Multiscale modelling of gas-liquid bioreactors : Biological Methanation Application

Vincent Ke Sen Ngu

THÈSE

En vue de l'obtention du

DOCTORAT DE L'UNIVERSITÉ DE TOULOUSE

Délivré par l'Institut National des Sciences Appliquées de Toulouse

Présentée et soutenue par

Vincent Ke Sen NGU

Le 17 novembre 2022

Modélisation multi-échelle de bioréacteurs gaz-liquide: Application à la méthanation biologique

Ecole doctorale : **MEGEP - Mécanique, Energétique, Génie civil, Procédés**

Spécialité : **Génie des Procédés et de l'Environnement**

Unité de recherche :
TBI - Toulouse Biotechnology Institute, Bio & Chemical Engineering

Thèse dirigée par
Arnaud COCKX et Jérôme MORCHAIN

Jury

Mr. Krist V. GERNAEY	**DTU Denmark**	Rapporteur
Mr. Roland RZEHAK	**HZDR Dresden**	Rapporteur
Mr. Benoît HAUT	**ULB Bruxelles**	Examinateur
Mr. Cees HARINGA	**TU Delft**	Examinateur
Mrs. Claire DUMAS	**TBI Toulouse**	Examinatrice
Mrs. Anne-Marie BILLET	**LGC Toulouse**	Présidente du jury
Mr. David F. FLETCHER	**USYD Sydney**	Invité
Mr. Arnaud COCKX	**TBI Toulouse**	Directeur de thèse
Mr. Jérôme Morchain	**TBI Toulouse**	Co-directeur de thèse

THESIS

Submitted for the title of

Doctor of Philosophy of Université de Toulouse

Issued by Institut National des Sciences Appliquées de Toulouse

---

Presented and defended by

Vincent Ke Sen NGU

On 17 November 2022

Multiscale modelling of gas-liquid bioreactors:

Applied to biological methanation

PhD School: **MEGEP - Mécanique, Energétique, Génie civil, Procédés**

Discipline: **Process and Environmental Engineering**

Research Laboratory:

TBI - Toulouse Biotechnology Institute, Bio & Chemical Engineering

PhD supervised by

Arnaud COCKX et Jérôme MORCHAIN

Jury

Mr. Krist V. GERNAEY	**DTU Denmark**	Reviewer
Mr. Roland RZEHAK	**HZDR Dresden**	Reviewer
Mr. Benoît HAUT	**ULB Bruxelles**	Examiner
Mr. Cees HARINGA	**TU Delft**	Examiner
Mrs. Claire DUMAS	**TBI Toulouse**	Examiner
Mrs. Anne-Marie BILLET	**LGC Toulouse**	President of jury
Mr. David F. FLETCHER	**USYD Sydney**	External guest
Mr. Arnaud COCKX	**TBI Toulouse**	Supervisor
Mr. Jérôme Morchain	**TBI Toulouse**	Co-supervisor

Abstract

Upscaling biochemical processes from the laboratory scale to industrial scale is very challenging as performance losses are typically observed along the scale-up process. In this context, numerical models are required to perform predictive modelling and bioreactor simulations which facilitate the scale-up procedure, leading to an optimum reactor design and improved performances. In this thesis, the bioreactor design of interest is the bubble column reactor.

Bubble column reactors are widely used in the chemical and bioprocess industries due to their good mixing, heat and mass transfer properties. However, the modelling of bubble columns is very challenging due to highly coupled multiphysics phenomena in terms of multiphase flow, mass transfer and (bio)reaction. The present work aims to unravel the coupling mechanisms by using a multiscale modelling approach and attempts to model bubble column bioreactors under a wide range of conditions and applications.

In this PhD thesis, a novel two-way coupled spatio-temporal 1D model is proposed to tackle the hydrodynamics and (bio)reactive mass transfer two-way coupling phenomenon. The model validation has been conducted using own-measured hydrodynamics data and biological methanation experimental data obtained by the Symbiose team at Toulouse Biotechnology Institute. Furthermore, literature data and numerical test cases have been used to validate the model, particularly the hydrodynamics and mass transfer aspects of the model. Following the model validation, the comprehensive, dynamic 1D model has been applied to perform multiphysics simulations of different (bio)processes, including CO_2 physical absorption, CO_2 chemisorption, oxygen transfer, biological methanation, and yeast fermentation, highlighting the robustness of the model. For instance, the 1D model predicts the substrate gradients in industrial-scale fermenters just as well as the CFD model. Similarly, in the chemical engineering context, the 1D model yields relatively well the CO_2 mass transfer in a reactive bubble column, compared with the CFD model.

The particularity of these processes is the fact that the major substrates are fed through the gas phase, leading to the possibility of a gas-liquid mass transfer limitation regime. For example, biological methanation is usually limited by the hydrogen mass transfer phenomenon. In this work, a practical biological methanation model is proposed to handle the bioreaction descriptions in both biological and physical transport limiting regimes. Moreover, Eulerian CFD model is also developed for biological methanation process and a detailed comparison with the experimental data and 1D model predictions is conducted. Asymptotic 0D models and analytical solutions have also been developed for some

applications to shed light on the underlying process and highlight the controlling parameters. This multiscale modelling strategy has drawn new fundamental insights into multiphase reactor modelling, primarily the use of appropriate models according to the subject of research, the implementation of suitable closures in the modelling of multiphysics coupling phenomena, and the identification of controlling parameters of such processes.

In short, through this PhD thesis, efficient numerical modelling tools (0D, 1D, and CFD models) have been developed for primarily bubble column applications to gain an understanding of the multiscale physical and biological phenomena in order to minimise the risk of upscaling the bioprocess.

Keywords: Gas-liquid mass transfer, Multiscale modelling, Bubble column, Biological methanation, CFD, Scale-up

Résumé

Le changement d'échelle des bioprocédés de l'échelle de laboratoire à l'échelle industrielle est très complexe car des pertes de performance sont généralement observées tout au long du processus de changement d'échelle. Dans ce contexte, les modèles numériques sont nécessaires pour effectuer des modélisations prédictives et des simulations de bioréacteurs qui facilitent la procédure de changement d'échelle, en menant à une conception optimale du réacteur et à de meilleures performances. Dans cette thèse, la conception du bioréacteur qui nous intéresse est le réacteur à colonne à bulles.

Les réacteurs à colonne à bulles sont largement utilisés dans les industries chimiques et de bioprocédés grâce à leurs bonnes propriétés de mélange, de transfert de chaleur et de masse. Cependant, la modélisation des colonnes à bulles est très difficile en raison des phénomènes multiphysiques fortement couplés en termes d'écoulement multiphasique, de transfert de masse et de (bio)réaction. Le présent travail vise à élucider les mécanismes de couplage en utilisant une approche de modélisation multi-échelle et tente de modéliser les bioréacteurs à colonne à bulles dans une large gamme de conditions et d'applications.

Dans cette thèse, un nouveau modèle 1D spatio-temporel couplage à double sens est proposé pour aborder le phénomène de couplage à double sens de l'hydrodynamique et du transfert de masse (bio)réactif. La validation du modèle a été réalisée sur la base de mesures hydrodynamiques et de données expérimentales de méthanation biologique obtenues par l'équipe Symbiose de Toulouse Biotechnology Institute. De plus, des données de la littérature et des cas tests numériques ont été utilisés pour valider le modèle, en particulier les aspects hydrodynamiques et de transfert de masse du modèle. Après la validation du modèle, le modèle 1D dynamique et complet a été appliqué pour réaliser des simulations multiphysiques de différents (bio)procédés, y compris l'absorption physique du CO_2, la chimisorption du CO_2, le transfert d'oxygène, la méthanation biologique et la fermentation de la levure, démontrant la robustesse du modèle. Par exemple, le modèle 1D prédit les gradients de substrat dans les fermenteurs à l'échelle industrielle tout aussi bien que le modèle CFD. De même, dans le contexte du génie chimique, le modèle 1D rend relativement bien le transfert de masse du CO_2 dans une colonne de bulles réactives, comparé au modèle CFD.

La particularité de ces procédés est le fait que les principaux substrats sont alimentés par la phase gazeuse, ce qui conduit à la possibilité d'un régime de limitation du transfert de masse gaz-liquide. Par exemple, la méthanisation biologique est généralement limitée par le phénomène de transfert de masse de l'hydrogène. Dans ce travail, un modèle pratique de méthanation biologique est proposé

pour traiter les descriptions de la bioréaction dans les régimes de limitation du transport biologique et physique. En outre, un modèle CFD eulérien est également développé pour le processus de méthanation biologique et une comparaison détaillée avec les données expérimentales et les prédictions du modèle 1D est effectuée. Des modèles 0D asymptotiques et des solutions analytiques ont également été développés pour certaines applications afin de démêler le processus fondamental et de mettre en évidence les paramètres de contrôle du procédé. Cette stratégie de modélisation multi-échelle a permis d'acquérir de nouvelles connaissances fondamentales sur la modélisation des réacteurs multiphasiques, principalement l'utilisation de modèles pertinents en fonction du sujet de recherche, la mise en œuvre de fermetures appropriées dans la modélisation des phénomènes de couplage multiphysique, et l'identification des paramètres de contrôle de ces procédés.

En bref, grâce à cette thèse de doctorat, des outils de modélisation numérique efficaces (modèles 0D, 1D et CFD) ont été développés pour des applications de colonnes à bulles, afin de mieux comprendre les phénomènes physiques et biologiques multi-échelles et de minimiser le risque de changement d'échelle de bioprocédés.

Mots-clés : Transfert de matière gaz-liquide, Modélisation multi-échelle, Colonne à bulles, Méthanation biologique, CFD, Changement échelle

To my parents, Woh Tai and Guek Hua,

To my sister, Vivian,

To my love, Ze Ying

Acknowledgement

Most of the PhD work has been conducted at Toulouse Biotechnology Institute, attached to INSA Toulouse. This work would not have been possible without the help and support of colleagues, families, and friends. First, I would like to thank my supervisors Arnaud Cockx and Jérôme Morchain for their guidance and assistance over the last three years, leading to this fruitful and successful collaboration. I greatly appreciated your feedback and advice that helped me improve the quality of the papers, conference presentations and my manuscript. Arnaud, I acknowledged your critical and analytical thinking which consistently pushed me to question the results, investigate the underlying problems, and provide more explicit physical discussions. Thank you for helping me through all the administrative papers works, such as application for the funding. Jérôme, I always appreciate your ability to put complex problems into simpler terms and see things from another perspective. Your unique way of explaining biological systems by taking analogies with daily life examples is much valued as it makes sophisticated biological engineering comprehensible to me. Both of you are my role model in research and I hope one day I will be able to reach such achievements in my career. I would also want to thank the jury members for accepting this role, especially the two reviewers: Professor Krist Gernaey and Dr. Roland Rzehak for taking the time to review this lengthy manuscript. I appreciated the rich discussions we had during the viva, which suggested many interesting perspectives.

Special thanks to John and David who accepted my research stay to the University of Sydney. It was a great pleasure to collaborate with you. David, thank you for sharing your knowledge of Computational Fluid Dynamics and your life experiences working with the industry and academics. John, thank you for welcoming me and always finding time for discussions. I enjoyed having coffee catch-ups with you both and it truly was a fulfilling scientific and cultural experience for me in Australia.

Furthermore, I also want to thank my professors at INSA Toulouse who taught me ever since I was still an undergraduate. I acknowledged all academic staff for their patient mentoring and dynamic yet informative teaching which eventually developed my research interest in chemical and biochemical engineering, in particular, the design and modelling of multiphase reactors. Specifically, I thank Alain Liné, Gilles Hebrard, Etienne Paul and Matthieu Spérandio whose teaching in the field of fluid mechanics, mass transfer and bioreaction had attracted me to the field of bioreactor modelling.

I would also like to thank Lionel Gamet and Matthieu Roland from IFPEN who were my Master's internship supervisors. Thanks to you, I have learnt to have a rigorous approach to research (numerical investigations, questioning hypotheses, presentations of results, report writing) and interpersonal

skills since my early career. Some of your career advice also helped me get through my PhD journey, such as some wise word from Matthieu: “la recherche n’est pas linéaire”, which regularly remind me to keep grinding and never give up.

A big thank you to all technical staff and my colleagues in TBI, especially from the TIM, SOPHYE and SYMBIOSE teams. The experimental part could not have been done without the technical support from Claude and Yan. Among my colleagues in TBI, first, I want to thank Irem and Maike for being such caring friends: Irem for constantly reminding me to take a break and have some coffee, and Maike for regularly checking on and taking care of us. Thank you, Ugo, for running the Kfete operation with me and of course for being such a supportive basketball teammate and a wonderful friend and neighbour. I also treasured Eliot for organising hiking trip in the Pyrenees which was always a good moment to “relax” in the mountains and lakes. It was a shame I wasn’t able to travel to Ottawa for the conference with you that could be so much fun! I also value the conversations with Pla and Gleeza who also come from South-East Asia as we have so many common points. A warm thank you to Ernest, Matthis, Meghan, Ali, Rita, Maxence, Solomon, Ming, Han bin, and Paul for your supportive words and warm discussions during coffee time. I would also want to thank all my seniors (Mei Mei, Alberto, Ibrahima, Alexandre, Gaëlle, Ryma, Vincent, Dylan, Carlos) for sharing tips and advice on things related to research, administrative related tasks, and career choices.

I am blessed to be surrounded by Spanish-speaking Latin Americans over the past three years who have taught me *un poquito* of Spanish words. You are definitely some of the warmest people and best dancers I have ever met. I want to thank Carlos, César, Juan Camilo, Gina, Suzy, Nia, Marco, Christel, Joel, Alberto, Santiago, Gary, Anaid for being such wonderful friends and most importantly my Spanish and Salsa teacher. Moreover, weekends can’t be fun without basketball and it was a pleasure to hoop with Ugo, Shen Zhou, Tee Wei, and other members of “WeChat ISAE basketball group”. I cherish the fun we had and I improved my game playing alongside with you all.

Furthermore, I would also want to thank all my friends in France and Malaysia. I want to thank the Kinabalu group (Clement, Edmund, Teck Wan, Zi Kang, Zi Wei, Theresa, Luna) for all the memorable ski and hiking trips to the French Alpes, Ardèche, Grenoble and Rhône-Alpes region. Moreover, I also thank my Paris gang (Ming Han, Arianne, Peggy, Cheng, Cheng Dong, Xia, Clement, Clara, Cassandra, Heeran, Bei Ning, Juan), as it is always nice to meet you guys in Paris for catch-up and delicious food. I appreciated the constant supportive and warm wishes from Dharshana and Agnes who were also pursuing their PhD. I am grateful for the support of my friends in Malaysia, Aaron, Kee win, Crystal and my high school boys, Stanly, Eric, “Wary Gong”, Christopher, Gordon, and Mervyn.

I acknowledged the financial support provided by 3BCAR and EUR BioEco that made the mission to Australia possible. I also acknowledged the HPC resources of CALMIP for providing the computational resources necessary for the CFD simulations (P22025).

Finally, I would like to thank my family for encouraging me to pursue my PhD dream, especially my parents. Thank you, Dad, for your financial support of for early education. It is a classic joke that we say Asian parents would like their children to be a doctor (the kind that treat sick patients) growing up. Likewise, mum, you always wanted me to be a doctor but I've resisted this idea ever since I was young. Today, I am happy to have earnt my Doctor title (in Sciences), which I am proud of. Last but not least, I want to thank my love, Ze Ying for her encouragement and care over the past 8 years. I am glad you are always there to listen to my problems and all those puzzling bubble column and bioreactor stories. The last three years have been very challenging with the long-distance intercity travel and I deeply valued your patience. Now, I am very glad to be living with you again.

List of Publications

1. "H_2 mass transfer – a key factor for efficient biological methanation: Comparison between pilot-scale experimental data, 1D and CFD models."
   Ngu V., Fletcher D.F., Kavanagh J.M., Rafrafi Y., Dumas C., Morchain J., Cockx A.

   Submitted to Chemical Engineering Science on 17/06/2022. Under review.

2. "In-depth analysis of reactive bubbly flow using two-way coupled spatio-temporal 1D model." Chemical Engineering Science 261, 117963
   Ngu V., Morchain J., Cockx A.

   Link: https://doi.org/10.1016/j.ces.2022.117963

3. "Spatio-temporal 1D gas–liquid model for biological methanation in lab scale and industrial bubble column." Chemical Engineering Science 251, 117478

   Ngu V., Morchain J., Cockx A.

   Link: https://doi.org/10.1016/j.ces.2022.117478

4. "Towards anaerobic digestion (ADM No.1) model's extensions and reductions with in-situ gas injection for biomethane production." IFAC-PapersOnLine Volume 55, 20, 635-640.
   C. Acosta-Pavas J., Morchain J., Dumas C., **Ngu V.**, Cockx A., A. Aceves-Lara C.

   Link: https://doi.org/10.1016/j.ifacol.2022.09.167

List of Communications

1. Accepted oral presentation at the 18th Conference on French Society of Chemical Engineering (SFGP), Toulouse, France, November 2022.

   "Study of the effect of hydrogen transfer on biological methanation with a multi-scale modelling approach."
   Ngu V., Fletcher D.F., Kavanagh J.M., Rafrafi Y., Dumas C., Morchain J., Cockx A.

2. Oral presentation at the 15th International Conference on Gas–Liquid and Gas–Liquid–Solid Reactor Engineering (GLS-15), Ottawa, Canada, August 2022.

   "H_2 mass transfer – a key factor for efficient biological methanation: Comparison between pilot-scale experimental data, 1D and CFD models."
   Ngu V., Fletcher D.F., Kavanagh J.M., Rafrafi Y., Dumas C., Morchain J., Cockx A.

3. Oral presentation at the Dispersed Two-Phase Flow (DTPF) Conference, Lyon, France, October 2021.

   "Reactive bubbly flow using two-way coupled 1D model."
   Ngu V., Morchain J., Cockx A.

4. Oral presentation at the 13th European Congress of Chemical Engineering (ECCE) and 6th European Congress of Applied Biotechnology (ECAB), Berlin, Germany, September 2021

   "H_2 mass transfer – a key factor for efficient biological methanation: Establishment of 1D gas-liquid model for biological bubble column."
   Ngu V., Morchain J., Cockx A.

Nomenclature

Roman symbols

Symbol	Description	Unit
a	Volumetric interfacial area	$m^2.m^{-3}$
C^*	Solubility	$mg.L^{-1}$
C_0	Distribution coefficient of the drift-flux model	$-$
C_D	Drag coefficient	$-$
C_G	Gas concentration	$mg.L^{-1}$
C_L	Liquid concentration	$mg.L^{-1}$
D_i	Species diffusivity	$m^2.s^{-1}$
d_{32}	Sauter mean diameter	m
d_b	Bubble diameter	m
D_G	Gaseous axial dispersion coefficient	$m^2.s^{-1}$
D_L	Liquid axial dispersion coefficient	$m^2.s^{-1}$
D_r	Reactor Diameter	m
E	Enhancement factor	$-$
F_i	Species gas molar flowrate	$mol.s^{-1}$
g	Gravity acceleration	$m.s^{-2}$
H	Reactor Height	m
He	Henry's constant	$mg.L^{-1}.Pa^{-1}$
j_G	Superficial gas velocity	$m.s^{-1}$
j_L	Superficial liquid velocity	$m.s^{-1}$
K	Biological affinity constant	$mg.L^{-1}$
k_L	Liquid side mass transfer coefficient	$m.s^{-1}$
k_La	Volumetric mass transfer coefficient	s^{-1}
m	Maintenance rate	$g_{H_2}.g_X.h^{-1}$
M	Molar mass	$g.mol^{-1}$
MPR	Methane production rate per unit volume of reactor	$mL\ CH_4.L^{-1}.h^{-1}$
P	Pressure	Pa
P_{atm}	Atmospheric pressure	Pa
P_0	Pressure at the top of the column	Pa
q	Specific bioreaction rate	$g_{H_2}.g_X.h^{-1}$
Q	Gas volumetric flowrate	$m^3.s^{-1}$

R	Ideal gas constant	$J.mol^{-1}.K^{-1}$
R_i	Species reaction term per unit volume of liquid	$mg_i.L^{-1}.s^{-1}$
S	Cross-section area	m^2
r	Reaction rate vector	$g_{H_2}.L^{-1}.h^{-1}$
T	Temperature	K
t	Time	s
T_i	Species mass transfer rate	$mol.s^{-1}$
t_∞	Steady state	$-$
u'	Instantaneous velocity	$m.s^{-1}$
u_∞	Bubble terminal velocity	$m.s^{-1}$
u_{rel}	Relative velocity	$m.s^{-1}$
$\vec{u}$	Velocity vector	$m.s^{-1}$
u	Local velocity	$m.s^{-1}$
V	Volume	m^3
y	Gas molar fraction	$-$
$Y_{A/B}$	Conversion yield of A on B	$g_A.g_B^{-1}$
z	Axial coordinate	m

Greek symbols

Symbol	Description	Unit
α	3D Local phase holdup	$-$
ε	1D Local phase holdup	$-$
η	H_2 conversion	$-$
μ	Dynamic fluid viscosity	$Pa.s$
μ	Biological growth rate	$g_X.g_X^{-1}.h^{-1}$
ν	Kinematic fluid viscosity	$m^2.s^{-1}$
ρ	Fluid density	$kg.m^{-3}$
σ	Surface tension	$N.m^{-1}$
φ	Specific uptake rate	$g.g_X^{-1}.h^{-1}$
ϕ	Local volumetric molar fluxes	$mg.L^{-1}.s^{-1}$

Subscripts and superscripts

Symbol	Description
0	Inlet
G	Gaseous phase
i	Species
in	Inlet
k	Phase
L	Liquid phase
n	Nodes
out	Outlet

Chemical species

Symbol	Description
CH_4	Methane
CO_2	Carbon dioxide
H_2	Hydrogen
H_2O	Water
N_2	Nitrogen
NaOH	Sodium hydroxide
O_2	Oxygen
X	Biomass

Dimensionless numbers

Symbol	Description
Eo	Eötvös number
Fr	Froude number
Ha	Hatta number
Mo	Morton number
Pe	Péclet number
Re	Reynolds number
Sc	Schmidt number
Sh	Sherwood number
We	Weber number

General Introduction

Biotechnologies have expanded in recent years as there is increasing manufacturing of different commodities and added-value products from bio-based feedstocks, replacing fossil fuel as raw materials. This is fuelled by the transition towards sustainable development and decarbonisation of the industries. In this PhD thesis, the bioprocess of interest is biological methanation which is the production of methane through two major gas-fed substrates: hydrogen and carbon dioxide via hydrogenotrophic methanogens. Biological methanation is an interesting technological breakthrough in the field of renewable energy and waste treatment. We have seen lately more catastrophic events linked to climate change taking place around the globe, ranging from record-breaking European heat waves in the northern hemisphere to extreme east coast flooding in Australia in the southern hemisphere. Therefore, swift actions have to be made to cut down CO_2 emissions and reduce the risks of climate change.

To act against global warming and its associated threats, countries around the world are likely to step up the proportion of renewable energy in their energy mix. In this regard, biological methanation plays an important role alongside the installation of renewable energy such as wind and solar energy. Due to the intermittent behaviour of renewable energy, disequilibrium between energy supply and demand is expected. In this context, biological methanation acts as an excellent energy buffer for the surplus electricity. First, surplus electricity is used to produce hydrogen via the electrolysis of water. Energy storage in terms of methane has a better edge than hydrogen storage as natural gas storage and transport infrastructures are already in place, reducing the capital expenditure for installing new equipment. Thus, the hydrogen produced is further converted into methane through biological methanation. Moreover, biogas production from anaerobic digestion has soared over the past decades. A biogas upgrade facility is required to increase the methane content. A biological methanation plant is an interesting option for biogas upgrading coupled with a renewable energy source. On a large-scale, synergy effects between a wastewater treatment plant, an anaerobic digestor, renewable energy wind farms, and a biological methanation plant have been demonstrated in the industrial park at Avedøre, Denmark.

For the last decade, research on biological methanation focuses mostly on proof-of-concept experimental studies, particularly, the optimisation of bioreactor design and the characterisation of microbiological activities. As a result, few numerical models for biological methanation reactor exists in the literature which hampers the scale-up of this technology. Upscaling biochemical processes from the laboratory scale to the industrial scale is very challenging as performance losses are typically

observed along the scale-up process. Numerical simulations provide an alternative to costly and time-consuming experiments for bioreactor studies by studying unplanned operating conditions and elucidating the interactions between physical and biological processes. Moreover, sensitivity analysis can be conducted by numerical models to search for bioreactor improvement strategies. In short, numerical models are able to perform predictive modelling and bioreactor simulations which facilitate the scale-up procedure, leading to an optimum reactor design and improved performances. In this thesis, the bioreactor design of interest is the bubble column reactor in which bio-methanation takes place. Biological methanation experiments had been performed in a pilot-scale bubble column by the SYMBIOSE team at Toulouse Biotechnology Institute and future demonstration and industrial plants are under construction and planning stage, respectively.

Bubble column reactors are widely used in the chemical and bioprocess industries due to their good mixing, heat and mass transfer properties. However, the modelling of bubble columns is very challenging due to highly coupled multiphysics phenomena in terms of multiphase flow, mass transfer and (bio)reaction. The present work aims to unravel the coupling of these physical and biological phenomena by using a multiscale modelling approach and attempts to model bubble column bioreactors under a wide range of conditions, scales, and applications.

Figure 1 summarises the multiscale modelling strategy implemented in this thesis. In a first step, a comprehensive gas-liquid spatio-temporal 1D model coupling hydrodynamics, mass transfer and bioreaction are developed. The driving reason to begin with a macroscopic 1D reactor model is to keep a low numerical cost yet be able to yield satisfactory results that encompass all aspects of bioreactors modelling. Based on the 1D model results, further investigations can be performed by mesoscopic CFD models, if necessary, for example, to characterise more precisely the local spatiotemporal heterogeneities. Alternatively, the 1D model results can be used to develop asymptotic relationships and motivates the research of analytical solutions. Asymptotic 0D models and analytical solutions help to shed light on the underlying process and highlight the controlling parameters in asymptotic situations.

The model validation is necessary to evaluate the accuracy and performance and ensure the robustness of the model. The 1D spatio-temporal model validation had been conducted using own-measured hydrodynamics data and biological methanation experimental data obtained by the SYMBIOSE team. Therefore, in the second step, bubble size distribution and transient gas holdup experiments were conducted in the same pilot column to obtain information on hydrodynamics. Furthermore, literature data and numerical test cases have been used to challenge the model,

particularly the coupling between hydrodynamics and mass transfer. In a third step, following the model validation, the 1D model was used to perform multiphysics simulations of different (bio)processes, including CO_2 physical absorption, CO_2 chemisorption, oxygen transfer, biological methanation, and yeast fermentation, highlighting the robustness of the model.

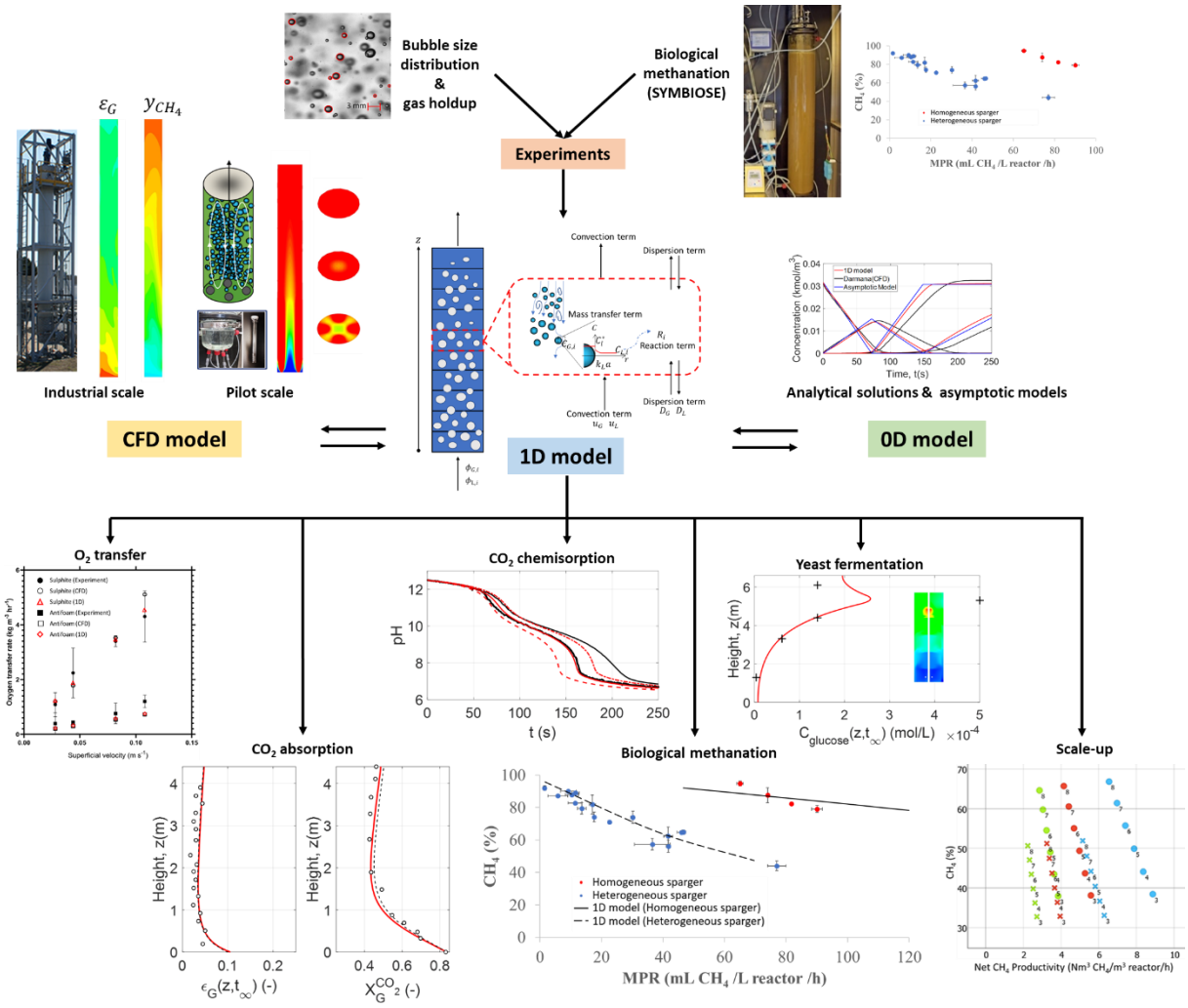

Figure 1: Schematic representation of the multiscale modelling strategy for the development of efficient bubble column models coupling fluid dynamics and (bio)reaction dynamics.

The particularity of these processes is that the main substrates are fed through the gas phase, leading to the possibility of a gas-liquid mass transfer limitation regime. For example, biological methanation is usually limited by the hydrogen mass transfer phenomenon due to its low solubility. This particular reason motivated us to develop a fully-coupled bubble column model to address the coupling between fluid dynamics and (bio)reaction dynamics. In this work, a practical biological methanation model was also proposed to handle the bioreaction descriptions in both biological and physical transport limiting regimes.

This dissertation is composed of **7 chapters** and it is structured as follows. **Chapter 1** is a general bibliography overview of this PhD work. The first part will review the field of biological methanation. The second part consists of a literature review about multiphyscis coupling in bioreactors modelling. The third part briefly discusses the fundamentals of bubble column hydrodynamics. The last part presents the recent development of bubble column modelling using CFD and 1D models. In **Chapter 2**, experimental techniques and the numerical model structure are presented. The image processing techniques for the optical methods are detailed. The numerical methods, closure models, and initial and boundary conditions are discussed. **Chapter 3** is dedicated to validating the 1D model, particularly the hydrodynamics and mass transfer aspects. Then in **Chapter 4**, the 1D model is extended to two industrial applications: scale-up of biological methanation reactor and investigation of substrate gradients in large-scale fermenters. In the former, we have been mandated by industry partner ENOSIS Energies to provide design guidelines for two bioreactors at the demonstration and industrial scales. In the latter, the 1D model is used to analyse the formation of substrate gradients during yeast fermentation inside a 22 m^3 fermenter. Similarly, in **Chapter 5**, an in-depth analysis of reactive bubbly flow is performed using the 1D model. Along the way, asymptotic models are developed to describe the transient reactive mass transfer and bubble shrinkage. In **Chapter 6**, the Eulerian CFD model for biological methanation is developed resolving the fluid flow, multispecies mass transfer, and bioreaction simultaneously. CFD simulations are also performed for the industrial-scale biological methanation reactor of Electrochaea. Lastly, in **Chapter 7**, concluding remarks and important insights obtained through this multiscale modelling approach are reported. Future perspectives on possible outlook for this work are also listed.

Table of contents

Chapter 1 Bibliography

1.1 Biological methanation

The energy demand for economic development has soared over the last few decades. To satisfy this energy demand, many countries still rely heavily on the fossil fuels such as oil, coal, and natural gas ("IEA Data overview," 2019). The increasing use of fossil fuels has caused climate change and global warming. Climate change has brought catastrophic mortality events, such as wildfires, drought, rising sea levels, and severe flooding (Dupuy et al., 2020; Westerling and Bryant, 2008; Xu et al., 2009). This has driven policymakers to develop alternative renewable energy for limiting the impact of global warming due to the overuse of fossil fuels (Grimalt-Alemany et al., 2018). The 2015 Paris agreement (COP21) sets the framework for participating countries to limit the rise of global temperature below 2°C by lowering greenhouse gas emissions (European Commission, 2016a). An imminent restructuring of the global energy system is necessary to achieve net-zero CO_2 emissions by 2050.

To ensure energy transition away from fossil fuels, a massive deployment of renewable energy such as wind and solar energy is strongly required (Thema et al., 2019; Zwart and Nap, 2017). However, solar and wind energy are both intermittent energy sources with unpredictable power production. In order to maintain an equilibrium between the fluctuating power production and the power demand, the presence of an energy buffer is much needed. For example, more than 26% of the electricity produced from wind parks in Denmark is a temporary surplus (Carton and Olabi, 2010; Sharman, 2005). This surplus electricity needs to be stored with an energy buffer, such as methane to prevent energy loss (Götz et al., 2016). In fact, different propositions for energy storage have been proposed in the literature, as shown in Figure 1.1. The most promising technology is chemical storage, either in the form of hydrogen (H_2) or methane (CH_4) as they can be stored for long periods with relatively long discharge time and large storage capacity (Schaaf et al., 2014).

The utilisation of H_2 as a renewable energy carrier poses unsettled major challenges, mainly due to its low density that requires high storage volume infrastructure. It is also extremely explosive and diffuses easily, causing leakage and other concomitant issues with safety (Zwart and Nap, 2017). While the direct exploitation of H_2 as a transport fuel is still under development, H_2 storage also encounters other aforementioned problems. Alternatively, CH_4 can be used as an energy carrier. It can be generated from H_2 and CO_2 by either chemical or biological pathways.

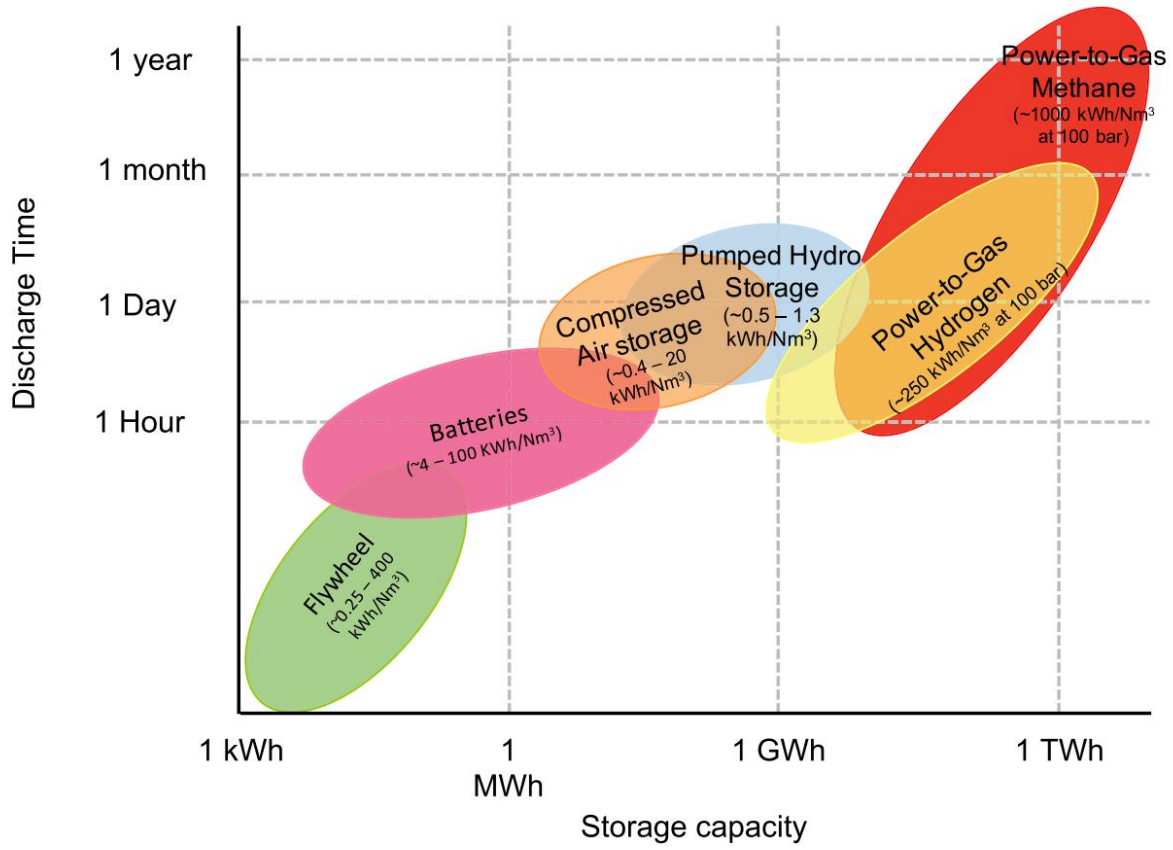

Figure 1.1: Power-to-methane provide sufficient storage capacity and long discharge times to be in line to meet future energy demands at the global energy network scale. Adapted from: Schaaf et al. (2014)

The biological methanation process is depicted in Figure 1.2. H_2 can be produced via the electrolysis of water using the electricity generated by the surplus of renewable energy. The carbon supply can be obtained from CO_2 emission streams of power plants or biogas/wastewater treatment plants (Strübing et al., 2017). The methane produced can be injected directly into the gas network if it reaches the gas grid's requirements. The regulative standards and regulations on natural gas quality vary according to country, but the majority of the countries in Europe require > 95% of CH_4 purity to be injected into the natural gas grid (Thema et al., 2019). Therefore, Power-to-Methane technology provides interconnectivity between the gas and the electricity network, resulting in a more flexible energy storage and delivery system.

Recently, a collaborative study in France between GRDF and GRTgaz coordinated by the French Agency for Environment and Energy Management (ADEME) outlines the possibility of a "100% renewable gas mix by 2050" (ADEME, 2018). The theoretical primary feedstock (anaerobic digestion of agriculture waste, biowastes, pyro-gasification of woods, etc) could produce up to 460 TWh superior calorific

value[1] of renewable gas. To achieve this ambitious goal of 100% renewable electricity production by 2050 in France, it is important to optimise the current biogas production process or syngas to methane enrichment process via biological methanation to obtain high purity of methane for storage in the gas reserves. The biological methanation plays an important role in substituting natural gas originating from fossil fuels. It is projected that almost 1/3 of the renewable gas will be produced via biological methanation by 2050 in France (ADEME, 2018).

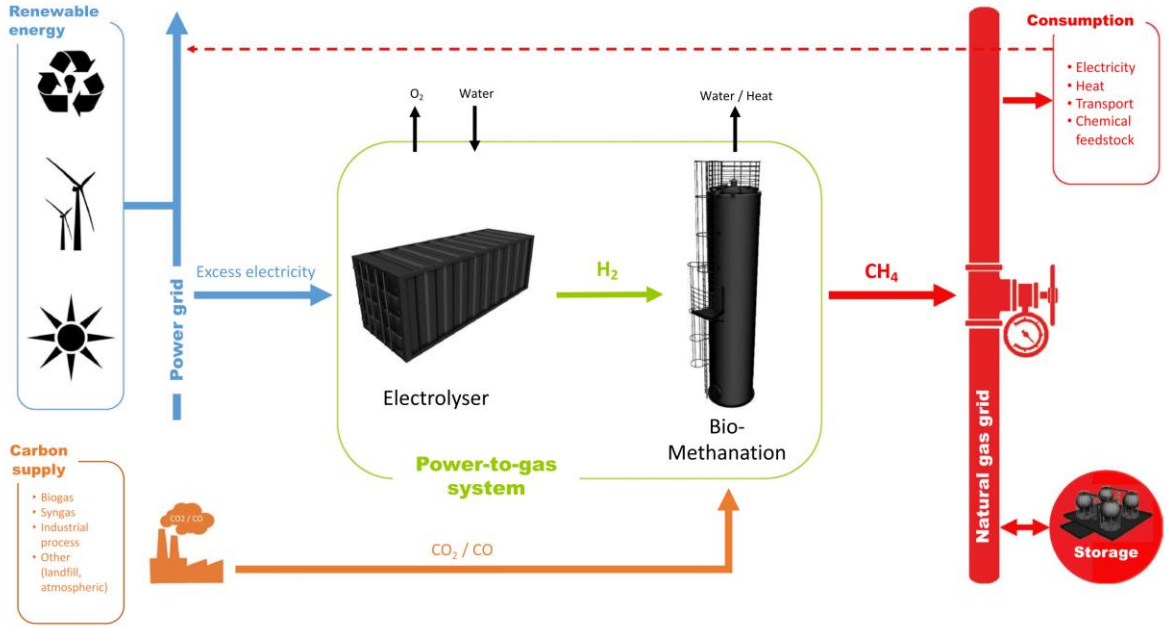

Figure 1.2: Synergy effect of biological methanation. Adapted from: Rafrafi et al. (2020)

Besides interconnecting with the renewable energy electricity grid, biological methanation can be integrated with wastewater treatment plants (WWTP) and anaerobic digestors, such as the biological methanation plant on the BIOFOS site in Avedøre, Denmark (Lardon et al., 2018). Additionally, the by-product of the electrolysis of water, oxygen (O_2) can be fed to nearby WWTP. The biogas from anaerobic digestion containing mainly CH_4 and carbon dioxide (CO_2) can be upgraded by biological methanation. The heat produced from biological methanation can be used to heat the anaerobic digestor. Indeed, biological methanation is an exothermic process which operates typically with T>50°C while the anaerobic digestion of sewage sludge is an endothermic process, that operates usually at the

[1] An units of energy which signifies the amount of heat which would be released by the complete combustion in 1 Nm^3 of air, in such a way that the pressure at which the reaction takes place remains constant, and all the products of combustion are returned to the same specified temperature θ as that of the reactants, all of these products being in the gaseous state except for water formed by combustion, which is condensed to the liquid state at θ.

mesophilic condition that requires heating at a temperature around 35-37°C. Thermal integration can be done between these two processes (Angenent et al., 2018). Such synergistic effects between industries have shown that a positive energy balance is achievable at a large-scale (Lardon et al., 2018).

$$4\,H_2 + CO_2 \rightarrow CH_4 + 2\,H_2O \qquad \Delta_R H^0 = -165\text{kJ/mol} \tag{1.1}$$

The overall methanation reaction is presented in equation (1.1). The reaction is exothermic; thus, heat removal is required. Methanation can be accomplished based on two different pathways: catalytic-chemical methanation or biological methanation (Lecker et al., 2017). Catalytic-chemical methanation operates at a rather high temperature and high pressure which ranges between 300-500°C and 100 bar respectively. Biological methanation operates under milder operating conditions, with pressure at about P_{atm} to 10 bar. Temperature-wise it can operate in either mesophilic (37°C) or thermophilic conditions (55°C-70°C) (Zwart and Nap, 2017). The catalysts for catalytic methanation are metal-based catalysts which are very sensitive to the impurities such as sulfur compounds, ammonia, and particles. It requires periodic regeneration or the installation of gas cleaning infrastructure to remove impurities from the raw syngas before entering the reactor. In contrast to catalytic-chemical methanation, the biological methanation is catalysed by autotrophic hydrogenotrophic methanogens which have a higher tolerance to impurities (Grimalt-Alemany et al., 2018). However, catalytic-chemical methanation has already been exploited at a commercial scale, whereas biological methanation has only reached a pilot/demonstration plant size (Rafrafi et al., 2020). Biological methanation is less exploited than catalytic methanation due to its low reaction rate and low hydrogen solubility (Lecker et al., 2017). Nevertheless, studies have shown that the synergy effect of combining biological methanation and anaerobic digestion demonstrates a tremendous increase in methane productivity and purity, which could eventually match the requirement of the natural gas grid (Grimalt-Alemany et al., 2018; Lardon et al., 2018; Lecker et al., 2017). Indeed, biological methanation requires lower energy demand as it operates at milder condition (T < 70°C and P < 10 bar) and tends to be more robust as a biological catalyst has higher tolerance of impurities, e.g. hydrogen sulfide H_2S. (Götz et al., 2015).

Biological methanation can be performed either in the in-situ or ex-situ systems (Angelidaki et al., 2018; Jensen et al., 2018; Rafrafi et al., 2020). The difference between in-situ and ex-situ systems is shown in Figure 1.3. For the in-situ system, hydrogen gas is injected directly into the anaerobic digester, as shown in Figure 1.3(a). In an ex-situ system, hydrogen gas from electrolysers and CO_2 from external sources, such as syngas gasification, biogas, and flue gas are injected into another bioreactor and converted by hydrogenotrophic methanogens into methane, as shown in Figure 1.3(b).

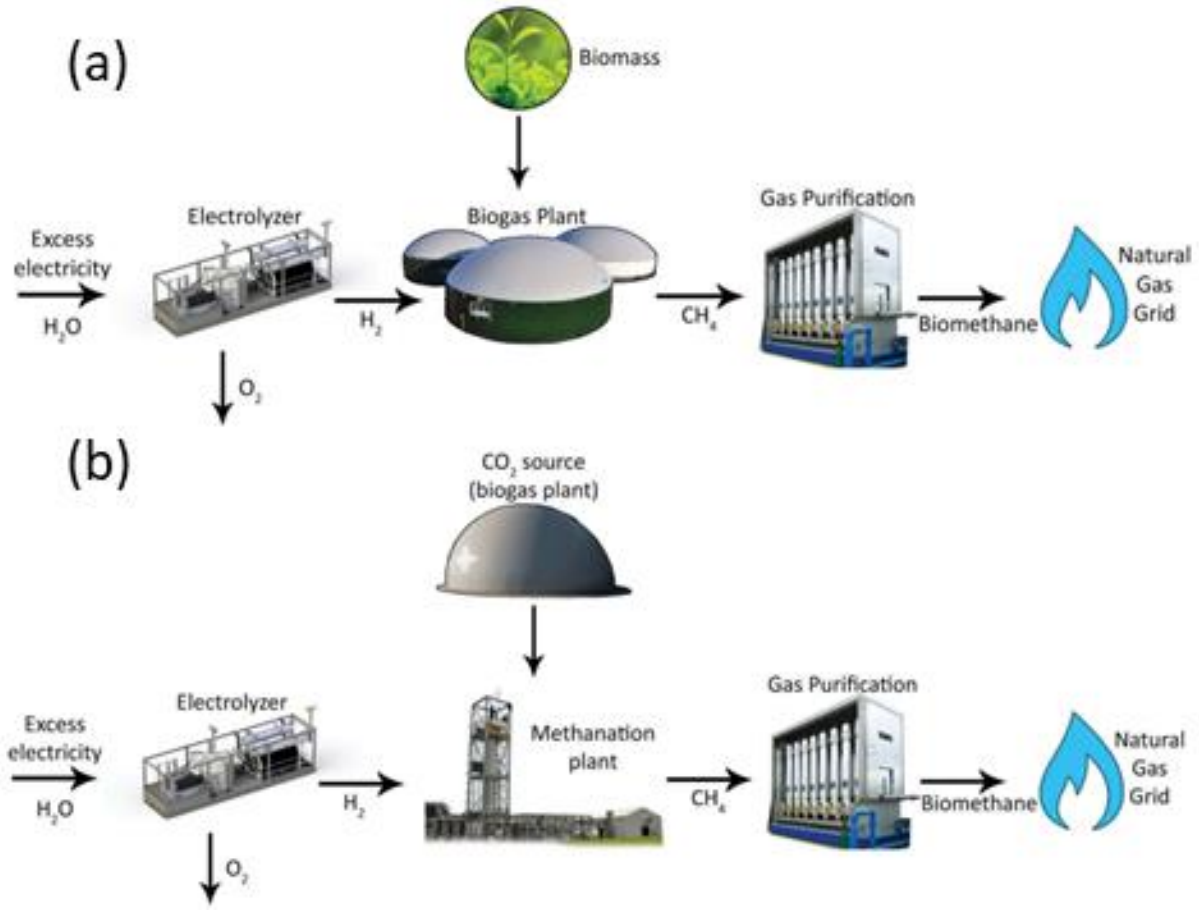

Figure 1.3: (a) In-situ and (b) ex-situ biological methanation. Adapted from: Rusmanis et al. (2019)

As the in-situ system happens in an anaerobic digestor, a brief summary of anaerobic digestion is presented hereafter. Anaerobic digestion is a process that occurs widely in nature and it converts organic matter into majorly methane and carbon dioxide, in the absence of oxygen (Toerien and Hattingh, 1969). The process is widely used to treat organic effluents, municipal solid waste, and the stabilisation of sewage sludge (De Bere, 2000; Rajeshwari et al., 2000). In essence, anaerobic digestion is a successive bioprocess of breaking down complex organic wastes into precursors for biogas production. The biological methanation is situated at the last step of the anaerobic digestion process.

Figure 1.4 depicts the typical pathway of the anaerobic digestion of organic wastes. Generally, the anaerobic digestion process starts with the pre-treatments and hydrolysis of complex organic matter into simpler molecules, classified as carbohydrates, proteins and lipids. The pre-treatments are conducted to facilitate the hydrolysis process which is agreed as the rate-limiting step (Mata-Alvarez et al., 2000). The hydrolysis process breaks down insoluble organic matter into simple sugar - monosaccharides, amino acids and volatile fatty acids or long chain fatty acids. Hydrolysis is followed by acidogenesis to degrade monosaccharides and amino acids to organic acids. Small amounts of

ethanol and lactate may be present. The organic acids (e.g. propionate, butyrate, long chain fatty acids) are further broken down into acetate by acetogenesis process. Acetogenesis is the process of breaking down higher volatile fatty acids and other intermediates into acetate, hydrogen and carbon dioxide. The last step is the methanogenesis process whereby methane is produced by the methanogenic microorganisms. The biomethane is typically produced through acetoclastic methanogenesis and hydrogenotrophic methanogenesis.

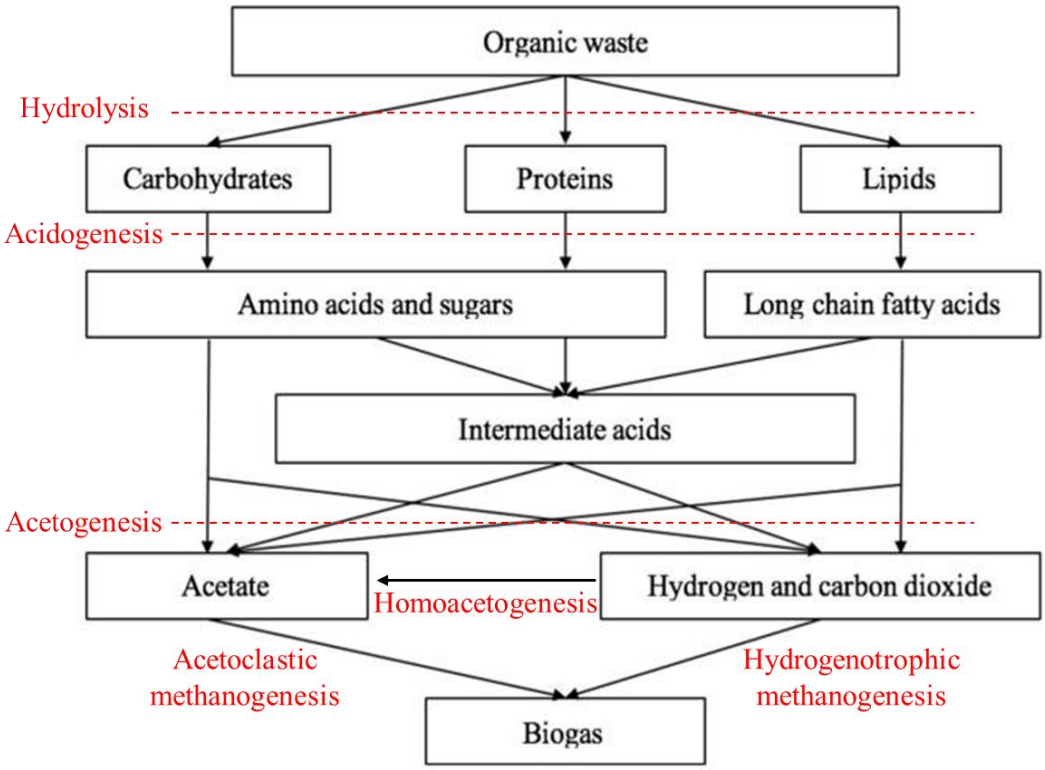

Figure 1.4: Anaerobic digestion pathways to produce biogas. Adapted from: Meegoda et al. (2018)

For ex-situ biological methanation, regardless of the use of pure culture or mixed culture system, hydrogenotrophic methanogenesis is the key process during the biological methanation process. The CO_2 produced in the biogas reacts with exogeneous H_2 supply to yield CH_4.

Although the in-situ system does not require any extra infrastructure for post-gas treatment, a recent study showed that the hydrogen uptake rate is very low, even with a high volume of H_2 injected. Thus, the H_2 conversion is much lower in an in-situ system, leading to lower biological methanation efficiency (low CH_4 purity and productivity) than ex-situ system (Götz et al., 2016). The rise of pH due to CO_2 depletion can be observed as it is consumed progressively. This could lead to C-source limitation for autotrophic hydrogenotrophic methanogens, thus restraining the CH_4 production (Aryal et al., 2018). The addition of exogenous hydrogen also affects acetogenesis, as it inhibits the oxidation of long chain

volatile fatty acids into acetate (Voelklein et al., 2019). However, some authors suggested that a balanced in-situ system with an adequate level of hydrogen can promote successful biogas upgrading. The exogenous hydrogen can stimulate Wood-Ljungdahl pathway (homoacetogenesis) where 40% of hydrogen can be consumed to produce acetate and subsequently methane, as shown in Figure 1.4 (Voelklein et al., 2019). Therefore, it balances up the acetate loss from acetogenesis inhibition.

The initial stages of anaerobic digestion (hydrolysis and acidogenesis) are not present in an ex-situ system. Thus, reactor stability and performance only depend on the sufficient provision of CO_2, H_2, hydrogenotrophic methanogens and nutrients (Angenent et al., 2018). In the literature, it is generally found that the ex-situ system leads to better biological methanation in terms of purity and productivity, as shown in Figure 1.5. The purity signifies the methane content in terms of molar fraction in the outlet gas. The productivity is generally defined as the amount of methane produced (in mass/mole or in volume) per reactor volume per unit time. Despite the increasing number of scientific articles about biological methanation, they lack a coherent and standardised nomenclature which hinders the comparison between studies (Thema et al., 2019).

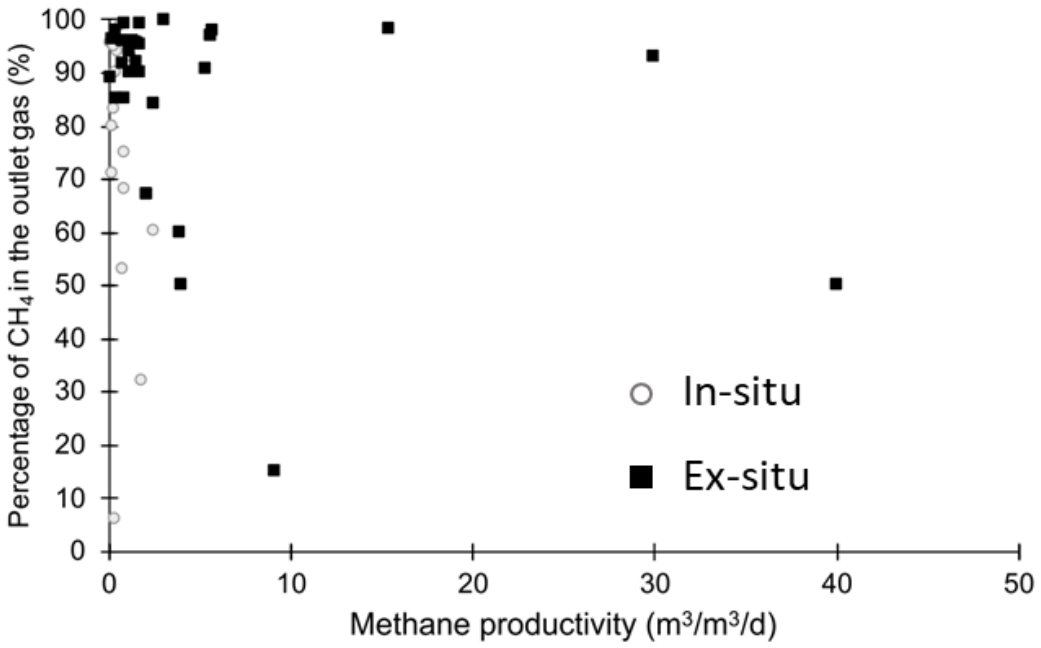

Figure 1.5: (a) CH_4 purity and productivity for in-situ (circles) and ex-situ (squares) system. Adapted from: Rafrafi et al. (2020).

Despite the numerous benefits of biological methanation, there are still several unsolved bottlenecks before commercially implementing this technology. The major challenge of the biological methanation, which is comparable to the challenge of aerobic bioprocesses is the gas-liquid mass

transfer limitation. (Lecker et al., 2017; Rafrafi et al., 2020; Rusmanis et al., 2019). This is due to the poor solubility of H_2 (of the order 1 mg/L at atmospheric pressure compared with that of O_2 at 40 mg/L). Only a few large-scale biological methanation plants with a range of volume between 3.5-100 m^3 are referenced in the literature, signifying that the technology is only at the early stage of its commercial application (Rafrafi et al., 2020). Extensive investigations on reactor design, system configurations and operating conditions are still mainly at the laboratory or pilot scale. Several reactor designs, such as stirred tank reactors (Figueras et al., 2021; Martin et al., 2013; Peillex et al., 1990), bubble column reactors (Bassani et al., 2017; Kougias et al., 2017; Laguillaumie et al., 2022; Voelklein et al., 2019), membrane reactors (Díaz et al., 2015; Luo and Angelidaki, 2013), fixed-bed reactors (Lee et al., 2012) and trickled bed reactors (Markthaler et al., 2020; Sieborg et al., 2020; Strübing et al., 2018; Ullrich et al., 2018), have been studied to demonstrate the feasibility of biological methanation. Different strategies for the operating configurations and conditions have been investigated to improve H_2 mass transfer efficiency (Bassani et al., 2017; Kougias et al., 2017; Ullrich and Lemmer, 2019).

Each reactor technology applied for biological methanation has its advantages and drawbacks. But optimisations of the reactor design and operating conditions have to be conducted to ensure a good gas-liquid mass transfer in the system (Grimalt-Alemany et al., 2018). Several initiatives have been discussed in the literature to improve the mass transfer rate in different reactor configurations. The next section presents a mini technical review of bioreactor design for biological methanation studied in the literature.

1.1.1 Bioreactor design for biological methanation

1.1.1.1 Stirred-tank reactor (STR)

The most common reactor system studied for the biological methanation process is a stirred tank reactor (STR) (Grimalt-Alemany et al., 2018; Lecker et al., 2017). The mass transfer rate depends on several factors, such as the reactor design, the impeller configuration, the volumetric power input, and the gas flow rate. In STR, increasing gas flowrate requires higher volumetric power input to maintain a high interfacial area, otherwise, coalescence may occur, leading to a decrease in interfacial area. Peillex et al. (1988) compared the biological methanation efficiency of a Rushton turbine with a straight blade impeller. It is found that the Rushton turbine promotes better radial flow and improved the volumetric mass transfer coefficient by 124% in comparison to a straight blade impeller.

Another common solution to enhance the mass transfer in a stirred tank is to increase the bubble break-up by increasing the agitator's power-to-volume ratio. Luo and Angelidaki (2012) showed that the gas-liquid mass transfer is the rate-limiting factor when they studied the biogas upgrading in a 1 L laboratory stirred-tank reactor under thermophilic condition. They observed a CH_4 content improved from 90% to 95% when the mixing speed was increased from 500 to 800 rpm. They also demonstrated that a high gas injection rate improves the biogas productivity but the CH_4 purity decreases. However, it is costly to increase the mass transfer by increasing the agitation power in a commercial large-scale stirred tank reactor. This scale-up effect was elucidated in the work of Savvas et al. (2017). By considering a stirring speed of 1200 rpm, a 2 L and 5 L STR equipped with 2 Ruston type impeller would have a power consumption of 28 $kWh.m^{-3}.d^{-1}$ and 360 $kWh.m^{-3}.d^{-1}$, respectively. This means that for a CH_4 production of 40 $L.L^{-1}.d^{-1}$, the energy spent by the system would be 7% and 90%, respectively of the energy contained in the end product. The power consumption of a STR can be calculated using equation (1.2).

$$\mathrm{P} = N_p \rho N^3 D^5 \tag{1.2}$$

Where N_p is the power number, ρ is the fluid density, N is the angular velocity of the impeller, and D is the impeller diameter. The increase in the impeller diameter due to scale-up will increase significantly the mixing power consumption, as the power is directly proportional to the diameter raised to the power of 5. The power number N_p depends on the impeller design and hydrodynamic regime, but in the turbulent regime, the power number becomes independent of the Reynolds

number, as shown in Figure 1.6. Table 1.1 summarises the power number for some typical impellers for $Re > 2 \times 10^4$.

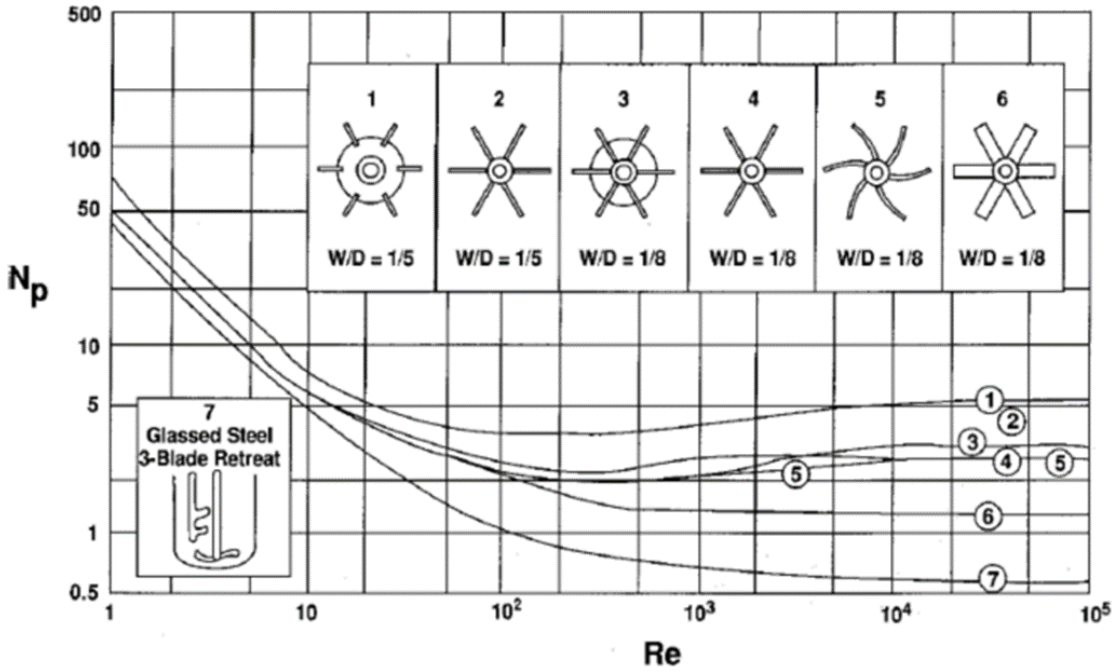

Figure 1.6: Power number as a function of Reynolds number. Adapted from: Paul et al. (2004)

Table 1.1: Power number in the turbulent regime for different impellers in standard STR. Adapted from: Nienow (1998)

Impeller type	N_p
6-blade Rushton	5
12-blade Rushton	7.5
Scaba	1.45
4-blade, 45° pitch turbine	1.27
6-blade, 45° pitch turbine	1.70
A315	0.84

Moreover, the achievable gas retention time in a STR is relatively short, gas bubbles formed after injection will rise to the surface within seconds, leading to a low mass transfer rate (Ullrich et al., 2018). Seifert et al. (2014) investigated the gas flow rates and the reactor pressure in the off-gas quality and productivity. The authors demonstrated that increased gassing rates improve the CH_4 productivity due to the increase of volumetric mass transfer coefficient but the H_2 conversion efficiency decreases. This conversion efficiency can be compensated by a simultaneous increase of the reactor pressure (Seifert et al., 2014).

1.1.1.2 Trickle-bed reactor (TBR)

Trickle bed reactors are reactors with packed solid support material which offers a high volumetric surface area for mass transfer. Generally, the interfacial area is independent of the gas flowrate, provided the wetting is perfect. The interfacial area is dependent on the support material and the gas retention time is controlled by the gas substrate feed rate. The microorganisms are immobilised on the surface of the packing, with the liquid continuously wetting the microorganisms' surfaces (Lecker et al., 2017; Ullrich et al., 2018). Due to the high specific interfacial area, the gas substrates in contact with the liquid ensure continuous substrates mass transfer. Ullrich et al. (2018) reported a higher CO_2 and H_2 conversion rates and higher methane contents in the outlet can be achieved by raising the operating pressure in the trickle-bed reactor. They tested three operating pressures of 1.5, 5 and 9 bar absolute and they observed a higher methane fraction and a higher methane formation rate at high pressure. Some authors also confirmed that a higher methane fraction (> 90%) in the product gas can be achieved for a trickle-bed reactor compared to a STR at (85%) (Alitalo et al., 2015; Burkhardt and Busch, 2013; Ullrich et al., 2018). Ullrich and Lemmer (2019) conducted a gas-liquid mass transfer enhancement experiment in a trickle-bed reactor by performing liquid flow modulation. The methane purity in the outlet was significantly increased as pause intervals without liquid sprinkling became longer. It is shown that the CH_4 purity increases from 89% to 97% by switching from the liquid circulation interval of 2 minutes to 1-day. The liquid modulation offers various advantages: (1) better distribution of nutrient solution on the microorganisms' surface, (2) a thinner liquid film for a better mass transfer and (3) lower energy consumption of the process. Alitalo et al. (2015) also do not observe any loss in biological activity if the packing material is wetted once every 72 h. Although the liquid is only supplied occasionally, homogeneous distribution of liquid over the packing material is essential to limit dead zones without methanogenic activity (Dupnock and Deshusses, 2019). This depends on several parameters, including the packing material's wettability, the liquid velocity and the liquid viscosity (Jensen et al., 2021). The hydrodynamic particularly the gas-liquid dispersion in the trickle-bed reactor is also very important in order to achieve efficient biological methanation. Kimmel et al. (1991) compared the CH_4 productivity in two trickle-bed reactors of different diameters in response to an increase in the H_2 gas loading rate. The smaller TBR was reported to have higher productivity due to better liquid distribution, thus better wetting, which favour enhanced CH_4 productivity. The plug flow conditions might not have been ideal because of a wider diameter; thus, the wetting is imperfect, and therefore lower CH_4 productivity was observed. Figure 1.7 presents some packing materials that have been tested in the literature.

(a) (b) (c)

Figure 1.7: Different packing material used in the trickle-bed reactor. (a) Commercial packing material Bioflow40 made by company RAUSCHERT used in Burkhardt and Busch (2013), (b) Spherical porous clay granule used in Markthaler et al. (2020), (c) Commercial packing material Hel-X bio carrier made by company Christian Stöhr GmbH used in Strübing et al. (2018, 2017).

1.1.1.3 Membrane reactor

In a hollow fibre membrane reactor, membrane modules are submerged in the liquid and the gas is sparged through the small pores into the surrounding liquid. The gas retention time is dependent on the gas feed rate, thus independent of the gas-liquid mixing (Jensen et al., 2021). The fibre design is classified as hydrophilic or hydrophobic. If hydrophilic fibres are applied, the water is absorbed into the pores, thus the gas can be transferred directly into the liquid without the formation of bubbles. Luo and Angelidaki (2013) reported a 90% CH_4 content in the off-gas and they studied the H_2 gas flow rate on the reactor performance. The authors showed an increase in CH_4 content (78.4% to 90.2%) when the H_2 flowrate increases from 0.93 to 1.44 L/L/d. In the literature, high volumetric mass transfer coefficient ($k_L a$) are reported for this novel technology which is translated to high CH_4 purity (Díaz et al., 2015; Luo and Angelidaki, 2013; Munasinghe and Khanal, 2012). Díaz et al. (2015) explained the high $k_L a$ by the fact that the sparging area of the membrane module is much larger compared to other diffusers used in STR or bubble column (gas sparging area to reactor volume ratio of $30 m^2/m^3$). While hollow fibre membranes provide instantaneous gas-liquid mass transfer, the gas and liquid flowrates are limited due to the porosity and relatively small surface area, leading to low CH_4 productivity (Jensen et al., 2021; Rusmanis et al., 2019). It also suffers from some other drawbacks, such as high operating costs caused by membrane fouling (Rusmanis et al., 2019). The build-up of biofilm on the membrane over the system lifespan will decrease the operational efficiency as higher diffusional resistance is obtained resulting from biofouling. Eventually, backwashing is needed which leads to lower biological

methanation efficiency. Figure 1.8 shows two examples of membrane reactor design used in the literature.

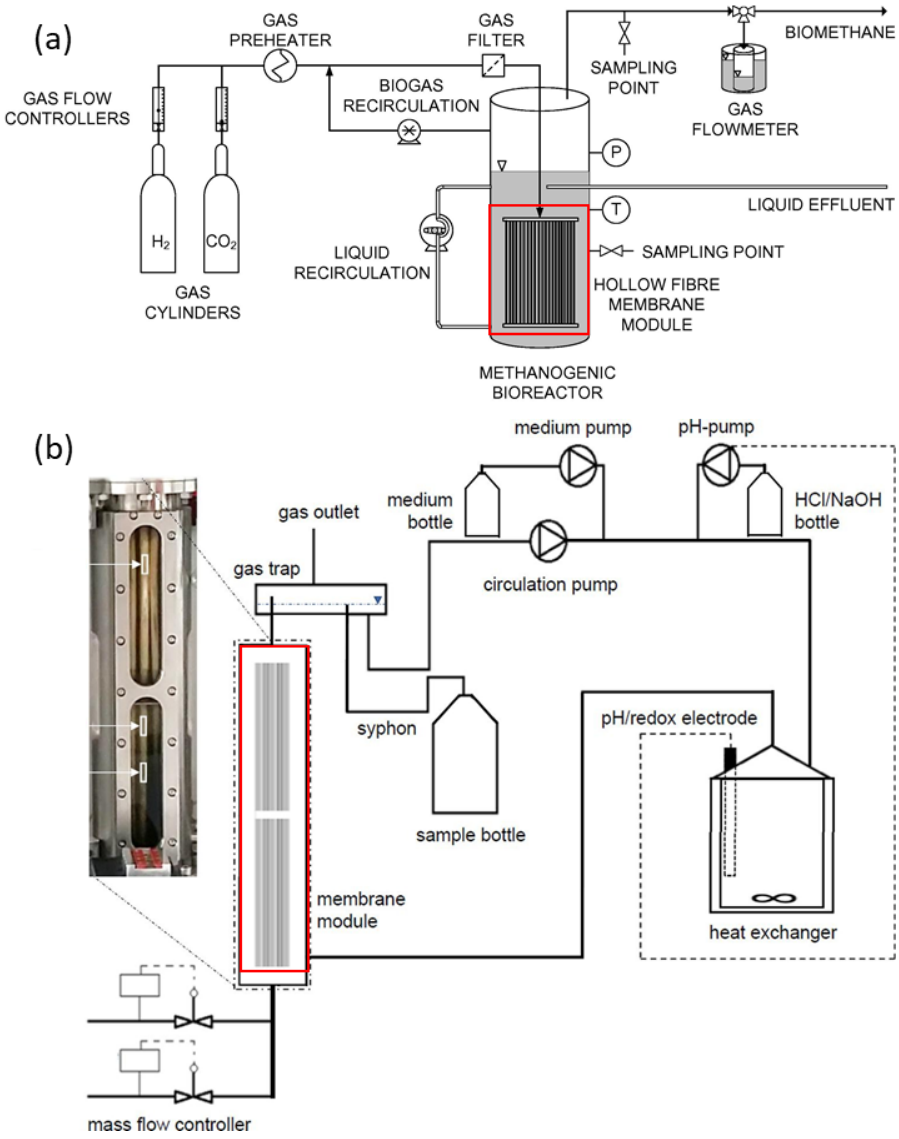

Figure 1.8: Membrane reactor design. (a) Hollow-fiber membrane module used in Díaz et al. (2015) was composed of 232 polymeric fibers with a pore size of 0.4 µm, a length of 550 mm and a total membrane surface of 0.93 m^2. (b) Hollow-fiber membrane module used in Pratofiorito et al. (2021) was composed of 19 polypropylene fibers with a pore size of 0.2 µm, a length of 390 mm and a total membrane surface of 0.198 m^2.

1.1.1.4 Bubble column reactor

In the literature, bubble column reactor for biological methanation is relatively less present than STR and trickle-bed reactor (Rusmanis et al., 2019). Ironically, the bubble column design is very simple without any mechanical stirring device, yet it provides good mixing and mass transfer properties (Shah et al., 1982). The gas bubbles are dispersed in the liquid via different gas sparger systems. The mass transfer rate in a bubble column is governed by several parameters, such as the superficial gas velocity, the gas and liquid phase properties, the solid concentration, the reactor design, the gas diffuser, and the operating conditions (Kantarci et al., 2005). The reason behind such many dependent parameters is the fact that multiphysics phenomena are highly coupled in a bubble column (Darmana et al., 2007). Namely, mixing is induced by buoyancy effects which depend heavily on bubble size and gas holdup (Laupsien et al., 2017; León-Becerril et al., 2002; McClure et al., 2015a; Mudde and Simonin, 1999). Bubble column enables to achieve higher average mass transfer driving force due to favourable gas composition spatial profiles and higher gas retention time (Chen et al., 2015). It offers non-mechanical mixing and hence it has a relatively low operation cost (Grimalt-Alemany et al., 2018). However, due to the low solubility of H_2, the biological methanation performance using bubble column reactor is poor with the CH_4 purity found below 90% (Bassani et al., 2016; Voelklein et al., 2019). Therefore, optimisation is required to enhance the mass transfer efficiency in bubble column reactor. Voelklein et al. (2019) demonstrated that a grid standard purity of CH_4 is only achievable through a 24 h gas-batch system using a 9.5 L bubble column reactor, hampering the application of continuous gas feed system. Guiot et al. (2011) showed that a gas recirculation-to-feed ratio of 18:1 is able to improve the CH_4 productivity from 0.49 mmol CH_4/gVSS/d to 2.55 mmol CH_4/gVSS/d. Different authors also confirmed that gas recirculation enhances the productivity of CH_4 (Grimalt-Alemany et al., 2018; Kougias et al., 2017). The sparger design becomes important for the mass transfer limiting process, whereby fine sparger is shown to be enhancing the mass transfer compared to coarse sparger, as shown in Figure 1.9. In general, fine sparger gives a smaller bubble size and promotes homogeneous flow, resulting in higher volumetric mass transfer coefficient (Deckwer et al., 1974; Möller et al., 2017).

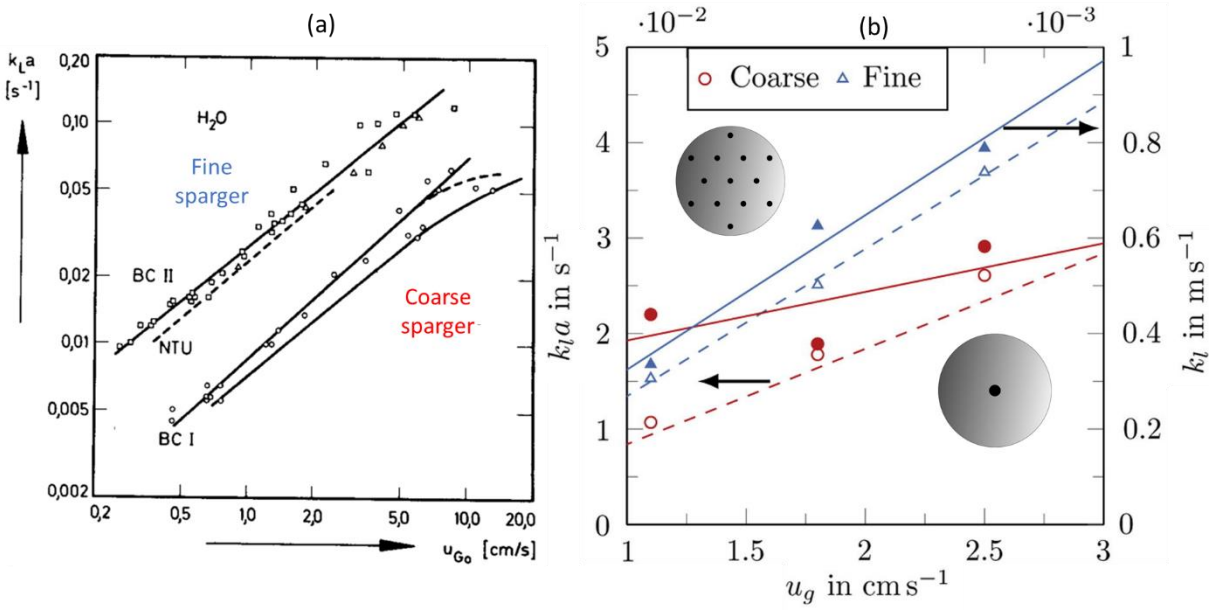

Figure 1.9: Comparison of mass transfer coefficient according to sparger design. (a) Adapted from the work of Deckwer et al. (1974). The coarse sparger is composed of a cross with 56 nozzles of 1 mm diameter. The fine sparger is composed of a glass sintered porous plate. The lines are predictions using NTU method and correlations. (b) Adapted from the work of Möller et al. (2017). The fine sparger is composed of 13 nozzles of 0.8 mm diameter. The coarse sparger is composed of a centred hole distributor with a diameter of 2.9 mm. The lines are best fitted curve.

1.1.1.5 Conclusion on bioreactor design for biological methanation

Different reactor technologies have been used to study biological methanation with the objective to reach grid-quality CH_4 purity and high productivity. It is found that the optimisation of operating conditions and reactor configurations is often necessary to achieve high biological methanation performance. For STR, the optimisation of reactor and impeller designs and agitation speed is necessary to obtain high mass transfer efficiency. For trickle-bed reactors, the key to efficient mass transfer is to distribute homogeneously the liquid nutrient in order to ensure perfect wetting and thin liquid film. High pressure also intensifies the mass transfer. For membrane reactors, the optimisation of high surface per volume ratio and backwashing is required to avoid biofouling. For bubble column reactors, increasing gas retention time via gas recycling is beneficial for gas conversion and therefore CH_4 productivity. Different reactor configurations offer distinct mass transfer performance, translated by a different range of volumetric mass transfer coefficient ($k_L a$), leading to very different biological methanation efficiency. Munasinghe and Khanal (2010) reported the characteristic values of $k_L a$ obtained for different reactor designs. It offers a very general guideline on optimisation parameters for mass transfer performance. Thema et al. (2019) also generalised the typical hydrodynamic and

mass transfer performance for different bioreactor designs. Table 1.2 and Table 1.3 summarise the findings of Munasinghe and Khanal (2010) and Thema et al. (2019). It should be emphasised that these values can only be used as a reference for the order of magnitude, as a large difference in the $k_L a$ value can be observed, e.g. $k_L a$ varies between 18 – 860 h^{-1} in bubble columns, as presented in Table 1.2. Figure 1.10 shows the gas-liquid interfacial area generated in different reactor systems. In STR and bubble column, the bubble generated is dispersed in the liquid bulk. In the membrane reactor, gas is diffused through the membrane to the biofilm forming on the outer layer of the membrane. In TBR, the gas is in contact with the liquid film formed on the packing material.

Table 1.2: Performance parameters of various bioreactors. Adapted from: Munasinghe and Khanal (2010)

Reactor configuration	$k_L a$ (h^{-1})	Performance parameters	References
Stirred tank	10-500	Agitation speed, gas flow rate	(Charpentier, 1981)
Bubble columns	18-860	Gas flow rate, bubble size	(Bouaifi et al., 2001; Charpentier, 1981; Datar et al., 2004)
Packed bubble columns	18-430	Packing media properties, liquid and gas flow rate	(Charpentier, 1981)
Packed columns co-current flow	1.5-3670	Packing media, liquid and gas flow rate	(Charpentier, 1981)
Packed columns trickled flow	36-360	Packing media, liquid and gas flow rate	(Charpentier, 1981)
Microbubble sparged bubble column	200-1800	Bubble size	(Bredwell and Worden, 1998)
Internal loop airlift reactor	140-220	Aeration rate, pumped liquid flow rate	(Fadavi and Chisti, 2005)
Airlift reactor with net draft tube	18-160	Superficial gas velocities, reactor pressure	(Wu et al., 1992)

Table 1.3: Order of magnitude for some key parameters of bioreactors. Adapted from: Thema et al. (2019)

Parameter	Unit	Trickle-Bed Reactor	Continuous Stirred Tank Reactor	Bubble Column Reactor	Membrane Reactor
Gas holdup	-	0.75-0.98	0.05-0.3	0.02-0.4	-
Liquid holdup	-	0.5-0.2	0.7-0.95	0.7-0.95	-
Specific area	m^2/m^3	60-640	100-1500	100-1000	70-180
Mass transfer coefficient	m/s	$0.4\text{-}2x10^{-4}$	$0.3\text{-}4x10^{-4}$	$1\text{-}4x10^{-4}$	$1\text{-}10x10^{-4}$
Volume specific power input	Wh/m^3	4.3	50	12.5-15.6	-

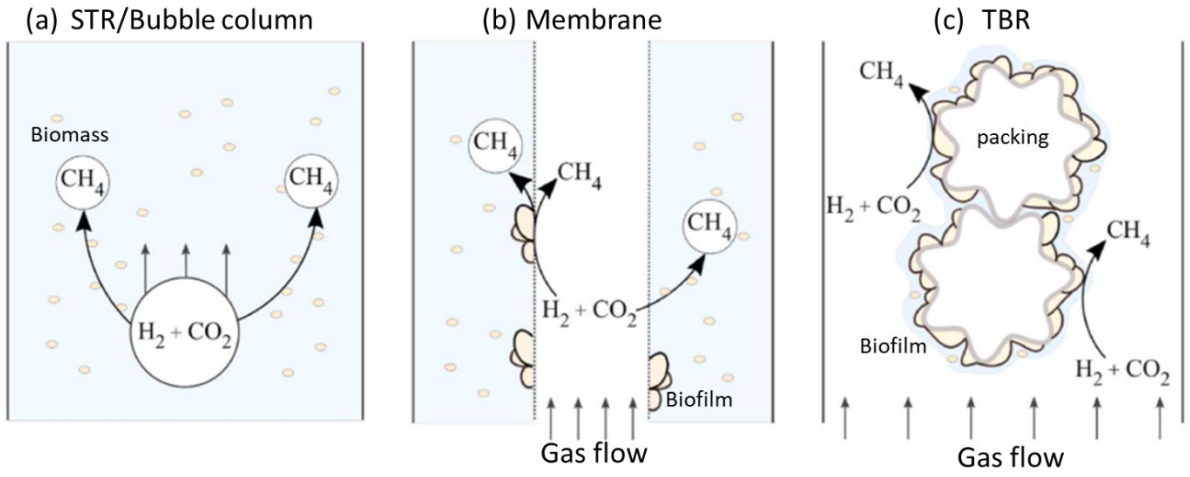

Figure 1.10: Gas-liquid interfacial area generation in (a) bubble dispersion system, namely STR and bubble column, (b) membrane and (c) TBR reactors. Adapted from: Jensen et al. (2021)

Table 1.4 reports the ex-situ biological methanation performance achieved using different reactor designs, configurations, and operating conditions. Only the ex-situ biological methanation is highlighted as it is more efficient than the in-situ configuration. As discussed in Section 1.1.1.4, very few biological methanation works using bubble column reactors are reported in the literature. It is found that trickle-bed reactor is highly studied to obtain efficient biological methanation. The reason is related to the optimal equilibrium between high mass transfer efficiency and low energy input. It is possible to achieve high CH_4 purity and productivity using STR, but it requires intense mixing with some reported agitation speed up to 1500 rpm (Peillex et al., 1990; Seifert et al., 2014). It is reported in Peillex et al. (1990) whereby a high CH_4 purity and productivity of 96% and 288 L/L/d was obtained in a 1.5 L laboratory-scale STR with an agitation speed of 1200 rpm and an airflow rate of 2 L/min (see

Table 1.4). Therefore, STR is not a viable option for large-scale biological methanation due to high energy demand. In comparison to STR, a trickle bed reactor requires less energy input as no stirring is necessary. The gas substrates that enter the reactor are in contact with the methanogens that are immobilised as a biofilm on the packing. The liquid nutrient trickles through the reactor with a very thin liquid film (if the hydrodynamic is well controlled), leading to very low diffusion resistance for mass transfer. Furthermore, increasing the pressure in trickle-bed reactors has a direct positive impact on H_2 mass transfer, and thus the CH_4 purity and productivity (Burkhardt et al., 2019). This is in contrast with a bubble column reactor whereby for the same gas molar feed, increasing pressure will not bring any positive impact to the mass transfer (Maalej et al., 2003). Nevertheless, it is found that existing industrial-scale biological methanation plants are installed with the STR technology (Rafrafi et al., 2020), probably due to well-known physics as STR is used traditionally in bioprocesses (Garcia-Ochoa and Gomez, 2009).

In this thesis, the reactor design of interest is the bubble column reactor for the following reasons:

- Pilot-scale ex-situ biological methanation experimental data is available for model validation. They are measured by the SYMBIOSE research group in our lab (Rafrafi et al., 2019).
- Wide range of experimental and numerical data on pilot-scale and industrial-scale bubble columns exist in the literature for chemical and biochemical processes. These data can be used to validate our numerical developments at several scales and for different (bio)reactive bubble column utilisations.

Table 1.4: Ex-situ biological methanation performance for different reactor design reported in the literature.

[1]Pressure is not specified. It is assumed to be ambient pressure P_{atm}

Reactor design	T (°C)	P	H_2 :CO_2 :CH_4	Max CH_4 % (corresponding CH_4 productivity in L/L/d)	Max productivity in L/L/d (corresponding CH_4 %)	Reference
Bubble column. Working volume of 1.4 L	52	P_{atm}[1]	62%:15%:23%	98% (-)	(-)	(Kougias et al., 2017)
Bubble column with ceramic diffuser. Reactor volume of 9.5 L.	55	P_{atm}	80%:20%:0%	92% (1.7)	3.7 (92%)	(Voelklein et al., 2019)
Bubble column with ceramic diffuser. Reactor volume of 9.5 L.	55	P_{atm}	73%:18%:9%	23% (5.1)	5.1 (23%)	(Voelklein et al., 2019)
STR. Working volume of 1.4 L	52	P_{atm}[1]	62%:15%:23%	79% (-)	-	(Kougias et al., 2017)
STR from Biostat C+, Sartorius Stedium biotech AG, Göttingen, Germany. Reactor volume of 10 L. Working volume of 3.5 – 5 L.	65	1 bar – 2 bar	80%:20%:0%	85% (137.17)	511 (60%)	(Seifert et al., 2014)
STR with magnetic stirrer. Working volume of 2 L.	55	P_{atm}[1]	-	89% (0.1)	0.36 (85%)	(Bassani et al., 2015)
STR with magnetic stirrer. Reactor volume of 1 L. Working volume of 0.6 L.	55	P_{atm}[1]	60%:15%:25%	95.4% (1.5)	5.3 (90.8%)	(Luo and Angelidaki, 2012)
STR with Rushton-type impeller. Working volume of 3.5 L	60	1 bar – 1.2 bar	80%:20%:0%	84.81% (9.93)	34 (48.77%)	(Martin et al., 2013)
STR with Rushton-type impeller. Working volume of 1.5 L	65	P_{atm}[1]	80%:20%:0%	96% (288)	288 (96%)	(Peillex et al., 1990)
Membrane reactor. Working volume of 0.75 L	37	P_{atm}[1]	80%:20%:0%	97% (20)	25 (73%)	(Savvas et al., 2017)
Membrane reactor. Working volume of 0.195 L	37	P_{atm}[1]	80%:20%:0%	90% (1.13)	3.95 (60%)	(Ju et al., 2008)

Membrane reactor. Working volume of 31 L	55	P_{atm}[1]	80%:20%:0%	84% (2)	9.5 (65%)	(Díaz et al., 2015)
Membrane reactor. Working volume of 3.42 L	37	P_{atm}[1]	80%:20%:0%	97% (1.05)	1.17 (80%)	(Pratofiorito et al., 2021)
TBR with packing material of glass rings from Sigma-Aldrich. Specific area of 0.002m^2/g. Working volume of 1 L	54	P_{atm}	62%:15%:23%	99.1% (0.88)	1.74 (95.1%)	(Porté et al., 2019)
TBR with Polypropylene packing rings (Hiflow rings type 15-7, RVT Process Equipment). Specific area of 312 m^2/m^3. Reactor volume of 7.5 L. Working volume of 5.8 L.	37	P_{atm}[1]	80%:20%:0%	98.26% (1.3)	2.52 (84%)	(Rachbauer et al., 2016)
TBR with packing material of Bioflow 40 from RAUSCHERT. Specific area of 305m^2/m^3. Reactor volume of 26.8 L. Working volume of 5 L.	37	P_{atm}	80%:20%:0%	97.5 % (0.65)	1.17 (94%)	(Burkhardt and Busch, 2013)
TBR with packing material of Bioflow 40 from RAUSCHERT. Specific area of 305m^2/m^3. Reactor volume of 90 L. Working volume of 61 L.	37	P_{atm}	80%:20%:0%	98% (0.4)	1.49 (92%)	(Burkhardt et al., 2015)
TBR with packing material of Bioflow 40 from RAUSCHERT. Specific area of 305m^2/m^3. Reactor volume of 90 L. Working volume of 61 L.	37	1-25 bar	80%:20%:0%	99.7% (3.1)	5.75 (97.7%)	(Burkhardt et al., 2019)
TBR with two packing material: at the bottom RFK 25 L type carrier with a specific area of 313 m^2/m3. and at the top Hel-X bio carrier HXF12KLL from Christian Stöhr GmbH & Co. KG, Germany with a specific area of 859 m^2/m3. Reactor volume of 72.6 L. Working volume of 58.1 L.	55	P_{atm}	80%:20%:0%	99.1% (1.7)	15.4 (98.1%)	(Strübing et al., 2017)
Two FBR in series. Solid support made up of vermiculite shales and graunilar perlite submerged in biological broth. Reactor volume of 4.4 L. Working volume of 4 L.	53	P_{atm}[1]	80%:20%:0%	90% (1.73)	4.03 (50%)	(Alitalo et al., 2015)
Two upflow reactor in series. Reactor volume of 1.4 L each.	52	P_{atm}[1]	62%:15%:23%	66% (-)	-	(Kougias et al., 2017)
3 TBR in series with random packing material from Christian Stöhr GmbH & Co. KG, Germany. Specfic srface area of 861 m^2/m^3 Reactor volume of 22.5 L each.	40	1 – 5 bar	80%:20%:0%	97% (5.62)	5.62 (97%)	(Ullrich and Lemmer, 2019)

1.1.1.6 Large-scale biological methanation plant

As mentioned previously in the introduction, biological methanation technology is still in its early stage of development, very few large-scale projects are referenced in the literature. Nevertheless, some examples are starting to emerge through joint-venture of different companies (Rafrafi et al., 2020).

- MicrobEnergy (Viessmann, HZI)

Recently, the Viessmann group sold their subsidiary MicrobEnergy company which has carried out large-scale tests with in-situ and ex-situ biological methanation to a Swiss-Japanese cleantech company Hitachi Zosen Inova (HZI) (Viessmann, 2021). It is reported that the 100 m^3 in-situ biological methanation plant is situated in Allendorf, Germany. The anaerobic digestor produces 175 Nm^3/h of CH_4 at 53% purity. The injection of 20 Nm^3/h of H_2 upgrades the biogas to 60% CH_4 at 198 Nm^3/h productivity (Reuter, 2013). Another 5 m^3 ex-situ plant is also installed by MicrobEnergy in Allendorf, Germany. The ex-situ bioreactor operates between 50 to 80°C and 5 to 15 bar. The agitation speed is indicated to be at 400 rpm. Two electrolysers of 150kW capacity provide a maximum hydrogen flowrate of 60 Nm^3/h to the reactor. It is shown that with an input of 15 Nm^3/h of H_2, the biogas produced CH_4 at 96% purity and at a flowrate of 5.5 Nm^3/h (Heller, 2015; IEA Bioenergy, 2018).

- Electrochaea

Electrochaea is a growth-stage company that provide grid-scale energy storage solution in North America and Europe. Electrochaea patented an ex-situ single culture highly efficient strain with *Methanothermobacter thermautotrophicus* (www.electrochaea.com). In 2016, Electrochaea commissioned the world's largest 1 MW Power-to-gas plant in the framework of the BioCat project. The system includes a commercial scale methanation reactor, an anaerobic digestor plant, an electrolyser, a gas polishing system and a gas grid injection station, all located at the BIOFOS wastewater treatment facility in Avedøre, near Copenhagen (www.electrochaea.com/technology). The reactor operates at 65°C and under 9 bar. The reactor design is a tall STR with multiple-stage impeller. The exact dimension of the reactor varies according to the literature, but it is agreed to reach approximately 10 m (Rafrafi et al., 2020; Rusmanis et al., 2019) The electrolyser provides a capacity of 200 Nm^3/h of hydrogen to upgrade the biogas up to 98% purity and 50 Nm^3/h productivity (Lardon et al., 2018; Rusmanis et al., 2019; Sveinbjörnsson and Münster, 2017).

Figure 1.11 presents the biological methanation demonstration plant of MicrobEnergy and Electrochaea. It shows that Electrochaea's bioreactor adapted a higher height-to-diameter ratio and it

is designed to treat higher hydrogen loading up to 200 Nm^3/h compared to that of MicrobEnergy of 15 Nm^3/h.

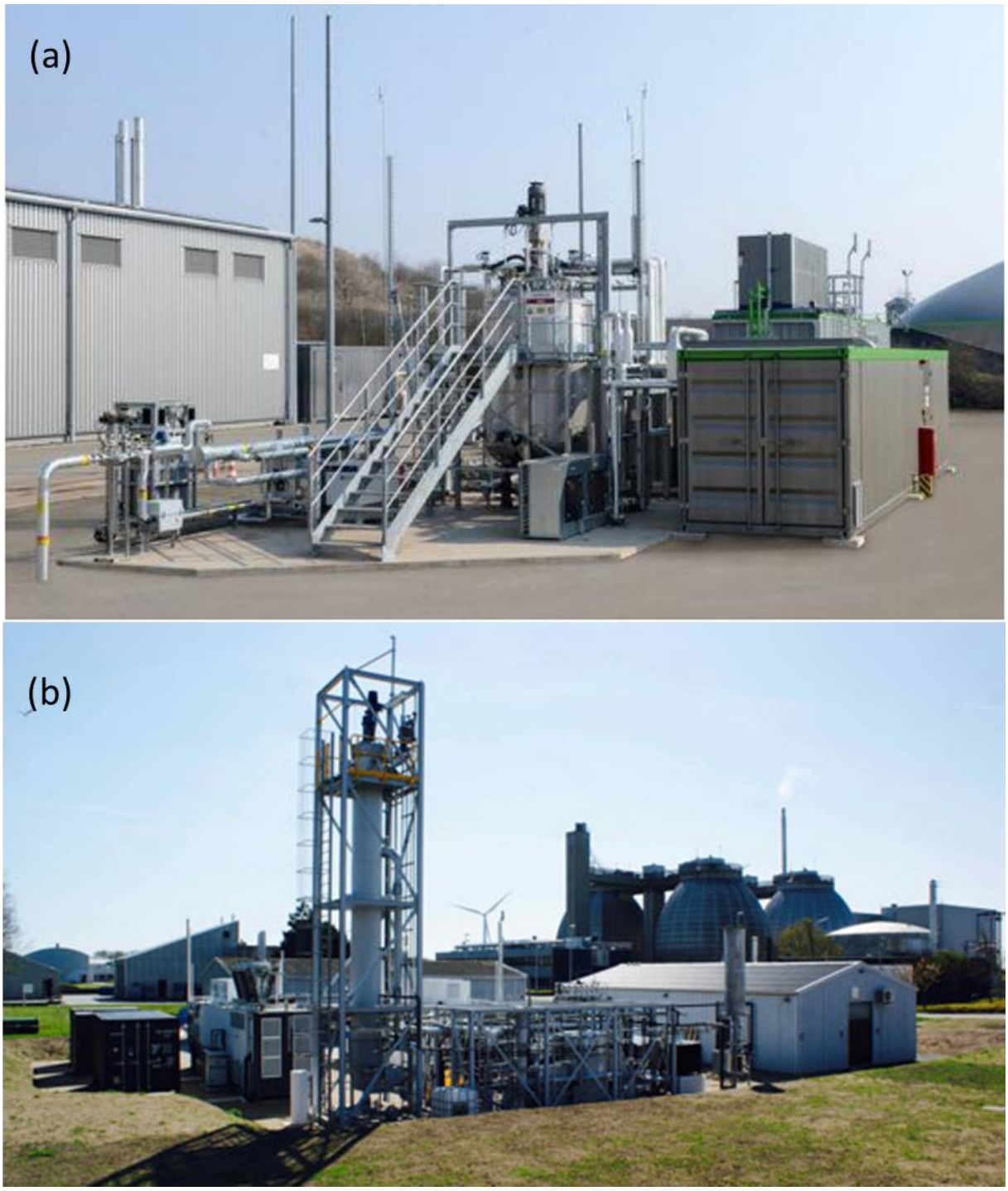

Figure 1.11: (a) 5 m^3 ex-situ biological methanation plant of MicrobEnergy in Allendorf, Germany (b) Electrochaea biological methanation plant in Avedøre, Denmark

1.2 Multiphysics coupling in bioreactors

The bioreactor has been used since early ancient times, primarily for beer brewing, cheese and winemaking. The discovery of antibiotics in the 30's pushed a breakthrough in the pharmaceutical industry to establish large-scale production in order to meet global medical needs. Apart from antibiotics, pharmaceutical groups and big food & beverage companies also developed bioprocesses that use micro-organisms to synthesize added-value products such as amino acids, enzymes, organic acids and proteins which become equally interesting as the manufacturing of commodity chemicals and food & beverages. This industrial biotechnology evolution challenges engineering skills in understanding the optimisation of reactor design and the operation of bioreactors (Mandenius, 2016).

Although there are some advances in biotechnology, a major challenge for current industries is to define a more standardised scale-up criteria rather than using empirical and traditional heuristics methods. To meet large-scale productions, industrial bioreactors are usually ten to thousand times larger than lab-scale bioreactors, hence, they could exhibit very different culture conditions than lab-scale bioreactors. Enfors et al. (2001) demonstrated the existence of spatial heterogeneities in industrial-scale culture when *E. Coli* cultivations were compared between a 22m^3 reactor and a lab-scale culture. Indeed, the operating conditions (pH, temperature, substrates concentration, etc) are better controlled in the small-scale compared to the large-scale. The mixing time is short to ensure homogeneous culture for the microorganisms. The difficulty arises when the length scale of the system studied increases. The mixing time increases with the reactor size, while the time constant associated with the bioreaction remains constant. This leads to non-ideal mixing and it creates heterogeneities and nutrient concentration gradients. Under these conditions, microbial cells will experience fluctuating conditions, forcing them to adapt to the environment they encountered according to the locally available substrates (Haringa et al., 2016; Morchain et al., 2013; Nadal-Rey et al., 2021b). These spatial gradients and environmental fluctuations require in-depth analysis to elucidate their effects on the metabolism and overall performance. In-silico predictions and simulation tools gain interest to investigate these multiphysics coupling phenomena as researchers used these tools to design bioprocesses, study mixing, and perform parametric studies on the operating conditions in order to reduce undesired concentration gradients and maximise production yields (Delafosse et al., 2010; Gernaey et al., 2010; Gernaey and Jeppsson, 2014; Haringa et al., 2017; Morchain et al., 2013; Nadal-Rey et al., 2021a; Nauha, 2019; Pigou and Morchain, 2015; Siebler et al., 2020; Sin et al., 2009). Because of the strong coupling between different physical phenomena with the biological phase and the complexity of cellular metabolism, it is generally challenging to predict and model bioreactor

performance. Due to the presence of multiphysics phenomena at different time and spatial scales in the bioreactor, it requires various modelling strategies to achieve the objective of the study, depending on the computational resources. Figure 1.12 depicts the coupling phenomena between hydrodynamics, gas-liquid mass transfer and gas-fed bioreaction in a bubble column reactor.

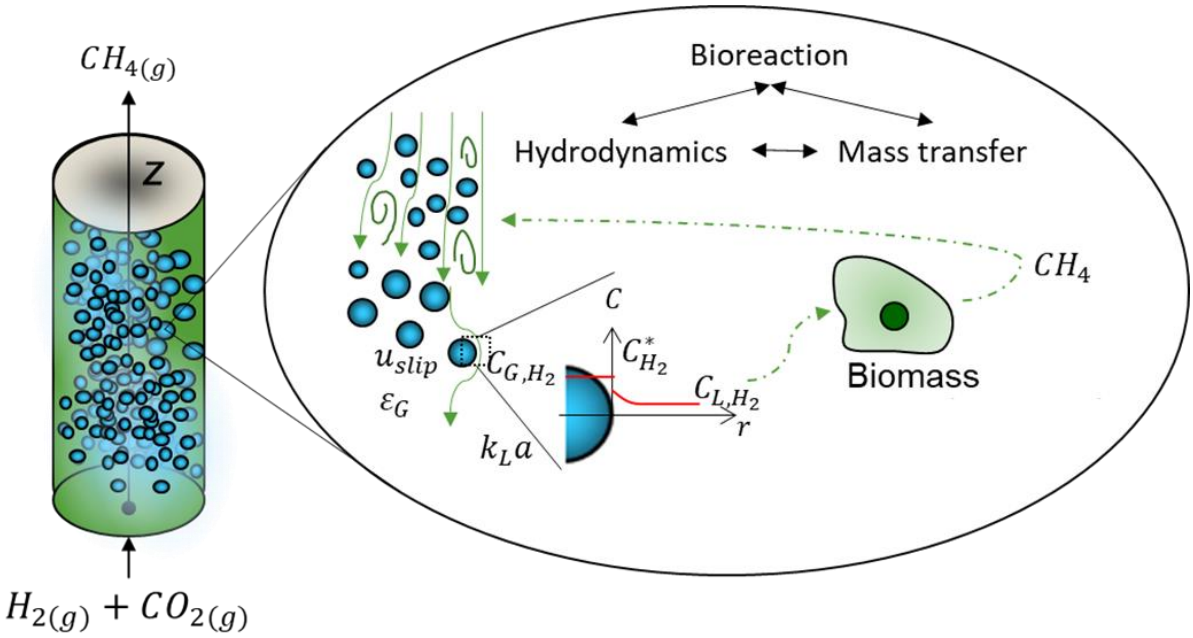

Figure 1.12: Multiphysics coupling in a bubble column reactor applied to biological methanation. Adapted from: Ngu et al. (2022a)

A prerequisite to studying bioreactors is the definition of a suitable model, which represents a closed set of equations describing the dynamic evolution of the biological culture, and the use of numerical methods to ensure stable resolution of the equations. As widely used in chemical reactor modelling, the most generic model that can be used to describe the dynamic evolution of the biological phase is the conservation equation that solved for the local mass balance of any species present in the bioreactor. It is written such as:

$$\frac{\partial C(\vec{x},t)}{dt} + \vec{u}(\vec{x},t).\vec{\nabla}C(\vec{x},t) - \vec{\nabla}.\left(D\vec{\nabla}C(\vec{x},t)\right) = R(C(\vec{x},t)) \tag{1.3}$$

with $\vec{x}$ is the vector location in the reactor, t is the time, $\vec{u}$ is the local velocity, and C is the concentration of the transported species. Equation (1.3) describes the variation in time of any species at a certain location in the reactor. It is influenced by the convective fluid motion (LHS 2nd term) and the diffusive fluid motion (LHS 3rd term) and the existence of sink/source term (RHS term). The last term usually deals with the mass transfer term and the reaction term. Even though Equation (1.3)

represents a general form of a species transport model, it is important to emphasise two aspects that are the core of bioreactor modelling: physical transport on the LHS and the mass transfer or the bioreactions on the RHS. On one hand, the description of physical transport deal with the hydrodynamic behaviour of multiphase flow in the bioreactor. On the other hand, the bioreaction modelling has to deal with the contribution of each viable microorganism to the overall local bioreaction rate. Both aspects need to be dealt with caution and will bring complementary challenges to bioprocess modelling. The coupling between the physical transport and bioreaction has to be addressed in detail to capture the relative events in the bioreactor. The challenges in bioreactor modelling will be addressed in the following.

1.2.1 Challenges in bioreactor modelling

1.2.1.1 Describing gas-liquid hydrodynamics

Bioreactors are often multiphase systems with the presence of gas bubbles, liquid culture medium, and solid biomass suspensions. The gases are supplied to ensure aerobic respiration or are sometimes produced by microorganisms. Due to the low Stokes number of microorganisms, the biological phase is supposed to follow the same trajectories as the liquid. Hence, a two-phase flow approach is generally sufficient to address the hydrodynamic description in a bioreactor, while the three-phase approach is relevant to address mass conservation aspects (Delafosse, 2008; Linkès, 2012). Depending on the operating conditions, the gas-liquid mixing flow can be chaotic and therefore very challenging to model in large-scale bioreactors. A complete hydrodynamic model is necessary to describe the velocity field of the two-phase bubbly flow. The velocity field of large-scale bioreactors can be modelled by solving 3D fluid mechanics equations, namely Reynolds Averaged Navier-Stokes (RANS) equations (Bach et al., 2017; Elqotbi et al., 2013; Haringa et al., 2017; Sarkizi Shams Hajian et al., 2020) or by enforcing a circulation map through so-called Compartment models (Delafosse et al., 2014; Pigou and Morchain, 2015; Vrábel et al., 1999) or by simplified 1D flow models when the two-phase flow occurs essentially in one preferential direction (Chen et al., 2015, 2016; Ngu et al., 2022a; Siebler et al., 2020).

1.2.1.2 Physical and biological regimes

The next challenge in bioreactor modelling is the description of the reaction term $R(C(\vec{x},t))$ in equation (1.3) as it involves a broad range of phenomena whose modelling is not straightforward. Depending on the bioreaction of interest, different microorganisms assimilate various substrates (e.g. glucose, oxygen, carbon dioxide, organic molecules, etc.) and metabolise these substrates for growth, maintenance and intercellular activities. Strictly speaking, chemical transformations take place inside the cell and they are preceded by mass transfer between the liquid phase and the biological phase. Hence, the context is that of heterogeneous catalysis.

Intercellular activities or metabolic pathways of microorganisms may differ between strains and also between individuals of the same strain, depending on the living environment and the physiological state of each individual cell. Recent progress in experimental techniques has led to novel databases and models to understand and predict the intercellular activities and overall functioning of cells for common stains used in industrial bioprocesses (Heavner et al., 2013, 2012; Orth et al., 2011).

For the bioreaction to occur within a cell, the substrate from the culture medium must be first assimilated by the cell. These microorganisms can be treated as reactive heterogeneous catalysts. The

substrate is first brought to the vicinity of a cell through external physical transport. The assimilation will occur as the substrate passes through the cell membrane via diffusion or transporters. The state of these transporters depends on the external (pH, substrate concentration, light, temperature) and internal fluctuations (metabolite concentration, storage, famine, etc.) (Pigou, 2018). In the field of chemical engineering, the standard approach for heterogeneous catalysis is to compare the characteristic time of external mass transfer and reaction in order to identify whether the reaction is controlled by kinetic or physical transport aspects. Morchain et al. (2017) introduced the concept of biological and physical transport limitation regimes and proposed a general formulation of a bioreaction sink term.

$$\begin{gathered} R\big(C(\vec{x},t)\big) = \varphi.X \\ \varphi = \varphi^b\left(1 - e^{-\varphi^e/\varphi^b}\right) \\ \varphi^e = \frac{C}{\tau_m X} \end{gathered} \tag{1.4}$$

φ is the specific mass transfer rate. X is the cell mass per unit volume. φ^e is the specific rate of transport due to micromixing. φ^b is the current cell specific uptake capacity, expressed as Monod model, for example. τ_m the micromixing time. In brief, mass transfer proceeds at a specific rate corresponding to the current cell capacity unless external transport is limiting. In contrast to standard heterogeneous catalysis, the Damkhöler number φ^e/φ^b varies not only with the external conditions but also with the physiological state of the cell since φ^b evolves in time. The concept of limitation is now based on a ratio of specific rates rather than in an absolute manner using concentration thresholds. In the end, the calculation of the “apparent reaction rate” results from a trade-off between external supply and biological demand (Morchain et al., 2021).

1.2.2 Multiphase bioreactor modelling approaches

Bioreactor behaves as a multiphase system and a more rigorous approach is necessary to consider the interactions between the phases, including mass and momentum transfer. The description of these transport and transfer phenomena is crucial for bioreactor modelling, especially when the transfer of substrates or products occurs between different phases. First, the hydrodynamic description for the gas-liquid phase is addressed. Next, the interfacial mass transfer is described with different closure models. Finally, models for biological kinetics are presented.

1.2.2.1 Euler-Euler modelling of gas-liquid hydrodynamics

Depending on the bioreactor scale and the variable of interest, different hydrodynamic models are needed to address the gas-liquid interactions. For the complete 3D model, the CFD approach is mostly used to simulate the hydrodynamics of the bioreactor. In this aspect, two CFD modelling approaches to treat the continuous and discrete phase can be further differentiated, namely Euler-Euler and Euler-Lagrange approaches. For the Euler-Euler approach, both phases are considered as inter-penetrating continua, and it solves for the local phase fraction, α_k and local velocity vector, $\overrightarrow{u_k}$ by formulating the continuity and momentum conservation equations on each phase. For the Euler-Lagrange approach, we choose to simulate the behaviour of a group of inclusions by following individually a large number of these inclusions in their movement. The statistical quantities are then obtained by a simple average. The Euler-Lagrange approach is also called the discrete bubble model as the dispersed phase (the bubbles) is followed individually. The continuous phase is often treated in Eulerian, which gives the name of the Euler-Lagrange approach. In terms of chemical engineering, the Euler-Euler approach can be found to model large-scale gas-liquid contactors (Cockx et al., 1999; Fayolle et al., 2007; Nadal-Rey et al., 2022; Rzehak and Krepper, 2016) and also lab-scale bubble columns (Chen and Brooks, 2021; Deen et al., 2001) whereas Euler-Lagrange approach is mostly reserved for the simulation of a lab-scale bubble column with low gas holdup (Huang et al., 2021; Jain et al., 2015; Taborda et al., 2021b; Taborda and Sommerfeld, 2021). In biochemical engineering, the Euler-Euler approach is still preferable for large-scale bioreactors (Gunyol and Mudde, 2009; Haringa et al., 2017; Morchain et al., 2014; Nadal-Rey et al., 2022; Puiman et al., 2022; Sarkizi Shams Hajian et al., 2020). Since the treatment of gas-liquid hydrodynamics using the 3D Euler-Lagrange approach is limited in bioreactor modelling, the Lagrangian equations for the discrete bubble model are not presented here. However, the Euler-Lagrange CFD model from the microbial point of view is discussed hereafter when the statistical analysis is of great interest, pioneered by the work of (Lapin et al., 2006, 2004), the so-called “life-line analysis”.

1.2.2.2 3D Euler-Euler equations

The general 3D Euler-Euler two fluid model are obtained by multiplying the single-phase flow RANS equations by the phase indicator function. After statistical averaging, one yields:

- **Continuity equation**

$$\frac{\partial \alpha_k \rho_k}{\partial t} + \vec{\nabla}.(\alpha_k \rho_k \overrightarrow{u_k}) = \overline{m_k} \tag{1.5}$$

where

- $k \in \{G, L\}$ designates respectively the gas, liquid phase
- α_k: local volume fraction of phase k
- ρ_k: density of phase k
- $\overrightarrow{u_k}$: velocity vector of phase k
- $\overline{m_k}$: statistical averaged interfacial mass transfer

- **Momentum conservation equation**

$$\frac{\partial \alpha_k \rho_k \overrightarrow{u_k}}{\partial t} + \vec{\nabla}.(\rho_k \alpha_k \overrightarrow{u_k} \otimes \overrightarrow{u_k}) = \alpha_k(\rho_k \vec{g} - \vec{\nabla} P) + \overrightarrow{\nabla}.(\tau_k - \rho_k \overline{u_k' u_k'}) + \overline{u_k\, m_k} + \overrightarrow{M_k} \tag{1.6}$$

where:

- $\otimes$: tensor product
- P: local pressure which is equal for all phases
- $\vec{g}$: body acceleration due to gravity force
- τ_k: stress tensor of phase k
- $\overline{u_k' u_k'}$: Reynolds turbulence stress tensor
- $\overline{u_k\, m_k}$: statistical averaged momentum transfers due to mass transfer
- $\overrightarrow{M_k}$: interfacial momentum exchange

- **Species transport equation**

$$\frac{\partial \alpha_k C_k}{\partial t} + \vec{\nabla}.(\alpha_k u_k C_k) = \alpha_k S_k - \overrightarrow{\nabla}.\alpha_k(\overrightarrow{J_k} + \overline{c_k' u_k'}) + \overline{c_k\, m_k} + L_k \tag{1.7}$$

where:

- C_k : local concentration of phase k

- $\overrightarrow{J_k}$: laminar diffusive flux of species in phase k (written analog to Fick's law). $\overrightarrow{J_k} = -\overrightarrow{\nabla}.(D_k C_k)$
- $\overrightarrow{c_k' u_k'}$: turbulent diffusive flux of species in phase k
- S_K : source or sink term
- $\overrightarrow{c_k \, m_k}$: species mass transport at interphase
- L_k : interfacial mass transfer term

If no mass transfer happens between phases, the RHS of equation (1.5) is equal to zero. The interfacial mass transfer term m_k needs to be integrated if the mass transfer causes a strong volume change in the gas phase. For the source term, S_k no significant chemical reaction occurs in gas and liquid phases, except for acid-base reactions which are present in the regulation of pH of the culture medium.

Turbulence plays an important role in bubbly flow and it contributes to the momentum exchange between phases. Industrial bioreactors usually operate in the turbulent regime, hence, there is a need to discuss the appropriate turbulent scale to be solved and the associated modelling strategy. Since the main objective of this thesis is not to investigate the turbulence behaviour in bioreactors, the discussion on turbulence models is kept short but concise. Turbulence exerts in all three-dimensional directions and has a transient behaviour. Different turbulence models exist in the literature, such as standard $k-\epsilon$, realizable $k-\epsilon$, RNG $k-\epsilon$, and $k-\omega$ which are typically available in commercial CFD software, e.g. ANSYS Fluent or open source code OpenFOAM.

Direct Numerical Simulation (DNS) with a sufficiently fine grid resolves all scales, ranging from the smallest Kolmogorov eddies to the integral scale of turbulence. However, it is rarely used to model industrial bioreactors with such details as it requires high-resolution time. Another method named Large Eddy Simulation (LES) only solves for the large eddy structures in the main flow and the smallest scales of turbulence are solved using the sub-grid scale model.

While the Navier-Stokes equations are applicable to describe instantaneous turbulent flow, very often, it is impractical and unnecessary to resolve all the fluctuating components of the turbulent quantities. Instead, the Reynolds Averaged Navier-Stokes (RANS) approach consists in splitting instantaneous variables into a time-averaged term and a fluctuating term. This is the most common way to compute turbulence by averaging over time the Navier-Stokes equations by Reynolds decomposition, resulting in an additional Reynolds turbulence stress tensor $\overline{u_k' u_k'}$ in equation (1.6). The Reynolds stress tensor is expressed in terms of turbulent viscosity ν_t in the liquid as

$$\overline{u_k' u_k'} = \nu_t \left(\frac{\partial \overline{u_i}}{\partial x_j} + \frac{\partial \overline{u_j}}{\partial x_i} \right) - \frac{2}{3} k_L \delta \tag{1.8}$$

The turbulent Reynolds stress has to be modelled to close the problem. Since there is no universal turbulence model available as the physics of turbulence is still an open research field, a number of semiempirical correlations have been developed, such as the mixing length model (one-equation model), the $k-\epsilon$ model (two-equation model), and the Reynolds stress model (seven-equation model). In this thesis, we applied mostly the $k-\epsilon$ model, thus, the brief presentation is limited to this model. The $k-\epsilon$ model is robust and economical and it has been used in many CFD applications in reactive and (bio)reactive flows. It supposes that the flow is fully turbulent with the rate at which the largest eddies extract energy from the mean flow being paired with the dissipation rate at which turbulent kinetic energy goes from larger to smaller eddies (Versteeg and Malalasekera, 2007).

From the dimensional analysis, it can be shown that k_L and ε_L are the two independent scaling parameters of time and length scales. Thus, the turbulent viscosity $\nu_t = \mu_{tL}/\rho_L$ as a function of turbulent kinetic energy k_L and dissipation rate ε_L is given by

$$\mu_{tL} = \mathrm{C}_\mu \rho_L \frac{k_L^2}{\varepsilon_L} \tag{1.9}$$

The transport equations for the turbulent kinetic energy (TKE) and the dissipation rate of TKE in the liquid phase are written as

$$\frac{\partial \rho_\mathrm{L} \alpha_\mathrm{L} \mathrm{k_L}}{\partial \mathrm{t}} + \vec{\nabla}.\left(\alpha_\mathrm{L}\left(\rho_\mathrm{L}\mathrm{k_L}\overrightarrow{\mathrm{u_L}} - \left(\mu_\mathrm{L} + \frac{\mu_\mathrm{tL}}{\mathrm{C}_2}\right)\nabla \mathrm{k_L}\right)\right) = \alpha_\mathrm{L}(\mathrm{Pr_L} - \rho_\mathrm{L}\varepsilon_\mathrm{L}) + \mathrm{T_{LG,k}} \tag{1.10}$$

$$\frac{\partial \rho_\mathrm{L} \alpha_\mathrm{L} \varepsilon_\mathrm{L}}{\partial \mathrm{t}} + \vec{\nabla}.\left(\alpha_\mathrm{L}\left(\rho_\mathrm{L}\varepsilon_\mathrm{L}\overrightarrow{\mathrm{u_L}} - \left(\mu_\mathrm{L} + \frac{\mu_\mathrm{tL}}{\mathrm{C}_3}\right)\nabla \varepsilon_\mathrm{L}\right)\right) = \alpha_\mathrm{L}\frac{\varepsilon_\mathrm{L}}{\mathrm{k_L}}(\mathrm{C}_4\mathrm{Pr_L} - \mathrm{C}_5\rho_\mathrm{L}\varepsilon_\mathrm{L}) + \mathrm{T_{LG,\varepsilon}} \tag{1.11}$$

Where C_2, C_3, C_4, C_5, and C_μ are constants having values of 1.0, 1.3, 1.44, 1.92, and 0.09, respectively as suggested by Launder and Spalding (1972). $\mathrm{T_{LG,k}}$ and $\mathrm{T_{LG,\varepsilon}}$ are terms accounting for interfacial transfer of TKE and its dissipation rate and it can be modelled using different models in the literature, such as the model of Pfleger and Becker (2001).

$$\mathrm{T_{LG,k}} = \alpha_L C_3 |M_{LG}||u_G - u_L| \tag{1.12}$$

$$\mathrm{T_{LG,\varepsilon}} = C_5 \frac{\varepsilon_L}{k_L}\alpha_\mathrm{L}\mathrm{C}_3 |M_{LG}||u_G - u_L| \tag{1.13}$$

For the $|M_{LG}|$ momentum transfer term, it can be simplified such that only drag is considered as this is regarded as the most dominant mechanism (McClure et al., 2014b).

In two-phase flow modelling, special attention needs to be given to the momentum exchange term $\overrightarrow{M_k}$, to account for all relevant forces. The most common forces considered are the drag, lift, wall, turbulent dispersion and virtual mass forces. These forces are usually characterised by three dimensionless numbers, namely Reynolds number, Eötvös number, and Morton number.

The bubble Reynolds number signifies the ratio of inertial to viscous force, written as:

$$Re_b = \frac{u_{slip}.d_B}{\nu_L} \tag{1.14}$$

The Eötvös number represents the ratio of hydrostatic pressure force to surface tension force, and it is evaluated as:

$$Eo = \frac{\Delta\rho.g.d_B^2}{\sigma} \tag{1.15}$$

The Morton number characterises the liquid medium which represents the ratio between viscous force and surface tension, and it is defined as:

$$Mo = \frac{\Delta\rho.g.\mu_L^4}{\rho_L^2\sigma^3} \tag{1.16}$$

- Drag force

The drag force is usually considered as the most important force. It reflects the resistance force opposing the bubble rising motion, written as equation (1.17). The drag is characterised by the drag coefficient C_D with different correlations to model it. Different correlations for C_D are discussed in Section 1.3.3.

$$F_{drag} = -\frac{3}{4d_b}C_D\rho_L\alpha_G|u_G - u_L|(u_G - u_L) \tag{1.17}$$

- Lift force

A bubble moving in an unbounded shear flow experiences a lift force perpendicular to the direction of the rising bubble. It is calculated as

$$F_{lift} = -C_L\rho_L\alpha_G(u_G - u_L) \times rot(u_L) \tag{1.18}$$

Spherical bubbles usually experience a positive shear lift coefficient in a manner that the lift force acts in the direction of decreasing liquid velocity. Experimental investigation of Tomiyama et al. (2002) shows that the lift force changes direction if a substantial deformation of the bubbles occurs. The following lift coefficient was derived from experimental observation of single air bubble trajectories in a simple shear flow of glycerol water solution:

$$C_L = \begin{cases} \min[0.288\, tanh(0.121\, Re_b)\,; f(Eo_\perp)] & Eo_\perp < 4 \\ f(Eo_\perp) & for \quad 4 < Eo_\perp < 10 \\ -0.27 & Eo_\perp < 10 \end{cases} \tag{1.19}$$

With $f(Eo_\perp) = 0.00105Eo_\perp^3 - 0.0159Eo_\perp^2 - 0.0204Eo_\perp + 0.474$

The modified Eötvös number is calculated the same as equation (1.15) but with a modified bubble diameter $d_\perp = d_b \sqrt[3]{1 + 0.163Eo^{0.757}}$ the maximum horizontal dimension of the bubble.

Based on this lift correlation, the lift coefficient changes sign when the bubble diameter is around 6 mm.

- Wall force

A bubble rising near a wall will also experience a wall lift force. It has the general form of:

$$F_{wall} = \frac{2}{d_b} C_W \rho_L \alpha_G |u_G - u_L|^2 \hat{y} \tag{1.20}$$

With $\hat{y}$ is the unit normal perpendicular to the wall pointing on the fluid. The wall force coefficient C_W is positive, signifying that the bubble is pushed away from the wall and the magnitude depends on the bubble distance to the wall. C_W is given as

$$C_W(y) = f(Eo)\left(\frac{d_b}{2y}\right)^2 \tag{1.21}$$

With $f(Eo) = 0.0217Eo$

- Turbulent dispersion force

Turbulent dispersion force acts on the phase fraction gradient. It describes the turbulent fluctuations of liquid velocity on the bubbles, resulting in random bubble movement in turbulent flows. Burns et al. (2004) derived an explicit expression by Favre averaging the drag force:

$$F_{TD} = -\frac{3}{4d_b} C_D \alpha_G |u_G - u_L| \frac{\mu_L^{turb}}{\sigma_{TD}} \left(\frac{1}{\alpha_L} + \frac{1}{\alpha_G}\right) \nabla \alpha_G \quad (1.22)$$

In analogy to molecular diffusion, $\frac{\mu_L^{turb}}{\sigma_{TD}}$ is referred to as a diffusion coefficient. σ_{TD} can be seen as a Schmidt number, which typically used a value of 0.9 (Rzehak et al., 2017b).

- Virtual mass force

When a bubble experiences acceleration, a certain amount of liquid is set into motion as well. This can be described by the virtual mass force, expressed as

$$F_{VM} = -C_{VM} \rho_L \alpha_G \left(\frac{D_G u_G}{Dt} - \frac{D_L u_L}{Dt}\right) \quad (1.23)$$

Where $\frac{D_G}{Dt}$ and $\frac{D_L}{Dt}$ are the material derivatives with respect to the inclusion velocity. For the virtual mass coefficient C_{VM}, a value of 0.5 is typically used.

The closures on mass transfer and reaction terms are discussed in Section 1.2.3 and Section 1.2.4.

1.2.2.3 Biological phase description

Similar to hydrodynamics, two approaches can be envisaged to represent the biological phase with distinct consequences on hydrodynamics and sink/source term modelling (Morchain, 2017):

- Suspended particle approach: the presence of cells is treated via Lagrangian particles transported by the liquid phase. Each particle represents a cell (or a collection of cells in the same state) and their trajectory is tracked from a force balance. The mathematical expression of each force experienced by the individual depends on the scale chosen for the resolution of the flow of the continuous phase. The accurate calculation of the reaction term in each elementary volume requires a large number of particles per unit volume and leads to the track of several millions of particles within the CFD simulation.

- Dissolved species approach: the presence of cells is considered via a scalar (its concentration in the liquid phase). This is the most common approach. However, since cells are actually suspended particles care must be taken when expressing the mass transfer and reaction terms at the elementary control volume level. Also, if cell-to-cell heterogeneity is of interest, one has to define several scalars to distinguish between groups of cells characterised by distinct properties.

An additional difficulty in calculating the sink term $R(C(\vec{x},t))$ of equation (1.3) lies in the heterogeneity within the cell population. The differences between individuals are constitutive of biological systems and population balance equations are the natural way of handling this complexity (Fredrickson and Tsuchiya, 1963). Biological diversity originates from extrinsic and intrinsic noises. Extrinsic noise corresponds to environmental fluctuations (Delvigne and Goffin, 2014) and intrinsic noise encompasses intracellular stochastic phenomena from gene expression to unequal partitioning of cell matter at cell division (Morchain et al., 2017, 2013).

When both spatial and biological heterogeneity are at stake, the consumption and production rate $R(C(\vec{x},t))$, must consider the distribution of cell properties, leading to

$$R\big(C(\vec{x},t)\big) = \frac{1}{V}\sum_{i=1}^{N_{cell}} m_i(\vec{x},t)\, r(C(\vec{x},t),\xi_i) \tag{1.24}$$

$m_i(\vec{x},t)$ is the mass of the i^{th} cell present at time t in the volume V. N_{cell} is the total number of cell in that volume. $r(C(\vec{x},t),\xi)$ is the specific reaction rate (including the previously mentioned considerations regarding physical and biological regimes). The vector ξ may contain information such as cellular mass, age, internal metabolites concentration, uptake capacity or any other variables of interest.

Rather than summing the contribution of each individual cell, the continuous formulation using density function is also possible

$$R\big(C(\vec{x},t)\big) = \int m(\vec{x},t,\xi)\, r(C(\vec{x},t),\xi)\,\mathrm{d}\xi \tag{1.25}$$

$m(\vec{x},t,\xi)\mathrm{d}\xi$ is the mass of cells per unit volume with the properties ξ. It is possible to calculate more than one cell property ξ. However, increasing the dimension of ξ increases the modelling and numerical challenges. It is not easy to access cell-scale information in experimental data. The initial multivariate distribution of biological state $m(\vec{x},0,\xi)$ is also hardly known, but strongly influences the evolution of microorganisms state over time (Pigou, 2018). The calculation of multidimensional integral is cumbersome.

In the end, the choice made for the formulation of the reaction term, discrete or continuous, is closely related to the description of biological phase in the fluid flow model. The discrete approach naturally coincides with a Lagrangian vision whereas the continuous approach naturally combines with a Eulerian approach.

Microorganisms modelled as Lagrangian particles follow liquid streamlines and for each trajectory, a set of ordinary differential equations that define the evolution of particle-attached properties is solved. The Lagrangian equations are expressed as:

$$\frac{\partial \vec{x}_{@p}}{\partial t} = \overrightarrow{u_L}(\vec{x}_{@p}) \tag{1.26}$$

$$\frac{\partial \xi_{@p}}{\partial t} = \mathrm{f}\left(\xi_{@p}, C_L\left(\vec{x}_{@p}\right)\right) \tag{1.27}$$

where:

- Subscript $@p$: variables attached to a Lagrangian particle
- $\vec{x}_{@p}$: location of a particle
- $\xi_{@p}$: vector of biological properties attached to a particle
- f: rate of change of cell properties ξ

Now, the advantages and disadvantages of Eulerian and Lagrangian approach for microbial analysis is addressed.

In the Eulerian approach, an ensemble average of all individuals is considered as the biological phase is represented by the concentration of each species. The behaviour of the population is described through an average individual of average composition. This may not be true as the dynamics of the population are not that of the average individual. The Lagrangian approach offers a wider possibility in terms of transfer and reaction aspects modelling. By following the trajectory of each cell, it gives access to the individual information and realises a statistical average at the population scale. The main interest of the Lagrangian approach is to describe the functioning of the biological system through a large number of variables. The effect of concentration variations (one-way coupling) seen along the trajectory of the cell is accessible easily by the Lagrangian approach (Haringa et al., 2017, 2016; Lapin et al., 2004). However, difficulties arise when describing the inverse-coupling whereby the liquid concentration field is modified due to assimilation or excretion by the microorganisms. This is due to the nature of the Lagrangian approach as the hydrodynamics/mass transfer/reaction coupling necessitates a sufficiently high number of distinct individuals in each control volume to ensure the statistical convergence of the ensemble average of the particles. From the practical point of view, the Lagrangian approach requires managing a high volume of files containing the particle trajectories. A high number of particles is necessary to ensure high local particle density for statistical averaging. This high density is essential to obtain statistical convergence and no skewed distribution. It is usually

achieved in small-scale reactors, and very rare in large-scale simulations. Another drawback of the Lagrangian approach is related to the modelling of the turbulence effect on the particle trajectory. If the Reynolds-averaged approach is applied to model the continuous phase velocities, a correct trajectory calculation should involve a model to calculate the turbulence-induced velocity fluctuations (Morchain, 2017). Table 1.5 summarises the direct comparison between the two approaches to describe the biological phase.

Table 1.5: Comparison of advantages and disadvantages of Eulerian and Lagrangian approach for the numerical simulation of bioreactor. Adapted from: Morchain (2017)

Approach	Eulerian	Lagrangian
One-way coupling	Simple and direct	Simple and direct
Inverse coupling	+ Phase transfer terms are explicit, easier to describe	- Requires a high number of particles per control volume
Biological model	- Structured model	+ No limitation in complexity or number of variables
Population heterogeneity	+ Accessible via the addition of a population balance equation	+ The global heterogeneity accessible starting from few thousands of particles
Numerical complexity	Stationary or transient simulations	Transient simulations - High computational costs
History effect	- No direct access to the particles' history	+ Individual knowledge of trajectories. Frequency analysis is possible

1.2.2.4 Compartment model approach

While CFD simulations yield a high spatial resolution of fluid flow, it tends to require high computation time. Another approach to cut down the computational cost of bioreactors study is the so-called compartment model approach (CMA). In the CMA model, the reactor's volume is split into N sub-volumes, referred to as compartments and each compartment is considered perfectly mixed (homogeneous and uniform concentration). A circulation map indicating the flow pattern circulating between these compartments is needed. The circulation map can be deduced from experimental data (Mayr et al., 1993; Vrábel et al., 1999; Zahradník et al., 2001) or from CFD simulations (Delafosse et al.,

2014; Le Moullec et al., 2010; Nadal-Rey et al., 2021a; Tajsoleiman et al., 2019). The compartments defined from CFD simulations can be identified either manually or automatically (zone segregation based on one or several properties that reached a constant value with respect to a given tolerance). The CMA model provides a basic understanding of the complex velocity flow field in a gross sense (Vrábel et al., 1999). It has been widely used in the literature for bioreactor modelling in regard to studying the mixing behaviour (Delafosse et al., 2010; Nadal-Rey et al., 2021a; Nauha, 2019; Pigou and Morchain, 2015; Vrábel et al., 1999). Figure 1.13 illustrates an example of the CMA model applied to an industrial 22 m^3 fermenter with the associated flowing pattern obtained through experimental observation. The CMA model was used to predict the mixing time and study the hydrodynamics of large-scale bioreactors (Vrábel et al., 2000, 1999).

The hydrodynamic model of an N compartments model is given by equation (1.28).

$$\frac{\partial C_i^n}{\partial t} = \sum_{m=1}^{N} \left(M_{m,n} C_i^m\right) - C_i^n \sum_{m=1}^{N} \left(M_{n,m}\right) + R_i + T_i \tag{1.28}$$

where:

- C_i^n: concentration of species i in compartment $n \in \{1, \dots, N\}$
- $M_{m,n}$: Volumetric flow matrix going from m-th compartment to the n-th one with m and $n \in \{1, \dots, N\}$
- T_i: gas-liquid mass transfer rate
- R_i : overall reaction rate

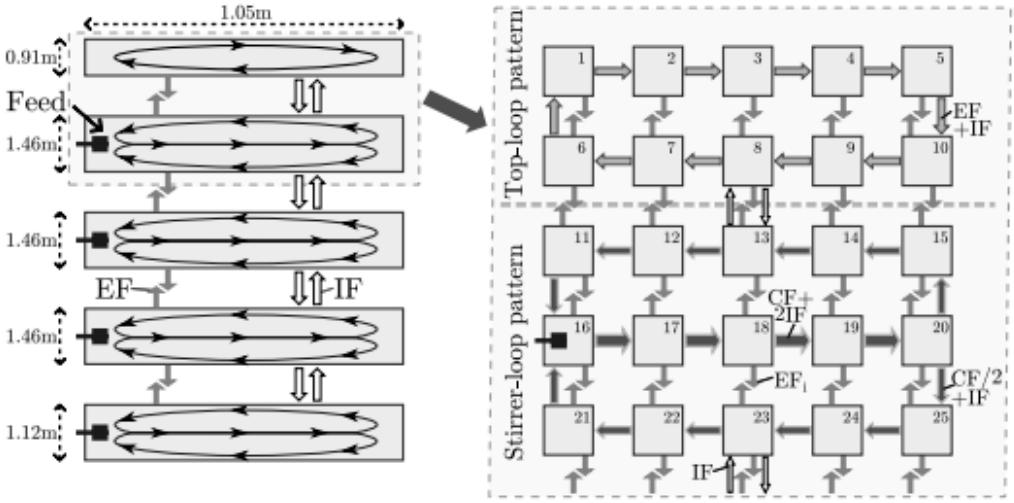

Figure 1.13: Representation of compartment model and flow pattern in a 22 m^3 fed-batch bioreactor. Adapted from: Vrábel et al. (1999)

1.2.2.5 1D model approach

For some multiphase flow problems, a complete 3D description is sometimes unnecessary as in bubble columns and airlifts (Camarasa et al., 2001; Cockx et al., 1997; Wallis, 1969). If the characteristic quantities vary essentially in the direction of the flow, the problem can be described using the 1D approach. The 3D mathematical description can be integrated across the cross-section to establish 1D conservation equations.

Supposed ε_k the spatial averaged of α_k by the surface-averaged operator $\langle\rangle$

$$\varepsilon_k = \langle \alpha_k \rangle = \frac{1}{S} \iint \alpha_k dS \tag{1.29}$$

For a given function F_k :

$$\varepsilon_k \langle F_k \rangle = \langle \alpha_k F_k \rangle = \frac{1}{S} \iint \alpha_k F_k dS \tag{1.30}$$

$$\varepsilon_k \langle u_k F_k \rangle = \langle \alpha_k u_k F_k \rangle = \frac{1}{S} \iint \alpha_k u_k F_k dS \tag{1.31}$$

To simplify the notation, $\langle F_k \rangle$ will be noted as F_k.

Notice that $\langle u_k F_k \rangle \neq \langle u_k \rangle \langle F_k \rangle$ if U_k and F_k are not distributed uniformly across the cross-section. If cross-sectional heterogeneity exists, a spatial dispersion term $\langle \widetilde{u_k} \widetilde{F_k} \rangle$ has to be considered as:

$$\langle u_k F_k \rangle = \langle u_k \rangle \langle F_k \rangle + \langle \widetilde{u_k} \widetilde{F_k} \rangle \tag{1.32}$$

In a 1D cylindrical bubble column, the radial homogeneity is often supposed, but the spatial dispersion can be estimated either by PIV experiments or by CFD simulation (Bauer and Eigenberger, 1999; Talvy et al., 2007a). The spatial averaging of the local continuity equation of equation (1.5), leads to

$$\frac{1}{S} \iint \frac{\partial \alpha_k \rho_k}{\partial t} + \frac{1}{S} \iint \nabla \alpha_k \rho_k u_k = \frac{1}{S} \iint \overline{m_k} \tag{1.33}$$

Assuming the flow is mainly in the direction of z, equation (1.33) is integrated to

$$\frac{\partial \varepsilon_k \rho_k}{\partial t} + \frac{\partial \varepsilon_k \rho_k u_k}{\partial z} = \langle \overline{m_k} \rangle \tag{1.34}$$

If the flow regime is in steady-state and no interfacial mass transfer between phases, equation (1.34) for a gas-liquid system can be simplified to

$$\varepsilon_G \rho_G u_G = cst = \rho_G \frac{Q_G}{S} = \rho_G j_G \tag{1.35}$$

$$\varepsilon_L \rho_L u_L = cst = \rho_L \frac{Q_L}{S} = \rho_L j_L \tag{1.36}$$

With j_G and j_L the superficial gas and liquid velocities, respectively.

The spatial averaging of the momentum equation (equation (1.6)) leads to

$$\begin{gathered} \frac{\partial \varepsilon_k \rho_k u_k}{\partial t} + \frac{\partial \varepsilon_k \rho_k \langle u_k u_k \rangle}{\partial z} = \\ \varepsilon_k \rho_k g - \frac{\partial \varepsilon_k P_k}{\partial z} + \frac{\partial}{\partial z}\left(\varepsilon_k \left[\overline{\tau_k} - \rho_k \left(\langle \overline{u_k' u_k'} \rangle + \langle \widetilde{u_k' u_k'} \rangle\right)\right]\right) + \langle \overline{u_k\, m_k} \rangle + \langle \overline{M_k} \rangle \end{gathered} \tag{1.37}$$

For the species concentration equation (equation (1.7)), the spatial averaging leads to

$$\frac{\partial \varepsilon_k C_k}{\partial t} + \frac{\partial \varepsilon_k \langle C_k u_k \rangle}{\partial z} = \varepsilon_k S_k + \frac{\partial}{\partial z}\left(\varepsilon_k \left(\langle \overline{J_k} \rangle + \langle \overline{c_k' u_k'} \rangle + \langle \widetilde{c_k' u_k'} \rangle\right)\right) + \langle \overline{c_k\, m_k} \rangle + \langle \overline{L_k} \rangle \tag{1.38}$$

Equations (1.34), (1.37), and (1.38) represents the 1D model after spatial averaging of the 3D model.

Noted that the spatial averaging of equations (1.6) and (1.7), additional terms due to the contribution of spatial dispersion appear in the RHS: $\langle \widetilde{u_k' u_k'} \rangle$ and $\langle \widetilde{c_k' u_k'} \rangle$. The second term at the RHS of equation (1.38) refers to the diffusive term due to molecular, turbulent and spatial diffusions. All these phenomena contribute to axial dispersions of the species concentration, and it is modelled as the axial dispersion term in the classical axial dispersion model. The last term at the RHS of equation (1.38) refers to interfacial mass transfer term which will be detailed in the next section.

1.2.3 Mass transfer modelling

In a bioreactor that functions either in aerobic or anaerobic conditions, gaseous bubbles are often sparged into the liquid to ensure growth, respiration or fermentation activities. The gas will then diffuse through the bubble interface towards the liquid phase. The gas-to-liquid mass transfer rate itself is dependent on the volumetric mass transfer coefficient ($k_L a$) and the concentration gradient defined as the difference between the equilibrium and the dissolved liquid concentration ($C^* - C_L$). The concentration gradient due to thermodynamic disequilibrium acts as the driving force for mass transfer. Most of the mass transfer resistance in bioreactors is encountered in the boundary layer near the bubbles represented by a gas-liquid film (Farzan et al., 2017). The volumetric gas-liquid mass transfer flux Φ_{GL} in mol.m^{-3}.s^{-1} is classically modelled as:

$$\Phi_{GL} = k_L a(C^* - C_L) \tag{1.39}$$

with

- k_L: liquid side mass transfer coefficient (m.s^{-1})
- a: volumetric interfacial area (m².m^3)
- C^*: equilibrium concentration (mol.m^{-3})
- C_L: liquid concentration (mol.m^{-3})

The volumetric specific area is a function of bubble diameter and gas holdup. Experimental measurements have shown that it exists a Bubble Size Distribution (BSD) in bubble columns (Colombet, 2012; Laupsien et al., 2019; McClure et al., 2013). Supposed $n_b(d_b)$ the distribution in a volume of reference V, the specific area for the BSD can be calculated as

$$\mathrm{a} = \frac{\int \pi d_b^2 n_b(d_b) \mathrm{d}d_b}{\int \frac{\pi}{6} d_b^3 n_b(d_b) \mathrm{d}d_b} \cdot \frac{Total\ bubble\ volume\ in\ V}{V} = \frac{6\alpha_G}{d_{32}} \tag{1.40}$$

d_{32} is the Sauter mean diameter and is an integral property of the BSD.

C^* can be calculated from Henry's law and it signifies a thermodynamic equilibrium between the liquid and the gas phase concentration. A library of Henry's constant for most of the gas components can be found form the work of Sander (2015). The Henry's constant varies with the temperature and it exists different expressions. Some expressions are more practical than others, depending on the formulation of the problem and application. For example, both Henry's constant defined in the units of mol.m^{-3}.Pa^{-}

[1] and dimensionless Henry's constant are used in this thesis. The dimensionless Henry's constant has the advantage to access directly the solubility of gas at a certain temperature and pressure.

The mass transfer coefficient k_L is controlled by both convection and diffusion phenomena at the gas-liquid interface. It exists a plentiful of theoretical analytical solutions and correlations in the literature to estimate k_L. Some of these correlations and the physical mechanisms are summarised in the work of Garcia-Ochoa and Gomez (2009), Rzehak (2016) and Solsvik (2018). The application of these correlations depends on different operating conditions. Most of the correlations take the form of:

$$Sh = a + b.Re^{c}.Sc^{d} \tag{1.41}$$

with

- $Sh = \frac{k_L.d_b}{D} = \frac{Convective\ mass\ transfer}{Diffusive\ mass\ transfer}$, Sherwood number
- $Re = \frac{u_{slip}.d_b}{\nu_L} = \frac{Inertial\ force}{Viscous\ force}$, Reynolds number
- $Sc = \frac{\nu_L}{D} = \frac{Momentum\ diffusivity}{Mass\ diffusivity}$, Schmidt number

a, b, c, d are the fitting parameters.

According to Huang et al. (2010), there are generally four categories of k_L models (i) correlations derived from dimensional analysis and after fitting with experimental data, (ii) spatial models such as the film model, (iii) time models such as Higbie's penetration model and (iv) combined film-penetration models. The correlations of Higbie (1935) and Frössling (1938) are considered the two asymptotic models of the mass transfer coefficient (Larsson et al., 2022). Higbie (1935) correlation is usually used for clean bubbles, whereas Frössling (1938) is used for contaminated bubbles. They are expressed as:

$$k_{L,Higbie} = \frac{D}{d_B}\left(\frac{2}{\sqrt{\pi}}Re^{0.5}Sc^{0.5}\right) \tag{1.42}$$

$$k_{L,Frossling} = \frac{D}{d_B}(2 + 0.66Re^{0.5}Sc^{0.33}) \tag{1.43}$$

with

- D: molecular diffusivity ($m^2.s^{-1}$)
- d_B: bubble diameter (m)

The Higbie (1935) correlation can be simplified to $k_{L,Higbie} = 2\sqrt{\frac{D}{\pi\theta}}$ whereby θ is the contact time between the bubble and the bulk liquid, estimated as the ratio of bubble diameter and the bubble slip velocity $\frac{d_B}{u_{slip}}$. The Higbie's model is usually used in gas-liquid bubbly flows, such as bubble column (Cockx et al., 1999; Rahimi et al., 2018; Talvy et al., 2007b) and airlift (Huang et al., 2010; Talvy et al., 2007b). Another approach to estimate the contact time is using the eddy cell model, proposed by Lamont and Scott (1970). Applying the Kolmogorov time scale of energy dissipation of small-scale eddies, the surface renewal time can be estimated by $\theta = \left(\frac{\nu}{\varepsilon}\right)^{0.5}$, where ν is the kinematic viscosity, ε is the turbulent energy dissipation rate. This model is commonly used in the simulation of mass transfer in a stirred-tank reactor (Bashiri et al., 2016; Linek et al., 2004; Prasher and Wills, 1973). For the calculation of k_L, it is often necessary to know the molecular diffusivity of the species. The molecular diffusivity and the Henry's constant are temperature dependent. Table 1.6 reports the molecular diffusivity, Henry's constant and the solubility of some common gases involved in bioprocess (Pauss et al., 1990; Sander, 2015).

Table 1.6: Physical data of different common gases

Gas	Molecular diffusivity ($cm^2.s^{-1}$)	Henry's constant at 25°C ($mol.m^{-3}.Pa^{-1}$)	Solubility ($mg.L^{-1}$) T=25°C, P=1atm, Pure water
O_2	1.98×10^{-5}	1.20×10^{-5}	38.91
H_2	4.65×10^{-5}	7.80×10^{-6}	1.58
CO_2	1.98×10^{-5}	3.30×10^{-4}	1471.24
CO	2.03×10^{-5}	9.70×10^{-6}	27.52
CH_4	1.57×10^{-5}	1.4×10^{-5}	22.70

The $k_L a$ is specific for a given reactor configuration and operating conditions. It is mainly dependent on the system's parameters, such as stirrer speed, gas recirculation, gas diffusion device, bubble size distribution, and the gassing rate. The concentration gradient ($C^* - C_L$) in a gas-limited culture, is dependent on the partial pressure of a gas in the gas phase which can be varied either over the fraction of that gas in the reactant gas or the pressure inside the reactor. The gas-liquid mass transfer in submerse cultures is influenced by several parameters, for example, reactor geometry, number, positioning and type of used stirrers, agitation, gas concentration, reactor pressure etc.

1.2.4 Bioreaction kinetics modelling

Bioreactors are more challenging to model compared to chemical reactors. Chemical reaction engineering is governed by a set of rigorous thermodynamics reactional schemes. In contrast, biological systems are more sensitive to exogenous perturbations and therefore it is more difficult to describe and predict biological behaviour. In terms of metabolisms, two distinctions of the model can be made (Gernaey et al., 2010; Pigou, 2018):

- Kinetic/metabolic model
- Structured/unstructured model (with the use of intracellular activities/without)

Kinetic models are constant yield models of a simple pseudo-reaction. They do not account for the actual complex metabolism network of the micro-organisms. They are formulated based on the hypothesis of balanced growth during which the biomass concentration remains constant. Thus, small-scale biological phenomena are filtered/averaged and provide information about the growth scale (Morchain, 2017).

Conversely, metabolic models rely upon a description of the metabolic network/pathway and from the material fluxes entering and exiting the cell to calculate the specific substrate consumption rates and the metabolite production rates. The yield of each reactional pathway is known but the distribution of substrate flow results in a global conversion yield varying as a function of the external environment and internal physiological state.

Structured models track the intracellular attached quantities, for example, internal composition, and physiology parameters (size, mass, age, etc.). Structured models describe the evolution of the microorganisms' properties, hence making a distinction between the liquid-phase compounds and the intracellular compounds.

The unstructured model is derived from mass balance conservation equations, resulting from a double averaging in time and space. This offers a global average description of the population, using an apparent kinetic rate. Without any distinction between the individuals, this makes the unstructured model more suitable for quasi-steady state simulations. Under transient conditions, the model failed to give reasonable predictive results. The presence of concentration gradients often hinders the metabolic functionality of the cells as they travel through fluctuating concentration signals. The metabolic dysfunction will lead to the over-assimilation of substrates, the formation of by-products, and eventually an overall reactor dysfunction (Pigou and Morchain, 2015). This is usually the case for

large-scale industrial reactors where resources could be depleted in certain zones, making the use of Monod kinetic law inappropriate for this type of modelling.

1.2.4.1 Unstructured kinetic model

The unstructured kinetic model describes biomass without reference to its internal composition. It is analogue to the chemical kinetics model in the homogeneous phase. They rely on an algebraic relationship between liquid-phase concentrations and growth rates. The growth rate is often defined using Monod-type law (Monod, 1950). Consider the following pseudo-reaction:

$$Y_{S/X}S + Y_{O_2/X}O_2 \xrightarrow{\mu} X + Y_{P/X}P \tag{1.44}$$

with S: substrate, O_2: oxygen, X: biomass and P: product. $Y_{A/\mathrm{B}}$: the conversion yield of A to B. The specific growth rate, μ of equation (1.44) formulated by Monod's law is expressed as:

$$\mu = \mu_{max}\frac{C_{L,S}}{K_S + C_{L,S}}\frac{C_{L,O_2}}{K_{O2} + C_{L,O_2}} \tag{1.45}$$

with μ_{max} : maximum specific growth rate without limiting factor, K_S and K_{O2}: respective saturation constant of the substrates and the oxygen.

The corresponding consumption or production rates (R_i expressed as $g_i/g_X/h$) of S, O_2, X and P can be expressed with μ according to the set of following equations

$$r_X = \mu X\ (Biomass\ growth) \tag{1.46}$$

$$r_S = -\frac{\mu}{Y_{X/S}}X\ (Substrate\ consumption) \tag{1.47}$$

$$r_{O2} = -\frac{\mu}{Y_{O2/S}}X\ (Oxygen\ consumption) \tag{1.48}$$

$$r_P = -\frac{\mu}{Y_{P/S}}X\ (Product\ formation) \tag{1.49}$$

Monod's model assumes that the growth rate is limited by the enzymatic kinetics of the substrates' metabolism. If several substrates $i \in \{1, \dots, n\}$ are assimilated by the cell, the formulation of Monod's law is extended to equation (1.44), expressed as the product of the hyperbolic functions.

$$\mu = f(C_{L,i}) = \prod_{1<i,n} \frac{C_{L,i}}{K_i + C_{L,i}} \tag{1.50}$$

If the microorganism has several growth modes, according to different chemical compounds and/or metabolisms, a function $\alpha(C_{L,i})$ can be used to describe the switching between growth modes, as expressed in equation (1.51).

$$\mu = \alpha(C_{L,i})\mu_1 + \left(1 - \alpha(C_{L,i})\right)\mu_2 \tag{1.51}$$

The unstructured kinetic model such as Monod's model is based on the algebraic relationship between liquid concentration and growth rate. As the notion of dynamics is absent in the biological system, it is also named as equilibrium model or zero-equation model (Morchain, 2017). The main advantage of the model is its simplicity and it is used particularly to monitor bioreactors in steady-state or pseudo-steady state conditions. However, care must be taken for the fact that no distinction is made between the microorganisms.

1.2.4.2 Unstructured metabolic model

The unstructured metabolic model depends solely on the metabolic model and the environmental conditions. Most microorganisms are able to assimilate different carbon sources for growth, depending on the availability of the substrates, thus resulting in various global conversion yields. A notable example includes the baker's yeast fermentation model of Sonnleitner and Käppeli (1986) and the *E. Coli* growth model of Xu et al. (1999). These models state that the microorganism will yield different behaviour, depending on the environmental conditions. The switch of these behaviours is defined by biological constants and local concentrations, hence the unstructured aspect of this model.

1.2.4.3 Structured kinetic model

The structured kinetic model tracks the internal properties of the cell to predict the bioreaction kinetics. The internal properties can be the composition, intracellular processes rate, and physiology. Simple tracking of an intracellular component can be used to relate the average specific growth rate to the mean specific synthesis rate of the main constituents of the cell. Morchain and Fonade (2009)

developed a structured biological model which can be easily coupled with any hydrodynamic model to simulate a spatially heterogeneous bioreactor. The originality of the model is the ability of the biological systems to adapt to the concentration fluctuations in the environment. It deployed an internal variable to compute the growth rate of the population according to its environment. The actual growth rate of the individual is defined as the minimum of the biological and equilibrium growth rate $\mu_a = \min(\mu^b, \mu^0)$. Later, Morchain et al. (2013) applied a coupled population balance model (PBM) and structured kinetic model to account for biological heterogeneity. The PBM was implemented in the CFD code FLUENT and the total biomass and substrate profiles are well captured. Besides, the dynamic changes in the population-specific growth rate according to the environment can be observed.

1.2.4.4 Structured metabolic model

The structured metabolic model tracks the internal properties of the cell, and the latter is used to identify the metabolic pathway used and define eventually the reaction rate. For example, the model can track internal metabolic regulations, metabolites' availability, and cell-cycle effects. This type of model is the most seen for cell modelling in the literature. The biological rate described using this model can be computed in different ways, but the most common being (Pigou, 2018):

- Use of kinetic expressions based on internal concentrations.
- Optimisation algorithm aiming at maximising one rate or yield, usually the growth rate.
- Decision tree-based closure (Sweere et al., 1988)

1.2.4.5 Existing work on ex-situ biological methanation model

In the literature, we found two numerical models describing the ex-situ biological methanation process. The first work consists of a 1D axial dispersion model applied to a stirred-tank reactor coupled with Monod-type biological kinetics to model biological methanation (Inkeri et al., 2018). The second work is related to a CFD simulation of a trickle-bed reactor coupled with an Arrhenius-type heterogeneous reaction model for biological methanation (Markthaler et al., 2020). For the model of Inkeri et al. (2018), an unstructured kinetic Monod-type model based on the biological kinetics described by Schill et al. (1996) is applied. Schill et al. (1996) proposed the following growth and maintenance reactions, respectively:

$$H_2 + Y_{CO_2/H_2} CO_2 + Y_{NH_3/H_2} NH_3 \rightarrow Y_{X/H_2} X + Y_{CH_4/H_2} CH_4 + Y_{H_2O/H_2} H_2O \quad (1.52)$$

$$4\mathrm{H}_2 + CO_2 \rightarrow CH_4 + 2H_2O \tag{1.53}$$

In the end, the hydrogen uptake rate was given in Inkeri et al. (2018) as

$$\mathrm{r}_{\mathrm{H}_2} = q_{max} \frac{C_{L,H_2}}{K_{s,H_2} + C_{L,H_2}} X \frac{C_{L,CO_2}}{10^{-3} + C_{L,CO_2}} \tag{1.54}$$

Equation (1.54) resembles the Monod-type description of H_2 substrate uptake. However, the $\frac{C_{L,CO_2}}{10^{-3}+C_{L,CO_2}}$ term remains questionable. It is reported by the author that it corresponds to an additional factor that limits the reactions when CO_2 is lacking. However, CO_2 is rarely lacking as it is more soluble than H_2. In the case when C_{H_2} approaches zero, as if the case of the mass transfer limiting regime if the $\mathrm{r}_{\mathrm{H}_2}$ term is given as $= q_{max} \frac{C_{L,H_2}}{K_{s,H_2}+C_{L,H_2}}$, numerical instabilities are awaited. This is due to the nature of Monod's law which is a hyperbolic function. It is believed that the $\frac{C_{L,CO_2}}{10^{-3}+C_{L,CO_2}}$ term act as a damper to smooth the numerical issue.

Markthaler et al. (2020) applied an Arrhenius-type model to represent the biological methanation. It is expressed as

$$R_{H_2} = A_0 . e^{\frac{-E_A}{R.T}} . C_{L,CO_2} . C_{L,H_2} \tag{1.55}$$

The authors explained that since the major microkinetic limitation of biological methanation ensues from interfacial H_2 mass transfer, the implementation of detailed reaction mechanisms plays a minor role. Thus, the preexponential factor A_0 and activation energy E_A were simply adjusted to very high reaction kinetics so that the overall process is limited by absorption.

The model of Inkeri et al. (2018) and Markthaler et al. (2020) consists of a homogeneous reaction problem formulation. It is clear that the biological methanation process depends on the convective and diffusive species transport and specific biological uptake rate, the biomass is a heterogeneous catalyst. Therefore, the bioreaction rate should be treated by a classical chemical engineering approach based on the rate-limiting flux. This is further detailed in our model, as explained in Section 2.2.3.

1.3 Two-phase flow modelling of bubble column

In this section, a brief review of bubble column reactors is detailed. Bubble column reactors are commonly used in the industry, such as metallurgical, petrochemical, biochemical, and water treatment. These reactors have numerous advantages: (a) simple design, (b) absence of a mechanical stirring device (c) good mixing (d) low energy input requirements and (e) large gas-liquid contact area (Deckwer and Schumpe, 1993; Kantarci et al., 2005; Shah et al., 1982). Many topics regarding bubble columns have attracted considerable interest in the literature, including gas-liquid or gas-liquid-solid hydrodynamics, mass transfer and (bio)reactive bubbly flow. Bubble column modelling becomes an important issue for design and industrial process optimisation. However, complex and highly coupled phenomena in terms of multiphase flow, mass and heat transfer, and (bio)reaction prevail in such system, making the modelling of bubble columns very challenging.

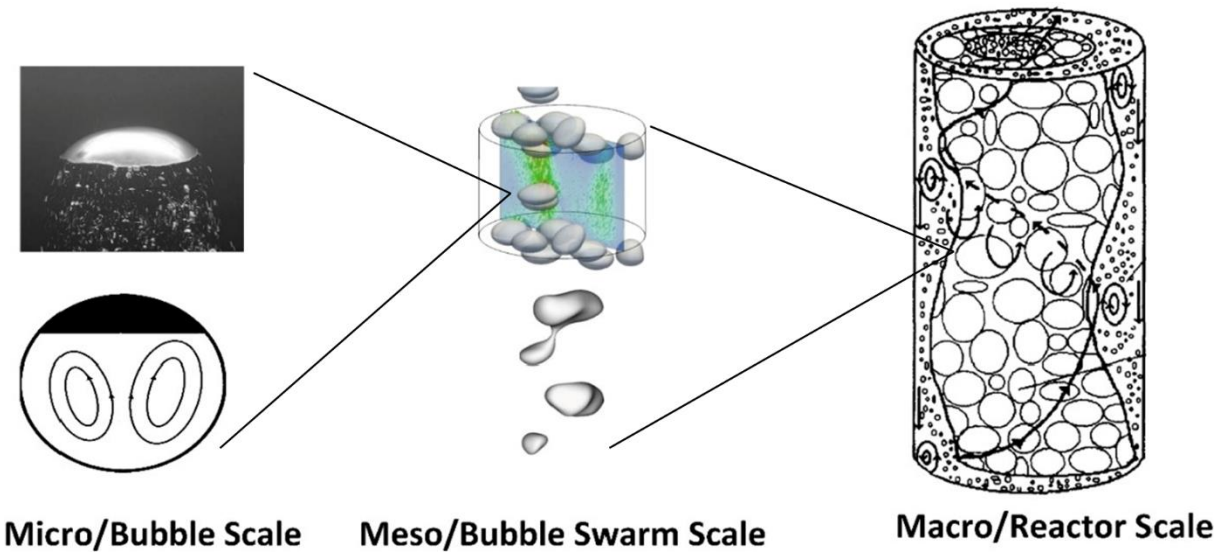

Figure 1.14: The multiscale phenomena of bubbly flow occurring in bubble column. Adapted from: Shu et al. (2019)

In terms of hydrodynamics, the complexity arises as the overall gas holdup and mixing time involves phenomena occurring at the micro-scale (bubble coalescence and breakage), meso-scale (bubble-bubble interaction), and macro-scale (large-scale liquid recirculation), as shown in Figure 1.14 (Shu et al., 2019). For a gas-liquid two-phase bubble column, the gaseous phase is the disperse phase injected via a sparger and the continuous phase is the liquid. The liquid phase can operate in batch mode, co-courant and counter-courant flow, with recirculation of either gas or liquid or both. Bubble column hydrodynamics is controlled by its geometry and the operating conditions, mainly the superficial gas

velocity j_G. The bubble column hydrodynamics and mass transfer are partly related to its global gas holdup, formulated as the ratio of the volume of gas to the reactor volume.

$$\alpha_G = \frac{V_G}{V_G + V_L} \tag{1.56}$$

1.3.1 Flow regime

Depending on the superficial gas velocity and the reactor geometry, several flow regimes can be differentiated with their respective flow characteristics. Krishna (2000) classifies the bubble column hydrodynamics into three main regimes: homogeneous, transition and heterogeneous, as depicted in Figure 1.15.

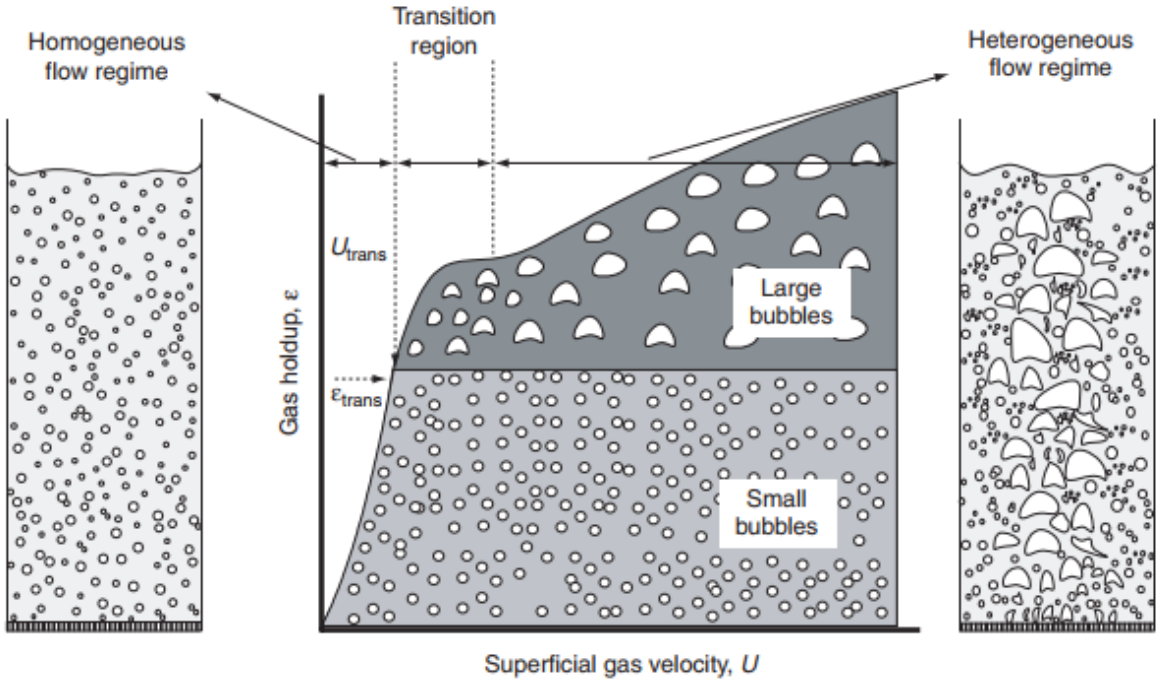

Figure 1.15: Flow regime in bubble column. Adapted from: Krishna (2000)

At low superficial gas velocity, the bubble column operates at the so-called homogeneous regime, which is also called the bubbly regime. The bubbles are mostly spherical in shape and their path is quite linear. The bubble break-up and coalescence are negligible here. The global gas holdup is quasi-linear versus the superficial gas velocity. The bubble size population are mostly homogeneous with a very narrow bubble size distribution. If the superficial gas velocity is further increased, the global gas holdup will reach a local maximum, and the transition regime is established. Large bubbles start to appear in the centre of the column rising in a helical form with liquid recirculation down the column near the

wall to have a net liquid downward flow. Finally, the heterogeneous regime appears at high superficial gas velocity. Two classes of bubbles are very visible with the large bubbles rising at higher velocities at the centre of the column, whereas smaller bubbles are found near the wall, entrained by the down flow of liquid recirculation. Shah et al. (1982) also proposed a regime map that stated that the hydrodynamic regime depends on the column diameter and the superficial gas velocity, as shown in Figure 1.16.

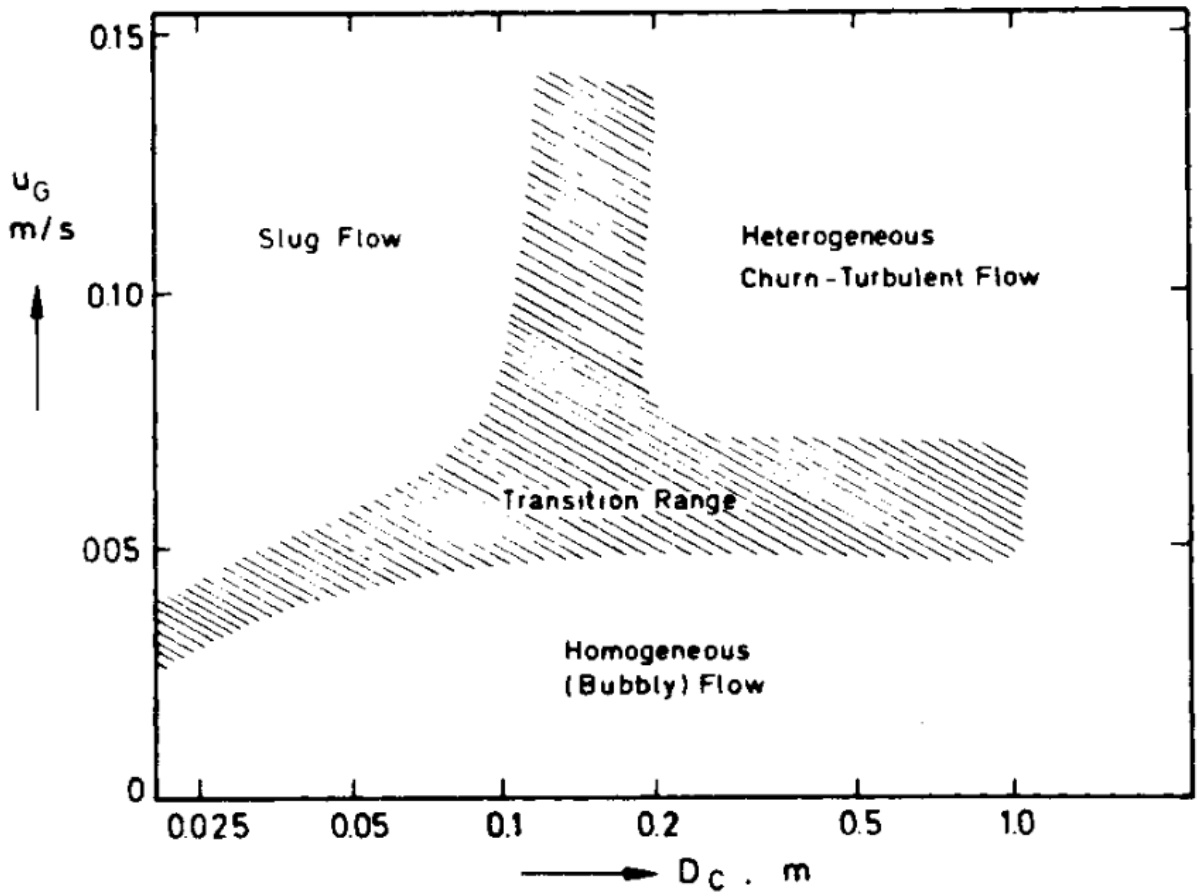

Figure 1.16: Bubble column flow regime dependency on superficial gas velocity and column diameter. Adapted from: Shah et al. (1982)

However, it is found that the hydrodynamic regime is more complicated and depends on other additional parameters. For example, McClure et al. (2016b, 2015d) explained that the overall gas holdup also depends on the sparger design and the liquid physicochemical properties. The authors tested a tree sparger design but with three different configurations: sparger #1 (sparger with 0.5 mm orifices), sparger #2 (sparger with 3 mm orifice), sparger #3 (sparger with 0.5 mm orifices but with half activated). It is also found that in the heterogeneous regime (at high superficial gas velocity), the sparger design does not play any role in the hydrodynamic as the gas holdup is the same. At low

superficial gas velocity (i.e., in the homogeneous regime), the sparger #1 holds a much higher gas holdup. It is explained by the formation of smaller bubbles and the interactions between bubbles lead to the hindered rise of bubbles, resulting in a much higher gas holdup. This observation is also reported by Chaumat et al. (2006) and (Colombet et al., 2015). When surfactants are present in the liquid, the bubble size distribution becomes narrower, leading to smaller mean bubble size. The surfactant also inhibits bubble coalescence. These effects lead to higher gas holdup in a liquid system with the addition of surfactant such as 2-propanol. These results are presented in Figure 1.17.

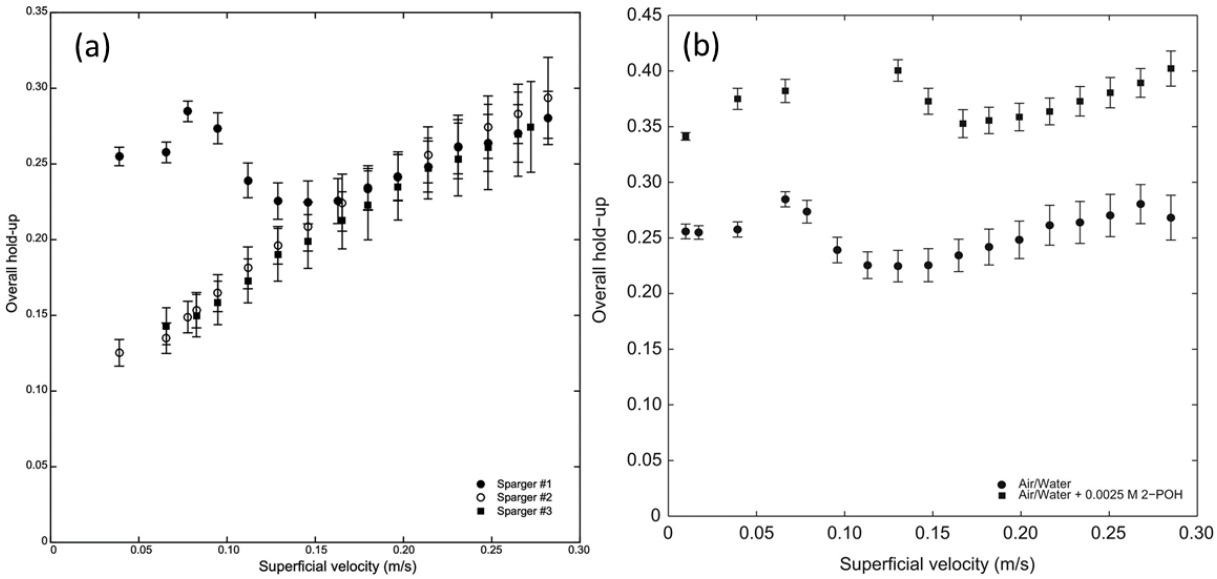

Figure 1.17: (a) Hydrodynamic regime depends on the sparger design. Adapted from: McClure et al. (2016b). (b) Effect of liquid physicochemical properties on the bubble column hydrodynamics. Adapted from: McClure et al. (2015d)

1.3.2 Bubble shape and size

The understanding and the study of bubble size is still a recurrent research topic due to its importance in bubble column hydrodynamics and mass transfer. The bubble size changes with the break-up and coalescence phenomena. But, its shape can be predicted with the bubble regime map proposed by Clift et al. (1978), as shown in Figure 1.18, using three dimensionless numbers: Reynolds number, Eötvös number and Morton number (see the respective definitions in equations (1.14)-(1.16)). The bubble shape depends on the superficial gas velocity and the flow regime. The regime map proposed by Clift et al. (1978) gives a general idea of the bubble shape and bubble terminal velocity provided the liquid properties are known.

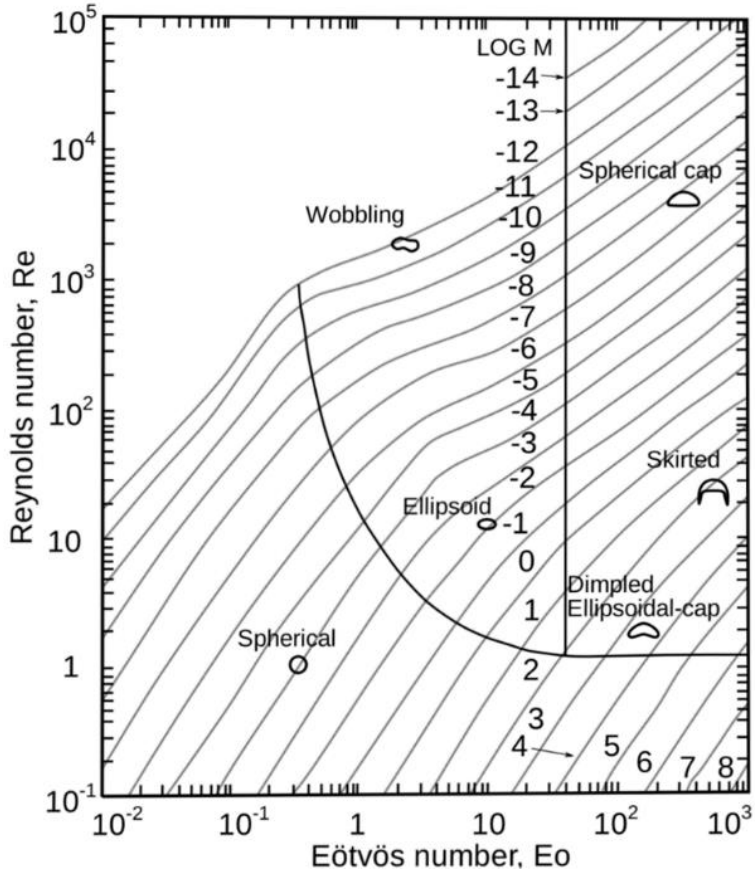

Figure 1.18: Bubble shape regime map in unhindered gravitational motion. Adapted from: Clift et al. (1978)

The sparger design is very important as it determines largely the initial bubble size, and thus the bubble rise velocity (Kulkarni and Joshi, 2011). Different types of sparger designs have been studied in the literature to determine the hydrodynamics and mass transfer properties, such as tree sparger, ring sparger, spider sparger, porous plate, perforated plate, and needle sparger. These spargers can be classified into two major categories: plate-type spargers and pipe-type spargers (Kulkarni and Joshi, 2011). At a given superficial gas velocity, these spargers will produce different bubble sizes and flow regimes, depending on the uniformity of gas injection, the pore size, and the number of holes (Besagni et al., 2018a; Sharaf et al., 2016; Veera and Joshi, 1999). In this section, some correlations for the prediction of the initial bubble diameter are presented.

One of the most common spargers is the orifice-type sparger. In the literature, it exists numerous correlations to estimate the bubble size generated by an orifice sparger. These expressions are derived mostly from the physical mechanisms controlling the forming of the bubbles. In general, three regimes of bubble formation can be distinguished: quasi-static, dynamic bubbling and inertial jet formation regimes (Colombet, 2012).

At very low superficial gas velocity, the bubble formation is under a quasi-static regime. The force balance between the buoyancy force and capillary force of a single bubble leads to Tate's law:

$$\frac{\mathrm{d_b}}{d_o} = \left[\frac{6\sigma}{d_o^2 \Delta\rho g}\right]^{1/3} = \left[\frac{6}{Eo_o}\right]^{1/3} \tag{1.57}$$

With Eo_o the Eötvös number (equation (1.15)) at the orifice, d_o the diameter of the orifice.

The transition from quasi-static regime to dynamic bubbling regime is observed when the flow exceeds a critical value, characterised as the critical superficial gas velocity:

$$\mathrm{u}_{crit} = \frac{4}{d_o^2}\left(\frac{16}{3g^2}\right)^{1/6}\left(\frac{\sigma d_o}{2\rho_L}\right)^{5/6} \tag{1.58}$$

Under the dynamic bubbling regime, Gaddis and Vogelpohl (1986) proposed an expression for initial bubble diameter, following the integration of buoyancy force, capillarity force, added-mass, and drag force:

$$\frac{\mathrm{d_b}}{d_c} = \left[\left(\frac{6\sigma}{d_o^2 \Delta\rho g}\right)^{4/3} + \frac{81}{\pi}\frac{\nu_L Q_o}{g d_o^4} + \left(\frac{135 Q_o^2}{4\pi^2 g d_o^5}\right)^{4/5}\right]^{1/4} \tag{1.59}$$

With Q_o the gas volumetric flow rate passing through the orifice. Equation (1.59) can be written in dimensionless form as:

$$\frac{\mathrm{d_b}}{d_c} = \left[\left(\frac{6}{Eo_o}\right)^{4/3} + \frac{81}{\pi}\left(\frac{Fr_o}{Ar_o}\right)^{1/2} + \left(\frac{135 Fr_o}{64}\right)^{4/5}\right]^{1/4} \tag{1.60}$$

With Fr_o the orifice Froude number, Ar_o the orifice Archimedes number.

Under the inertial jet formation regime, the bubble diameter can be estimated with the correlation written as:

$$\frac{\mathrm{d_b}}{d_c} = C_2 Fr_o^{1/5} \tag{1.61}$$

In the literature, different values of C_2 have been proposed, ranging from 1.12 – 1.35. But, an arbitrary mean value of 1.2 can be taken as an estimation (Colombet, 2012).

Other correlations for the prediction of the initial bubble diameter for the orifice sparger are reported in Table 1.7. Most of these correlations described the bubble diameter with the orifice diameter d_o

and the orifice superficial gas velocity j_{Go}. Among the correlations in Table 1.7, only that of Bhavaraju et al. (1978) considers the properties of the liquid phase instead of the gas phase. The complex correlation of Geary and Rice (1991) is actually derived from the force balance and it is valid also for rigid and flexible sparger.

The inlet bubble diameter usually does not retain its initial size due to hydrostatic pressure and breakup and coalescence events. Some authors proposed the correlations for the prediction of the mean bubble diameter $\overline{d_b}$ which is also called generally the Sauter mean diameter d_{32}. Table 1.8 summarises the correlation for mean bubble diameter prediction. Most of the correlations show the dependence with superficial gas velocity j_G, with the predicted mean bubble diameter increasing with j_G. The liquid properties such as viscosity and surface tension are also included in the correlations. The pressure effect is evidenced in the correlation of Wilkinson et al. (1994) whereby it is translated with the gas density ρ_G. The higher the pressure, the higher the gas density, and the lower the mean bubble diameter. Jamialahmadi et al. (2000) related the mean bubble diameter to the initial bubble diameter.

Table 1.7: Correlations for initial bubble diameter $\mathbf{d_{b0}}$ prediction. Adapted from: Azizi et al. (2019)

Reference	Correlation
Leibson et al. (1956)	$\mathrm{d_{b0}} = 0.18 d_0^{1/2} \left(\frac{\rho_G j_{G0} d_0}{\mu_G}\right)^{1/3}$ for $\frac{\rho_G j_{G0} d_0}{\mu_G}$ <2000
Miller (1974)	$\mathrm{d_{b0}} = \left(\frac{6\sigma d_0^{0.48}}{\Delta\rho g}\right)^{1/3}$
Bhavaraju et al. (1978)	$\mathrm{d_{b0}} = 3.23 d_o \left(\frac{\rho_L j_{G0} d_0}{\mu_L}\right)^{-0.1} \left(\frac{\pi j_{Go}^2/4}{g d_o^3}\right)^{0.21}$
Moo-Young and Blanch (1981)	$\mathrm{d_{b0}} = 0.19 d_0^{0.48} \left(\frac{\rho_G j_{G0} d_0}{\mu_G}\right)^{0.32}$
Geary and Rice (1991)	$y = \frac{d_i^3}{d_o^3}$ $\frac{0.5g\left(\frac{d_{b0}^3}{6}\right)^2}{11(d_o^2 j_{G0})^2}(y^2 - 1 - 2\ln y) + N_r(y - 1 - \ln y) - 2$ $- N_\mu\left(2\left(y^{1/2} - 1\right) - \ln y\right)$ $- \frac{2\left(\frac{\pi d_{b0}^3}{6}\right)^{1/3}}{d_o}\left(\frac{1}{36\pi}\right)^{1/6}\left(3\left(y^{1/3} - 1\right) - \ln y\right) = 0$

	$N_r = \frac{32}{11}\frac{\pi d_{b0}^3/6}{\rho_L(\pi d_o^2 j_{G0})^2 d_o}\left(\frac{\pi d_o^2 j_{G0}^2 \rho_G}{4} - \pi\sigma d_o\right)$ $N_\mu = \frac{128}{11}\frac{\sqrt[5]{\pi d_{b0}^3/6}}{d_o^3 j_{G0}}\sqrt{\frac{2\mu_L}{\rho_L}}\left(\frac{d_o^2 j_{G0}}{16}\right)^{3/2}\left(\frac{4\pi}{3}\right)^{1/2}$

Table 1.8: Correlations of mean bubble diameter $\overline{d_b}$ prediction. Adapted from: Azizi et al. (2019)

Reference	Correlation
Akita and Yoshida (1973)	$\overline{d_b} = 26D\left(\frac{D^2 g\rho_L}{\sigma}\right)^{-0.5}\left(\frac{j_G D^3 \rho_L^2}{\mu_L}\right)^{-0.12}\left(\frac{j_G}{\sqrt{gD}}\right)^{0.12}$
Wilkinson et al. (1994)	$\overline{d_b} = \left(8.8\frac{\sigma}{\rho_L g}\right)^{0.5}\left(\frac{j_G\mu_L}{\sigma}\right)^{-0.04}\left(\frac{\sigma^3\rho_L}{g\mu_L}\right)^{-0.12}\left(\frac{\rho_L}{\rho_G}\right)^{0.22}$
Jamialahmadi et al. (2000)	$\overline{d_{bl}} = \left(\frac{6\sigma d_0^{0.48}}{\Delta\rho g}\right)^{1/3}$ $\overline{d_t} = 0.45 j_G^{0.87}\alpha_G^{0.85}$ $\overline{d_b} = \sqrt[3]{\overline{d_{bl}}^3 + \overline{d_t}^3}$
Kumar et al. (1976)	$\overline{d_b} = \begin{cases} 1.56\left(\frac{\rho_G j_{G0} d_0}{\mu_G}\right)^{0.058}\left(\frac{\sigma d_0^2}{\Delta\rho g}\right)^{0.25}, 1 < \frac{\rho_G j_{G0} d_0}{\mu_G} < 10 \\ 0.32\left(\frac{\rho_G j_{G0} d_0}{\mu_G}\right)^{0.425}\left(\frac{\sigma d_0^2}{\Delta\rho g}\right)^{0.25}, 10 < \frac{\rho_G j_{G0} d_0}{\mu_G} < 2100 \\ 100\left(\frac{\rho_G j_{G0} d_0}{\mu_G}\right)^{-0.4}\left(\frac{\sigma d_0^2}{\Delta\rho g}\right)^{0.25}, 4000 < \frac{\rho_G j_{G0} d_0}{\mu_G} < 70000 \end{cases}$

1.3.3 Bubble dynamics

After examining the bubble diameter size, it is interesting to discuss the bubble dynamics, particularly the forces encountered by the bubble. In equation (1.6), the $\overrightarrow{M_k}$ term represent the interfacial momentum exchange between the gas and liquid phase. This momentum transfer is only considered between the gaseous bubbles and the surrounding liquid. This momentum transfer between phases can be modelled as the following forces per unit volume:

$$\overrightarrow{M_G} = -\overrightarrow{M_L} = \overrightarrow{f_B} + \overrightarrow{f_D} + \overrightarrow{f_{VM}} + \overrightarrow{f_L} \tag{1.62}$$

With

- $\overrightarrow{f_B}$ = buoyancy force resulting from density difference

$$\overrightarrow{f_B} = (\rho_L - \rho_G)\vec{g} \tag{1.63}$$

- $\overrightarrow{f_D}$ = drag force is the force oppose to buoyancy force, usually results from the pressure and viscous effect on the gas-liquid interface

$$\overrightarrow{f_D} = F_D(\overrightarrow{u_L} - \overrightarrow{u_G}); F_D = \frac{18\mu_L}{d_b^2}\frac{C_D Re_b}{24} \tag{1.64}$$

C_D is the bubble drag coefficient.

- $\overrightarrow{f_{VM}}$ = added mass force originated from the relative acceleration between gas and liquid

$$\overrightarrow{f_{VM}} = C_{VM}.\rho_L(\frac{\partial\overrightarrow{u_L}}{\partial t} - \frac{\partial\overrightarrow{u_G}}{\partial t}) \tag{1.65}$$

C_{VM} is the added mass coefficient, which is usually 0.5.

- $\overrightarrow{f_L}$= lift force comes into effect with the presence of high shear flow, and the unbalanced distribution of pressure and viscous constraint.

$$\overrightarrow{f_L} = C_L.\rho_L.\rho_G(\overrightarrow{u_L} - \overrightarrow{u_G}) \times (\vec{\nabla} \times \overrightarrow{u_L}) \tag{1.66}$$

C_L is the lift force coefficient, which is equals to 0.5 for high Re number. For 10 < Re < 500, the following equation can be used for C_L (Legendre and Magnaudet, 1998).

$$C_L = \frac{1}{2} - \frac{6.5}{Re_b} \tag{1.67}$$

The drag force merits further discussion as it is considered the most important force in describing the two-phase bubbly flow. It determines the bubble slip velocity, and therefore the gas holdup and the volumetric interfacial area. The drag force varies according to the bubble shape, contamination level and gas volume fraction.

For a single spherical bubble rising at its terminal velocity, the equilibrium between the drag force and the buoyancy force leads to

$$0 = (\rho_G - \rho_L)V_b g - A_p C_D \frac{1}{2}\rho_L \left|\left|\overrightarrow{u_{rel}}\right|\right|\overrightarrow{u_{rel}} \tag{1.68}$$

With $\overrightarrow{u_{rel}}$ the relative bubble velocity. This equality leads to bubble terminal velocity and the drag coefficient is expressed as

$$\mathrm{C_D} = \frac{4}{3}\frac{\Delta\rho g d_b}{\rho_L u_r^2} \tag{1.69}$$

The C_D correlation can be obtained from experimental observation or numerical simulation. Table 1.9 reports the drag coefficient for spherical bubbles found in the literature.

Table 1.9: Correlation for drag coefficient of spherical bubbles

Range of Re	Correlation	Reference
$Re_b \ll 1$	$\frac{16}{Re_b}$	Hadamard (1911)
$Re_b \leq 1$	$\frac{16}{Re_b}(1+\frac{1}{8}Re_b+\frac{1}{40}Re_b^2\ln(Re_b)+O(Re_b^2)$	Taylor and Acrivos (1964)
$Re_b \gg 1$	$\frac{48}{Re_b}$	Levich (1962)
$Re_b > 50$	$\frac{48}{Re_b}\left(1-\frac{2.211}{Re_b}\right)$	Moore (1963)
$\forall\, Re_b$	$\frac{16}{Re_b}\left(1+\frac{Re_b}{8+0.5(Re_b+3.315Re_b^{0.5})}\right)$	Mei et al. (1994)

In the case of isolated small spherical bubbles without deformation (Re << 1), Stokes equation can be used to estimate the terminal velocity (Stokes, 2005):

$$u_{rel} = \frac{1}{18}.\frac{\Delta\rho.g.d_b^2}{\mu_L} \tag{1.70}$$

For non-spherical bubbles, the drag coefficient depends generally on the Reynolds number, Eötvös number, Morton number and the contamination level.

For an air-ParathermNF system and for an operating condition of $1 \leq P \leq 193$ bar and $T = 27 - 47 - 78$°C, Fan et al. (1999) validated the following empirical expressions for three bubble regimes: spherical, ellipsoidal and cap bubbles.

$$\mathrm{u_{rel}} = \left(\frac{\sigma g}{\rho_L}\right)^{0.25}\left[\left(\frac{Mo^{-0.25}}{K_b}\left(\frac{\Delta\rho}{\rho_L}\right)^{1.25}d'^2\right)^{-n}+\left(\frac{2c}{d'}+\frac{\Delta\rho d'}{2\rho_L}\right)^{-\frac{n}{2}}\right]^{-1/n} \tag{1.71}$$

with

- $d' = d_b \left(\frac{\rho_L g}{\sigma}\right)^{0.5}$
- $n = 0.8$ for contaminated system, $n = 1.6$ for pure system
- $c = 1.2$ for one liquid component and $n = 1.6$ for multi liquid component
- $K_b = \max(K_{b0} Mo^{-0.038}, 12)$
- $K_{b0} = 14.7$ for aqueous solution, $K_{b0} = 10.2$ for organic solution

Another correlation for relative velocity of non-spherical bubble proposed by Mendelson (1967) is expressed as

$$\mathrm{u_{rel}} = \sqrt{\frac{2\sigma}{\rho_L d_b} + \frac{\Delta\rho g d_b}{2\rho_L}} \tag{1.72}$$

Dijkhuizen et al. (2010) derived the drag coefficient for both spherical and non-spherical bubble as

$$\begin{aligned} \mathrm{C_D} &= \sqrt{C_D(Re_b)^2 + C_D(Eo)^2} \\ C_D(Re_b) &= \frac{16}{Re_b}\left(1 + \frac{Re_b}{8 + 0.5\left(Re_b + 3.315 Re_b^{0.5}\right)}\right) \\ C_D(Eo) &= \frac{4Eo}{9.5 + Eo} \end{aligned} \tag{1.73}$$

With $C_D(Re_b)$ issued from the correlation of Mei et al. (1994). Equation (1.73) is obtained through 3D Direct Numerical Simulation (DNS) of rising bubbles via the method of "Front Tracking". This correlation is valid for ultrapure water.

Tomiyama et al. (1998) also proposed generic drag coefficient model for both spherical, ellipsoidal and cap bubbles for

- Pure system:

$$C_D = max\left\{\min\left[\frac{16}{Re_b}\left(1 + 0.15 Re_b^{0.687}\right), \frac{48}{Re_b}\right], \frac{8}{3}\frac{Eo}{(4 + Eo)}\right\} \tag{1.74}$$

- Slightly contaminated system:

$$C_D = max\left\{\min\left[\frac{24}{Re_b}\left(1 + 0.15 Re_b^{0.687}\right), \frac{72}{Re_b}\right], \frac{8}{3}\frac{Eo}{(4 + Eo)}\right\} \tag{1.75}$$

- Contaminated system:

$$C_D = max\left\{\frac{24}{Re_b}\left(1 + 0.15Re_b^{0.687}\right), \frac{8}{3}\frac{Eo}{(4 + Eo)}\right\} \tag{1.76}$$

For small bubbles, the drag coefficient is governed by the viscous force which is characterised by the Reynolds number, whereas, for ellipsoidal bubbles, the governing factor is the gravity and surface tension forces which are characterised by the Eötvös number.

Ishii and Zuber (1979) proposed a drag model for spherical, distorted and cap bubbles, given by

- Spherical bubbles:

$$C_{D,spherical} = \frac{24}{Re_b}\left(1 + 0.1Re_b^{0.75}\right) \tag{1.77}$$

- Distorted bubbles:

$$C_{D,distorted} = \frac{2\sqrt{Eo}}{3}\left[\frac{1 + 17.67(1 - \alpha_G)^{9/7}}{18.67(1 - \alpha_G)^{3/2}}\right]^2 \tag{1.78}$$

- Cap bubbles:

$$C_{D,cap} = \frac{8}{3}(1 - \alpha_G)^2 \tag{1.79}$$

If $C_{D,spherical} > C_{D,distorted}$,
$C_D = C_{D,spherical}$ else $C_D = \min(C_{D,distorted}, C_{D,cap})$ (1.80)

Another drag model commonly used in gas-liquid flow simulations was that proposed by Harmathy (1960). The author proposed a constant bubble slip velocity when their Reynolds reaches an order of 1000. The slip velocity is given by equation (1.81). It corresponds to a constant slip velocity of 0.25 $m.s^{-1}$, when the properties of water and air at 25°C, 1 atm is considered.

$$u_{rel} = 1.5\left(\frac{\sigma g \Delta\rho}{\rho_L^2}\right)^{0.25} \tag{1.81}$$

Until now, we discussed the bubble drag according to the bubble shape. In practice, the gas-liquid bubble interface can be clean, partially contaminated or totally contaminated by surfactants or other impurities. These impurities will adsorb on the bubble interface and therefore immobilise the interface, leading to lower bubble terminal velocity.

Cuenot et al. (1997) described the adsorption of impurities on the bubble interface in 4 steps:

- The impurities are advected in the bubble wake before reaching the interface.
- The impurities reach the interface and are adsorbed to it at low concentration, without immobilising the interface
- Overtime, more impurities are adsorbed strongly on the surface and are transported to the bubble rear, dividing the bubble into two zones: mobile interface in the bubble front and immobile interface in the bubble rear. This can be explained by the stagnant cap model proposed by Sadhal and Johnson (1983).
- Further adsorption of impurities on the interface leads to a completely contaminated interface, making the bubble to behave like a solid sphere.

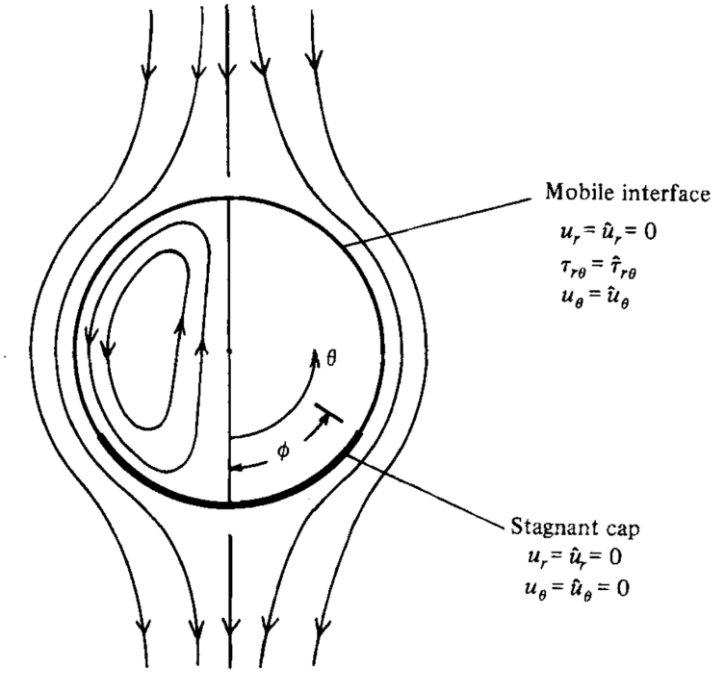

Figure 1.19: Stagnant cap model proposed by Sadhal and Johnson (1983). Adapted from: Sadhal and Johnson (1983)

Sadhal and Johnson (1983) proposed a stagnant cap model to describe the contamination level of the bubble interface, as shown in Figure 1.19. In the clean interface, the liquid is slipped along the interface until an angle of θ_{cap}. Beyond θ_{cap} is the contaminated immobile interface. When $\theta_{cap} = 180°$, the bubble is completely immobilised. At this point, the bubble drag force is equivalent to that of a solid sphere. This stagnant cap model has been used to describe the contamination level of the bubble

interface (Cuenot et al., 1997; Dani et al., 2022, 2006; Huang et al., 2011; Larsson et al., 2022; Sadhal and Johnson, 1983).

For a completely contaminated bubble, the drag coefficient of a solid sphere can be used, such as that of Schiller and Nauman (1933), expressed as:

$$\mathrm{C_D} = \frac{24}{Re_b}\left(1 + 0.15Re_b^{0.687}\right) \tag{1.82}$$

(Tomiyama et al., 2002a) proposed a terminal velocity expression for a completely contaminated deformed bubble as:

$$\mathrm{u_{rel}} = \frac{\sin^{-1}\sqrt{1-E^2} - E\sqrt{1-E^2}}{1-E^2}\sqrt{\frac{8\sigma}{\rho_L}E^{4/3} + \frac{\Delta\rho g d_b}{2\rho_L}\frac{E^{2/3}}{1-E^2}} \tag{1.83}$$

With $E = 1/(1 + 0.163Eo^{0.757})$

To summarise, spherical bubbles (small d_b and high σ) tend to rise rectilinearly. The terminal velocity is influenced by the degree of contamination on the gas-liquid interface. If the interface is pure and clean, an internal circulation is induced in the bubble, which decreases the viscous drag and increases the terminal velocity. On the other hand, the accumulation of impurities on the bubble interface which is characterised by the degree of contamination θ_{cap} will cause the interface to behave like a rigid surface. For ellipsoidal bubbles (high d_b and low σ), the bubble rises in zig-zag and helicoidal motion, the terminal velocity becomes lower and the bubbles are little affected by the contamination Tomiyama et al. (1998), as shown in Figure 1.20. Figure 1.21 shows the typical bubble terminal velocity diagram proposed by Clift et al. (1978) and Tomiyama et al. (1998). These two diagrams can be served as a rule of thumb for direct estimation of bubble terminal velocity. According to Clift et al. (1978), bubbles of 3-8 mm in contaminated water will rise with an averaged terminal velocity of 0.2 $m.s^{-1}$, whereas bubbles at that size in pure water will rise with an averaged terminal velocity of 0.25 ± 0.01 $m.s^{-1}$. In contrast, the drag coefficient model of Tomiyama et al. (1998), as shown in equations (1.74)-(1.76) stated that the terminal velocity varies with the contamination level only for bubbles smaller than 2.5 mm. After this threshold value, the bubbles will have the same terminal velocity of 0.25 ± 0.01 $m.s^{-1}$ regardless of the contamination level.

Shape	spherical		non-spherical
Motion	rectilinear		fluctuating
Purity	pure	contaminated	both
Flow pattern	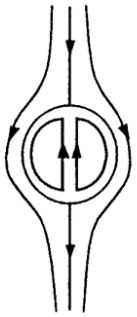	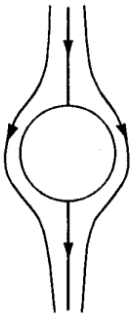	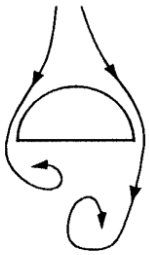
Governing effects	viscosity	viscosity	surface tension and gravity
Relevant dimension-less number	Re	Re	Eo

Figure 1.20: Governing factor for different bubbles shape at terminal velocity. Adapted from: Tomiyama et al. (1998)

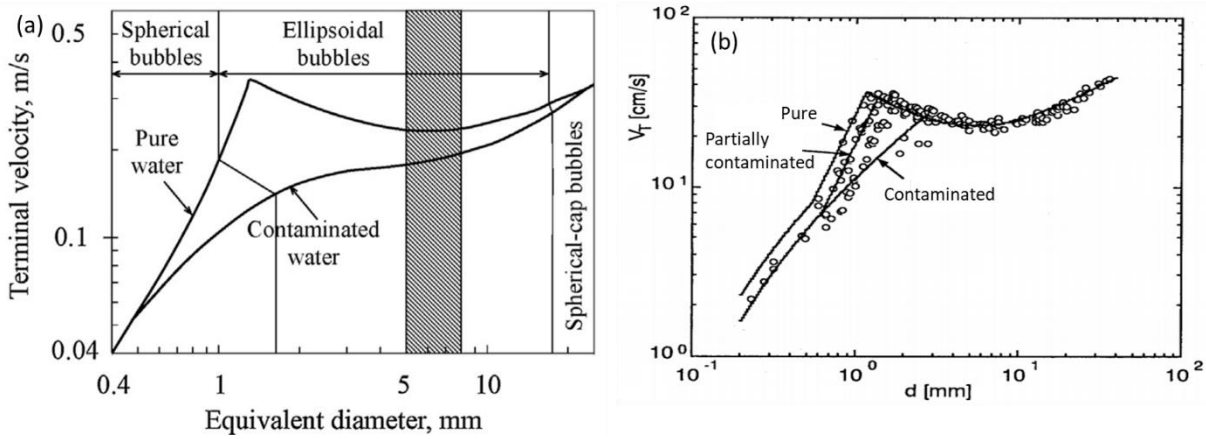

Figure 1.21: (a) Terminal velocity diagram adapted from Clift et al. (1978). (b) Terminal velocity diagram adapted from Tomiyama et al. (1998).

1.4 Recent emblematic achievements of bubble column modelling

After discussing different numerical models for bubble column simulations (Section 1.2) and the fundamentals of bubble dynamics (Section 1.3), this section is devoted to addressing the recent advances in bubble column modelling. The discussion is divided into the 3D fully-resolved CFD modelling and the 1D modelling. For the CFD model, the discussion is further distinguished between the development of hydrodynamics in bubbly flow, hydrodynamics coupled with mass transfer in bubbly flow, reactive bubbly flow and (bio)reactive bubbly flow. It should be emphasised that the advancements in bubble column modelling have been made since the 70s (Deckwer, 1977; Deckwer et al., 1974; Joshi and Sharma, 1979) in parallel with the progress in instrumentation techniques and computational capacities. Since then, many research works have been published to deal with different aspects of bubble column modelling, such as mixing, turbulence, hydrodynamics, population balance and (bio)reactive bubble column using different simulation approaches (Bauer and Eigenberger, 2001; Becker et al., 1994; Chen et al., 2004; Deen, 2001; Deen et al., 2004; Jakobsen et al., 1997; Krishna et al., 1999; Mudde and Simonin, 1999; Sokolichin et al., 1997; Sokolichin and Eigenberger, 1994). However, it is chosen that the discussion in this section is only restricted to the recent developments of bubble column models, i.e. after the year 2005, with a general overview of notable bubble column simulations using CFD and 1D models.

- **Application of CFD model for bubble column**
    - **Hydrodynamics in bubbly flow**

Recently, the research group from Politecnico di Milano, Italy published a comprehensive experimental investigation of bubble column hydrodynamics operating at a wide range of superficial gas velocities, in hope of remapping the bubble column flow regime map (Besagni et al., 2015, 2016, 2018a, 2019; Besagni, 2021; Besagni and Inzoli, 2016, 2017). The extensive datasets on different bubble column operating modes, sparger designs, and liquid properties were then used to validate the developed CFD models (Besagni et al., 2018b, 2017, 2015). Contrary to the "classic" three hydrodynamic regimes – homogeneous, transition and heterogeneous regime, the authors suggested a novel theory: "*The fluid dynamics of large-diameter bubble columns explicates in six flow regimes and is interpreted by a function of two global fluid dynamics parameters (the drift flux and the gas holdup); the analytical form of the function builds on five flow regime transition points*" (Besagni, 2021). This theory is illustrated graphically in Figure 1.22. On the right axis, each vertical position represents a time-averaged drift-flux value J_T calculated from its definition (Wallis, 1969; Zuber and Findlay, 1965). With the experimental database, the CFD model using the Eulerian multi-fluid approach was conducted to validate the model.

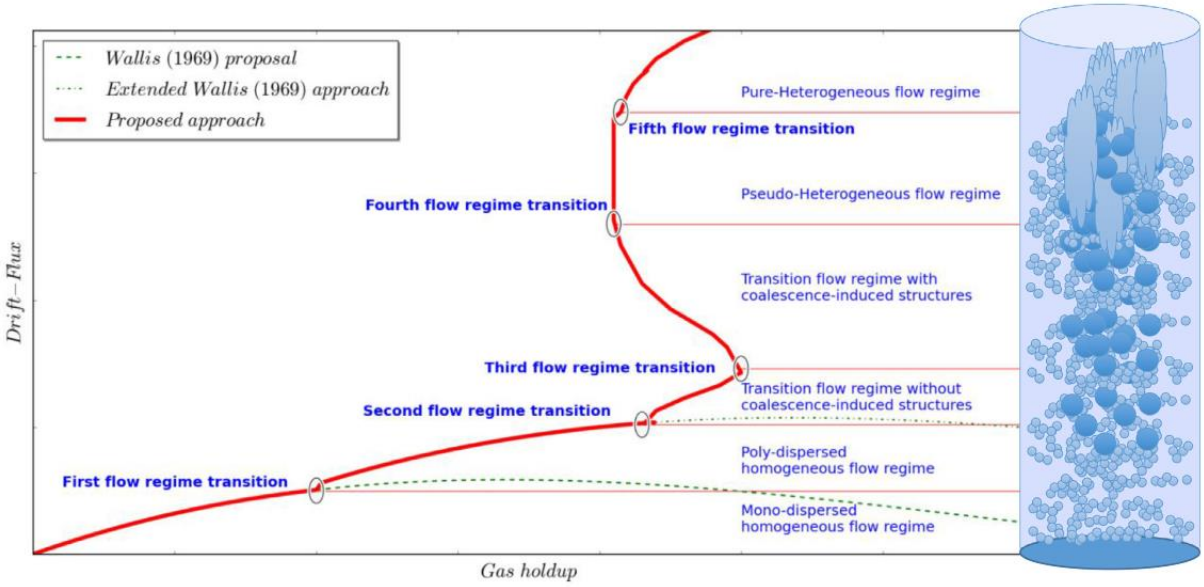

Figure 1.22: Flow regime map and regime transition point suggested by Besagni (2021)

Table 1.10: Transition regime coordinates

Transition Regime	Criteria
1	Transition from the mono-dispersed homogeneous flow regime to the poly-dispersed homogeneous flow regime occurs at $J_T \neq J_E$, with Volumetric flux: $J_T = j_G(1-\varepsilon_G) \pm j_L\varepsilon_G$ Theoretical drift-flux: $J_E = v_b(1-\varepsilon_G)$
2	Transition from the poly-dispersed homogeneous flow regime to the transition regime (without coalescence-induced structures) occurs at $J'_T \neq J'_E$, with Volumetric flux with changes in origin: $J_T = j'_G(1-\varepsilon'_G) \pm j_L\varepsilon'_G$ Theoretical drift-flux with changes in origin: $J'_E = v_b(1-\varepsilon'_G)$ $\varepsilon'_G = \varepsilon_G - \varepsilon_{G,trans-1}$ $j'_G = j_G - j_{G,trans-1}$
3	The transition from the absence of coalescence-induced structures to the presence of coalescence-induced structures is found at the maximum of the $J_T = f(\varepsilon_G)$ curve
4	Transition from the transition regime to the pseudo-heterogeneous regime is determined on the basis of the constant value of ε_G at high J_T.
5	The transition to the pure heterogeneous regime is determined based on the increase of ε_G with respect to the constant value found in the 4th regime.

The recent advances in hydrodynamic modelling of bubbly flow are also highlighted in the baseline Eulerian model established by the work of a research group from the Helmholtz-Zentrum Dresden-Rossendorf (HZDR), Institute of Fluid Dynamics, Dresden, Germany (Krepper et al., 2014; Liao et al., 2018; Rzehak et al., 2017b, 2017a, 2015; Rzehak and Krepper, 2015, 2013a, 2013b; Ziegenhein et al., 2017). Over the years, the research group has contributed to the development of the CFD model for multiphase flows, focusing on the Euler-Euler two or multi-fluid approach (Putra and Lucas, 2016). These models require suitable closure relations describing the interfacial exchange processes. Progress in the modelling of dispersed gas-liquid multiphase flow has been made by comparing existing bubble-induced turbulence (BIT) models in the literature to unravel suitable closures for modelling bubbly turbulence (Rzehak and Krepper, 2013a, 2013b). Several source terms for the turbulent kinetic energy and dissipation are tested and the prediction of the radial gas holdup, liquid velocity, and the square root of turbulent kinetic energy is compared with a comprehensive set of experimental data on upward vertical gas-liquid flow in round pipes of different diameters. It is found that most of the BIT model gives weak turbulent dispersion force prediction near the wall causing a steep gradient of liquid velocity and a strong lift force towards the wall, leading to overprediction of gas holdup near the pipe walls. By using a physically better-founded wall force of Hosokawa et al. (2002) over that of Antal et al. (1991), it is shown that a better prediction of wall peak gas holdup was obtained (Rzehak and Krepper, 2013b). Another objective is to propose a unified set of closures for the Euler-Euler two-fluid model for different configurations, i.e. pipe flow, bubble column on the air-water system and air-liquid molten system, and airlift. The set of bubble force correlations is summarised in Table 1.11. The baseline model has been validated using literature data for different applications (Krepper et al., 2018; Lucas et al., 2020; Rzehak et al., 2017b; Rzehak and Krepper, 2015; Ziegenhein et al., 2015). It has been shown that the Eulerian baseline model is capable to reproduce hydrodynamics behaviour for the aforementioned cases with acceptable accuracy for engineering design estimations (Rzehak et al., 2017b). It is found that the bubble size is of utmost importance as it appears in all closure relations. Earlier, the validation of the baseline closure model as shown in Table 1.11 has been conducted by Rzehak and Krepper (2015) by fixing the bubble's polydispersity (inhomogeneous MUSIG model) similar to the experiments conducted in a vertical pipe (Lucas et al., 2010b, 2010a). This way the modelling of complex and not well-understood bubble coalescence and rupture processes can be bypassed by imposing the measured bubble size distribution and the investigation can be focused solely on the closure terms. The overall agreement with the experimental data is quite good, except for the bubble migration to the centre of the pipe at the highest level of the column which is underpredicted by the model. The baseline model is also validated in a laboratory scale bubble column equipped with 4 nozzles sparger which offers high spatial data and is suitable for the validation of the

multiphase CFD model (Rzehak et al., 2017a). This type of experiment setup highlighting spatial heterogeneities that provide excellent local information for CFD model validation is still scarce in the literature.

Table 1.11: Closure relations for interfacial forces based on Rzehak et al. (2015)

Interfacial forces	Correlation
Drag	Ishii and Zuber (1979)
Lift	Tomiyama et al. (2002)
Wall	Hosokawa et al. (2002)
Turbulent dispersion	Burns et al. (2004)
Virtual mass	Constant coefficient of 0.5

In the context of hydrodynamic in bubble column fermenters, the research group from the School of Chemical and Biomolecular Engineering, University of Sydney, Australia developed extensive works on the modelling of large-scale bubble column hydrodynamics, mixing and O_2 mass transfer (Ertekin et al., 2021; Fletcher et al., 2017; McClure et al., 2013, 2014b, 2014a, 2015d, 2015a, 2016b, 2017). The developed CFD model has been successfully validated in bubble columns at various scales ranging from 0.19 m diameter and 1 m height to 0.39 m diameter and 2 m height to 3 m diameter and 6.6 m height (Ertekin et al., 2021; McClure et al., 2014c, 2013). For example, the developed CFD model is used to simulate hydrodynamics in industrial fermenters, generally in high superficial gas velocity ($j_G > 0.1$ m.s^{-1}) and in the presence of surfactants. The drag force experienced by the bubbles in such heterogeneous regime with the presence of surfactants is different from that at the homogeneous regime and pure system. At high superficial velocity (high gas holdup, $\alpha_G > 15\%$) accompanied by the presence of large bubbles, there is no hindered rise as observed in the lower gas holdup system. This has been shown in the work of Simonnet et al. (2007) whereby the relative bubble velocity increases due to decreasing bubble hindrance effect when $\alpha_G > 15\%$. It is caused by the aspiration of bubbles in the wake of the leading bubbles, resulting in decreasing drag force, increasing relative velocity and lower gas holdup. The swarm factor for gas holdup lower than 30% is given by Simonnet et al. (2007) as

$$\frac{C_D}{C_{D_\infty}} = (1-\alpha_G)\left[(1-\alpha_G)^{25} + \left(4.8\frac{\alpha_G}{1-\alpha_G}\right)^{25}\right]^{-2/25} \quad (1.84)$$

Whereby C_{D_∞} is the drag coefficient for an isolated bubble.

McClure et al. (2014c) modified slightly equation (1.84) into a conditional expression, as shown in equation (1.85) to better fit their experimental data.

$$\frac{C_D}{C_{D_\infty}} = f(\alpha_G)$$
$$f(\alpha_G) = \begin{cases} \min(h, 1)\ for\ h > 1 \\ 0.8h\ for\ h < 1 \end{cases} \tag{1.85}$$

Where h is the swarm factor of Simonnet et al. (2007), expressed in equation (1.84). Later, McClure et al. (2017) proposed an alternative empirical swarm factor for gas holdup larger than 25% as

$$f(\alpha_G) = \min\Big(\big(1 - f(\alpha_G)\big)^a + b, 1\Big) \tag{1.86}$$

Where a and b are empirical constants obtained through data fitting. A value of 50 for a was proposed and b depends on the sparger design. It is reported b = 0.2 for fine opening sparger and b = 0.08 coarse opening sparger. It is found that the inclusion of gas holdup correction term is necessary to obtain accurate predictions, particularly at higher superficial gas velocity whereby the omission of these terms leads to unphysical results, such as water being 'blown out' of the top of the column (McClure et al., 2014b).

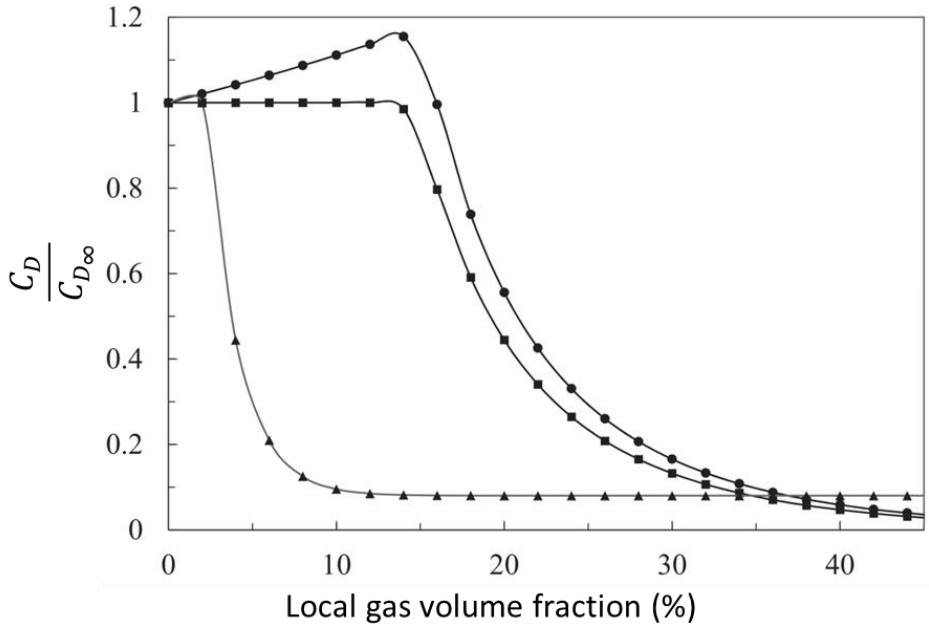

Figure 1.23: Swarm factor in function of the gas volume fraction. ● Equation (1.84), ■ Equation (1.85), ▲ Equation (1.86). Adapted from: Gemello (2018)

Gemello et al. (2018) suggested another swarm factor to model hydrodynamic with gas holdup over 30% as

$$\frac{C_D}{C_{D_\infty}} = \max\left\{(1-\alpha_G)\left[(1-\alpha_G)^{25} + \left(4.8\frac{\alpha_G}{1-\alpha_G}\right)^{25}\right]^{-2/25}; h_{min}\right\} \quad (1.87)$$

The value of h_{min} varies with the bubble column scale, generally between 0.12 and 0.18.

In the presence of surfactant, the bubble interface becomes immobile with the adsorption of the surfactant. Consequently, the drag of the bubbles increases. McClure et al. (2014a) proposed to multiply the drag coefficient by a coefficient of $k_{surfactant}$ which varies according to the type of surfactant. For example, it is proposed to use a value of 2 for systems containing 2-propanol and 0.75 for systems containing antifoams (Ertekin et al., 2021; McClure et al., 2014a). In the end, the effects of surfactant and reduced hindrance effect at high superficial gas velocity are modelled as:

$$C_D = C_{D_\infty} f(\alpha_G) k_{surfactant} \quad (1.88)$$

It should be emphasised that these swarm factor correction terms are empirical, issued from the fitting of experimental data. Nevertheless, the effectiveness of these correlations has been shown in predicting large-scale bubble columns (diameter > 1 m) hydrodynamics, such as overall gas holdup, radial gas holdup, the axial and radial liquid velocity at industrial conditions with high superficial gas velocity and the presence of surfactant (Ertekin et al., 2021; Fletcher et al., 2017; Gemello et al., 2018; McClure et al., 2017). There is still a lack of general consensus in the modelling of heterogeneous bubbly flow. A more generic model considering the swarm factor at low and high gas holdup coupled with the existence of surfactants must be developed with general application.

- **Hydrodynamics coupled with mass transfer in bubbly flow**

The advances in mass transfer modelling in bubble columns focus mostly on the prediction of oxygen uptake rate (OTR) in the context of wastewater treatment and fermentation (Cockx et al., 2001; Fayolle et al., 2007; McClure et al., 2015b). The satisfactory prediction of OTR relies on the correct description of interfacial area (hydrodynamics) and the mass transfer coefficient (mass transfer). The case of oxygen mass transfer is mostly modelled as a one-way coupling problem. This is characterised as the O_2 bubble mass loss from the bottom rising up to the top of the column is negligible to cause a change to the hydrodynamics. However, this may not be true in large-scale bubble column whereby the

changes in gas holdup becomes non-linear (Deckwer et al., 1978; Giovannettone and Gulliver, 2008). As demonstrated in the work of Larsson et al. (2022), the exponential mass loss of gas for the entire column can be described by the depletion factor (DF), defined as

$$DF = 6m\frac{k_L}{d_b}\frac{H}{u_G} \tag{1.89}$$

With m the dimensionless Henry's constant, H the height of the column, k_L the mass transfer coefficient, d_b the bubble diameter and u_G the bubble velocity. The DF for a bubble column of 4.4 m height with a 3 – 4 mm bubble diameter is estimated to be 0.4, which causes the O_2 mole fraction to decrease from 21% in the inlet to approximately 13% at the outlet (Larsson et al., 2022). This implies a constant description of equilibrium concentration C^* can lead to the wrong mass transfer rate, especially in a deep bubble column.

It is very challenging to achieve a detailed mass transfer model validation. Rzehak and Krepper (2016) have pointed out that the progress in the Euler-Euler simulation of mass transfer in bubbly flow has been hampered by a lack of spatially resolved data, particularly measurements of local concentration, which are necessary for CFD model validation. To fully validate a mass transfer CFD model, the validation experiments must include velocity field, gas holdup, interfacial area (Sauter mean diameter), mass transfer coefficient, and mass transfer rate. Chen and Brooks (2021) also mentioned the lack of comprehensive experiments on mass transfer covering all measurements in the open literature. Most of the early studies on bubble columns are generally devoted to global characteristics like overall gas holdup and volumetric mass transfer coefficient (Akita and Yoshida, 1973; Charpentier, 1981; Hikita et al., 1976), but no localised measurement of flow or mass transfer is tracked. One of the rare local measurements of gas holdup and CO_2 concentration is featured in the work of Deckwer et al. (1978). Rzehak and Krepper (2016) validated their CFD mass transfer model based on the measurement of Deckwer et al. (1978). However, the mass transfer coefficient was not modelled, instead, the reported experimental value of k_L from Deckwer et al. (1978) was used in the CFD model.

Due to higher computational costs of the CFD model, it is very common to model monospecies mass transfer. The work of multispecies gas-liquid mass transfer is still scarce in the literature. Nonetheless, local measurement of monospecies mass transfer is already challenging, needless to mention multi-component system. It has been demonstrated in the work of Troshko and Zdravistch (2009) in the simulation of an industrial-scale Fischer-Tropsch slurry bubble column reactor by considering two gas

components of the syngas: H_2 and CO. The CFD model is considered a reactive mass transfer model as the validation of mass transfer was conducted by comparing the syngas conversion.

In addition, the gas-liquid mass transfer is hampered in the presence of surfactant. This is due to additional mass transfer resistance caused by the adsorption of surfactant on the bubble interface. This effect has to be included in the CFD model for mass transfer modelling in such liquid system. Many numerical works focusing on Direct Numerical Simulation (DNS) approach have been conducted to investigate the closures to model the surfactant effect on mass transfer (Bothe et al., 2009; Dani et al., 2022; Falcone et al., 2018; Pesci et al., 2018). In conjunction with hydrodynamics, future work should focus on how the liquid phase composition affects mass and momentum transfer, with the aim of developing improved predictive approaches for the bubble drag and the liquid film mass transfer coefficient.

- **Reactive bubbly flow**

As discussed by Rzehak and Krepper (2016), the progress in reactive bubbly flow modelling requires a good quality experimental dataset. A correct inlet bubble diameter is crucial for the bubble column model as closures involving bubble hydrodynamics and mass transfer are linked to this information. Information about the measurement of concentration (primarily in the axial direction) is important for model validation. In the pioneering work of Darmana et al. (2007), the coupling of hydrodynamics and the chemical reaction was investigated extensively via the monitoring of CO_2 chemisorption in aqueous sodium hydroxide NaOH solution. Measurements on bubble size, global gas holdup, radial gas holdup, bubble velocity, and liquid velocity were performed. With the presence of chemical reactions, the gas substrate experiences an enhanced gas-liquid mass transfer. The reactive mass transfer was tracked with a pH probe. The pH dynamics are related to the intensity of CO_2 reactive mass transfer. The reactive bubbly flow has gained the interest of researchers (both experimental and numerical), and extensive studies at different scales have been published, ranging from the reactive flow of a single bubble (Falcone et al., 2018; Felis et al., 2019; Merker et al., 2017) to Taylor bubble (Hori et al., 2017; Kastens et al., 2017; Felix Kexel et al., 2021b, 2021a; F. Kexel et al., 2021; Sa'adiyah et al., 2021) and bubble swarm (Hlawitschka et al., 2017; Jain et al., 2015; Kipping et al., 2021, 2017; Krauß and Rzehak, 2018). It has been featured in the work of Darmana et al. (2007) that the coupling of reactive mass transfer and hydrodynamics is strong as the Sauter mean diameter shrink considerably during the transient CO_2 chemisorption process. To model this observation, Buffo et al. (2017) performed 3D CFD simulations coupled with the population balance model. In the literature, the use of the population balance model for bubble columns is still divided. Some considered that the overall hydrodynamics

and mass transfer are well captured by assuming a single class bubble size (Ertekin et al., 2021; Huang et al., 2018; McClure et al., 2014c), others reported better prediction by including the population balance model (Besagni et al., 2017; Buffo et al., 2017; Gemello et al., 2019). The use of the bubble population balance model requires suitable closures on bubble breakage and coalescence models which are still under active research (Liao and Lucas, 2010, 2009). Whilst the implementation of the bubble population balance model may improve the physical modelling, the use of a single bubble size has the advantage of simplicity and computational efficiency.

- **Bio-reactive bubbly flow**

The study of bioreactors using the CFD model has been widely documented in the literature. This approach has been particularly useful in identifying substrate gradients and their consequences on the metabolism of the microorganisms, such as productivity and substrate yield (Larsson et al., 1996; Morchain et al., 2014, 2013; Nadal-Rey et al., 2021b; Sarkizi Shams Hajian et al., 2020; Siebler et al., 2019; Wright et al., 2018). This is due to the nature of the fully-resolved 3D CFD simulation which offers local information about the substrate concentration field and the bioreaction kinetics. It is very often that the substrate gradients appear in large-scale bioreactors as the mixing time is in the same order of magnitude as the substrate uptake rate (Enfors et al., 2001; Haringa et al., 2017; Nadal-Rey et al., 2021b). In this context, many studies on bioreactor mixing using CFD and CMA models (flow maps issued from CFD simulation) have been done to predict the mixing evolution (Delafosse et al., 2014; Delvigne et al., 2006; Nadal-Rey et al., 2022; Vrábel et al., 1999) with the purpose to understand the mixing behaviour and improving reactor design. For the study of substrate gradients two distinct approaches can be found: Eulerian (Morchain et al., 2014; Sarkizi Shams Hajian et al., 2020) and Lagrangian (Haringa et al., 2017, 2016; Lapin et al., 2006, 2004; McClure et al., 2016a), as discussed in Section 1.2.2.3. This gradient analysis is further differentiated whether the population (physiological) state is included in the study, as the so-called structured-segregated biological model, as shown in the work of Morchain et al. (2014) and Lapin et al. (2006, 2004). By using this approach, the substrate uptake rate of each distinct individual depends not only on the extracellular substrate concentration but also on the intracellular concentration which in turn is a function of the history of the individual cells. These models can fully characterise the heterogeneous cell population behaviour due to non-ideal mixing and thus the apparition of substrate gradient. Amid the computational costs of the CFD model in investigating the dynamic behaviour of bioreactors in regard to substrate gradients, alternative approach such as the CMA model or the 0D model is also efficient (Morchain and Fonade, 2009; Pigou et al., 2017; Pigou and Morchain, 2015). Another approach based on the Euler-Lagrange framework for the biological phase has been applied in several applications to study the response of

microorganisms to the extracellular substrate concentration fluctuations in terms of frequency and magnitude (Haringa et al., 2018, 2017, 2016; McClure et al., 2016a; Siebler et al., 2019). This work was pioneered by Lapin et al. who introduced the approach of following the trajectory of the microorganism and its associated metabolisms encountered according to the extracellular substrate concentrations, so-called lifeline analysis (Lapin et al., 2006, 2004). First, the approach essentially begins with classic CFD simulation to capture the overall bioreactor gas-liquid hydrodynamics. The gas phase can be solved by including the bubble population balance model (Siebler et al., 2019) or imposed if the dissolved gas gradients are not expected to cause any significant change in the growth rate (Haringa et al., 2016). The bioreaction is then solved to calculate the substrate uptake rate. Next, from the converged substrate gradients and flow field, the cell lifelines are recorded in terms of particle number, position and substrate concentration viewed by the particle. To analyse the recorded lifelines, the metabolic regime has to be defined. Typically, the normalised specific substrate uptake rate (Haringa et al., 2017, 2016), growth rate (Kuschel et al., 2017) or the total product-biomass yield (Siebler et al., 2019) is used to distinguish the metabolic regime. By setting threshold values for each metabolic regime, regime transition patterns can be defined. Lifelines are characterised by a sequence of regime changes thereby integrating all extracellular stimuli exposed to the cell. Typically, three gradient zones ranging from high cellular activity to low cellular activity are identified, leading to six regime transition events, as illustrated in Figure 1.24.

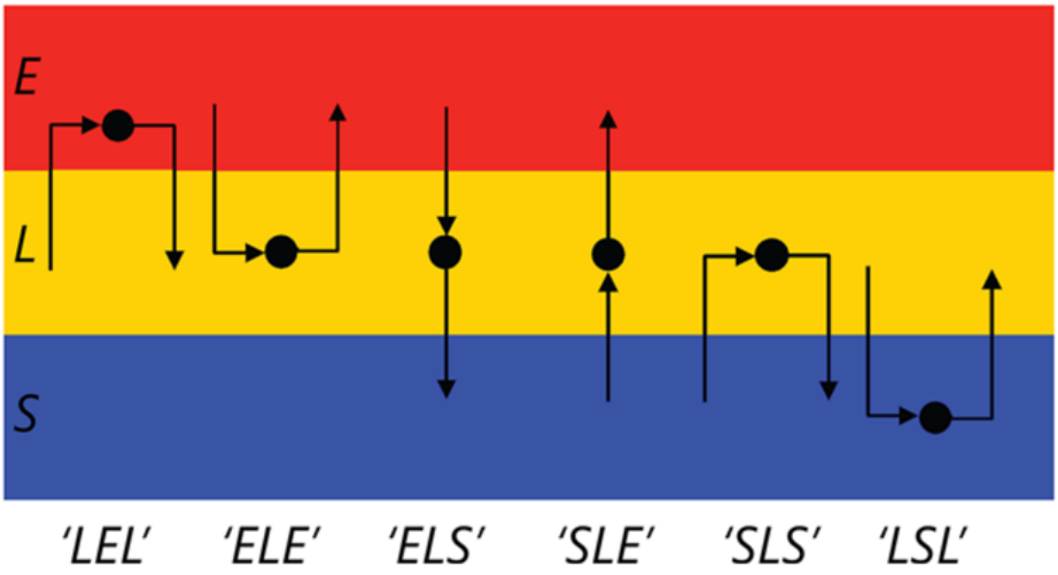

Figure 1.24: Graphical illustration of 6 possible transition patterns, ranging from high concentration (RED), intermediate concentration (YELLOW), and low concentration (BLUE). The example represents the metabolic regime of *Penicillium chrysogenum* which can be identified as glucose excess (E), glucose limitation (L), and glucose starvation (S). Adapted from: Haringa et al. (2016)

Subsequently, the regime residence time can be quantified and further analysis can be conducted, such as the quantification of intra-regime circulation time distribution and the design of a scale-down simulator. The analysis of large-scale bioreactors based on this approach has been highlighted in the literature and some interesting results can be discussed. Siebler et al. (2019) simulated *C. ljungdahlii* syngas fermentation in a 125 m^3 bubble column and the results revealed that most of the cells (97%) in the column experienced CO limitation and 84% of the cells were likely to undergo transcriptional changes after exposure in the stress-inducing zone longer than 70 s. Haringa et al. (2016) investigated the fermentation of *Penicillium chrysogenum* in a 54 m^3 stirred-tank reactor. The lifeline analysis showed that 57% of the vessel is substrate limited with the timescales associated with the migration of the microorganism between zones with excess substrate and substrate depletion of the same order of magnitude as the global circulation time at $O(10^1)$ seconds. Haringa et al. (2017) simulated a 22 m^3 *Saccharomyces cerevisiae* fermenter and the large-scale substrate concentration gradient impact on the microorganisms is quantified. From the lifeline analysis, different scale-down simulators were proposed based on fluctuating feed and multiple compartment approach.

- **Application of 1D model for bubble column**

The 1D model has been widely used to model multiphase flow due to its simplicity and lower computational cost than more complex 3D simulations. Nevertheless, the 1D model provides satisfactory physical modelling whereby valuable insights can be drawn, such as rational scale-up strategy and development of a simplified model/analytical solution. For instance, it has been applied to study the hydrodynamics of the airlift loop reactor (Camarasa et al., 2001; Cockx et al., 1997; Colombet et al., 2013; Sáez et al., 1998; Talvy et al., 2005). These models rely on macroscopic spatial-averaged mass and momentum balances to obtain information about the gas holdup, liquid recirculation velocity, and pressure drop. In general, these models supposed steady-state fully developed gas-liquid flow, which allows the simplification of the model. Typically, satisfactory agreement with the experimental data can be obtained using the 1D model, provided important closures are applied, such as the bubble drag coefficient. Because of the simplicity of the 1D model description, the 1D model may depend on closures issued from the fully-resolve CFD simulation, as shown in the work of Cockx et al. (1997), Talvy et al. (2005), and (Bauer and Eigenberger, 1999). The CFD model can be useful to better understand the local phenomena, and thus introducing the closure terms in the 1D model. This back-and-forth modelling approach between the CFD and 1D models has proven the existence of the multiscale nature of the bubble column with different physical phenomena occurring at different spatial and temporal scales, making the modelling of bubble columns extremely challenging (Shu et al., 2019).

In terms of industrial chemical engineering application, the 1D model based on the macroscopic axial dispersion model has been used extensively in the literature. In the context of chemical engineering, the 1D axial dispersion model has been used to study Fischer-Tropsch process (de Swart and Krishna, 2002; Rados et al., 2005; Schweitzer and Viguié, 2009). Fischer-Tropsch process is usually conducted in a slurry bubble column reactor with the solid catalyst suspended in the liquid phase. The reactor usually operates under high superficial gas velocity, reflecting the heterogeneous behaviour in the large-scale bubble column. de Swart and Krishna (2002) and Rados et al. (2005) used the 1D axial dispersion model with two bubble classes ("small" and "large" bubble, with the "small" bubble size estimated through an empirical correlation) to model large-scale Fischer-Tropsch slurry bubble column reactor (diameter of 7.5 m and height of 30 m for de Swart and Krishna (2002) case and diameter of 0.5 m and height of 10 m for Rados et al. (2005) case). Several empirical correlations were applied in the model, such as the rise velocity of bubbles, transition gas holdup, and interfacial area. Nevertheless, these works provided insights on reactor design for efficient Fischer-Tropsch process, such as the importance of having a high reactor and good backmixing to ensure high substrate conversion.

The use of the 1D axial dispersion model has also been demonstrated in other chemical engineering applications, such as carbon capture (Hissanaga et al., 2020; Inkeri and Tynjälä, 2020). The 1D model has been applied in the work of Inkeri and Tynjälä (2020) to study the reactor design and operating conditions on the carbon dioxide capture efficiency. It is found that low gas flowrate and high liquid flowrate promote CO_2 capture. Meanwhile, Hissanaga et al. (2020) developed a 1D plug-flow model based on spatial averaging of the two-fluid model to model CO_2 absorption in water. The validation is based on the experimental data of Deckwer et al. (1978) conducted in a 4.4 m high bubble column. The work of Hissanaga et al. (2020) highlights the modelling of non-linear gas holdup and mass transfer profiles in a large-scale bubble column reactor. The non-linear hydrodynamic behaviour is classic, as has been shown in the literature (Deckwer et al., 1978; Giovannettone et al., 2009; Giovannettone and Gulliver, 2008; Rzehak and Krepper, 2016). This is caused by the mutual interaction between mass transfer and the bubbly flow. This effect is amplified in the case of reactive bubbly flow, as shown by the work of Darmana et al. (2007).

The 1D model has also been used to study industrial bioprocesses, such as syngas fermentation (Chen et al., 2016, 2015; de Medeiros et al., 2019; Li et al., 2019; Siebler et al., 2020), bioethanol production (de Medeiros et al., 2020), and biological methanation (Inkeri et al., 2018; Ngu et al., 2022a). The 1D axial dispersion model of Chen et al. (2016, 2015) is coupled with the syngas fermentation metabolic model described via flux balance analysis to investigate the impact of reactor design and operating

parameters on bubble column performance. It is found that the ethanol-acetate selectivity depends highly on the H_2/CO feed ratio. Increasing liquid velocity also favours ethanol production. Due to mass transfer limitations, it is proved that gas recycling improves gas conversion by consuming unreacted substrate. These simulations demonstrated the benefits of the 1D model in studying the bioprocess without conducting additional experiments (hence cost and time-saving), once the model is validated. The 1D model can also be coupled with other optimisation tools, such as a multi-objective genetic algorithm, as shown in the work of de Medeiros et al. (2020). The work aims at defining the optimal reactor design and operating conditions for bioethanol production. The 1D axial dispersion model is used to generate an array of steady-state responses to the bubble column performance. These data will be provided to the distillation column which is modelled using the artificial neural networks (ANN) surrogate model. Above all, an optimisation framework was employed to perform techno-economic optimisation.

Siebler et al. (2020) applied the 1D axial dispersion model to study syngas fermentation in a large-scale bubble column reactor (height of 30 m). Again, the objective was to perform sensitivity analysis on operating parameters and study their impact on the bioreactor performance. Some interesting results can be discussed here: first, the fundamentals of bubble columns and its impact on the bioreaction are examined: (i) increasing $k_L a$ while keeping ε_G constant is the same as increasing bubble numbers, leading to a higher product yield. (ii) increasing ε_G while keeping $k_L a$ constant leads to decreasing bubble size and a higher product yield but is less pronounced that the changes in (i). (iii) varying ε_G and liberating $k_L a$ improves the product yield, more than that of scenarios (i) and (ii). Comparison of 1D with CFD results was also conducted in the study. In comparison with the CFD model results, the 1D model obtains a smaller mean bubble diameter and larger gas holdup, which leads to an overestimation of $k_L a$ by factor of 14. Consequently, the 1D model overpredicts the biological efficiency with 40% more product yield than CFD (Siebler et al., 2020). By adopting the Sauter mean diameter and the gas holdup by the values from the CFD model, the 1D model obtained closer results than CFD, as expected. Inkeri et al. (2018) developed a 1D axial dispersion model for STR to describe biological methanation reaction. Similarly, sensitivity analysis on liquid and gas feed, impeller design and power consumption were performed.

Despite the wide use of the 1D model for engineering applications, several drawbacks can be identified in the current state-of-the-art. First, most of the 1D models do not model the hydrodynamics of the bubbly flow (particularly the gas holdup), instead, it is calculated via empirical correlations (Chen et al., 2015; de Medeiros et al., 2020; de Swart and Krishna, 2002; Inkeri et al., 2018; Inkeri and Tynjälä,

2020; Li et al., 2019; Siebler et al., 2020). The correlations used by these 1D models are reported in Table 1.12 using nomenclatures of the respective original paper.

Table 1.12: Empirical correlation and relation used to calculate gas holdup in some existing 1D model

Reference	Gas holdup correlation
(Chen et al., 2015)	$\varepsilon_G = \frac{\varepsilon_G u_G}{K_G + u_G}$
(de Medeiros et al., 2020)	$\varepsilon_G = 0.6\left(\frac{u_G}{3600}\right)^{0.7}$
(de Swart and Krishna, 2002)	$\varepsilon_{G,trans} = 2.16\exp\left(-13.1\rho_g^{-0.1}\mu_L^{0.16}\sigma^{0.11}\right)\exp(-5.86C_s)$
(Inkeri et al., 2018)	$\frac{\varepsilon_G}{1-\varepsilon_G} = 0.819\frac{u_G^{2/3}N^{2/5}d_{im}^{4/15}}{g^{1/3}}\left(\frac{\rho_L}{\sigma}\right)^{1/5}\left(\frac{\rho_L}{\rho_L-\rho_G}\right)\left(\frac{\rho_L}{\rho_G}\right)^{-1/15}$
(Inkeri and Tynjälä, 2020)	$\varepsilon_G = \frac{u_G}{0.3 + 2u_G}$
(Li et al., 2019)	$\frac{u_G}{\varepsilon_G} = C_0(u_G + u_L) + v_b(1-\varepsilon_G)$
(Siebler et al., 2020)	$\varepsilon_G = \frac{v_s}{0.23}$

The use of empirical correlation restricts the gas holdup calculation to the range of application. The gas holdup has to be estimated precisely as it is involved in the calculation of $k_L a$ for mass transfer. Sometimes, the gas holdup was assumed as constant for the sake of simplicity (Chen et al., 2016). Taking the example of biological methanation, a huge loss of gas is awaited between the inlet and the outlet, as 5 moles of gas reactants are consumed to form 1 mole of product, as shown in equation (1.1). The assumption of constant gas holdup is thus prohibited to model applications with great loss of gas fraction. We only found the work of Hissanaga et al. (2020) that successfully predicted the non-linear gas holdup profile when compared with the literature data. Second, the coupling of (bio)reactive mass transfer with the hydrodynamics, meaning that the bubble size variation due to (bio)reactive mass transfer is scarcely discussed in the literature. This has to be included in the 1D model if one wishes to study reactive bubbly flow. Recently, Breit et al. (2021) developed a 1D model coupled with population balance model for batch bubble columns. The model is able to describe bubble size distribution based on different breakage and coalescence model. To validate the model, the gas holdup and Sauter mean diameter at 4 axial locations were measured and calculated in a 0.1 m diameter and 1 m height bubble column, operated at high superficial gas velocity ($j_G = 2{,}3{,}4$ m.s^{-1}). However, the model is not developed with mass transfer between gas-liquid phases. Thus, the two-way coupling effect of mass transfer and hydrodynamics was not assessed. Third, the multispecies mass transfer

effect has rarely been implemented in the 1D model. In the case of biological methanation, more than one species is present in the gaseous phase, having H_2, CO_2, and CH_4 as the major components. The huge disparity in terms of solubility between H_2 and CO_2 (see Table 1.6) will generate mass transfer fluxes at different intensities. The cost of filling this third gap is not very high (simply solving the same equations for two or more species), but it is interesting to carry out this exercise to gain more insights into multispecies mass transfer coupling. As the aforementioned reasons, some gaps in the literature needed to be filled for the development of a comprehensive spatio-temporal 1D model.

Nevertheless, some meaningful conclusions can be drawn from the use of 1D model in different fields of applications. The first conclusion is clear: the 1D model provides necessary information about the physical phenomena at a lower computational cost than 3D CFD simulations. Researchers were able to leverage the low computational cost of the 1D model to perform more engineering applications such as probing different reactor designs and operating parameters. The second conclusion is that despite the simplicity of the 1D model, closure relations play an important role and occasionally these closures have to be obtained through 3D fully-resolved CFD simulations. This highlight both numerical tools of 1D and CFD models have to be properly used to achieve satisfactory bubble column performance prediction and keep the computational cost as low as possible. The third conclusion concerns the actual advances in the 1D modelling approach in incorporating the coupling of hydrodynamics, mass transfer and (bio)reaction. It is clear that a more generic model is necessary to describe the coupling of several mutual multiphysics interactions, i.e. Sauter mean diameter variation according to hydrostatic pressure effect and mass transfer (with or without reaction); mechanistic model describing the gas holdup variation with height; and the impact of multispecies mass transfer on the hydrodynamics.

1.5 Thesis objective and outline

The main goal of this PhD thesis is to develop a model structure that encompasses all physical phenomena involved in (bio)reactive bubble column modelling while keeping a low computational cost. The main application of this model is to simulate ex-situ biological methanation reaction. In particular, we are interested to model gas-fed reactions in bubble column reactors. Thus, applications such as reactive bubbly flow and yeast fermentation are also considered.

The choice for the hydrodynamic modelling at low computation cost is obvious which is the 1D model. The bubbly flow is mostly unidirectional; thus, the 3D representation of the bubble column can be simplified to a 1D model. The choice of CMA is not considered as the mixing is not an issue in ex-situ biological methanation process. The major carbon and energy substrates are fed through the gas phase and not the liquid phase. Contrary to in-situ biological methanation system whereby the limiting step is the hydrolysis of organic matter that requires good mixing, the ex-situ biological methanation system bypass this rate-limiting process. Nevertheless, due to significative gas reduction between the inlet and the outlet, the two-way coupling between the hydrodynamics and the (bio)reactive mass transfer has to be considered. The gas holdup reduction and the Sauter mean diameter variation, as well as the hydrostatic pressure effect on the local hydrodynamics, has to be included in the model. For these aforementioned reasons, a two-way coupled spatio-temporal 1D model is developed in this thesis. This also addresses the drawback of the current 1D model in the literature.

In this thesis, only ex-situ biological methanation is treated under thermophilic condition. Under such conditions, hydrogenotrophic methanogens outcompete homoacetogenic methanogens. Therefore, it is supposed that the biological methanation is only ensured by the archaeon *Methanobacterium thermoautotrophicum* in this work. It is further assumed that the timescale of gaseous substrate mass transfer is relatively longer than the substrate uptake timescale, which is generally admitted in the literature (Jensen et al., 2021; Lecker et al., 2017; Rafrafi et al., 2020; Rusmanis et al., 2019; Sposob et al., 2021). Nevertheless, the hypothesis is checked in the subsequent chapters. This is in contrast with liquid-fed bioreactors whereby the yield loss and bottleneck are issued from insufficient mixing, characterised by the circulation timescale equalling or exceeding the turnover of substrates (Wang et al., 2015). Therefore, the investigation of lifeline analysis might not be relevant. Interestingly, lifeline analysis conducted by Siebler et al. (2019) has shown that less than 1% of the total volume of 125 m^3 bubble column is operating with maximum CO transfer, showing that the majority of the microorganisms are experiencing a substrate limiting regime. The biological methanation is very similar to the CO fermentation process studied by Siebler et al. (2019) as both H_2 and CO have very close

solubility (0.79 mol.m^{-3} vs. 0.92 mol.m^{-3} at 25°C, P=1atm in pure water, see Table 1.6). Therefore, a similar conclusion can be drawn with the gas-liquid mass transfer phenomenon as the limiting step. In terms of biological methanation description, it is treated as a heterogeneous reaction with the energy and carbon substrates originating from the gas phase and dissolved in the liquid phase to be assimilated by the microorganism. A novel biological methanation model based on the standard approach in multiphase chemical engineering modelling will be investigated to handle the limiting regime between the biological uptake capacity regime and the physical substrate transport regime.

The 1D model validation is conducted using in-house experimental data and literature data. For the biological methanation, the 1D model is validated using the experimental data provided by the SYMBIOSE team at Toulouse Biotechnology Institute. The effectiveness of the 1D model for biological methanation is also compared with that obtained through the Eulerian CFD simulations. The developed 1D model is also applied to different applications: the physical absorption of CO_2 in water, the chemisorption of CO_2 in NaOH, and the study of substrate gradients in large-scale fermenters.

This thesis is structured as follows:

- Chapter 2 details the experimental methods and the model structure.
- Chapter 3 is devoted to the thorough validation of each aspect of the complete model, ranging from the hydrodynamics to mass transfer and (bio)reaction.
- Two industrial applications using the 1D model are highlighted in Chapter 4 - biological methanation scale-up and investigation of substrate gradients in large-scale fermenters.
- Chapter 5 presents the application of reactive bubbly flow which gains lately the interest of chemical engineers and researchers. It aims to present the coupling between hydrodynamics and reactive bubbly flow.
- Chapter 6 reveals the comparison study between pilot-scale experimental data, 1D and CFD model predictions for the biological methanation process.
- Chapter 7 lists the general conclusions of this work and some outlooks.

Chapter 2 Materials and methods

2.1 Experimental study in pilot-scale bubble column

In this thesis, some experiments on bubble size distribution and gas holdup were conducted in the air-water system. The objective was to validate the hydrodynamic part of the 1D model with own-measured experimental data. It exists different measuring techniques to study the hydrodynamic of gas-liquid bubble columns, which can be classified into non-intrusive and intrusive techniques. More details on the measuring techniques can be found in Boyer et al. (2002) who provided an extensive review of the instrumentation techniques developed for multiphase flow analysis. In this work, due to some constraints, it had been narrowed down to the optical methods to quantify the hydrodynamics behaviour, namely the shadowgraphy method. In the same bubble column, biological methanation experiments had been performed by the SYMBIOSE team of TBI, and the bioprocess was monitored for more than a year, yielding some experimental data available for model validation. The biological methanation experiment was carried out before the start of this thesis, the discussion is limited to the extent of the understanding of the process and for model validation. Further discussions and details can be found in the previous work (Laguillaumie et al., 2022; Rafrafi et al., 2019).

2.1.1 Experimental setup

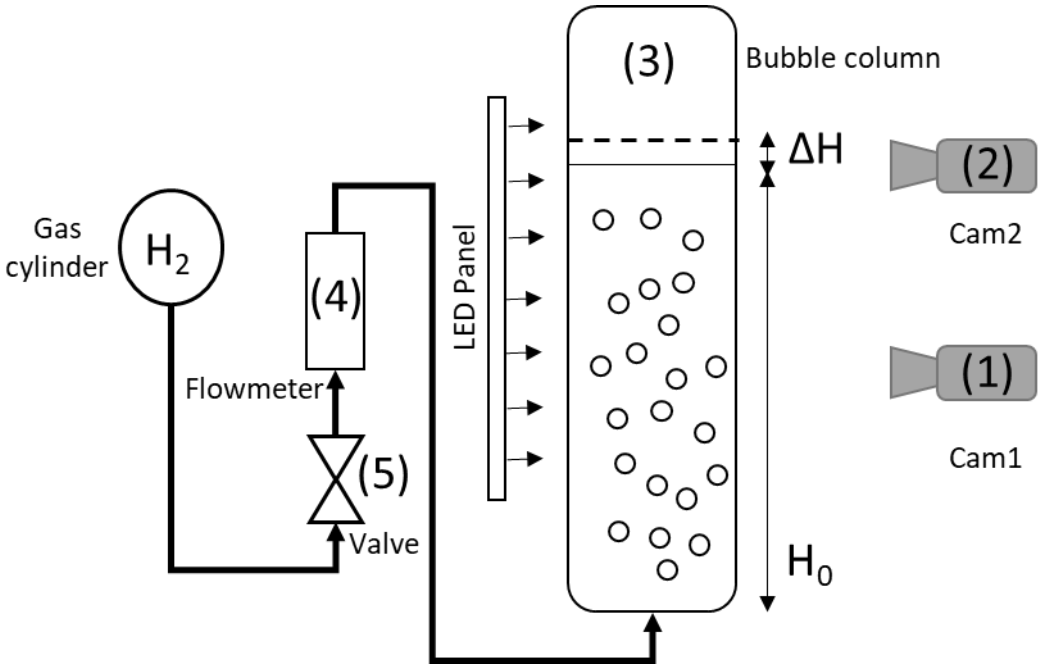

Figure 2.1: Simplified experimental setup for bubble size and gas holdup measurements

Figure 2.1 shows the simplified sketch of the experimental setup with the required components numbered in the figure. The experimental setup is composed of a 22 L cylindrical glass bubble column with an internal diameter and height of 0.15 m and 1.24 m, respectively. The initial liquid height (H_0) was kept at 1 m. Bubbles were injected through a ceramic porous plate with a porosity of 100-160 µm at the bottom of the column occupying the entire section of the column in order to favour a homogeneous flow regime in the column. The gas feed line was equipped with a flowmeter (4) with a measuring range of 0-2 NL/min. A camera, Cam1 (1) was installed at column's mid-height to identify the bubble geometrical characteristics. The bubble images were captured near to the wall to avoid image deformation due to the cylindrical shape of the column. A second camera, Cam2 (2) was placed at the free surface to detect the rising water level for the overall transient gas holdup calculation. Cam1 provides an acquisition window of 26 x 26 mm² with a spatial resolution of 40-pixel mm^{-1}. Cam2 has a narrower but longer view of 9.7 x 38.7 mm² with a spatial resolution of 27-pixel mm^{-1}. Due to space constraints, no square box was placed around the column during the image acquisition. Besides, the visualisation window was very tiny and the possible effect of the optical density correction is negligible. Cam2 and Cam1 operated simultaneously at the same frequency of 20 Hz with a total of 1000 images shot for each measurement. Thus, for each dynamic gas loading, the bubble size distribution was also measured. A homogeneous light-emitting diode (LED)-panel was installed behind the column to increase the luminosity.

Note: Previously, the bubble column was used for biological methanation experiments. No hydrodynamics study, particularly the bubble size and gas holdup measurement had been conducted. By the time this thesis began, another trickle-bed reactor is stacked on top of the bubble column. This complicated the use of optical probe for local bubble size and local gas holdup measurement. The mass transfer experiment, particularly the $k_L a$ characterisation was not conducted either due to this space constraint.

2.1.2 Bubble size distribution measurement

Among the model parameters, bubble diameter is not easily predictable for hydrodynamics modelling. It can be estimated through correlations, analytical solutions or experimental measurements. In this work, some experiments were conducted to determine the Sauter mean diameter (d_{32}). The bubble size distribution measuring technique in this thesis followed the work of Laupsien et al. (2019).

For bubble size measurement, the gas-liquid system employed was H_2-water. H_2 was chosen due to its very low solubility (see Table 1.6). This ensures that the mass transfer impact on the hydrodynamics is the minimum. Another practical reason is due to biological methanation is performed in the same reactor with the available H_2 gas feed line already in place. The superficial gas velocity, $j_G = Q_G/S$ defined as the gas flow rate (Q_G) per column cross-section (S) was varied between [0 – 0.16] cm/s. The recorded images were then treated using Matlab® image processing toolbox. The image processing algorithm used to extract the bubble geometrical characteristics followed the work of Laupsien et al. (2019) and the step-by-step method is briefly recalled here.

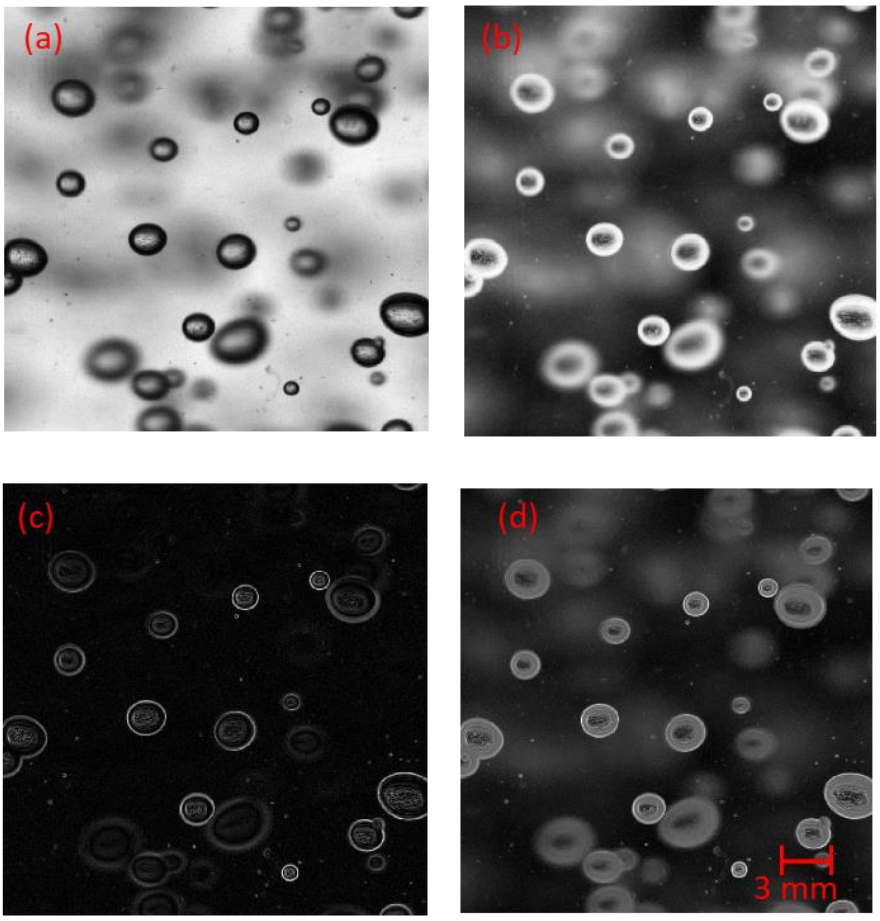

Figure 2.2: Preprocessing of raw image. (a) Raw image. (b) Normalized and inverted image (c) Contour detected image (d) Resulting image from image (b) plus image (c)

The preprocessing step of the raw image is presented in Figure 2.2. First, the raw image (Figure 2.2(a)) is normalized and inverted (black → white and vice versa) in order to compare to the same threshold for all the images (Figure 2.2(b)). The bubble contour is next determined by applying a grey level gradient using the Sobel method with a threshold value of 0.85, as shown in Figure 2.2(c). In the end, the normalized and inverted image is added to the contour-detected image to form a pre-processed image (Figure 2.2(d)), ready for the next image processing step.

The step-by-step image processing algorithm is shown in Figure 2.3. A hierarchy filtering criteria based on a set of control parameters as presented in Laupsien et al. (2019) is applied to the image. The control parameters include the border removal, minimum equivalent diameter, solidity, and eccentricity. The solidity is defined as the area of a convex hull (smallest possible polygon with an area $A_{polygon}$) surrounding the object under consideration relative to its raw projected area A_{raw}, as shown in equation (2.1) (Laupsien et al., 2019). The eccentricity is defined as the ratio between the major and minor axes of a projected ellipse, as written in equation (2.2). M is the large semiaxis and m is the small semiaxis length. For the equivalent diameter determination, it is assumed that the bubbles formed have an oblate ellipsoidal form. The equivalent diameter d_{eq} of a sphere can be obtained by assuming the equality between the volume of the sphere V_{sphere} (equation (2.3)) and the volume of the ellipsoid $V_{ellipsoid}$ (equation (2.4)). The equivalent diameter can be expressed using equation (2.5).

$$Solidity = \frac{A_{Raw}}{A_{polygon}} \tag{2.1}$$

$$Eccentricity = \frac{M}{m} \tag{2.2}$$

$$V_{sphere} = \frac{\pi d_{eq}^3}{6} \tag{2.3}$$

$$V_{ellipsoid} = \frac{4}{3}\pi m M^2 \tag{2.4}$$

$$d_{eq} = \sqrt[3]{8mM} \tag{2.5}$$

$$d_{32} = \frac{\sum_{i=1}^{n} w_i {d_{eq}}_i^3}{\sum_{i=1}^{n} w_i {d_{eq}}_i^2} \tag{2.6}$$

The first step of the filtering strategy is to binarize the image (Figure 2.3(a)). From the binarized image, all apparent holes inside the bubbles due to light refraction or alignment of the light source, bubbles and camera are filled (Figure 2.3(b)). This operation will only work if the object has an enclosed contour. Next, all objects with more than 10% of their contour length at the image borders are removed. A minimum diameter of 0.5 mm is then applied to remove any tiny particles that exist in the

liquid. Finally, the solidity and eccentricity filters are applied to remove all objects with a convex shape and overlapping bubbles. The threshold value for solidity and eccentricity are fixed at a minimum of 0.97 and a maximum of 2, respectively, following the work of Laupsien et al. (2019). For all experiments, a minimum of 1000 bubbles are considered to ensure the statistical convergence of the bubble size distribution. The Sauter mean diameter is therefore calculated based on its definition, as written in equation (2.6), with w_i the number density function associated to the equivalent diameter class d_{eq_i}.

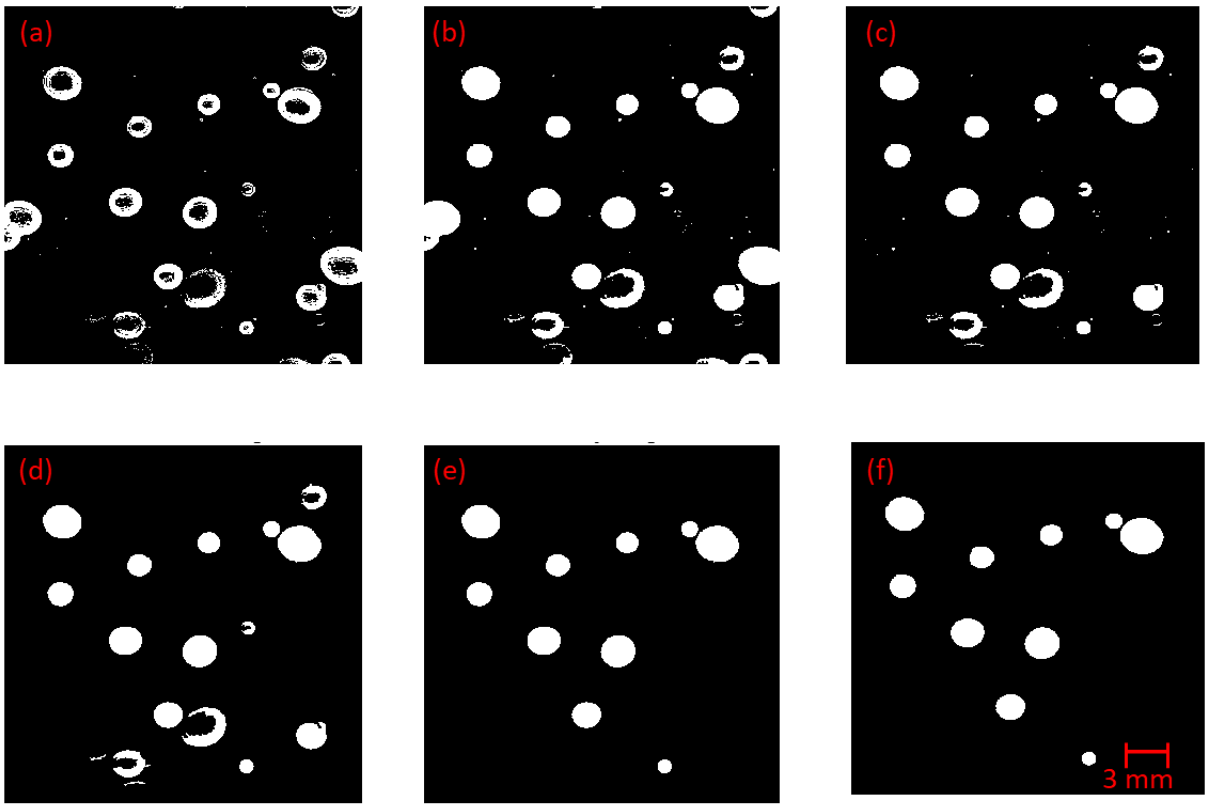

Figure 2.3: (a) Sequential step of image processing algorithm. (a) Binarized image (b) Hole-filled image (c) Border removed image (d) Mini-particle removed image (e) Solidity filtered image (f) Eccentricity filtered image

2.1.3 Global gas holdup measurement

The gas holdup is an important parameter that quantifies the fraction of gas that is present in the system. The changes of gas holdup profile in the function of superficial gas velocity is commonly used to characterise the flow regime (Besagni et al., 2018c; Shah et al., 1982; Wallis, 1969). It is also very useful for the characterisation of industrial applications where the mass transfer is the main point of interest.

The present bubble column was constructed without any hole or opening for pressure tapping. Moreover, the space constraint limits the use of an optical probe to assess local gas holdup. As aforementioned reason, the gas holdup can then only be measured via the non-intrusive optical method. In this work, the dynamic gas holdup was measured using the bed expansion method as typically done in the literature (Krepper et al., 2007). Instead, a camera was applied rather than a ruler to better capture the liquid swelling at milliseconds precision (Sasaki et al., 2017). The algorithm to determine the global gas holdup is depicted in Figure 2.4. The first 64-pixel nearest to the wall (Figure 2.4(b)) were extracted to calculate the mean pixel value for each row. The grey profile obtained was then normalized so that all images can be compared to the same threshold value. The lower meniscus level $H(t)$ was detected by applying a threshold of 70% of the maximum pixel value (Figure 2.4(c)). The process was repeated for all images to obtain a temporal rising water level profile (Figure 2.4(d)).

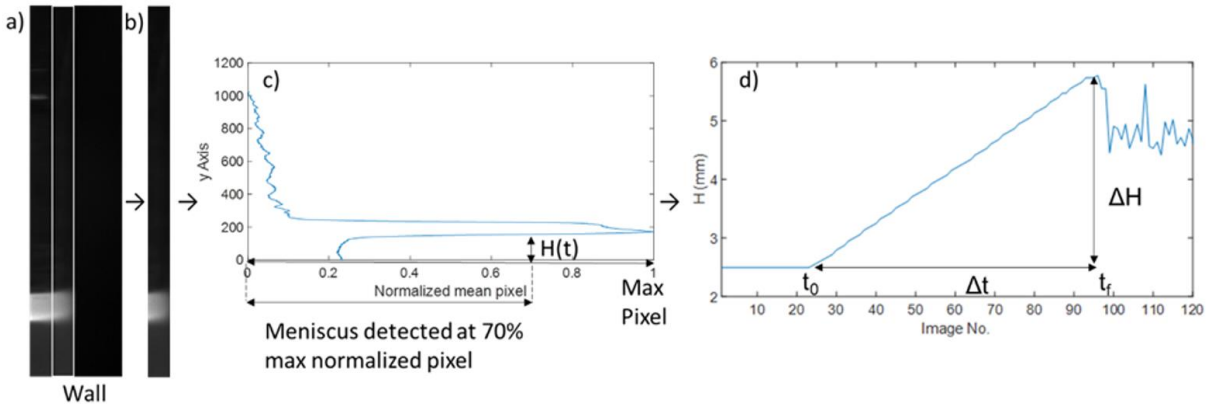

Figure 2.4: Global gas holdup measurement from image processing of raw data. (a) Raw image (b) Cropped image (c) Normalized pixel profile (d) Instantaneous liquid level

The experimental gas holdup was then calculated using equation (2.7). In this equation, H_0 corresponds to the initial liquid height and $\Delta H(t)$ holds for the instantaneous liquid elevation ($H(t) - H_0$), as shown in Figure 2.4. It was found experimentally that the slope of the rising water level profile corresponds to the superficial gas velocity.

$$< \varepsilon_{G,exp}(t) > = \frac{\Delta H(t)}{\Delta H(t) + H_0} \tag{2.7}$$

$$j_G = \frac{Q_G}{S} = \frac{\Delta H}{\Delta t} \tag{2.8}$$

The abovementioned methods with two cameras are a non-intrusive way of direct and simultaneous measurement of bubble size, superficial gas velocity, and global gas holdup.

2.1.4 Biological methanation experiment

The biological methanation experiments were carried out in the same bubble column. It must be emphasised that the biological experiment was not conducted in this thesis, but it was conducted previously before the thesis by the SYMBIOSE team (EAD9) of Toulouse Biotechnology Institute. The biological methanation results were communicated in the past in Rafrafi et al. (2019). The simplified sketch of the biological methanation experimental setup is presented in Figure 2.5(a) which is composed of the same 22 L bubble column with an initial liquid height and internal diameter of 1200 mm and 150 mm, respectively. The experiment was conducted at atmospheric pressure and in thermophilic conditions (temperature of 55°C). H_2:CO_2 with a ratio of 4:1 was fed to the column with any unreacted gas being recirculated at a rate (Q_r) of 2 NL/min. Gases were supplied from gas cylinders from Air Liquide®. The gas composition at the bubble column outlet was quantified by gas chromatography (Hewlett Packard HP 5890 Series II, Agilent Technologies). The carbon dioxide and methane output gas flowrate were measured with infrared gas analysers (X-Stream Enhanced Series, Rosemount), while hydrogen was measured with a thermal conductivity analyser (Binos 100 2M, Rosemount). The inoculum was composed of a mix of anaerobic digestion sludges from three different plants treating household wastes, duck manures and bovine manures (Laguillaumie et al., 2022). To characterise the bioreactor performances, two parameters were chosen, namely outlet methane gas purity ($y_{CH_4,out}$) and methane production rate (MPR). MPR is defined in equation (2.9) as the outlet methane volumetric flowrate per unit volume of the reactor. These two parameters represent the quality and the quantity of methane contained in the off-gas.

$$MPR = \frac{y_{CH_4,out} \cdot Q_{G,out}}{V} \tag{2.9}$$

where $Q_{G,out}$ is outlet gas flowrate and V is the reactor volume.

Two types of gas sparger, presented in Figure 2.5(b) and Figure 2.5(c), were tested experimentally. The first, named the heterogeneous sparger, is composed of 4 small porous sintered diffusers with a diameter of 10 mm each. The second, a homogeneous sparger, consists of a single porous sintered diffuser occupying the bottom cross-section of the column. Both spargers have the same properties with a pore size between 100-160 µm. The total area of the spargers is 0.00314 and 0.0177 m² for the heterogeneous and homogeneous sparger, respectively. The inlet gas flowrate ($Q_{G,in}$) varied between 0.001 to 0.16 NL/min. Considering the maximum gas flowrate possible flowing into the bubble column is 2.16 NL/min, the expected maximum superficial gas velocity can be calculated. Taking the normal

condition ($P_N = 101325\ Pa$, $T_N = 273.15\ K$) and the pressure (supposing 2% of gas and an initial height of 1.2 m) and temperature at the inlet with $P = 101325 + 1000 \cdot 9.81 \cdot (1 - 0.02) \cdot 1.2 = 112861\ Pa$ the expected maximum gas flowrate is $Q_{G,in} = 3.88 \times 10^{-5} m^3.s^{-1}$, which correspond to an expected maximum superficial gas velocity of 0.002 m.s^{-1}. We must highlight the low superficial gas velocity applied during biological methanation in this experimental configuration. This is in contrast with other bioprocesses which operates mostly in high superficial gas velocity, such as yeast fermentation whereby the superficial gas velocity can rise up to 0.3 m.s^{-1} (McClure et al., 2014c).

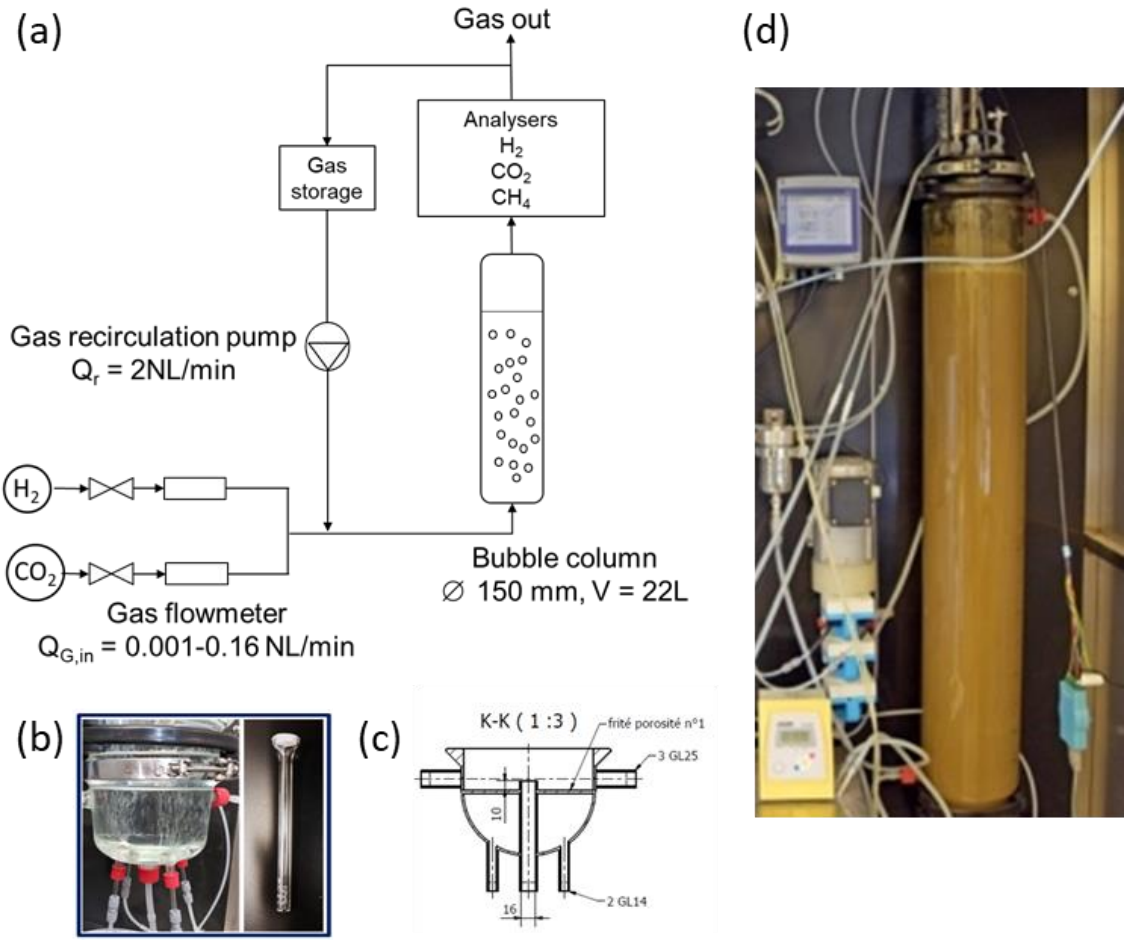

Figure 2.5: (a) Simplified experimental setup. (b) Heterogeneous (4 inlets) sparger (c) Homogeneous sparger. (d) Bubble column used for biological methanation

2.2 Numerical tools for bioreactor modelling

2.2.1 Eulerian approach

The use of the multiphase fluid mechanics approach is necessary to calculate explicitly the hydrodynamics, concentration fields, and transport of species in the reactor volume. The conservation of mass, momentum, and energy equations can be established in a control volume at the scale of the system studied. These equations can be written as Lagrangian or Eulerian depending on the chosen reference frame. In this thesis, the Eulerian approach is used to address the conservation equations. These conservation equations are a set of partial differential equations with no easy analytical solutions. Numerical methods are necessary to solve them, by discretising in time and space, which approximate a continuous nature of the problem to a discrete solution. This resolution method requires a numerical algorithm, (e.g. finite volume, finite element, finite difference) that is related to the choice of the 3D geometrical mesh. This complex and hard to implement 3D resolution often requires high computational resources. It exists a simple alternative method when the variations of all quantities in the cross-section perpendicular to the main flow direction could be neglected. This pares down the 3D model to a 1D model by integrating the 3D equations in the cross-section. The physical quantities vary only in the direction of the flow and time. Regardless of the complexity of the approach, the resolution requires the closure models to express non-resolved local phenomena, such as the interfacial transfer term.

In the following section, the formulation of the general Eulerian equations of the conservation of mass, momentum and species transport is recalled here, as it is already presented in Section 1.2.2.2. Next, a detailed description of the 1D model developed during the thesis is presented.

2.2.2 3D General Eulerian equations

For an elementary volume in a multiphase flow system, the conservation equations for the mass, momentum and species transport are given by:

$$\frac{\partial \alpha_k \rho_k}{\partial t} + \vec{\nabla}.(\alpha_k \rho_k \overrightarrow{u_k}) = \overline{m_k} \tag{2.10}$$

$$\frac{\partial \alpha_k \rho_k \overrightarrow{u_k}}{\partial t} + \vec{\nabla}.(\rho_k \alpha_k \overrightarrow{u_k} \otimes \overrightarrow{u_k}) = \alpha_k\left(\rho_k \vec{g} - \vec{\nabla} P\right) + \overrightarrow{\nabla}.\left(\tau_k - \rho_k \overline{u_k' u_k'}\right) + \overline{u_k\, m_k} + \overrightarrow{M_k} \tag{2.11}$$

$$\frac{\partial \alpha_k C_k}{\partial t} + \vec{\nabla}.(\rho_k \alpha_k C_k) = \alpha_k S_k - \overrightarrow{\nabla}.\alpha_k\left(\overrightarrow{J_k} + \overline{c_k' u_k'}\right) + \overline{c_k\, m_k} + L_k \tag{2.12}$$

The definition of each term of equations (2.10)-(2.12) was presented in the bibliography chapter (see equations (1.5)-(1.7)). These equations are textbook Eulerian equations for conservation equations solved by any commercial or open source CFD simulation software (ANSYS Fluent, OpenFOAM, etc). If the flow is mostly unidirectional, the 3D model can be rendered to a 1D model which still offers meaningful physical modelling, provided appropriate closures are applied.

In this thesis, we developed a spatio-temporal 1D model which is formulated as the axial dispersion model. In fact, the 1D model can be interpreted as a macroscopic reactor-scale model derived from the cross-sectional integration of the local conservation equations (2.12), as shown in Figure 2.6. This approach is used extensively in the literature to study multiphase contactors at the laboratory scale (Camarasa et al., 2001; Cockx et al., 1997; Talvy et al., 2005) and at the industrial scale (Chen et al., 2016; de Swart and Krishna, 2002; Li et al., 2019; Siebler et al., 2020). The next section is devoted to the description of the 1D model, including the closure models, the discretisation schemes, the resolution strategy and the originalities.

2.2.3 1D spatio-temporal axial dispersion model

2.2.3.1 General equations

The 1D spatio-temporal gas-liquid model developed in this work aims to study the multispecies mass transfer coupled with (bio)reaction kinetics. It is chosen that α_k be the holdup of each phase k in the 3D volume, and after cross-sectional integration of α_k, we denoted ε_k as the spatial averaged holdup at a certain axial location. The 1D model approach is very similar to the examples in the literature discussed in Section 1.4, but some new particularities are developed and discussed in this section. The motivation to develop this model has also been discussed in Section 1.4. The 1D model is composed of the following partial mass balances for any species i in the gas and liquid phase, respectively.

$$\frac{\partial \phi_{G,i}}{\partial t} + \frac{\partial u_G \phi_{G,i}}{\partial z} = D_G \frac{\partial}{\partial z}\left(\varepsilon_G \frac{\partial C_{G,i}}{\partial z}\right) - k_{L,i} a (C_i^* - C_{L,i}) \tag{2.13}$$

$$\frac{\partial \phi_{L,i}}{\partial t} + \frac{\partial u_L \phi_{L,i}}{\partial z} = D_L \frac{\partial}{\partial z}\left(\varepsilon_L \frac{\partial C_{L,i}}{\partial z}\right) + k_{L,i} a (C_i^* - C_{L,i}) + \varepsilon_L R_i \tag{2.14}$$

$$\varepsilon_G + \varepsilon_L = 1 \tag{2.15}$$

$$\phi_{G,i} = \varepsilon_G C_{G,i} \tag{2.16}$$

$$\phi_{L,i} = \varepsilon_L C_{L,i} \tag{2.17}$$

$$\rho_G = \sum_i \frac{M_i P_i}{1000RT} = \sum_i \frac{C_{G,i}}{1000} \tag{2.18}$$

$$\varepsilon_G = \frac{\sum \phi_{G,i}/M_i}{P} RT \tag{2.19}$$

The resolution of the 1D model provides the spatial and temporal profiles of gas and liquid holdup, as well as the species concentrations in both phases. u_G and u_L are the gas and liquid velocities, respectively. ε_G and ε_L are the gas and liquid holdup, summing to one, as stated in equation (2.15). $C_{G,i}$ and $C_{L,i}$ are the concentration of species i in each phase: mass per unit volume of the gas and liquid phase, respectively. Hence, $\phi_{G,i}$ and $\phi_{L,i}$ of equations (2.16) and (2.17) are the concentration of species i: mass per unit volume of the column.

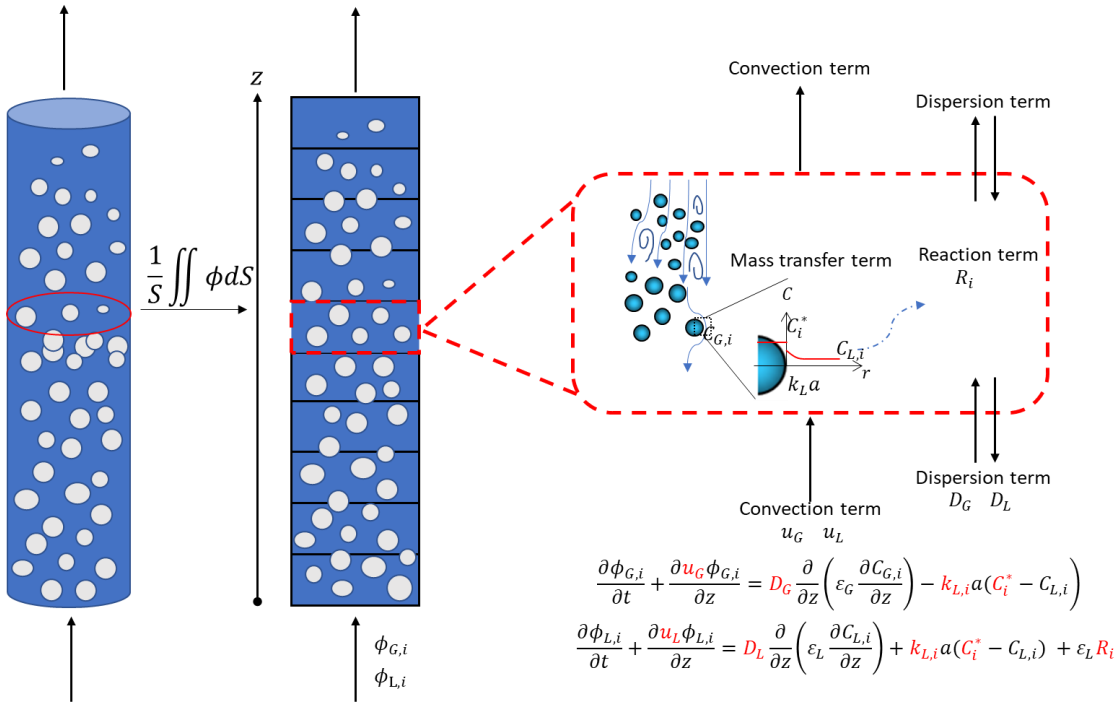

Figure 2.6: Schematic representation of the 1D model. The variables highlighted in red font requires closure relations to complete the model

Equations (2.13) and (2.14) signify the evolution of the species mass at an elementary volume ∂z over time depend on the convective flux, the dispersive flux, the mass transfer flux and the reactive flux (in the liquid phase). The transported variables are $\phi_{G,i}$ and $\phi_{L,i}$ in the units of $mg_i.L^{-1}$. Therefore,

equations (2.13) and (2.14) are the species transport equations analogous to the 3D species conservation equations, after cross-sectional integration of equation (2.12). The momentum conservation equation (2.11) is not solved in the 1D model, but closures are applied to model the gas-liquid hydrodynamics. Omitting the dispersion term, the summation of equations (2.13) and (2.14) for each species i yield the continuity equation (2.10) for gas and liquid phase, respectively. The continuity equation (2.10) is not solved but the local gas density ρ_G and the gas holdup ε_G can be calculated from equations (2.18) and (2.19), respectively. Here, M_i is the species-dependent molecular weight.

By analysing equations (2.13) and (2.14) , the axial dispersion term is the specific term to the 1D model that characterises all diffusivity phenomena, i.e. spatial dispersion, molecular diffusivity, and turbulent diffusivity (Talvy et al., 2007a). D_G and D_L stand for the dispersion coefficients in each phase which are assumed independent of z in this work. The mass transfer rate is obtained from the product of a species-dependent mass transfer coefficient, $k_{L,i}$, the interfacial area per unit volume of the column, a, and the driving force $(C_i^* - C_{L,i})$. R_i is the volumetric consumption/production rate per unit volume of liquid $(mg_i.L^{-1}.s^{-1})$. The schematic representation of the 1D model is shown in Figure 2.6.

2.2.3.2 Closure equations

Besides the resolved variables $\phi_{L,i}\ and\ \phi_{G,i}$, closure equations or additional models are needed to define the parameters in the conservation equations. These closures parameters reflect the local physical phenomena occurring on-the non-resolved scale of the axial 1D model.

- Dispersion coefficients

The gaseous axial dispersion coefficient D_G is mainly related to large velocity differences between the bubbles of different sizes when coalescence between bubbles is low (Bardin-Monnier et al., 2003). The liquid axial dispersion coefficient D_L describes the mixing in the liquid phase, attributed to different reasons such as large-scale liquid recirculation, radial exchange flow, bubble-induced agitation and liquid entrainment induced by density gradient (Deckwer and Schumpe, 1993). These recirculation flow induce an axial mixing and appears mostly under the heterogeneous regime (Heijnen and Van't Riet, 1984). In this work, D_L is calculated from the correlation proposed by Deckwer et al. (1974), as presented in equation (2.20) while D_G was estimated from the correlation of Wachi and Nojima, (1990), as written in equation (2.21). Both correlations are a function of the superficial gas velocity, j_G, and bubble column diameter, D_r.

$$D_L = 2.7 \cdot 10^{-4} \cdot (D_r \cdot 100)^{1.4} \cdot (j_G \cdot 100)^{0.3} \quad (2.20)$$

$$D_G = 20 \cdot D_r^{1.5} \cdot j_G \quad (2.21)$$

- Gas and liquid velocity

Instead of solving the momentum conservation equation, the hydrodynamics of the 1D model is simplified and modelled using algebraic equations. For the bubble velocity, it is assumed that the bubbles rise at its terminal velocity u_∞ which can be derived from a momentum balance between buoyancy, drag and gravity forces. The terminal velocity is defined by the drag coefficient C_D and the Sauter mean diameter d_b, as expressed in equation (2.22). For the liquid velocity, it varies according to the bubble column operation mode. If the bubble column is closed to the liquid, the liquid velocity is considered as $u_L = 0$. If the bubble column operates in co-current or counter-current mode, a non-zero velocity has to be considered. In general, the bubble rises at a relative velocity $u_{rel} = |u_G - u_L|$ (also called slip velocity) which considers the contribution of the liquid velocity on the bubbles.

$$u_\infty = \sqrt{\frac{4}{3}\frac{g.(\rho_L - \rho_G)\, d_b}{\rho_L.C_D}} \quad (2.22)$$

The terminal velocity depends strongly on the drag coefficient. Various correlations for C_D have been discussed in Section 1.3.3.

In the case of non-uniform hydrodynamics due to non-homogeneous gas injection or with the presence of strong liquid recirculation, the bubble velocity can be better described by the drift-flux model (Zuber and Findlay, 1965). It is commonly used in 1D modelling such as for airlift contactors whereby liquid recirculation is inevitable (Camarasa et al., 2001; Talvy et al., 2007a). The drift-flux model is composed of two components: (i) gas transport induced by the mixture velocity $< j >$, which is the sum of gas and liquid superficial velocity ($j = j_G + j_L$) and (ii) the buoyancy-driven gas transport u_{rel}. The gas velocity in the drift-flux model is expressed as:

$$u_{df} = C_0 < j > + u_{rel} \quad (2.23)$$

The distribution coefficient C_0 is defined as

$$C_0 = \frac{< \varepsilon_G . j >}{< \varepsilon_G > . < j >} \tag{2.24}$$

It can be determined from the experimental or 3D numerical simulation spatial profiles.

- Interfacial mass transfer

The mass transfer term changes with the vertical coordinate z because it involves other variables that are spatially dependent ($\varepsilon_G, d_b, u_{rel}, C_i^*, C_{L,i}$). This indicates that the mass transfer intensity will vary axially. The local volumetric interfacial area a is computed from the local gas volume fraction ε_G and the local Sauter mean diameter d_b. It is assumed that the Sauter mean diameter is similar to the mean diameter of the bubble size distribution having the same volume of an equivalent sphere, in a manner that $d_b \approx d_{32} \approx d_{30}$. The local $k_{L,i}$ value can be estimated using the classical Higbie (1935) correlation, as written in equation (2.25) and it is species-dependent due to different values of liquid-side diffusion coefficient D_i. Different closure models for the mass transfer coefficient can be found in the literature (Rzehak, 2016; Solsvik, 2018). Some are empirical, others are derived analytically as it is still a wide research area in progress (Dani et al., 2022, 2006; Kentheswaran et al., 2022). It is very flexible to implement different mass transfer closure models in the 1D model according to the Sauter mean diameter, fluid properties and contamination effect. For different closure models, it can be referred to Section 1.2.3.

$$k_{L,i} = 2\sqrt{\frac{u_{rel}\, D_i}{\pi\, d_b}} \tag{2.25}$$

$$a = \frac{6\varepsilon_G}{d_b} \tag{2.26}$$

The solubility of each species C_i^* changes depending on the local partial pressure of the gas P_i. It is calculated from the Henry's constant but different forms of Henry's constant exist Sander (2015). Generally, the solubility is higher at the bottom of the column due to higher hydrostatic pressure. Using Henry's constant He_i of the units $mg_i . L^{-1} . Pa^{-1}$, the solubility can be calculated as

$$C_i^* = He_i . P_i = He_i y_i\, P = \, He_i C_{G,i} RT \tag{2.27}$$

The local pressure depends on the overall gas holdup in the volume of fluid above a given location z:

$$P(z,t) = P_0 + \left(1 - \widetilde{\varepsilon_G(z)}\right) \rho_L g(H - z) \tag{2.28}$$

With P_0 the pressure at the top of the column and $\widetilde{\varepsilon_G(z)} = \frac{1}{H-z}\int_z^H \varepsilon_G(\zeta,t)\,.\,d\zeta$.

Due to mass transfer, bubble shrinkage is expected. The changes in the Sauter mean diameter d_b is described by

$$d_b = d_{b0}\sqrt[3]{\frac{\varepsilon_G}{\varepsilon_{G0}}} \tag{2.29}$$

Whereby d_{b0} is the inlet bubble diameter, ε_{G0} is the inlet gas holdup. Equation (2.29) is derived by assuming the number of bubbles per unit volume remains constant throughout each cross-section of the column. It indicates that the bubble diameter changes accordingly with the local gas holdup. The local gas volume fraction changes depending on the mass transfer and (bio)reaction intensity, as well as the pressure dependence, in agreement with the ideal gas law. This approach is similar to the work of Bauer and Eigenberger (1999), but the original work includes the bubble number density in the diameter variation as it is tracked locally, whereas, in our work, we supposed the bubble number is constant and assumed the coalescence and breakup mechanisms are neglected since the gas flowrate is low, signifying that the flow regime remains in the homogeneous regime.

- Source term due to bioreaction/chemical reaction

In the case of (bio)reactive bubbly flow, closure models describing the consumption/production rate of the species have to be included in the 1D model. In this thesis, the reaction of interest is biological methanation. In this section, the biological methanation model as developed in Ngu et al. (2022a) is presented.

The biological methanation model is based on the original model of Schill et al. (1996). The authors proposed that the bio-catalysed conversion of hydrogen and carbon dioxide into methane is represented through equations (2.30) and (2.31), which signifies biomass growth (r_1) and maintenance (r_2), respectively.

$$H_2 + \nu_{CO_2,1} CO_2 + \nu_{NH_3,1} NH_3 \underset{r_1}{\rightarrow} \nu_{X,1}\,X + \nu_{CH_4,1} CH_4 + \nu_{H_2O,1} H_2O \tag{2.30}$$

$$H_2 + \nu_{CO_2,2} CO_2 \underset{r_2}{\rightarrow} \nu_{CH_4,2} CH_4 + \nu_{H_2O,2} H_2O \tag{2.31}$$

In our model, we consider a third reaction, the death of biomass (r_3).

$$X \underset{r_3}{\rightarrow} \emptyset \tag{2.32}$$

From equations (2.30)-(2.32), a metabolic flux-based model is developed which consists in computing the vector of reaction rates $r = \{r_1, r_2, r_3\}$ expressed in $g_{H_2}.L^{-1}.h^{-1}$. Let φ_{H_2} be the specific hydrogen uptake rate and m the specific maintenance rate (both in $g_{H_2}.g_X^{-1}.h^{-1}$). In contrast to the work of Schill et al. (1996), we do not assume that $r_2 = mX$ (the maintenance rate is no longer constant) and we alternatively use m to set the upper bound for the maintenance reaction rate ($r_2 \in [0, mX]$). The second constraint is $r_1 + r_2 = \varphi_{H_2}X$. Finally, priority is given to the maintenance reaction.

$$\begin{aligned} \varphi_{H_2} > m \;&\rightarrow\; r = \{\varphi_{H_2} - m, m, 0\}.X \\ \varphi_{H_2} < m \;&\rightarrow\; r = \{0, \varphi_{H_2}, m - \varphi_{H_2}\}.X \end{aligned} \tag{2.33}$$

As a consequence of the calculation procedure (2.33), biomass growth is only possible if the maintenance requirement is met, which is translated by the condition $\varphi_{H_2} > m$. In that case, the death rate is negligible. Otherwise, if the hydrogen supply is insufficient to satisfy the energy demand for maintenance ($\varphi_{H_2} < m$), the growth stops, maintenance proceeds at a rate defined by the hydrogen uptake rate φ_{H_2} and the cell death rate is proportional to the energy lacking for maintenance.

The calculation of the specific hydrogen uptake rate, φ_{H_2} uses basic principles of multiphase heterogeneous reactive systems: the reaction rate in the suspended phase (here it is the biological catalyst) is either set by the kinetics in that phase or limited by the external (physical) transport rate. Considering that the physical transport of substrate precedes uptake by the microorganisms, i.e. the two phenomena occur in series, the actual consumption rate can be expressed as the rate of the limiting step: biological consumption φ_{bio} or physical transport φ_{phy} rate (Morchain et al., 2017). A standard approach in multiphase reactor modelling is to define the actual consumption rate as the smallest of the two rates.

$$\varphi_{H_2} = \min\{\varphi_{bio}, \varphi_{phy}\} \tag{2.34}$$

The biological specific uptake capacity is calculated from the maximum hydrogen uptake capacity $q_{H_2}^{max}$, and the hydrogen concentration in the liquid phase C_{L,H_2}, through a Monod type equation.

$$\varphi_{bio} = q_{H_2}^{max} . \frac{C_{L,H_2}}{K_{H_2} + C_{L,H_2}} \tag{2.35}$$

The physical transport rate, φ_{phy} in equation (2.34) involves two phenomena: the gas-liquid mass transfer and the micromixing (responsible for the transport of dissolved species toward the cell-liquid interface). These phenomena are in parallel and the specific mass flux supplied to the cell is therefore set by the largest of the two rates, as expressed in equation (2.36).

$$\varphi_{phy} = max\left(\frac{k_L a_{H_2}(C_{L,H_2}^{*} - C_{L,H_2})}{\varepsilon_L X}, \frac{C_{L,H_2}}{X.\tau_m}\right) \tag{2.36}$$

In the limit of the local dissolved hydrogen going to zero, the physical supply is set by the specific gas-liquid mass transfer rate. Otherwise, the physical supply is set by the rate of micromixing in the liquid phase (τ_m). This second term is needed in the case where the local interfacial area would approach zero, for any reason, at some location, during the calculation. This situation may occur when performing CFD simulation whereby the local gas holdup turns zero. Altogether, equations (2.33)-(2.36) provide a physically consistent and numerically stable way to include a non-constant maintenance rate in the biological methanation model. It thus improves the model of Schill et al. (1996) who considers a constant maintenance rate and avoids the introduction of new arbitrary parameters in additional damping functions, as proposed by Inkeri et al. (2018). It also provides a more significant meaning to the physics rather than employing a homogeneous Arrhenius reaction rate (see Section 1.2.4.5), as in the work of Markthaler et al. (2020).

To help illustrate the proposed biological methanation model, Figure 2.7 shows the specific hydrogen uptake rate calculated by the Monod model, as shown in equation (2.35) and the specific substrate transport rate considering only the hydrogen mass transfer, i.e. $\varphi_{phy} = \frac{k_L a_{H_2}(C_{L,H_2}^{*} - C_{L,H_2})}{\varepsilon_L X}$. The temperature is considered as 55°C. The partial pressure of hydrogen is considered as 80% of the atmospheric pressure and the Henry's constant from Sander (2015), leading to C_{L,H_2}^{*} in an order of 1 mg.L^{-1}. The $k_L a$ is assumed to be 100 h^{-1}, which is a reasonable estimation as it is approximately the typical $k_L a$ value for a pilot-scale batch bubble column operating at a superficial gas velocity below 0.1 m.s^{-1} (Bouaifi et al., 2001; Deckwer and Schumpe, 1993; Deckwer et al., 1974; Deshpande et al., 2019; Heijnen and Van't Riet, 1984).

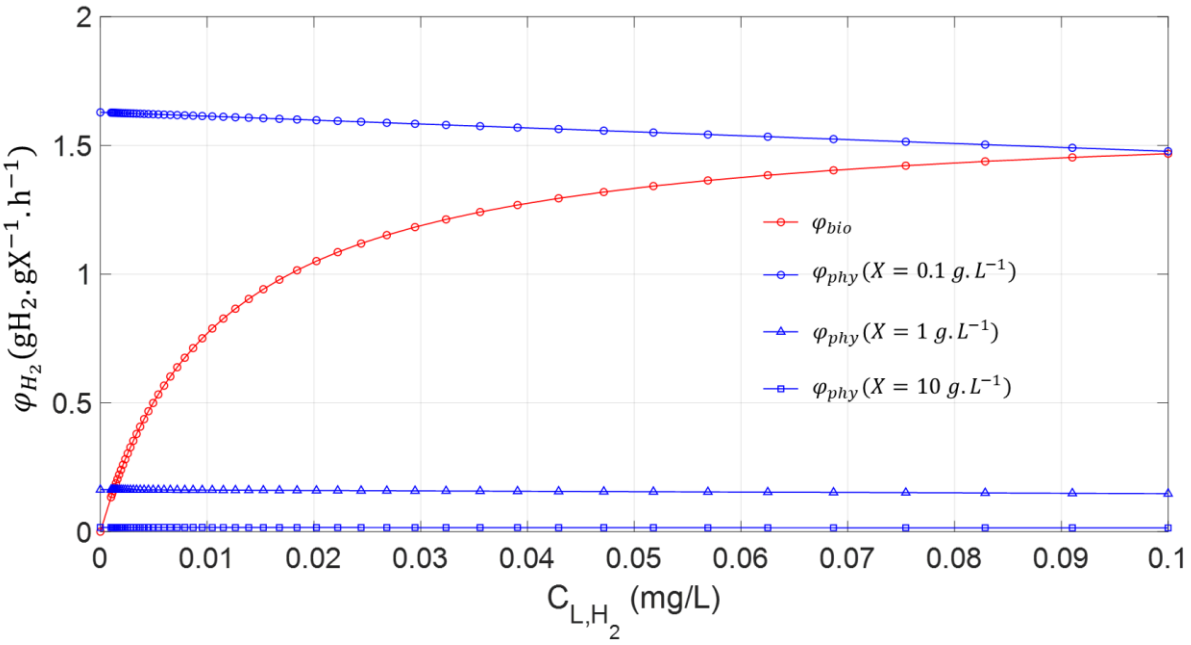

Figure 2.7: Specific hydrogen uptake rate as a function of dissolved hydrogen concentration. The physical transport rate for several biomass concentration is calculated.

Three biomass concentrations are also considered to demonstrate the effect of biomass concentration X to the specific hydrogen uptake rate φ_{H_2}. At very low biomass concentration (X = 0.1 g.L^{-1}), the dissolved hydrogen is sufficient that the hydrogen uptake is limited by the biological own uptake capacity. However, once the biomass concentration increases to very high value (generally once the steady-state is reached), the specific hydrogen uptake is set by the substrate transport rate: gas-liquid mass transfer rate. At this stage, the dissolved hydrogen concentration is very low and the hydrogen supply is not sufficient to balance the biological demand, the specific hydrogen uptake rate is thus calculated from the specific hydrogen mass transfer rate. It is shown that the biological specific uptake rate drops exponentially to zero when the hydrogen concentration approaches zero. Numerically, this could pose a stability problem as the set of equations becomes very stiff and unstable. If the hydrogen concentration equals to zero, the hydrogen reaction rate is zero if the uptake rate is calculated by the Monod model. However, the biological methanation is by nature a heterogeneous reaction, the continuity of flux imposed that the reaction rate is non-null but equal to the rate of substrate transport which is considered the gas-liquid mass transfer. In such conditions, increasing biomass concentration will not lead to higher methane productivity. The only solution to increase the productivity of the methane is by improving the mass transfer intensity, i.e. $k_L a C^*_{L,H_2}$. In this thesis, it is demonstrated the importance of $k_L a$ in determining the biological methanation efficiency, as discussed in Chapter 4 and Chapter 6.

Thus, the individual reaction terms R_i in equation (2.14) for the simulated species involved during the biological methanation are computed as

$$R_{H_2} = (r_1 + r_2) = \varphi_{H_2} X \tag{2.37}$$

$$R_{CO_2} = \left(Y_{CO_2/H_2} r_1 + Y^m_{CO_2/H_2} r_2\right) \tag{2.38}$$

$$R_{CH_4} = \left(Y_{CH_4/H_2} r_1 + Y^m_{CH_4/H_2} r_2\right) \tag{2.39}$$

$$R_X = Y_{X/H_2}(r_1 - r_3) \tag{2.40}$$

with $Y_{i/j}$ being the yield coefficient in grams of i per gram of j consumed. The values for the biological methanation kinetic rates and yield coefficient are reported in Ngu et al. (2022a) and the same values are applied in the following of this work, as reported in Table 2.1.

Table 2.1: Biological parameters proposed in Schill et al. (1996).

Parameters	Definition	Value	Units
$\mathrm{Y_{X/H_2}}$	$\nu_{X,1}\frac{M_X}{M_{H_2}}$	0.22	g_X/g_{H_2}
$\mathrm{Y_{CO_2/H_2}}$	$\nu_{CO_2,1}\frac{M_{CO_2}}{M_{H_2}}$	5.70	g_{CO_2}/g_{H_2}
$\mathrm{Y_{CH_4/H_2}}$	$\nu_{CH_4,1}\frac{M_{CH_4}}{M_{H_2}}$	1.92	g_{CH_4}/g_{H_2}
$\mathrm{Y^m_{CO_2/H_2}}$	$\nu_{CO_2,2}\frac{M_{CO_2}}{M_{H_2}}$	5.5	g_{CO_2}/g_{H_2}
$\mathrm{Y^m_{CH_4/H_2}}$	$\nu_{CH_4,2}\frac{M_{CH_4}}{M_{H_2}}$	2	g_{CH_4}/g_{H_2}
$q^{max}_{H_2}$	Maximum H_2 specific uptake rate	1.77	$g_{H_2}/g_X/h$
m	Maintenance rate	0.14	$g_{H_2}/g_X/h$
K_{H_2}	Affinity constant	0.01	mg_{H_2}/L

Other types of reaction can also be implemented in the 1D model. For example, the application of the 1D model to yeast fermentation and CO_2 chemisorption is demonstrated in Chapter 4 and Chapter 5, respectively.

2.2.3.3 Numerical discretisation and boundary condition

Equations (2.13) and (2.14) are partial differential equations that describe a continuous phenomenon, evolving in space and time. Due to the non-linearities nature of the equation, no analytical solution is available. Therefore, it is solved numerically via discretisation based on the finite difference method. Equations (2.13) and (2.14) are discretised on a regular grid with N nodes at constant node size so that the solution is approximated by the vector of discrete values $\phi_{G,i,n}$ and $\phi_{L,i,n}$ where $n \in [1, N]$. The spatial derivatives and the boundary conditions are discretised to second-order. The same order of accuracy preserves the stability of the numerical scheme. The convection term is calculated using second order upstream differences, as shown in equations (2.41)-(2.42). The dispersion term is calculated using second-order central difference, as shown in equations (2.44). The numerical is shown for the gas phase but the same is applied to the liquid. The suffix i that signifies the species is omitted for the clarity of the expressions.

For $n = 2$

$$\frac{\partial u_G \phi_G}{\partial z}|_n = \frac{u_G \phi_G|_{n+1} - u_G \phi_G|_{n-1}}{2\Delta z} \tag{2.41}$$

For $n = 3{:}N$

$$\frac{\partial u_G \phi_G}{\partial z}|_n = \frac{3u_G \phi_G|_n - 4u_G \phi_G|_{n-1} + u_G \phi_G|_{n-2}}{2\Delta z} \tag{2.42}$$

For $n = 2{:}N-1$

$$\frac{\partial u_G \phi_G}{\partial z}|_n = \frac{3u_G \phi_G|_n - 4u_G \phi_G|_{n-1} + u_G \phi_G|_{n-2}}{2\Delta z} \tag{2.43}$$

$$\frac{\partial}{\partial z}\left(\varepsilon_G \frac{\partial C_G}{\partial z}\right)|_n = \frac{\varepsilon_G C_G|_n - 2\varepsilon_G C_G|_{n-1} + \varepsilon_G C_G|_{n-2}}{\Delta z^2} \tag{2.44}$$

The boundary conditions depend on the operating condition of the bubble column. For example, for a bubble column operating in semi-continuous mode (open for the gas but closed for the liquid), a zero-flux (zero gradient) boundary condition is imposed to the liquid at both inlet and outlet of equation (2.14). The same boundary condition is applied to the gas only at the outlet. A Dirichlet boundary condition is always imposed to the gas inlet as the gas is injected into the bubble column, identical to the work of (Chen et al., 2015; Li et al., 2019; Siebler et al., 2020). If the bubble column includes a liquid feed, a Dirichlet boundary condition is also applied to the liquid, either at $n = 1$ or N, depending on

the operating mode as co-current or counter-current to the gas phase. Mathematically, a zero-gradient boundary condition is translated as equation (2.45). These boundary conditions are treated with second-order accuracy as shown in equations (2.46) and (2.47), the same as the spatial derivatives described earlier. The Dirichlet condition for the gas phase is shown in equation (2.48). P is calculated as the absolute pressure, considering the hydrostatic pressure, as shown in equation (2.28). P_0 is specific to the system studied. The gas holdup at the inlet $\varepsilon_{G,0}$ is computed as the ratio between the superficial gas velocity and the bubble relative velocity determined by the associated drag model. The spatial discretisation of equations (2.13) and (2.14) leads to a system of ordinary differential equations which is solved using the MATLAB® stiff solver ode15s at adaptative timestep. The stiff solver is necessary as the overall system is very stiff with different relaxation times for the convective term, mass transfer term and the reaction source term. In addition, different substrate uptake rates may exist between two nodes, due to the nature of the biological metabolic model, leading to more stiffness. The "nonnegative" option is also set for the ode15s solver.

$$\frac{\partial \phi}{\partial z}|_n = 0 \qquad n = 1 \text{ or } N \tag{2.45}$$

$$\frac{\partial \phi}{\partial z}|_{n=1} = \frac{-3\phi|_1 + 4\phi|_2 - \phi|_3}{2\Delta \mathrm{z}} \tag{2.46}$$

$$\frac{\partial \phi}{\partial z}|_{n=N} = \frac{3\phi|_n - 4\phi|_{n-1} + \phi|_{n-2}}{2\Delta \mathrm{z}} \tag{2.47}$$

$$\phi_{G,i}|_{n=1} = \frac{\varepsilon_{G,0} \mathrm{y_i} P}{\mathrm{RT}} \tag{2.48}$$

2.2.3.4 Resolution strategy

The set of equations in the 1D model is algebro-differential since the calculations of the right-hand terms in equations (2.13) and (2.14) require the local gas and liquid holdup, as well as the concentrations of all species in each phase to be retrieved from the known $\phi_{G,i,n}$ and $\phi_{L,i,n}$. These unknowns are solutions of a non-linear system (2.49) which connects the hydrodynamics and the mass transfer to the local pressure calculated using equation (2.28).

$$\begin{cases} \phi_{G,i,n} = \varepsilon_{G,n} \cdot C_{G,i,n} \\ \phi_{L,i,n} = (1 - \varepsilon_{G,n}) \cdot C_{L,i,n} \\ \dfrac{\mathrm{P_n}}{R.T} = \displaystyle\sum_i \frac{C_{G,i,n}}{M_i} \qquad n \in [1, N] \\ \mathrm{P}_n = P_0 + (1 - \widetilde{\varepsilon_G})\, \rho_L g (H - z_n) \end{cases} \tag{2.49}$$

The resolution algorithm for non-linear system (2.49) follows a successive substitution procedure. Starting from the initial imposed local molar fluxes ($\phi_{G,i}$, $\phi_{L,i}$) and the local gas holdup (ε_G), the local pressure profile (P), the local gas holdup (ε_G) as well as $C_{G,i}$ and $C_{L,i}$ are updated before the next timestep is taken.

The following procedure is used at the beginning of each timestep.

Step 1. $\phi_{G,i} \leftarrow \phi_{G,i}(t)$ and $\varepsilon_G \leftarrow \varepsilon_G(t)$

Step 2. $C_{G,i} \leftarrow \frac{\phi_{G,i}}{\varepsilon_G}$

Step 3. Update P from ε_G using equation (2.28)

Step 4. Update the local gas fraction $\varepsilon_G \leftarrow \frac{\sum \phi_{G,i}/M_i}{P} RT$

Step 5. Repeat Step 2 to 4 until the difference between two iterations falls below a given tolerance (10^{-5})

Step 6. Update the liquid phase concentrations $C_{L,i} = \phi_{L,i}/(1-\varepsilon_G)$

The updated $C_{G,i}$, $C_{L,i}$ and ε_G are used in the right-hand side of equations (2.13) and (2.14) to compute the time derivatives $\frac{\partial \phi}{\partial t}$. The time derivatives are solved using the ode15s solver of MATLAB® until the end time whereby the steady-state is reached.

2.2.4 Novel specificities of the 1D model

As stated in Section 1.5, some gaps need to be filled in the existing 1D model to provide a more generic 1D numerical description of the bubble column reactor. We recall briefly again the limitation of some existing 1D models: (i) constant gas fraction or calculation of gas holdup via empirical correlation (ii) one-way coupling of hydrodynamics and (reactive) mass transfer and (iii) partial exploration of multispecies mass transfer. In this context, we proposed a comprehensive 1D model that responds to these aforementioned drawbacks. First, the calculation of the gas holdup and the multiphysics coupling, in particular, the two-way coupling of hydrodynamics and mass transfer is embedded in the subroutine – a non-linear system of equations (2.49). It begins with the fact that the right-hand side of equations (2.13) and (2.14) involves the calculation of mass transfer term and reaction term spatially. The advancement of each timestep updates the local mass fluxes $\phi_{G,i,n}$ and $\phi_{L,i,n}$, by solving for the convective, dispersive, mass transfer and (bio)reaction fluxes. The updated local mass fluxes $\phi_{G,i,n}$ and $\phi_{L,i,n}$ together with local pressure P are used to solve recursively the non-linear system (2.49). The resolution of this subroutine provides the necessary elements to complete the definition of the time derivatives of equations (2.13) and (2.14) at the new timestep. This operation is repeated until the imposed end time of the simulation. This approach eliminates the use of empirical correlation for the gas holdup calculation, ensuring a more realistic model. Next, the example of (bio)reactive bubbly flow of biological methanation was simulated with the 1D model. In particular, the huge disparity in the solubility between the gas substrate H_2 and CO_2 will be explored in this work.

This formulation reflects that the local gas holdup is a function of the local pressure and local mass fluxes, extracted from the transported $\phi_{G,i,n}$ and $\phi_{L,i,n}$. The local mass fluxes vary with the mass transfer intensity and reaction rate. The Sauter mean diameter is not assumed constant but varies axially according to the gas holdup. The mass transfer fluxes and reaction rate vary axially according to the locally available substrate concentrations and the bifurcation of substrate uptake rate presented in the biological description.

With this novel 1D modelling approach, several applications will be shown in the following chapters. Chapter 3 demonstrates the validation of the 1D model using literature data. Chapter 4 features the use of the 1D model for industrial applications. Chapter 5 is devoted to studying reactive bubbly flow. The strong coupling between the reactive mass transfer and the hydrodynamics is showcased in this example, having the Sauter mean diameter varies considerably along the axial direction. This subject is widely treated using the CFD approach in the literature. We aim to reach the same goal as the CFD model – decipher the coupling of hydrodynamics and reactive mass transfer by using the 1D model.

Chapter 6 presents a comparison study between biological methanation pilot-scale experimental results, 1D and CFD models. The industrial biological methanation reactor of Electrochaea was also simulated using the CFD model and the results were compared with the 1D model predictions.

2.2.5 Model setup and problem initialisation

In the following chapters, the 1D model is used to study different bubble column applications. But the principle of the 1D model setup is identical for all cases. The only difference is the closures model applied that changes according to the situation. These closures are inlet bubble diameter, gas and liquid velocities, gas and liquid dispersion coefficients, mass transfer coefficient, and reaction terms, as already discussed in Figure 2.6. To avoid repetition in the subsequent chapters, the simulation setup in the 1D model is only detailed here but the closures model used for each case will be reported in the following chapters.

- **Preamble**

For all case studies, basic information on the reactor geometry, operating pressure at the outlet, operating temperature, liquid and gas properties at the given temperature and pressure (density, viscosity, surface tension), thermodynamic parameters (Henry's constant, molecular diffusivity) are required before running any simulation. The Henry's constant is mostly adapted from Sander (2015).

- **Hydrodynamic setup**

To mimic the experimental conditions of transient gas loading in tap water, the 1D model is set up under the same conditions as the pilot experiment. The mass transfer term is set to zero. The model is spatially discretised to 100 nodes. The initial gas holdup in the column from node 2 to N is set to very low value of 10^{-6} to represent the absence of the gaseous phase initially in the column. The experimental gas holdup is compared to the global spatial-averaged gas holdup given by the model at steady-state. The procedure of the comparison between the experimental transient loading and the 1D model prediction is also explained in our first paper, presented at the end of Chapter 3.

- **Mass transfer and reaction setup**

If no (bio)chemical reaction exists, only the mass transfer term is activated. The mass transfer closure model varies from case to case and it will be specified for each simulation in the following chapters. The reaction kinetics also changes according to different applications. The initial hydrodynamics start usually from the converged hydrodynamic case with the previous setup. If the initial liquid phase is

dissolved with the gaseous species, the initial liquid concentration is calculated from the equilibrium with the gaseous phase based on the Henry's constant.

Note: The 1D model developed in this thesis is a dynamic model which signifies that all simulations correspond to transient simulations. A sufficient end time is necessary to reach the steady state. Moreover, most of the mass transfer and reaction studies start with the convergence of hydrodynamics, as usually done in bubble column simulation (Chen et al., 2016, 2015; Darmana et al., 2007; Hissanaga et al., 2020; Sarkizi Shams Hajian et al., 2020). This ensures numerical stability and also respect the experimental condition whereby the mass transfer is usually activated after the development of the flow.

Chapter 3 1D Model Validation

In this chapter, the 1D model is validated using self-measured experimental data and confronted with the data collected from the literature of previous studies. Some literature data are issued from experimental measurements, while others are obtained through numerical simulations. The 1D model numerical methods and the setup have been explained in Chapter 2. Therefore, the resolution method is not repeated here, but the closure relations applied for each example are reported in a table. The goal is to illustrate the robustness of the spatio-temporal 1D model in simulating different applications. Some conclusions can be drawn from each example. The first part is to validate the hydrodynamics aspect of the two-phase model. The discussion on the experimental measurement of the bubble size and the gas holdup is also presented. The next section is devoted to the validation of the coupling with mass transfer. This is crucial as the (bio)chemical reactions often depend on the mass transfer rate. For instance, biomass requires oxygen for respiration and intracellular activities, which could be a two-way coupled problem with hydrodynamics.

3.1 Two-phase flow hydrodynamics

3.1.1 Bubble size measurement and transient gas loading in tap water system

In this section, we present the Sauter mean diameter and overall gas holdup calculated from the image processing of images captured from a pilot bubble column with tap water and hydrogen injection.

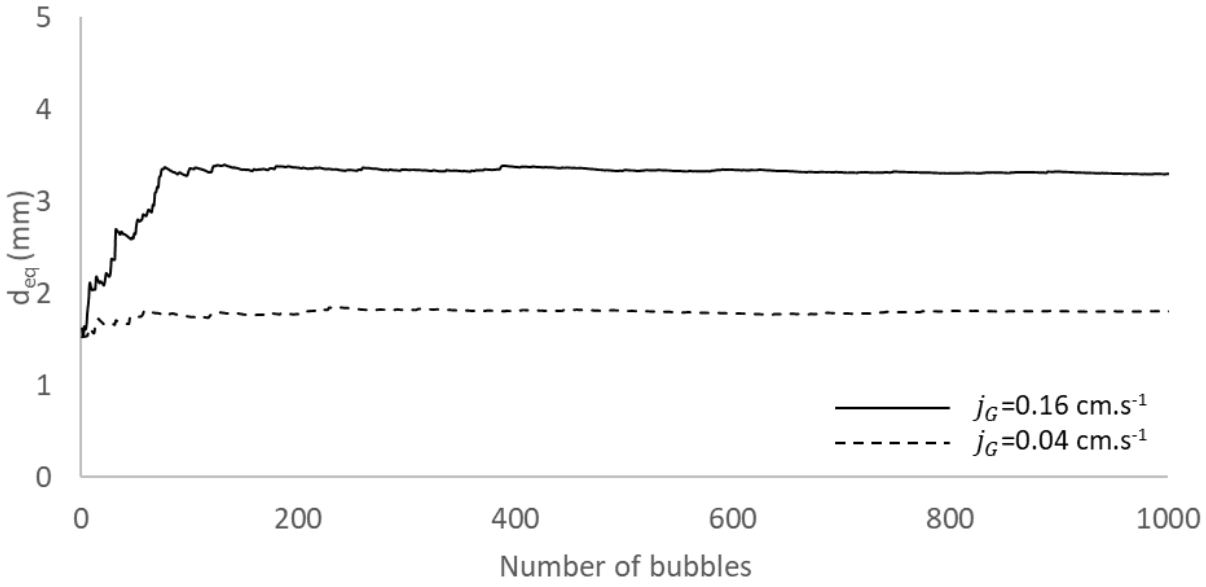

Figure 3.1: Statistical convergence of equivalent diameter measurements.

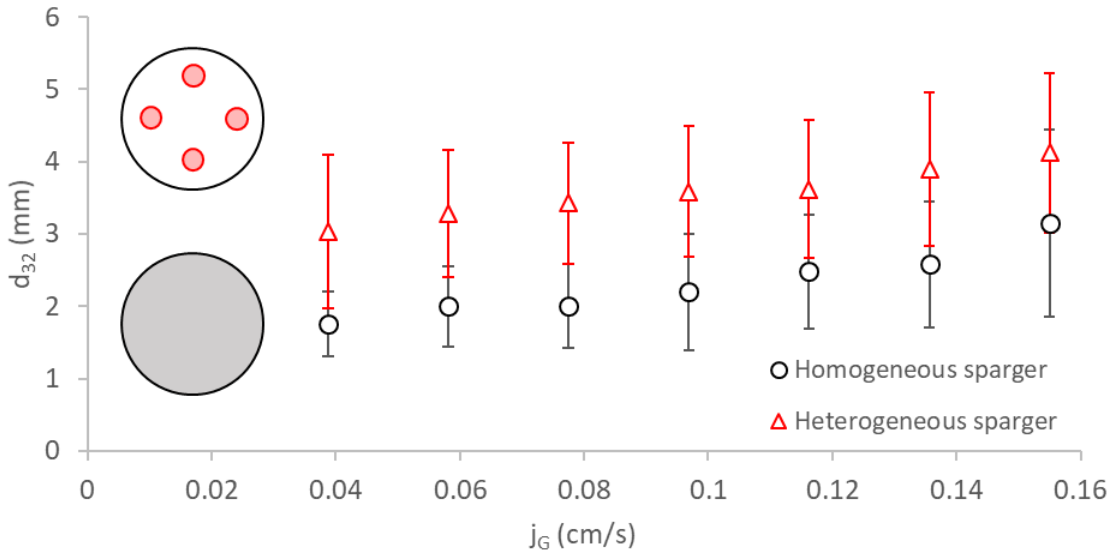

Figure 3.2: Sauter mean diameter vs. superficial gas velocity. The homogeneous sparger is shaded in grey while the heterogeneous sparger is shaded in red.

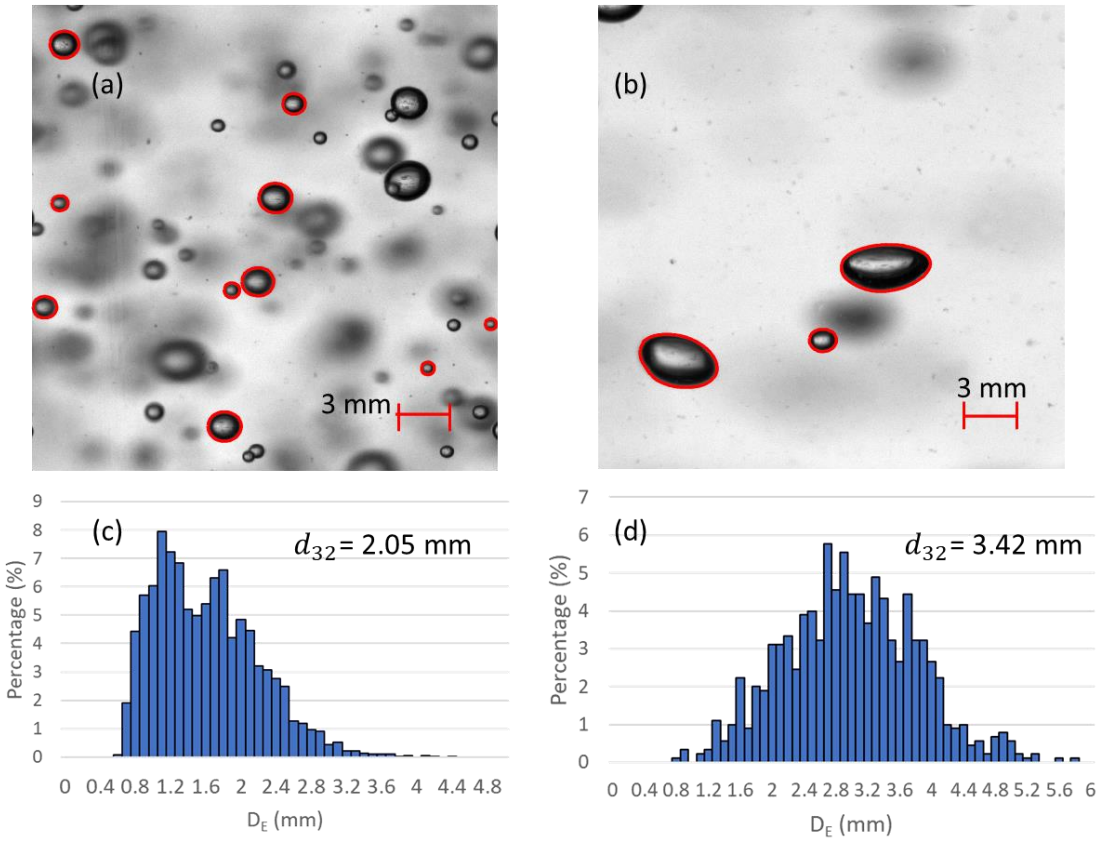

Figure 3.3: (a and b) Detected bubbles by the image processing algorithm at j_G = 0.78 mmm/s. (c and d) Histogram of bubble size distribution for a bin size of 0.2 mm equivalent diameter and the calculated Sauter mean diameter. (a) and (c) homogeneous sparger, (b) and (d) heterogeneous sparger.

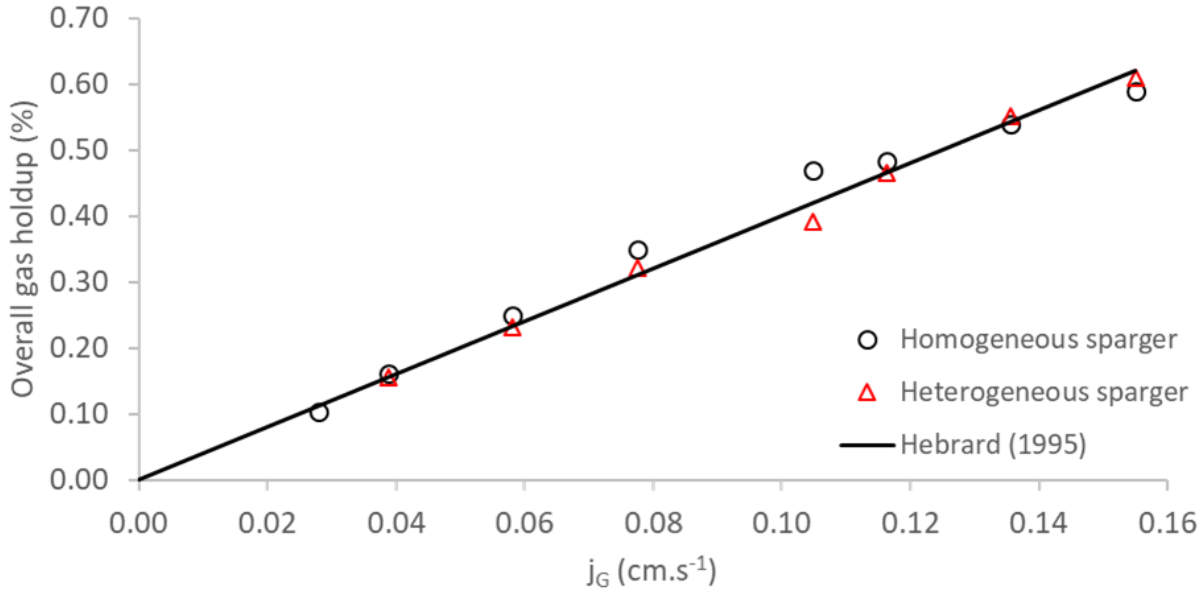

Figure 3.4: Overall ε_G vs. superficial gas velocity. Black line corresponds to correlation of Hebrard (1995) which stated that $\varepsilon_G = 4.j_G$

With a minimum of 1000 bubbles detected, the statistical convergence of equivalent diameter was reached for all measurements. The example given in Figure 3.1 is for the two superficial gas velocities but the statistical convergence was also achieved for all other measurements.

Each simultaneous measurement of bubble size distribution and transient gas holdup was performed either two or three times and averaged to obtain a mean value. The reported error bars in Figure 3.2 indicate one standard deviation around the mean diameter. It is found that the Sauter mean bubble diameter increases slightly with the flowrate for the two spargers. For the same superficial gas velocity, the heterogeneous sparger generates a larger Sauter mean diameter than that of the homogeneous sparger, approximately 30-60% larger in size. The example of the bubbles formed by the two spargers is illustrated in Figure 3.3, with its associated bubble size distribution. As the interfacial area for mass transfer is inversely proportional to the Sauter mean diameter, the heterogeneous sparger offers a smaller interfacial area for mass transfer. Figure 3.4 presents the overall gas holdup measured for the two spargers. It is found that at a certain superficial gas velocity the homogeneous sparger gives slightly higher gas holdup and vice versa. The experimental results are also compared to the correlation of Hebrard (1995), as shown in Figure 3.4. The correlation relates a simple relationship between superficial gas velocity, gas holdup and bubble terminal velocity, based on the fact that bubbles of 2-5 mm have a terminal velocity in the air-water system around 0.25 $m.s^{-1}$, as stated in the homogeneous slip velocity (Wallis, 1969). The correlation works mostly at low superficial gas velocity and low gas holdup, as demonstrated in the work of Colombet (2012). It is found that the overall gas holdup

obtained from the two spargers correlates well with the correlation of Hebrard (1995), as expected, as the correlation works for low superficial gas velocity.

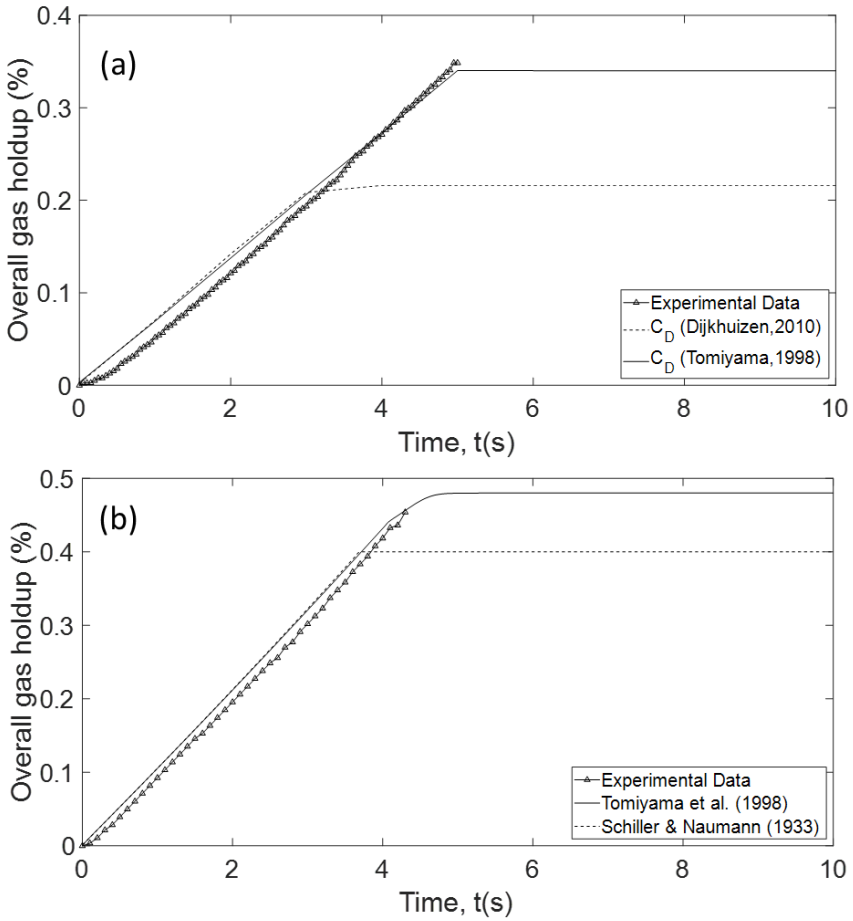

Figure 3.5: Transient gas holdup compared with different drag models for (a) $j_G = 0.78$ mm.s^{-1} and (b) $j_G = 1.1$ mm.s^{-1}

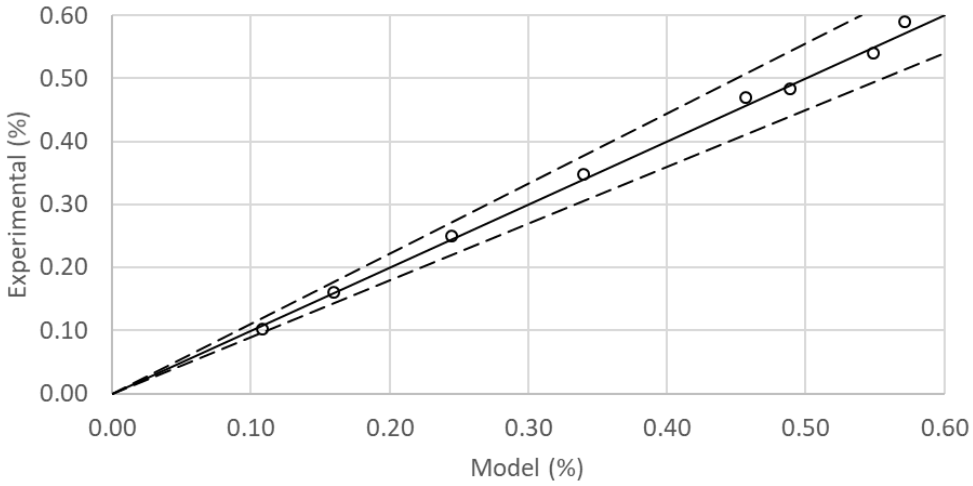

Figure 3.6: Parity plot of experimental and 1D prediction of $< \varepsilon_G >$ with $\pm$ 10 % error for the homogeneous sparger

To compare with the overall gas holdup experimental data, we tested different drag models in the 1D model. It is found that the Tomiyama et al. (1998) drag model developed for partially contaminated systems corresponds well with the experimental transient data when compared with other drag models, as shown in Figure 3.5. Figure 3.6 shows that the 1D model predicts satisfactorily well the measured gas holdup. The results show that the hydrogen-tap water system is well described by Tomiyama et al. (1998) partially contaminated drag coefficient. The drag correlation of Dijkhuizen et al. (2010) developed for the ultrapure system yields higher bubble terminal velocity, leading to underprediction of the overall gas holdup. The correlation of Schiller and Nauman (1933) developed for the drag coefficient of a solid sphere also underpredicts the overall gas holdup. The overall hydrodynamic is well captured with an overall error within +/- 10% range. Some additional experimental results on bubble size distribution and gas holdup have been reported in our first paper given in Section 3.4. Noted that the range of the overall gas holdup obtained is below 1%, with the superficial gas velocity in the order of $mm.s^{-1}$ (typical operating range of the biological methanation experiment which is detailed in Section 6.1). For the validation of the model in higher superficial gas velocity, we have turned to literature data whereby extensive hydrodynamics studies have been published. The following section highlights the 1D model prediction with some cases reported in the literature. The literature results are then analysed using the 1D model and further discussion is presented.

3.1.2 Comparison with Colombet (2012) case in pure water system

In the work of Colombet (2012), the hydrodynamics study had been conducted in a square (15 x 15 cm) glass bubble column of 100 cm high (initial liquid height at 76 cm). Filtered tap water and air were used as the liquid and gas system, respectively. The gas bubbles were injected through 841 capillaries with an inner diameter of 0.2 mm, covering the cross-section of the bubble column. Gas holdup and bubble size distribution were measured for a wide range of superficial gas velocity with the global gas holdup ranging from 0 – 30%. The gas holdup was measured using optical probes placed at the centre of the column at mid-height. The bubble size was measured through two techniques: non-invasive (optical method) and invasive (dual-tip optical probe). For the optical method, two lenses were used: a fixed-focal lens that measured the bubble size up to a gas holdup of 15% and a telecentric lens for gas holdup over 15%. The experimental data have also been reported in Colombet et al. (2015, 2011). As the bubble diameter and global gas holdup are measured experimentally, it is attempted to use the 1D model to predict the gas holdup and compare it with the experimental data. Considering the pure liquid system used, two drag correlations were tested, i.e. the drag coefficient of Tomiyama et al. (1998) for the pure system and that of Dijkhuizen et al. (2010) developed from direct numerical

simulation (DNS) using ultrapure water as the liquid phase. A collective factor of Wallis (1961) is included in the 1D model to take into account the hindered rise due to bubble swarm in the bubble column as observed in Colombet (2012). The closures used in the 1D model is summarised in Table 3.1.

Table 3.1: Closure relations used in the 1D model to simulate Colombet (2012) case.

Variables	Closure model
d_b	From the experiment data. The measured bubble diameter evolution is scaled to the following correlations which can be used: $\frac{d_b-d_0}{d_0} = 15\varepsilon_G$ for $\varepsilon_G \leq 2\%$ $\frac{d_b-d_0}{d_0} = 2.3\varepsilon_G^{0.52}$ for $\varepsilon_G > 2\%$ ε_G is dimensionless, d_0 = 0.0014 m, and d_b in meters
u_G	Tomiyama et al. (1998) pure system $C_{D_\infty} = max\left\{\min\left[\frac{16}{Re_b}\left(1+0.15Re_b^{0.687}\right), \frac{48}{Re_b}\right], \frac{8}{3}\frac{Eo}{(4+Eo)}\right\}$ Dijkhuizen et al. (2010) $C_{D_\infty} = \sqrt{C_D(Re_b)^2 + C_D(Eo)^2}$ $C_D(Re_b) = \frac{16}{Re_b}\left(1+\frac{Re_b}{8+0.5\left(Re_b+3.315Re_b^{0.5}\right)}\right)$ $C_D(Eo) = \frac{4Eo}{9.5+Eo}$ Collective effect from Wallis (1961) : $C_D = C_{D_\infty}(1-\varepsilon_G)^{-2}$
u_L	0 m.s^{-1} bubble column closed to the liquid.
D_G	Neglected due to high Peclet number as reported in Colombet (2012)
D_L	Neglected due to high Peclet number as reported in Colombet (2012)

Figure 3.7 reports the results obtained from the 1D model using two different drag correlations. It shows that at low superficial gas velocity the Dijkhuizen's correlation fits well with the experimental data but at higher gas velocity, Tomiyama's correlation fits better that the Dijkhuizen's correlation. The water quality is considered very clean as it is reported that any particle in the tap water that is larger than 15 µm is filtered (Colombet, 2012). This matches the quality of pure water as considered in the DNS study of Dijkhuizen et al. (2010), which yields a good agreement until j_G > 10 mm.s^{-1}. It is shown in Dijkhuizen et al. (2010) that at Reynolds > 500, the drag coefficient of Tomiyama et al. (1998) is larger than that of Dijkhuizen et al. (2010), leading to lower slip velocity, and higher gas holdup, as reflected in Figure 3.7. Figure 3.8 shows the transient gas loading with the two drag models. Again,

Tomiyama's drag model leads to a later establishment of gas holdup due to lower bubble terminal velocity. Overall, the 1D model yields good agreement compared to the experimental data. This is due to the fact that the bubble swarm generated by the needle-sparger (fine sparger) are very uniform, as reported in Colombet (2012), and classical closures on the drag forces are appropriate to obtain very close gas holdup.

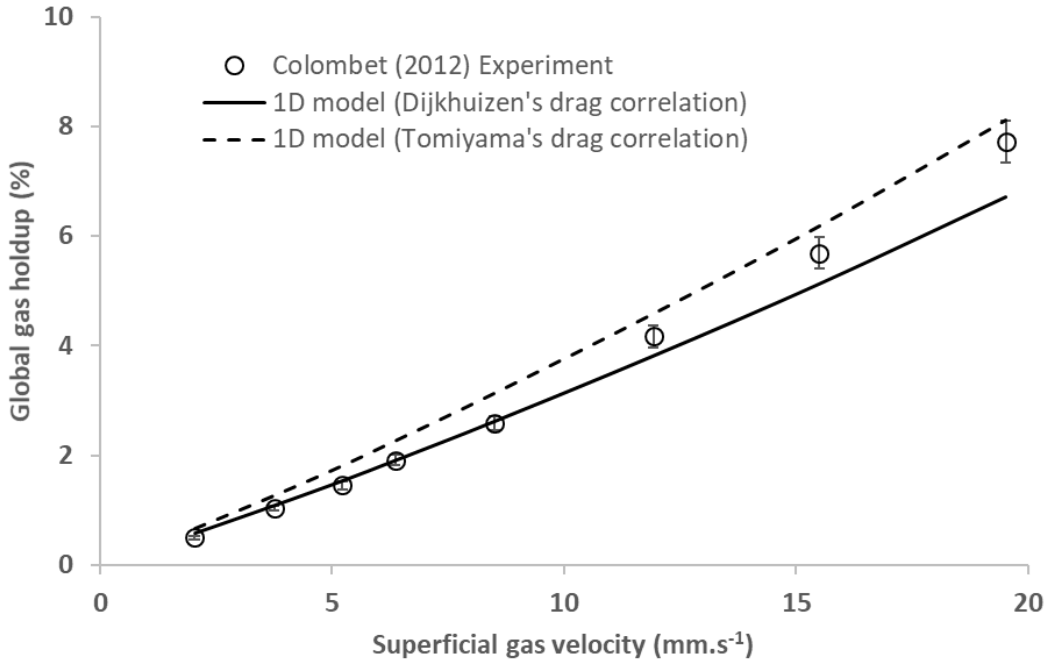

Figure 3.7: Global gas holdup for different superficial gas velocities compared between experimental data and 1D model prediction. Error bar signifies $\pm$ 5% error

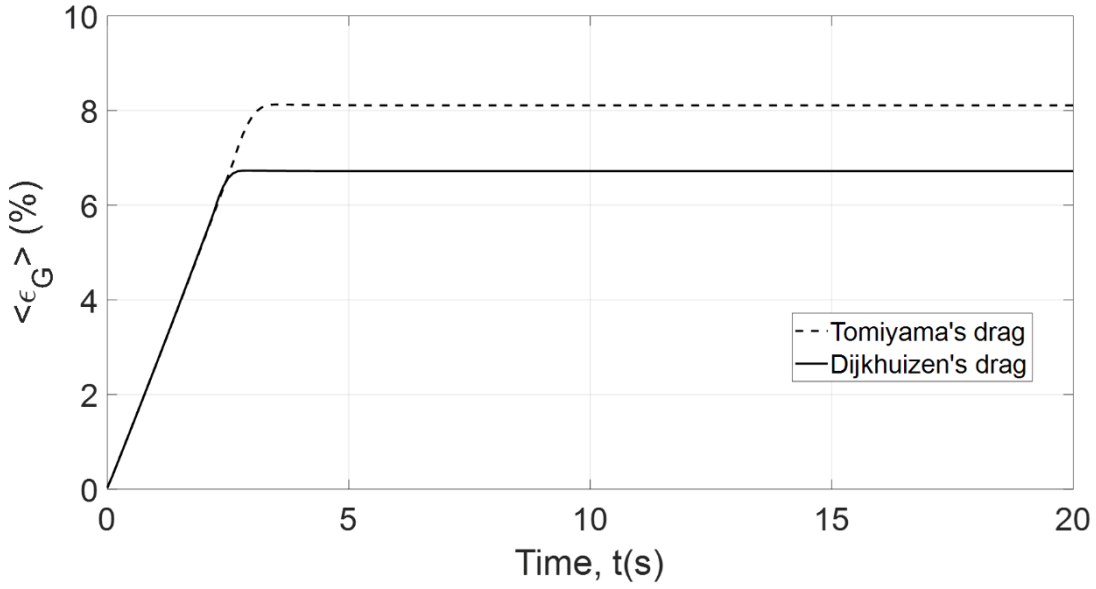

Figure 3.8: Simulation of transient gas loading using the 1D model for superficial gas velocity of 19.5 mm.s^{-1}.

3.1.3 Comparison with the McClure et al. (2015c, 2014a) case as in Ertekin et al. (2021) in water with surfactants system

Extensive experimental datasets on bubble size and global gas holdup have been reported in the work of McClure et al. (2015b, 2014b, 2014a, 2013) for different liquid mediums (with or without the presence of surfactants) to mimic the biological fermentation broths. Besides, CFD models have been developed and validated using these datasets (McClure et al., 2015b, 2014b, 2014c). The objective is to develop numerical models for bubble columns operating in industrial conditions, including the presence of surfactant, typically the industrial bubble column fermenter. In this section, the 1D model will be used to compare with some of the datasets. Recently, the work of Ertekin et al. (2021) reported and summarised some findings based on the datasets of (McClure et al., 2015c, 2014a) case. The same datasets are used in the comparison with the 1D model. In the work of Ertekin et al. (2021), part of the hydrodynamics study was conducted in a bench-top bubble column with a diameter of 0.19 m, and a height of 1 m (liquid height of 0.5 m). The measurements were performed with different air-liquid systems, but here, only three systems will be compared, particularly: air/water, air/water + 0.02 M 2-propanol, and air/water + 0.01% (v/v) Antifoam A. Due to the presence of surfactants, the measured bubble diameter varies differently. The bubble diameters in the 1D model are kept the same as the experimental values. The 1D model follows the closures used in the CFD model that have been validated using the experimental datasets (Ertekin et al., 2021). The bubble diameter is considered as constant as a narrow bubble size distribution was obtained in the experiment.

Table 3.2: Closure relations used in the 1D model to simulate (McClure et al., 2015c, 2014a) case.

Variables	Closure model
d_b	Constant 6 mm for air/water system Constant 4 mm for air/water + 0.02 M 2-propanol system Constant 15 mm for air/water + 0.01% (v/v) Antifoam A system Followed the work of (Ertekin et al., 2021; McClure et al., 2014a)
u_G	Grace drag coefficient (C_{D_∞}) plus swarm correction factor $f(\alpha_G)$ $C_D = C_{D_\infty} f(\alpha_G) k_{surfactant}$ $f(\alpha_G) = \min((1-\alpha_G)^{50} + 0.2, 1)$ $k_{surfactant} = 1$ for water, $k_{surfactant} = 2$ for propanol, $k_{surfactant} = 0.75$ for Antifoam, McClure et al. (2015c, 2014a)
u_L	0 m.s^{-1} bubble column closed to the liquid.
D_G	Calculated from Wachi and Nojima (1990)
D_L	Calculated from Deckwer et al. (1974)

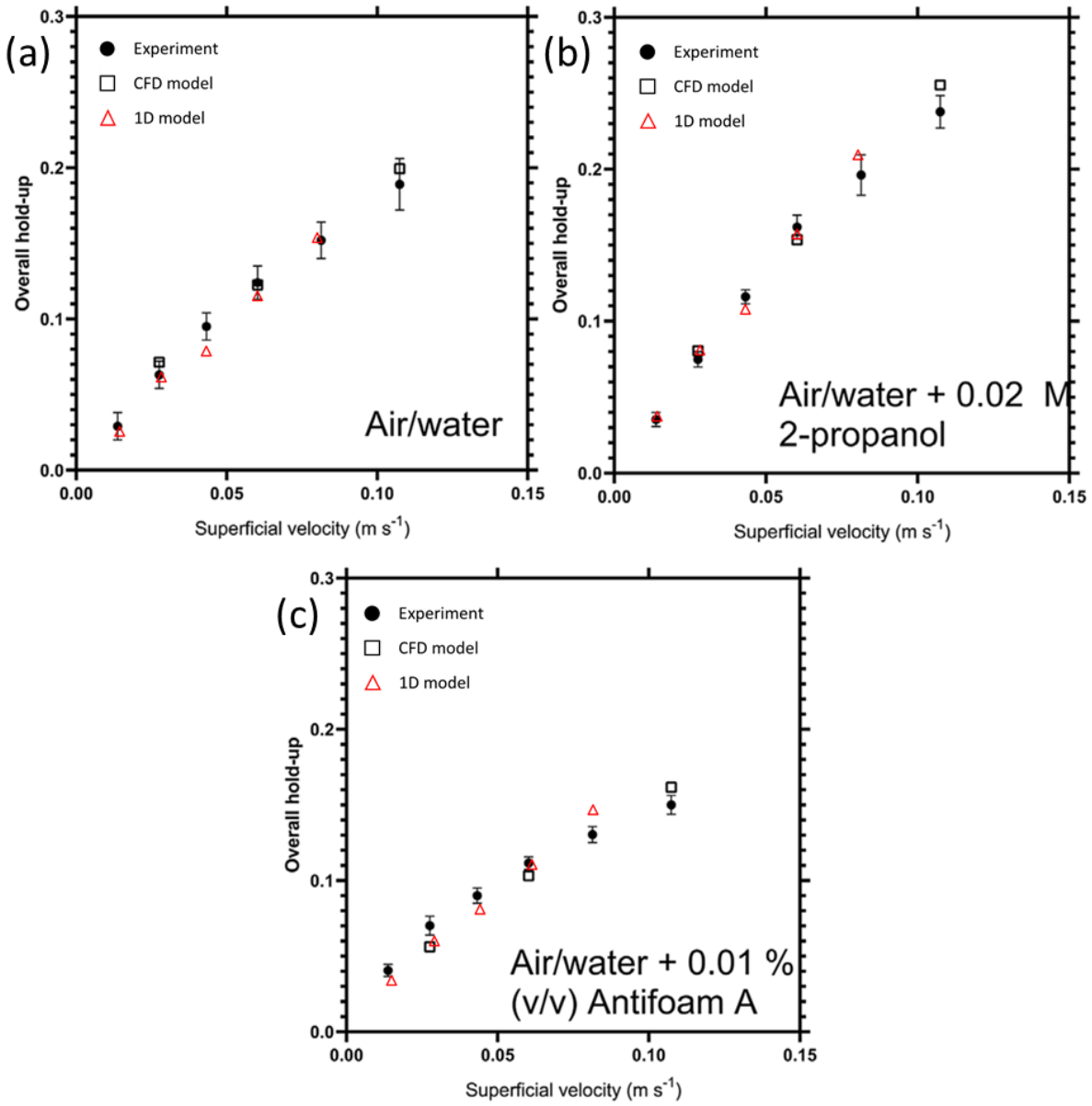

Figure 3.9: Comparison of overall gas holdup between experimentally measured, CFD and 1D model predictions (a) Air/Water (b) Air/Water + 0.02 M 2-propanol (c) Air/Water + 0.01% (v/v) Antifoam A.

Figure 3.9 shows the 1D model results compared with the experimental data and the CFD prediction of McClure et al. (2014a). With the same closure relations, the global gas holdup is satisfactorily calculated by the 1D model. It is found that the overall gas holdup increases in the system containing 2-propanol. With the addition of alcohol, the bubble coalescence is inhibited. The bubble size distribution becomes narrower and it shifted left to a smaller mean bubble size. The presence of surfactant on the bubble interface has a significant impact on the drag (McClure et al., 2014a). The drag modification effect also depends on the nature of the surfactant. As measured by McClure et al.

(2014a) the drag coefficient for water + 0.02 M 2-propanol is relatively higher than water system but for Antifoam-A, the drag coefficient is lower than water. To model this contamination effect, the drag coefficient was modified by multiplying with an empirical factor issued from experimental measurements ($k_{surfactant} = 2$ for 2-propanol and $k_{surfactant} = 0.75$ for Antifoam A). Consequently, the overall gas holdup for water + 2-propanol is higher than that of water, while the gas holdup for water + Antifoam is lower than that of water. With the modification of the drag, the overall gas holdup can be predicted correctly, as shown in Figure 3.9(b) and Figure 3.9(c).

3.1.4 Comparison with the Chen and Brooks (2021) and Krepper et al. (2007) case for low overall gas holdup system

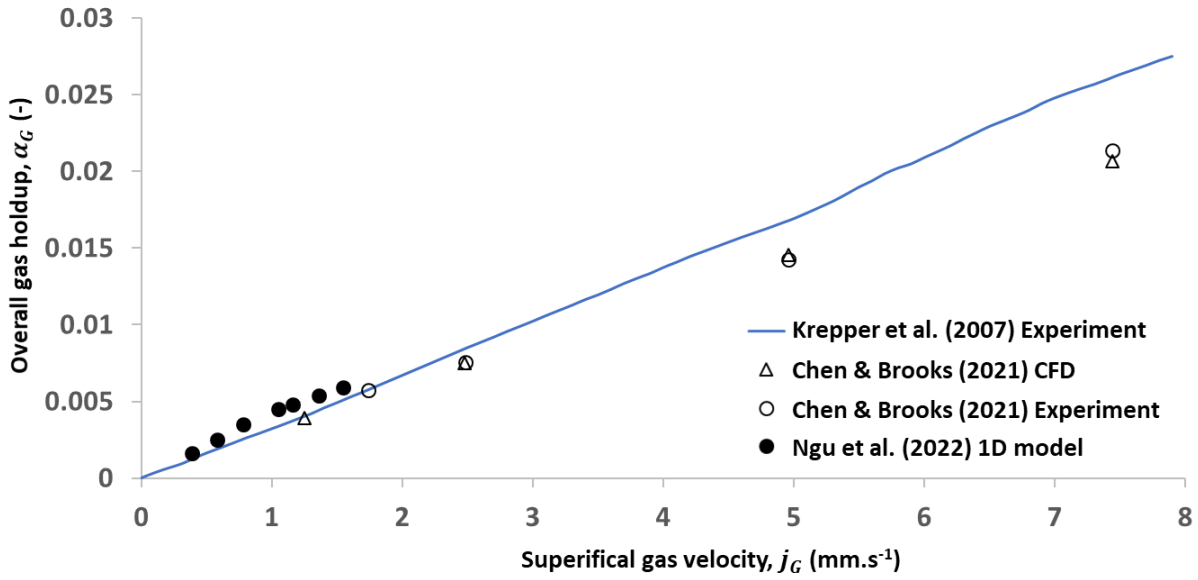

Figure 3.10: Comparison of the overall gas holdup predicted by the 1D model with literature data.

Figure 3.10 shows the comparison of the global gas holdup predicted by the 1D model as reported in (Ngu et al., 2022a) with the literature work, including both experimental measurements (Chen and Brooks, 2021; Krepper et al., 2007) and numerical simulation (Chen and Brooks, 2021). Krepper et al. (2007) measured the global gas holdup in a rectangular bubble column (0.1 m wide, 0.02 m depth) equipped with a porous sparger by the liquid swelling method. In a more recent study, Chen and Brooks (2021) measured the global gas holdup in a small-scale cylindrical bubble column (Dr = 0.13 m, and H = 0.166 m) via the optical method. The global gas holdup was measured as the 2D projected void fraction. The projection is done by weighing the bubble by its relative dimension in the projection direction. This correction considering the curvature of the bubble is necessary to produce the correct projected void fraction. Instead of using the bubble equivalent radius as the weighing factor, the distance between the furthest point of the bubble circumferences and the bubble centre was chosen.

From the identified bubble diameter and estimated volume, the instant bubble distribution is projected onto a 2D plane and averaged in time (Chen and Brooks, 2021). 3D CFD Eulerian simulations were also carried out by Chen and Brooks (2021) to compare with their experimental data. The global gas holdup reported in Ngu et al. (2022a) is slightly higher than that obtained by Krepper et al. (2007), probably due to the reactor geometry as the pseudo-2D rectangular column was used in Krepper et al. (2007). Nevertheless, the order of magnitude is quite close to those measured by Krepper et al. (2007) and Chen and Brooks (2021) which remain as some of the few studies that measured the global gas holdup at such low superficial gas velocity. It can be observed that the overall gas holdup of Chen and Brooks (2021) is relatively lower than obtained by Krepper et al. (2007). This could be due to the narrow rectangular column used by Krepper et al. (2007) as the small depth of 0.02 m hinder the bubble rise, leading to lower bubble velocity and higher gas holdup at high superficial gas velocity.

The 1D model is also used to compare with the transient gas holdup measurement of Krepper et al. (2007). It is mentioned that the column operated in the dispersed homogeneous bubbly regime with the absence of bubble coalescence and breakup for superficial gas velocities below 10 mm.s^{-1}. The gas phase employed is air and the liquid phase is mentioned to be water. However, the contamination level of the water used experimentally is not specified. In this context, the drag coefficient of Tomiyama et al. (1998) and Dijkhuizen et al. (2010) is tested using the 1D model. The results for three different superficial gas velocities (j_G = 6, 8, and 10 mm.s^{-1}) are compared here. The bubble size distribution was also given for the three superficial gas velocities but it was shown that the average bubble size for the three superficial gas velocities does not vary much with an average bubble size of 3 mm. The same bubble size is used in the 1D model. The closure relations used are summarised in Table 3.3.

Figure 3.11(a)-(c) show the transient gas holdup profiles for j_G = 6, 8, and 10 mm.s^{-1} obtained by the 1D model superposed with the results of Krepper et al. (2007). It is found that the Tomiyama et al. (1998) for partially contaminated drag coefficient agrees better with Krepper et al. (2007) results than the Dijkhuizen et al. (2010) drag coefficient. This shows that the water used may be tap water rather than filtered ultrapure water, which is more adapted to the Dijkhuizen et al. (2010) drag coefficient. It is unclear whether the transient profiles of Krepper et al. (2007) correspond to experimental measurements or CFD predictions as they are not specified in the paper. Nevertheless, if the steady-state value is referred to the overall results in Figure 3.11(d), it seems that the transient profiles correspond to the CFD predictions by ANSYS CFX. It shows that the 1D model predicts the overall gas holdup just as well as the CFD model. The slight overvaluation of the gas holdup compared to the experimental measurements could be due to the omission of radial heterogeneity and liquid

recirculation velocity of the pseudo-2D bubble column, which is often integrated into the bubble velocity as the drift-flux model (Zuber and Findlay, 1965), as shown in the work of (Ngu et al., 2022b).

Table 3.3: Closure relations used in the 1D model to simulate Krepper et al. (2007) case.

Variables	Closure model
d_b	Constant 3 mm
u_G	Tomiyama et al. (1998) and Dijkhuizen et al. (2010) drag coefficient models
u_L	0 m.s^{-1} bubble column closed to the liquid.
D_G	Calculated from Wachi and Nojima (1990)
D_L	Calculated from Deckwer et al. (1974)

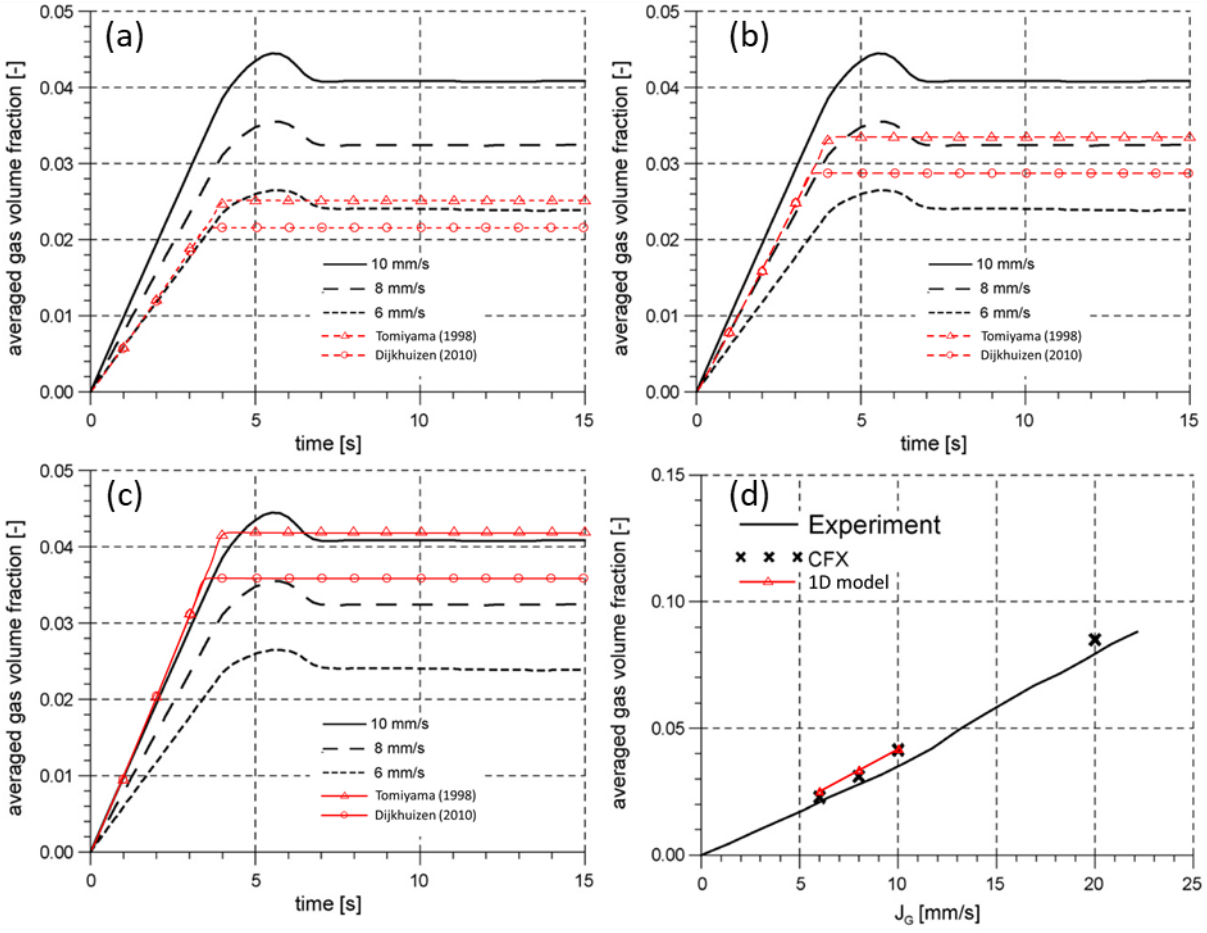

Figure 3.11: Comparison of transient gas holdup profile between 1D model prediction and Krepper et al. (2007) work. (a) j_G=6 mm.s^{-1}, (b) j_G=8 mm.s^{-1}, (c) j_G=10 mm.s^{-1} (d) Overall results

In short, the global gas-liquid hydrodynamics of a bubble column is characterised by the overall gas holdup. It is shown that the 1D spatio-temporal model is capable to reproduce the overall gas holdup for different bubble column designs provided that appropriate closure models and bubble diameter

are applied to the model. When the bubble diameter and the drag coefficient are similar to experimental measurements, a good agreement can be obtained. Through our own experimental data, it is proved that the Tomiyama et al. (1998) drag correlation is adequate for the tap-water system, whilst the (Dijkhuizen et al., 2010) drag correlation is more suitable for the ultrapure water system. The drag coefficient for the surfactants system remains empirical, nevertheless, good prediction can be obtained when it matched the drag coefficient matched that of experiments McClure et al. (2015c, 2014a). Future perspectives include the need to develop mechanistic and generic drag model for surfactant system (Ertekin et al., 2021). The hydrodynamics aspect of the model is checked and it is expected to provide a reliable prediction of the bubbly flow upon validation using experimental data and literature data. Next, the hydrodynamics coupled with the mass transfer is studied for model validation.

3.2 Interfacial gas-liquid mass transfer

3.2.1 Comparison with the Chen and Brooks (2021) case

Apart from the hydrodynamics experiment, Chen and Brooks (2021) also determined the oxygen mass transfer coefficient by monitoring the transient oxygen loading using an oxygen probe. The deoxygenation was not conducted by bubbling nitrogen gas as usually done in the literature. Instead, the deionised water was first boiled and sealed to remove dissolved oxygen. The liquid was then cooled before conducting the dynamic reoxygenation. The $k_L a$ was calculated by fitting a homogeneous CSTR model to the experimental dynamic oxygen curve. The experiment was conducted at three superficial gas velocities: 2.5, 5, and 7.5 mm.s^{-1}. For j_G of 2.5 mm.s^{-1}, the result was also compared with the CFD simulation. However, the initial bubble diameter used in the CFD simulation was not specified, which deterred the validation process. Nevertheless, the 1D model is still used to simulate the same experiment and it is attempted to compare with the experimental $k_L a$ value. The 1D model simulation is set up as the experimental conditions. The pressure at the outlet is set to atmospheric pressure and the temperature of the bubble column is kept at 25°C. The composition of air is imposed at the inlet. The initial dissolved oxygen concentration is set to zero. Other closure models used in the 1D model are reported in Table 3.4. An example of the dynamic oxygenation obtained by the 1D model for the superficial gas velocity of 2.5 mm.s^{-1} is shown in Figure 3.12. The obtained transient oxygen curve is analysed by a homogeneous CSTR model to yield the volumetric mass transfer coefficient that will be compared to the experimental measurements.

Table 3.4: Closure relations used in the 1D model to simulate Chen and Brooks (2021) case.

Variables	Closure model
d_b	Between 5-7 mm. Estimated from Gaddis and Vogelpohl (1986) correlation.
u_G	Tomiyama et al. (1998) drag coefficient for pure system.
u_L	0 m.s^{-1} bubble column closed to the liquid.
D_G	2.2×10^{-3}, 4.5×10^{-3}, and 6.8×10^{-3} m².s^{-1} for $j_G = 2.5$, 5, 7.5 mm.s^{-1}, respectively. Calculated from Wachi and Nojima (1990)
D_L	6.3×10^{-3}, 7.7×10^{-3}, and 8.7×10^{-3} m².s^{-1} for $j_G = 2.5$, 5, 7.5 mm.s^{-1}, respectively. Calculated from Deckwer et al. (1974)
k_L	Higbie (1935)
C^*	Sander (2015)

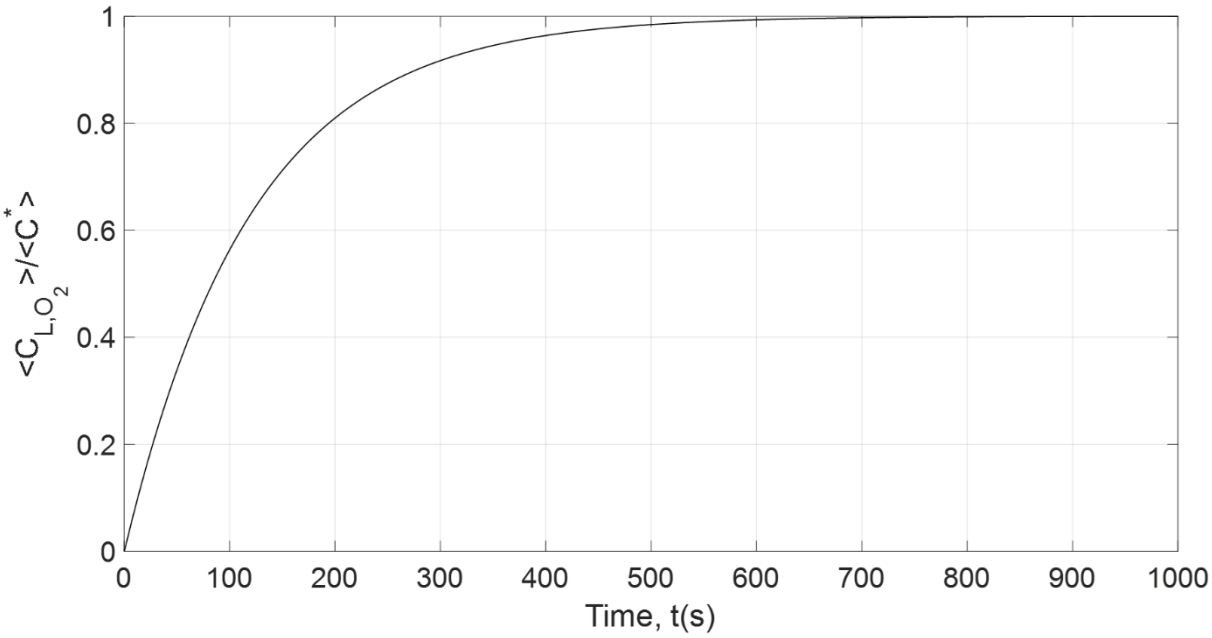

Figure 3.12: Dynamic oxygenation curve for superficial gas velocity of 2.5 mm.s^{-1}

The dissolved oxygen concentration variation in a closed vessel based on the CSTR model can be written as

$$\frac{dC_L}{dt} = \frac{k_L a}{\varepsilon_L}(C^* - C_L) \tag{3.1}$$

By taking the characteristic time for the mass transfer as the time needed to reach 63% of the final value (C_{63}), the $k_L a$ can be expressed as

$$k_L a = -\frac{\varepsilon_L}{t_{63}} ln\left(1 - \frac{C_{63}}{C^*}\right) \tag{3.2}$$

Sensitivity analysis of the initial bubble diameter is carried out between 5 – 7 mm. The overall results on the $k_L a$ is shown in Figure 3.13. Figure 3.13 shows that for a given superficial gas velocity, the smaller the bubble diameter, the higher the $k_L a$, in line with the fact that a smaller diameter gives a higher interfacial area for mass transfer. As the superficial gas velocity increases, the bubble diameter that gives the best fit to the experimental results of Chen and Brooks (2021) also increases. The bubble diameter of best fit for the superficial gas velocity of 2.5, 5, and 7.5 mm.s^{-1} are 6, 7, and 7 mm. It should be emphasised that this validation remains very global, as no information on the bubble diameter is given. Nonetheless, the 1D model comes in handy to estimate this unknown bubble size, assuming a classical mass transfer closure of Higbie (1935) model. Thorough validation must include bubble

velocity, gas holdup, interfacial area, volumetric mass transfer coefficient and finally the local concentration profile. Nevertheless, this work represents the first attempt to mass transfer validation.

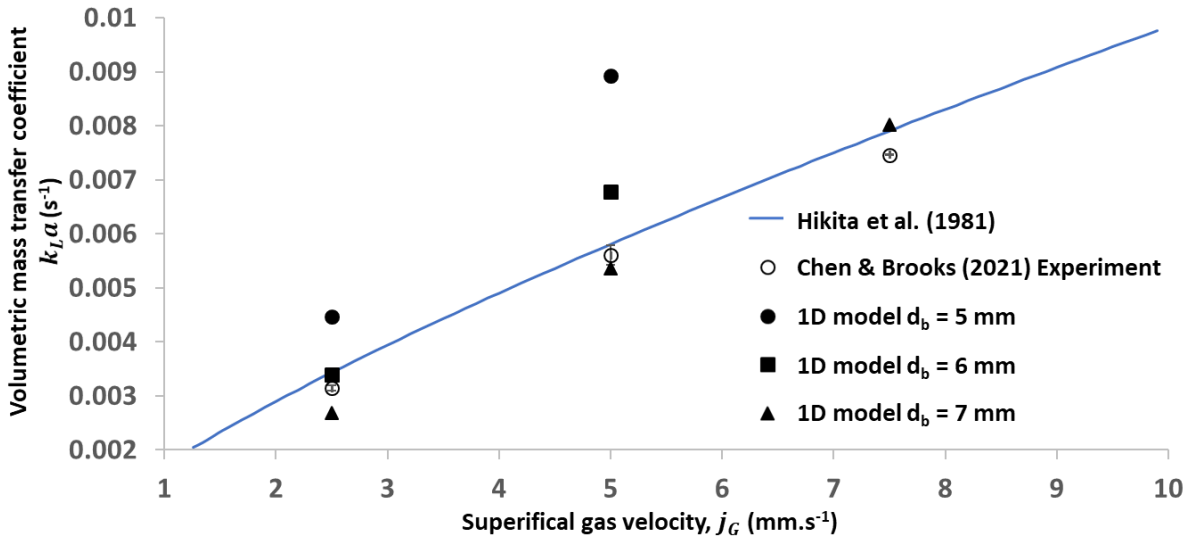

Figure 3.13: 1D model prediction compared to the work of Chen and Brooks (2021) and the correlation of Hikita et al. (1981)

3.2.2 Comparison with the Han and Al-Dahhan (2007) case with high pressure system

Another dataset on mass transfer experiments can be found in the work of Han and Al-Dahhan (2007). The authors characterised the oxygen mass transfer coefficient for different sparger designs and quantified the pressure effect on the mass transfer. The bubble column was made up of stainless steel to withstand high pressure, with a reactor diameter of 0.162 m and a free-surface height of 1.8 m diameter, which corresponds to a height-to-diameter ratio of 11.2. Filtered tap water was used as the liquid phase. Three sparger designs were tested, namely a perforated plate with 163 holes of 0.5 mm (distributor #1), a perforated plate with 163 holes of 1.32 mm (distributor #2) and a cross sparger with four holes of 2.54 mm (distributor #3). The monitoring of the transient oxygen loading was conducted with an oxygen probe. Two models were used to treat the dynamic oxygenation curve: the CSTR model and the axial-dispersion model. Due to high height to diameter ratio (H/D_r = 11.2), it is shown that the axial dispersion model fits the data better than the CSTR model. The gaseous dispersion coefficient used in the work of Han and Al-Dahhan (2007) varied between 0.017 – 0.4 m^2.s^{-1}, whereas the liquid dispersion coefficient was calculated from the correlation of Deckwer et al. (1974), which varied between 0.013 – 0.045 m^2.s^{-1}. The experiment was conducted at superficial gas velocity, j_G = 0 – 0.6

m.s^{-1}, which cover all hydrodynamic regime at a pressure between atmospheric pressure up to 10 bar. The bubble diameter was not given directly but can be derived explicitly, as data on global gas holdup, interfacial area, and volumetric mass transfer coefficient were given. Regardless, no explanation was detailed in the paper on how the interfacial area and global gas holdup were obtained. The bubble diameter was calculated from the known global gas holdup and interfacial area as $d_b = \frac{6\varepsilon_G}{a}$. In this work, only the results obtained from distributor #1 (porous plate covering the majority of the cross-section with fine holes) are compared here to that of the 1D model as it is considered the most suitable sparger for the 1D model validation (fine and homogeneous sparger). Besides, most of the superficial gas velocity tested is over 0.1 m.s^{-1}, meaning that the column operated in the heterogeneous regime, most of the time (Deckwer and Schumpe, 1993; Shah et al., 1982). In such regime, large-scale liquid recirculation and drag swarm factor have to be considered. This makes the 1D model validation relatively challenging because the bubble hydrodynamics can no longer be determined by a simple slip velocity considering only the drag coefficient. Nevertheless, there are a few experimental points that can be compared with the 1D model, particularly when j_G is below 0.1 m.s^{-1}. For the comparison, the same numerical experiment as that of Chen and Brooks (2021) was conducted and the closure relations are summarised in Table 3.5.

Table 3.5: Closure relations used in the 1D model to simulate Han and Al-Dahhan (2007) case.

Variables	Closure model
d_b	Between 4-7 mm. Calculated from the reported experimental data.
u_G	Tomiyama et al. (1998) drag coefficient for pure system.
u_L	0 m.s^{-1} bubble column closed to the liquid.
D_G	Calculated from Wachi and Nojima (1990)
D_L	Calculated from Deckwer et al. (1974)
k_L	Higbie (1935)
C^*	Sander (2015)

Table 3.6: Comparison between experimental results and 1D model predictions

Experimental data from Han and Al-Dahhan (2007)					1D model	
j_G (m.s^{-1})	ε_G (-)	a (m².m^{-3})	d_b (mm)	k_La (s^{-1})	ε_G (-)	k_La (s^{-1})
0.02	0.09	126	0.0043	0.038	0.095	0.037
0.83	0.25	241	0.0062	0.097	0.37	0.109

Table 3.6 reports the comparison of the 1D model results with the selected datasets of Han and Al-Dahhan (2007). Another reason for such few datapoints is that not every For j_G = 0.02 m.s^{-1}, the 1D model yield consistent results with the reported value. The global gas holdup is slightly overvalued, but the volumetric mass transfer coefficient is relatively well predicted. However, for j_G = 0.83 m.s^{-1}, the global gas holdup is highly overpredicted. At such high gas holdup, the bubbles are usually churn-up and the drag force is strongly reduced due to collective effects and bubbles coalescence (McClure et al., 2017; Simonnet et al., 2007). The omission of this swarm correction term leads to overprediction of the gas holdup, which eventually overpredicts the $k_L a$. Moreover, in the heterogeneous regime, the bubble size distribution is likely to be bimodal (Krishna et al., 1999; Laupsien et al., 2022), which includes the need of solving the bubble population balance model (Gemello et al., 2019).

3.2.3 Comparison with the McClure et al. (2015b) case in water with surfactants system

McClure et al. (2015b) investigated the impact of surfactant addition on the oxygen mass transfer rate. The same bubble column described in Section 3.1.3 was used in the experiment. Measurements on bubble size distribution, overall gas holdup, and $k_L a$ were conducted to determine subsequently the liquid film mass transfer coefficient k_L. The oxygen transfer rate (OTR) was determined experimentally by the sulfite method. The dissolved oxygen reacts with the sulfite ions to form sulfate ions, thus the monitoring of the OTR can be conducted by following the sulfite concentration. The oxygen concentration is zero as the sulfite concentration is sufficiently high and the rate of reaction is relatively fast. The experiment was repeated with different types of surfactants, including 2-propanol, 1,2-propanediol, n-hexane, D-mannitol, and Antifoam A. It is found that the addition of hydrophilic or hydrophobic surface-active compounds led to an approximately threefold reduction in k_L. As mean bubble size was reported in McClure et al. (2015b), it is interesting to use the 1D model to compare with their experimental results. Besides, CFD simulations were also developed for such system and the comparison results have been published in Ertekin et al. (2021). The closures on the bubble velocity in the CFD model were modelled using Grace drag coefficient with the swarm factor correction term, the same as the hydrodynamics study explained in Section 3.1.3. For the liquid film mass transfer coefficient, the CFD model applied a fixed value of 1×10^{-4} m.s^{-1} for systems containing surfactant (Antifoam) and a fixed value of 4×10^{-4} m.s^{-1} for clean system (water+ sulfite). In the 1D model, the Higbie (1935) and Frössling (1938) mass transfer models are used for clean and surfactant-containing systems, respectively. As explained in Ertekin et al. (2021), to model the function of sulphite as an oxygen scavenger, a sink term sufficiently large is necessary, such that the dissolved oxygen concentration reaches zero. In the 1D model, it is modelled as 99.995% of the oxygen mass transfer

term. Table 3.7 summarises the closure models used in the 1D model which followed the CFD work of Ertekin et al. (2021). The OTR expressed in equation (3.3) is calculated as the time-averaged mass transfer term by the liquid volume, with the time averaging of 30 s, followed the work of Ertekin et al. (2021).

$$OTR = k_L a\left(C^* - C_{L,O_2}\right) \tag{3.3}$$

Table 3.7: Closure relations used in the 1D model to simulate McClure et al. (2015b) case

Variables	Closure model
d_b	Constant 5 mm for both air/water + sulfite and air/water + sulfite + Antifoam system Followed the work of (Ertekin et al., 2021; McClure et al., 2015b)
u_G	Grace drag coefficient (C_{D_∞}) plus swarm correction factor ($f(\alpha)$) $C_D = C_{D_\infty} f(\alpha_G) k_{surfactant}$ $f(\alpha) = \min((1-\alpha_G)^{50} + 0.2, 1)$ $k_{surfactant} = 2$ for sulfite, $k_{surfactant} = 0.75$ for Antifoam
u_L	0 m.s^{-1} bubble column closed to the liquid.
D_G	Calculated from Wachi and Nojima (1990)
D_L	Calculated from Deckwer et al. (1974)
R_{O_2}	$-0.99995 T_{O_2}$
k_L	Higbie (1935) for tap water and Frössling (1938) for surfactants

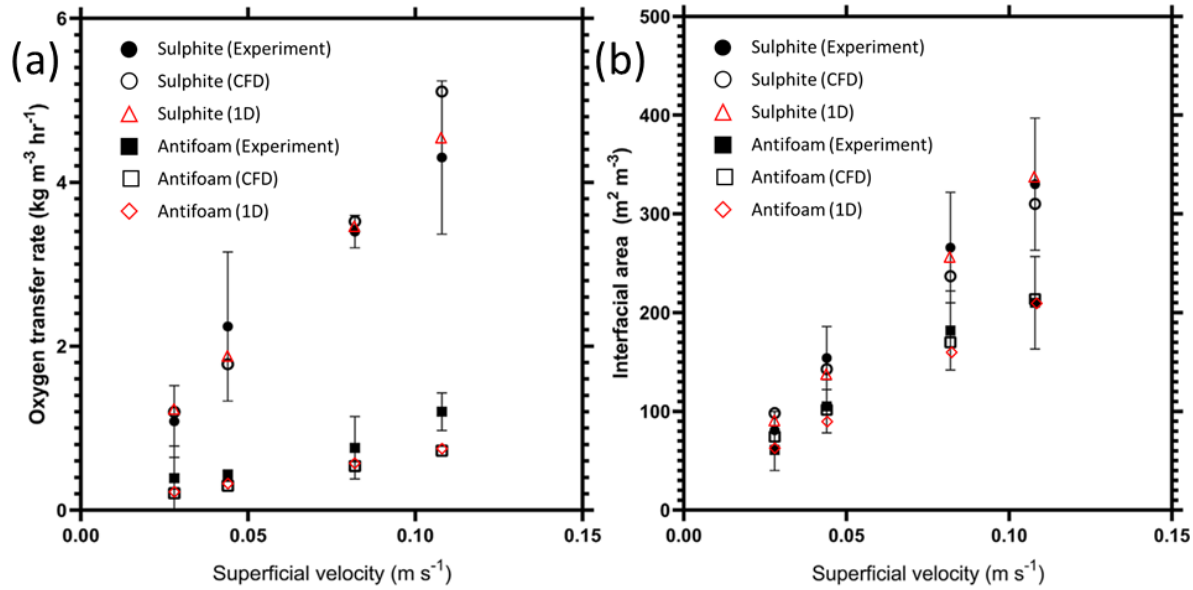

Figure 3.14: Comparison between experimental data, CFD and 1D model predictions of (a) oxygen transfer rate and (b) interfacial area for tap water and for tap water with antifoam.

Figure 3.14 reports the results obtained from the 1D model compared to the experimental measurements and CFD results. The 1D model predicts relatively well both the interfacial area and the OTR. The interfacial area is proportional to the bubble diameter and the gas holdup. The bubble diameter is obtained from the experimental measurement and the gas holdup has been validated in Section 3.1.3, hence, the predicted interfacial area is in good agreement with the experimental value. As previously discussed, the closures for drag were issued from experimental measurements, as well as the liquid film mass transfer coefficient k_L. These closures have been validated by the developed CFD model (Ertekin et al., 2021; McClure et al., 2015b, 2015c). Contrary to a fixed value of k_L, the Higbie (1935) and Frössling (1938) correlation are used here, which turned out to be appropriate closures as both models yield approximately 4.13×10^{-4} m.s^{-1} and 1.05×10^{-4} m.s^{-1} for clean and surfactant containing system, respectively, which is close to the experimentally measured values. Similar to the experiment, the presence of Antifoam on the bubble surface creates a barrier for mass transfer, which causes the bubbles to behave like a solid sphere. The liquid film mass transfer coefficient k_L can be well described by the Frössling (1938) correlation. Meanwhile, for the clean system, the classical Higbie (1935) proved again to be sufficient to predict the OTR.

3.2.4 Comparison with the Deckwer et al. (1978) case with CO_2 physical absorption in a tall bubble column

For a thorough validation of the 1D model, the spatially resolved measurement data on the species concentration are greatly necessary. The local measurement of the dissolved concentration and therefore the interfacial mass transfer intensity are scarce in the literature (Rzehak and Krepper, 2016). Here, a thorough validation of mass transfer terms in the 1D model is conducted using the literature data of Deckwer et al. (1978), as had been done in the CFD model of Rzehak and Krepper (2016). Deckwer et al. (1978) conducted CO_2 interfacial mass transfer study in a bubble column operating under co-current and counter-current regimes. Due to high CO_2 interphase mass transfer rate, the gas holdup varies considerably with the axial position. The authors reported the complex behaviour of gas-liquid hydrodynamics at such high interphase mass transfer rate with absorption at the bottom and desorption at the top of the column. Only the co-current case is considered in this work. The experiment was conducted in a bubble column with a height and internal diameter of 4.4 m and 0.14 m, respectively. The gas sparger is a glass sintered plate with a pore size of 150 µm which ensures homogeneous injection of bubbles. The gas phase is a mixture of air and CO_2 at various molar fractions of CO_2 (X_{CO_2}) and different superficial gas velocities (j_G). Whereas, the liquid phase was fed free of CO_2 and it is maintained at a constant superficial liquid velocity (j_L) of 4.72 cm.s^{-1}. The temperature is maintained at 14°C. The gas holdup was measured using pressure taps and the manometric method.

The bubble size was measured using the photography method. The gas phase was analysed using gas chromatography or absorption in KOH solution to quantify the CO_2 content. The dissolved CO_2 was measured using the electrochemical method.

Table 3.8: Experimental data reported in Deckwer et al. (1978) for experiment number 15 – 20

Exp.	Inlet data		Outlet data		P (kPa)	Averaged data		
	j_G (cm.s^{-1})	X_{CO_2} (-)	j_G (cm.s^{-1})	X_{CO_2} (-)		$<\varepsilon_G>$ (-)	$<j_G>$ (cm.s^{-1})	$<k_La>$ (s^{-1})
15	1.64	0.766	0.75	0.274	102.0	0.017	0.69	0.0071
16	2.75	0.835	1.20	0.467	102.7	0.027	1.15	0.0119
17	3.42	0.673	2.49	0.377	103.9	0.072	2.20	0.0264
18	4.01	0.56	3.55	0.324	107.2	0.105	3.08	0.0396
19	4.63	0.478	4.59	0.293	109.6	0.126	3.94	0.0431
20	5.16	0.425	5.42	0.269	110.7	0.135	4.64	0.0490

If the interfacial CO_2 mass transfer flux is well captured by the 1D model compared with the experimental data of Deckwer et al. (1978), then it can be considered that the mass transfer part of the 1D model is also validated in a relevant two-way coupled situation.

The CO_2 mass transfer results of Deckwer et al. (1978) had also been used by Rzehak and Krepper (2016) to validate their Eulerian CFD model. Similarly, Hissanaga et al. (2020) developed a one-dimensional (1D) two-fluid model to study the mass transfer modelling of homogeneous bubbly flow. The numerical predictions of Rzehak and Krepper (2016) and Hissanaga et al. (2020) were also taken to serve as a comparison with the present 1D model results. However, extra care needs to be taken when comparing these results with the 1D model as Rzehak and Krepper (2016) and Hissanaga et al. (2020) models may apply different closure models and assumptions. Hissanaga et al. (2020) summarised the experimental data of Deckwer et al. (1978) as reported here in Table 3.8. Table 3.8 shows that the superficial gas velocity and the CO_2 molar fraction decrease from the inlet to the outlet, signifying a loss of gas fraction due to the gas-to-liquid mass transfer.

For the CFD model of Rzehak and Krepper (2016), the interfacial forces considered were the drag, the lift, the wall lubrication, the turbulent dispersion and the virtual mass forces. The drag is modelled

using the correlation of Ishii and Zuber (1979), the lift force is modelled with the correlation of Tomiyama et al. (2002), the wall lubrication force is modelled with the correlation of Hosokawa et al. (2009), and the turbulent dispersion force is modelled with the correlation of Burns et al. (2004). Meanwhile, the bubble size (d_b) and the mass transfer coefficient (k_L) were kept constant spatially and identical to the experimental values of Deckwer et al. (1978).

The 1D model of Hissanaga et al. (2020) also considers the drag correlation of Ishii and Zuber (1979) which is valid for sphere, ellipsoidal and cap bubbles. It is expressed as:

$$\mathrm{C_D} = \max[C_D^{sph}, \min(C_D^{ell}, C_D^{cap})] \tag{3.4}$$

$$C_D^{sph} = \frac{24}{\mathrm{Re}}(1 + 0.1\mathrm{Re}^{0.75}) \tag{3.5}$$

$$C_D^{ell} = \frac{2}{3}\sqrt{\mathrm{Eo}} \tag{3.6}$$

$$C_D^{cap} = \frac{8}{3} \tag{3.7}$$

Where Re and Eo are the Reynolds and Eötvos number, respectively, given by

$$Re = \frac{|u_G - u_L| d_b}{\nu_L} \tag{3.8}$$

$$\mathrm{Eo} = \frac{(\rho_L - \rho_G) g d_b}{\sigma} \tag{3.9}$$

The mass transfer coefficient used is derived from the Sherwood (Sh) correlation of (Lochiel and Calderbank, 1964), written as:

$$Sh = \frac{2}{\sqrt{\pi}}\left(1 - \frac{2.96}{\sqrt{Re}}\right)^{1/2} Re^{1/2} Sc^{1/2} \tag{3.10}$$

Noticed that equation (3.10) is reduced to the classical Higbie (1935) model in the case of high Re.

The closures of the 1D model are reported in Table 3.9. The bubble velocity is modelled as its terminal velocity derived from the momentum balance. The drag coefficient is calculated from the correlation of Tomiyama et al. (1998) which is valid for spherical and non-spherical bubbles. The inlet bubble diameter is taken the same as experiment at 2.86 mm. In contrary with the work of Rzehak and Krepper (2016) and Hissanaga et al. (2020), the bubble diameter is not modelled as a constant but it can vary

axially. The mass transfer coefficient of Higbie (1935) is applied whereby the liquid system is tap water. The axial dispersion coefficients are set to zero, following the suggestions of Rzehak and Krepper (2016) and Hissanaga et al. (2020) whereby the authors neglected the dispersion phenomena as the Peclet number is high. Another difference is that the current 1D model considers oxygen mass transfer alongside with carbon dioxide mass transfer, whereas the models of Rzehak and Krepper (2016) and Hissanaga et al. (2020) only considers CO_2 mass transfer.

Table 3.9: Closure relations used in the 1D model to simulate Deckwer et al. (1978) case.

Variables	Closure model
d_b	Inlet bubble diameter = 2.86 mm. d_b non-constant axially, followed the equation (2.29)
u_G	Tomiyama et al. (1998) drag coefficient for pure system.
u_L	0 m.s^{-1} bubble column closed to the liquid.
D_G	Neglected. Followed the suggestions of Rzehak and Krepper (2016) and Hissanaga et al. (2020)
D_L	Neglected. Followed the suggestions of Rzehak and Krepper (2016) and Hissanaga et al. (2020)
k_L	Higbie (1935)
C^*	Sander (2015)

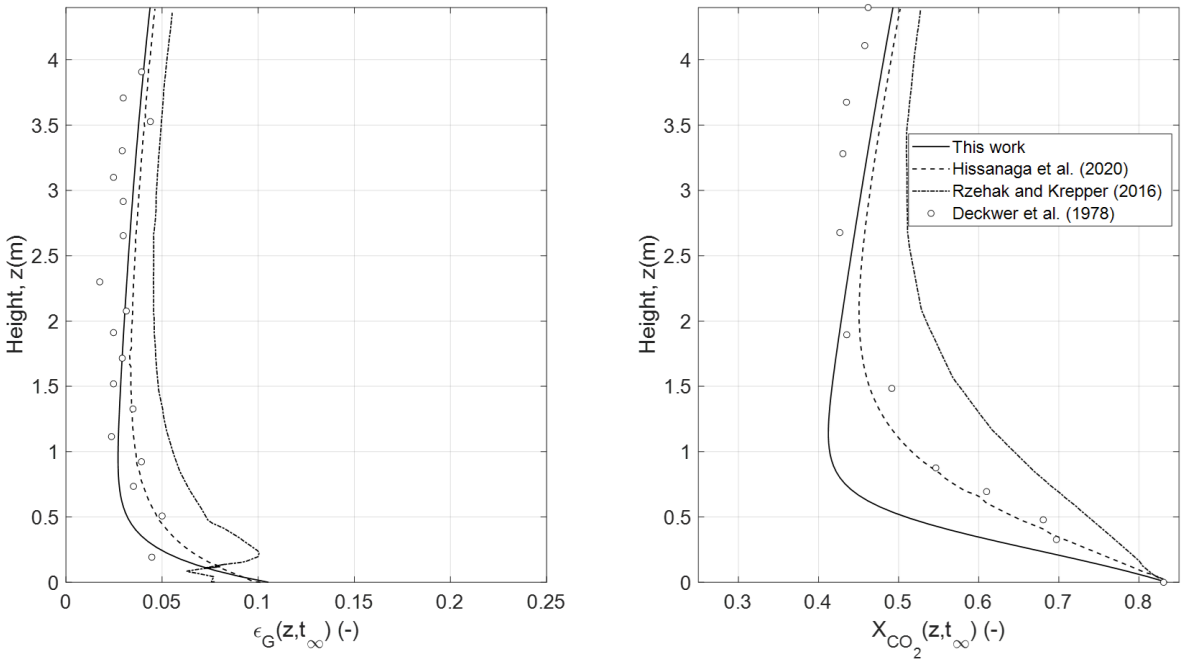

Figure 3.15: Local gas holdup and CO_2 molar fraction at steady-state for experiment 16

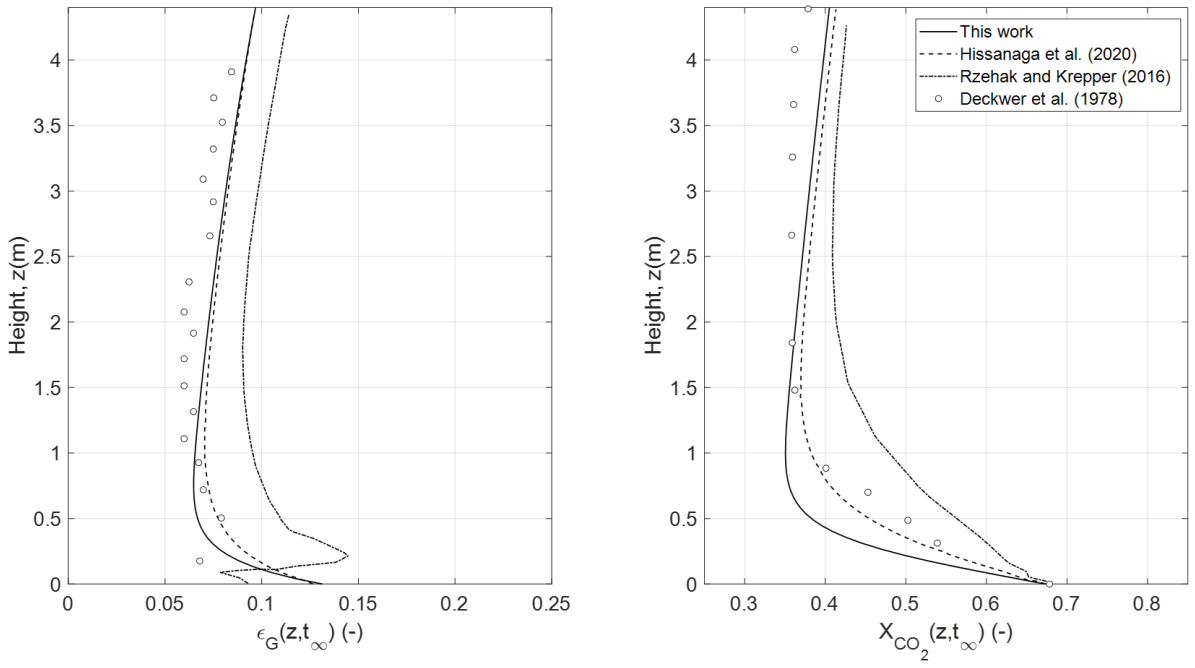

Figure 3.16: Local gas holdup and CO_2 molar fraction at steady-state for experiment 17

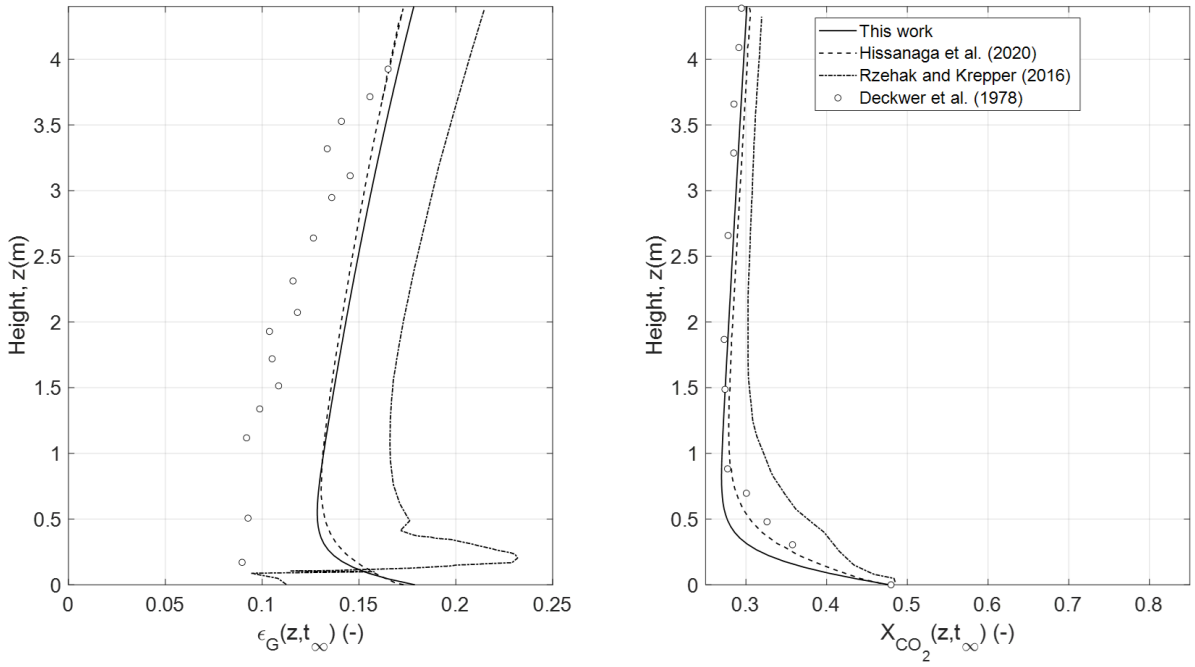

Figure 3.17: Local gas holdup and CO_2 molar fraction at steady-state for experiment 19

Figure 3.15, Figure 3.16, and Figure 3.17 show the local gas holdup and CO_2 molar fraction profile obtained by the 1D model and compared with Deckwer et al. (1978) experimental data. Globally, the 1D model follows the experimental trend. The local gas holdup varies considerably with the axial location. For experiments 16 and 17, the local gas holdup decreases at the bottom and then increases

at the top of the column, signifying the gas-liquid mass transfer passes from absorption to desorption along the column. At such tall column, gas expansion due to lower hydrostatic pressure also causes the gas holdup to increases at the top of the column. For the CO_2 molar fraction, a similar trend can be observed with a modest increase of X_{CO_2} at the top. Both the 1D model of this work and that of Hissanaga et al. (2020) fail to capture the local gas holdup variation of experiment 19. This could be due to the fact that both 1D models are developed in the homogeneous bubbly flow regime without considering bubble coalescences and does not include the swarm correction term (Gemello et al., 2019; McClure et al., 2017; Simonnet et al., 2007) whereas experiment 19 was conducted near the transition - heterogeneous regime. In this regime, complex fluid structures prevail in the bubble column with the presence of bubble coalescence. At high superficial gas velocity, bubble coalescence occurs and it increases the Sauter mean diameter, drastically reducing the drag, leading to higher bubble velocity and lower gas holdup. It is interesting to see that the 1D model is sufficient to capture the local gas holdup and the interfacial mass transfer flux as the profiles are well captured compared with the CFD model of Rzehak and Krepper (2016). It can be observed in experiments 16 and 17 that the CO_2 mass transfer is overpredicted by the 1D model, resulting in a lower CO_2 molar fraction as compared to the experiment and the prediction of Hissanaga et al. (2020). This is due to the difference in the mass transfer closure term applied and the non-constant bubble diameter. High absorption flux leads to bubble diameter reduction, which in return increases the CO_2 mass transfer flux, resulting in a higher loss in the CO_2 molar fraction. It is reported that the measured bubble diameter remained relatively constant throughout the column (Deckwer et al., 1978). The bubble diameter measurement was conducted at two axial locations using the photography method. The reason given by Rzehak and Krepper (2016) and Deckwer et al. (1978) was that since the bubbles lose mass due to absorption but the simultaneous occurrence of coalescence must have compensated for the effect, resulting in quasi-constant bubble diameter throughout the column. For the aforementioned reason, new simulations are carried out by assuming constant bubble diameter and the mass transfer closure of Lochiel and Calderbank (1964) which is the one applied by Hissanaga et al. (2020).

Figure 3.18 compares the axial profiles of different variables obtained for case 16, depending on whether constant or non-constant bubble diameter is assumed. When the bubble diameter is supposed axial-dependent, it is found that a decrease in bubble diameter is observed at the bottom of the column, with an approximately 40% decrease reached, from 2.86 mm at the inlet to 1.82 mm, as shown in Figure 3.18(a). As the bubble diameter is inversely proportional to the interfacial area a, the drop in a and $k_L a$ for the non-constant bubble case is less than that of the constant bubble case, as shown in Figure 3.18(b) and Figure 3.18(c). Here, only the $k_L a$ profile for O_2 is shown as the $k_L a$ profile

of CO_2 is proportional to that of O_2 with a ratio of 0.9, which corresponds to the ratio of diffusivity between the two species.

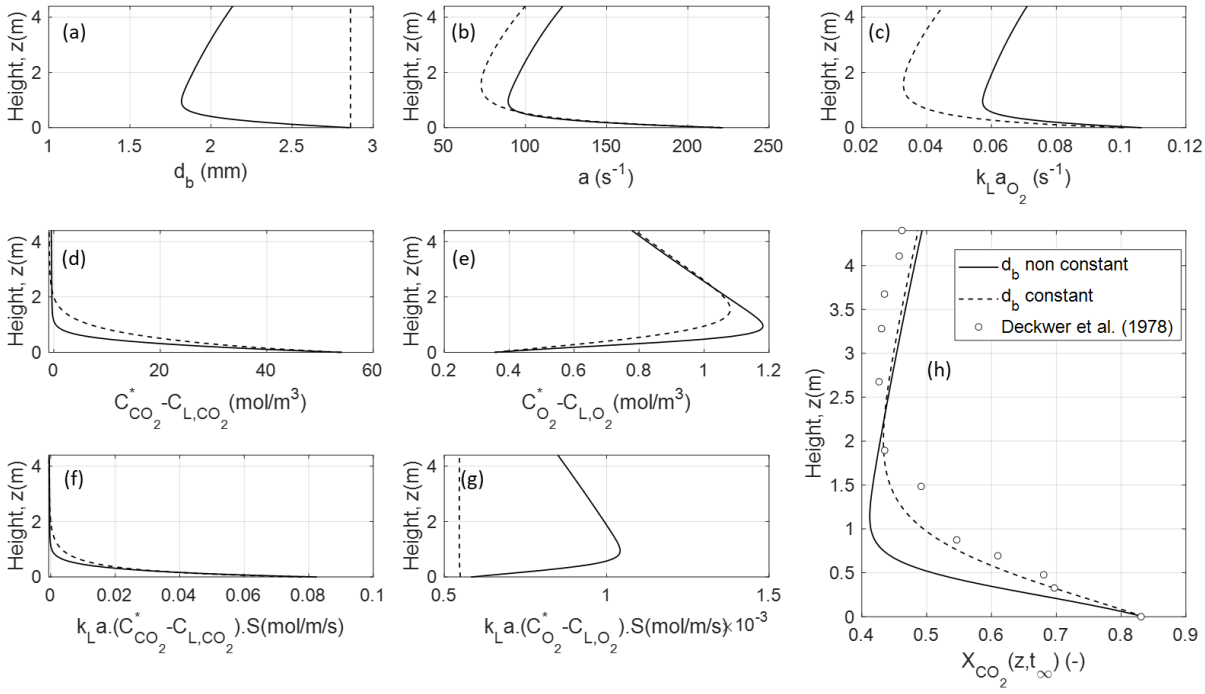

Figure 3.18: Comparison between constant diameter and non-constant diameter for the axial profiles of (a) bubble diameter, (b) Interfacial area, (c) $k_L a$ for H_2 (d) CO_2 concentration gradient, (e) H_2 concentration gradient, (f) CO_2 mass transfer flux per unit height, (g) H_2 mass transfer flux per unit height, (h) CO_2 molar fraction for case 16 at steady-state.

Figure 3.18(d) and Figure 3.18(e) show the concentration gradients (driving force for mass transfer) of CO_2 and O_2, respectively. For CO_2, the concentration gradient is positive at the bottom half of the column but it turns weakly negative in the upper half, signifying a change of the mass transfer direction from absorption (gas → liquid) to desorption (liquid → gas). For O_2, the concentration gradient is always positive, signifying that only absorption occurs and the equilibrium is never reached in the system. Interestingly, the high CO_2 concentration gradient at the bottom of the column causes an increase in the O_2 concentration gradient by a maximum of 237%, highlighting the multispecies mass transfer effect. This is mostly due to higher hydrostatic pressure at the bottom of the column, higher CO_2 partial pressure and higher CO_2 Henry's constant, as calculated by Sander (2015), yielding $H_{CO_2}(14°C) = 4.49 \times 10^{-4} mol.m^{-3}.Pa^{-1}$ vs. $H_{O_2}(14°C) = 1.49 \times 10^{-5} mol.m^{-3}.Pa^{-1}$. The multispecies mass transfer effect is also observed in the local mass transfer flux, as shown in Figure 3.18(f) and Figure 3.18(g). The local mass transfer flux profiles are equivalent to that of concentration gradients except for the case of O_2 flux with constant bubble diameter. It is noticed that the O_2 mass

transfer flux is almost constant throughout the column. In fact, the increase in the concentration gradient is compensated by the drop in $k_L a$ at the bottom of the column and the inverse observation is made at the top of the column. In the end, a better fit is obtained with the constant bubble diameter case, as shown in Figure 3.18(h), similar to the conclusion of Rzehak and Krepper (2016) and Hissanaga et al. (2020). It confirms that coalescence occurs and compensates the gas loss, leading to constant bubble diameter at gas holdup up to 10% at the bottom.

When the mass transfer closure model of Lochiel and Calderbank (1964) with the constant bubble diameter assumption is applied, our 1D model results are very similar result to those of Hissanaga et al. (2020), as shown in Figure 3.19, Figure 3.20, and Figure 3.21. The results confirm the previous assumption that the constant bubble diameter was observed throughout the column. It also shows that the Higbie model overestimates the mass transfer flux as the correlation yields a more optimistic k_L, resulting in a higher drop in the gas holdup and the CO_2 molar fraction at the inlet, as shown in Figure 3.17. The choice of mass transfer closure model in bubbly flow modelling is still an open question in the literature. In this work, we applied the mass transfer coefficient k_L of Higbie (1935), derived from the theoretical solution of mass transfer across a mobile sphere. For simplification, some of the mass transfer modelling in bubbly flow conducted in the literature uses the experimental measured k_L value (Ertekin et al., 2021; Krishna and van Baten, 2003; McClure et al., 2015b; Rzehak and Krepper, 2016)

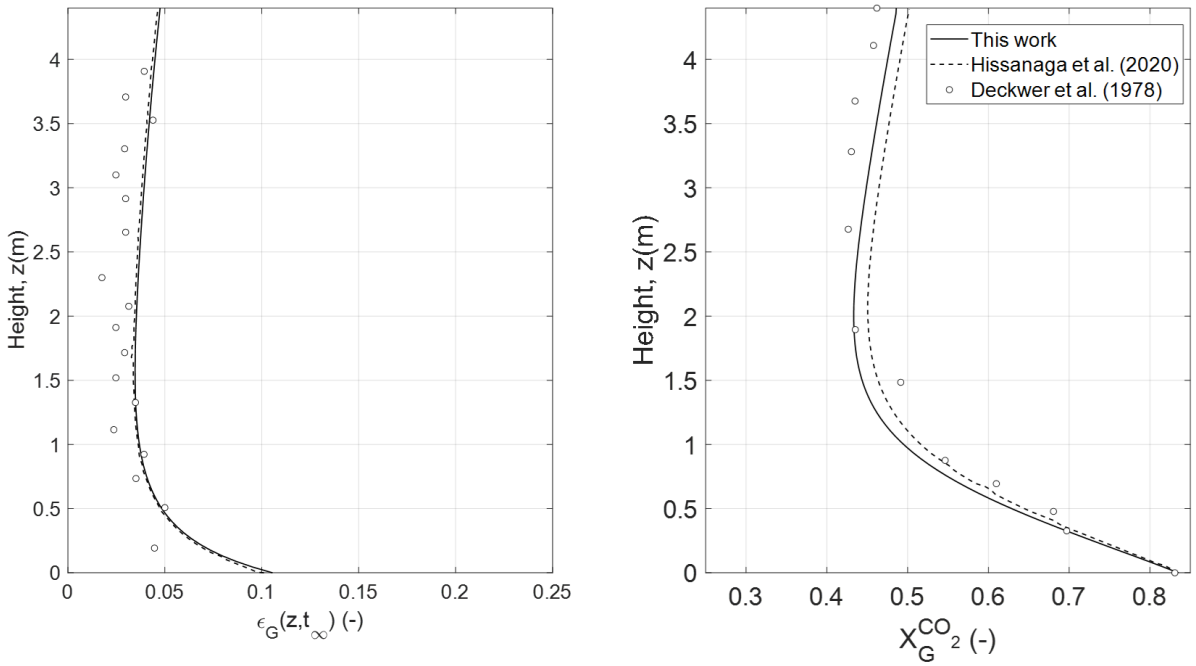

Figure 3.19: Local gas holdup and CO_2 molar fraction at steady-state for experiment 16 with the mass transfer coefficient calculated from Lochiel and Calderbank (1964) and a constant bubble diameter.

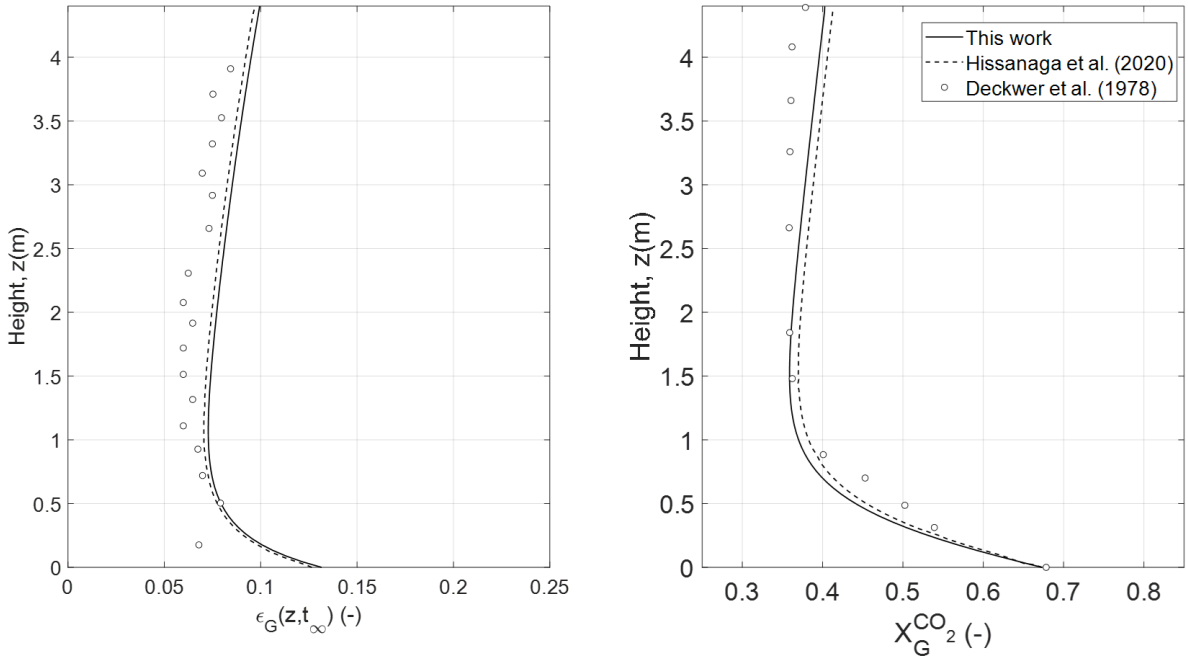

Figure 3.20: Local gas holdup and CO_2 molar fraction at steady-state for experiment 17 with the mass transfer coefficient calculated from Lochiel and Calderbank (1964) and a constant bubble diameter.

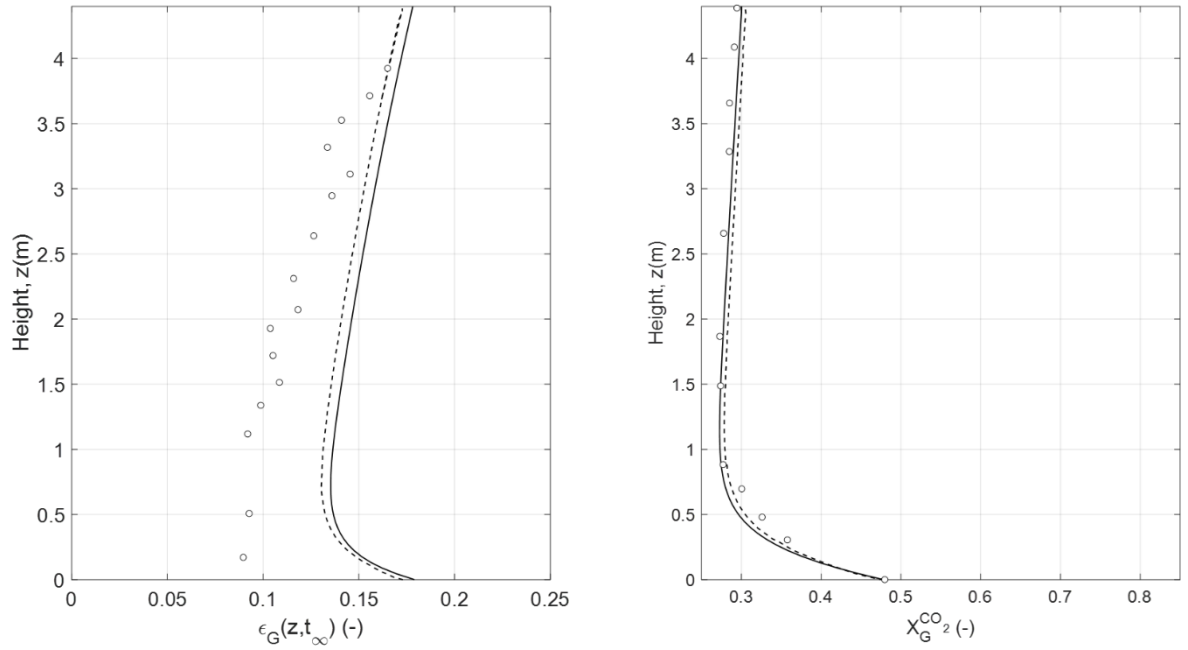

Figure 3.21: Local gas holdup and CO_2 molar fraction at steady-state for experiment 19 with the mass transfer coefficient calculated from Lochiel and Calderbank (1964) and a constant bubble diameter.

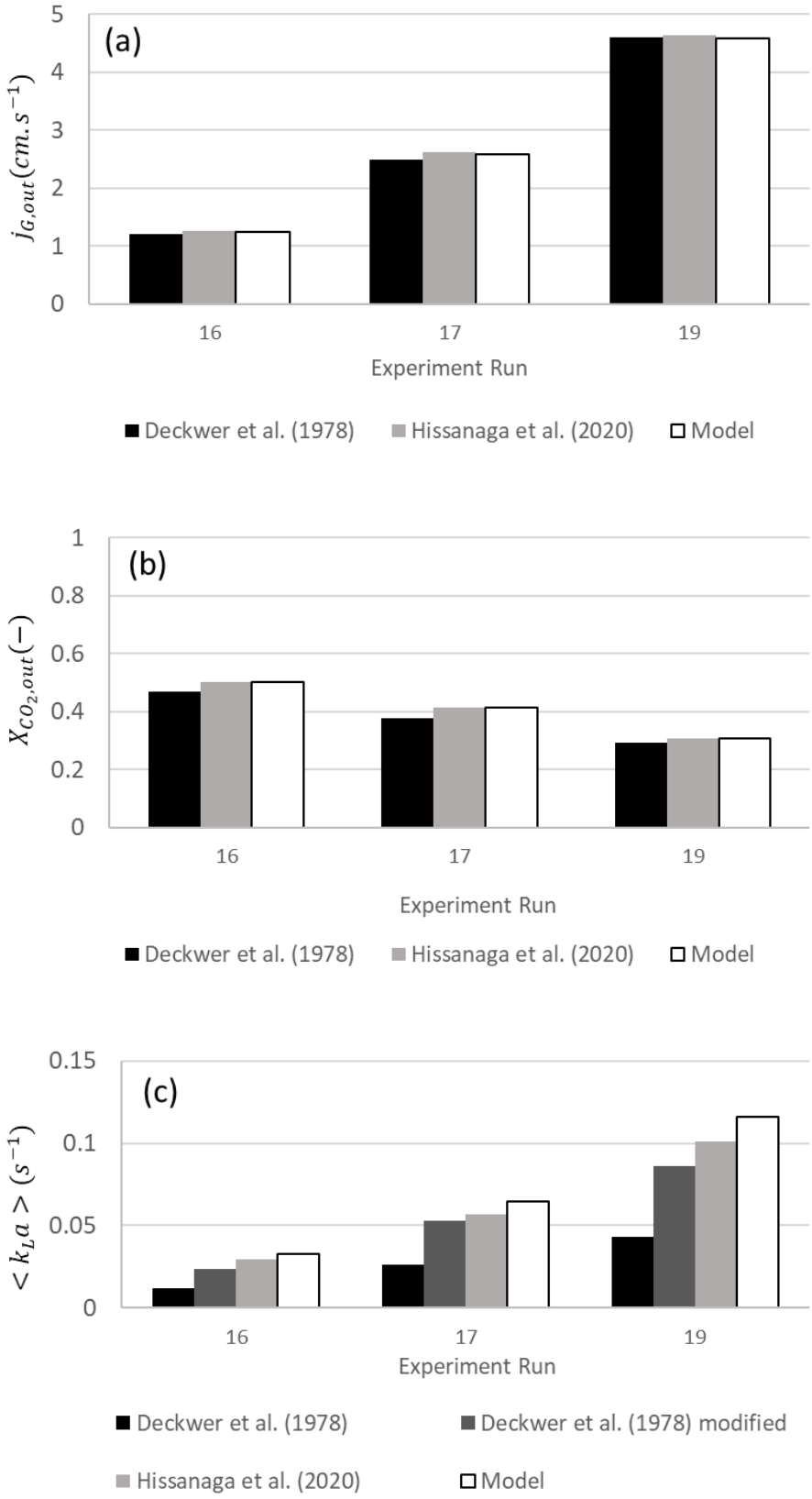

Figure 3.22: Comparison of (a) Outlet superficial gas velocity (b) Outlet CO_2 molar fraction (c) Global averaged $k_L a$ between 1D model and literature data.

Figure 3.22(a) and (b) present the results obtained at the column outlet, namely the superficial gas velocity and the CO_2 molar fraction. It shows that the 1D model is capable of capturing hydrodynamics in large-scale bubble columns as the outlet superficial gas velocity after experiencing interfacial mass transfer is validated correctly compared with Deckwer et al. (1978) experimental data. Figure 3.22(c) reports the averaged $k_L a$ value from the 1D model, Deckwer et al. (1978) and Hissanaga et al. (2020). The experimental $k_L a$ measured by Deckwer et al. (1978) is relatively too low. The underprediction could probably be due to non-linearities in the spatial gas holdup and associated variables induced by the huge CO2 mass loss. This makes the determination of $k_L a$ extremely challenging by fitting to the model, as many phenomena have to be considered simultaneously. The authors mentioned that the mass transfer coefficient has to be multiplied by a factor of 2 or 3 from the experimental value in their model to obtain the experimental results. The k_L value of Deckwer et al. (1978) was determined by fitting the own developed theoretical model with the experimental results through the trial-and-error method.

3.3 General conclusion

The developed 1D model is able to predict relatively well the overall gas holdup provided the closure models used are valid in the experimental conditions. It is found that with a suitable bubble diameter, drag model and bubble swarm correlation, the overall gas holdup is well predicted for various systems, operating under different conditions. For example, in the case of dense swarm flow, as in the case of Colombet (2012), the bubble swarm corrective factor of Wallis (1961) has to be included. The spatial variation of the gas holdup during CO_2 absorption of Deckwer et al. (1978) case is also well captured by the 1D model and it is also compared with the results of Rzehak and Krepper (2016) CFD model and Hissanaga et al. (2020) 1D model.

Upon validation of the hydrodynamics, the mass transfer modelling in bubbly flow is investigated using the 1D model. Different test cases have been conducted using literature data, covering all ranges of superficial gas velocity, bubble column dimension, gas and liquid properties. These validation studies show the robustness of the present spatio-temporal 1D model in studying mass transfer in bubbly flow. The most complete study conducted by Deckwer et al. (1978) has been used for comparison. It is found that the Sauter mean diameter does not vary much axially throughout the column, signifying the coupling may be weak. However, in the case of reactive bubbly flow, the mass transfer is expected to have a more significant coupling with the chemical reaction. This is highlighted in the study of CO_2 reactive mass transfer in NaOH solution in Chapter 5.

3.4 First paper: Spatio-temporal 1D gas–liquid model for biological methanation in lab scale and industrial bubble column

Our first paper is published in Chemical Engineering Science and it is accessible with the following link: https://doi.org/10.1016/j.ces.2022.117478. The paper reports the development of the 1D model and the successive validation with the experimental data, literature data and numerical test cases. It also features our attempt to simulate an industrial-scale biological methanation plant of Electrochaea described in Section 1.1.1.6.

Chemical Engineering Science 251 (2022) 117478

Contents lists available at ScienceDirect

Chemical Engineering Science

journal homepage: www.elsevier.com/locate/ces

Spatio-temporal 1D gas–liquid model for biological methanation in lab scale and industrial bubble column

Vincent Ngu, Jérôme Morchain, Arnaud Cockx *

TBI, Université de Toulouse, CNRS, INRAE, INSA, Toulouse, France

HIGHLIGHTS

- A dynamic multiple-way coupled 1D model for biological methanation is developed.
- H_2 and CO_2 mass transfer fluxes are accurately predicted at various scales.
- Novel bioreaction closure model relying upon physical supply and biological demand.
- The model allows predictive 1D simulation of industrial-scale bioprocess performances.

GRAPHICAL ABSTRACT

A comprehensive 1D multiple-way coupled gas–liquid model for the scale-up of biological methanation process in bubble column reactor. Industrial scale reactor image taken from www.electrochaea.com.

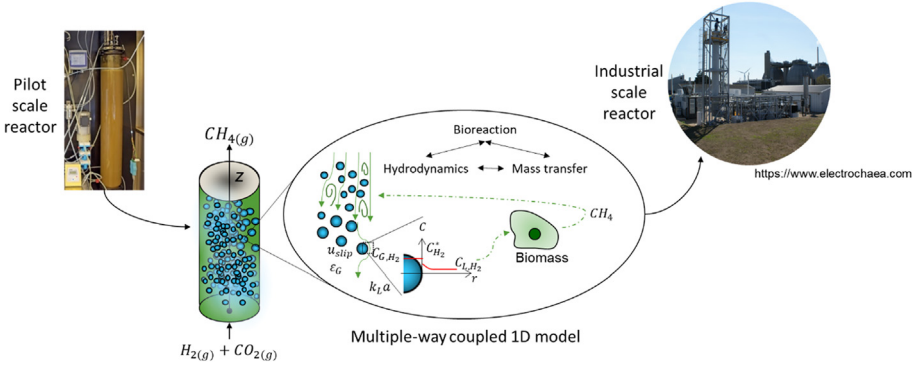

ARTICLE INFO

Article history:
Received 13 September 2021
Received in revised form 17 December 2021
Accepted 22 January 2022
Available online 29 January 2022

Keywords:
Biological methanation
Bubble column
Gas-liquid mass transfer
1D modeling
Power-to-Gas
Biogas upgrading

ABSTRACT

Numerical simulation of biological methanation in bubble column reactors is challenging due to strong coupling between hydrodynamics, mass transfer and bioreaction. A satisfactory prediction of the mass transfer coefficient and the gas solubility is crucial to couple hydrodynamics and biokinetics. A comprehensive 1D multispecies multiple-way coupled gas–liquid model is developed. The hydrodynamics of the model is validated using experimental gas loading data at very low gas holdup. The local mass transfer is validated using literature data on CO_2 mass transfer in the large-scale. The local gas holdup and interfacial CO_2 mass transfer flux are correctly described thanks to a two-way coupling between hydrodynamics and mass transfer, including changes in bubble diameter and pressure effects. When a mixture of H_2, CO_2 and CH_4 is used, highly non-linear mass transfer profiles due to differences in solubilities are observed. An original flux-based metabolic model is proposed to simulate an industrial biological methanation process. This allows smooth transition between biologically and physically controlled regimes as the culture reaches a steady-state. The comprehensive model enlightens that the biological methanation performances are governed by the H_2 mass transfer limitation balanced by growth in the transient state and biological maintenance in the steady-state.

* Corresponding author.
E-mail addresses: ngu@insa-toulouse.fr (V. Ngu), morchain@insa-toulouse.fr (J. Morchain), cockx@insa-toulouse.fr (A. Cockx).

https://doi.org/10.1016/j.ces.2022.117478
0009-2509/

1. Introduction

In the last decades, the implementation of renewable energy such as wind and solar energy has been increased worldwide, primarily due to a decline in production costs and an increasing global warming threat. However, solar and wind energy are both intermittent with unpredictable power production. In order to maintain an equilibrium between the fluctuating power production and the power demand, the presence of an energy buffer is much needed. Biological methanation emerges as an interesting solution as the surplus electricity can be stored in the form of biomethane (CH_4) through the process commonly called as "Power-to-Gas". Compared to catalytic methanation, biological methanation operates at milder condition, hence a lower investment and operation cost. A synergy effect of biological methanation with anaerobic digestor can also be established to upgrade carbon dioxide (CO_2) in the biogas to CH_4. Despite biological methanation advantages, the overall process is strongly limited by hydrogen (H_2) mass transfer (Lecker et al., 2017; Bassani et al., 2016; Rusmanis et al., 2019).

Investigation of local mass transfer phenomena in biological methanation through in silico approach is challenging especially in full scale bubble column. The hydrostatic pressure effect on the mass transfer in such tall column has to be taken into consideration. In biological methanation where the origin of the substrates and the final product CH_4 are in gas phase, a multispecies mass transfer approach has to be considered too. The strong coupling of hydrodynamics, mass transfer and reaction is evidenced through experimental findings. Giovannettone et al. carried out gas holdup measurement in a 24 m high bubble column at different liquid height. The gas holdup was found to increase with column height regardless of the sparger type or initial liquid height; with taller columns exhibiting a larger difference in gas holdup between the top and the bottom than that in shorter columns. The out of date assumption of constant gas holdup throughout the column, caused large errors in performance prediction during scale-up to industrial-scales (Giovannettone et al., 2009). In such large-scale reactors, the gaseous phase may actually undergo continuous and drastic changes in volume. As pointed out by (Di Giuliano and Pellegrino, 2019), assuming a constant superficial velocity in a 1D axial dispersion model is equivalent to imposing a constant gas holdup. Neither the case with high mass transfer rate nor the situation with volume expansion and contraction due to rapid mass transfer/reaction could valid this assumption. (Deckwer et al., 1978) conducted absorption and desorption of CO_2 in water using tall columns (4.4 m and 7.2 m high) and observed that, due to high CO_2 mass transfer rate, the gas holdup varies considerably from the bottom to the top of the column. For multispecies mass transfer, which is the most common case in industrial reactor, when one species has a higher solubility than the others, the mass transfer leads to a decrease in bubble size (Hlawitschka et al., 2017); in return, it offers a higher interfacial area for other species mass transfer. The strong coupling resides in that any changes in bubble size will influence the overall hydrodynamics behavior, resulting in a completely different slip velocity, residence time and gas fraction. In the very case of bioreactions, the spatial dependence of interfacial area and partial pressure impacts the ratio of interfacial mass transfer fluxes which determine the local availability of nutrients. These heterogeneities may induce undesired metabolic behavior as reported in many industrial bioreactor applications (Morchain et al., 2014; Pigou and Morchain, 2015).

In short, the reaction rate of biological methanation depends on the local availability of the dissolved substrates which is controlled by the gas–liquid mass transfer process and the mixing. The interphase mass transfer flux depends on (1) the local prevailing hydrodynamics which are controlled by the gas and liquid motion and (2) the spatially-dependent consumption by the biomass. This complex coupling of different phenomena makes the overall reactor performance prediction and scale-up of bubble column very difficult (Darmana et al., 2007). Therefore, a two-way coupling approach needs to be considered when one tries to model such strongly coupled phenomena.

The two-way coupled hydrodynamic-mass transfer problem was already addressed in the literature (Darmana et al., 2007; Nauha and Alopaeus, 2015; Inkeri et al., 2018; de Medeiros et al., 2020). Nauha and Alopaeus (2015) considered the changes in gas holdup and gas density in their compartmental model to simulate a stirred-tank bioreactor. Without including these changes, the correct interfacial area and mass transfer flux could not be estimated, leading to bad prediction of reactor performances. In Chen et al.'s works, dedicated to the simulation of synthesis gas fermentation using a 1D bubble column model, the gas holdup changes was not considered in (Chen et al., 2018, 2016, 2015). The gas–liquid mass transfer coefficients, bubble diameter, gas velocity, and gas and liquid volume fractions were treated as constants. But in a later paper of the same research group, the model included hydrodynamic spatial variation by introducing the drift-flux model (Li et al., 2019). The drift-flux model is solved according to local bubble diameter in order to obtain the local gas holdup. Inkeri et al. applied a semi-fundamental approach for the coupling of hydrodynamics and mass transfer to simulate a stirred-tank bioreactor (Inkeri et al., 2018) and a bubble column reactor (Inkeri and Tynjälä, 2020). In both studies, the local gas holdup is estimated from literature correlation through local dependent superficial gas velocity. Much like Inkeri et al. de Medeiros et al. (2020) mentioned that their 1D model accounts for the variation of gas velocity. The gas holdup is not solved, but rather estimated using literature correlation involving superficial gas velocity. Nonetheless, the results of this coupling on local concentration profile and reactor performance are not shown in their work, as it is not the objective of the paper. More recently, Hissanaga et al. (2020) developed a 1D spatio-temporal model to describe CO_2 absorption. In their work, only CO_2 is considered for mass transfer whilst the others (oxygen and nitrogen gas) behave as inert species. To our best knowledge, the two-way coupling is either empirical (through literature correlation and not-fully resolved) or its effect has not been thoroughly discussed in a 1D model framework.

Furthermore, the difficulties in modeling any biological reaction lie in the formulation of the reaction term addressing the mixing, mass transfer and bioreaction. Chen et al. (2018) developed a 1D model to simulate bioreaction using flux balance analysis. The flux balance model is a complex model which involve linear programming problem through hierarchical fixed-priority preemptive (lexicographic) optimization procedure (Chen et al., 2016). In their work on synthesis gas fermentation reactor, Siebler et al. (2020), inspired by (Linkès, 2012), proposed to compute liquid-cell mass transfer as the steady-state solution of a continuity of fluxes equation involving a Monod expression for uptake law and mass transfer diffusion limitation in the liquid phase. In the context of biological methanation, Inkeri et al. (2018) employed unstructured kinetics model, originally introduced by Schill et al. (1999) to model the bioreaction. However, they introduce an artificial stabilizing function in their model to avoid numerical issues when the substrates concentration approaches zero. Recently, Markthaler et al. (2020) used a second order kinetic law, rather than a Monod law, to model biological methanation process.

As the reaction rate of biological methanation is limited by H_2 gas–liquid mass transfer, the detailed reaction mechanism

becomes less important (Markthaler et al., 2020). In fact, the correct modeling of methanogens growth and methane production depends mainly on satisfactory prediction of the mass transfer coefficient (k_La) and the gas solubility (C^*) (Schill et al., 1999). A more practical and realistic model for biological methanation with the possibility to switch between biological regime and physical regime is therefore necessary. In this work, a comprehensive 1D spatio-temporal model considering multispecies mass transfer (H_2, CO_2, CH_4), variable gas volume fraction due to local pressure changes and mass transfer flux applied to biological methanation process is developed. The first originality is to perform a predictive resolution of partial mass balance coupled through two-phase hydrodynamics and multi-species mass transfer. The second originality lies in the formulation of the hydrogen consumption rate handling the transition from biological to physical regimes. In continuation of previous works, a universal approach to model substrate uptake rate, including gas–liquid mass transfer rate limitation is implemented (Pigou, 2018).

In a first step, the model is validated in terms of transient hydrodynamics (using experimentally measured gas holdup) and spatial mass transfer flux (using literature data). In a second step, after checking local gas liquid mass transfer fluxes for each species and global mass balances, the influences of operating pressure and reactor's height on the mass transfer and the effect of multispecies mass transfer are discussed. Lastly, an industrial-scale biological methanation plant is simulated using the proposed bioreaction expression. A step by step thorough validation of the numerical code is presented through a series of test cases along with a comparison to some experimental data when available. The goal of this model is to discuss scale-up issues as faced in the industry when multispecies mass transfer is coupled with bioreaction.

2. Material and methods

This section is dedicated to present the mathematical model and the experimental setup. The set of equations solved with the closure equations and the resolution strategy are described in Sections 2.1 and 2.2 respectively. The experimental setup and measurements are depicted in Section 2.3.

2.1. Model structure

2.1.1. General equations

The conservation of mass for the species, $i = [H_2, CO_2, etc]$ in an elementary volume of height dz takes the following form

$$\frac{\partial \phi_{G,i}}{\partial t} + \frac{\partial u_G \phi_{G,i}}{\partial z} = D_G \frac{\partial}{\partial z}\left(\varepsilon_G \frac{\partial C_{G,i}}{\partial z}\right) - k_{L,i}a(C_i^* - C_{L,i}) \quad (1)$$

$$\frac{\partial \phi_{L,i}}{\partial t} + \frac{\partial u_L \phi_{L,i}}{\partial z} = D_L \frac{\partial}{\partial z}\left(\varepsilon_L \frac{\partial C_{L,i}}{\partial z}\right) + k_{L,i}a(C_i^* - C_{L,i}) + \varepsilon_L R_i \quad (2)$$

$$\varepsilon_G + \varepsilon_L = 1 \quad (3)$$

Eqs. (1) and (2) are partial mass balance for each species, i transported in gaseous and liquid phase respectively. u_G and u_L are the gas and liquid velocities, respectively. ε_G and ε_L are the volume fraction of the gas and liquid phase summing at one, as stated in Eq. (3). $C_{G,i}$ and $C_{L,i}$ are the concentration of species i per unit volume of the gas and liquid phase respectively. Hence, $\phi_{G,i}$ is the concentration of species i present in the gas phase per unit volume of the column, i.e. $\phi_{G,i} = \varepsilon_G C_{G,i}$. Similarly, $\phi_{L,i} = \varepsilon_L C_{L,i}$ holds for the same species in the liquid phase.R_i is the volumetric consumption/production rate per unit volume of liquid ($mg_i \cdot L^{-1} \cdot s^{-1}$). D_G and D_L stand for the dispersion coefficient in each phase. The mass transfer rate is obtained from the product of a species dependent mass transfer coefficient, $k_{L,i}$, the interfacial area per unit volume of the column, a, and the driving force ($C_i^* - C_{L,i}$).

In these equations, any variable, $\psi \in \{\phi, u, \varepsilon, C_i, C_i^*, k_L, a, R\}$ actually refers to $\psi(z,t)$ a spatio-temporal dependent variable at any instant time t and with $z = 0$ and $z = H$ corresponding to inlet and outlet conditions respectively. Additionally, $\psi(z, t_\infty)$ refers to the local value of ψ at any z-coordinate at steady-state. Finally, $< \psi(z,t) >$ indicates the spatial average at time t.

Noted that ε_G and ε_L in Eqs. (1) and (2) are defined in the temporal and spatial derivatives, which is not the case for some model proposed in the literature to treat the two-way coupling (Inkeri et al., 2018; de Medeiros et al., 2020; Li et al., 2019). These models used empirical or semi-empirical correlations to describe the coupling of hydrodynamics and mass transfer, with the parameters of these correlations usually obtained via spatial-dependent local values, typically calculated through global mass balance (Inkeri et al., 2018; Li et al., 2019).

2.1.2. Closure equations

Besides the resolved variables $\phi_{L,i}$ *and* $\phi_{G,i}$, closure equations or additional models are needed to define the parameters in the conservation equations. Theses closures parameters reflect the local physical phenomena occurring on-the non-resolved scale of the axial 1D model.

Dispersion coefficients: D_G is related to large velocity differences between the bubbles of different sizes (Bardin-Monnier et al., 2003). D_L describes the mixing in the liquid phase, attributed to different reasons such as large-scale liquid recirculation, radial exchange flow, bubble-induced agitation and liquid entrainment induced by density gradient (Deckwer and Schumpe, 1993). These recirculation flow induce an axial mixing and appears mostly under heterogeneous regime (Heijnen and K. Van't Riet, , 1984). Different correlations exist in the literature to estimate D_G and D_L (Heijnen and Van't Riet, 1984; Wachi and Nojima, 1990). Here, D_L is estimated from the correlation of (Deckwer et al., 1974) and it was kept constant throughout the column. D_G is estimated from the correlation of (Wachi and Nojima, 1990) and it was also kept constant for the sake of simplicity. These coefficients depend on the bubble column diameter (D_r) and the superficial gas velocity (j_G), expressed as:

$$D_L = 2.7 \cdot 10^{-4} \cdot (D_r \cdot 100)^{1.4} \cdot (j_G \cdot 100)^{0.3} \quad (4)$$

$$D_G = 20 \cdot D_r^{1.5} \cdot j_G \quad (5)$$

Slip velocity: the expression for the slip velocity valid in homogeneous bubbly flow regime is defined in Eq. (6). It is obtained from a momentum balance on an isolated bubble having reached its terminal velocity and it involves the Sauter mean diameter d_b and a drag coefficient C_D.

$$u_{slip} = u_G - u_L = u_\infty = \sqrt{\frac{4}{3}\frac{g(\rho_L - \rho_G)\, d_b}{\rho_L C_D}} \quad (6)$$

Various correlations for the drag coefficient, obtained from (Tomiyama et al., 1998), (Mei et al., 1994), and (Dijkhuizen et al., 2010) are implemented in the model. The Tomiyama correlation is valid for slightly contaminated systems, and the two others apply for clean bubbles. These correlations are reported in Appendix A.

Mass transfer term: The mass transfer term changes with the vertical coordinate z because it involves other variables that are spatially dependent ($\varepsilon_G, d_b, u_{slip}$). The local $k_{L,i}$ value is estimated using the correlation of (Higbie, 1935) as written in Eq. (7) and it is species dependent due to different value of liquid-side diffusion coefficient D_i. The local interfacial area is computed from the local gas volume fraction ε_G and the local bubble diameter d_b.

$$k_{L,i} = 2\sqrt{\frac{u_{slip} D_i}{\pi d_b}} \tag{7}$$

$$a = \frac{6\varepsilon_G}{d_b} \tag{8}$$

The solubility of each species (C_i^*) is set from the Henry constant He_i and the local partial pressure P_i.

$$C_i^* = He_i \cdot P_i = He_i y_i P = He_i C_{G,i} RT \tag{9}$$

Here, it is important to provide more details on the calculation of the local total pressure which depends on the overall gas retention in the volume of fluid above a given location z. It is expressed as:

$$\mathrm{P}(z,\mathrm{t}) = P_0 + \left(1 - \widetilde{\varepsilon_G(z)}\right)\rho_L g(H - z) \tag{10}$$

with $\widetilde{\varepsilon_G(z)} = \frac{1}{H-z}\int_z^H \varepsilon_G(\zeta, t)\cdot d\zeta$

The volume fraction of the gas phase changes due to mass transfer/bioreaction and pressure dependence on the vertical coordinate z. It is assumed that the number of bubbles per unit volume remains constant throughout the column which leads to the following relationship.

$$\frac{d_b^3(z,t)}{\varepsilon_G(z,t)} = \frac{d_b^3(0,0)}{\varepsilon_G(0,0)} \tag{11}$$

Consumption/production rates:

(Schill et al., 1999) proposed that the biocatalysed conversion of hydrogen and carbon dioxide into methane is represented through Eqs. (12) and (13).

$$H_2 + \nu_{CO_2,1} CO_2 + \nu_{NH_3,1} NH_3 \underset{r_1}{\rightarrow} \nu_{X,1} X + \nu_{CH_4,1} CH_4 + \nu_{H_2O,1} H_2O \tag{12}$$

Besides growth, the authors indicate that hydrogen is also consumed to produce maintenance energy, through the following reaction

$$H_2 + \nu_{CO_2,2} CO_2 \underset{r_2}{\rightarrow} \nu_{CH_4,2} CH_4 + \nu_{H_2O,2} H_2O \tag{13}$$

Here, we consider a third reaction, the death of biomass.

$$X \underset{r_3}{\rightarrow} \varnothing \tag{14}$$

The metabolic flux-based model consists in computing the vector of reaction rates $r = \{r_1, r_2, r_3\}$ in $(g_{H2} \cdot L^{-1} \cdot h^{-1})$. Let φ_{H_2} be the hydrogen specific uptake rate and m the specific maintenance rate (both in $g_{H2} \cdot g_X^{-1} \cdot h^{-1}$). In contrast to the work of Schill et al., we do not assume that $r_2 = mX$ (the maintenance rate is no longer constant) and we alternatively use m to set the upper bound for the maintenance reaction rate ($r_2 \in [0, mX]$). The second constraint is $r_1 + r_2 = \varphi_{H2} X$. Finally, the priority is given to the maintenance reaction.

$$\begin{aligned} &\varphi_{H2} > m \rightarrow r = \{\varphi_{H2} - m, m, 0\} \cdot X \\ &\varphi_{H2} < m \rightarrow r = \{0, \varphi_{H2}, m - \varphi_{H2}\} \cdot X \end{aligned} \tag{15}$$

As a consequence of the calculation procedure (15), growth is only possible if the maintenance requirement is met ($\varphi_{H2} > m$) and, in that case, the death rate is negligible. Otherwise, if the hydrogen supply is insufficient to satisfy the energy demand for maintenance ($\varphi_{H2} < m$), growth stops, maintenance proceeds at a rate defined by the hydrogen uptake rate φ_{H2} and the cell death rate is proportional to the energy lacking for maintenance.

The calculation of the hydrogen specific uptake rate,φ_{H_2}, uses basic principles of multiphase reactive systems: the reaction rate in the suspended (biological) phase is either set by the kinetics in that phase or limited by the external (physical) transport rate. Considering that the physical transport of substrate precedes uptake by the microorganisms, i.e. the two phenomena occur in series, the actual consumption rate can be expressed as the rate of the limiting step: biological consumption or physical transport rate (Morchain et al., 2017). A standard approach in multiphase reactor modeling is to define the actual consumption rate as the smallest of the two rates.

$$\varphi_{H_2} = \min\left\{\varphi_{bio}, \varphi_{phy}\right\} \tag{16}$$

The biological specific uptake capacity is set from the maximum hydrogen uptake capacity $q_{H_2}^{max}$, and the hydrogen concentration in the liquid phase $C_{L,H2}$, through a Monod type equation.

$$\varphi_{bio} = q_{H_2}^{max} \cdot \frac{C_{L,H_2}}{K_{H_2} + C_{L,H_2}} \tag{17}$$

The physical transport rate, φ_{phy} in Eq. (18) involves two phenomena: the gas–liquid mass transfer and the micromixing (responsible for the transport of dissolved species toward the cell-liquid interface). These phenomena are in parallel and the specific mass flux supplied to the cell is therefore set by the largest of the two rates, as expressed in Eq. (18):

$$\varphi_{phy} = max\left(\frac{k_L a_{H_2}(C_{L,H_2}^* - C_{L,H_2})}{\varepsilon_L X}, \frac{C_{L,H_2}}{X.\tau_m}\right) \tag{18}$$

In the limit of the local dissolved hydrogen going to zero, the physical supply is set by the specific gas–liquid mass transfer rate. Otherwise, the physical supply is set by the rate of micromixing in the liquid phase (τ_m). In this work, it is set to 0.01 s. This second term is needed in the case where the local interfacial area would approach zero, for any reason, at some location, during the calculation. Altogether, Eqs. (15)–(18) provide a physically consistent and numerically stable way to include a non-constant maintenance rate in the modelling. It thus improves the model of (Schill et al., 1999) (constant maintenance rate) and avoids the introduction of new arbitrary parameters in additional damping functions, as proposed by Inkeri et al. (2018) (Eqs. (46) and (47) in the cited paper).

In the end, the reaction terms per unit volume of liquid, in Eq. (2), are computed as

$$\begin{aligned} R_{H_2} &= r_1 + r_2 = \varphi_{H2} X \\ R_{CO_2} &= \mathrm{Y}_{CO_2/H_2} r_1 + \mathrm{Y}^{\mathrm{m}}_{CO_2/H_2} r_2 \\ R_{CH_4} &= \mathrm{Y}_{CH_4/H_2} r_1 + \mathrm{Y}^{\mathrm{m}}_{CH_4/H_2} r_2 \\ R_X &= \mathrm{Y}_{X/H_2}(r_1 - r_3) \end{aligned} \tag{19}$$

$Y_{i/j}$ is the yield coefficient in gram of i per gram of j consumed. The values of all biological parameters reported in Table 1 are taken from the work of (Schill et al., 1999). M_i is molar mass of species i.

The consequences and advantages of this formulation are further detailed in the last part of the discussion section dedicated to the fully coupled simulation of an industrial scale methanation bubble column.

To sum up the proposed 1D model relies on the following choices and assumptions:

Table 1
Biological parameters.

Parameters	Definition	Value	Units
Y_{X/H_2}	$v_{X,1}\frac{M_X}{M_{H2}}$	0.22	g_X/g_{H_2}
Y_{CO_2/H_2}	$v_{CO_2,1}\frac{M_{CO2}}{M_{H2}}$	5.70	g_{CO_2}/g_{H_2}
Y_{CH_4/H_2}	$v_{CH_4,1}\frac{M_{CH_4}}{M_{H2}}$	1.92	g_{CH_4}/g_{H_2}
$Y^m_{CO_2/H_2}$	$v_{CO_2,2}\frac{M_{CO2}}{M_{H_2}}$	5.5	g_{CO_2}/g_{H_2}
$Y^m_{CH_4/H_2}$	$v_{CH_4,2}\frac{M_{CH_4}}{M_{H_2}}$	2	g_{CH_4}/g_{H_2}
$q^{max}_{H_2}$	Maximum H_2 specific uptake rate	1.77	$g_{H_2}/g_X/h$
m	Maintenance rate	0.14	$g_{H_2}/g_X/h$
K_{H_2}	Affinity constant	0.01	mg_{H_2}/L

i. One dimensional two-phase flow in homogeneous bubbly flow regime
ii. Constant bubble number without breakup and coalescence
iii. Interfacial bubble contamination considered in the drag law formulation
iv. Hydrodynamics & multispecies mass transfer & bioreaction multiple-way coupling
v. Potential limitation of biological uptake rates by gas–liquid mass transfer

2.2. Numerical resolution

Partial differential equations (1) and (2) are solved using the finite difference method on a regular grid with N nodes, so that the solution is approximated by the vector of discrete values $\phi_{G,i,n}$ and $\phi_{L,i,n}$ where $n \in [1, N]$. A second order discretization in space is used for transport equations and boundary conditions, i.e. the convection term is calculated using second order upstream differences and the dispersion term is calculated using second order central difference, similar to the work of Giovannettone and Gulliver (2008). The spatial discretization of Eqs. (1) and (2) leads to a system ordinary differential equation which is solved using the MATLAB 2017b stiff solver ode15s.

Boundary and initial condition:

Dirichlet boundary condition for the gas mass flow rate, ϕ_G is imposed at the inlet, whereas zero-slope boundary condition is imposed at the outlet. As the simulated bubble columns operates in semi continuous mode, a zero-flux boundary condition is imposed for ϕ_L at the inlet and the outlet. The initial condition for the gas phase is computed based on the ideal gas law using spatially dependent pressures. Whereas, for the liquid phase, ϕ_L is initialized to 0, indicating the absence of dissolved gas components initially for instance.

Numerical procedure:

The set of equation is actually algebro-differential since the calculation of the right-hand terms in Eqs. (1) and (2) require that the retention and concentrations of all species in each phases are retrieved from the known $\phi_{G,i,n}$ and $\phi_{L,i,n}$. These $(2i+1).N$ unknowns are solution of a non-linear system (20) which connects hydrodynamics and mass transfer to the local pressure calculated using Eq. (10).

$$\begin{cases} \phi_{G,i,n} = \varepsilon_{G,n} \cdot C_{G,i,n} \\ \phi_{L,i,n} = (1-\varepsilon_{G,n}) \cdot C_{L,i,n} \\ \frac{P_n}{R.T} = \sum_i \frac{C_{G,i,n}}{M_i} \\ P_n = P_0 + (1-\widetilde{\varepsilon_G})\rho_L g(H - z_n) \end{cases} \quad n \in [1, N] \qquad (20)$$

Thus, the non-linear system (20) resolution as explained in Appendix B is embedded within the time stepping procedure presented in Fig. 1 to provide the local retention and concentrations of each species in both phases at every grid point.

The resolution starts with the preprocessing of the problem: specifying the reactor geometry, the operating conditions, the species involved, and defining boundary and initial conditions. The non-linear system of Eq. (20) is solved iteratively until the relative difference of ε_G, $C_{G,i}$, and $C_{L,i}$ between consecutive iterations (*Crit)* is below the given tolerance ($Tol = 10^{-6}$). The bubble diameter and slip velocity are updated (Eqs. (11) and (6) respectively) and used to compute the right hand side of Eqs. (1) and (2). In the end, time integration is performed by MATLAB solver.

2.3. Experimental setup

Among the model's input, d_b is not modellable. A series of experiment was therefore conducted in a lab-scale bubble column with tap water to obtain the Sauter mean diameter d_{32} of the equivalent sphere diameter which serves as an inlet parameter, $d_b(0,t)$. Some results on d_{32} are shown in Appendix C. Alongside with the bubble size measurement, the corresponding gas holdup was also measured dynamically in order to validate the hydrodynamics aspect of the model.

The experimental setup is shown in Fig. 2. It is composed of a 22 L glass cylinder column (3) with a diameter of 0.15 m. The initial liquid height (H_0) is kept at 1 m. Bubbles are injected through a ceramic porous plate with a porosity of 100–160 μm at the bottom of the column occupying the entire section of the column in order to favor homogeneous flow regime in the column. The gas feed line is equipped with a flowmeter (4) with measuring range of 0–2 NL/min. A camera, Cam1 (1) was installed at column's mid-height to identify the bubble geometrical characteristics. A second camera, Cam2 (2) was placed at the free-surface to detect the rising water level for the gas holdup calculation. Cam1 provided an acquisition window of 26 × 26 mm^2 with a spatial resolution of 40-pixel mm^{-1}. Cam2 has a narrower but longer view of 9.7 × 38.7 mm^2 with a spatial resolution of 27-pixel mm^{-1}. Cam2 and Cam1 operated simultaneously at the same frequency of 20 Hz with a total of 1000 images shot for each measurement. A homogeneous light-emitting diode (LED)-panel was installed behind the column to increase the luminosity.

2.3.1. Bubble size and dynamic gas holdup measurement

Tap water was used as the liquid phase and H_2 was used as the gas phase. H_2 was chosen to study the column hydrodynamics because of its very low solubility which guaranties that the mass transfer effect on hydrodynamics is minimal.

Pictures of the rising water level were taken near the column wall to reduce the negative effect of the continuous disturbance of the unalterable changes between the refractive indices due to the curved surface of the glass column. The superficial gas velocity, $j_G = Q_G/S$ defined as the gas flow rate (Q_G) per column cross-section (S) was varied between [0–0.16] cm/s. The recorded images from both cameras were then treated using Matlab®.

The image processing algorithm used to extract the bubble geometrical characteristics followed the methodology of Laupsien et al. (2019). Bubble images and its associated experimental results are provided in Appendix C. The dynamic gas holdup was measured using bed expansion method but a camera was applied rather than a ruler to better capture the liquid swelling. The algorithm to determine the global gas holdup is depicted in Fig. 3. 64-

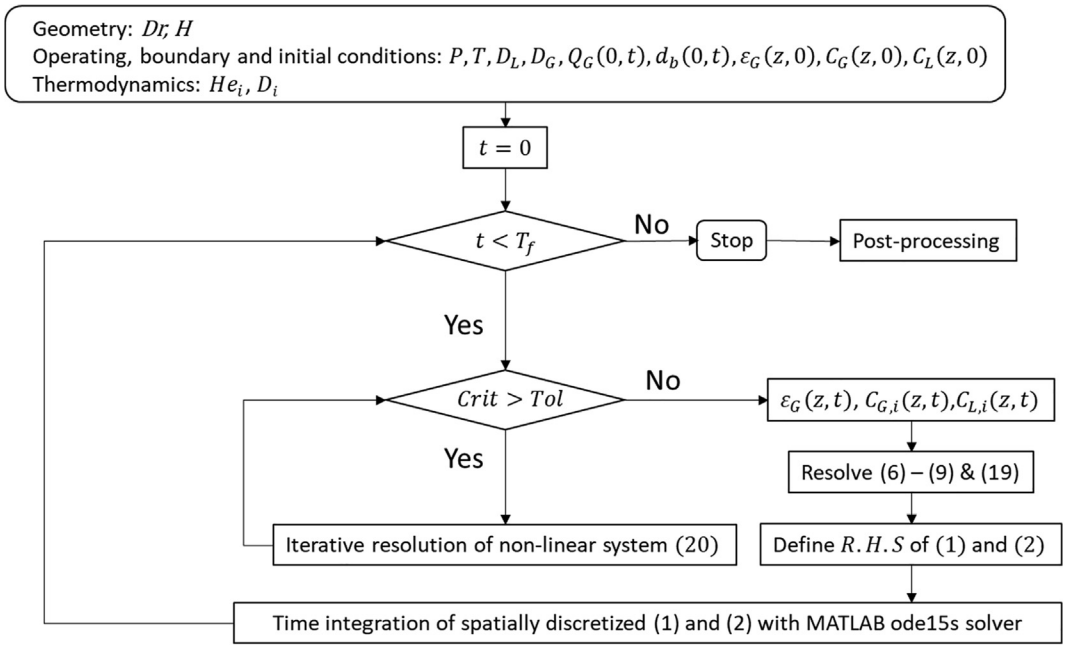

Fig. 1. Algorithm flowchart for the resolution of the model.

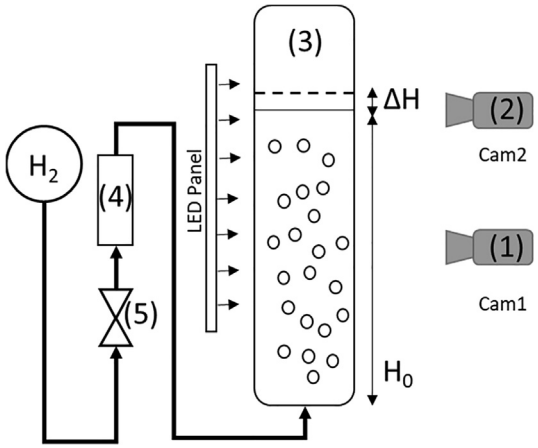

Fig. 2. Experimental setup for gas holdup and bubble size measurements.

pixel column nearest to the wall were extracted to calculate the mean pixel value for each level. The profile obtained was then normalized so that all images was compared to the same threshold value. The lower meniscus level was detected by applying a threshold of 70% of the maximum pixel value. The process was repeated for all images to obtain the water level time profile. The difficulty of this method lies in identifying the water level when the first bubble reaches the free surface. Indeed, the water level profile becomes chaotic when the bubbles reach the free liquid surface and, from that point onward, exploiting the real water level height is tedious, due to foaming. We chose to track the water level change, ΔH, until the first bubble reaches the free surface. In order to prove that the difference between these two methods is insignificant, the cumulative statistical average of ΔH at steady state was compared to the ΔH upon arrival of the first bubble and the difference was quantified. A relative difference of less than 5% was found, even for gas holdup below 1%. The details on the comparison is elaborated in Appendix D. For this reason, the ΔH was considered until the image on the arrival of bubbles at the free surface. Moreover, the precision of the method can be improved by increasing the camera speed to better capture the last instant before the perturbation of the water level by the bubbles. Besides, the flow rate studied is low (j_G below 0.16 cm/s with reactor diameter of 0.15 m), the column is operated in the homogeneous bubbly flow regime, with weak liquid circulation, according to (Shah et al., 1982) regime map. (Sasaki et al., 2017) employed a very similar method for the study of gas holdup. However, the gas flow rate in Sasaki et al. work is rather high and the flow regime is heterogeneous with large liquid recirculation. The establishment of the flow regime, leading to constant gas holdup, is much longer in their case.

The experimental gas holdup was then calculated using Eq. (21). In this equation, H_0 corresponds to the initial liquid height and $\Delta H(t)$ holds for the instantaneous liquid elevation $(H(t) - H_0)$, as shown in Fig. 2. It was found experimentally that the slope of the rising water level profile corresponds to the superficial gas velocity. The abovementioned methods are non-intrusive way of direct and concise measurement of both bubble size, superficial gas velocity, and global gas holdup simultaneously.

$$\langle \varepsilon_{G,exp}(t) \rangle = \frac{\Delta H(t)}{\Delta H(t) + H_0} \tag{21}$$

$$j_G = \frac{Q_G}{S} = \frac{\Delta H}{\Delta t} \tag{22}$$

2.3.2. Comparison with model

The H_0, Q_G and experimentally measured bubble size were used in the model as inlet parameters. The gas holdup at the inlet is computed as the ratio between the superficial gas velocity and the u_{slip} from Eq. (6). Different drag laws were tested and the model prediction compared with experimental data. As already mentioned, a measurement of dynamic gas holdup allows to evaluate both the superficial gas velocity (from the slope in Fig. 3) and the final gas holdup. The former serves as a check of gas flow rate applied experimentally and the latter can be compared to that pre-

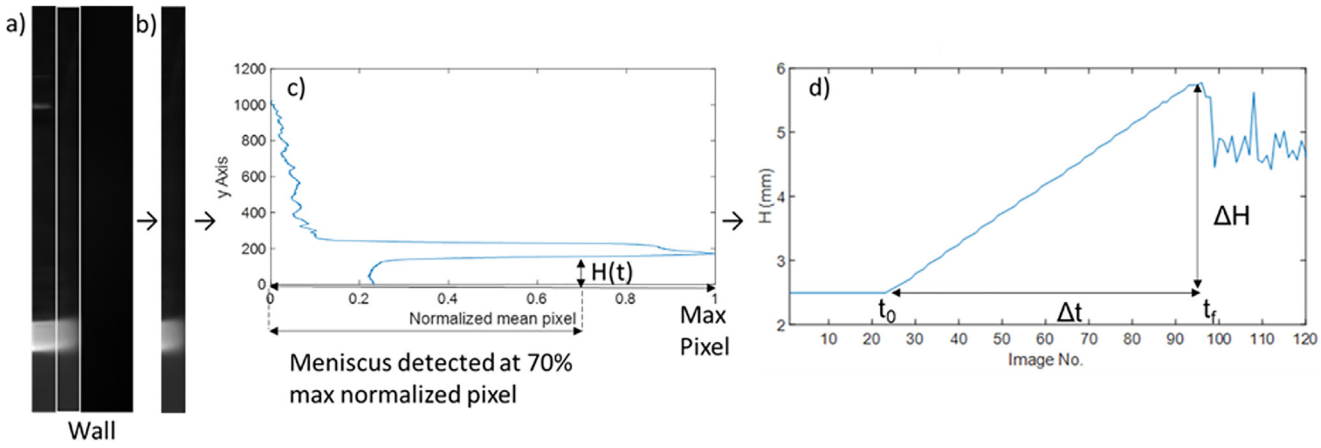

Fig. 3. Global gas holdup measurement from image processing of raw data. (a) Raw image (b) Cropped image (c) Normalized pixel profile (d) Instantaneous liquid level.

dicted by the model. The $\langle \varepsilon_{G,exp} \rangle$ was compared with the global gas holdup given by the model, $\langle \varepsilon_G(z, t_\infty) \rangle$ which is the total spatial average of gas retention at steady-state. The model is also expected to reproduce the dynamic evolution of $\langle \varepsilon_{G,exp} \rangle$. This approach is similar to (Besagni et al., 2019) work whereby, the bubble size experimental measurements served as inlet conditions for the numerical CFD model and the model's gas holdup was compared to that of experiment.

To mimic the experimental conditions, whereby the global gas holdup is followed dynamically, the following model parameters, initial and boundary conditions are set for the model. The initial gas holdup in the column from node 2 to N (except the inlet, reserved for the boundary condition) was fixed to a relatively small value of 10^{-6} rather than 0; on one hand to represent the absence of gaseous phase initially in the column and on other hand to facilitate the numerical convergence and to reduce initial stiffness. The outlet pressure, $P(H, t)$ was kept constant as the atmospheric pressure of 1 atm.

3. Results

3.1. Hydrodynamics validation through transient gas holdup measurement

A key feature of the model is its ability to describe spatio-temporal changes in the gas retention and bubble diameter through which the evolution of interfacial area can be predicted. This section is devoted to the validation of the transport terms of our equation through a comparison of the model results with the experimental measurement of gas holdup in the transient period following gas injection in a column initially filled with liquid.

The results presented in Fig. 4 indicate that the gas retention increases linearly in time. The slope of the experimental curve corresponds to the superficial gas velocity: imposed gas flow rate divided by the column cross section. The numerical slope also closely matched that of experiment.

The slope of the simulated retention curve given is fully determined by the superficial gas velocity. This slope is independent of the bubble slip velocity. The bubble slip velocity actually defines the gas retention at steady state. The drag law dependent bubble slip velocity sets the gas residence time.

This case was investigated with three different drag laws. Mei model did not fit well as it is more applicable to spherical bubbles. Spherical bubbles rise in a rectilinear manner, hence it has higher bubble velocity and a lower residence time, which explain a lower

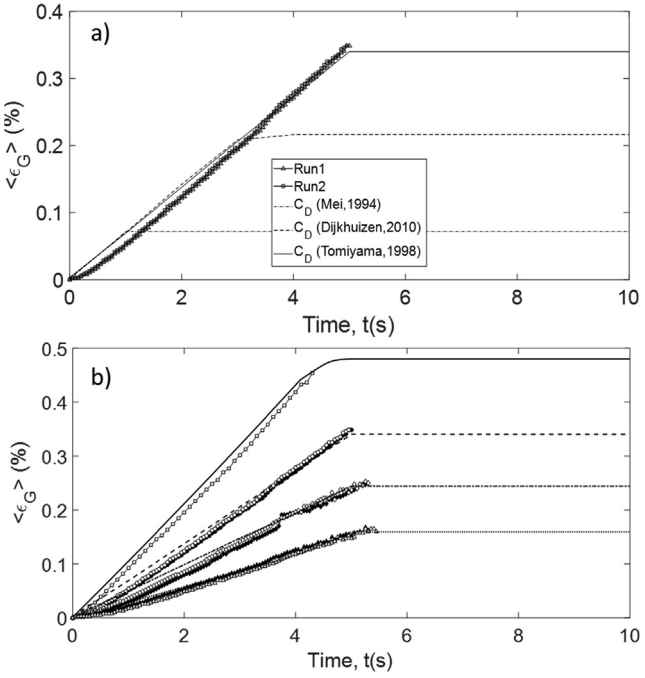

Fig. 4. (a) Experimental and model predicted dynamic gas loading with different drag model. The repeatability is very good. (b) Examples of experimental and model predicted dynamic gas loading using Tomiyama drag model (Tomiyama et al., 1998).

final retention value (Tomiyama et al., 1998). The correlation proposed by (Dijkhuizen et al., 2010) are more suitable for ultrapure medium, which clearly is not the case of tap water. Therefore, the drag force is less important than that calculated from Tomiyama, hence the bubble velocity is much higher, thus a lower final gas holdup. As expected, Tomiyama correlation has the best fit for our cases as the quality of water used is similar to ours. Tomiyama drag model is applicable for a wide range of conditions, such as different fluid properties and bubbles size, which is the reason why it was used for different simulation cases to be presented in Section 4.

The model yields a good agreement with the experimental measured gas holdup as the relative error between the two is less than 10% (for very low gas holdup, i.e. less than 0.6%), as shown in Table 2. The good agreement also confirms that collective effects on bubble velocity could be neglected at such low gas holdup.

Table 2
Overall experimental and model results.

	j_G (cm/s)	0.039	0.058	0.078	0.105	0.116	0.136	0.155
	d_{32} (mm)	1.76	2.00	2.00	2.20	2.48	2.60	3.15
Experiment	$\langle \varepsilon_{G,exp} \rangle$ (%)	0.16	0.25	0.35	0.45	0.48	0.54	0.59
Model	$\langle \varepsilon_G \rangle$ (%)	0.16	0.24	0.34	0.47	0.49	0.55	0.57

This work demonstrated the present method is suitable to measure extremely low gas holdup. To the authors' best knowledge, the measurement of such low global gas holdup (<0.6%, j_G between [0–0.16] cm/s) is rare in the literature. The closest works were reported by Kováts et al., Chen & Brooks and Besagni et al. whereby the minimum j_G tested were 0.007 cm/s, 0.15 cm/s, and 0.4 cm/s respectively (Chen and Brooks, 2021; Kováts et al., 2020; Besagni and Inzoli, 2016). To conclude this experimental section, the proposed dynamic gas holdup measurement yields a very neat slope during gas loading which corresponds to the superficial gas velocity imposed at the inlet and it quantifies the global gas holdup at steady-state via optical means without perturbating the hydrodynamic flow.

3.2. Local mass transfer validation through experimental axial measurement

Our model is further used for the simulation of CO_2 mass transfer in a large-scale bubble column (H = 4.4 m) fed with a liquid flow rate of 3 m^3/h, operated in co-current mode. The local gas holdup and local CO_2 profile measured by (Deckwer et al., 1978) is used to validate our model. Similar work has been reported by Hissanaga et al. (2020) and Rzehak and Krepper (2016). In fact, (Rzehak and Krepper, 2016) pointed out that local measurement of both concentration and bubble size distribution is scarce in the literature, which makes this work very meaningful for the validation of our model. In all these works, the reaction of CO_2 with water was neglected, the same assumption is made here. The temperature is set as 14 °C. The CO_2 liquid diffusivity D_{CO_2} and Henry constant He_{CO_2} at this temperature is calculated from the expression given by (Versteeg and Van Swaaij, 1988) which yield $1.4663 \cdot 10^{-9}$ m^2/s and 0.0192 mg/L/Pa respectively.

Fig. 5 and Table 3 show the results of our model compared to that of Hissanaga et al. 1D model and Deckwer et al. experimental data. For our model, the inlet bubble diameter was taken the same as experimental value measured by Deckwer et al., which equals to 2.86 mm for the two flow rates. Following the work of Hissanaga et al., plug flow condition is supposed for both phases. Therefore, D_L and D_G are equal to 0 in this particular case. In Fig. 5a, the local gas holdup varies noticeably with axial location due to large column size and high interphase mass transfer rates. For experiment 17, the local gas holdup decreases at the bottom of the column due to an intense gas to liquid mass transfer flux. Then, the local gas holdup reaches a minimum and increases again as one approaches the surface. A similar trend is also observed in the X_{CO_2} profile. This reveals that the gas–liquid mass transfer first operates from gas to liquid at the bottom of the column, then in the opposite way in the upper part. Obviously, the gas holdup, the interfacial area and k_La are not constant and making such hypothesis negatively impacts the prediction of reactor performances in an industrial bubble column. It is interesting to see that both models fail to represent the retention profile of experiment 19. This is because, both models are valid in the homogeneous bubbly flow regime whereas experiment 19 was conducted near the transition regime where some coalescence could occur and increase the mean Sauter bubble diameter and bubble velocity, thus a lower gas holdup. Nevertheless, both models capture reasonably well the local CO_2 profile. Our model slightly overestimates the absorption CO_2 flux at the inlet because our $k_{L,i}$ value is calculated from the Higbie correlation which gives a slightly higher value than the correlation used by Hissanaga et al. Lastly, the outlet flow rate ($j_{G,out}$) and the outlet CO_2 mass fraction are correctly quantified by our model, as shown in Table 3, which shows that our model is capable to reproduce large-scale hydrodynamics and spatially dependent mass transfer rate. In our model, oxygen (O_2) is treated as an active species together with CO_2, which is not the case in Hissanaga et al. model. However, the O_2 mass transfer has not any huge impact on the results. This confirms their hypothesis that O_2 can be treated as an inert species for the mass transfer in this case.

To conclude Section 3, our 1D model is validated temporally and spatially through own-experimental data and literature data.

4. Discussion on multispecies mass transfer/bioreaction

In Section 4, the link between reactor's design, operating conditions and the intensity of multispecies mass transfer is investigated. First, the effect of column's height is studied. Secondly, H_2 mass transfer is studied at two different heights. Next, the effect of multi-species mass transfer is explored with its sensitivity to column's height. In the related Sections 4.1 and 4.2, all the simulations utilized d_b = 2.5 mm at the inlet, in order to facilitate a direct comparison between the results. Finally, a full-scale biological methanation reactor is simulated.

4.1. Case 0: Effect of hydrostatic pressure on interfacial area

Two bubble columns of H = 2 m and H = 10 m fed with the same molar flow rate and operated at $P = 1atm$, are simulated using 20 nodes and 100 nodes grid respectively. In this section, the mass transfer coefficient k_L is set to zero. Steady-state results are presented in term of normalized vertical profiles in Fig. 6c and d and global mass balances in Table 4. In Table 4, the local and instantaneous molar flux of species i is calculated as:

$$F_i(z,t) = \frac{y_i(z,t) \cdot P(z,t) \cdot Q_G(z,t)}{R \cdot T} \tag{23}$$

Fig. 6a and b also show that the time to reach a steady state is roughly equal to the bubble residence time (H/u_{slip}). This is consistent with the fact that the pressure-induced changes in bubble diameter have little effect on the rising velocity in the present case. For H = 2 m and H = 10 m, bubble diameter ranges in [2.5–2.7] mm and in [2.5–3.2] mm respectively (graph not shown) leading to u_{slip} approximately constant when using Tomiyama drag correlation. The effects of bubble expansion due to decreasing pressure however explain the slightly non-linear $\langle \varepsilon_G \rangle = f(t)$ and $\langle a \rangle = f(t)$ curves in the 10 m high column. At steady-state, the changes in gas retention and interfacial area with height are much more pronounced in the tall column than in the small column and the spatial profile is clearly non-linear. The hydrostatic pressure decreases with decreasing height, which causes an expansion in gas volume, hence, the gas holdup increases. This implies, in the same time, an increase in bubbles size due to Eq. (11). Similar observations are reported in the experimental study of Giovannettone et al. (2009).

We compare the interfacial area, $\langle a(z, t_\infty) \rangle$, and its approximation based on averaged quantities $6\langle \varepsilon_G \rangle / \langle d_b \rangle$. Results are reported

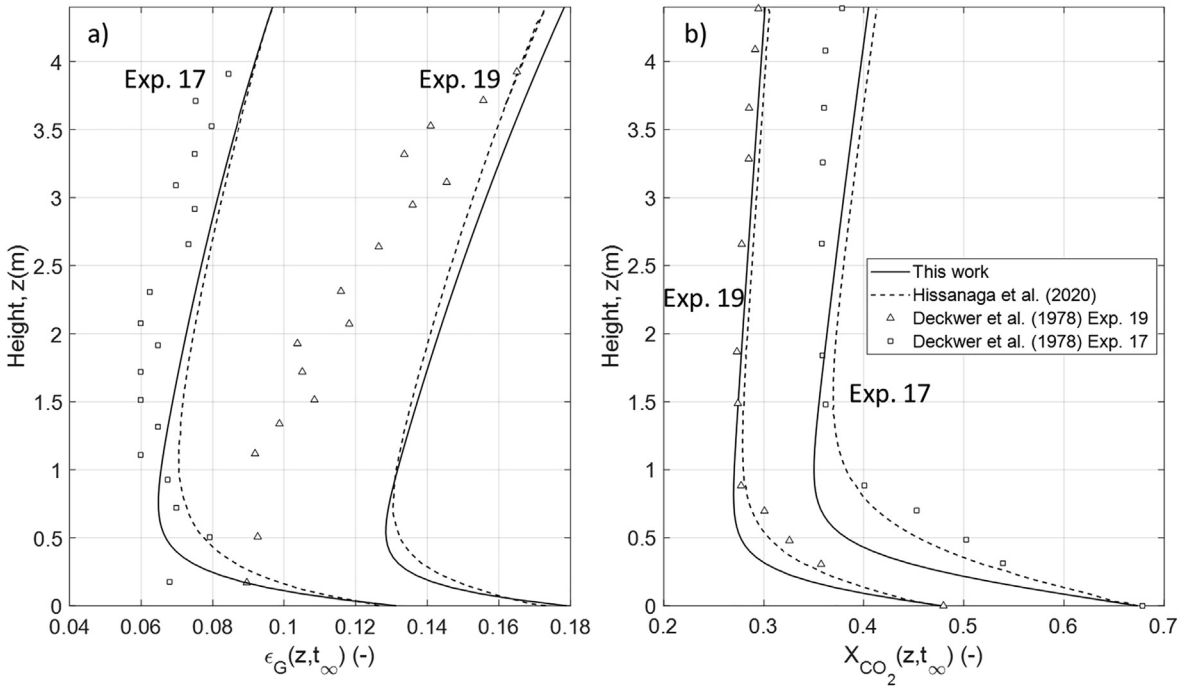

Fig. 5. (a) Local gas holdup and (b) local gaseous CO_2 mass fraction (X_{CO_2}) at steady-state. □: Experiment 17 and Δ: Experiment 19.

Table 3
Model output compared to Deckwer et al. experimental work and Hissanaga et al. 1D model.

		Deckwer et al. (1978)		Hissanaga et al. (2020)		This work	
Exp.	$j_{G,in}$ (cm/s)	$j_{G,out}$ (cm/s)	$X_{G,out}$ (–)	$j_{G,out}$ (cm/s)	$X_{G,out}$ (–)	$j_{G,out}$ (cm/s)	$X_{G,out}$ (–)
17	3.42	2.49	0.377	2.62	0.413	2.58	0.405
19	4.63	4.59	0.293	4.64	0.306	4.58	0.301

in Table 4. Note that if $\langle \varepsilon_G \rangle$is accessible in experiments, the information about $\langle d_b \rangle$ is much difficult to obtain in an industrial scale column. In a 10 m high column, the relative error between $\langle a(z,t_\infty) \rangle$ and $6\langle \varepsilon_G \rangle / \langle d_b \rangle$is only 1% because the change in diameter due to hydrostatic pressure is negligible. However, non-linearities are more pronounced in tall columns and the evaluation of mass transfer related quantities from global measurements becomes a risky exercise in real systems.

4.2. Two-way coupled hydrodynamics and mass transfer problem

4.2.1. Case 1: Effect of hydrostatic pressure on H_2 mass transfer

Case 1 evaluates the impact of scale-up on the H_2 mass transfer (a weakly soluble gas) in two columns fed with the same constant gas molar flow rate as in Case 0 (column diameter D_r =0.15 m). The mass transfer term is now activated and the initial hydrodynamic conditions are taken from the converged hydrodynamics of case 0. This represents the experimental situation when the column is initially fed with an inert gas at t < 0 and the switch to a transferable gas is performed at t > 0 without perturbating the hydrodynamics. The model parameters D_L and D_G , set through Eqs. (4) and (5) are provided in Table 4. The temperature is set as 25 °C. The H_2 liquid diffusivity D_{H_2} and Henry constant He_{H_2} at this temperature are taken as $5.1488 \cdot 10^{-9}$ m^2/s and $1.56 \cdot 10^{-5}$ mg/L/Pa respectively (Sander, 2015).

The gas holdup, bubble size and interfacial area profiles are not shown as they remain the same as that of case 0. This is expected since the solubility of H_2 is extremely low and the hydrodynamics is not impacted by the H_2 mass transfer (one-way coupling case). From this information and using concentration profiles, the local mass transfer fluxes are computed and presented in Fig. 7c.

Intuitively, the global mass transfer rate is null when a bubble column operated in semi-continuous mode reaches a steady-state. The liquid phase gets saturated by the dissolved gas components leading to $C_L = C^*$ throughout the column. Fig. 7c depicts that the global mass transfer is indeed null whilst the mass transfer flux evolves spatially even at steady-state. From Fig. 7a the C_{G,H_2} is higher at the bottom of the 10 m high column due to the elevated hydrostatic pressure whilst the value is identical at the free surface due to the same atmospheric pressure. The linear decrease of C_{G,H_2} due to decreasing local pressure shows that the gaseous phase is spatially heterogeneous. Fig. 7b presents the concentration in the liquid phase as well as the equilibrium concentration C^*. In the 2 m high column, the liquid mixing time at 63% homogeneity is estimated from the analytical solution of Inoue (1973); $\tau_m \approx 140s$ is comparable to the mass transfer characteristic time, $\tau_{tr} = \frac{1}{\langle k_L a \rangle} \approx 150s$, and despite the saturation concentration change, the liquid concentration remains homogeneous throughout the column. For H = 10 m, the liquid concentration profile is non-uniform because of insufficient mixing in the liquid phase ($\tau_m = 3400s \gg \tau_{tr} = 225s$). The mass transfer coefficient is averaged from the value presented in Fig. 8b. Fig. 7b shows that the saturation concentration C^* follows the trend of gaseous concentration. At steady-state, the local C_L are everywhere different from C^*, but the overall mass transfer is zero. Note that the (net transfer flux = 10^{-8}/F_{in} = 10^{-4}). Fig. 7c displays that absorption

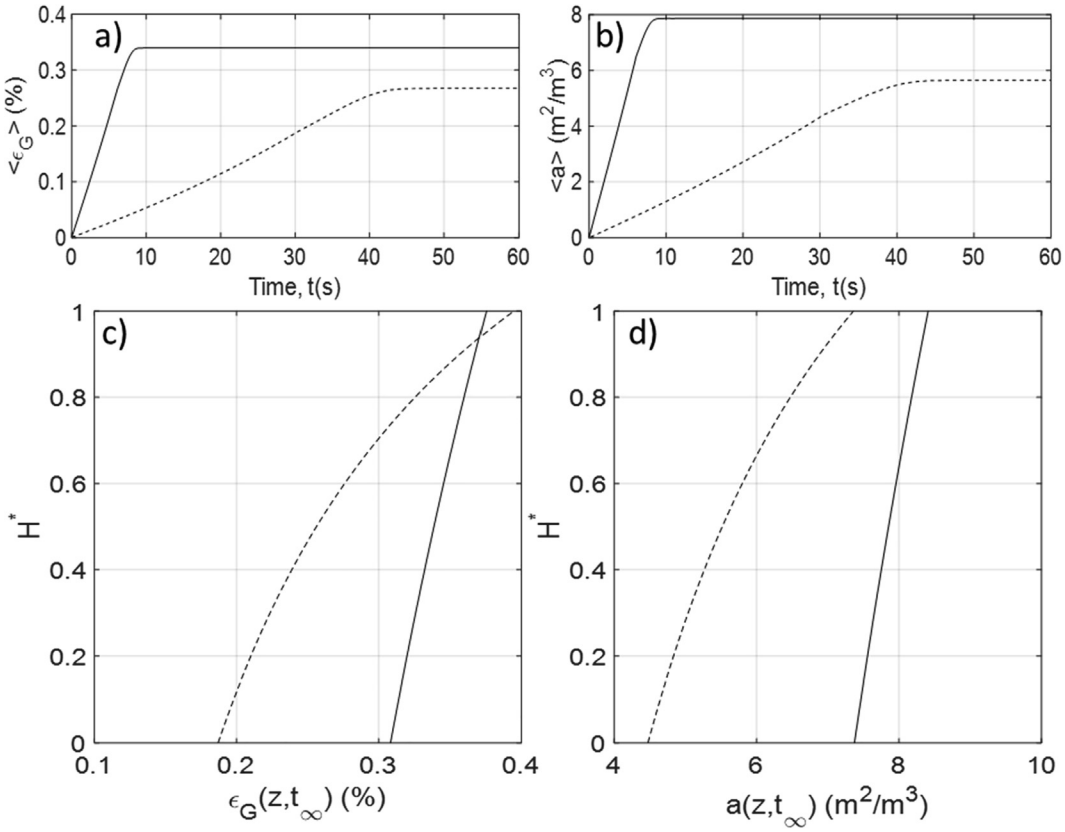

Fig. 6. (a–b) Dynamic simulation of mean gas holdup and interfacial area until steady-state for two column heights. (c–d) Normalized vertical profiles of gas holdup and interfacial area at steady-state. – H = 2 m, – – H = 10 m.

Table 4
Model's input and steady-state hydrodynamic results for two different column's height.

Model Inputs	H (m)	2	10
	$F_{H_2}(0,t)$ (10^{-4} mol/s)	6.8286	
	$j_G(0,t)$ (cm/s)	0.081	0.049
	D_L (m^2/s)	$5.6{\cdot}10^{-3}$	$4.8{\cdot}10^{-3}$
	D_G (m^2/s)	10^{-3}	$5.7\ 10^{-4}$
Model Outputs	$P(0,t_\infty)$ (Pa)	120,880	199,240
	$F_{H_2}(H,t_\infty)$ (10^{-4} mol/s)	6.8293	6.8293
	$F_{H_2}(0,t) - F_{H_2}(H,t_\infty)$ (10^{-4} mol/s)	−0.0007	−0.0007
	$\langle\varepsilon_G(z,t_\infty)\rangle$ (%)	0.34	0.25
	$\langle a(z,t_\infty)\rangle$ (m^2/m^3)	7.866	5.65
	$6\ \langle\varepsilon_G(z,t_\infty)\rangle/\langle d_b(z,t_\infty)\rangle$ (m^2/m^3)	7.872	5.71

occurs in the lower half of the column, desorption takes place in the upper half. This observation is also reported in Giovannettone's experimental work where positive gas transfer rate was found in the lower part of the column and negative gas transfer rate in the upper part (Giovannettone and Gulliver, 2008). This is an interesting illustration to the fact that macroscopic observations (the net transfer rate is equal to zero) cannot be used to infer local phenomena (the local mass transfer rate is nowhere equal to zero).

A benefit of the spatially discretized model is the opportunity to compute the integral mass transfer over the total column height or over sub intervals. The global mass transfer rate, T_i (g/s or mol/s) is computed through Eq. (24) as the integral of local mass transfer rate (the spatial reference to z for each variable is omitted for clarity).

$$T_i = S \cdot \int_0^z k_L a \cdot \left(C_i^* - C_{i,L}\right) \cdot dz \tag{24}$$

Due to higher hydrostatic pressure in large column, the mass transfer rate is 2 times higher than that at small column, as indicated in Table 5. For the same inlet molar flow rate, the mass transfer is enhanced due to column height. Thus, it can be claimed that it is advantageous to have higher column for low soluble gas as used in biological methanation.

4.2.2. Case 2: Effect of CO_2 ($y_{CO2,in}$ = 20%) on H_2 mass transfer

For case 2, the impact of scale-up on the multispecies mass transfer, especially the substrates involved in biological methanation process: H_2 & CO_2 is studied. The model parameters, initial and boundary conditions are the same as case 1. The proportion of H_2:CO_2 is set to 4:1 as the condition usually found in the study of biological methanation, which is in line with the reaction stoichiometry (Rusmanis et al., 2019). A constant pH = 7 assumption is made, therefore dissolved CO_2 remain at their CO_2 form. The temperature is again set as 25 °C. The D_{H_2} and He_{H_2} are kept the same as previous case. The CO_2 liquid diffusivity D_{CO_2} and Henry constant He_{CO_2} at this temperature are taken as $2.2884{\cdot}10^{-9}$ m^2/s and 0.0145 mg/L/Pa respectively (Sander, 2015).

The hydrostatic pressure profile remains unchanged due to low gas holdup and it is not presented here. The presence of CO_2 alters the local gas holdup, even at low concentration (here, $y_{CO2,in}$ = 20%). A more significative effect is observed at the large scale. A slight decrease in ε_G is detected near the inlet which is explained by the preferential and significant mass transfer of CO_2 at the bottom of the column. The variation in ε_G implies changes in the interfacial area and thus in the k_La profile as shown in Fig. 8.

With the same molar flow rate for both reactors, the model revealed very different local gaseous and liquid concentration profiles. Compared to a linear decrease of gaseous concentration pro-

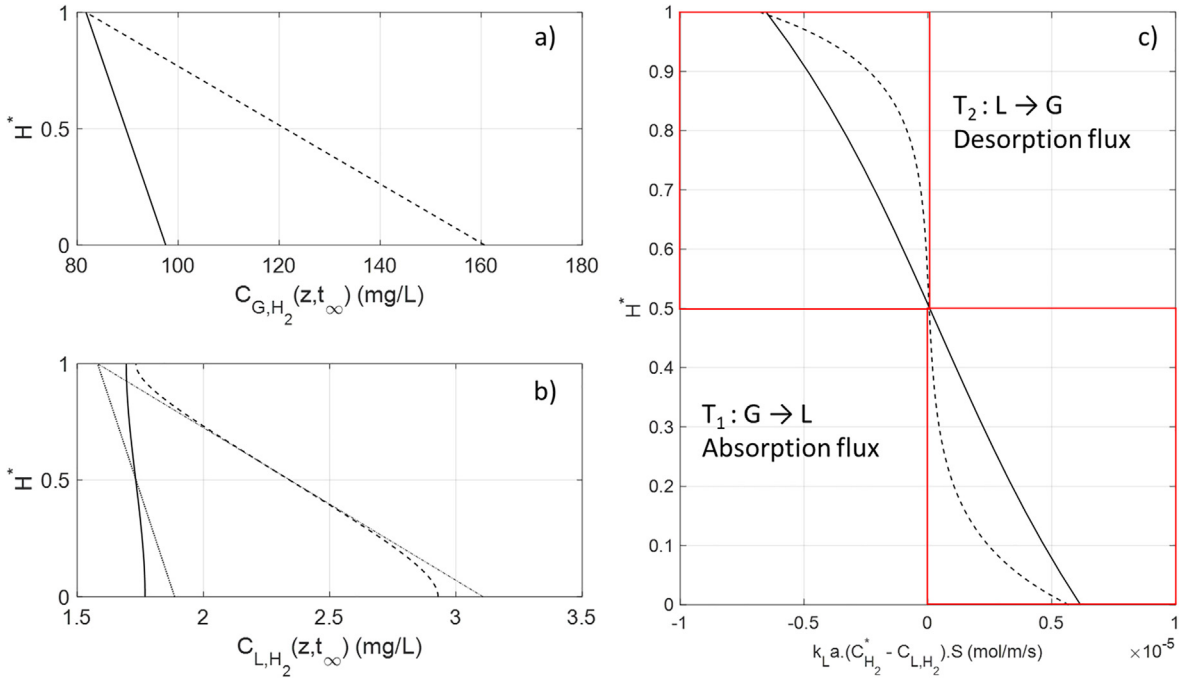

Fig. 7. (a–b) Normalized vertical profiles of concentrations and (c) mass transfer rate at steady-state. Graph legend as follows: – H = 2 m, – – H = 10 m, ■ ■ ■ and – ■ – are C^* profile for H = 2 m and H = 10 m respectively.

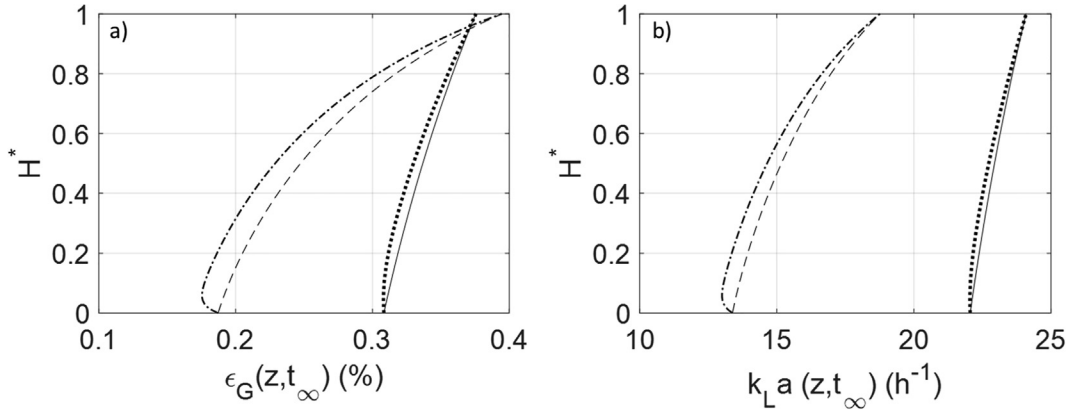

Fig. 8. Normalized vertical profiles ε_G and k_La at steady-state for monospecies, H_2 vs multispecies H_2 & CO_2 for two reactor heights. – and – – are for monospecies cases (case 1: H_2 only) at H = 2 m and H = 10 m respectively. ■ ■ ■ and – ■ – are for multispecies cases (case 2: H_2 & CO_2) at H = 2 m and H = 10 m respectively.

Table 5
Hydrogen local mass transfer fluxes in the lower and upper part of the column.

H (m)	2	10
F_{in} (10^{-4} mol/s)	6.8286	6.8287
T_1 (10^{-4}mol/s)	0.0290	0.066
T_2 (10^{-4}mol/s)	−0.0292	−0.064
$T = T_1 + T_2$ (10^{-4}mol/s)	−0.0002	0.002

file in the absence of CO_2 in Fig. 7a, in this case, the volume contraction due to the intense CO_2 mass transfer (refer to Fig. 9c) causes an enrichment of the gaseous phase in H_2 (see Fig. 9a) at the bottom of the column. An increase in H_2 gas concentration leads to a higher H_2 saturation concentration $C^*_{H_2}$ and consequently increases the hydrogen mass transfer rate. The transfer of the two species is coupled. The phenomenon is amplified in the high column because of stronger pressure effects. Again, the liquid concentration is rather homogeneous at H = 2 m but heterogeneous at H = 10 m, as shown in Fig. 9b and d. The mass-transfer profile appear to be complex mainly due to the existence of two species with high contrast in terms of solubility (Solubility CO_2 ×100 times higher than that of H_2). Fig. 9e and f reveal that the multi-species mass-transfer effect can be observed even at H = 2 m. Fast dissolution of CO_2 implies high absorption rate at the inlet, but quickly diminished afterward as the liquid concentration approaches the saturation concentration. The strong two-way coupling is clearly exhibited in this example. Non-linear evolution of C^* prompts error in calculating local flux if linear approximation of C^* is used. The estimation of mass transfer flux with the arithmetic mean of C^* will therefore be wrong as C^* profile is no longer linear.

Fig. 9g depicts that the inlet H_2: CO_2 gaseous molar flux ratio of 4:1 is not conserved throughout the reactor as this is caused by the huge contrast in term of solubility. CO_2 is much more soluble than H_2, hence, a huge drop of CO_2 causes an increase of the ratio. As displayed in Table 6, the CO_2 absorption flux ($T_{CO2,1}$) is 6 times higher than that of H_2 ($T_{H2,1}$) at the small scale and also nearly 6

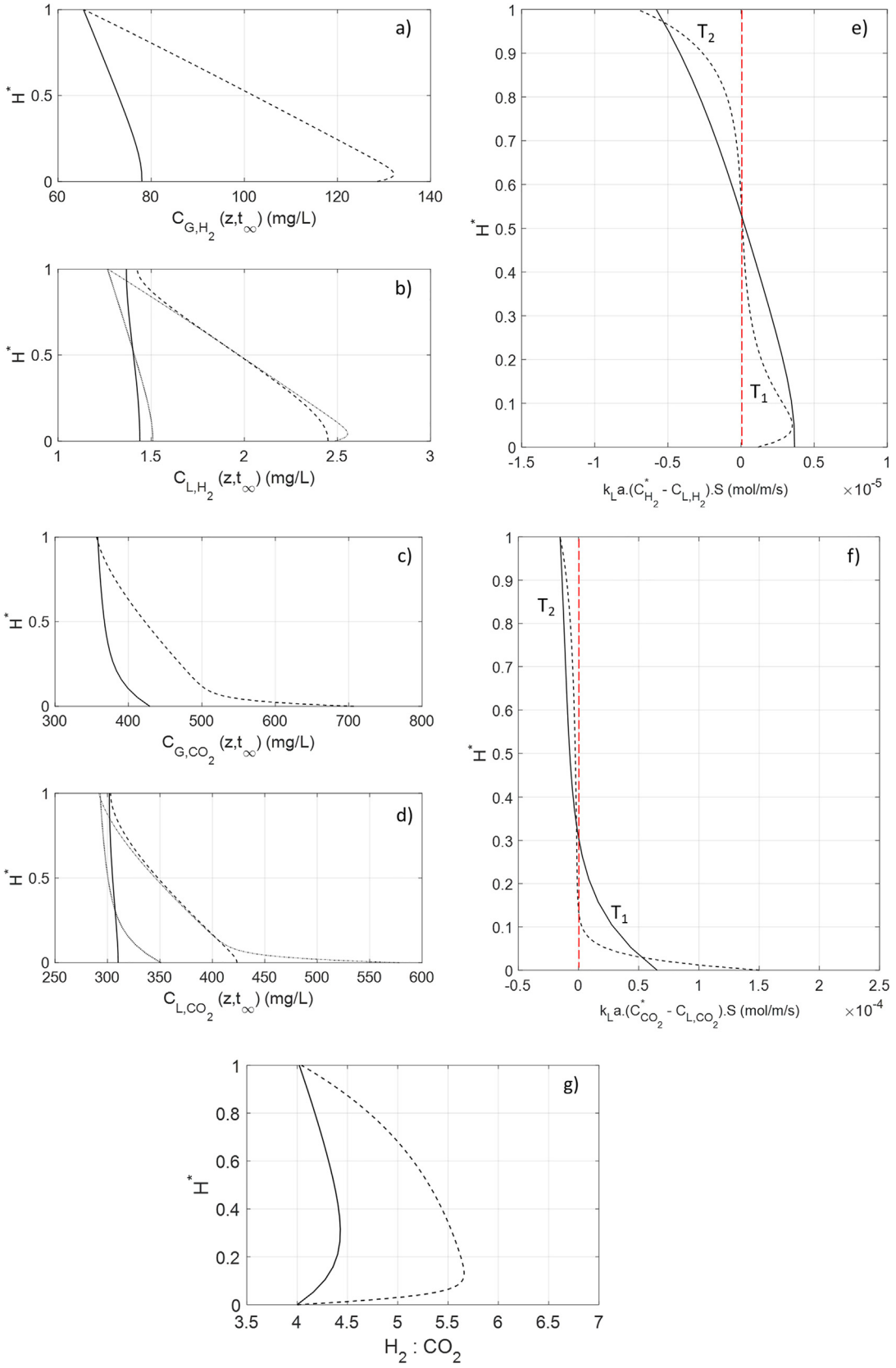

Fig. 9. (a–d) Normalized vertical profiles of gas and liquid concentrations (e–f) Normalized vertical profiles of mass transfer rate, and (g) local H_2: CO_2 ratio at steady-state. Graph legend as follows: – H = 2 m, – – H = 10 m, ■ ■ ■ and – ■ – are C^* profile for H = 2 m and H = 10 m respectively.

times higher at the large scale. Nevertheless, at the small scale, the absorption flux of CO_2 is nearly 10% of the inlet molar flux ($T_{CO2,1}$/F_{in}), which leads to an increase in the H_2: CO_2 ratio around 10% in the similar way. At the larger scale, the absorption flux of CO_2 rep-

Table 6
H_2 & CO_2 local mass transfer flux.

H (m)	2		10	
Species, *i*	H_2	CO_2	H_2	CO_2
$F_{i,in}$ (10^{-4}mol/s)	5.463	1.366	5.463	1.366
$T_{i,1}$ (10^{-4}mol/s)	0.023	0.137	0.068	0.410
$T_{i,2}$ (10^{-4}mol/s)	−0.024	−0.131	−0.069	−0.392
$T_i = T_{i,1} + T_{i,2}$ (10^{-4}mol/s)	−0.001	0.006	−0.001	0.018

resents 30% of the inlet molar flux, which results in an even higher H_2:CO_2 ratio.

However, the ratio 4:1 is recovered at the outlet, which is expected, as the net global mass transfer flux is always null at steady-state. The mass transfer profile is different than that of case 1 for H_2 mass transfer (Fig. 9e and f vs. Fig. 7c). Here, it is no longer symmetrical. At the small scale, the only similarity with case 1 is that the H_2 absorption and desorption still occur at the bottom half and the upper half of the column respectively, as shown in Fig. 7c and Fig. 9e. Although the presence of CO_2 alters the linear mass transfer profile (see Fig. 7), the overall mass transfer flux is still conserved. The mass balances for each species are again accurately satisfied as shown in Table 6.

Due to the multispecies mass transfer, the H_2:CO_2 ratio of the absorption flux rate ($T_{H2,1}/T_{CO2,1}$) is 0.023/0.137 = 0.168 and 0.068/0.410 = 0.166 at the small scale and at the large scale respectively. This is far from the expected stoichiometry ratio (4:1). The hydrogen is in large default compared to CO_2, as previously observed by Gerhard and it is repeated in Schill et al. (1999). Gerhard suggested that in order to obtain the ideal stoichiometric proportion of H_2 to $C0_2$ in the liquid phase (i.e., 4:1), the molar ratio between H_2 and $C0_2$ in the gaseous phase has to be greater than 35:1. In this work, we suggest to obtain a stoichiometric proportion in terms of absorption flux to satisfy the biological reaction and not in terms of concentration. In order to better analyze this competition between mass transfer and bioreaction, the next case study addresses biological methanation reaction.

4.3. Case 3: Effect of CH_4 bioproduction on H_2 and CO_2 multispecies mass transfer – Hydrodynamics, mass transfer and bioreaction coupled problem

For the final case, the model is further challenged with an industrial-scale problem including bioreaction. To our best knowledge, the world first full-scale biological methanation demonstration plant is located in Avedore, Denmark (Rusmanis et al., 2019). It operates at a full electrical power load capacity of 1 MW. The reactor is designed to treat up to 50 Nm^3/h of CO_2 contained in a mixture of biogas (65% CH_4 and 35% CO_2) issuing from a nearby anaerobic digestor. From a recent study, the objective of the plant is to demonstrate the capability to produce 125 Nm^3/h of biomethane at 97% of purity. This is done by upgrading the raw biogas with the addition of 200 Nm^3/h of H_2 generated from the hydrolysis of water using the surplus renewable electricity. With these input collected from the literature, it is attempted to use the current model to reproduce the reported results obtained at an industrial scale (Rusmanis et al., 2019; Electrochaea – Carbon and Energy storage, 2017; Electrochaea GmbH, n.d.; Sveinbjörnsson and Münster, 2017). The bubble diameter at the inlet is supposed to be 2 mm as no information is found. A 10-meter high bubble column operated under pressure ≈8 bar and 65 °C, fed with a H_2: CO_2: CH_4 gas molar mixture of 60%:15%:25% was considered. At this temperature, the liquid phase diffusivities of D_{H_2}, D_{CO_2}, and D_{CH_4} are taken as $1.2097{\cdot}10^{-8}$, $5.3765{\cdot}10^{-9}$, and $3.9518{\cdot}10^{-9}$ m^2/s respectively. The Henry constants of He_{H_2}, He_{CO_2}, and He_{CH_4} at this temperature is taken as $1.2641{\cdot}10^{-5}$, 0.0056 and $1.0541{\cdot}10^{-5}$ mg/L/Pa respectively (Sander, 2015). Due to a larger column's diameter (0.72 m), the model parameter, D_L is computed as 10^{-1} m^2/s by Deckwer correlation. The bioreaction is solved using equations described in Section 2.1.2. (Rafrafi et al., 2020) stated that the increase of pH in ex-situ biological methanation reactor is less problematic than in-situ system. Thus, the effect of pH is not studied and the dissolved CO_2 remain at their CO_2 form, similar to previous works (Inkeri et al., 2018; Markthaler et al., 2020).

In the presence of reaction, the hydrodynamics behavior differs from case 2 (without reaction). The later has already a very distinct hydrodynamic behavior from case 1 (without the presence of CO_2). As depicted in Fig. 10a, the pressure is slightly higher in the presence of bioreaction. The local pressure profile depends on the local ε_G which in turns depends on the mass transfer and the bioreaction. Due to a huge consumption of CO_2 and H_2 (confirmed in Fig. 11a and Fig. 11c), ε_G falls sharply from about 10% to lower than 5% and non-linearly with the height especially in the first half of the column. The impact of bioreaction on the hydrodynamics and the mass transfer is profound, as ε_G reduces almost two-fold because of bioreaction. As expected, this leads to a non-linear decrease in k_La in a similar manner. Due to high pressure system (P varies between 8 and 9 bar) coupled with high mass transfer flux, it is likely favorable to maintain in homogeneous bubbly flow regime as $\langle\varepsilon_G\rangle$ reaches 6% throughout the column as shown in Fig. 10b.

Fig. 11a and c shows that both H_2 and CO_2 gas concentration plunge and every substrate transferred to the liquid phase is consumed by the reaction to produce CH_4. As presented in Fig. 11b, C_{L,H_2} reaches 0 at the top of the reactor as dissolved H_2 from gas to liquid mass transfer is totally consumed by the bioreaction to form CH_4. Fig. 11d reveals that the dissolved CO_2 is not limiting the reaction as the C_{L,CO_2} is close to its saturation concentration. Dissolved CH_4 is always higher than the saturation C^*, as depicted in Fig. 11f. Therefore, dissolved CH_4 is transferred from the liquid to the gas and C_{L,CH_4} almost reaches the saturation value at the top of the column. The methane concentration in the gas phase is enriched throughout the column, as shown in Fig. 11e, C_{G,CH_4} increases in the same trend as C_{L,CH_4}. From Fig. 11g, the local CH_4 mass transfer profile is opposite of that of CO_2. Moreover, due to the limitation of bioreaction by the H_2 mass transfer at steady state, the local CO_2 transfer is stoichiometrically controlled by the bioreaction: with every 4 mol of H_2 transferred, 1 mol of CO_2 is transferred as well (see Table 8). Thus, the H_2 local mass transfer profile is nearly 4 times larger than that of CO_2.

Fig. 12 shows the local profile obtained at steady state. The gaseous substrates (H_2 & CO_2) enter the column are transferred and consumed. The model predicts more than 95% CO_2 removal and conversion into CH_4. The outlet CH_4 fraction reaches 95% with a flow rate of 123 Nm^3/h which corresponds closely to the output reported at the full industrial scale (Table 7) and validate thus globally the 1D comprehensive model in a real installation. This result was obtained by setting the initial bubble diameter to 2 mm and using the Higbie correlation for k_L. Some other combination might work equally well. The satisfactory comparison to the

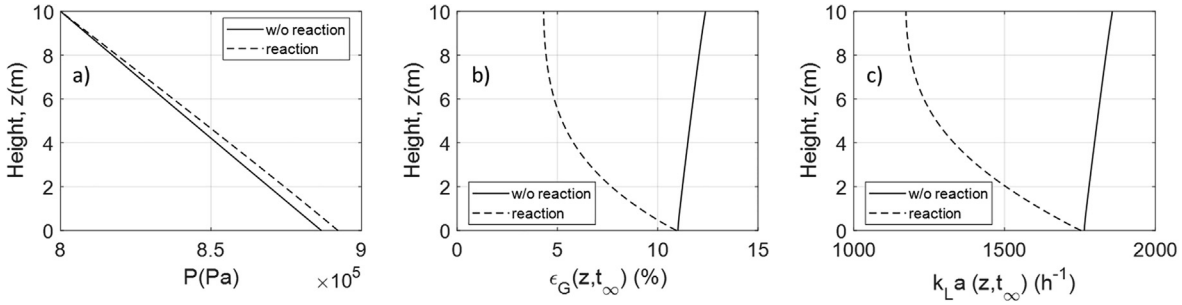

Fig. 10. Steady-state hydrodynamic variables spatial profile. The legend **w/o reaction** and **reaction** refer to the case without reaction and with reaction respectively.

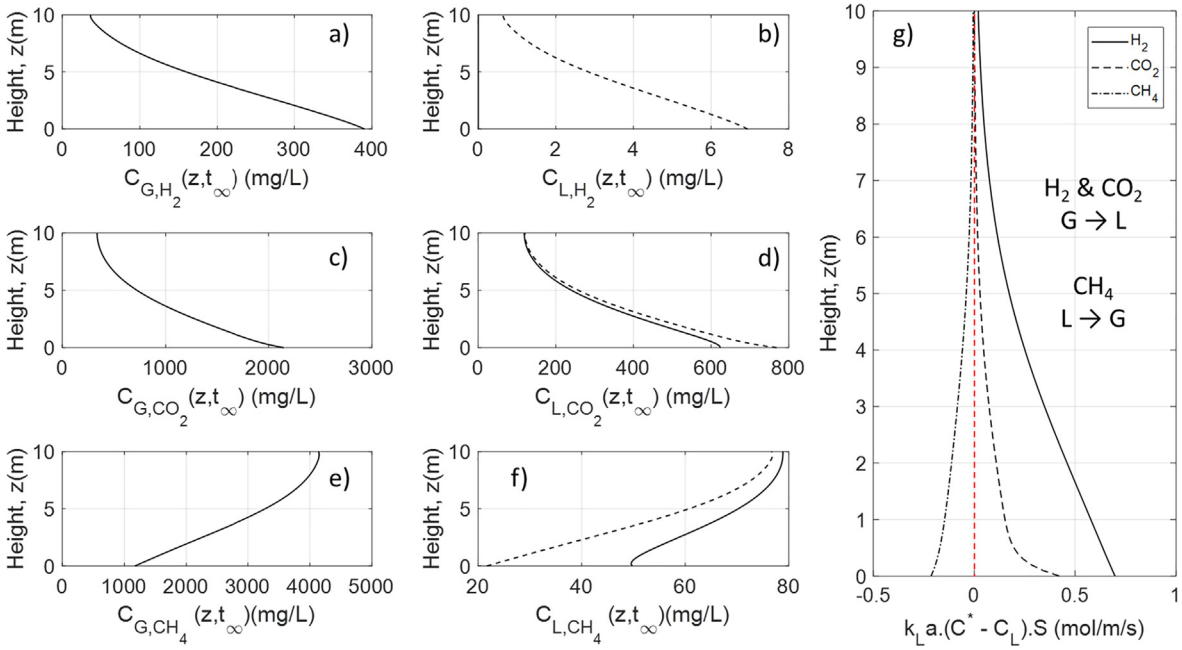

Fig. 11. Steady-state concentration spatial profile. Graph legend for liquid and equilibrium concentration as follows: – and – – are for $C_{L,i}$ and C^* profile respectively.

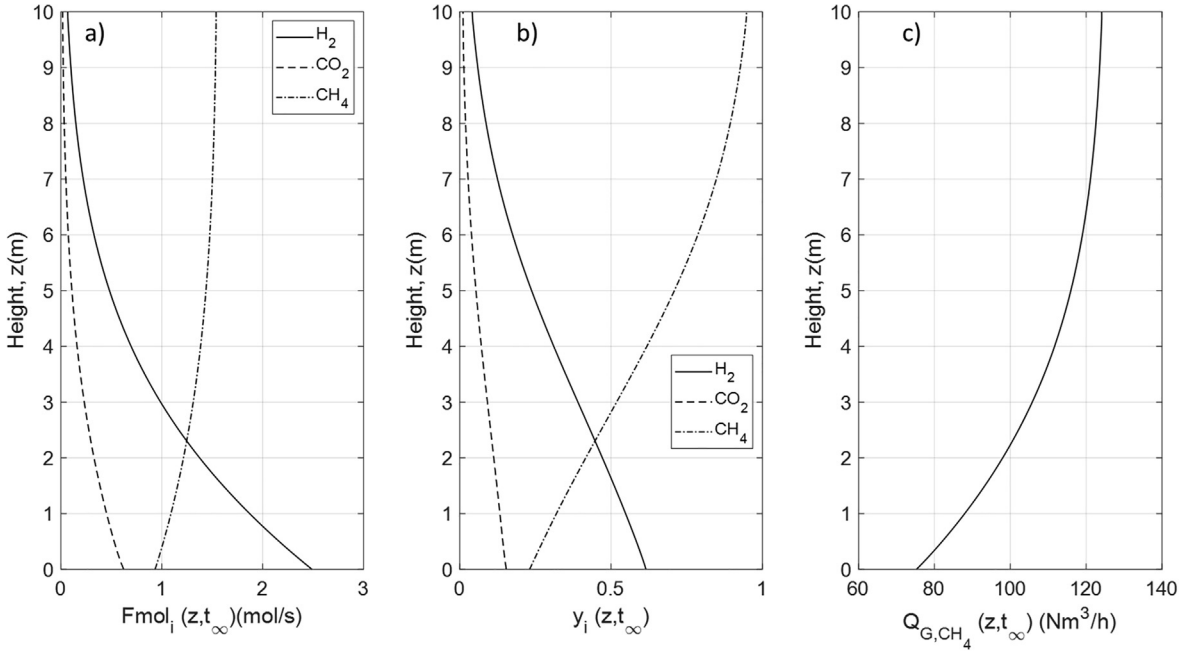

Fig. 12. Industrial scale biological methanation performance. (a) Gas phase local molar flux (b) gas phase molar fraction and (c) methane production.

Table 7
Model predicted results vs. reported values from the literature.

Outlet value	Reported data from (Electrochaea – Carbon and Energy storage, 2017; Forstmeier, n.d.)	This work
$Q_{G,CH4}$ (Nm^3/h)	125	123
yCH_4 (%)	95–97	95

outlet concentration actually validates the integral value of k_La at the reactor scale as no concentration profile like in the work of Deckwer et al. in Section 3.2 are available for local validation at industrial scale.

From Table 8, it is observed that the H_2: CO_2 gaseous molar ratio of 4:1 imposed at the inlet corresponds to the ratio of the gas transferred (T_{H2}: T_{CO2}) at the steady state. This is due to the overall limiting process is originated from the H_2 mass transfer. Therefore, the CO_2 and CH_4 mass transfer are conditioned by the stoichiometry of the bioreaction, as stated in Eq. (13).

A strength of the proposed approach is to handle the transition from the biological regime to the physical regime. Indeed, in a bioreactor where substrates are provided in the gas phase only, biomass keeps growing until the gas–liquid mass transfer becomes the limiting phenomena as reported in Table 9. In order to illustrate this succession of events, the vertical profiles of local H_2 consumption rate φ_{H_2}, expressed either as the biological consumption rate or the physical supply of H_2 mass transfer rate, are plotted in Fig. 13 at different times.

At the beginning of the process around t = 400 s (Fig. 13a), H_2 is abundant in the reactor with very little biomass in it (initial concentration at 1 g/L, as shown in Fig. 14), the mass transfer is not limiting the overall reaction. It is observed that φ_{H_2} is equals to $q_{H_2}^{max}$ and the column operates in the biological regime. As the biomass concentration increases in the reactor, the demand for H_2 increases. At t = 19,900 s (Fig. 13b), this demand is fulfilled in the lower part of the column which still operates in the biological regime, but it is insufficient in the upper part where the actual specific uptake rate is limited by the local mass transfer. In the lower part, the gas phase is still rich in H_2 while H_2 is depleted in the gas phase in the upper part. A steady-state is reached when the H_2 mass transfer becomes the limiting step everywhere.

Fig. 14 depicts the evolution of biomass concentration until steady state. Dynamic simulation shows that the biomass reaches a concentration of 35 g/L at steady state. This value can be compared to an estimate based on the assumption that gas–liquid mass transfer is limiting the bioreaction everywhere in the reactor. Such a situation is actually taking place at steady state as shown in Fig. 13c (t = 59,900 s). This implies that the amount of hydrogen supplied is used for maintenance purposes only and the overall specific growth rate is null. Therefore, the steady state biomass concentration can be obtained from the solution of $R_X = Y_{X/H_2}(r_1 - r_3) = Y_{X/H_2} \cdot \left(\varphi_{H_2} - m\right) \cdot X = 0$. Using Eq. (16) in the regime of gas liquid mass transfer limitation, one gets $\langle \varepsilon_L X \rangle = \frac{\langle k_L a_{H_2} C^*_{L,H_2} \rangle}{m}$ which leads to a value of 35.8 g/L for the biomass concentration. This value is very close to the biomass concentration at steady state, suggesting that the model for biological reaction calculation is consistent and correctly implemented into the numerical simulation.

Table 8
H_2, CO_2 & CH_4 local mass transfer flux.

Species, i	H_2	CO_2	CH_4
$F_{i,in}$ (mol/s)	2.48	0.62	0.93
T_i (t = t_∞) (mol/s)	2.43	0.61	−0.61
Yield = T/F_{in} (%)	98	98	–

Table 9
Evaluation of H_2 biological demand and physical supply in Eq. (16) at three different time instants valued in mol/s.

Time	Total biological demand $S \cdot \int_0^z q_{H_2}^{max} \cdot \frac{C_{L,H_2}}{K_{H_2}+C_{L,H_2}} \cdot X \cdot dz$	Total physical supply $S \cdot \int_0^z max\left(\frac{k_L a_{H_2} C^*_{L,H_2}}{\varepsilon_L}, \frac{C_{L,H_2}}{\tau_m}\right) \cdot dz$
t = 400 s	2.30	2689
t = 19,900 s	6.41	376
t=t_∞	11.88	6.72

With the new formulation of substrate uptake rate as written in Eq. (16), it can be observed that:

i. This rate limiting-step formulation provides an elegant way to circumvent the numerical issues related to extremely low values for K_{H2}, which led Inkeri and co-workers to introduce artificial stabilizing function I_D and I_C in their model (see Eqs. (46) and (47) in (Inkeri et al., 2018)
ii. At low biomass concentration, the uptake rate is set by the biological capacity of the microorganisms and is almost constantly equal to $q_{H_2}^{max}$ since the value of K_{H2} is extremely low (5.6 $\mu mol \cdot L^{-1}$ as reported by Schill et al. (1999)
iii. As the biomass increases, the specific uptake rate will become limited by the gas–liquid mass transfer rate.
iv. Mass transfer limitation coincides with almost zero hydrogen concentration. However, when the hydrogen concentration is close to zero, the actual specific uptake rate is not zero (typically the case when the uptake rate is expressed in terms of concentration, such as Monod-type expression) but equals the maximum mass transfer rate per cell mass indicating that bioreactions are limited by the gas–liquid mass transfer rate. Thus, growth will still be possible.
v. According to Eqs. (15)–(19), growth will finally stop when $\varphi_{H_2} = m$. Thus, a constant biomass concentration will be reached when hydrogen uptake is limited by gas–liquid mass transfer and the amount of hydrogen is just sufficient to meet the cell's requirements for maintenance. From that point onward, we will observe that $k_L a_{H_2} \cdot C^*_{L,H_2} = m \cdot \varepsilon_L \cdot X$ and the other kinetic equations indicate that constant carbon dioxide consumption and methane production rates will be attained, both being proportional to $k_L a_{H_2} C^*_{L,H_2}$.
vi. (Markthaler et al., 2020) used a second order kinetics law to describe biological methanation. In accordance with (Schill et al., 1999) conclusions, these authors observed that the kinetic rate constant itself is of minor importance since biological reactions rates are, in the end, controlled by the interfacial mass transfer rate. Here, we proposed a more meaningful formulation for the biokinetics model capable to capture the competitive balance between biological demand and mass transfer supply.

5. Conclusion and outlook

It is well-known in the literature that the modeling of biological processes requires a two-way coupling approach for mass transfer and hydrodynamics. But in practice, either very few models have done so or the two-way coupling has not been implemented delicately and discussed in details (Inkeri et al., 2018; de Medeiros et al., 2020; Chen et al., 2016, 2015). Therefore, a new 1D gas–liquid multispecies mass transfer and spatio-temporal model is established to model the biological methanation process in bubble

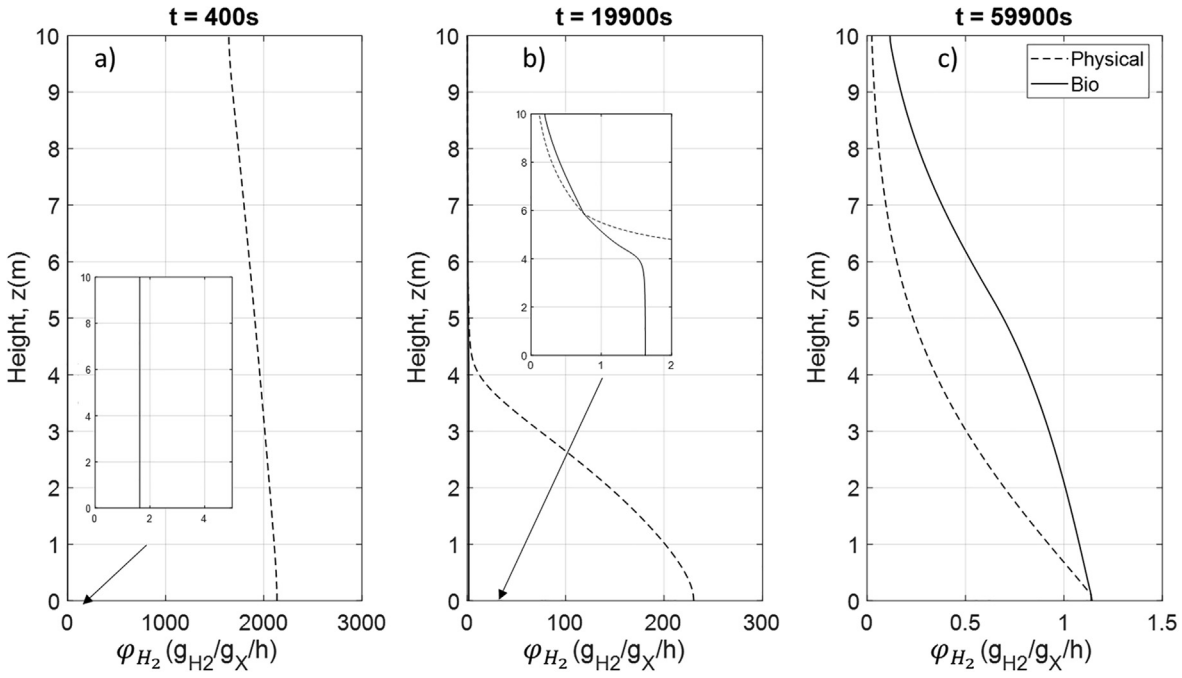

Fig. 13. Revealing the regime transition: biological consumption rate and specific H_2 mass transfer rate as presented in Eq. (16).

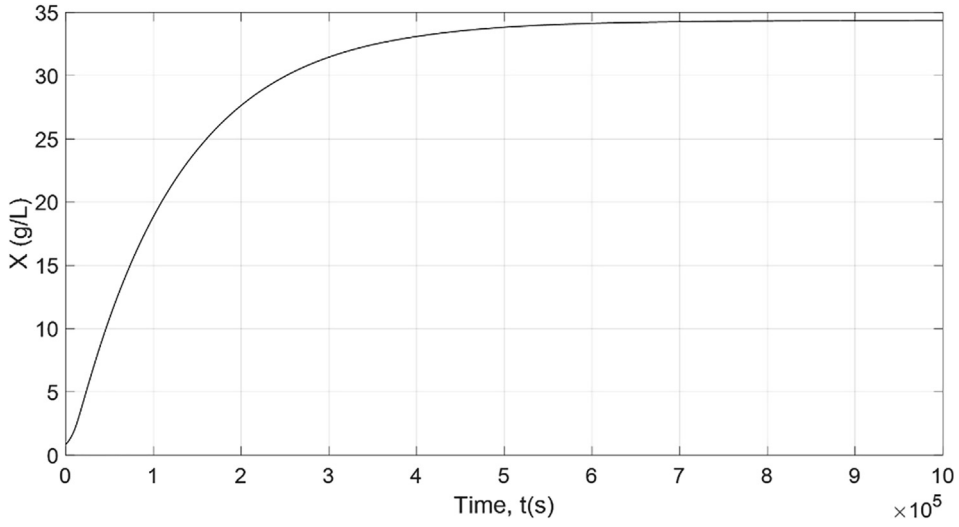

Fig. 14. Temporal evolution of biomass weight in g per L of total reactor volume.

columns. The model developed considers the 1D two phase flow, whereby the mass transfer and bioreaction rate impact the hydrodynamics local profile, in return the hydrodynamics quantifies the interphase mass transfer rate and the bioreaction rate. The two-way coupled 1D model developed here is in good agreement with previous experimental and literature data. The knowledge of bubble size is crucial but no further fitting parameters are needed to obtain good prediction in the very case where bioreaction rates are controlled by gas–liquid mass transfer. For the bubbly flow hydrodynamics, the model is validated using our experimental transient gas holdup measurements and literature data. A satisfactory predication of the local gas holdup profile and mass transfer, behavior was shown in comparison to the results of Deckwer et al. (1978) and Hissanaga et al. (2020). Strong variation of local gas holdup due to high interphase CO_2 mass transfer flux are correctly addressed. Local mass transfer flux of each species *i* are captured precisely by the model which is crucial to simulate the biological reaction. The effect of hydrostatic pressure and column height was studied and it is found that non-linearities and heterogeneities prevails in tall bubble column. Due to differences in the gaseous substrates' solubility (H_2 & CO_2), the local concentrations and therefore the local mass transfer fluxes of each species vary along the height of the column. As a result, the molar ratio imposed at the inlet is not conserved, signifying that the mass transfer rate changes according to the species. Lastly, the model has been extended to an industrial-scale biological methanation plant. In this type of bioprocess, where the substrates are fed through the gaseous phase only the performances are limited by the slowest mass transfer rate (H_2 for biomethanation). Contrary to (Inkeri et al., 2018) and (Markthaler et al., 2020) work, the new proposed biological uptake rate has a more physical significance. As pointed out by Schill et al., the description of the kinetics of growth should

be written as the uptake kinetics of the limiting substrate that controls the whole bioreaction process (Schill et al., 1999). In this work, we proposed to describe the substrate uptake rate by using the minimum between the biological Monod-type uptake rate and the locally available specific H_2 supply. The latter is expressed as the maximum between the specific mass transfer rate (when the dissolved H_2 in the environment is depleted) and the specific local concentration renewed by the micromixing. This signifies the limiting factor can either comes from the biological origin or the physical origin. The results of this formulation have been demonstrated in the simulation of industrial-scale biological methanation as the results is closely matched the reported values. In future work, this comprehensive 1D model will be used to study scale-up and addresses two-way coupling issues faced in the industrial biological bubble column. The 1D model with the novel bioreaction closure model will also be used as a baseline reference for multispecies two-phase flow in a more complex geometry whereby two-fluid CFD model could be extended to study multispecies two-way coupling with bioreaction.

CRediT authorship contribution statement

Vincent Ngu: Methodology, Conceptualization, Writing – original draft, Software, Data curation, Validation. **Jérôme Morchain:** Supervision, Methodology, Conceptualization, Writing – review & editing, Software. **Arnaud Cockx:** Supervision, Methodology, Conceptualization, Writing – review & editing.

Declaration of Competing Interest

The authors declare that they have no known competing financial interests or personal relationships that could have appeared to influence the work reported in this paper.

Acknowledgement

The authors would like to thank Claude Le Men who installed the optical setup for image acquisition and provided technical support on the experimental setup.

Appendix A

Drag model

Tomiyama et al. (1998)

$$C_D = \max\left\{\min\left[\frac{24}{Re_b}\left(1+0.15Re_b^{0.687}\right), \frac{72}{Re_b}\right], \frac{8}{3}\frac{Eo}{(4+Eo)}\right\} \quad (A.1)$$

Mei et al. (1994)

$$C_D = \frac{16}{Re_b}\left(1+\frac{Re_b}{8+0.5(Re_b+3.315Re_b^{0.5})}\right) \quad (A.2)$$

Dijkhuizen et al. (2010)

$$C_D = \sqrt{C_D(Re_b)^2 + C_D(Eo)^2}$$

$C_D(Re_b) = C_D$ from Eq. (A.2)

$$C_D(Eo) = \frac{4.Eo}{9.5+Eo} \quad (A.3)$$

Appendix B

Details of iterative resolution of system (20)

The algorithm is a successive substitution procedure. Starting from the known local molar fluxes ($\phi_{G,i}$, $\phi_{L,i}$) and the local gas holdup (ε_G), the local pressure profile (P), the local gas holdup (ε_G) as well as $C_{G,i}$ and $C_{L,i}$ are updated before the next timestep is taken.

The following procedure is used at the beginning of each timestep.

Step 1. $\phi_{G,i} \leftarrow \phi_{G,i}(t)$ and $\varepsilon_G \leftarrow \varepsilon_G(t)$
Step 2. $C_{G,i} \leftarrow \frac{\phi_{G,i}}{\varepsilon_G}$
Step 3. Update P from ε_G using equation (10)
Step 4. Update the local gas fraction $\varepsilon_G \leftarrow \frac{\sum \phi_{G,i}/M_i}{P} RT$
Step 5. Repeat Step 2 to 4 until the difference between two iterations falls below a given tolerance
Step 6. Update the liquid phase concentrations $C_{L,i} = \phi_{L,i}/(1-\varepsilon_G)$

The updated $C_{G,i}, C_{L,i}$ and ε_G are used in the right-hand side of Eqs. (1) and (2) to compute the time derivatives.

Appendix C

Bubble geometrical characteristics

With a total of 1000 images taken, the statistical convergence was reached as a significative number of bubbles were detected. Example of bubble images provided from Cam1 centered in the cylindrical bubble column are presented in Fig. C.1. The acquisition window of 26 × 26 mm^2 is small in comparison to the column diameter of 150 mm. It is noticeable that the bubble number and bubble sizes increase with increasing flow rate. The equivalent diameter calculated were represented in the form of histogram with a bin of 0.2 mm, as shown in Fig. C.2. The bubble size detected

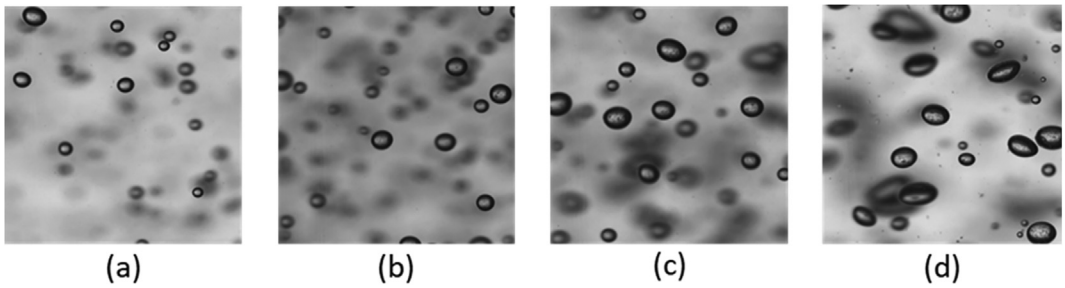

Fig. C.1. Raw images (a)–(d) refers to j_G = 0.039 cm/s, 0.078 cm/s, 0.116 cm/s and 0.156 cm/s respectively.

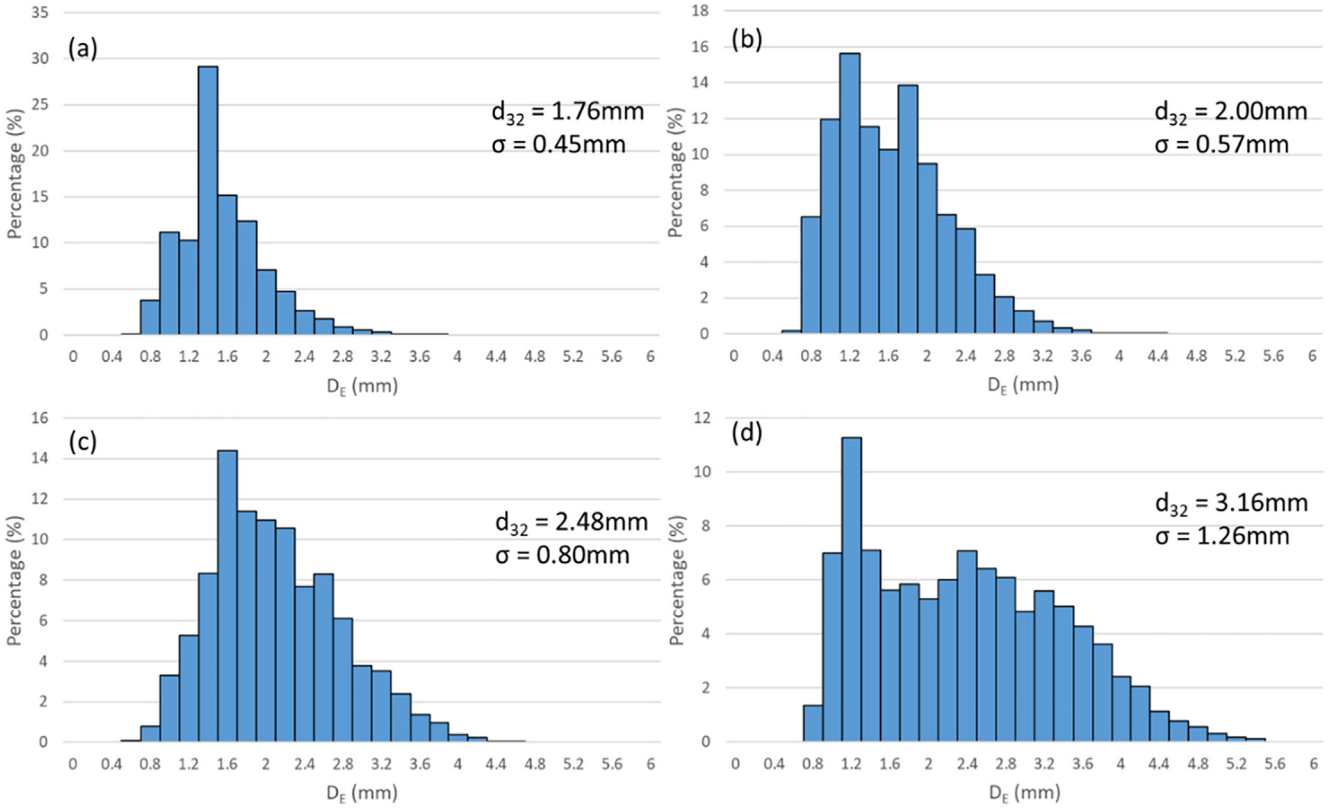

Fig. C.2. Histogram of bubble size distribution (a)–(d) refers to j_G = 0.039 cm/s, 0.078 cm/s, 0.116 cm/s, and 0.156 cm/s respectively.

and its standard deviation increased with the flow rate. The bubble size distribution was mostly mono-dispersed which is almost the case in homogeneous bubbly flow regime. This also validates the choice of using single-bubble class for our model by using the d_{32} of each case.

Appendix D

Statistical average of ΔH

Fig. D.1 plots the cumulative average of ΔH versus the image number. The curve is not constant which indicates the fluctuating nature of the free surface, but they eventually reach a stable value with increasing image number. As observed, the difference between the cumulative statistical average of ΔH and the ΔH taken at the last image upon the first bubble arrival is insignificant. Here, the ΔH obtained was 2.91 vs 2.98 mm. This result in a $\langle \varepsilon_{G,exp} \rangle$ of 0.277% vs 0.283%, a negligible relative difference of 5%.

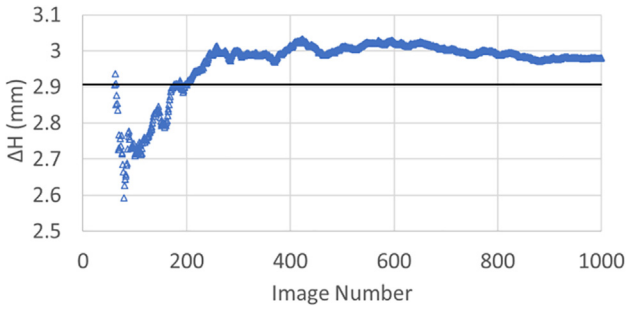

Fig. D.1. Continuous line is ΔH taken at the last image vs Δ symbol the cumulative average of ΔH.

References

Bardin-Monnier, N., Guiraud, P., Gourdon, C., 2003. Lagrangian simulations contribution to the knowledge of discs and doughnuts pulsed solvent extraction columns hydrodynamics. Chem. Eng. Process. Process Intensif. 42 (7), 503–516. https://doi.org/10.1016/S0255-2701(02)00072-7.

Bassani, I., Kougias, P.G., Angelidaki, I., 2016. In-situ biogas upgrading in thermophilic granular UASB reactor: key factors affecting the hydrogen mass transfer rate. Bioresour. Technol. 221, 485–491. https://doi.org/10.1016/j.biortech.2016.09.083.

Besagni, G., Inzoli, F., 2016. Comprehensive experimental investigation of counter-current bubble column hydrodynamics: Holdup, flow regime transition, bubble size distributions and local flow properties. Chem. Eng. Sci. 146, 259–290. https://doi.org/10.1016/j.ces.2016.02.043.

Besagni, G., Inzoli, F., Ziegenhein, T., Lucas, D., 2019. The pseudo-homogeneous flow regime in large-scale bubble columns: experimental benchmark and computational fluid dynamics modeling. Petroleum 5, 141–160. https://doi.org/10.1016/j.petlm.2017.12.004.

Chen, J., Brooks, C.S., 2021. Experiments and CFD simulation of mass transfer and hydrodynamics in a cylindrical bubble column. Chem. Eng. Sci. 234,. https://doi.org/10.1016/j.ces.2020.116435 116435.

Chen, J., Gomez, J.A., Höffner, K., Barton, P.I., Henson, M.A., 2015. Metabolic modeling of synthesis gas fermentation in bubble column reactors. Biotechnol. Biofuels 8, 89. https://doi.org/10.1186/s13068-015-0272-5.

Chen, J., Gomez, J.A., Höffner, K., Phalak, P., Barton, P.I., Henson, M.A., 2016. Spatiotemporal modeling of microbial metabolism. BMC Syst. Biol. 10, 21. https://doi.org/10.1186/s12918-016-0259-2.

Chen, J., Daniell, J., Griffin, D., Li, X., Henson, M.A., 2018. Experimental testing of a spatiotemporal metabolic model for carbon monoxide fermentation with Clostridium autoethanogenum. Biochem. Eng. J. 129, 64–73. https://doi.org/10.1016/j.bej.2017.10.018.

Darmana, D., Henket, R.L.B., Deen, N.G., Kuipers, J.A.M., 2007. Detailed modelling of hydrodynamics, mass transfer and chemical reactions in a bubble column using a discrete bubble model: Chemisorption of CO2 into NaOH solution, numerical and experimental study. Chem. Eng. Sci. 62, 2556.

de Medeiros, E.M., Noorman, H., Maciel Filho, R., Posada, J.A., 2020. Production of ethanol fuel via syngas fermentation: Optimization of economic performance and energy efficiency. Chem. Eng. Sci.: X 5,. https://doi.org/10.1016/j.cesx.2020.100056 100056.

Deckwer, W.-D., Adler, I., Zaidi, A., 1978. A comprehensive study on CO_2-interphase mass transfer in vertical cocurrent and countercurrent gas-liquid flow. Can. J. Chem. Eng. 56 (1), 43–55.

Deckwer, W.-D., Burckhart, R., Zoll, G., 1974. Mixing and mass transfer in tall bubble columns. Chem. Eng. Sci. 29 (11), 2177–2188. https://doi.org/10.1016/0009-2509(74)80025-4.

Deckwer, W.-D., Schumpe, A., 1993. Improved tools for bubble column reactor design and scale-up. Chem. Eng. Sci. 48 (5), 889–911. https://doi.org/10.1016/0009-2509(93)80328-N.

Di Giuliano, A., Pellegrino, E., 2019. Numerical integration strategies of PFR dynamic models with axial dispersion and variable superficial velocity: the case of CO2 capture by a solid sorbent. Heliyon 5,. https://doi.org/10.1016/j.heliyon.2019.e02040 e02040.

Dijkhuizen, W., Roghair, I., Van Sint Annaland, M., Kuipers, J.A.M., 2010. DNS of gas bubbles behaviour using an improved 3D front tracking model—Drag force on isolated bubbles and comparison with experiments. Chem. Eng. Sci. 65 (4), 1415–1426. https://doi.org/10.1016/j.ces.2009.10.021.

Electrochaea – Carbon and Energy storage, 2017. https://www.europeanbiogas.eu/wp-content/uploads/2017/09/7.-Electrochaea_EBA_Sept2017.pdf.

Electrochaea GmbH, n.d. http://www.electrochaea.com/ (accessed March 8, 2021).

Forstmeier, D.M., n.d. Biological methanation for grid scale carbon & energy storage. Vol. 17.

Giovannettone, J.P., Gulliver, J.S., 2008. Gas transfer and liquid dispersion inside a deep airlift reactor. AIChE J. 54 (4), 850–861. https://doi.org/10.1002/aic.11449.

Giovannettone, J.P., Tsai, E., Gulliver, J.S., 2009. Gas void ratio and bubble diameter inside a deep airlift reactor. Chem. Eng. J. 149 (1-3), 301–310. https://doi.org/10.1016/j.cej.2008.11.024.

Heijnen, J.J., Van't Riet, K., 1984. Mass transfer, mixing and heat transfer phenomena in low viscosity bubble column reactors. Chem. Eng. J. 28, B21–B42. https://doi.org/10.1016/0300-9467(84)85025-X.

Higbie, R., 1935. The Rate of Absorption of a Pure Gas into a Still Liquid during Short Periods of Exposure. Trans. AIChE. 31, 365–389.

Hissanaga, A.M., Padoin, N., Paladino, E.E., 2020. Mass transfer modeling and simulation of a transient homogeneous bubbly flow in a bubble column. Chem. Eng. Sci. 218,. https://doi.org/10.1016/j.ces.2020.115531 115531.

Hlawitschka, M.W., Kováts, P., Zähringer, K., Bart, H.-J., 2017. Simulation and experimental validation of reactive bubble column reactors. Chem. Eng. Sci. 170, 306–319. https://doi.org/10.1016/j.ces.2016.12.053.

Inkeri, E., Tynjälä, T., Laari, A., Hyppänen, T., 2018. Dynamic one-dimensional model for biological methanation in a stirred tank reactor. Appl. Energy 209, 95–107. https://doi.org/10.1016/j.apenergy.2017.10.073.

Inkeri, E., Tynjälä, T., 2020. Modeling of CO2 Capture with Water Bubble Column Reactor. Energies 13, 5793. https://doi.org/10.3390/en13215793.

Inoue, K., 1973. Method of determining the coefficient of longitudinal mixing for the continuous phase under conditions of a non flow-through system in high rate extractors. Theoreticheskie Osnovy Khimicheskoi Tekhnologii, 550–556.

Kováts, P., Thévenin, D., Zähringer, K., 2020. Influence of viscosity and surface tension on bubble dynamics and mass transfer in a model bubble column. Int. J. Multiph. Flow 123,. https://doi.org/10.1016/j.ijmultiphaseflow.2019.103174 103174.

Laupsien, D., Le Men, C., Cockx, A., Liné, A., 2019. Image processing for bubble morphology characteristics in diluted bubble swarms. Phys. Fluids 31,. https://doi.org/10.1063/1.5088945 053306.

Lecker, B., Illi, L., Lemmer, A., Oechsner, H., 2017. Biological hydrogen methanation – A review. Bioresour. Technol. 245, 1220–1228. https://doi.org/10.1016/j.biortech.2017.08.176.

Li, X., Griffin, D., Li, X., Henson, M.A., 2019. Incorporating hydrodynamics into spatiotemporal metabolic models of bubble column gas fermentation. Biotechnol. Bioeng. 116 (1), 28–40. https://doi.org/10.1002/bit.26848.

Linkès, M., 2012. Numerical Simulation and modelling of substrate assimilation by microorganisms in a turbulent flow, phd. http://ethesis.inp-toulouse.fr/archive/00002128/ (accessed May 25, 2021).

Markthaler, S., Plankenbühler, T., Weidlich, T., Neubert, M., Karl, J., 2020. Numerical simulation of trickle bed reactors for biological methanation. Chem. Eng. Sci. 226,. https://doi.org/10.1016/j.ces.2020.115847 115847.

Mei, R., Klausner, J.F., Lawrence, C.J., 1994. A note on the history force on a spherical bubble at finite Reynolds number. Phys. Fluids 6, 418–420. https://doi.org/10.1063/1.868039.

Morchain, J., Gabelle, J.-C., Cockx, A., 2014. A coupled population balance model and CFD approach for the simulation of mixing issues in lab-scale and industrial bioreactors. AIChE J. 60 (1), 27–40. https://doi.org/10.1002/aic.14238.

Morchain, J., Pigou, M., Lebaz, N., 2017. A population balance model for bioreactors combining interdivision time distributions and micromixing concepts. Biochem. Eng. J. 126, 135–145. https://doi.org/10.1016/j.bej.2016.09.005.

Nauha, E.K., Alopaeus, V., 2015. Modeling outdoors algal cultivation with compartmental approach. Chem. Eng. J. 259, 945–960. https://doi.org/10.1016/j.cej.2014.08.073.

Pigou, M., Morchain, J., 2015. Investigating the interactions between physical and biological heterogeneities in bioreactors using compartment, population balance and metabolic models. Chem. Eng. Sci. 126, 267–282. https://doi.org/10.1016/j.ces.2014.11.035.

Pigou, M., 2018. Modélisation du comportement cinétique, des phénomènes de mélange et de transfert locaux, et des effets d'hétérogénéité de population dans les fermenteurs industriels, These de doctorat, Toulouse, INSA. http://www.theses.fr/2018ISAT0038 (accessed June 9, 2021).

Rafrafi, Y., Laguillaumie, L., Dumas, C., 2020. Biological Methanation of H2 and CO2 with Mixed Cultures: Current Advances, Hurdles and Challenges. Waste Biomass Valor. https://doi.org/10.1007/s12649-020-01283-z.

Rusmanis, D., O'Shea, R., Wall, D.M., Murphy, J.D., 2019. Biological hydrogen methanation systems – an overview of design and efficiency. Bioengineered 10 (1), 604–634. https://doi.org/10.1080/21655979.2019.1684607.

Rzehak, R., Krepper, E., 2016. Euler-Euler simulation of mass-transfer in bubbly flows. Chem. Eng. Sci. 155, 459–468. https://doi.org/10.1016/j.ces.2016.08.036.

Sander, R., 2015. Compilation of Henry's law constants (version 4.0) for water as solvent. Atmos. Chem. Phys. 15 (8), 4399–4981. https://doi.org/10.5194/acp-15-4399-2015.

Sasaki, S., Uchida, K., Hayashi, K., Tomiyama, A., 2017. Effects of column diameter and liquid height on gas holdup in air-water bubble columns. Exp. Therm Fluid Sci. 82, 359–366. https://doi.org/10.1016/j.expthermflusci.2016.11.032.

Schill, N.A., Liu, J.-S., von Stockar, U., 1999. Thermodynamic analysis of growth of Methanobacterium thermoautotrophicum. Biotechnol. Bioeng. 64, 74–81. https://doi.org/10.1002/(SICI)1097-0290(19990705)64:1<74::AID-BIT8>3.0.CO;2-3.

Shah, Y.T., Kelkar, B.G., Godbole, S.P., Deckwer, W.-D., 1982. Design parameters estimations for bubble column reactors. AIChE J. 28 (3), 353–379. https://doi.org/10.1002/aic.690280302.

Siebler, F., Lapin, A., Takors, R., 2020. Synergistically applying 1-D modeling and CFD for designing industrial scale bubble column syngas bioreactors. Eng. Life Sci. 20 (7), 239–251. https://doi.org/10.1002/elsc.201900132.

Sveinbjörnsson, D., Münster, E., 2017. Gas conditioning and grid operation: Upgrading of Biogas to Biomethane with the Addition of Hydrogen from Electrolysis. https://futuregas.dk/wp-content/uploads/2018/06/FutureGas-WP1-Deliverable-1.1.1.-Technologies-and-status-of-methanation-of-biogas-2017_Final.pdf.

Tomiyama, A., Kataoka, I., Zun, I., Sakaguchi, T., 1998. Drag Coefficients of Single Bubbles under Normal and Micro Gravity Conditions. JSME Int. J. Ser. B 41 (2), 472–479. https://doi.org/10.1299/jsmeb.41.472.

Versteeg, G.F., Van Swaaij, W.P.M., 1988. Solubility and diffusivity of acid gases (carbon dioxide, nitrous oxide) in aqueous alkanolamine solutions. J. Chem. Eng. Data 33 (1), 29–34. https://doi.org/10.1021/je00051a011.

Wachi, S., Nojima, Y., 1990. Gas-phase dispersion in bubble columns. Chem. Eng. Sci. 45 (4), 901–905. https://doi.org/10.1016/0009-2509(90)85012-3.

Chapter 4 Industrial application of 1D model

Upon validation at different scales of the 1D spatio-temporal gas-liquid model in Chapter 3, we envisioned its use for different engineering applications, such as bioreactor design, optimisation, and process diagnostics. The bioreactor performance depends on various parameters and this often makes it difficult to quantify thoroughly the influence of each parameter. Consequently, scaling up or optimising a biological process remains a challenging task without in-depth knowledge and accurate predictions of the bioreactor behaviours, such as the flow characteristics and bioreaction kinetics at the micro and reactor scales. The comprehensive 1D model developed in the previous parts includes new and often ignored features about two-phase bubbly flow modelling and associated multiphysics coupling regarding mass transfer and bioreactions. Owing to these, in silico design studies as well as sensitivity analysis can be performed within minutes (to be compared with days when a more complex unsteady 3D model is used). Two applications will be demonstrated in this Chapter: the scale-up of the biological methanation plant starting from the pilot-scale experiments and the analysis of substrate gradients in a large-scale fermenter, as shown in Figure 4.1. In the former, the 1D model is used to design an optimal bioreactor for biological methanation in terms of performance and costs. In the latter, the 1D model simulates substrate gradients resulting from a strong coupling between mixing, transfer and reaction in a mechanically agitated 22 m^3 industrial fermenter in Stavanger.

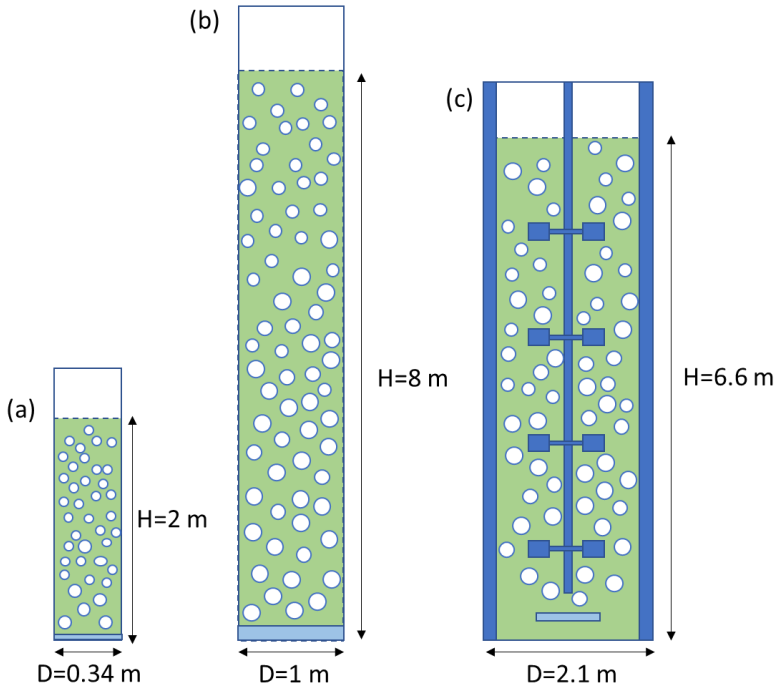

Figure 4.1: Schematic representation of the final bioreactor design studied in this chapter. Biological methanation reactor in (a) demonstration scale and (b) industrial scale. (c) Industrial fermenter

4.1 Pressure effect on bubble column

As the reactor design for biological methanation will be operating under pressure, i.e. 4 bar for the demonstration unit and 13 bar for the industrial unit, the pressure effect on the bubble column is first assessed. The elevated pressure allows direct injection of the reactor off-gas into the gas well and the gas network (4 bar) for storage and transport. The pressure has several important effects in a bubble column: on hydrodynamics through gas compression and gas holdup, on the mass transfer through again gas holdup and solubility. Also, it can be suspected that the bubble generation at the inlet is also dependent on the pressure.

4.1.1 Effect of pressure on bubble size generation

Giovannettone et al. (2009) measured the bubble size with an immerged camera inside a 24 m depth air-water bubble column/air-lift reactor using both fine and coarse spargers with superficial gas velocity up to 0.01 m.s^{-1}. They concluded that the Sauter mean bubble diameter does not change with the gas flow rate and depth. Therefore, the hydrostatic pressure seems to not affect the bubble size for mass transfer in their conditions tested (j_G below 0.05 m.s^{-1}). Lin et al. (1998) measured the bubble size through photography method in two bubble columns (D_r = 50.8mm, H = 0.8m and D_r = 101.6mm, H = 1.58m) equipped with a multi-orifice sparger in a ring arrangement (orifice diameter of 3 mm) for pressure ranging from 0.1 MPa to 19.4 MPa. The gas-liquid system tested was nitrogen and paratherm NF heat transfer fluid. Zhen et al. (2019) measured the bubble size via a high-speed camera in a cylindrical stainless-steel column (D_r = 50mm, H = 0.6m) equipped with a single orifice nozzle (orifice diameter of 3 mm) for pressure ranging from 0.1 MPa to 6 MPa. The gas-liquid system tested were nitrogen and paraffin/silicon oil, respectively to simulate the condition of the Fischer-Tropsch process. In the work of Lin et al. (1998) and Zhen et al. (2019), the authors demonstrated that the bubble diameter decreases with pressure. Idogawa et al. (1985) conducted the bubble size measurement with different sparger designs at a superficial gas velocity ranging from 0.005 to 0.05 m.s^{-1} and pressure varies between 1 to 150 bar. Their results are reported in Figure 4.2. The bubble size formed via a coarse sparger (single orifice) is larger than that formed via a fine sparger (porous plate). The effect of gas sparger design decreases with increasing pressure, and above P = 100 bar no significant effect of gas sparger on the bubble size can be observed. The bubble size remains constant above this pressure. The decrease in bubble size due to pressure effect is more pronounced for the coarse sparger than the fine sparger.

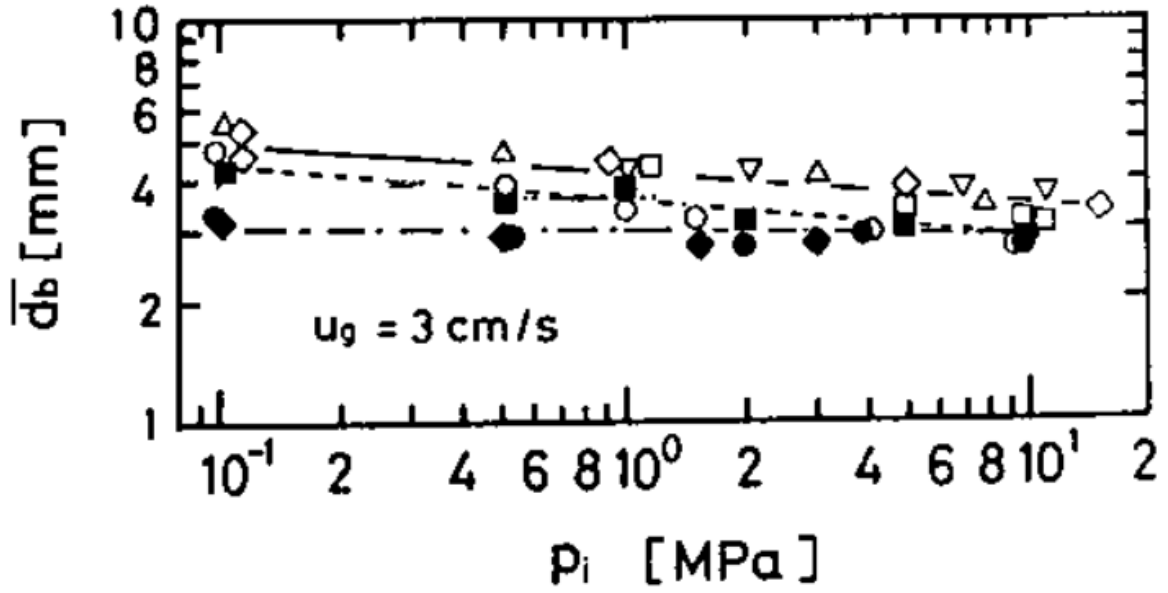

Figure 4.2: Evolution of bubble size with pressure (1 < P < 150 bar) with different gas injection devices at superficial gas velocity of 3 cm.s^{-1}. Unique orifice: ○ d_o = 1mm (We_o = 90 – 9000), △ d_o = 3mm (We_o = 3 – 300), ▽ ◇ □ d_o = 5mm (We_o = 0.7 – 100). Perforated plate: ■ d_o = 1mm. Porous plate: ● ◆ Adapted from: Idogawa et al. (1985)

The pressure effect on the bubble size can be quantified using some correlations developed for bubble size estimation. The correlations proposed by Gaddis and Vogelpohl (1986) and Kazakis et al. (2008) developed for orifice sparger and porous sparger, respectively are used for this analysis.

$$\frac{d_b}{d_o} = 1.2 Fr_o^{\frac{1}{5}}$$
$$Fr_o = \frac{u_o^2}{g.d_o} \tag{4.1}$$

With d_o the orifice diameter, u_o the superficial gas velocity passed through the orifice. Equation (4.1) proposed by Gaddis and Vogelpohl (1986) can be used to estimate the bubble size formed by a single orifice sparger under jet regime. If the gas volumetric flowrate is substituted into equation (4.1), the pressure effect can be quantified.

$$\frac{d_b}{d_o} = 1.2\left[\frac{u_o^2}{g.d_o}\right]^{\frac{1}{5}} = 1.2\left[\frac{16.Q_o^2}{\pi^2 g.d_o^5}\right]^{\frac{1}{5}} \tag{4.2}$$

$$d_b = 1.2 d_o\left[\frac{16.Q_o^2}{\pi^2 g.d_o^5}\right]^{\frac{1}{5}} = 0.84.Q_o^{\frac{2}{5}} = K.Q_o^{0.4}$$

Equation (4.2) shows that the bubble diameter varies proportionally to the flowrate to the power of 0.4 ($d_b \propto Q_o^{0.4}$). To illustrate the effect of pressure on the bubble size formed via single orifice sparger, the example of 4 and 10 bar is taken. For a fixed mass/molar gaseous flow rate, $PQ = constant$, according to ideal gas law. Therefore, $PQ|_{10\ bar} = PQ|_{4\ bar}$, which leads to equation (4.3).

$$d_b|_{10\ bar} = d_b|_{4\ bar}.\left(\frac{Q_{10}}{Q_4}\right)^{0.4} = d_b|_{4\ bar}.\left(\frac{P_4}{P_{10}}\right)^{0.4} \tag{4.3}$$

If the bubble diameter formed at 4 bar is between 2 to 4 mm, it will be reduced to between 1.4 and 2.8 mm at 10 bar for a single orifice sparger which corresponds to a 30% decrease in size.

If the gas distributor system used is a porous sparger plate, Kazakis et al. (2008) proposed an equation to estimate the bubble size.

$$\frac{d_b}{d_s} = 7.35\left[We^{-1.7}.Re^{0.1}.Fr^{1.8}.\left(\frac{d_p}{d_s}\right)^{1.7}\right]^{\frac{1}{5}}$$
$$We = \frac{\rho_L.j_{Gs}^2.d_s}{\sigma_L}, Re = \frac{\rho_L.j_{Gs}.d_s}{\mu_L}, Fr = \frac{j_{Gs}^2}{g.d_s} \tag{4.4}$$

With d_s the sparger plate diameter, j_{Gs} the superficial gas velocity through the sparger, d_p the pore size, ρ_L the liquid density, μ_L the liquid viscosity, and σ_L the liquid surface tension. With the same analogy (taking a pore size of 40 µm), it can be demonstrated that the bubble diameter varies proportionally to the flowrate to the power of 0.06 ($d_b \propto Q_o^{0.06}$). If the bubble diameter formed at 4 bar is 2 mm, it will only be reduced to 1.89 mm at 10 bar, which is just a 5.5% decrease in size. This finding matched the conclusion of (Idogawa et al., 1985) whereby the pressure has a more significant effect on the bubble size if a single orifice gas distributor is used compared to that of a porous plate, meaning that the pressure has a more significant effect on bubble column hydrodynamics operated in the heterogeneous flow than in the homogeneous flow.

$$d_b = 7.35 d_s\left[\frac{\rho_L^{-1.6}.d_s^{-3.4}}{\sigma_L^{-1.7}.\mu_L^{0.1}.g^{1.8}}.\left(\frac{d_p}{d_s}\right)^{1.7}\right]^{0.2}.j_{Gs}^{0.06} = K.j_{Gs}^{0.06} \tag{4.5}$$

4.1.2 Effect of pressure on gas hold up and interfacial area

As far as the gas holdup is concerned, the following formula can be used as first approximation of the expected value

$$\langle \varepsilon_G \rangle = \frac{Q_G}{u_{rel} S} = \frac{Q_{G0}}{u_{rel} S} \frac{P_N}{P} \tag{4.6}$$

P_N: pressure at normal condition 1 atm, Q_{G0}: normalised gas flow rate in Nm^3/h, P: operating pressure, S: cross section of the column, and u_{rel}: bubble slip velocity (constant between 1 and 4 mm). Equation (4.6) is similar to the gas holdup correlation of Heijnen and Van't Riet (1984), as given in equation (4.7).

$$\langle \varepsilon_G \rangle = \frac{Q_G}{v_{b\infty} S} = \frac{Q_{G0}}{v_{b\infty} S} \frac{P_N}{P} \tag{4.7}$$

With $v_{b\infty}$ = 0.25 $m.s^{-1}$.

Equations (4.6) and (4.7) show that the gas holdup is inversely proportional to the operating pressure. The pressure effect on the interfacial area is harder to predict as it is a function of gas holdup and bubble diameter. Supposed a porous sparger is used in which the bubbles remain insensitive to the pressure and the interfacial area will decrease accordingly with the gas holdup (for the same flow rate expressed under normal conditions).

4.1.3 Effect of pressure on the transition between flow regimes

Many investigations have been reported in the literature regarding the effect of operating pressure on bubble column hydrodynamics (Campani et al., 2015; Clark, 1990; Deckwer et al., 1980; Giovannettone et al., 2009; Idogawa et al., 1985; Kemoun et al., 2001; Lin et al., 1998; Liu et al., 2019). Some important works are recalled here to understand the pressure effect on the reactor performance. First, in terms of the gas holdup, Deckwer et al. (1980) measured the gas holdup in a slurry bubble column reactor for the Fischer-Tropsch process with a porous plate distributor at pressure up to 11 bar with superficial gas velocity below 0.04 $m.s^{-1}$. The author reported no significant effect of pressure on the gas holdup.

It is not until the work of Kemoun et al. (2001) and Lin et al. (1998) that showed a more pronounced pressure effect on the gas holdup. The results are depicted in Figure 4.3. They found that the pressure has little to no effect on the gas holdup at low superficial gas velocity (homogeneous regime), while the gas holdup increases significantly at high superficial gas velocity (heterogeneous regime). This increase in gas holdup is due to the presence of smaller bubbles under pressurised conditions. The

authors explained that the rate of bubbles breakup increases with pressure. This leads to a reduction in bubble size with increasing pressure which is not the case under ambient pressure heterogeneous regime where the bubble coalescence rate is rather high.

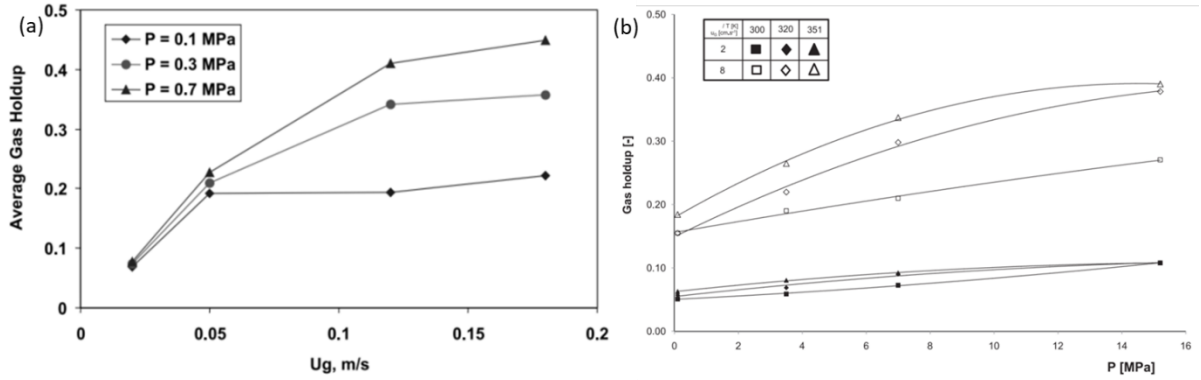

Figure 4.3: (a) Gas holdup as a function of superficial gas velocity for pressure = 1 bar, 3 bar and 7 bar. Adapted from: Kemoun et al. (2001). (b) Gas holdup as a function of pressure for superficial gas velocity = 0.02 m.s^{-1} and 0.08 m.s^{-1}. Adapted from: Lin et al. (1998).

They also linked their findings to the work of Wilkinson and v. Dierendonck (1990) who explained the effect of pressure on gas holdup in terms of the Kelvin-Helmhotz stability analysis (Kemoun et al., 2001). They indicated that the pressure mainly affects the stability of large bubbles (mostly present in the heterogeneous regime), which tend to break due to surface instabilities. Lin et al. (1998) also observed a shift in bubble size distribution to smaller bubbles at high flow rate under high pressure. The author attempted to characterise the reduction of bubble size with Kelvin-Helmhotz stability and other models, but the main message is clear: the increasing pressure causes an increase in instability of large bubbles, leading to bubble breakup only in high superficial gas velocity (j_G > 0.05 m.s^{-1}). At low superficial gas velocity (which is mostly under the homogeneous regime) the rate of bubble coalescence and breakup is relatively low, therefore the gas holdup is rather insensitive to pressure. This mainly explains the findings of Deckwer et al. whereby the gas holdup is not affected by pressure because the reported results were obtained at lower superficial gas velocity. This transition from the homogeneous regime to the heterogeneous regime occurs at j_G > 0.05 m.s^{-1} (Deckwer et al., 1980; Kantarci et al., 2005; Shah et al., 1982). This is also reflected in the findings of Maalej et al. (2003), whereby the experiments were conducted mostly in the homogeneous regime (with j_G up to 0.03 m.s^{-1}), therefore no major changes in bubble diameter are expected with the absolute pressure. Moreover, it is found that a high pressure system delays the transition from the homogeneous regime to the heterogeneous regime (Letzel et al., 1999; Wilkinson, 1991). A decrease in the rising velocity of "large bubbles" was observed in the heterogeneous regime in the pressurised column. Under these

conditions, the rise velocity of “large bubbles” decreases with the square root of the gas density, leading to lower rise velocity and higher gas holdup.

4.1.4 Effect of pressure on volumetric mass transfer coefficient

Maalej et al. (2003) showed no positive effect of pressure to mass transfer at constant inlet molar flowrate (or mass flowrate), as shown in Figure 4.4. The author reported that for a given inlet molar flowrate, the higher the pressure, the lower gas flowrate (and thus the lower the superficial gas velocity), the lower the gas holdup (fewer bubbles are present), the lower the interfacial area, and consequently the lower the $k_L a$. In other words, the high pressure increases the gas density as the gas volume contracts. This leads to fewer bubbles per unit volume. The impact of pressure on the biological methanation performance was also investigated using the 1D model. The results are discussed in Section 4.2.2, after presenting the context of reactor design and the base case.

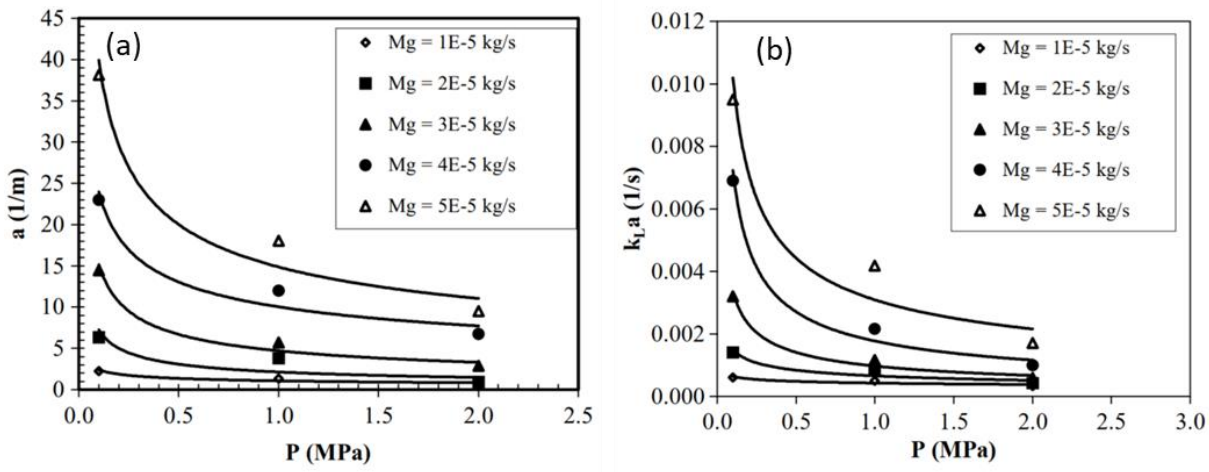

Figure 4.4: (a) Interfacial area and (b) Mass transfer coefficient as a function of pressure for different gas mass flowrate. Adapted from: Maalej et al. (2003)

4.2 Biological methanation plant design & sizing

During the thesis, we are solicited by the company ENOSIS Energies to design two ex-situ biological methanation plants at different scales: (a) a demonstration unit to treat a biogas feed of 5 Nm^3/h and (b) an industrial unit treating biogas feed of 85 Nm^3/h. We have worked together with CRITT Toulouse to define some guidelines and provide recommendations for a coherent scale-up of the biological methanation plant. The planned bioreactor design is a high height-to-diameter ratio stirred-tank reactor equipped with impellers and under pressure. The objective is to design an optimal bioreactor for biogas upgrading to grid-quality biomethane. Indeed, the biogas usually produced in the anaerobic digesters reaches about 60% of methane but still contains more than 35% of carbon dioxide that can be converted into methane in a bio-methanation unit.

4.2.1 Demonstration plant

The demonstration biological methanation plant is planned to be integrated with an existing anaerobic digestor situated at SOLIDIA site, Bélesta-en-Lauragais (France). The typical composition of the biogas issuing from the anaerobic digestor is 58.2% CH_4, 38.9% CO_2, 2.9% N_2, 0.7% O_2, and 20 ppm NH_3 with a flowrate of 5 Nm^3/h. An electrolyser with a capacity to produce 10 Nm^3/h of H_2 has been installed. In this part, it will be assumed that the biogas is composed of 60% CH_4 and 40% CO_2 and the electrolyser operates at maximum capacity. As a result, the gas composition at the inlet of the biological methanation reactor is set to 10 Nm^3/h of H_2, 2 Nm^3/h of CO_2, and 3 Nm^3/h of CH_4, corresponding to a total gas flowrate at the inlet of 15 Nm^3/h. Thus, an inlet, a H_2:CO_2 ratio of 5:1 is imposed and the inlet gas molar fractions are 0.67 for H_2, 0.13 for CO_2, and 0.2 for CH_4.

Another constraint is the upper limit for the reactor volume V_{max} set to 500 L. We tested different reactor dimensions (H and D_r) with regard to the maximum volume allowed. The reactor pressure was kept to 4 bar which allows the direct injection to the nearby gas network and the temperature was maintained at 55°C. The initial bubble diameter is assumed to be 2 mm and this value is fixed for all parametric studies. Another important assumption was to consider that the biological methanation process would be operated in, or very close to, the physical regime. This means that the bioreaction rate is limited by the hydrogen mass transfer rate which is related to the nature of the bioprocess where nutrients are fed through the gas phase only. This can be done by setting a high biomass concentration in our previously developed biological methanation model (Ngu et al., 2022a). The overall strategy can be explained in Figure 4.5. For the bubble velocity, the drag model of Tomiyama

et al. (1998) contaminated system is used. The mass transfer coefficient is modelled using Higbie (1935) penetration model.

Variables	Closure model
d_b	Constant 2 mm
u_G	Tomiyama et al. (1998) drag coefficient
u_L	0 m.s^{-1} bubble column closed to the liquid
D_G	Calculated from Wachi and Nojima (1990)
D_L	Calculated from Deckwer et al. (1974)
k_L	Higbie (1935)
R_i	Ngu et al. (2022) with biomass concentration fixed at 10 g.L^{-1}

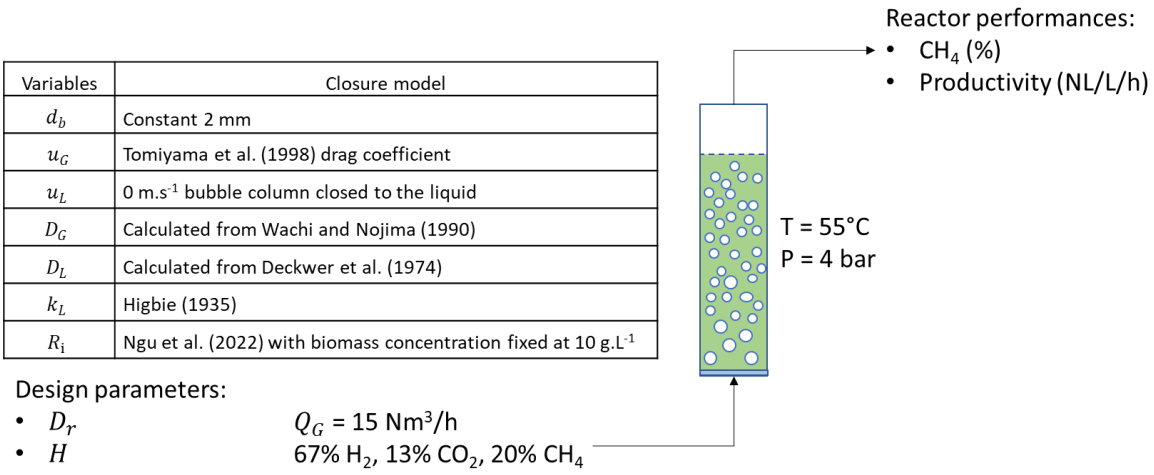

Figure 4.5: Bubble column design using the 1D model and the associated closure models.

The strategy was to perform a large number of simulations using different sets of design parameters in order to map the domain of possible design. Typically, the reactor volume was taken between 200 - 500 L, the column diameter between 0.3 and 0.5 m, leading to a height between 2 and 8 m with the H/D_r ratio between 4 and 25. This strategy is driven by the objective to provide guidelines for the industrial partner. It was chosen over an optimisation approach as it provides a more comprehensive view of the effect of each design choice on the performances. The reactor performances are assessed through the composition of the outlet gas (% CH_4 or purity) and the amount of methane produced per unit time and unit volume (productivity).

4.2.1.1 Bubble column without gas recirculation

The 1D model is used to perform preliminary reactor design. First, a reactor consisting of a single bubble column without gas recirculation was assessed.

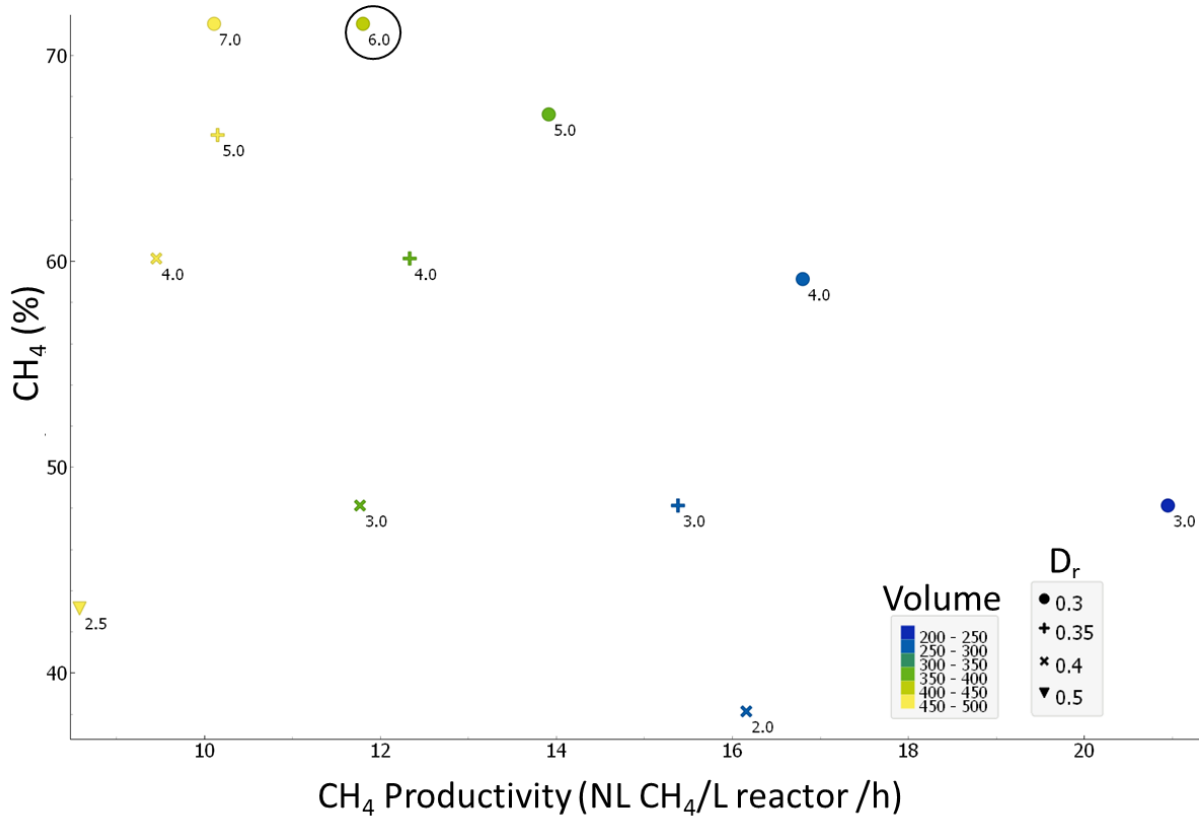

Figure 4.6: Biomethane quality and associated productivity at the bubble column outlet for different combination of H and D_r. The shape represents the column diameter, the code color indicates the reactor volume and the label below the point indicates the column height. The circled point reads D_r = 0.3 m, H = 6m and V between 400-450 L. (constant inlet gas flow rate and inlet bubble diameter of 2 mm).

Figure 4.6 presents the results of twelve simulations corresponding to various design options in a single graph. Symbols refer to the reactor diameter, colours to the reactor volume and numbers indicate the corresponding reactor height. It shows that reactor productivity and gas outlet purity in % of methane are mutually exclusive: high productivity is associated with low purity and vice versa. Three important insights can be drawn from Figure 4.6.

→ For a given reactor diameter D_r (same symbols) and for the same molar gas flowrate imposed at the inlet, the higher the reactor, the higher the purity but the lower the productivity.

This can be understood as follows. The higher the reactor, the longer the gas residence time, leading to a larger mass transfer flux and a better H_2 conversion (mass of hydrogen transferred per mass of hydrogen supplied). More H_2 being transferred and more CH_4 being produced, the purity increases with the column height. The productivity is expressed as the outlet CH_4 flowrate per unit volume of

the reactor. It can be interpreted as the space yield. Higher H_2 conversion is achieved in a tall reactor but the increase in hydrogen conversion is not linear with the increase of the reactor height (whilst the increase in volume is). As a result, the productivity decreases with reactor height H at constant D_r and constant inlet gas flow rate.

→ For a given reactor height H, the smaller the column diameter D_r, the higher the productivity but no effect is observed on the purity. This is because H_2 conversion essentially depends on the gas residence time only.

If we now take a look at a group of points labelled with the same number, we examine the effect of changing the reactor volume while keeping the height constant. Increasing the column diameter at constant height does not, or marginally affects the off-gas purity. In contrast, the productivity increases as the reactor diameter is decreased (from left to right).

The model proved that the mass transfer is not affected by the column diameter. The model does not incorporate any major effect of column's diameter on mass transfer. The underlying hypothesis is that the generation of bubbles of the same given size is accessible whatever the reactor diameter (in the ranged covered here). Besides, the H/D_r ratios simulated here fulfil the criteria for scale-up of bubble columns (Sasaki et al., 2017; Wilkinson et al., 1992). Sasaki et al. (2017) provided an updated version for the scale-up criteria of bubble column previously proposed by Wilkinson et al. (1992). Sasaki et al. (2017) stated that the effects of D_r and H on the gas holdup are negligible when scaling up from small to large bubble columns, provided that gas holdup in the small columns are obtained for D_r > 200 mm and H > 2200 mm. The hydrodynamics can thus be expected to be similar to that of a small column.

In Chapter 6, analytical solutions are developed for predicting biological methanation performance. It is found that the CH_4 purity depends essentially on the hydrogen conversion which itself is a function of mass transfer rate. The higher the column, the longer the gas residence time, the higher the hydrogen conversion, hence the higher the CH_4 purity.

→ For D_r = 0.3m (filled circles), an asymptote in methane purity (around 70%) is reached when the column is increased beyond 6 m.

This result is not surprising as the H_2:CO_2 ratio injected is not in stoichiometric conditions. Therefore, the reaction could be limited by CO_2. A simple theoretical mass balance calculation can derive the expected maximum CH_4 fraction, as shown in Table 4.1. Indeed, in the case of non-stoichiometric injection, an asymptotic CH_4 purity is reached due to the absence of bioreaction once CO_2 is exhausted.

Table 4.1: Stoichiometric table for the biological methanation reaction

Reaction	$4H_2 + CO_2 \rightarrow CH_4 + 2H_2O$			
$F_{i,in}$ (Nm^3/h)	10	2	3	-
$F_{i,out}$ (Nm^3/h)	2	0	5	-

Figure 4.7 reports the vertical concentration profiles of gaseous and dissolved species at the steady state and helps to understand the asymptotic behaviour in terms of CH_4 purity. The case presented hereafter corresponds to the 6-meter-high bubble column (black circled point in Figure 4.6). It is found that the CO_2 concentration in the gas phase approaches zero above 4.5 meters meaning that the total amount of CO_2 injected has transferred and reacted. When all the CO_2 gas is consumed, CO_2 gas-liquid mass transfer is halted, and no more CO_2 is dissolved in the liquid phase, consequently, the bio-catalysed CH_4 production ceases.

However, the mass transfer of hydrogen is still taking place. Thus, the H_2 liquid concentration, departs from zero, above z=4.5m, for it is no longer consumed by the biological reaction (bottom left graph). In the same upper zone of the column, the CH_4 liquid concentration drops as the CH_4 is desorbed to the gas phase. The H_2 injected in excess remains in the outlet stream and explains the 70% CH_4 purity.

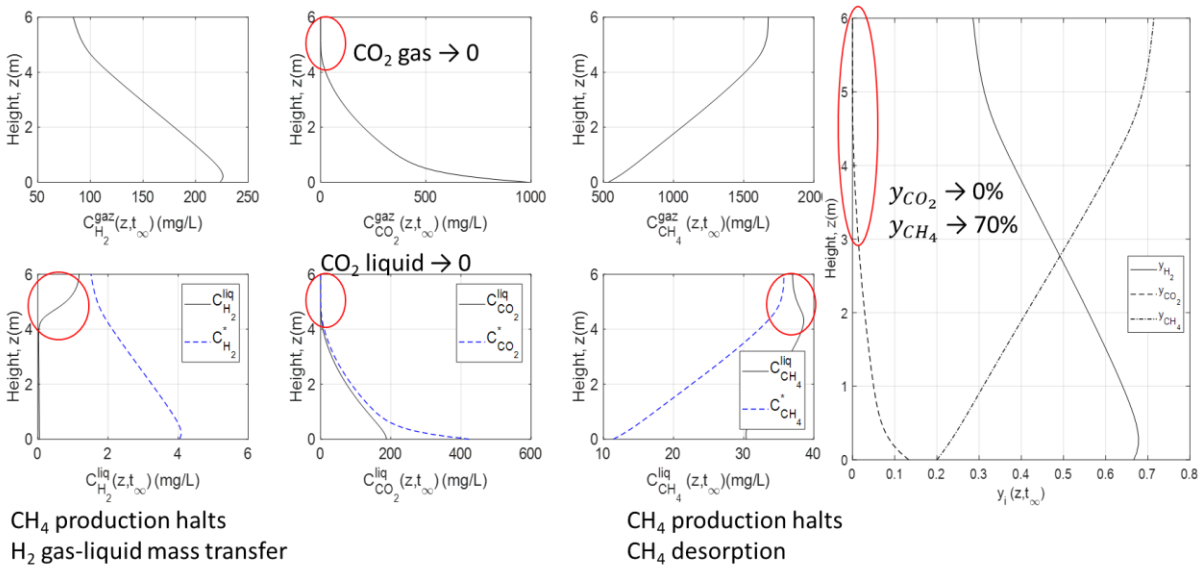

Figure 4.7: Local concentration vertical profiles (6 subgraphs on the left) and vertical profiles of molar fractions in the gas phase (right graph) at steady-state for D_r = 0.3m and H = 6m.

This case reveals the importance of H_2:CO_2 stoichiometric conditions at the inlet to ensure grid-quality biomethane at the outlet. A new set of simulations was conducted with the new inlet composition and the results are shown in Figure 4.8. When a 4:1 H_2:CO_2 ratio is imposed at the inlet (resulting in 8 Nm^3/h

of H_2, 2 Nm^3/h of CO_2, and 3 Nm^3/h of CH_4), the expected maximum purity is 95% and the corresponding productivity is 6.94 Nm^3/h. The related height would be 10 m. This point was not added to the graph to preserve readability. No asymptote is observed and the highest CH_4 purity reported is 84% for D_r = 0.3m and H = 7m.

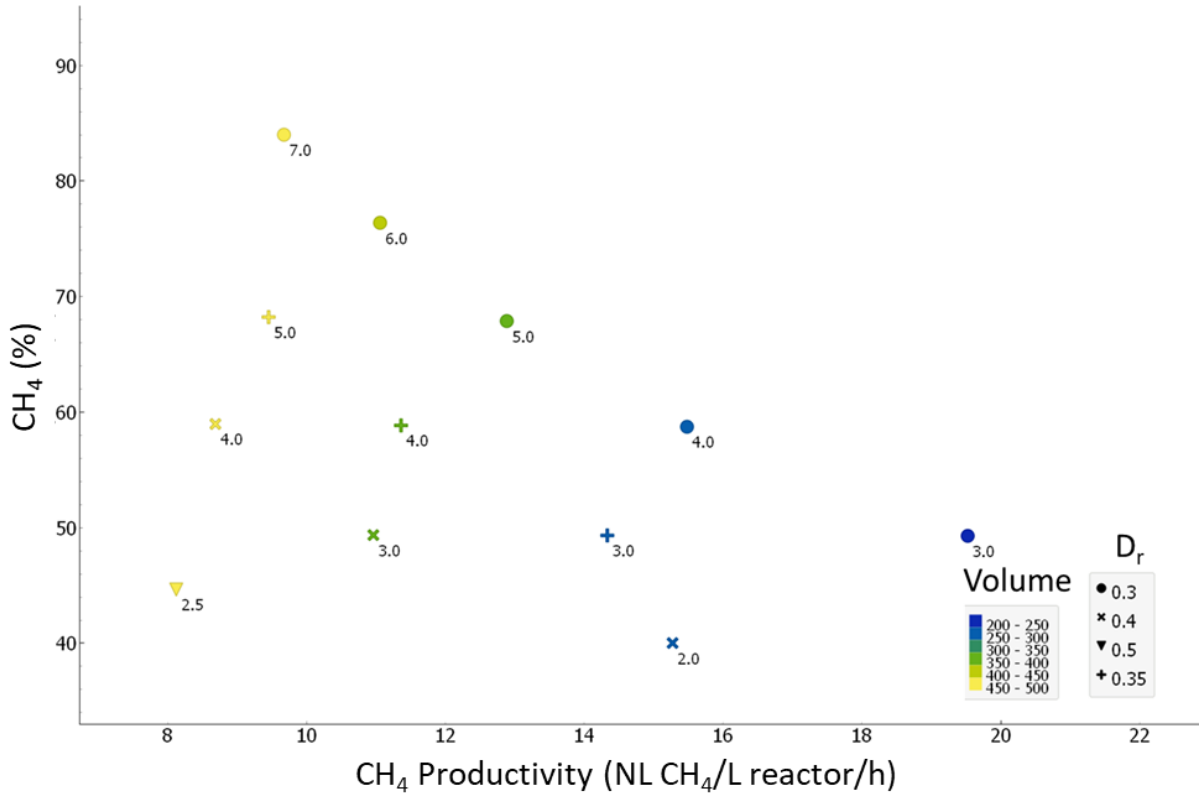

Figure 4.8: Biomethane quality and associated productivity at the bubble column outlet for different combination of H and D_r, with a H_2: CO_2 ratio of 4:1.

From these results, it can be concluded that a single pass bubble column without gas recirculation, at the given working conditions (P = 4 bar, T=55°C, d_b = 2 mm, V_{max} = 500 L, Q_G = 13 Nm^3/h) is not sufficient to reach a grid-quality CH_4 purity (CH_4% > 97%) at the outlet, as we are limited by the height of the column. It was not the case with the industrial biological methanation reactor of Electrochaea, whereby it is found by the 1D model that 95% CH_4 purity can be achieved in a 10-meter-high column (Ngu et al., 2022a).

4.2.1.2 Bubble column with gas recirculation

In order to increase the purity, the strategy of gas recirculation was set up with the view of improving the conversion of poorly soluble reactants (namely hydrogen in the present case). In order to comply with industrial and safety constraints of the production site (SOLIDIA), the reactor height is limited to 2 m and two reactor diameters are investigated (D_r = 0.54 and 0.34 m). These diameters are chosen as they correspond to the commercially available porous plate sparger, as used in the pilot-scale bubble column used by SYMBIOSE team. The gas recirculation flowrate $Q_{G,r}$ is varied from 0 to 40 Nm^3/h.

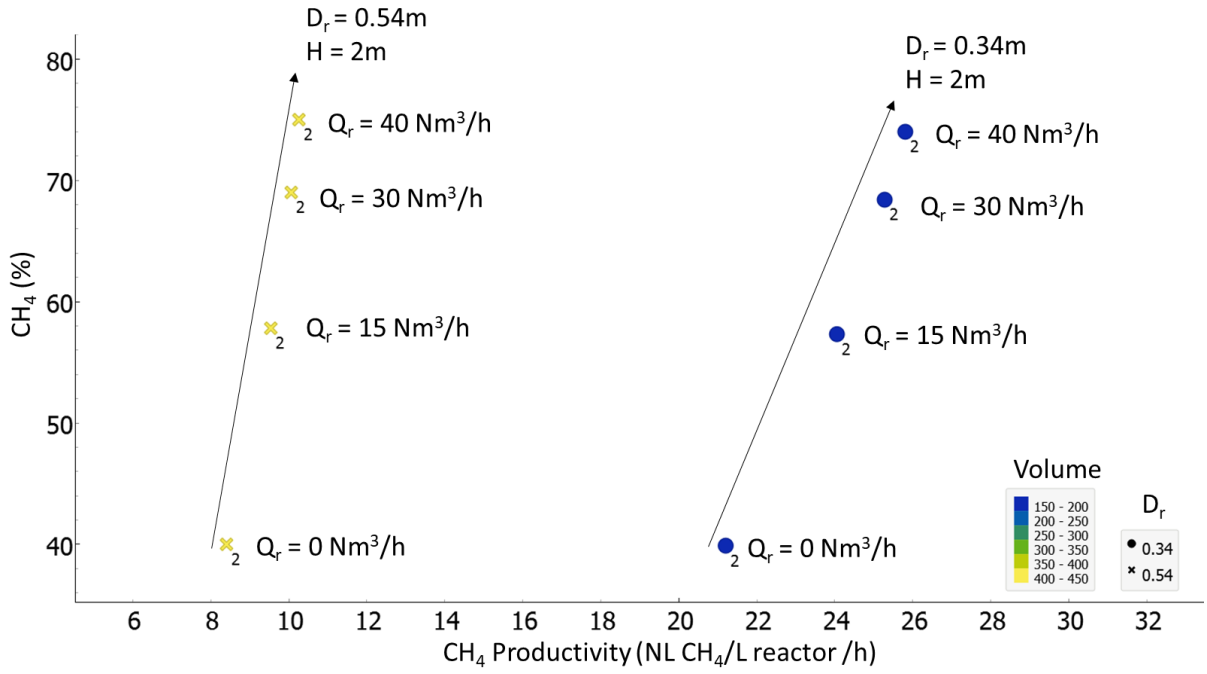

Figure 4.9: Biomethane quality and associated productivity at the bubble column outlet for two commercially-available diffuser size (D_r = 0.54 and 0.34 m). Constant inlet bubble size 2 mm

The new simulation with gas recirculation was conducted with a H_2: CO_2 ratio of 4:1 and a total inlet gas flowrate of 13 Nm^3/h. The results are shown in Figure 4.9 with the positive impact of gas recycling indicated by the arrows. In particular, the 2 m high bubble column with a diameter of 0.34 m reaches, without gas recycling, 40 % in purity and about 21 Nm^3 CH_4/L/h in productivity. When gas recycling is used, the performances reach 75 % purity and productivity of 26 Nm^3 CH_4/L/h. Here again, calculations are performed assuming a constant bubble diameter despite the 5-fold increase in gas flow rate.

The maximum purity is close to 80% for both diameters. This remains below the grid-quality standard when the height is limited to 2 m. The positive effect of gas recirculation is similar in terms of purity,

irrespective of the diameter whilst the effect on productivity is more pronounced for the smaller diameter. These results were used to orient the design of the bubble column reactor to be constructed at the SOLIDIA site.

To conclude the preliminary design of the demonstration plant, the column height H is limited to 2 m, and the reactor diameter D_r is taken as 0.34 m, resulting in a total volume of 180 L to treat 5 Nm^3/h of biogas. It is found that high H_2 and CO_2 molar flowrate at the inlet will lead to higher CH_4 productivity. However, higher productivity does not guarantee a higher conversion of substrates into CH_4, leading to a more dilute product. The reactor design and subsequently the hydrodynamics plays a key factor to achieve efficient biological methanation. It has been demonstrated by the 1D model that tall bubble columns ensure longer gas residence time and therefore a higher H_2 conversion, resulting in higher CH_4 purity. Unconverted H_2 at the outlet can be recycled to increase the mass transfer flux and thus the overall mass transfer efficiency to obtain a higher CH_4 purity. For the same molar flow rate of substrates in the inlet, gas recirculation is also highly beneficial to both purity and productivity. These claims are built upon the possibility to maintain the inlet bubble diameter in the millimetre range to ensure a high specific area for mass transfer. This could be done by deploying a fine sparger and adding a mechanical stirring device to prevent bubble coalescence that would appear mostly in the heterogeneous regime or gas fraction > 10%.

Table 4.2 summarises the overall gas holdup obtained for the majority of the simulations reported here. The overall gas holdup for all the cases remains below 6%, thus, the bubble column operates mostly in the homogeneous regime. This signifies that the coalescence phenomenon is limited and thus valid the constant bubble diameter assumption. It is proven experimentally that a homogeneous regime is critical to maintaining a high conversion rate due to improved hydrodynamics and mass transfer (Deckwer et al., 1974). Therefore, a fine and homogeneous sparger is recommended for the demonstration-scale biological methanation unit. During the writing of this manuscript, the demonstration unit at the SOLIDIA site is still under construction. The next study focuses on an industrial-scale biological methanation plant that is still in the preliminary planning stage.

Table 4.2: The overall gas holdup for different reactor design simulated in this section. Conditions: P = 4 bar, T=55°C, d_b = 2 mm, V_{max} = 500 L, Q_G = 13 Nm^3/h

D_r (m)	H (m)	Gas recirculation	$<\varepsilon_G>$ (%)
0.3	3	No	4.05
0.3	4	No	3.69
0.3	5	No	3.39
0.3	6	No	3.12
0.3	7	No	2.89
0.4	2	No	2.5
0.4	3	No	2.27
0.4	4	No	2.06
0.5	2.5	No	1.52
0.34	2	Yes (40 Nm^3/h)	6.39
0.54	2	Yes (40 Nm^3/h)	2.52

4.2.2 Case study on the effect of pressure using the 1D model

As mentioned in Section 4.1.4, the pressure effect is studied using the 1D model. Figure 4.10 shows that for the same molar flowrate (at a constant normalised gas flowrate, recall that Q_G = 13 Nm^3/h comprised of 8 Nm^3/h H_2, 2 Nm^3/h CO_2 and 3 Nm^3/h CH_4) a pressure increase has little effect on the productivity and the purity. Certainly, the solubility of gases increases with pressure, but this positive effect is counterbalanced by a lower gas fraction (and thus lower $k_L a$) due to gas compression. This is in line with the conclusion of Maalej et al. (2003). The quantitative results explaining the observed phenomena can be found in Table 4.3. It should be mentioned that the bubble diameter is kept constant when comparing the two pressures. Since the bubble size is controlled by the pressure drop through the porous plate rather than the absolute pressure itself, this assumption is justified.

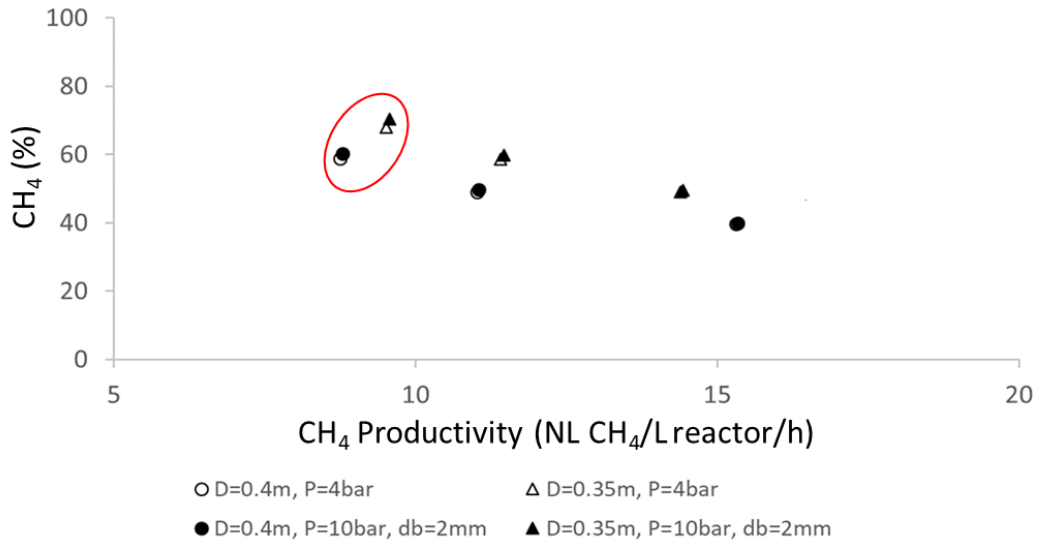

Figure 4.10: Effect of pressure on the reactor performance. The detailed quantitative data in Table 4.3 correspond to the red circled points.

Table 4.3 shows that the ratio of $k_L a|_{10bar}$ to $k_L a|_{4bar}$ is equivalent to the ratio of pressure. The pressure does have a positive impact on the gas solubility. But, the H_2 mass transfer flux, which is the product of both $k_L a$ and the concentration gradient $(C^* - C_L)$ increases only slightly when the pressure increases from 4 to 10 bar, leading to an insignificant increase in the mass transfer efficiency and thus contributes only to a very marginal increase in the CH_4 purity. It is important to emphasise that the results given in Figure 4.10 and Table 4.3 are obtained by the 1D model developed in the homogeneous bubbly flow regime without considering bubble coalescence and breakup, justified here as the overall gas holdup is less than 2.5%.

Table 4.3: Pressure effect for the data presented with the red circled points in Figure 4.10.

D_r (m)	0.35	0.35	0.4	0.4
H (m)	5	5	4	4
Pressure (bar)	4	10	4	10
Outlet CH_4 (%)	67.98	70.27	58.73	60.23
Productivity (NL/L/h)	9.51	9.57	8.74	8.79
$Q_{G,out}$ (Nm^3/h)	6.73	6.55	7.48	7.33
$Q_{G,CH_4 out}$(Nm^3/h)	4.57	4.60	4.39	4.42
$< \varepsilon_G >$ (%)	2.47	1.00	2.06	0.83
$< a >$ (m^2/m^3)	83	34	68	28
$< k_L a >$ (h^{-1})	**443**	**185**	**357**	**148**
$< C^*_{H_2} >$ (mg/L)	**2.58**	**6.25**	**2.74**	**6.67**
Hydrogen molar transfer flux T_{H_2} (mol/s)	0.077	0.078	0.068	0.069
Hydrogen conversion	0.778	0.787	0.689	0.696

4.2.3 Brief conclusion on the pressure effect on the biological methanation

Several experimental works in the literature claimed that high-pressure system in biological methanation reactor is beneficial to CH_4 purity and productivity (Martin et al., 2013; Seifert et al., 2014). However, our 1D model does not reflect this trend, as shown in the case study in Section 4.2.2. In this section, the effect of pressure on biological methanation is discussed thoroughly. First, the results from the literature which concluded on a positive effect of pressure are discussed.

Martin et al. (2013) conducted an ex-situ biogas upgrading in a 3.5 L CSTR. The effect of pressure on methane purity was not reported. But, they observed that higher pressure leads to higher productivity and higher H_2 conversion efficiency (Figure 3 of the cited paper). However, the experiment was not conducted at the same **inlet molar flowrate.** Seifert et al. (2014) studied the effect of pressure in a 10 L CSTR. It is reported that methane purity and productivity increase with pressure (see Figure 4 of the cited paper). Again, the experiments were not conducted at the same **inlet molar flowrate**.

It is then crucial to ensure the consistent use of inlet molar flowrate to investigate the pressure effect. Without this condition, no direct comparison can be done in terms of the same quantity of gas to be treated. In fact, increasing the pressure at a constant inlet gas flowrate will cause an increase in inlet molar flowrate (ideal gas law). It has been reported in the literature that productivity increases systematically with inlet hydrogen gas feed (Bassani et al., 2016; Kougias et al., 2017; Rafrafi et al., 2019; Voelklein et al., 2019). In terms of methane purity, the positive effect of pressure remains sceptical.

Nevertheless, it is reported that high pressure is beneficial in retarding the appearance of the heterogeneous regime by having a higher transition superficial gas velocity (Clark, 1990; Wilkinson, 1991). High pressure allows for delivering a higher flowrate per section of the column. Therefore, it is vital for industrial applications to operate bubble columns under pressure to treat a higher quantity of gas for example. However, the reasons for that are more related to the hydrodynamics of multiphase flow (the possibility to maintain the homogeneous flow regime at high gas flow rate) than to thermodynamic aspects (increases solubility).

4.2.4 Industrial plant

It is also planned to install a large-scale biological methanation plant in the Occitanie region, Toulouse, France. A driving reason to install this industrial biological methanation plant is to reach 100% renewable biogas in the natural gas grid. The plant will be integrated with a wastewater treatment plant (WWTP), an anaerobic digestor, renewable energy sources, and the natural gas grid. The process flow diagram is presented in Figure 4.11.

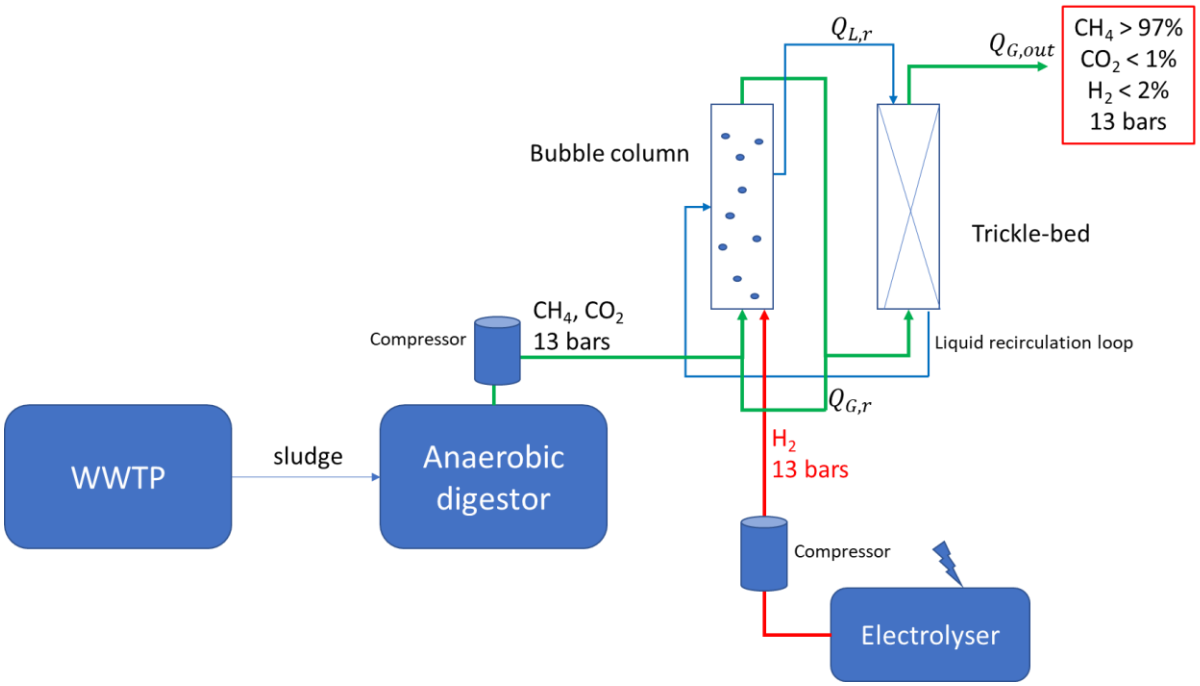

Figure 4.11: Process flow diagram of the integrated biological methanation plant. Green arrows: Gas flow, Blue arrows: liquid flow: Red arrows: hydrogen from electrolyser

The objective is to upgrade biogas from the anaerobic digestor (from 60% to grid-quality 97% CH_4 purity) and to increase biomethane production through a series of a bubble column and a trickle-bed reactor. Our mandate is to provide a preliminary study of the optimal reactor dimension. The specifications of the process are as follows:

- The biogas exits the anaerobic digestor at a flowrate of 85 Nm^3/h.
- The typical biogas composition can be simplified to 60% CH_4 and 40% CO_2, corresponding to a flowrate of CH_4 and CO_2 of 51 Nm^3/h and 34 Nm^3/h, respectively.
- Imposing a 4:1 ratio of H_2:CO_2, the requirement for H_2 flowrate is 136 Nm^3/h. Subsequently, the total gas flowrate entering the bubble column (without gas recirculation) is 221 Nm^3/h, with a composition of $y_{H_2} = 0.62$, $y_{CO_2} = 0.15$, and $y_{CH_4} = 0.23$.

- Both reactors are expected to operate at 13 bars and 55°C.

The liquid loop between the bubble column and the trickle-bed is required to provide nutrients to the biofilm which develops on the packing material. The gas recirculation, back to the bubble column is optional. The dimensions of the column (height H, diameter D_r), liquid and gas recirculation flowrate are treated as the unknowns of the problem. First, the bubble column bioreactor performance without gas recirculation is analysed to provide a point of comparison. The same closures as the previous study is used for the 1D model.

4.2.4.1 Bubble column reactor

We first attempted to estimate the possible bubble diameter formed in the industrial-scale bioreactor. As the bubble column operates under high pressure (13 bars), the correlation of (Wilkinson et al., 1994), as written in equation (4.8) is used. It is valid for P up to 15 bars and developed for a perforated ring sparger.

$$d_b = \left(\frac{8.8\sigma}{\rho_L g}\right)^{0.5} \cdot \left(\frac{j_G \mu_L}{\sigma}\right)^{-0.04} \cdot \left(\frac{\sigma^3 \rho_L}{g \mu_L^4}\right)^{-0.12} \cdot \left(\frac{\rho_L}{\rho_G}\right)^{0.22} \tag{4.8}$$

Using the specifications given and using the physical property of water, the correlation yields a bubble diameter of 4 mm. We first attempted to use an initial bubble diameter d_{b0} of 3 and 4 mm (the reference case) to design the bubble column.

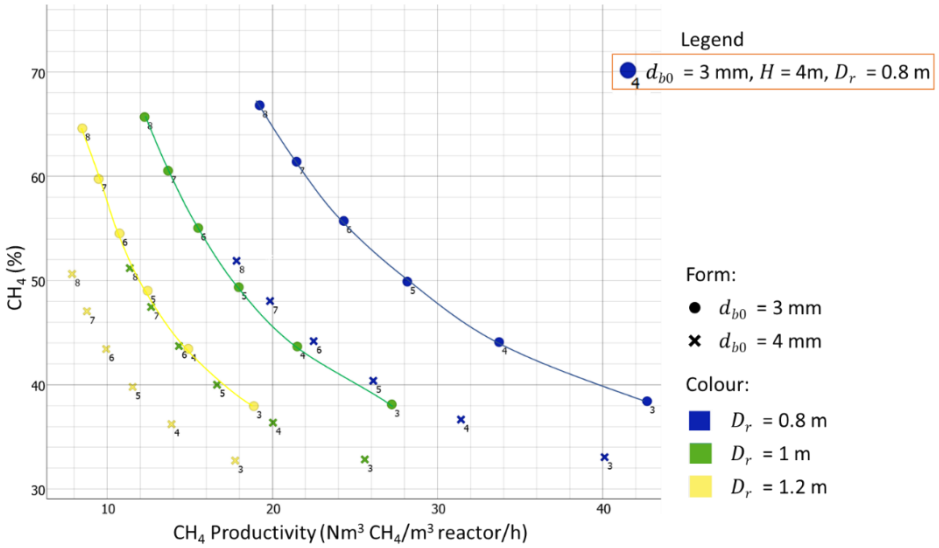

Figure 4.12: Biomethane quality at the bubble column outlet and associated productivity for different bubble diameter, reactor diameters, and column height (without gas recycling).

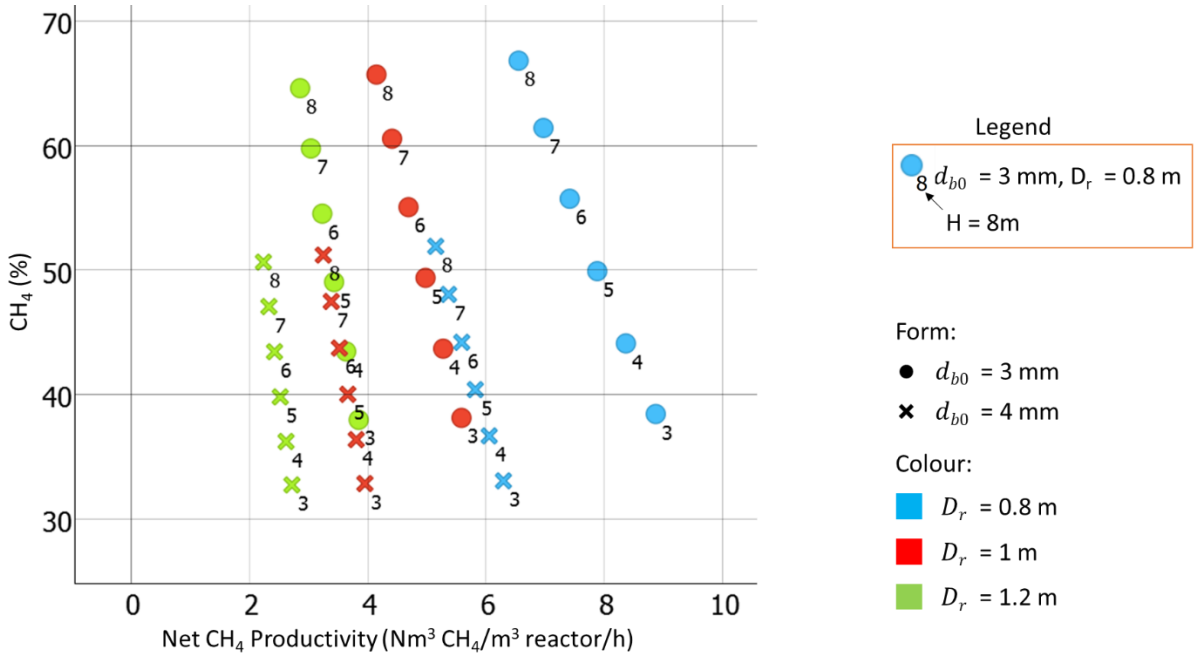

Figure 4.13: Biomethane quality at the bubble column outlet and the net productivity for different bubble diameter, reactor diameters, and column height (without gas recycling).

Figure 4.12 shows the CH_4 fraction plot against the total CH_4 flowrate per unit volume of the reactor (total productivity). Figure 4.13 reports the CH_4 fraction plot against the flowrate of the net CH_4 produced per unit volume of the reactor (net productivity). The net productivity is expressed as the net CH_4 produced by the biological methanation reactor excluding the initial 51 Nm^3/h of CH_4 issued from the anaerobic digestor.

The results show that the CH_4 purity is directly related to the column height and depends strongly on the bubble size.

- For a bubble diameter of **4 mm**, a height increment of 1 m increases the CH_4 content of the gas phase by 3.5%. Thus, the inlet biomethane of 23% is upgraded roughly to 33.5% and 51% for a column height of 3 m and 8 m, respectively. The outlet and inlet methane purity and the column height are linked through the following linear relationship

$$\%_{CH_4,out} \approx \%_{CH_4,in} + 3.5\,H \tag{4.9}$$

- For a bubble diameter of **3 mm**, a height increment of 1 m increases the CH_4 content by 5.5%. Thus, the inlet biomethane of 23% is improved approximately to 39.5% and 67% for a column height of 3 m and 8 m, respectively.

$$\%_{CH_4,out} \approx \%_{CH_4,in} + 5.5\,H \tag{4.10}$$

- A more general correlation relating the outlet and inlet methane purity with the column height in meters and the bubble diameter in mm can be expressed as

$$\%_{CH_4,out} \approx \%_{CH_4,in} + 15\frac{H}{d_b} \tag{4.11}$$

Considering the major effect of bubble size on hydrogen transfer performance, special attention must be paid to the biogas distribution system at the bottom of the column.

In general, the productivity decreases with reactor height and diameter. This is due to the productivity being inversely proportional to the reactor volume. As discussed previously, the productivity can be translated as a volumetric yield. However, it has been shown that a high column is necessary to achieve high CH_4 methane due to longer gas residence time. It is also advisable not to choose a column that is too narrow as it increases the risk of coalescence.

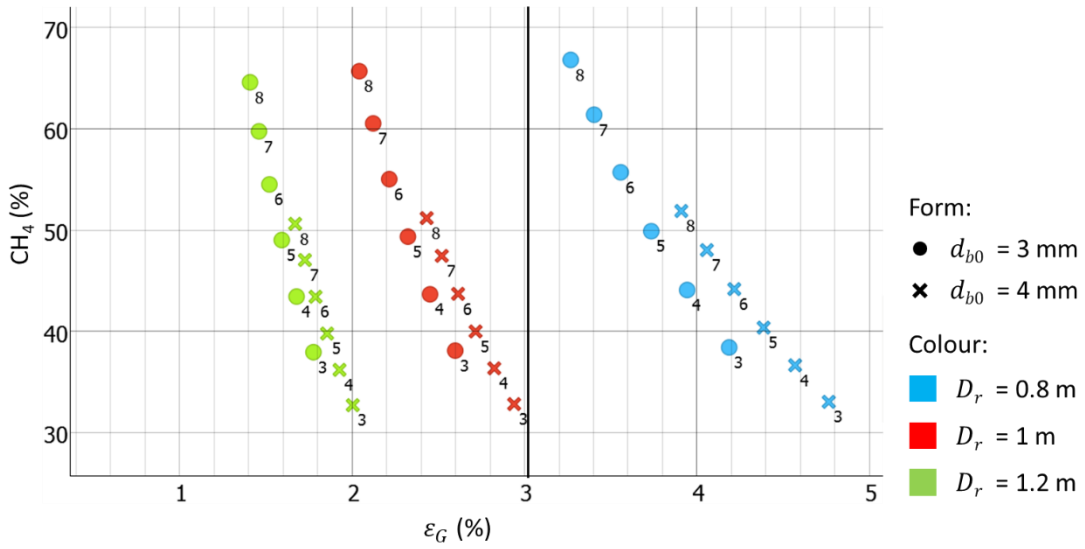

Figure 4.14: Biomethane quality and gas holdup for different bubble diameter, reactor diameters, and column height (without gas recycling).

Figure 4.14 shows that if the upper limit of the gas holdup is 3%, a wider bubble column such as D_r = 1 m should be chosen. The larger the column diameter, for the same inlet gas molar flowrate, the lower the gas holdup. It also shows that for the same column diameter, the higher the column, the lower the

gas holdup. As the inlet gas molar flowrate is conserved, higher hydrostatic pressure leads to higher gas compression, lower superficial gas velocity, and hence lower gas holdup.

In the absence of gas recycling, the bubble column of 1 m in diameter and 8 m in height with a bubble diameter of 4 mm delivers biomethane at a purity of 50% with a net productivity of 3.2 $Nm^3/m^3/h$ or a total productivity of 11.4 $Nm^3/m^3/h$. This gives an estimated total gas flowrate at the outlet of 150 Nm^3/h after round off.

Considering a large amount of hydrogen remaining at the top of the column for the 4 mm bubbles case, it is attempted to set up a recycling loop of the outlet gas to increase the conversion rate of the gaseous reactants.

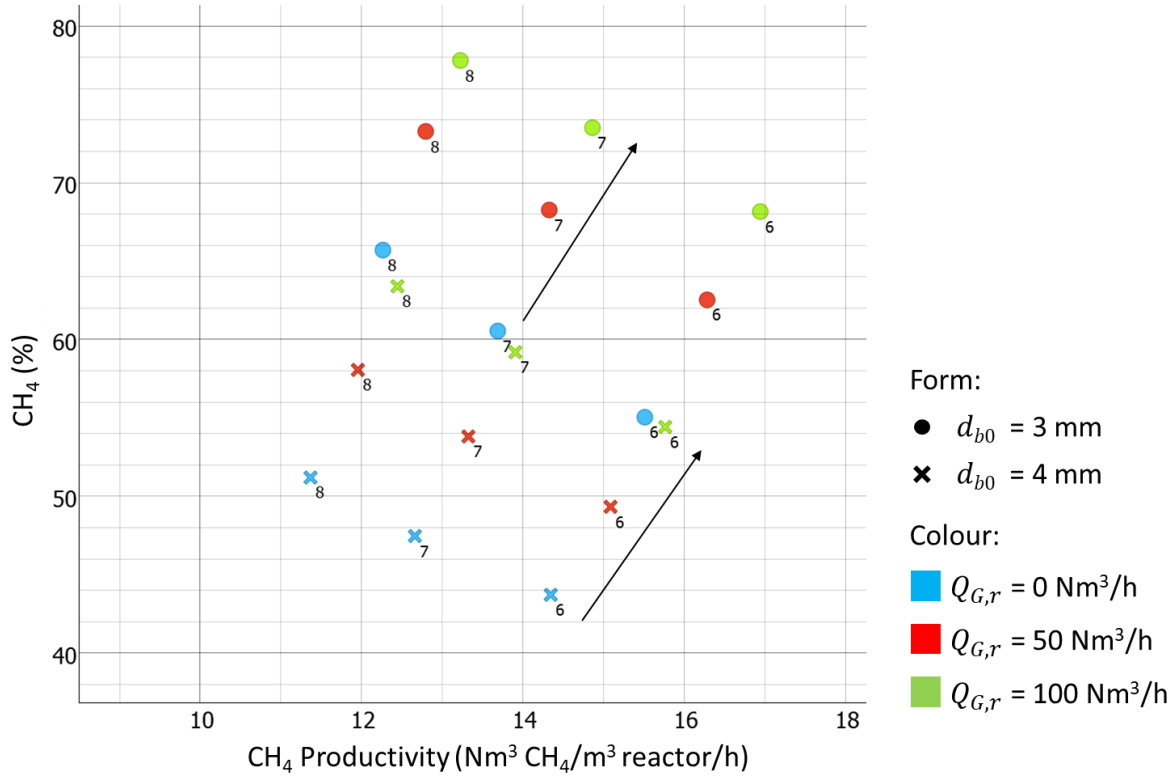

Figure 4.15: Biomethane quality at the bubble column outlet and associated productivity for different bubble diameter, reactor diameters, and column height. Impact of the recycled gas flow rate

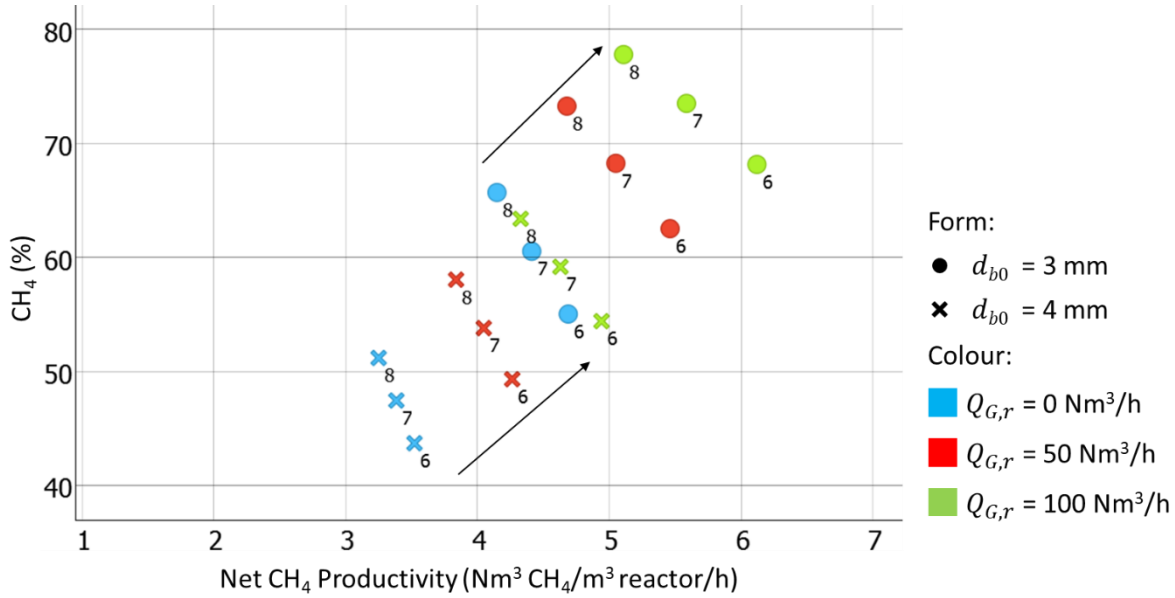

Figure 4.16: Biomethane quality and the net productivity at the bubble column outlet for different bubble diameter, reactor diameters, and column height. Impact of the recycled gas flow rate

Figure 4.15 and Figure 4.16 present the results for different gas recycling flowrates for total productivity and net productivity, respectively. In particular, the blue points correspond to the absence of gas recycling and thus are identical to the previous results reported in Figure 4.12 and Figure 4.13. The gas recirculation allows increasing significantly the CH_4 purity and productivity, as highlighted by the arrows. In terms of productivity gain, recycling the outlet gas is more advantageous for smaller bubbles. With the 1D model, it is interesting to report the local gas concentration and molar fraction profiles, as shown in Figure 4.17.

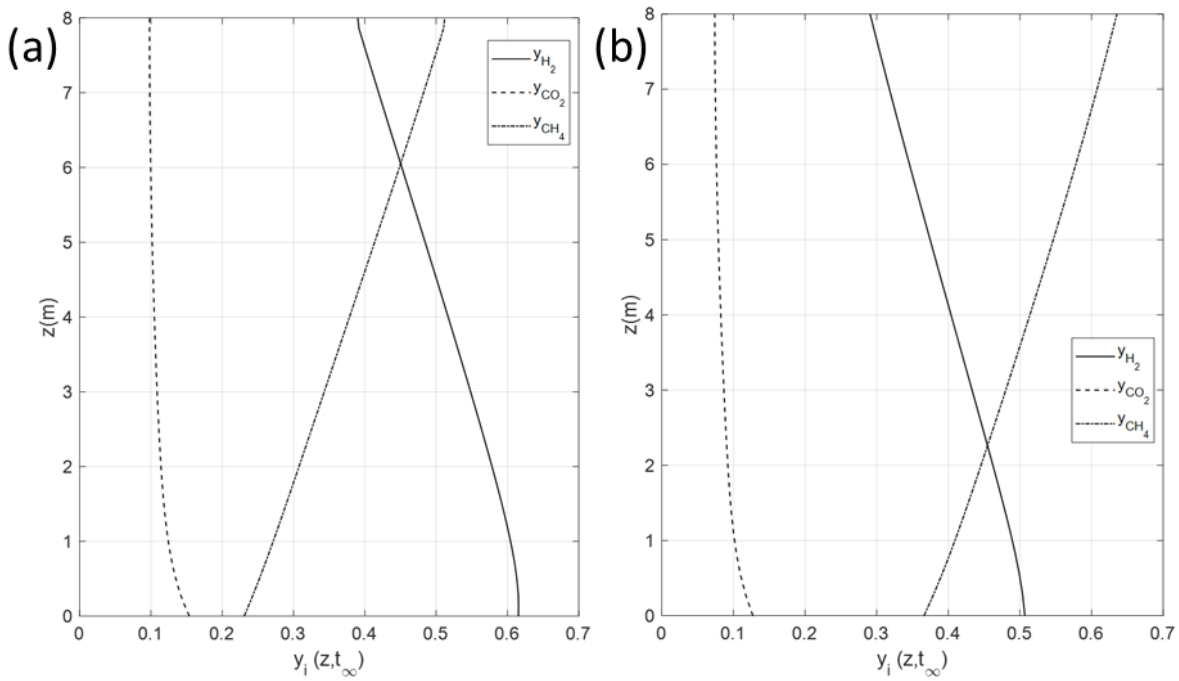

Figure 4.17: Vertical profiles of gas molar fraction in an 8-meter-high column (a) without or (b) with gas recycling

It is shown that CH_4 purity improves from roughly 50% to 63% with gas recycling. The substrate conversion is also improved as the H_2 and CO_2 outlet content drop from 39% to 29% and 10% to 8%, respectively. For a bubble diameter of 4 mm, the CH_4 purity increases by 6% for every 50 Nm^3/h of gas recycled. A correlation relating the outlet and inlet methane purity with the column height in meters, the bubble diameter in mm, and the gas recirculation flowrate in Nm^3/h can be written as

$$\%_{CH_4,out} \approx \%_{CH_4,in} + 15\frac{H}{d_b} + \frac{6}{50}Q_{G,r} \tag{4.12}$$

In general, the increase of the total gas feed is a priori detrimental to maintaining the mass transfer performance in optimal conditions. A high gas flow leads to an increase in the gas holdup, and thus favours the probability of bubble coalescence. However, as the whole operates under high pressure, it is possible to increase the gas flow in the column while maintaining a gas holdup lower than 5% due to gas compression. It is found that the overall gas holdup for all simulations was below 5% due to high pressure applied to the system (13 bar).

Based on the results obtained with the 4 mm bubble diameter, we recommended a column dimension of 1 m diameter (minimum) and 8 m height (to extend gas residence time) in the presence of gas recirculation. This allows achieving a purity of 64% at 12.5 $Nm^3/m^3/h$ total productivity before entering

the second bioreactor for further upgrading. The total gas flowrate at the outlet is thus estimated as 120 $Nm^3/m^3/h$. The gas recirculation allows an increase of 13% in CH_4 purity in comparison with the case without gas recirculation.

4.2.4.2 Trickle-bed reactor in series with the bubble column reactor

The trickle-bed reactor allows finalisation of the hydrogen conversion and thus increases the CH_4 purity (less than 3% hydrogen). The column operates in counter-current mode: the gas from the bubble column is injected at the bottom of the trickle-bed and the liquid is sprayed on the top and flows over the packing material. The characteristics of the packing material chosen is a 1-inch plastic PALL ring with a specific surface area of 207 $m^2.m^{-3}$. Interestingly, from a modelling point of view, the trickle-bed reactor can also be described using a 1D model. A counter-current circulation of phases has to be considered and the change in the volume fraction of the gas and liquid phase discarded (in contrast to the bubble column in which mass transfer and pressure effects modify the local gas holdup)

It is essential to know that the packing material is in relation to the column diameter and linked directly to the sizing constraints. The operating pressure is 13 bars, as in the bubble column. The liquid is recirculated at a flow rate between 50 and 100 m^3/h to wet ensure complete wetting of the packing material. The liquid wetting is vital for the gas-liquid mass transfer; thus, it must be ensured a sufficient wetted interfacial area (minimum 50%). The total gas flowrate is 150 Nm^3/h with a purity of 64%, which corresponds to the outlet gas flowrate of the designed bubble column ($H = 8$ m, $D_r = 1$ m, and $d_{b0} = 4$ mm). If the gas recycling is absent, the flowrate entering the trickle bed is reduced to 120 Nm^3/h and the CH_4 purity set to 50%. The trickle-bed reactor design is thus performed with or without gas recycling, and considering a minimum liquid flowrate of 50 m^3/h and a maximum liquid flowrate of 100 m^3/h. The sizing of the trickled bed is based on empirical correlations and global material balances (Copigneaux, 1993). Compared to the sizing of the bubble column obtained through the 1D model, the sizing of the trickle bed remains a global estimation. Nevertheless, the results serve as an initial approach for further work on developing numerical models for trickle bed reactors.

With the presence of gas recycling in the bubble column, the minimum dimension for the trickle-bed reactor is 2 m in diameter and 6 m in height to reach a CH_4 purity of 97% and the corresonding CH_4 production is 85 Nm^3/h with a liquid flowrate of 50 m^3/h. Without gas recycling in the bubble column, the dimension for the trickle-bed reactor is 2 m in diameter and 8 m in height to achieve the same performance. However, the liquid recirculation flowrate is increased from 50 m^3/h to 100 m^3/h.

To conclude the sizing of the industrial biological methanation plant, the optimal choice for the first bubble column reactor with a bubble size of 4 mm is to choose a minimum $D_r = 1$ m and $H = 8$ m, associated with a gas recirculation flowrate of $Q_{G,r} = 100$ Nm^3/h to achieve a CH_4 purity of 65% (only 50% without gas recirculation). The optimal choice for the second trickle-bed reactor with plastic PALL ring packing is to choose a column of $D_r = 2$ m and $H = 6$ m to achieve a final CH_4 purity of 97% (from 65% issued from the bubble column) and a CH_4 production of 85 Nm^3/h, with the liquid recirculation flowrate of $Q_{L,r} = 50$ m^3/h. The better biogas upgrading of the trickle bed reactor comes from a superior interfacial area as $a_{trickle\ bed}$ = 207 m^2.m^{-3} > $a_{bubble\ column}$ = 60 m^2.m^{-3}.

4.2.5 General conclusion on biological methanation scale-up study

Through examples given in Sections 4.2.1 and 4.2.2, it is obvious that the 1D model can be used as a practical tool for defining a rational scale-up strategy for biological methanation. Through this exercise, it is found that the reactor height has a vital impact on the bioreactor performance. High purity can be achieved in high H/D_r bubble columns to the detriment of productivity. The CH_4 purity evolves linearly with the reactor height. Next, the reactor diameter has a limited effect on the CH_4 purity. Nevertheless, for a certain gas molar flowrate, the smaller the column diameter, the higher the gas fraction to be injected per unit of column section. This heightens the concern of bubble coalescence which is detrimental to the mass transfer and hence the conversion. For a bioprocess that is strongly limited by hydrogen solubility, it is necessary to provide a high volumetric interfacial area for mass transfer.

Several experimental works reported on the positive pressure effect of biological methanation have been conducted using a non-constant mass flow rate (Martin et al., 2013; Seifert et al., 2014). Nevertheless, a considerable number of studies about the pressure effect in bubble columns (notably on hydrodynamics) have been reported in the literature. It is found that the positive pressure effect depends on the superficial gas velocity and the sparger design. If an orifice-type sparger is used, the bubble diameter decreases clearly with the pressure. It is also revealed that a negative pressure effect only prevails in the heterogeneous regime (high superficial gas velocity) as it promotes bubble breakage, leading to lower bubble size and higher gas holdup, and hence, stabilising the bubbly flow regime even at high flowrate. Whereas the biological methanation operates mostly in the homogeneous regime at low superficial gas velocity. Using the 1D model, it is found that at the same inlet molar flowrate, the higher the pressure, the higher the C^* but the lower the $k_L a$.

4.3 Substrate gradients in large-scale fermenters

In this section, the 1D model is applied to study large-scale bioreactors used for the baker's yeast fermentation process. In large-scale fermenters, the timescale associated with the glucose uptake is similar to the mixing timescale. As a result, non-ideal mixing in industrial bioprocesses leads to substrate gradients, resulting in by-product formation and yield loss. Whereas on the laboratory scale, the bioprocess has excellent yield due to a well-mixed environment under perfectly controlled conditions (Enfors et al., 2001; Haringa et al., 2016; Morchain, 2017). In the presence of substrate gradients, the microorganism experiences strong temporal variations in the extra-cellular substrate concentration along the cell trajectory. These variations may have an effect on their metabolism, which continuously needs to adapt to variations in substrate availability (Haringa et al., 2017). Other than substrate gradients, the microorganism may also experience gradients in dissolved oxygen, pH, and temperature. In the past, an array of researches on substrate gradients had been performed using the CFD framework (Delvigne et al., 2006; Haringa et al., 2017, 2016; Lapin et al., 2006, 2004; McClure et al., 2016a; Morchain et al., 2014; Nadal-Rey et al., 2021b, 2021a; Sarkizi Shams Hajian et al., 2020; Wright et al., 2018). In this subject, most of the CFD model is based on a well-documented reference case: a 22 m^3 industrial fermenter with extensive published experimental data and numerical results (Enfors et al., 2001; Larsson et al., 1996; Vrábel et al., 2001, 2000, 1999). It is shown that the CFD model provides detailed insight into the fermentation environment. In particular, Lapin et al. (2006, 2004) developed the Euler-Lagrange approach, whereby the microorganisms are tracked through their lifelines in a transient manner. The lifeline analysis records the duration and magnitude of substrate concentration variation experienced by the microorganisms. These approaches require a large number of particles to be tracked to ensure statistical convergence. Consequently, the computational cost is very high. Another CFD approach is the use of the Euler-Euler approach to predict substrate and product gradients, as shown in the work of Sarkizi Shams Hajian et al. (2020). In that work, an unstructured metabolic model is coupled to the CFD model to study by-product formation in a 22 m^3 fermenter. In the next section, a comparison of the 1D model predictions with the CFD results from Sarkizi Shams Hajian et al. (2020) is presented and a critical analysis of the case is discussed.

4.3.1 Brief description of the CFD based study

Sarkizi Shams Hajian et al. (2020) conducted a 3D CFD simulation based on Euler-Euler RANS two-fluid model. Figure 4.18 shows the geometry of the fermenter simulated with the CFD model. The mesh consisted of approximately 2.5 million hexahedron cells. The turbulence was modelled as realizable $k-\epsilon$. The concentration of chemical species, namely glucose, O_2, CO_2, and ethanol was modelled in the gas (O_2 and CO_2 only) and liquid phase. The physical properties of water were considered for the liquid phase. The gas phase was assumed to follow the ideal gas law with a constant bubble diameter of 9 mm. The drag model of Grace from Clift et al. (1978) was used with a swarm factor set to -1.2. Assuming zero liquid velocity for closed bubble column, the slip velocity at 9 mm is calculated as 0.206 $m.s^{-1}$. No additional bubble interface forces are considered. The operating pressure was set to 130 710 Pa close to the boundary and the operating density was set to zero. The temperature is mentioned to be 30°C. The operating conditions for the simulation case are summarised in Table 4.4. The biomass is not solved but instead assumed as a constant value. Two values of biomass concentration ($X = 10$ $g.L^{-1}$ and $X = 25$ $g.L^{-1}$) were considered to investigate the impact of the substrate gradients magnitude on the bioreactions.

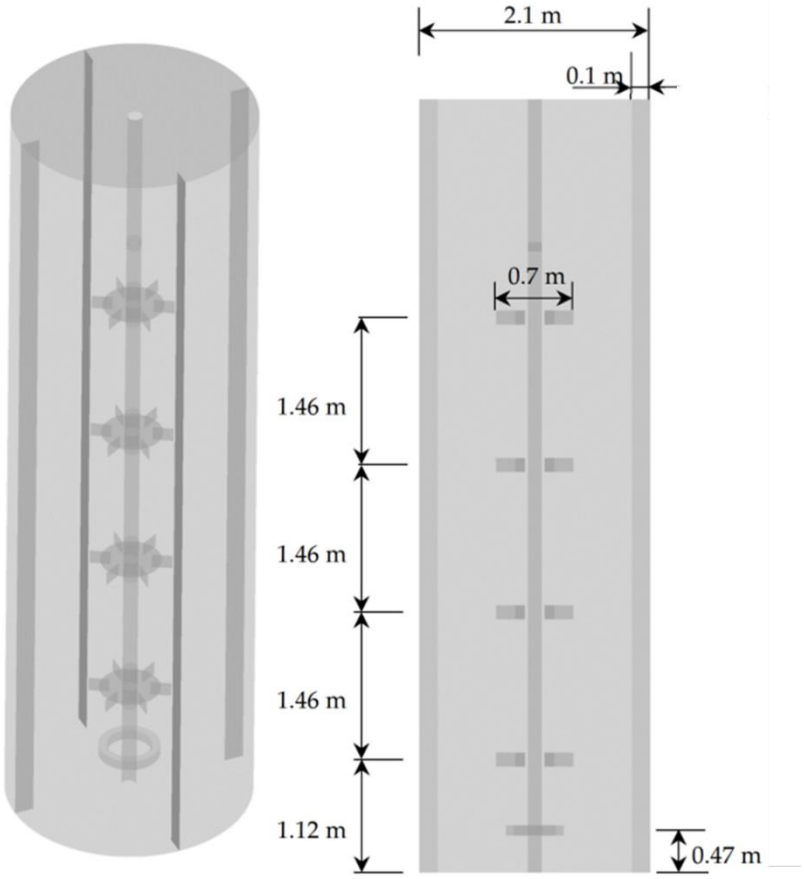

Figure 4.18: Geometry of the 22 m^3 fermenter studied by Sarkizi Shams Hajian et al. (2020)

Table 4.4: Operating conditions set up in the CFD simulation of Sarkizi Shams Hajian et al. (2020)

Operating parameters	Description
Primary phase (water)	$\rho_L = 1000$ kg.m^{-3}, $\mu_L = 0.001$ Pa.s
Secondary phase (air)	$\rho_G = 1.225$ kg.m^{-3} Ideal gas law $d_b = 0.009$ m
Interphase forces	Drag force only: Grace & Swarm coefficient -1.2
Aeration rate	0.231 kg.s^{-1}
Headspace pressure	130 710 Pa
Agitation rate	2.22 s^{-1}
Glucose feed	52 kg.h^{-1}

4.3.2 Biological model

The biokinetics model followed the *Saccharomyces cerevisiae* fermentation model proposed by Sonnleitner and Käppeli (1986). Glucose is served as the main substrate whereas ethanol can be considered as a substrate or a product depending on the environmental conditions. The model assumes the yeast respiratory capacity as the key metabolic bottleneck. If the glucose uptake exceeds the respiratory limits, the remaining electrons are channelled via reductive pathways, leading to the secretion of ethanol, commonly called as overflow mechanism. The model also allows ethanol uptake under aerobic conditions (if oxygen is in excess after glucose uptake). Under anaerobic condition, ethanol is the dominant product. Thus, the metabolic is divided into:

- Aerobic growth on glucose (indexed sae)
- Aerobic growth on ethanol (indexed san)
- Anaerobic growth of glucose (indexed eae)

The uptake rate of the substrates are assumed to follow Monod-type kinetics (Monod, 1950):

Glucose $$q_s = q_s^{max} \frac{C_s}{K_s + C_s} \quad (4.13)$$

Oxygen $$q_o = q_o^{max} \frac{C_o}{K_o + C_o} \quad (4.14)$$

Ethanol $$q_e = q_e^{max} \frac{C_e}{K_e + C_e} \quad (4.15)$$

To differentiate the metabolism state, the catabolic capacity to metabolise glucose serves as the threshold. Primarily, if the specific glucose uptake q_s exceeds the related oxygen demand for oxidation $Y_{s/o}q_o$, meaning that:

$$q_s > Y_{s/o}q_o \quad (4.16)$$

The overflow mechanism kicks in and aerobic ethanol is formed. In this case, acetaldehyde serves as an electron acceptor. Consequently, the "anaerobic" carbon flux refers to the remainder of the total substrate uptake, mathematically translated as equations (4.17)-(4.18), which signifies the ethanol secretion.

$$q_{sae} = min(q_s, Y_{s/o}q_o) \quad (4.17)$$

$$q_{san} = q_s - q_{sae} \quad (4.18)$$

The ethanol formed can be consumed as a substrate under aerobic conditions but priority is given to glucose. Given that (4.19) holds true, meaning that oxygen is in excess compared to glucose, the specific ethanol uptake rate is calculated by equation (4.20). Equation (4.20) compares whether oxygen demand for ethanol oxidation after glucose consumption $\frac{q_o - Y_{o/s}q_{sae}}{Y_{o/e}}$ exceeds the ethanol uptake q_e.

$$q_s < Y_{s/o}q_o \quad (4.19)$$

$$q_{eae} = min\left(\frac{q_o - Y_{o/s}q_{sae}}{Y_{o/e}}, q_e\right) \quad (4.20)$$

In the end, the overall metabolic model can be simplified down into the following three global reactions (with general stoichiometric coefficients):

- Aerobic growth on glucose

$$sC_6H_{12}O_6 + oO_2 + nNH_3 \rightarrow CH_{1.8}O_{0.6}N_{0.2} + cCO_2 + wH_2O \quad (4.21)$$

- Anaerobic growth on glucose

$$sC_6H_{12}O_6 + nNH_3 \rightarrow CH_{1.8}O_{0.6}N_{0.2} + eC_2H_5OH + cCO_2 + wH_2O \quad (4.22)$$

- Aerobic growth on ethanol

$$eC_2H_5OH + oO_2 + nNH_3 \rightarrow CH_{1.8}O_{0.6}N_{0.2} + cCO_2 + wH_2O \quad (4.23)$$

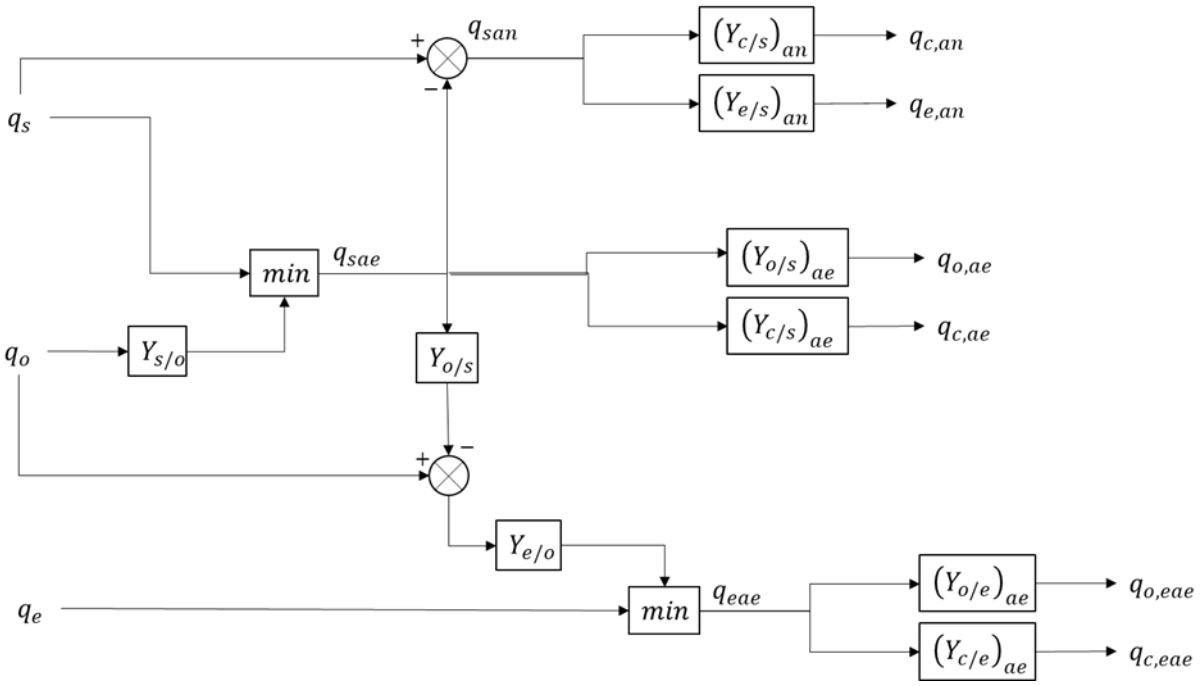

Figure 4.19: Schematic representation of the metabolic model network as presented in Sonnleitner and Käppeli (1986).

Figure 4.19 presents the graphical illustration of the metabolic pathway based on the respiratory bottleneck. It starts with the calculation of the specific uptake rate from equation (4.13)-(4.15) and the bioreaction is based on the comparison of uptake rate, as shown in Figure 4.19. The yeast fermentation model is an unstructured metabolic model. It assumes that the metabolism of microorganisms changes instantaneously when confronted with the fluctuating extra-cellular substrate concentration. In the reality, the intracellular state should be considered in the model, as in the work of (Pigou and

Morchain, 2015). The historical state of the microorganisms has to be included to yield a more realistic model. Nevertheless, this approach is not included in the 1D model as the objective is to compare the 1D model results with those of the CFD model by Sarkizi Shams Hajian et al, (2020).

4.3.3 1D modelling of the fermenter

The height and diameter in the 1D model are those of the CFD simulated fermenter. The number of grid points along the vertical direction is set to 100. The closure relations used in the 1D model are reported in Table 4.5. In particular, the dispersion coefficient is set so as to respect the hydrodynamic mixing time. The mixing time had been reported in Vrábel et al. (1999) to be 166 s and the numerical mixing simulation had also been reported in Haringa et al. (2017) to be 183 s. It is measured by monitoring the tracer concentration using a probe located at the bottom of the reactor while the tracer was injected at the top. Therefore, the liquid dispersion coefficient D_L can be calculated by fitting the analytical solution of Inoue and Kafarov (1973) with the mixing time. The analytical solution of Inoue and Kafarov (1973) is presented in

$$y = \frac{C(z,t)}{C_0} = 1 + 2\sum_{n=1}^{\infty} cos\left(\frac{n\pi z}{L}\right) exp\left(-\frac{n^2\pi^2}{L^2} D_L t\right) \tag{4.24}$$

With L the distance between the probe location and the injection point.

The gas-liquid mass transfer for O_2 and CO_2 was modelled via the film theory based on Henry's law. However, the Henry's constant was not reported in Sarkizi Shams Hajian et al. (2020). The modelled mass transfer coefficient is not explicitly reported either. But, it is believed Lamont and Scott (1970) correlation for mass transfer based on the eddy dissipation model is used. The ethanol gas-liquid mass transfer is modelled using a partition coefficient, meaning that only the ethanol in the liquid is solved. The ethanol concentration in the gas phase is assumed to be at equilibrium with that of liquid, the same hypothesis will be made in the 1D model.

As far as the biological model is concerned, the same bioreaction model used in the CFD simulation was implemented in the 1D model. The yield coefficient values were not reported in the work of Sarkizi Shams Hajian et al. (2020) but it is referenced in the work of Sweere et al. (1988). The same values are used in the 1D model and these coefficients are reported in Table 4.6.

Table 4.5: Closure relations applied in the 1D model

Variables	Closure model
d_b	Constant 9 mm same as Sarkizi Shams Hajian et al. (2020)
u_G	Same as Sarkizi Shams Hajian et al. (2020)
u_L	0 m.s^{-1} bubble column closed to the liquid
D_G	0.1 m².s^{-1} insensitive to D_G. Assumed the same as D_L
D_L	0.1 m².s^{-1} - Calculated from the analytical solution of Inoue and Kafarov (1973) using the mixing time obtained from the experiment of Vrábel et al. (1999)
k_L	Higbie (1935)
C^*	Sander (2015)
R_i	same as Sarkizi Shams Hajian et al. (2020)

Table 4.6: Biological parameters applied in the 1D model based on Sweere et al. (1988)

Biological parameters	Value (units)
q_s^{max}	$3.5\ \mathrm{gS.gX^{-1}.h^{-1}}$
q_o^{max}	$0.256\ \mathrm{gO_2.gX^{-1}.h^{-1}}$
q_e^{max}	$0.236\ \mathrm{gE.gX^{-1}.h^{-1}}$
K_s	$150\ mgS.L^{-1}$
K_o	$0.1\ mgO_2.L^{-1}$
K_e	$100\ mgE.L^{-1}$
$Y_{s/o}$	$2.592\ \mathrm{gS.gO_2^{-1}}$
$\left(Y_{c/s}\right)_{an}$	$0.4620\ \mathrm{gCO_2.gS^{-1}}$
$\left(Y_{e/s}\right)_{an}$	$0.480\ \mathrm{gE.gS^{-1}}$
$\left(Y_{c/s}\right)_{ae}$	$0.574\ \mathrm{gCO_2.gS^{-1}}$
$Y_{o/e}/\left(Y_{o/e}\right)_{ae}$	$0.890\ \mathrm{gO_2.gE^{-1}}$
$\left(Y_{c/e}\right)_{ae}$	$0.650\ \mathrm{gCO_2.gE^{-1}}$

4.3.4 Hydrodynamics results

First, the results without bioreaction are presented. It is reported that the average gas holdup in the fermenter corresponds to 19% (Sarkizi Shams Hajian et al., 2020). This value is slightly above the experimental measurements of 17.1% (Vrábel et al., 1999) and the previous numerical CFD Euler-Lagrange simulation of 17.6% (Haringa et al., 2017). With the obtained average gas holdup, the volume-averaged mass transfer coefficient $k_L a$ is reported to be 190 h^{-1} (Sarkizi Shams Hajian et al., 2020). This $k_L a$ value is quite close to the experimental value of 180 h^{-1} (Larsson et al., 1996) and a previous CFD Euler-Lagrange simulation yielded 144 h^{-1} (Haringa et al., 2017).

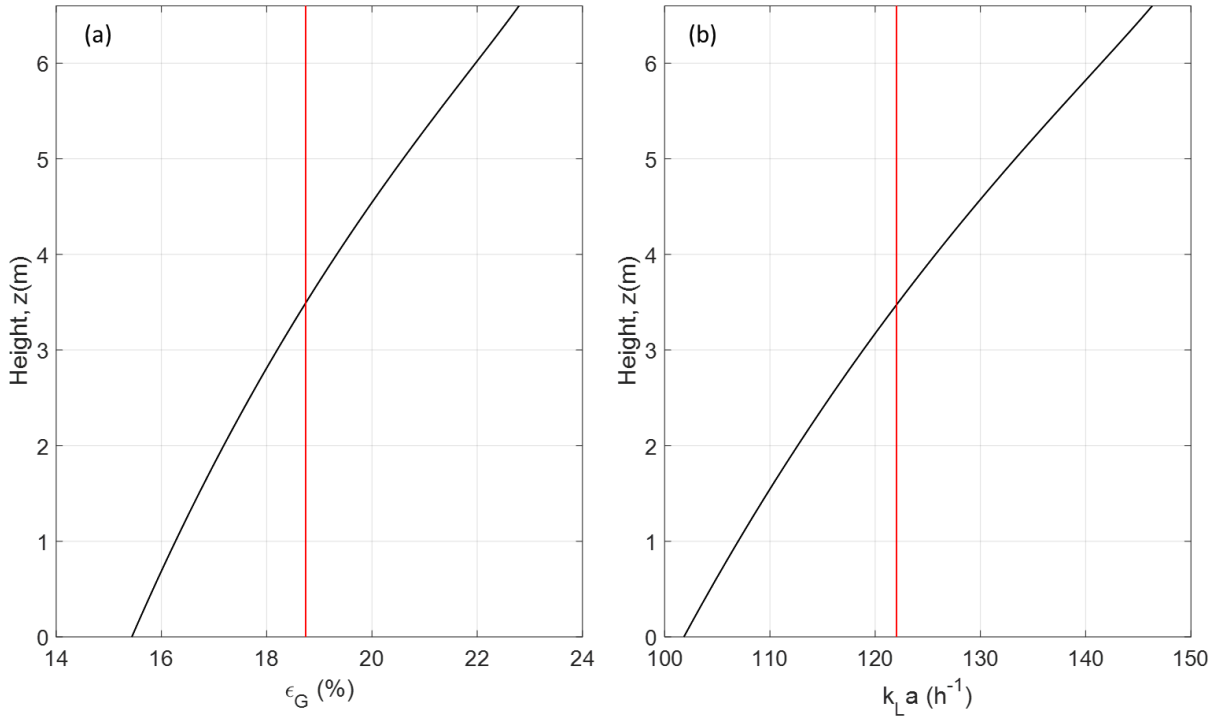

Figure 4.20: (a) Gas holdup and (b) $k_L a$ profiles at steady-state. Red line signifies the averaged value.

Figure 4.20 reports the hydrodynamic profile of the gas holdup and $k_L a$. It must be emphasised that the spatio-temporal 1D model developed in this thesis has been applied to bubbly flow applications, primarily validated in bubble column reactors. The current fermenter corresponds to a tall multistage stirred-tank reactor. Nevertheless, the physics of bubbly flow in stirred tanks exhibiting a high H/D_r ratio is still very close to that of a bubble column. The gas holdup and $k_L a$ increase linearly from the bottom to the top of the column, with the averaged gas holdup and $k_L a$ at steady state found to be 18.73% and 122 h^{-1}, respectively. The averaged gas holdup is very close to that of Sarkizi Shams Hajian et al. (2020). This is due to the fact that the same closure on the bubble drag is considered in the 1D model, which is the Grace drag model with the swarm factor of -1.2. However, the $k_L a$ is

underpredicted. By using the Higbie model, k_L is calculated as $2\sqrt{\frac{D.u_{rel}}{\pi d_b}}$ with the oxygen diffusivity at 30°C, $D = 2.6 \times 10^{-9}$ m².s^{-1}, the slip velocity, $u_{rel} = 0.206$ m.s^{-1}, and the bubble diameter $d_b = 0.009$ m, accordingly, the $k_L = 2.75 \times 10^{-4}$ m.s^{-1}. Considering the interfacial area of $a = \frac{6\varepsilon_G}{d_b}$ with $\varepsilon_G = 18.73\%$, the average $k_L a$ yields 122 h^{-1}. Since the bubble diameter is identical and the overall gas holdup is very close to that of the CFD model, the reason for the difference in $k_L a$ resides in the closure model for k_L. It is believed that the Lamont and Scott (1970) closure model is used in the work of Sarkizi Shams Hajian et al. (2020). The model of Lamont and Scott (1970) cannot be implemented in the 1D model as the energy dissipation is not calculated. Instead, the $k_L a$ is multiplied by a factor of 1.5 to match the $k_L a$ value of the CFD model. This numerical artefact corrects the volumetric mass transfer coefficient to the same value and will allow a direct comparison when the bioreaction is considered.

4.3.5 Yeast fermentation for $X = 10$ g.L^{-1}

Next, the yeast fermentation is simulated. The simulation considered two biomass concentrations. First, the biomass concentration of $X = 10$ g.L^{-1} is discussed. The glucose is injected at a rate of 52 kg.h^{-1} at the top of the fermenter. However, the exact location of the glucose feed is not mentioned in the work of Sarkizi Shams Hajian et al. (2020). Nevertheless, it is found in previous work that the glucose feed is located 6.5 m above the bottom of the tank, close to the liquid surface (Larsson et al., 1996). This is a bit contradictory to the results of Sarkizi Shams Hajian et al. (2020) whereby the feed location is estimated at around 5.5 m (notice the red spots in the glucose profiles reported in the reference paper of Sarkizi Shams Hajian et al. (2020) are located around 5.5 m). Nonetheless, sensitivity analysis on this feed location is performed using the 1D model, with two feed locations (i) 5.5 m from the ground and (ii) 6.5 m from the ground. The glucose feed is modelled as a local source term in the species transport equation of glucose. Besides, the glucose concentration profile for the same simulation case and setup is also reported in Haringa et al. (2017) whereby an Euler-Lagrange CFD simulation was performed. These results are also considered in the comparison with the 1D model.

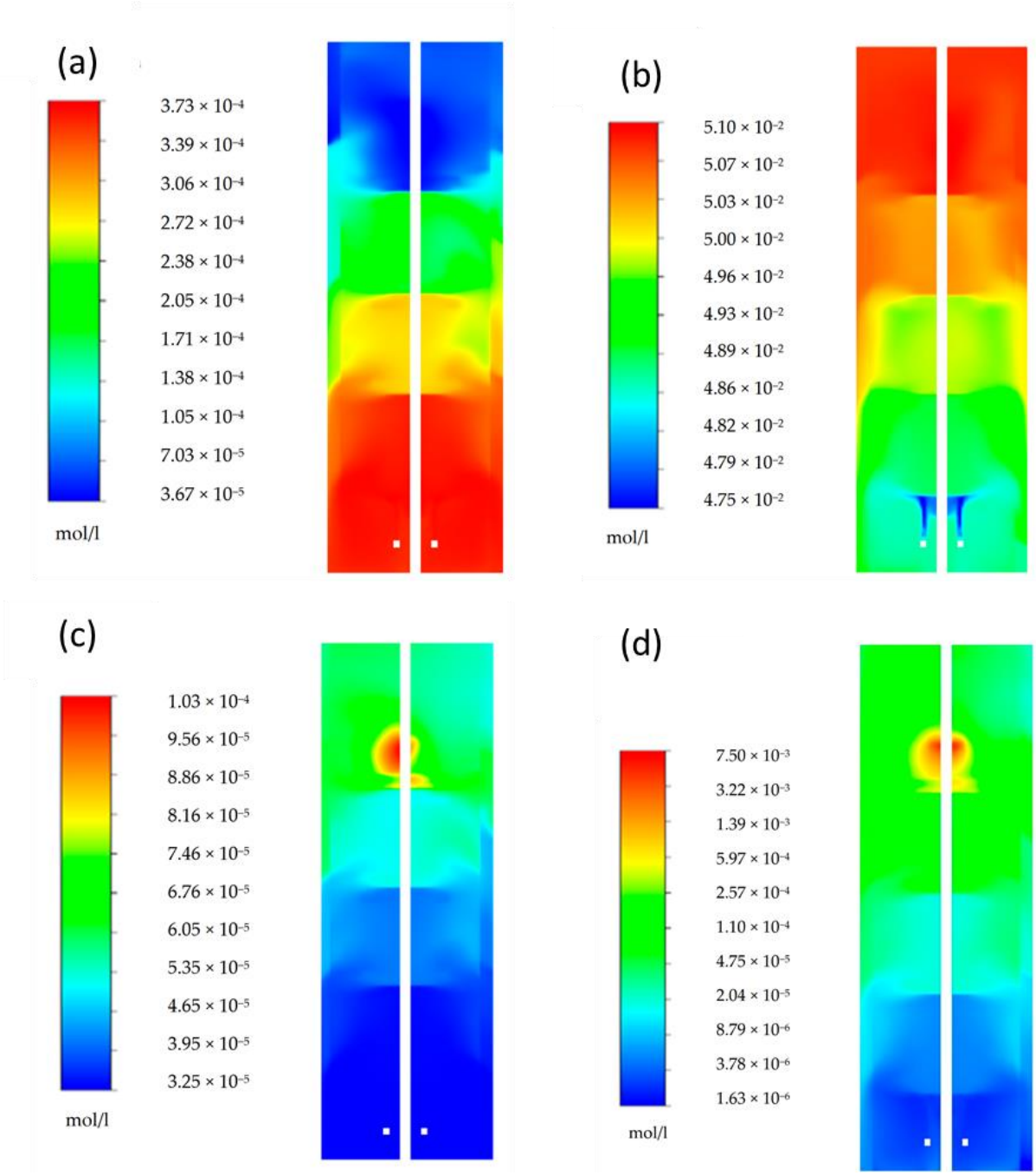

Figure 4.21: CFD concentration profiles of (a) oxygen (b) carbon dioxide (c) ethanol and (d) glucose for $X = 10$ g.L^{-1} as reported in Figure 4 of Sarkizi Shams Hajian et al. (2020)

The concentration fields issued from the CFD simulation of Sarkizi Shams Hajian et al. (2020) reveal some kind of compartmentation with almost uniform concentrations in the four zones where the impellers are installed, as shown in Figure 4.21. This can be related to the fact that the reactor is equipped with Rushton turbines (radial impeller). Figure 4.22 presents the concentration profiles obtained from the 1D model superposed with those of CFD. The mean concentration value in the four quasi-uniform concentration zones of the CFD model is reported together with the 1D model results

in Figure 4.22. The agreement is quite good if one considers that averaging the CFD results implies an image analysis procedure which is not error-free. Also, the 1D model obviously filters horizontal gradients that are actually present in the upper part of the column, close to the glucose feed point. The 1D model results have a better agreement with CFD for the glucose feed location situated at 5.5 m. The oxygen profile is slightly underpredicted but this is due to the different mass transfer closure models, as discussed previously. Nevertheless, the oxygen profile is still considered acceptable even if it was multiplied by a constant factor of 1.5. The glucose profile is also well predicted, considering the possible error committed during the calculation of the CFD mean concentration value. If the glucose feed had been located at 6.5 m, the peak of glucose concentration will not be observed. Nevertheless, the results for the glucose feed at 6.5 m can still be compared to the experimental measurement of Larsson et al. (1996) and the CFD simulation of Haringa et al. (2017). The results are reported in Table 4.7. The 1D model predictions are very close to both the experimental values (at discrete sampling positions) and the CFD ones for the glucose concentration. In essence, the 1D model underpredicts the glucose concentration at the bottom; very well predicts the value in the middle; while both CFD and 1D models overpredict the glucose concentration at the top.

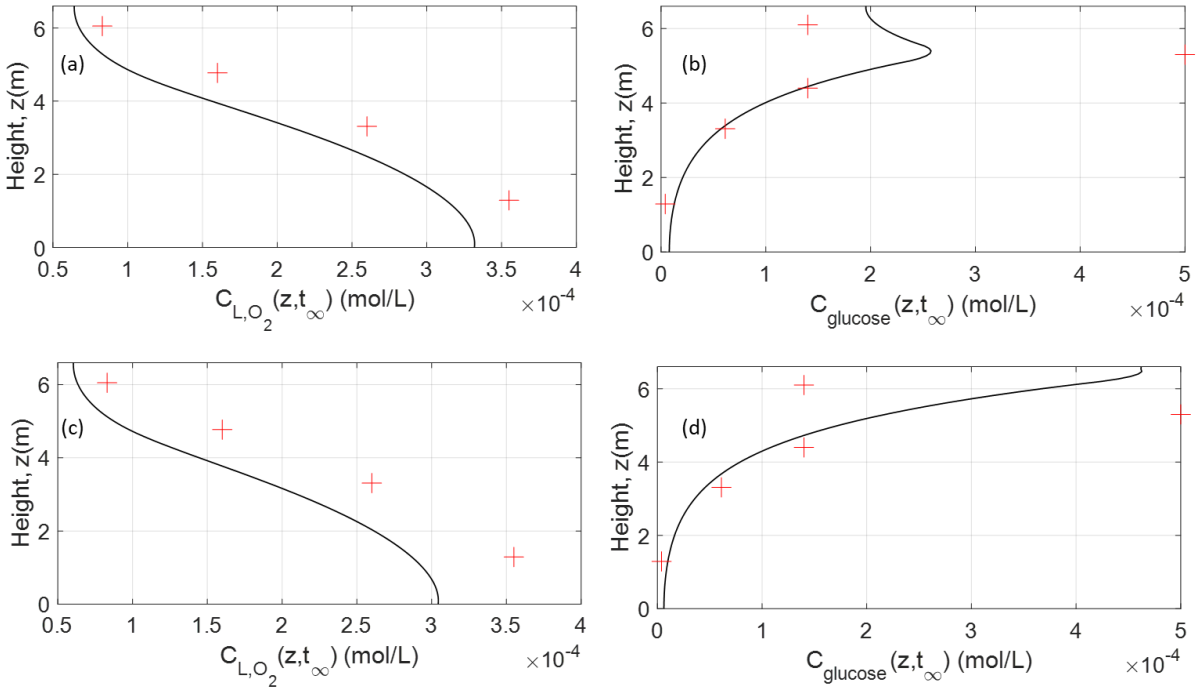

Figure 4.22: Concentration profiles of oxygen and glucose at steady state. (a) and (b) for glucose feed located approximately at 5.5 m. (c) and (d) for glucose feed located around 6.5 m. Red cross: CFD mean value from Sarkizi Shams Hajian et al. (2020)

Table 4.7: Mean glucose concentration in mg.L^{-1} (glucose molecular weight = 180 g.mol^{-1}) at three axial locations with the glucose feed located at 6.5 m.

Axial Location (m)	Experimental value from Larsson et al. (1996)	Euler-Lagrange CFD simulation from Haringa et al. (2017)	1D model
0.97	4.3	5.1	1.63
3.90	11.2	17.6	14.2
6.35	40.7	82.9	81.3

Overall, the 1D model predictions are in good agreement with the literature data, highlighting the advantage of the 1D model in the study of substrate gradients in large-scale bioreactors. For comparison, the simulation time for the 1D model is in the order of 10 minutes whereas the CFD simulations are mostly in the order of hours or days.

Apart from oxygen and glucose profiles, Sarkizi Shams Hajian et al. (2020) also provided the dissolved CO_2 concentration profile. It must be emphasised that the dissolved CO_2 concentration profile is much harder to compare for several reasons. First, CO_2 is produced in the liquid phase as a by-product, as shown in equations (4.21)-(4.23). Next, due to thermodynamic disequilibrium, it is stripped from the liquid phase to the gas phase with the mass transfer intensity defined by the concentration gradient $C^* - C_L$ and the volumetric mass transfer coefficient $k_L a$. More precisely, C^* depends on the CO_2 partial pressure and the Henry's constant, C_L depends on the pH and the production rate, and $k_L a$ depends on the gas holdup, bubble diameter and the closures for the mass transfer coefficient k_L. It is found that the CO_2 concentration predicted by the 1D model is not in the same order of magnitude as that provided by Sarkizi Shams Hajian et al. (2020).

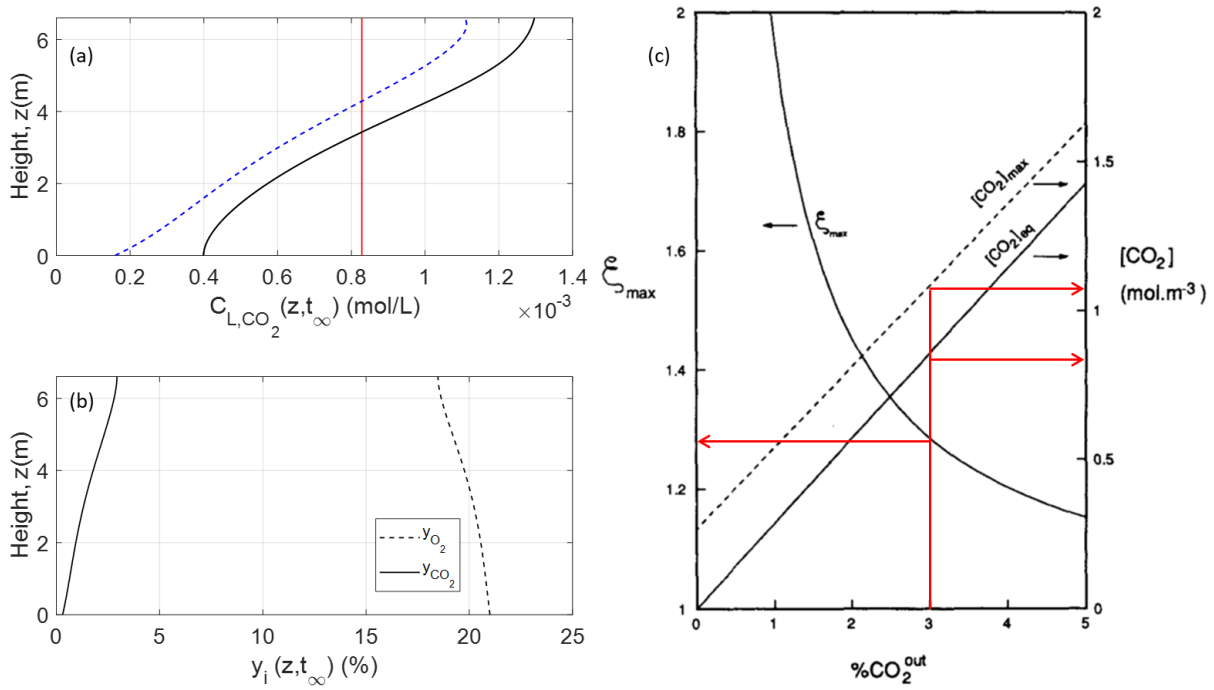

Figure 4.23: (a) Dissolved CO_2 concentration profile. Red line indicates the mean CO_2 concentration. Blue dotted line represents the CO_2 equilibrium concentration (b) O_2 and CO_2 molar fraction profile (c) Maximum CO_2 and equilibrium concentration and their ratio ξ as a function of outlet CO_2 molar fraction. Adapted from: Royce and Thornhill (1991)

Figure 4.23(a) shows that the dissolved CO_2 concentration increases from the bottom to the top of the column, with the maximum CO_2 concentration formed, being 1.3×10^{-3} mol.L^{-1} (1.3 mol.m^{-3}). The maximum CO_2 concentration is located at the top where the glucose feed is situated. The mean dissolved concentration is around 0.8×10^{-3} mol.L^{-1}, as shown with the red vertical line in Figure 4.23(a). Figure 4.23(b) shows that the CO_2 molar fraction increases from 400 ppm in the inlet to 3% at the outlet, which is consistent with the finding of Sarkizi Shams Hajian et al. (2020) who reported that the estimated CO_2 molar fraction reached between 2.1 and 2.9 %. For baker's yeast fermentation, Chen and Gutmanis (1976) reported that with an inlet molar fraction of CO_2 of 400 ppm (normal air condition), the CO_2 molar fraction formed at the outlet gas is between 0-5%.

Figure 4.23(c) presents the dissolved CO_2 concentration, the corresponding equilibrium concentration and their ratio according to the % of CO_2 in the outlet gas. For a 3% CO_2 outlet molar fraction, Royce and Thornhill (1991) model predict the dissolved CO_2 concentration and its equilibrium concentration are roughly 1.1×10^{-3} mol.L^{-1} and 0.85×10^{-3} mol.L^{-1}, respectively. Thus, the dissolved CO_2 concentration obtained by the 1D model agrees with the work of Royce and Thornhill (1991). For pH = 5 of fermentation condition and a CO_2 partial pressure of 3% atmospheric pressure, the dissolved CO_2

is roughly 10^{-3} mol.L^{-1} (Pourbaix, 1974). Many researchers also reported the dissolved CO_2 concentration to be in the range of 10^{-3} mol.L^{-1} in usual yeast fermentation conditions, namely temperature = 30°C, pH = 4-5, and pressure at atmospheric pressure (Chen and Gutmanis, 1976; Jones and Greenfield, 1982; Royce and Thornhill, 1991; Yagi and Yoshida, 1977)

Surprisingly, the dissolved CO_2 concentration reported in Sarkizi Shams Hajian et al. (2020) is roughly 5×10^{-2} mol.L^{-1}. It might be that the hydrostatic pressure was considered instead of the CO_2 partial pressure in the work of Sarkizi Shams Hajian et al. (2020) which could explain such a high dissolved CO_2 concentration. For a given pH in the liquid and CO_2 partial pressure in the gas phase, the dissolved CO_2 concentration is known. Indeed, from the data of (Pourbaix, 1974), a concentration of 5×10^{-2} mol.L^{-1} is achieved if the CO_2 partial pressure is considered as the atmospheric pressure. Nevertheless, the difference in CO_2 concentration between the 1D and CFD models has no impact on the prediction of other species gradients.

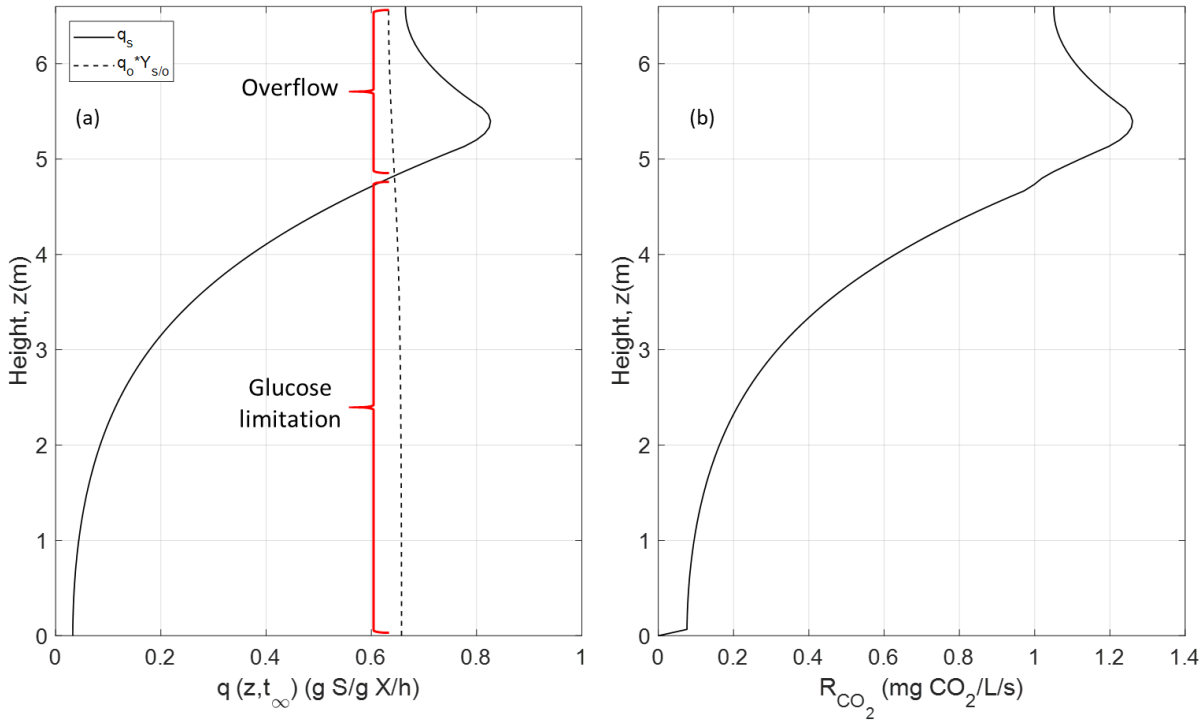

Figure 4.24: (a) Specific glucose uptake rate (b) Volumetric CO_2 production rate

The 1D model shows that the slope of the dissolved CO_2 concentration (Figure 4.23(a)) is not constant, signifying that different metabolic mechanisms coexist inside the fermenter. CO_2 is a by-product of yeast fermentation produced via metabolic pathways, according to equations (4.21)-(4.23) and each pathway gives a different carbon dioxide yield, as shown in Table 4.6.

Figure 4.24(a) presents the local variation of the specific glucose uptake q_s and the related oxygen demand for oxidation $Y_{s/o}q_o$. It shows that the glucose is in excess ($q_s > Y_{s/o}q_o$) at the top of the column near the feed zone, signifying the principal metabolic pathway is the aerobic growth of glucose with the rest of the glucose being converted to ethanol through the overflow mechanism. (see equation (4.21) and equation (4.22)). From the bottom to a height of 5 m, the specific glucose uptake rate is lower than the associated oxygen demand for oxidation ($q_s < Y_{s/o}q_o$). The main active metabolic pathway is the aerobic growth of ethanol, as written in equation (4.23). As a result, it can be observed in Figure 4.24(b) that the CO_2 production rate peaks near the glucose feed location, and decreases gradually down the column.

4.3.6 Yeast fermentation for $X = 25$ g.L^{-1}

We also compared the results for $X = 25$ g.L^{-1} between 1D and CFD models, as shown in Figure 4.25. The oxygen concentration decreases significantly from the bottom to the top of the column. Sarkizi Shams Hajian et al. (2020) stated that the dissolved oxygen level below 4×10^{-6} mol.L^{-1} is observed in a volume of 0.04 m^3 near the top of the column. We also found a very similar volume of 0.0395 m^3 for the region above 5.46 m height where the dissolved oxygen concentration is 4×10^{-6} mol.L^{-1}. Due to a higher biomass concentration, the substrate consumption rate is larger than in the previous test case. The aeration rate being constant, the substrate gradients are now more pronounced. The concentration value of 4×10^{-6} mol.L^{-1} is mentioned by Sarkizi Shams Hajian et al. (2020) as the threshold for aerobic growth of glucose. The dissolved CO_2 concentration profile was not reported in Sarkizi Shams Hajian et al. (2020). Nevertheless, the dissolved CO_2 profile predicted by the 1D model is still reported in Figure 4.25(b). The CO_2 concentration profile is very similar to that of $X = 10$ g.L^{-1}, with only slightly higher CO_2 near the glucose feed. This signifies the CO_2 production is not sensitive to the increase of biomass concentration. The dissolved CO_2 concentration is most likely due to thermodynamic equilibrium. It must be emphasised that the pH is not solved in either 1D or CFD models. In reality, the dissolved CO_2 concentration changes according to the pH. However, coupling the dynamics of pH in a complete model is rare, since the system equations become very stiff. The ethanol and glucose concentration are also predicted satisfactorily well compared with the CFD results, as shown in Figure 4.25(c) and Figure 4.25(d), respectively.

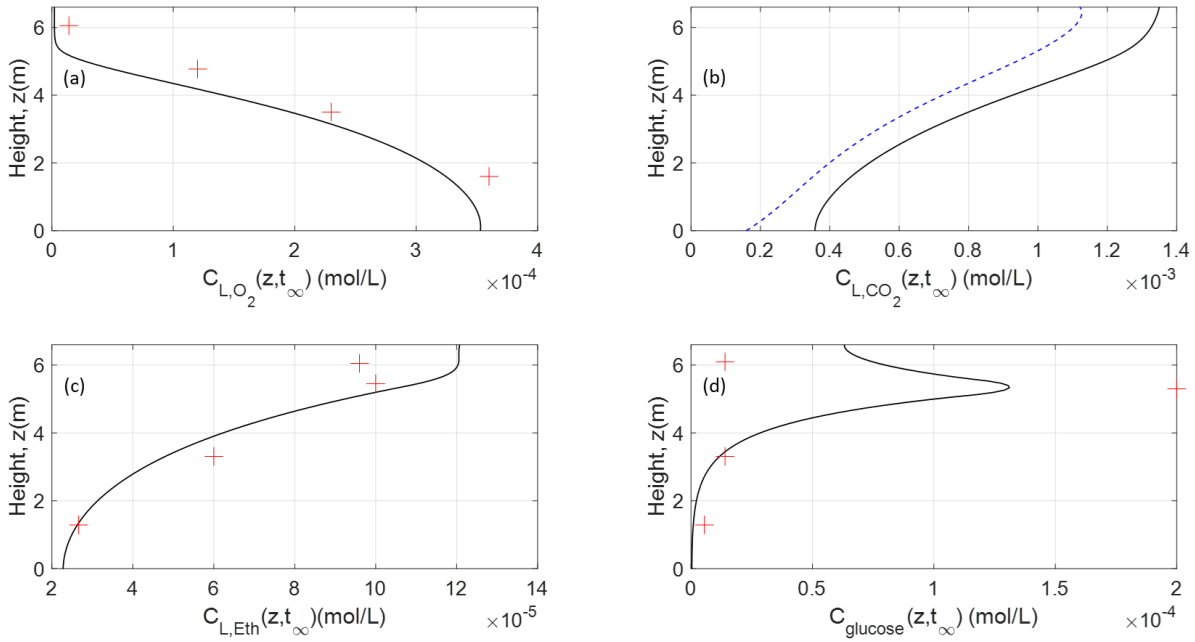

Figure 4.25: Concentration profiles of (a) oxygen (b) carbon dioxide (c) ethanol and (d) glucose for $X = 25$ g.L^{-1}. Red cross: CFD mean value from Sarkizi Shams Hajian et al. (2020)

4.4 General conclusion on substrate gradients in large-scale fermenters study

From this study, it is shown that the 1D model performed just as well as the CFD model in the investigation of substrate gradients in large-scale fermenters. The 1D model results have been compared to the results of Sarkizi Shams Hajian et al. (2020) who performed the 3D Euler-Euler CFD simulation of a well-known 22 m^3 industrial fermenter (Haringa et al., 2017; Larsson et al., 1996; Vrábel et al., 2001, 2000, 1999). The key parameters are kept the same as much as possible, such as the bubble diameter and the reported $k_L a$ value. It is found that substrate and by-product gradients exist in large-scale bioreactors and numerical modelling tools such as 1D and CFD models are useful to understand the existence of such gradients and the physics of the process. At higher biomass concentration, more severe substrate gradients are expected on glucose and oxygen concentrations, leading to poor product yield. To mitigate this problem, solutions such as multiple feed points can be envisaged. Although CFD models yield more precise local information about the substrate gradient, the 1D model offers a faster resolution with a satisfactory prediction which give the possibility to perform sensitivity analysis, such as probing design parameters, biological kinetics parameters, and operating conditions before moving into more advanced CFD simulation.

Chapter 5 Reactive bubbly flow analysis using 1D model

5.1 Reactive bubbly flow

Considering the scenario of high interfacial mass transfer rate without chemical reaction, the dissolution of the gas bubble in the liquid will lead to bubble size reduction, and in return impact the bubble rising velocity. This is characterised as a two-way coupling problem. Some of the earliest work on this subject include the study of carbon dioxide (CO_2) absorption in water which is relatively more soluble than oxygen (Deckwer et al., 1978; Takemura and Yabe, 1999). In the case of reactive bubbly flow, the presence of chemical reactions will accelerate the interfacial mass transfer, leading to a strong two-way coupling problem with the hydrodynamics. The coupling of reactive mass transfer and fluid dynamics are shown in Figure 5.1 with the respective parameters involved. The mass transfer rate $\dot{m}$ in kg.s^{-1} or mol.s^{-1} is a function of local fluid dynamics and chemical reaction kinetics.

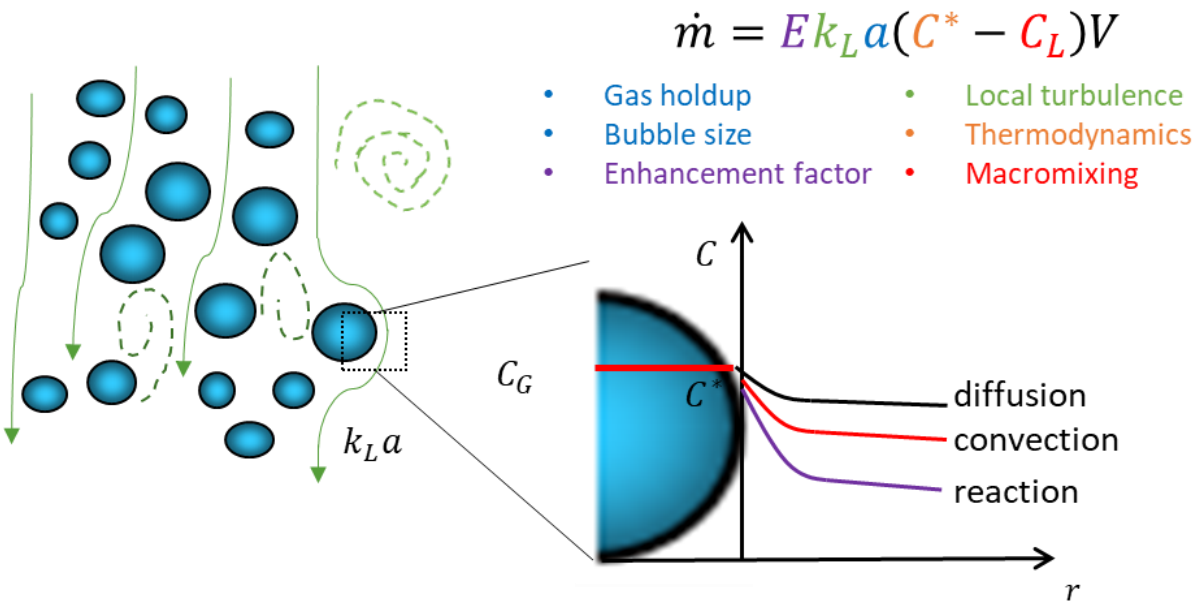

Figure 5.1: Diffusional, convective or reactive mass transfer mechanism

Recently, comprehensive research on the topic of reactive mass transfer has been published in the book *Reactive Bubbly Flows* (2021). It provides an extensive experiment dataset for future numerical model validation and it also presents recent numerical methods for detailed simulation of reactive bubbly flow. This review includes the study of different scales, ranging from a free-rising single bubble to confined Taylor bubbles and bubble swarms. Among the reactive systems studied, the chemisorption of CO_2 in aqueous sodium hydroxide solution (NaOH) is the most studied system, with three notable examples presented in *Reactive Bubbly Flows* (2021) are the studies of Darmana et al.

(2007), Kováts et al. (2017) and Taborda et al. (2021). These studies were conducted in laboratory-scale bubble columns with a height of ~1 m. These researchers used different experimental techniques to quantify the reactive mass transfer of CO_2. Darmana et al. (2007) follows the reactive mass transfer with a pH probe. Kováts et al. (2017) monitors the pH changes with an optical method of 2-tracer-PLIF. Taborda et al. (2021) records the electrical conductance using a wire-mesh sensor which tracks the pH changes.

In this work, we chose the reference case of Darmana et al. (2007) for our study due to a complete experimental dataset and also extensive research was published after this original work. Darmana et al. (2007) investigated the chemisorption of CO_2 in NaOH solution and the influence of fast reaction on the hydrodynamics behaviour was studied both experimentally and numerically with the CFD model using the Euler-Lagrange approach. The goal is to elucidate the coupling of hydrodynamics and chemisorption (mass transfer under the effect of chemical reaction). The authors developed a fully-resolved CFD Euler-Lagrange model to investigate the coupling, and the model was validated with experimentally measured bubble velocity profile, Sauter mean diameter, integral gas holdup and pH. The pH measurement serves as a monitoring of the CO_2 mass transfer flux. Overall, the model captures well the hydrodynamics but the overall mass transfer process is underpredicted. Another shortcoming of Darmana et al. CFD model is the necessity of huge computational resources and long simulation time as for every 4s simulation, the required calculation time is 24h. A short summary on this reference case is presented in Section 5.2.

Since 2007, many researchers have revisited Darmana et al. work, using different strategies but mostly focused on the CFD model, either the Eulerian approach (Hlawitschka et al., 2016; Krauß and Rzehak, 2018; Liu et al., 2021) or the Lagragian approach (Gruber et al., 2015; Huang et al., 2021; Taborda and Sommerfeld, 2021). These studies applied different strategies separately to investigate or reproduce the experimental data, such as detailed reaction pathways (Krauß and Rzehak, 2018; Krauβ and Rzehak, 2017), bubble population model (Buffo et al., 2017; Gruber et al., 2015), mass transfer closure model (Huang et al., 2021; Liu et al., 2021; Taborda and Sommerfeld, 2021), and enhancement factor model (Huang et al., 2021; Krauβ and Rzehak, 2017). Section 5.3 summarises shortly the originality and findings of each work.

5.2 Summary of Darmana et al. (2007) case

A brief description of the experimental and numerical works of Darmana et al. (2007) is presented in this section. The experimental setup consists of a pseudo-2D bubble column of 200 mm width, 30 mm depth and 1500 mm height. The liquid level was kept at 1000 mm for all experiments. The 2D geometry is chosen to enable the visualisation of the flow structures and the bubble size distribution. Measurements via the optical method can be carried out directly without correction of the optical index. The bubbles were introduced through 21 gas needles, forming a square pitch of 5 mm in the middle of the column. The inner diameter of the needles was 1 mm. The superficial gas velocity (j_G) was kept as 7 mm.s^{-1}. The bubble size formed at the inlet (d_{b0}) was mentioned to be 5.5 mm.

Two gas-liquid systems were measured to investigate the influence of fast chemical reactions on the hydrodynamics behaviour. First, nitrogen (N_2) and twice-distilled water was used to mimic the non-reactive system. Next, a reactive system composed of CO_2 and aqueous NaOH solution at an initial pH of 12.5 was utilised to study the effect of chemisorption on the hydrodynamics. All experiments were carried out after the flow pattern was fully developed in pseudo steady-state regime. Several measurements were conducted, namely:

- Integral gas holdup was calculated by the difference in liquid height with and without bubbles.
- Time-averaged gas velocity was measured by using Particle Image Velocimetry (PIV) as a tracking method of the bubble. The bubble velocity profile was reported at z/H = 0.75.
- Local bubble size measurements were obtained through the image processing technique of a series of images recorded via CCD camera. The time-averaged bubble size axial profile was reported only for the reactive case.
- Temporal evolution of pH was measured with a pH probe placed at 2 cm below the liquid surface in the centre of the column.

Besides the experimental work, Darmana et al. (2007) also carried out numerical simulations for both non-reactive and reactive cases using the CFD Euler-Lagrange approach. The motion of each individual bubble is computed from the bubble mass and momentum equations while considering all relevant fluid dynamical forces, namely gravity, buoyancy, drag, lift, virtual mass and wall forces. The drag, lift and wall forces are modelled using closures obtained from Tomiyama et al. (2002, 1995).

5.3 Summary of previous studies on the Darmana et al. (2007) case

In the literature different researchers applied different strategies to reproduce the experimental data of Darmana et al. (2007), of which they can be organised to the following strategies:

- Detailed reaction pathways (Krauß and Rzehak, 2018; Krauβ and Rzehak, 2017)

For the chemisorption process of CO_2 in aqueous NaOH solution, Darmana et al. (2007) considers only the reversible two-step reaction pathway in their CFD model. The dissolved CO_2 will react with the NaOH solution in a two-step reversible reaction, which will be denoted as the first and second reactions. The reactions are written as:

$$CO_2 + OH^- \rightleftharpoons_{k_{1,2}}^{k_{1,1}} HCO_3^- \tag{5.1}$$

$$HCO_3^- + OH^- \rightleftharpoons_{k_{2,2}}^{k_{2,1}} {CO_3}^{2-} + H_2O \tag{5.2}$$

Where $k_{1,1}$ and $k_{1,2}$ are the forward and backward rate constants, respectively for the first reaction while $k_{2,1}$ and $k_{2,2}$ are the forward and backward rate constants for the second reaction.

Krauβ and Rzehak (2017) proposed a third reactive pathway which is the water reaction pathway that becomes important when pH < 10 and even dominant at pH < 8. It is a two-step reaction, the first reaction which is reversible (Kern, 1960) is written as:

$$CO_2 + H_2O \rightleftharpoons_{k_{3,2}}^{k_{3,1}} {HCO_3}^- + H^+ \tag{5.3}$$

The second step is identical to the hydroxide pathway, as shown in equation (5.2). The two reactions are coupled with the auto-dissociation of water, characterised by the equilibrium constant K_w. The chemical reaction rates are therefore expressed as:

$$R_{1,1} = k_{1,1}.[CO_2].[OH^-] \tag{5.4}$$

$$R_{1,2} = k_{1,2}.[HCO_3^-] \tag{5.5}$$

$$R_{2,1} = k_{2,1}.[HCO_3^-].[OH^-] \tag{5.6}$$

$$R_{2,2} = k_{2,2}.[CO_3^{2-}] \tag{5.7}$$

$$R_{3,1} = k_{3,1}.[CO_2] \tag{5.8}$$

$$R_{3,2} = k_{3,2}.[HCO_3^-].[H^+] = k_{3,2}.[HCO_3^-].\frac{K_w}{[OH^-]} \tag{5.9}$$

Here, the reaction rate $R_{j,k}$ are expressed in kmol.m^{-3}.s^{-1} with $j = 1,2,3$ denotes the reactions of equations (5.1)-(5.3) and $k = 1,2$ denotes the forward and backward reaction, respectively.

To validate the newly proposed reactive pathways, the authors developed a 0D model to investigate this effect solely. This simplified approach excludes any possible error from hydrodynamic modelling. The authors found that the overall pH is very well predicted with this simplified approach. By including the third pathway, the second change of pH slope when pH < 8 is well captured by the model.

- Bubble size distribution by solving population balance model (Buffo et al., 2017)

To predict the bubble size distribution and eventually the specific surface area that defines the overall mass transfer rate, Buffo et al. (2017) developed a CFD model that coupled with the population balance model using open-sourced CFD OpenFOAM software. The population balance equation is solved by the quadrature method of moments method. The shortcoming of this work is that the inlet bubble diameter was not kept the same as 5.5 mm which is that of Darmana et al. (2007). Instead, a correlation is used to estimate the inlet bubble diameter. This leads to an overestimation of the bubble size profile. Otherwise, the use of bubble size population balance model should yield a relatively good bubble diameter profile as it should yield a more realistic mass transfer flux.

- Mass transfer closure model (Huang et al., 2021; Liu et al., 2021; Taborda and Sommerfeld, 2021)

The earliest attempt to compare different mass transfer models is reported in the work of Liu et al. (2021). The authors applied four Sherwood correlations (in the form of $Sh = 2 + a.Re^b.Sc^c$) to their Eulerian model and it was tested with or without the enhancement factor model. Table 5.1 reports the Sherwood correlation used in the work of Liu et al. (2021). The choice of the Sherwood correlation tested is debatable. For example, the two empirical correlations of (Jain et al., 2015) shows a power of 0.33 for the Sc, which is usually used for contaminated system, whereas for the case of Darmana et al. (2007), the system is considered pure as the experiment was conducted with twice distilled water or aqueous NaOH solution. In their model, the enhancement factor of Fleischer et al. (1996) which is previously validated by Hlawitschka et al. (2016) was used. The CFD simulations were conducted with a constant bubble diameter of 5.5 mm. However, some contradictory results were obtained. The authors proposed a ranking of the best fit using the four Sherwood correlations. Interestingly, in a later

paper by Huang et al. (2021), it is reported another ranking of the same Sherwood correlations tested by Liu et al. (2021). The authors explained the difference is due to different numerical approaches and the reactive kinetics model applied.

Table 5.1: Sherwood correlation used by Liu et al. (2021)

Sherwood correlation	Description	Reference
$Sh = 2 + 0.015Re^{0.89}.Sc^{0.7}$	Non-spherical bubbles with stochastic deformations of the interface	(Brauer, 1979)
$Sh = 2 + 0.6415Re^{0.5}.Sc^{0.5}$	Spherical bubbles under creeping flow regime	(Bird et al., 2002)
$Sh = 2 + 1.25Re^{0.5}.Sc^{0.33}$	Bubble swarm	(Jain et al., 2015)
$Sh = 2 + 0.43Re^{0.58}.Sc^{0.33}$	Bubble swarm	(Jain et al., 2015)

Other recent advances in describing reactive mass transfer can be found in the work of Taborda and Sommerfeld (2021) and Taborda et al. (2021b). The authors developed the so-called full dynamic model to study Darmana et al. (2007) reference case. Both Taborda and Sommerfeld (2021) and Taborda et al. (2021b) developed a CFD model based on the Euler-Lagrange approach with the Sherwood number modified to take into account the non-spherical bubble oscillation motion. The Sherwood number is multiplied with the oscillation term which yields the following expression

$$Sh = \frac{2}{\sqrt{\pi}} Pe^{\frac{1}{2}} \left[I_{n1} + I_{n2} \frac{A}{\omega_n^2} We^{\frac{1}{2}} \right]$$
$$We = \frac{\rho_L u_{rel}^2 d_b}{\sigma} \tag{5.10}$$

Where Pe is the Péclet number, I_{n1} and I_{n2} are integral constants dependent on the oscillation amplitude, ω_n the osccilation frequency, A the oscillation amplitude, and We the Weber number.

- Enhancement factor model (Huang et al., 2021; Krauβ and Rzehak, 2017)

The enhancement factor (E) is defined as the ratio between the mass transfer fluxes with and without reaction, supposing the same driving force of concentration. Besides evaluating the reactive pathway, Krauβ and Rzehak (2017) also provided a comprehensive review of enhancement factor that is widely used in the chemical engineering context. The fundamental findings of Krauβ and Rzehak (2017) are summarised hereafter.

For the chemisorption of CO_2 in NaOH, a fast single-step irreversible reaction of second order is considered by combining equations (5.1) and (5.2), which leads to equation (5.11).

$$CO_2 + 2OH^- \rightarrow CO_3^{2-} + H_2O \tag{5.11}$$

The Hatta number (Ha) is thus written as:

$$Ha = \frac{\sqrt{k_{1,1}.D_{CO_2}.[OH^-]}}{k_L} \tag{5.12}$$

Different mass transfer models (surface renewal model, penetration model, and film model) will give different expressions of E. Among these models, the one given by the surface renewal model yield an explicit expression of E, whereas the penetration and the film models give an implicit expression of E. Krauβ and Rzehak (2017) demonstrates that the differences between all three expressions are minor, with the surface renewal model provides a convenient formula, written as:

$$E = -\frac{Ha^2}{2(E_i - 1)} + \sqrt{\frac{Ha^4}{4(E_i - 1)^2} + E_i \frac{Ha^2}{4(E_i - 1)} + 1} \tag{5.13}$$

With E_i is the instantaneous enhancement factor. E_i must be greater or equal to one to always give a value of E greater or equal to one. Otherwise, the value is limited by $max(E, 1)$ (Westerterp et al., 1984). To apply this model, an expression of E_i is needed. An implicit solution given by Danckwerts and Lannus (1970) which dependent on $\beta(E_i)$ is the following:

$$E_i = \frac{1}{erf(\beta/\sqrt{D_{CO_2}})} = \frac{erf(\beta/\sqrt{D_{OH^-}})}{erf(\beta/\sqrt{D_{CO_2}})} + \frac{exp(-\beta^2/D_{OH^-})}{exp(-\beta^2/D_{CO_2})}.\frac{[OH^-]}{2.He.C_{G,CO_2}}.\sqrt{\frac{D_{OH^-}}{D_{CO_2}}} \tag{5.14}$$

Some asymptotic cases can be derived from equation (5.14). An analytical solution is obtained if $D_{OH^-} = D_{CO_2}$, where β drops out of equation (5.14) and E_i becomes

$$E_i = 1 + \frac{[OH^-]}{2.He.C_{G,CO_2}} \tag{5.15}$$

For the case of $\beta \rightarrow 0$, $\mathrm{E_i} \rightarrow \infty$. But, a direct evaluation of equation (5.14) is also possible by calculating the limit of the first term on the right-hand side according to de l'Hôpital's rule, which yields an approximate explicit expression valid for $E_i \gg 1$ (Krauβ and Rzehak, 2017). The expression of $\mathrm{E_i}$ becomes

$$E_i = \left(1 + \frac{D_{OH^-}.[OH^-]}{2.D_{CO_2}.He.C_{G,CO_2}}\right).\sqrt{\frac{D_{OH^-}}{D_{CO_2}}} \tag{5.16}$$

Equation (5.16) is used in the original work of Darmana et al. (2007). However, Krauβ and Rzehak (2017) pointed out that equation (5.16) is sensitive to the ratio of D_{OH}^{-}/D_{CO_2} as it is not guaranteed to satisfy the requirement of $\mathrm{E_i} > 1$. For this reason, it is improved in (Westerterp et al., 1987) to

$$\mathrm{E_i} = \left(1 + \frac{[OH^-]}{2.He.C_{G,CO_2}}\right).\sqrt{\frac{D_{OH^-}}{D_{CO_2}}} \tag{5.17}$$

Krauβ and Rzehak (2017) proposed a fit formula to resolve equation (5.14) which depends on the sign of $\delta - 1$ with $\delta = \sqrt{\frac{D_{OH^-}}{D_{CO_2}}}$. As δ is superior than 1, the solution for E_i is given as

$$(E_i - 1).\frac{\delta}{\chi} = 1 + \frac{1}{2}(\delta - 1).\left(\frac{2}{\pi}arctan\left(0.2.\frac{\pi}{2}ln(exp(\chi) - 1)\right) + 1\right) \tag{5.18}$$

With $\chi = \frac{[OH^-]}{2.He.C_{G,CO_2}}.\sqrt{\frac{D_{OH^-}}{D_{CO_2}}}$.

Krauβ and Rzehak (2017) also studied the expression of E considering a two-step reaction for CO_2 chemisorption process. However, they found that the two-step nature of the reaction does not play a significant role as the results are the same as that of a one-step reaction, therefore, the expression of E for a two-step reaction is not discussed here. Krauβ and Rzehak (2017) found that the explicit fit formula yields the same results as solving the implicit equation (5.14). This proves that it is more practical for modelling purposes to apply the explicit fit formula rather than performing numerical resolution of the implicit equation.

Another simple enhancement factor model (E) has been proposed by Fleischer et al. (1996) which is obtained from the fitting to the experimental data. The model stated that if the OH^- mass fraction is higher than a certain threshold, E is activated. It is expressed as:

$$E = \begin{cases} 1, & Y_{OH^-} < 1.8e-6 \\ 1241.3\,Y_{OH^-} + 1.0069, & Y_{OH^-} \geq 1.8e-6 \end{cases} \tag{5.19}$$

This model has been used in many existing works (Hlawitschka et al., 2016; Huang et al., 2021; Liu et al., 2021), primarily due to its simplicity. Up to pH of 10, the enhancement factor is close to unity (Hlawitschka et al., 2016).

Huang et al. (2021) also investigated different expressions for the enhancement factor. They pointed out that the E given by equation (5.19) gives the best fit to Darmana's experimental pH curve.

- General summary

Since the original work of Darmana et al. (2007), many researchers used their experimental datasets to validate their numerical model for reactive bubbly flow. Several advances and insights have been drawn from these studies which are important in the field of reactive bubbly flow simulation. To our best knowledge, no studies have been attempted using the 1D modelling approach for this reference case. It also lacks direct comparative studies between previous works and analysis of different approaches. In this work, we aim to achieve the same goal as the previous CFD studies which are to unravel the coupling mechanisms and underline the controlling parameters during the CO_2 chemisorption process, using a comprehensive spatio-temporal 1D model.

5.4 Second Paper: In-depth analysis of reactive bubbly flow using two-way coupled spatio-temporal 1D model

Our second paper is published in Chemical Engineering Science and it is accessible with the following link: https://doi.org/10.1016/j.ces.2022.117963. The paper reports the application of the previously developed 1D model to the Darmana et al. (2007) case and further detailed analysis on reactive bubbly flow is provided. Moreover, it highlights an asymptotic model describing the CO_2 chemisorption process, which is derived from the CSTR assumption. It also features some sensitivity analyses conducted using the 1D model.

Chemical Engineering Science 261 (2022) 117963

Contents lists available at ScienceDirect

Chemical Engineering Science

journal homepage: www.elsevier.com/locate/ces

In-depth analysis of reactive bubbly flow using two-way coupled spatio-temporal 1D model

Vincent Ngu, Jérôme Morchain, Arnaud Cockx *

TBI, Université de Toulouse, CNRS, INRAE, INSA, Toulouse, France

HIGHLIGHTS

- Two-way coupled 1D model successfully implemented for CO_2 reactive absorption.
- 1D model yields excellent agreement with experimental and literature data.
- Asymptotic model unravels the governing parameters at each pH zone.
- Sensitivity analyses show the importance of k_L in capturing the transient process.

ARTICLE INFO

Article history:
Received 8 April 2022
Received in revised form 24 June 2022
Accepted 29 July 2022
Available online 3 August 2022

Keywords:
Bubble column
Gas-liquid multiphase flow
Mass transfer
CO_2 absorption
Chemical reaction
1D modeling

ABSTRACT

This work aims to investigate reactive bubbly flow using a comprehensive spatio-temporal 1D model. The work of Darmana et al. (2007) who conducted experimental and numerical study on CO_2 chemisorption in NaOH solution is used as the reference case. The gas–liquid hydrodynamics are well captured using a drift-flux loop model. During the transient process, bubble diameter d_b shrinkage from 5.5 mm at the inlet to 3.7 mm at the outlet is captured by the 1D model. The pH evolution is also well predicted by the 1D model provided that appropriate closures are applied, including the recently proposed enhancement factor and reaction pathway by Krauβ & Rzehak (2017). An asymptotic 0D model is proposed to highlight the key parameters involved during the transient chemisorption process which are enhancement factor E, mass transfer coefficient k_L, and interfacial area a. Sensitivity analyses on liquid axial dispersion coefficient, enhancement factor and mass transfer coefficient are then performed to elucidate their impact on reactive mass transfer. As the process is controlled by interfacial mass transfer, the most important parameters are k_L and d_b description.

1. Introduction

Bubble column reactors are commonly used in the industry, such as metallurgical, petrochemical, biochemical, and water treatment. These reactors have numerous advantages: (a) simple design, (b) absence of mechanical stirring device (c) good mixing (d) low energy input requirements and (e) large gas–liquid contact area (Deckwer and Schumpe, 1993; Kantarci et al., 2005; Shah et al., 1982). However, complex and highly coupled phenomena in terms of multiphase flow, mass and heat transfer, and (bio) reaction prevail in such system.

In reactive bubble column, the hydrodynamics, mass transfer, and reactions are highly coupled with each other. The reaction rate depends on the local availability of the species, which is controlled by the convection, the mixing of the fluid flow, and the gas–liquid mass transfer (if the species is originated from the gaseous phase). The interphase mass transfer flux is driven by the species concentration gradient diffused between phases, which depends on the mass transfer coefficient and interfacial area (hence the local bubble size and gas holdup). Besides, the mass transfer coefficient is a function of the bubble size and local hydrodynamics, which are also affected by the overall gas–liquid reaction rate. In short, the coordinated and mutual influence of these complex processes make the overall reactor performance prediction and scale-up of reactive bubble column very challenging (Buffo et al., 2017; Darmana et al., 2007). Fig. 1a depicts the coupling of these phenomena through different physical parameters involved in reactive bubbly flow.

Recently, extensive efforts have been made to develop numerical code to simulate bubble column reactor (Hlawitschka et al., 2017; McClure et al., 2014; Rzehak et al., 2017; Rzehak and Krepper, 2016). Most of the works have been performed using

* Corresponding author.
E-mail addresses: ngu@insa-toulouse.fr (V. Ngu), morchain@insa-toulouse.fr (J. Morchain), cockx@insa-toulouse.fr (A. Cockx).

https://doi.org/10.1016/j.ces.2022.117963
0009-2509/

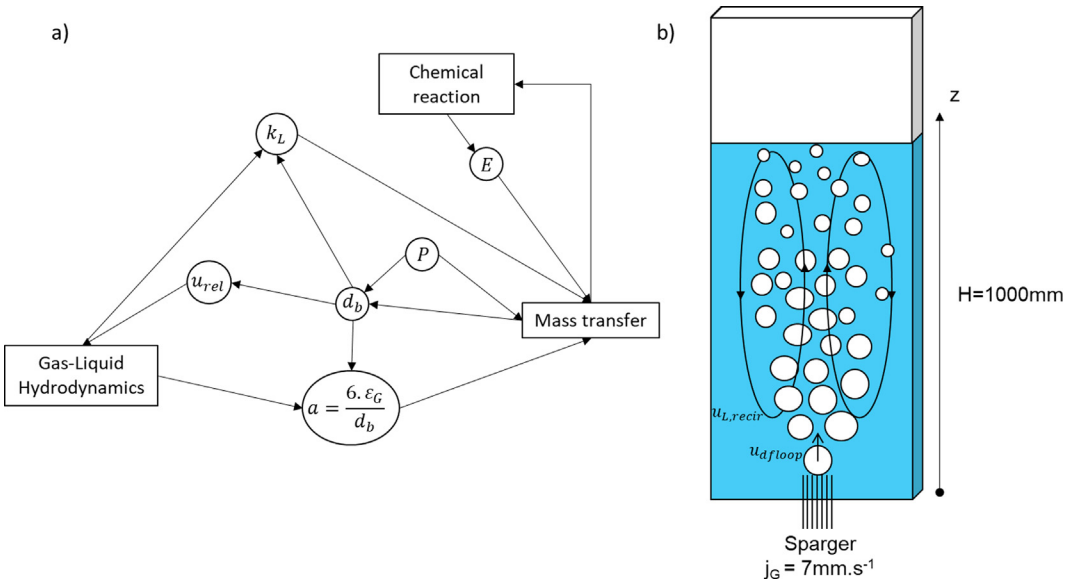

Fig. 1. (a) Interdependency diagram of hydrodynamics, mass transfer and chemical reaction through different parameters involved in reactive bubbly flow. (b) Simplified sketch of the pseudo-2D bubble column studied by Darmana et al. (2007).

Computational Fluid Dynamics (CFD) approach as it is a powerful tool to capture the spatial heterogeneities and to study the local interaction of multiphase systems. In general, two approaches are used in the CFD framework, i.e, Euler-Euler and Euler-Lagrange simulations. Apart certain studies on industrial-scale bubble column (Cockx et al., 1999; Ertekin et al., 2021; Rehman et al., 2017), most of the numerical work focus on lab-scale bubble column. Krauβ and Rzehak (2018) pointed out that most of the numerical work focus on the fluid dynamics of bubbly flows. The mass transfer modeling, particularly with the reactive flow is less common in the literature. The presence of reactive system coupled with mass transfer phenomenon, makes the mass transfer modeling highly challenging. Extensive studies are needed to unravel the influence of reactive mass transfer on the hydrodynamics behavior. Moreover, progress in simulation studies is hindered by a shortage of high-quality validation data. This is mostly due to the difficulty to access local value such as concentration measurements (Krauβ and Rzehak, 2018; Rzehak and Krepper, 2016). Lately, Chen and Brooks (2021) conducted a comprehensive experiment on local mass transfer in small-scale bubble column (5-inch diameter and 6.55-inch height) and the CFD model developed by the authors is validated in terms of hydrodynamics and mass transfer. A detailed study with local concentration measurements at a larger-scale bubble column was carried out by Deckwer et al. (1978) and their data was later used in the work of Rzehak and Krepper (2016) whereby Euler-Euler CFD simulation was performed. Rzehak and Krepper (2016) concluded that new measurements will be needed as spatially resolved data which are suitable for CFD model validation is still scarce in the literature.

In the reference work of Darmana et al. (2007), the chemisorption of carbon dioxide (CO_2) in aqueous sodium hydroxide solution (NaOH) was investigated and the influence of fast reaction on the hydrodynamics behavior was studied both experimentally and numerically with the CFD model using Euler-Lagrange approach. In the past, several numerical attempts have been conducted to compare with Darmana's work. As demonstrated in several literature findings, reactive absorption of CO_2 in NaOH is a fast and highly coupled reaction as the shrinkage of bubble size is observed which in returns affects the CO_2 mass transfer flux and the reaction rate (Buffo et al., 2017; Darmana et al., 2007; Gruber et al., 2015). Most of the studies on Darmana et al. (2007) reference case have been performed using CFD framework, either in Euler-Euler (Hlawitschka et al., 2016; Krauß and Rzehak, 2018; Liu et al., 2021) or Euler-Lagrange (Gruber et al., 2015; Huang et al., 2021; Taborda and Sommerfeld, 2021) approach. These studies applied different strategies separately to investigate or reproduce the experimental data, such as detailed reaction pathways (Krauβ and Rzehak, 2018; Krauβ and Rzehak, 2017), bubble population model (Buffo et al., 2017; Gruber et al., 2015), mass transfer closure model (Huang et al., 2021; Taborda and Sommerfeld, 2021), and enhancement factor model (Huang et al., 2021; Krauβ and Rzehak, 2017).

To our best knowledge, no studies have been done using one-dimensional (1D) modeling approach for this reference case. The 1D model requires less computational resources than sophisticated CFD model and it is easy to implement, hence it offers a fast and satisfactory prediction (Siebler et al., 2020). Although there is some trade-off in terms of highly precise spatial resolution offered by the CFD model, the 1D model is still very useful for probing and filtering off a wide range of design and operating parameters or closure models before moving into advanced CFD modeling which aims at studying the local field structure and the interactions between phases. The 1D model is commonly used to model bubble columns in the literature as it provides satisfactory performance prediction at low computational costs (Camarasa et al., 2001; Colombet et al., 2013; Hissanaga et al., 2020; Larsson et al., 2022; Talvy et al., 2007). However, most of the model make some assumptions such as constant gas holdup and constant bubble diameter. These assumptions cannot be made in the case of Darmana et al. (2007), as the bubble diameter changes considerably in the axial direction due to reactive absorption.

A two-way coupled and spatio-temporal approach have to be considered in the case of fast reaction. This paper aims to demonstrate that a full 1D two-way coupled spatio-temporal model is able to reproduce Darmana's results without performing computational-intensive calculations. The goal is to decipher and characterize the hydrodynamics-reactive mass transfer coupling process. Following the literature results, similar conclusions and some new insights are also drawn using the 1D model. This paper is organized as follows. A summary of the reference work of Darmana et al. (2007) is briefly recalled in Section 2.1. Next, the 1D model and the closure models applied are described in

Section 2.2. A comparison to some literature data is presented in Section 3. An asymptotic model based on CSTR assumption is also proposed in Section 4 to better understand the underlying physical mechanism that impact the temporal pH evolution. Besides, it helps to identify essential parameters which play an important role at different time zone in describing the CO_2 chemisorption process. Lastly, sensitivity analysis that highlights important parameters of reactive bubbly flow is presented in Section 5. Section 6 summarizes our findings and final remarks.

2. Materials & methods

2.1. Brief summary of Darmana's case

Full description of the methods and the results can be found in the original work of Darmana et al. (2007). For the sake of simplicity, a brief recap of the work is reported here. A simplified sketch of the bubble column used is shown in Fig. 1b.

The experimental setup consisted of a lab-scale pseudo-2D bubble column of 200 mm width and 30 mm depth. The initial liquid level (H) was kept at 1000 mm. The gas was sparged through 21 needles arranged with a square pitch of 5 mm and it was located at the column center. The superficial gas velocity (j_G) was kept as 7 mm.s^{-1}. The bubble size formed at the inlet (d_{b0}) was mentioned to be 5.5 mm.

Two gas–liquid systems were measured to investigate the influence of fast reaction on the hydrodynamics behavior. First, nitrogen (N_2) and twice distilled water was used to mimic the non-reactive system. Next, a reactive system composed of CO_2 and aqueous NaOH solution at an initial pH of 12.5 was utilized to study the effect of chemisorption on the hydrodynamics. Several measurements were conducted, namely:

- Integral gas holdup was calculated by the difference of liquid height with and without bubbles.
- Time-averaged gas velocity was measured by using Particle Image Velocimetry (PIV) as a tracking method of the bubble. The bubble velocity profile was reported at z/H = 0.75.
- Local bubble size measurements were obtained through image processing technique of a series of images recorded via CCD camera. The time-averaged bubble size axial profile was reported only for reactive case.
- Temporal evolution of pH was measured with a pH probe placed at 2 cm below the liquid surface in the center of the column.

Besides the experimental work, Darmana et al. (2007) also carried out numerical simulations for both non-reactive and reactive cases using the CFD Euler-Lagrange approach. The motion of each individual bubble is computed from the bubble mass and momentum equations while considering all relevant fluid dynamical forces, namely gravity, buoyancy, drag, lift, virtual mass and wall forces. The drag, lift and wall forces are modeled using closures obtained from Tomiyama et al. (2002, 1995).

2.2. Comprehensive 1D spatio-temporal model for reactive bubbly flow

2.2.1. Two-phase hydrodynamics model

Previously developed comprehensive two-way coupled 1D model is used in this work and it is recalled here. The numerical discretization and the applied scheme are kept the same as that described in Ngu et al. (2022). The 1D model is composed of the following species transport equations, and they are solved for 4 species $i \in \left\{CO_2; OH^-; HCO_3^-; CO_3^{2-}\right\}$:

Gas:

$$\frac{\partial \varepsilon_G C_{G,i}}{\partial t} + \frac{\partial u_G \varepsilon_G C_{G,i}}{\partial z} = D_G \frac{\partial}{\partial z}\left(\varepsilon_G \frac{\partial C_{G,i}}{\partial z}\right) - \mathrm{E}k_{L,i}a\left(C_i^* - C_{L,i}\right) \tag{1}$$

Liquid:

$$\frac{\partial \varepsilon_L C_{L,i}}{\partial t} + \frac{\partial u_L \varepsilon_L C_{L,i}}{\partial z} = D_L \frac{\partial}{\partial z}\left(\varepsilon_L \frac{\partial C_{L,i}}{\partial z}\right) + \mathrm{E}k_{L,i}a\left(C_i^* - C_{L,i}\right) + \varepsilon_L R_i \tag{2}$$

$$\varepsilon_G + \varepsilon_L = 1 \tag{3}$$

Equation (1) is solved only for CO_2, whereas equation (2) is solved for $CO_2, OH^-, HCO_3^-, CO_3^{2-}$. Apart from CO_2, the mass transfer term ($\mathrm{E}k_{L,i}a\left(C_i^* - C_{L,i}\right)$) is zero. ε_G and ε_L are the gas and liquid holdup summing as unity as shown in equation (3). $C_{G,i}$ and $C_{L,i}$ are the concentration of species i, which will also be represented with $[i]$ in this work, e.g. $[CO_2]$ concentration of CO_2.

The gas phase hydrodynamics is modeled via a drift-flux loop model (u_{dfloop}) which is derived hereafter. The relative gas velocity of the mixture (u_{rel}) can be derived from a momentum balance on an isolated bubble having reached its terminal velocity, expressed as:

$$u_{rel} = \sqrt{\frac{4}{3}\frac{g(\rho_m - \rho_G)d_b}{\rho_L C_D}} \tag{4}$$

With g the gravity (9.81 m^2.s^{-1}), ρ_m and ρ_G the mixture and gas density, respectively; d_b is the bubble diameter and C_D is the drag coefficient. The mixture density ρ_m is calculated as $(\rho_L\varepsilon_L + \rho_G\varepsilon_G) - \rho_G = \varepsilon_L(\rho_L - \rho_G)$. The density of water (1000 kg.m^{-3}) and carbon dioxide (1.78 kg.m^{-3}) at 298.15 K and 1 atm are taken for liquid and gas density, respectively. The drag coefficient proposed by Tomiyama et al. (1998) for pure system is used, similar to Darmana et al. (2007). It is written as:

$$C_D = max\left\{\min\left[\frac{16}{Re}\left(1 + 0.15Re^{0.687}\right), \frac{48}{Re}\right], \frac{8}{3}\frac{Eo}{(4+Eo)}\right\}$$

$$Re = \frac{u_{rel}d_b}{\nu_L} \quad Eo = \frac{(\rho_L - \rho_G)gd_b^2}{\sigma} \tag{5}$$

With Re the Reynolds and Eo the Eötvös number. The viscosity and surface tension of water is applied ($\mu_L = 10^{-3}$ Pa.s and $\sigma = 0.072$ N.m^{-1}). The variations of Re and Eo are between 800 and 1600 and 1.4 – 4.2, respectively for both non-reactive and reactive cases. In this range of Re and Eo, the drag coefficient is governed by the Eötvös term, signifying that the governing factor is no longer the viscous force but the pressure and surface tension forces (Tomiyama et al., 1998). No collective effect is included as the gas holdup shown in Darmana et al. (2007) is relatively low (lower than 3 %). The axial bubble velocity profile obtained by Darmana et al. (2007) is parabolic, showing the non-uniformity of the flow, due to the centered gas inlet. Considering this non-uniformity bubbly flow, the drift-flux model (u_{df}) suggested by Zuber and Findlay (1965), which is commonly used in 1D modeling is applied here (Camarasa et al., 2001; Talvy et al., 2007). It stated that the gas velocity is composed of two components: (i) gas transport induced by the mixture velocity $< j >$, which is the sum of gas and liquid superficial velocity ($j = j_G + j_L$) and (ii) the buoyancy driven gas transport u_{rel}. The drift-flux model is expressed as:

$$u_{df} = C_0 < j > + u_{rel} \tag{6}$$

Here, the coefficient C_0 is calculated from its definition $C_0 = \frac{<\varepsilon_G j>}{<\varepsilon_G>.<j>}$ using Darmana et al. (2007) reported profiles, and a value of 1.24 and 1.27 are obtained for non-reactive and reactive case, respectively.

The experimental liquid axial velocity profile obtained by Darmana et al. (2007) suggests that the bubbles rise in the column center with liquid recirculation down near the wall. This liquid recirculation phenomena leads to the hydrodynamic of the column to behave like an airlift system (Talvy et al., 2007, 2005). Thus, the liquid recirculation velocity $u_{L,recirc}$ is considered as j_L in the drift-flux model in equation (6), leading to drift-flux loop u_{dfloop} model, written as.

$$u_{dfloop} = C_0\left(j_G + u_{L,recirc}\right) + u_{rel} \tag{7}$$

The value of $u_{L,recirc}$ is also derived from the liquid axial velocity profile from Darmana et al. (2007) through spatial averaging till the inversion point of liquid velocity – point where the liquid flow direction changes to downward flow. This mean value of $u_{L,recirc}$ varies with or without reaction due to the gas holdup changes and they are given in Table 2. In the end, the gas velocity u_G is calculated with the drift-flux loop model u_{dfloop} expressed in equation (7).

The liquid side axial dispersion coefficient (D_L) is taken from the correlation of Deckwer et al. (1974) while the gaseous side axial dispersion coefficient (D_G) is estimated with the correlation of Wachi and Nojima (1990). The bubble column diameter (D_r) is taken as the equivalent diameter of a circular bubble column having the same cross sectional area as that of a rectangular column, similar to the work of Alexander and Shah (1976), which yields $D_r = 0.087$ m. These coefficients are expressed in equations (8) and (9). The correlations yield a value of 5×10^{-3} m^2.s^{-1} and 3.6×10^{-3} m^2.s^{-1} for D_L and D_G, respectively. D_L can be breakdown into several terms to assess the contribution of each dispersion phenomena (Talvy et al., 2007). The CO_2 molecular diffusivity in water is in the order of 10^{-9} m^2.s^{-1}, the turbulent diffusivity can be considered as the turbulent viscosity ν_t, which can be estimated using Chou model, given as $\nu_t = U^*\kappa\delta$ with $\kappa = 0.4$ (Chou, 1945; Launder and Spalding, 1974). The length scale δ is taken as the half depth of the column (15 mm), U^* can be supposed as 5 % of averaged bubble velocity initially estimated as 0.3 m.s^{-1}. Therefore, the turbulent velocity is estimated as $\nu_t = 0.05 \cdot 0.3 \cdot 0.4 \cdot 0.015 \approx 10^{-4}$ m^2.s^{-1}. Thus, the main contribution of axial dispersion in the liquid phase is the spatial dispersion as in Talvy et al. (2007).

$$D_L = 2 \cdot 7 \cdot 10^{-4} \cdot (D_r \cdot 100)^{1.4} \cdot (j_G \cdot 100)^{0.3} \tag{8}$$

$$D_G = 20 \cdot D_r^{1.5} \cdot j_G \tag{9}$$

Due to mass transfer, bubble shrinkage is expected. The changes in bubble diameter d_b is described by equation (10):

$$d_b = \mathrm{d_{b0}}\sqrt[3]{\frac{\varepsilon_G}{\varepsilon_{G0}}} \tag{10}$$

The inlet bubble diameter (d_{b0}) are taken the same as Darmana et al. (2007) at 5.5 mm. The interfacial area (a) is calculated with bubble diameter and gas holdup, expressed as:

$$a = 6\frac{\varepsilon_G}{d_b} \tag{11}$$

Table 1
Summary of reaction term for each species i.

Species i	$R_i(kmol.m^{-3}.s^{-1})$
CO_2	$-R_{1,1} + R_{1,2} - R_{3,1} + R_{3,2}$
OH^-	$-R_{1,1} + R_{1,2} - R_{2,1} + R_{2,2} - R_{3,1} + R_{3,2}$
HCO_3^-	$R_{1,1} - R_{1,2} - R_{2,1} + R_{2,2} + R_{3,1} - R_{3,2}$
CO_3^{2-}	$R_{2,1} - R_{2,2}$

Table 2
Input parameters applied in the 1D model for the reference case.

Input Parameters	Value	Units
d_{b0}	5.5	mm
T	298.15	K
j_G	0.007	m.s^{-1}
pH_0	12.5	–
C_0 without reaction	1.24	–
C_0 with reaction	1.27	–
$u_{L,recirc}$ without reaction	0.066	m.s^{-1}
$u_{L,recirc}$ with reaction	0.042	m.s^{-1}

The mass transfer closure model (k_L) is calculated from the Sherwood (Sh) correlation derived for non-spherical bubbles situated in the wobbling regime (Brauer, 1979). The expression is given in Table 3. The calculations of the solubility $C^*_{CO_2}$ and diffusivity D_{CO_2} are detailed in Appendix A and Appendix B, respectively.

2.2.2. Reactive model

The reaction term (R_i) calculation follows the recent work of Krauß and Rzehak (2018). The description of the reaction term R_i in the 1D model is briefly explained here. The dissolved CO_2 will react in a two-step reversible reaction which will be denoted as the first and second reactions in this work. The reactions are written as follows:

$$CO_2 + OH^- \rightleftharpoons^{k_{1,1}}_{k_{1,2}} HCO_3^- \tag{12}$$

$$HCO_3^- + OH^- \rightleftharpoons^{k_{2,1}}_{k_{2,2}} {CO_3}^{2-} + H_2O \tag{13}$$

Where $k_{1,1}$ and $k_{1,2}$ are the forward and backward rate constants, respectively for the first reaction while $k_{2,1}$ and $k_{2,2}$ are the forward and backward rate constants for the second reaction.

The water reaction path becomes important at pH less than 10 and even dominant at pH less than 8 (Kern, 1960). It consists of two steps, the first of which, is written as:

$$CO_2 + H_2O \rightleftharpoons^{k_{3,1}}_{k_{3,2}} {HCO_3}^- + H^+ \tag{14}$$

The first step is reversible (Kern, 1960). The second step is identical to hydroxide path (equation (13)), with the two pathways coupled by the auto-dissociation of water associated with the equilibrium constant K_w.

$$H_2O \rightleftharpoons OH^- + H^+ \tag{15}$$

Therefore, the corresponding chemical reactions rates for equations (12)-(14) are expressed as:

$$R_{1,1} = k_{1,1}.[CO_2].[OH^-] \tag{16}$$

$$R_{1,2} = k_{1,2}.\left[HCO_3^-\right] \tag{17}$$

$$R_{2,1} = k_{2,1}.\left[HCO_3^-\right].[OH^-] \tag{18}$$

Table 3
Closure models applied in the 1D model for the reference case.

Parameters	Correlation
u_G	$u_G = u_{dfloop} = C_0\left(j_G + u_{L,recir}\right) + u_{rel}$
D_L	$D_L = 2.7 \cdot 10^{-4} \cdot (D_r \cdot 100)^{1.4} \cdot (j_G \cdot 100)^{0.3}$
D_G	$D_G = 20 \cdot j_G \cdot D_r^{1.5}$
k_L	$Sh = 2 + 0.015Re^{0.89}.Sc^{0.7}$ $Sh = \frac{k_L d_b}{D_{CO_2}}$; $Re = \frac{u_{rel} d_b}{\nu_L}$; $Sc = \frac{\nu_L}{D_{CO_2}}$
E	$E = -\frac{Ha^2}{2(E_i-1)} + \sqrt{\frac{Ha^4}{4(E_i-1)^2} + E_i\frac{Ha^2}{4(E_i-1)} + 1}$
	E_i *from equations (B.4)-(B.6) of* Krauß and Rzehak (2017)

$$R_{2,2} = k_{2,2}.\left[CO_3^{2-}\right] \tag{19}$$

$$R_{3,1} = k_{3,1}.[CO_2] \tag{20}$$

$$R_{3,2} = k_{3,2}.\left[HCO_3^-\right].[H^+] = k_{3,2}.\left[HCO_3^-\right].\frac{K_w}{[OH^-]} \tag{21}$$

Here, the reaction rate $R_{j,k}$ are expressed in kmol.m^{-3}.s^{-1} with $j = 1, 2, 3$ denotes the reactions of equations (12)-(14) and $k = 1, 2$ denotes the forward and backward reactions, respectively. The calculation of the reaction rate constants $k_{j,k}$ are detailed in the Appendix C. The reaction term R_i for each species i in equation (2) is calculated with the expressions given in Table 1.

2.2.3. Enhancement factor model

Due to fast chemical reaction, enhancement of mass transfer flux has to be considered.

A simple enhancement factor model (E) has been proposed by Fleischer et al. (1996) which is obtained from the fitting to the experimental data. The model stated that if the OH^- mass fraction is higher than a certain threshold, E is activated. It is expressed as:

$$E = \begin{cases} 1, Y_{OH^-} < 1.8e-6 \\ 1241.3Y_{OH^-} + 1.0069, Y_{OH^-} \geq 1.8e-6 \end{cases} \tag{22}$$

This model has been used in many existing works (Hlawitschka et al., 2016; Huang et al., 2021; Liu et al., 2021), primarily due to its simplicity. Up to pH of 10, the enhancement factor is close to unity (Hlawitschka et al., 2016). It is pointed out by Huang et al. (2021) that this model gives the best fit to Darmana's experimental pH curve when the authors compared this correlation with other enhancement factor models.

Recently, Krauβ and Rzehak (2017) proposed another enhancement factor model based on the fit formula of an instantaneous one-step second-order reaction. The model is briefly presented here, as the details can be found in the original paper. Here, a fast single-step irreversible second order reaction is considered by combining equation (12) and (13). This leads to the following overall reaction equation:

$$CO_2 + 2OH^- \rightarrow CO_3^{2-} + H_2O \tag{23}$$

The Hatta number (Ha) is thus written as:

$$\mathrm{Ha} = \frac{\sqrt{k_{1,1}.D_{CO_2}.[OH^-]}}{k_L} \tag{24}$$

With the renewal theory, an expression for the enhancement factor derived by DeCoursey (1974) is expressed as:

$$\mathrm{E} = -\frac{Ha^2}{2(E_i - 1)} + \sqrt{\frac{\mathrm{Ha}^4}{4(E_i-1)^2} + E_i\frac{\mathrm{Ha}^2}{4(E_i-1)} + 1} \tag{25}$$

With E_i is the instantaneous enhancement factor. E_i must be greater or equal to one to always give a value of E greater or equal to one. Otherwise, the value is limited by max(E, 1) (Westerterp et al., 1998). To apply this model, an expression of E_i is needed. An implicit solution was given by Danckwerts and Lannus (1970), however, it is difficult to resolve and thus, less practical for modeling purpose. Krauβ and Rzehak (2017) proposed an explicit fit formula to overcome the complexity of the implicit model. The explicit E_i model is used in this work but it is not detailed here as it can be found in Appendix B of Krauβ and Rzehak (2017).

The impact of E is investigated in this work and it will be discussed in Section 5.2. The results given by the E of Fleischer et al. (1996) and Krauβ and Rzehak (2017) are compared. In the first step, the results presented hereafter used the latest development of E which is that of Krauβ and Rzehak (2017) unless it is stated otherwise.

In short, the input parameters and the closure models used for the reference study are summarized in Table 2 and Table 3, respectively. Apart from the reference results of Darmana et al. (2007), some additional and more recent CFD results in the literature are also used in the comparison with the 1D model, as indicated with a "x" in Table 4. These results included transient gas holdup, local gas holdup, local bubble velocity, local bubble diameter, and temporal pH evolution. For non-reactive case, the reactive term is not solved to calculate the integral gas holdup. The integral gas holdup is calculated by spatial averaging gas holdup at $t_\infty = 250$ s. The initial concentrations of sodium and hydroxide ions were set to match the initial pH value of 12.5, while all other species were set to zero. For reactive case, the reactive term is activated and the initial hydrodynamics start from the converged non-reactive case. The model is spatially discretized for 50 node grids and it is solved using MATLAB 2017b stiff solver ode15s where the timestep is adaptative as explained in Ngu et al. (2022).

3. Results of 1D model compared with previous works

3.1. Hydrodynamics with and without CO_2 reactive absorption

In this section, the hydrodynamics results on the non-reactive and the reactive system are addressed. In most cases, Darmana et al. (2007) employed time-averaging for the interpretation of the dynamic results. It is reported that a time interval of 20–80 s and 20–95 s was used for the non-reactive and the reactive case, respectively. The same time interval for time-averaging is used in this work.

Table 5 presents the 1D time-averaged local bubble velocity compared with that of Buffo et al. (2017), Darmana et al. (2007), and Krauß and Rzehak (2018). In all work, the non-reactive case shows higher bubble velocity compared with the reactive case. In the reactive case, high CO_2 mass transfer flux leads to a reduction in bubble size, causing a decline in the bubble velocity as expected. This is further confirmed in Fig. 3a where the bubble size decreases considerably during CO_2 chemisorption. Table 6 depicts the 1D time-averaged local gas holdup compared with that of Darmana et al. (2007), Huang et al. (2021), and Krauß and Rzehak (2018). Again, the high CO_2 interfacial mass transfer flux leads to a significant reduction in the gas holdup. The global hydrodynamics is well captured by the 1D model as the bubble velocity and the gas holdup are at the same order of magnitude to the experimental data and the literature CFD results.

Table 4
List of references used for comparison with 1D model. E-L: Euler-Lagrange. E-E: Euler-Euler.

Reference	CFD approach	Transient gas holdup	Local gas holdup	Local bubble velocity	Local bubble diameter	pH
(Darmana et al., 2007)	E-L	–	x	x	x	x
(Buffo et al., 2017)	E-E	x	–	x	x	x
(Krauβ and Rzehak, 2018)	E-E	x	x	x	x	x
(Huang et al., 2021)	E-L	–	x	–	–	x
(Hlawitschka et al., 2016)	E-E	–	–	–	–	x

Table 5
Time-averaged bubble velocity in $m.s^{-1}$ at z/H = 0.75 for non-reactive and reactive case. The experimental and CFD results are obtained by area-weighted average.

Case	Experiment	(Darmana et al., 2007) CFD	(Buffo et al., 2017) CFD	(Krauβ and Rzehak, 2018) CFD	1D model
Non-reactive	0.21	0.20	0.25	0.25	0.31
Reactive	0.19	0.20	0.23	0.24	0.29

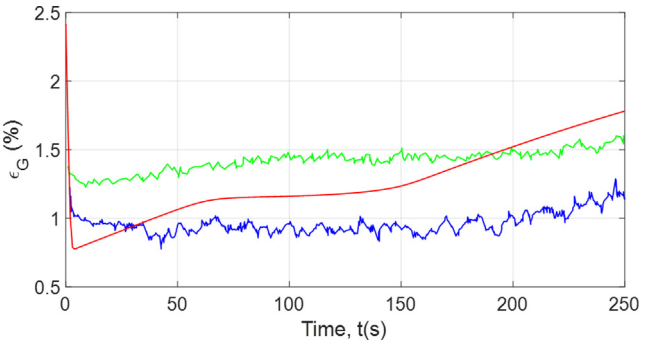

Fig. 2. Transient integral gas holdup during the CO_2 chemisorption. Red line from 1D model. Blue line from (Buffo et al., 2017) CFD results. Green line from (Krauβ and Rzehak, 2018) CFD results.

Table 7 reports the integral gas holdup obtained by the 1D model and Darmana et al. data. The global hydrodynamics are correctly captured for both non-reactive and reactive cases as the integral gas holdup closely match that of experiment. The gas phase hydrodynamics play an important role in reactive bubbly flow. The bubbles hydrodynamic characterizes the gas holdup which characterizes the specific area a for mass transfer. Consequently, as long as the gas velocity is correctly described, the gas holdup, the mass transfer flux and the reaction rate should be correctly predicted.

Table 7
Integral gas holdup in % from this work compared with experimental and simulation data of Darmana et al. (2007).

Case	Experiment	CFD Simulation	1D model
Non-reactive	2.3	2.2	2.42
Reactive	1.2	1.6	1.78

Fig. 2 depicts the transient evolution of integral gas holdup in the column. The gas holdup drops immediately when the chemical reaction commences. It remains almost constant during the course of the chemisorption process. However, once the reaction is over, the gas holdup increases subsequently. Buffo et al. (2017) yields a lower integral gas holdup, mainly due to a larger initial bubble diameter (see Fig. 3), leading to a lower residence time. At the end of the neutralization process ($t = t_\infty$), the 1D model yields an integral gas holdup close to that of Krauβ and Rzehak (2018). Two zones can be noticed for the transient gas holdup: (1) during the CO_2 chemisorption and (2) CO_2 physical absorption. During the chemical reaction process, the integral gas holdup remains almost

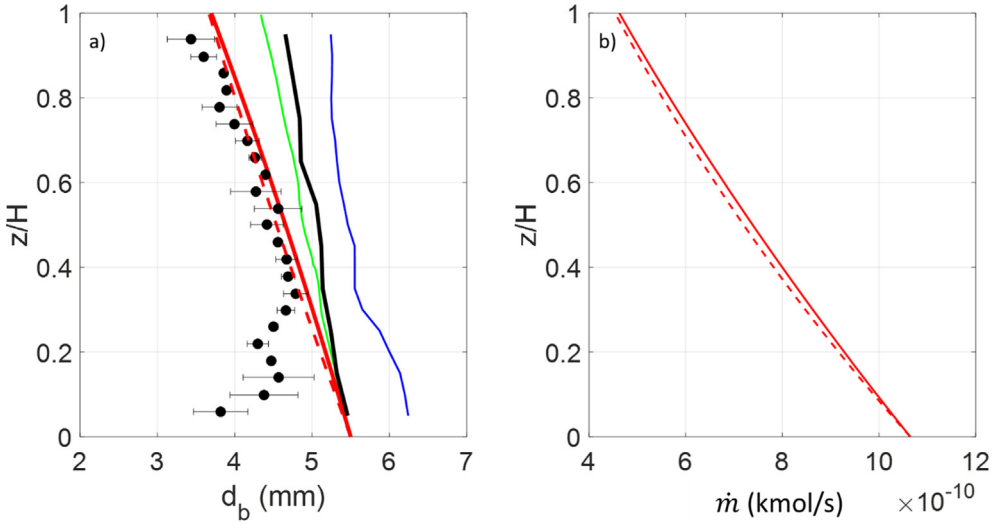

Fig. 3. (a) Time-averaged axial mean Sauter diameter profile. Blue line from (Buffo et al., 2017) CFD results, Green line from (Krauβ and Rzehak, 2018) CFD results, Magenta lines from (Huang et al., 2021), Black line from from (Darmana et al., 2007) CFD results, Black dots from (Darmana et al., 2007) experimental results, Red lines. – 1D model – – equation (29) (b) Time-averaged local mass transfer rate of a single bubble predicted with d_{b0} = 5.5 mm. – Lagrangian model – – equation (31).

Table 6
Time-averaged gas holdup in % at z/H = 0.75 for non-reactive and reactive case. CFD results are obtained by area-weighted average.

Case	(Darmana et al., 2007) CFD	(Huang et al., 2021) CFD	(Krauβ and Rzehak, 2018) CFD	1D model
Non-reactive	2.09	2.99	3.05	2.38
Reactive	1.48	1.39	1.48	1.07

constant, which is translated by a steady CO_2 mass transfer flux (confirmed in Fig. 7) to the liquid. When the reaction is terminated, CO_2 starts to accumulate in the liquid, the dissolved CO_2 concentration increases. This results in an increasing gas holdup as the CO_2 mass transfer flux is diminishing, due to a weaker driving force (concentration gradient $C^*_{CO_2} - C_{L,CO_2}$). This phenomenon is also evidenced in the temporal gas holdup profile of Buffo et al. (2017), although they reveal a more modest increase.

The time-averaged axial bubble diameter profile during dynamic CO_2 chemisorption is presented in Fig. 3a. It shows that the bubble diameter shrinks due to high mass transfer flux when the bubbles rises in the column. 1D model yields relatively good bubble size reduction as the predicted bubble diameter is very close to the experimental measurements. Experimental measured bubble diameter was judged as unreliable up to a height of approximately 400 mm. In this region most of the bubbles overlaps and this could not be handled by the image processing algorithm, resulting in underestimated bubble size (Darmana et al., 2007). Nonetheless, most CFD models underpredict the bubble size shrinkage. Regardless, the bubble diameter has to be correctly quantified as it strongly impacts the mass transfer rate, and consequently the reaction rate. Fig. 3a shows that Buffo et al. (2017) model has the largest difference with the experimental data. This is due to the inlet bubble diameter applied by the authors is calculated from literature correlation which yields 6.2 mm and not 5.5 mm that is used by all other CFD works. If d_{b0} = 5.5 mm had been used in Buffo et al. (2017), the results could be better as the authors solved the bubble size population balance equation, which should yield a more realistic mass transfer flux. Darmana et al. (2007) underpredicts the bubble diameter shrinkage, mostly due to a lower mass transfer flux prediction. As shown in Fig. 3b the mass transfer rate of a single bubble ($\dot{m} = k_L \pi d_b^2 C^*_{CO_2}$) decreases with a factor of 2 between the top and the bottom of the column. This demonstrates that a slight error in terms of the bubble diameter prediction will generate larger errors in the transfer rate and subsequently the final pH value. The changes in mass transfer flux due to bubble diameter shrinkage can be explained with a simplified Lagrangian model of which it is detailed hereafter.

3.2. Role of bubble size on reactive mass transfer

By measuring the variation of bubble size with a video camera, it is able to evaluate experimentally the mass transfer coefficient, by knowing the mass transfer rate (Hori et al., 2017; Saito and Toriu, 2015; Takemura and Yabe, 1999; Tanaka et al., 2020). The same analogy can be applied here to relate the changes in bubble size due to the mass transfer rate, similar to the work of Solsvik (2018). The change in moles of CO_2 inside a bubble over time can be written as:

$$\frac{dn}{dt} = -k_L A_b \left(C^*_{CO_2} - C_{L,CO_2} \right) \tag{26}$$

With $A_b = \pi d_b^2$ the bubble surface area for mass transfer and n is the number of moles. Using the ideal gas law, $PV = nRT$ and assuming an isothermal process, equation (26) can be rewritten as:

$$\frac{\pi}{6RT} \frac{d\left(P \cdot d_b^3\right)}{dt} = -k_L A_b \left(C^*_{CO_2} - C_{L,CO_2} \right) \tag{27}$$

During 20–95 s of the reactive absorption, the dissolved CO_2 concentration is nearly zero (see Fig. 6b), C_{L,CO_2} can be considered equal to 0. If the column height and gas holdup are low, the pressure P can be supposed constant with an estimated value of $< P >= P_{atm} + \frac{\rho_L g H}{2} = 106230 Pa$. The bubble velocity u_G for the range of d_b during the reactive absorption experiences little changes, leading to $dt = \frac{dz}{u_G}$. Equation (27) is rearranged to.

$$\frac{d\left(d_b^3\right)}{d_b^2} = -\frac{k_L}{u_G} \frac{C^*_{CO_2} 6RT}{< P >} \cdot dz \tag{28}$$

Assuming a constant u_G and k_L, integration of equation (28) leads to axial evolution of d_b expressed as.

$$d_b = d_{b0} \left(1 - \frac{k_L}{d_{b0}} \frac{z}{u_G} \frac{C^*_{CO_2} 2RT}{< P >} \right) \tag{29}$$

Equation (29) reveals the term $\frac{k_L}{d_{b0}} \frac{z}{u_G}$ which can be interpreted as the ratio of the convection characteristic time ($\frac{z}{u_G}$) to the mass transfer characteristic time ($\frac{k_L}{d_{b0}}$). The lower the u_G, the higher the gas residence time, the higher the mass transfer flux, the smaller the bubble size due to mass transfer. Similarly, the higher the k_L, the higher the mass transfer flux, the higher the bubble shrinkage.

From equation (29), the axial evolution of mass transfer rate ($\dot{m}$) can be calculated as the evolution of $\frac{\dot{m}}{\dot{m}_0}$ is related to $\left(\frac{d_b}{d_{b0}}\right)^2$, leading to.

$$\frac{\dot{m}}{\dot{m}_0} = \left(1 - \frac{k_L}{d_{b0}} \frac{z}{u_G} \frac{C^*_{CO_2} 2RT}{< P >} \right)^2 \tag{30}$$

By developing equation (30), it results in equation (31).

$$\dot{m} = \dot{m}_0 \left(1 - 2 \frac{k_L}{d_{b0}} \frac{z}{u_G} \frac{C^*_{CO_2} 2R.T}{P} + \left(\frac{k_L}{d_{b0}} \frac{z}{u_G} \frac{C^*_{CO_2} 2RT}{P} \right)^2 \right) \tag{31}$$

With $\left(\frac{k_L}{d_{b0}} \cdot \frac{z}{u_G} \frac{C^*_{CO_2} \cdot 2R.T}{P} \right)^2 \ll 2. \frac{k_L}{d_{b0}} \cdot \frac{z}{u_G} \frac{C^*_{CO_2} \cdot 2R.T}{P}$, which is verified (results not shown) equation (31) can be simplified to.

$$\dot{m} = \dot{m}_0 \left(1 - 2 \frac{k_L}{d_{b0}} \frac{z}{u_G} \frac{C^*_{CO_2} 2RT}{P} \right) \tag{32}$$

Comparing equation (29) to equation (32), the reduction of $\dot{m}$ is twice of that of d_b, meaning that any changes in d_b will lead to a two times modification in $\dot{m}$. The simplified expressions of axial evolution of d_b and $\dot{m}$ are plotted together with that given by 1D model in Fig. 3. It is shown that the simplified Lagrangian model predicts the axial evolution of d_b and $\dot{m}$ just as well as the 1D model. This is due to a small-scale column (H = 1 m), with relatively low-pressure effect, low gas holdup and no large changes in the bubble terminal velocity (bubble terminal velocity at 5.5 mm diameter nearly equals that at 4 mm diameter (Clift et al., 1978)).

The importance of the bubble diameter has already been highlighted in Buffo et al. (2017) and Liu et al. (2021). Indeed, the correct characterization of bubble diameter is crucial in the prediction of interfacial area (and thus the mass transfer flux) for such a highly-coupled fast reaction, as shown in Fig. 3.

Fig. 4a shows the significant pH evolution with different inlet bubble diameter. The results show the same conclusion as Buffo et al. (2017) (see Fig. 10 of Buffo et al. (2017)). A smaller bubble size creates higher specific gas–liquid contact area, resulting in a higher mass transfer flux. An inlet diameter of 4.5 mm overpredicts the mass transfer flux, hence, a faster drop in pH. The optimal inlet bubble diameter corresponds to the bubble diameter given by Darmana et al. (2007) – 5.5 mm. Inlet bubble diameter has a strong impact on the dynamic pH evolution ever since the beginning of the chemisorption process, as the CO_2 transfer flux has a direct influence on the OH^- conversion rate. Notice that this mean Sauter diameter of 5.5 mm could represent reasonably the polydisperse

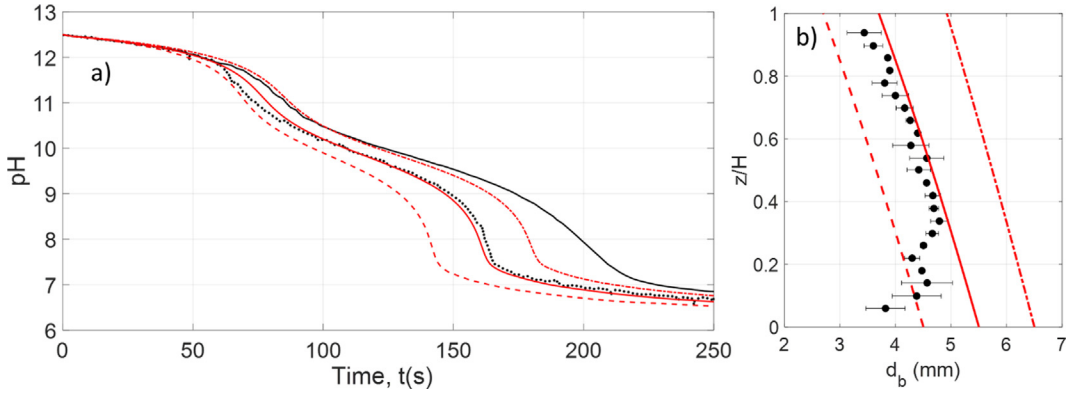

Fig. 4. (a) Time-dependent pH profile for 3 different inlet bubble diameters (d_{b0}). (b) Axial mean Sauter diameter profile. Black lines from (Darmana et al., 2007) CFD results, Black dots from (Darmana et al., 2007) experimental results, Red lines from 1D model. – d_{b0} = 5.5 mm, – – d_{b0} = 4.5 mm, – ■ – d_{b0} = 6.5 mm.

bubble population between 4.5 and 6.5 mm without any consequence on the average mass transfer rate (equation (32)) if no coalescence or breakage occurs in the homogeneous bubbly flow regime, as supposed by the 1D model. In the industry, inlet bubble diameter has a strong impact on the bubble column mass transfer and reaction conversion efficiencies. Thus, the sparger design becomes an important issue as it determines the bubble size distribution at the inlet, which consequently characterizes the bubble diameter in the developed region. (Camarasa et al., 1999; McClure et al., 2016; Schäfer et al., 2002; Tirunehe and Norddahl, 2016). In Fig. 4b, the axial variation of bubble size is compared with inlet bubble size d_{b0} between 4.5 mm and 6.5 mm. It shows that d_{b0} = 5.5 mm seems to be the best fit.

Although the bubble formed at the inlet is mentioned to be 5.5 mm, no further explanation is given in Darmana et al. (2007) on how this bubble diameter is calculated as the measurement at this zone is judged to be unreliable experimentally. Here, it is attempted to understand the proposed 5.5 mm. With the orifice diameter d_{or} = 1 mm, CO_2 gas viscosity μ_G of 1.49×10^{-5} $m^2.s^{-1}$ and the gas velocity at the orifice U_{or} = 2.5 $m.s^{-1}$ (supposing the gas flowrate is equally distributed in each orifice), the bubble Reynolds number at the orifice can be calculated using equation (33).

$$Re_{or} = \frac{\rho_G U_{or} d_{or}}{\mu_G} \tag{33}$$

One gets Re_{or} equals to 300 which suggests that the bubble formation is in the dynamic regime (McCann and Prince, 1971). Thus, the bubble diameter formed can be calculated with (Gaddis and Vogelpohl, 1986) model, written as.

$$\frac{d_{b0}}{d_{or}} = 1.16\left(\frac{U_{or}^2}{d_{or} g}\right)^{\frac{1}{5}} \tag{34}$$

Equation (34) yields an initial bubble size of 4.3 mm. Considering the size of the sparger pitch of 5 mm, bubble coalescence can occur, resulting in larger bubble diameter at formation, which explain the higher d_{b0} of 5.5 mm. It is believed that the initial bubble diameter comes from the extrapolation of bubble diameter profile from the zone whereby the measurement is reliable. This inlet information is necessary as an input to subsequent numerical simulation. Hence, d_{b0} = 5.5 mm will be used for the rest of this work.

3.3. Importance of reaction pathway

The importance of correct reaction pathway has been demonstrated in the study of Krauß and Rzehak (2017) and Krauß and Rzehak (2018).

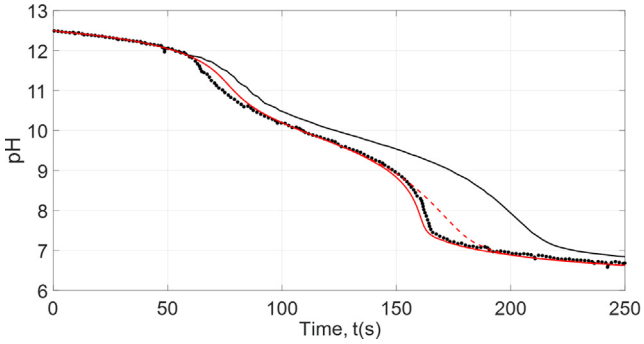

Fig. 5. Time-dependent pH profile using 2 or 3 reaction pathways. Black line from (Darmana et al., 2007) CFD results, Black dots from (Darmana et al., 2007) experimental results, Red lines from 1D model. – 3 reaction pathways, – – 2 reaction pathways.

Fig. 5 shows that including the water pathway is essential to reproduce the experimental data. At the initial stage (pH > 9), the two curves overlap with each other, as all other parameters were taken the same and the third reaction is not activated. When the pH is less than 9, roughly when the time instant is in the range of 130–170 s, the water pathway becomes more and more dominant, as the third reaction rate becomes higher, as confirmed in Fig. 7. At the same time, the first reaction rate is getting smaller. If the water pathway is neglected, the total CO_2 consumption is only the first reaction rate, thus a weaker decrease in pH. The final pH value for both reaction pathways at steady-state remains the same even though the reaction rates are different between t = 150–200 s. The final pH value depends solely on the equilibrium constant of the chemical reaction (Liu et al., 2021). The water pathway only impacts the results when pH less than 9. In short, 1D model is in agreement with previous CFD works of Huang et al. (2021) and Krauß and Rzehak (2018). The third reaction has to be considered to describe the second change of pH slope.

3.4. pH and chemical species concentration evolutions

Local concentration of chemical species was not measured experimentally in the work of Darmana et al. (2007). Nevertheless, the local pH value at the outlet was recorded dynamically with a pH probe. This dynamic pH evolution indicates the consumption of hydroxide ions by the dissolved CO_2. Therefore, an accurate CO_2 interfacial mass transfer flux prediction is required to reproduce the experimental pH curve with time. Fig. 6a shows that the pH evolution of the 1D model is consistent with the experi-

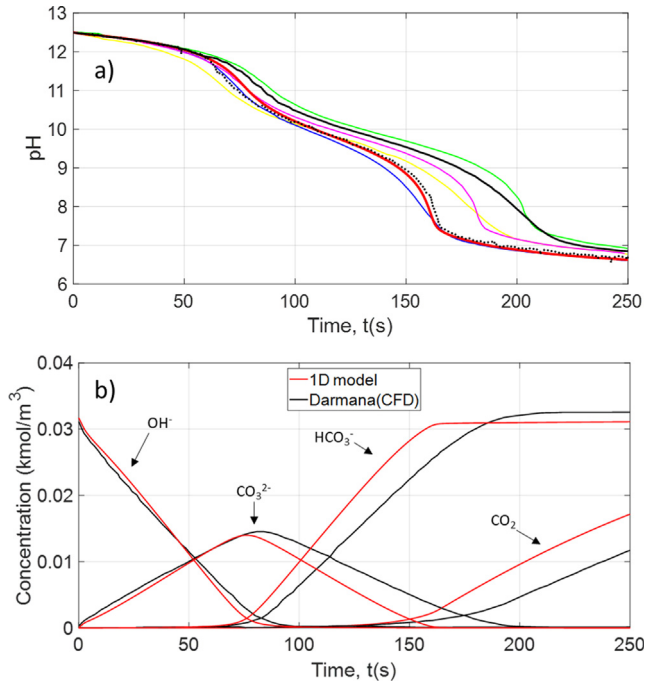

Fig. 6. (a) Time-dependent pH profile compared to existing literature results. Green line from (Krauß and Rzehak, 2018) CFD results, Magenta line from (Huang et al., 2021) CFD results, Blue line from (Buffo et al., 2017) CFD results, Yellow line from (Hlawitschka et al., 2016), Black lines from (Darmana et al., 2007) CFD results, Black dots from (Darmana et al., 2007) experimental results, Red lines from 1D model. (b) Temporal evolution of chemical species concentration.

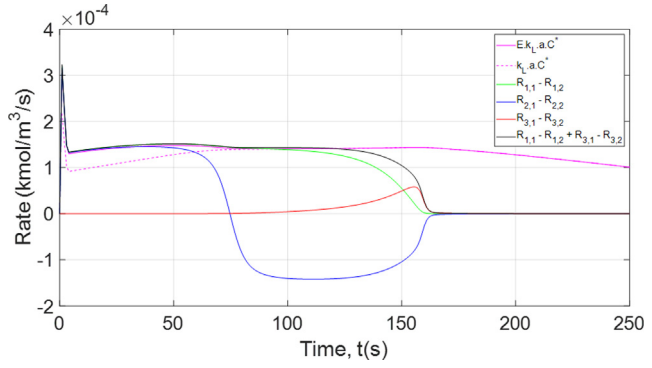

Fig. 7. Reaction rates and CO_2 mass transfer rate during the chemisorption process.

mental pH and other researchers work. The pH predicted by the 1D model also gives a better fit than Darmana's CFD model. The concentration temporal profile obviously has a slight difference than that of Darmana et al. (2007) CFD results, as reflected in the discrepancy of the two pH curves. In fact, the 1D model describes the pH evolution better than certain CFD model, mostly due to a better description of bubble size reduction – a key factor in determining the enhanced mass transfer flux (see Fig. 3a). By introducing an improved reaction pathway, as suggested by Krauß and Rzehak (2018), the second change in pH slope is also much better predicted. For example, for the case of Buffo et al., 2017, Darmana et al. (2007) and Hlawitschka et al., 2016, the second change in pH slope is not the same as that experimentally measured because the third pathway was not included in their model.

In Fig. 6b, it is interesting to observe that the final concentration of HCO_3^- corresponds to the initial concentration of OH^-, indicating that conservation of mass is achieved in the whole reaction process. This is also observed in all the work in the literature (Buffo et al., 2017; Hlawitschka et al., 2016; Huang et al., 2021; Krauß and Rzehak, 2018; Taborda and Sommerfeld, 2021), except in the original work of Darmana et al. (2007).

At the early stage of the reaction process, all the dissolved CO_2 reacts immediately with the hydroxide ions (OH^-) and is converted into carbonate ions (CO_3^{2-}). This is displayed in Fig. 6b with a decrease of $[OH^-]$ at the same time an increase in $\left[CO_3^{2-}\right]$, and in Fig. 7 whereby both $R_{1,1} - R_{1,2}$ and $R_{2,1} - R_{2,2}$ are positive, signifying the equations (12) and (13) are going in the forward reaction.

At approximately 75 s, $\left[CO_3^{2-}\right]$ reaches its maximum value and subsequently starts to decrease. This is reflected in Fig. 7 where $R_{2,1} - R_{2,2}$ turns negative, indicating that the equilibrium of the second reaction (equation (13)) starts to shift backward. Meanwhile, $R_{1,1} - R_{1,2}$ remains positive, meaning that the first reaction (equation (12)) is quasi irreversible. This results in an increase of bicarbonate (HCO_3^-) concentration, as shown in Fig. 6b. With the consumption of both CO_3^{2-} and OH^-, the pH continues to decrease. When the pH reaches 9, the third reaction commences, resulting in the formation of H^+ ions, which triggers a steep change in the slope of pH curve. This corresponds to the moment when $R_{3,1} - R_{3,2}$ turns positive. At about 180 s, CO_3^{2-} is completely consumed and HCO_3^- reaches a steady concentration. The pH reaches a value of 7. In Fig. 7, it can be noticed that the CO_2 transfer rate equals to the reaction rate throughout most of the process until the start of CO_2 accumulation in the liquid at around 130 s.

After 180 s, the chemical reaction process ends as no more reactants (OH^-) are present in the system. From this point onwards, the process switches to pure CO_2 physical absorption. Over time, the concentration of CO_2 increases meanwhile the CO_2 gas–liquid transfer rate decreases as the driving force decreases. The pH decreases gradually as the solution turns weakly acidic due to dissolved CO_2.

The CFD model provides more detailed local information on the reactive flow. Nevertheless, 1D model yields reliable axial evolution of the concentration, which is compared with the CFD work of Buffo et al. (2017). The results are shown in Fig. 8 whereby it reports the local concentration profiles of the dominant species at three different time instants (t = 10 s, 80 s and 200 s), as illustrated in Fig. 6b. At the early stage (t = 10 s), the pH is high as OH^- ions are the most abundant in the system. Dissolved CO_2 reacts immediately with OH^- and CO_3^{2-} is produced. At around 80 s, the CO_3^{2-} concentration peaks, and it acts as the dominant species. When the neutralization process reaches its late stage (t = 200 s), CO_2 accumulates in the liquid at a rate imposed by the physical absorption rate. Apart from the concentration of CO_2, all other species concentrations captured by 1D model are in the same order of magnitude with that of Buffo et al. (2017) CFD model. A slightly higher CO_2 concentration captured by the 1D model could likely due to the inlet bubble diameter d_{b0} applied is lower than that of Buffo et al. (2017) CFD model, as shown in Fig. 3a. At the final stage, the concentration of HCO_3^- reaches the initial concentration of OH^- (initial pH of 12.5 which is equivalent to 0.0316 kmol.m^{-3}). All concentration profiles show a very weak spatial heterogeneity behavior as also depicted in the CFD results of Buffo et al. (2017). It shows that the temporal evolution is more important than the spatial heterogeneity due to the relatively well mixed liquid phase. Nevertheless, for the gas phase, a steadily decreasing $C^*_{CO_2}$ implies a decreasing mass transfer driving force and reaction rate along the axial direction.

In this section, it can be concluded that the two-phase hydrodynamics and the reactive pathway are validated by the 1D model. The 1D model agrees with the findings of the literature in terms

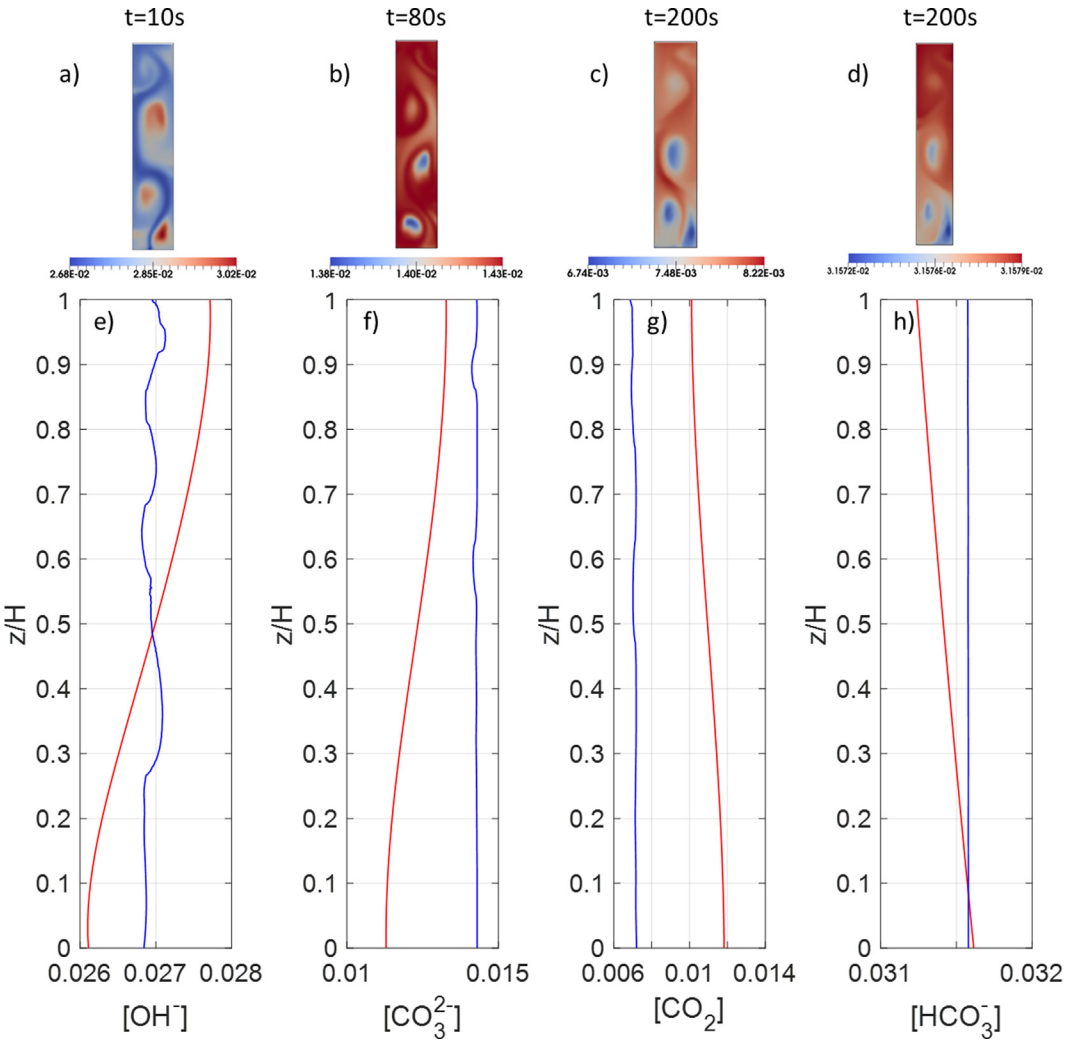

Fig. 8. Instantaneous spatial profiles of chemical species concentration at different instants. (a)-(d) CFD concentration contours are taken from Fig. 6 of (Buffo et al., 2017). (e)-(h) CFD results superposed with 1D results. Blue line from (Buffo et al., 2017) CFD results, Red lines from 1D model. CFD profiles are obtained through area-weighted average at each height.

of inlet bubble diameter (Buffo et al., 2017; Darmana et al., 2007; Liu et al., 2021) and the chemical kinetics model of Krauβ and Rzehak (2017). Prior to sensitivity analyses, an asymptotic model is discussed to provide fundamental insights of reactive bubbly flow physics and to underline the main coupling phenomena occurring in each stage of the pH curve.

4. Asymptotic 0D model

In this section, an asymptotic model is derived to better understand the neutralization process. This asymptotic model helps to select the main parameters for the sensitivity analysis. Basic equations are presented here with the detailed development available in the *supplementary material*.

The asymptotic model is established in three phases and it only considered successive predominant species of each time interval, as shown in Fig. 6. In Phase 1, the chemical reactive species present in the system are OH^- and CO_3^{2-}. Meanwhile in Phase 2, the concentration of OH^- becomes negligible compared to other species and it is considered equals to zero. The transferred CO_2 forms HCO_3^-, hence $[CO_2]$ is still zero. Lastly in Phase 3, $[OH^-]$ and $\left[CO_3^{2-}\right]$ remains zero and only dissolved $[CO_2]$ changes at this period. Therefore, the asymptotic model established for the three phases, after development, is given by the following equations:

Phase 1 ($t \in [0; t_1]$)

$$[OH^-] = [OH^-]_0 - 2.E.k_L.a.C^*_{CO_2}.t \tag{35}$$

$$\left[CO_3^{2-}\right] = E.k_L.a.C^*_{CO_2}.t \tag{36}$$

$$t_1 = \frac{[OH^-]_0}{2.E.k_L.a.C^*_{CO_2}} \tag{37}$$

Phase 2 ($t \in [t_1; t_1 + t_2]$)

$$\left[HCO_3^-\right] = 2.k_L.a.C^*_{CO_2}.(t - t_1) \tag{38}$$

$$\left[CO_3^{2-}\right] = \left[CO_3^{2-}\right]_{t_1} - k_L.a.C^*_{CO_2}.(t - t_1) \tag{39}$$

$$t_2 = \frac{[OH^-]_0}{2.k_L.a.C^*_{CO_2}} \tag{40}$$

Phase 3 ($t \in [t_1 + t_2; t_\infty]$).

$$[CO_2] = C^*_{CO_2}(1 - e^{-k_L.a.(t-(t_1+t_2))}) \tag{41}$$

From the asymptotic model, the pH evolution can be predicted by:

Phase 1

$$pH = 14 + log_{10}\left([OH^-]_0 - 2.E.k_L.a.C^*_{CO_2}.t\right) \quad t \in [0; t_1[\tag{42}$$

Phase 2

$$pH = -log_{10}(K_{a2}) - log_{10}\left(\frac{2.k_L.a.C^*_{CO_2}.(t-t_1)}{\left[CO_3^{2-}\right]_{t1} - k_L.a.C^*_{CO_2}.(t-t_1)}\right)$$

$$t \in]t_1; t_1 + t_2[\tag{43}$$

$$pH = -log_{10}(K_{a2}) - log_{10}\left(\frac{2.k_L.a.C^*_{CO_2}.(t-t_1)}{\left[CO_3^{2-}\right]_{t1} - k_L.a.C^*_{CO_2}.(t-t_1)}\right)$$

$$t \in]t_1; t_1 + t_2[\tag{44}$$

All parameters used in the asymptotic model are derived from time (0–250 s) and space averaged 1D complete model value and they are reported in Table 8. Fig. 9 reveals that the asymptotic model agrees well with 1D model results. The asymptotic model highlights that the essential parameters that control Phase 1 is related to E, k_L, and a. In Phase 2 and Phase 3, the most important parameters that control the pH evolution are just k_L and a. As CO_2 chemisorption rate is imposed by the mass transfer flux, it is actually not surprising to observe that the underlying mechanisms is totally controlled by mass transfer parameters, as proved by the asymptotic model and also discussed in the work of Huang et al. (2021). These parameters have to be modeled with utmost attention to give the most realistic prediction of temporal pH evolution. Sensitivity analyses on these parameters are thus carried out in Section 5.

Table 8
Parameters used in the asymptotic model.

Input Parameters	Value	Units
d_b	4.8	mm
ε_G	1.6	%
a	20	$m^2.m^{-3}$
u_G	0.289	$m.s^{-1}$
k_L	$3x10^{-4}$	$m.s^{-1}$
E	1.06	–
$C^*_{CO_2}$	0.0345	$kmol.m^{-3}$

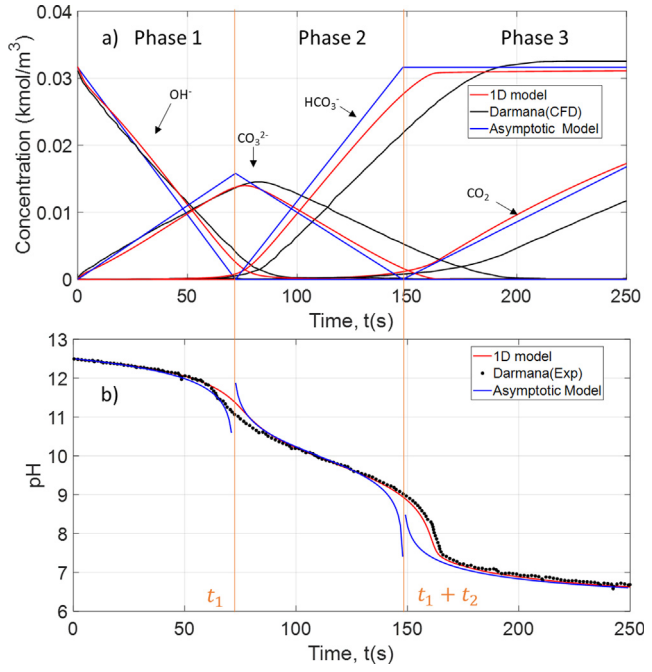

Fig. 9. (a) Temporal evolution of chemical species concentration with the asymptotic model described from equations (35)-(41) and (b) Time-dependent pH profile compared between (Darmana et al., 2007) CFD results, 1D model, asymptotic model (equations (42)-(44)).

Before sensitivity analysis, qualitative investigation can already be conducted with the asymptotic model, particularly from the expression of pH (equations (42)-(44)). The 0D model shows that the most impactful closure parameters in Phase 1 are E and k_L. From equation (42), it can be related that the higher the E, the higher the decrease in pH. Besides, it is proven through equation (37) that the higher the E, the shorter the t_1, displacing the pH curve to the left.

On the contrary, Phase 2 is barely impacted by E, as shown in Fig. 7, whereby the non-enhanced mass transfer rate is nearly equal to the enhanced mass transfer rate. Nonetheless, it is still controlled by the k_L value as shown in equation (43). The slope of the pH curve is highly dependent of the mass transfer coefficient k_L. Phase 3 is analogous to Phase 2, having k_L as the determining parameter. In Phase 3, the only concentration evolution is that of $[CO_2]$, which changes according to the physical absorption flux.

The interfacial area a appears to be sensitive in every phase, signifying the importance of bubble diameter and gas holdup in the prediction of mass transfer flux. This also justifies the previous work using CFD approach for gas fraction calculation and bubble population model to better capture the mass transfer (Buffo et al., 2017; Krauβ and Rzehak, 2018).

5. Discussions on sensitivity analyses using 1D model

With the good agreement of 1D and asymptotic model with experimental data, extensive sensitivity analyses have been conducted and they are compared with other researcher's work (Buffo et al., 2017; Hlawitschka et al., 2016; Huang et al., 2021; Krauß and Rzehak, 2018; Krauβ and Rzehak, 2017; Liu et al., 2021). It is important to emphasize that the transient CO_2 chemisorption is measured by a pH probe located near the liquid free surface Darmana et al. (2007). This probe response integrates all the physical coupling (hydrodynamics, mass transfer and chemical reactions) taking place in the bubble column during the transient measurement, implying that the validation process is tricky, as several parameters have to be adjusted or predicted. The CFD approach is more complex compared to the 1D approach as it requires high computational resources to follow the overall chemical reaction spatially and temporally (plus integrating population balance model will further increase the simulation time). Regarding the complexity of the problem and long simulation time, it is difficult to validate a high-quality parametric study without extra consideration. For these aforementioned reasons, 1D model provides an interesting alternative for sensitivity analyses in view of short calculation time. Upon validation of hydrodynamics, inlet bubble diameter and reactive pathway in Section 3, the impact of other important parameters such as liquid mixing and mass transfer closure model are studied with the 1D model here. These sensitivity analyses also serve as a comprehensive comparison with the most recent CFD work as only certain results were compared and analyzed between them.

5.1. Influence of mixing

The liquid mixing in the 1D model is characterized by the axial dispersion coefficient D_L, in contrast to previous CFD work whereby the mixing in the bubble column is resolved.

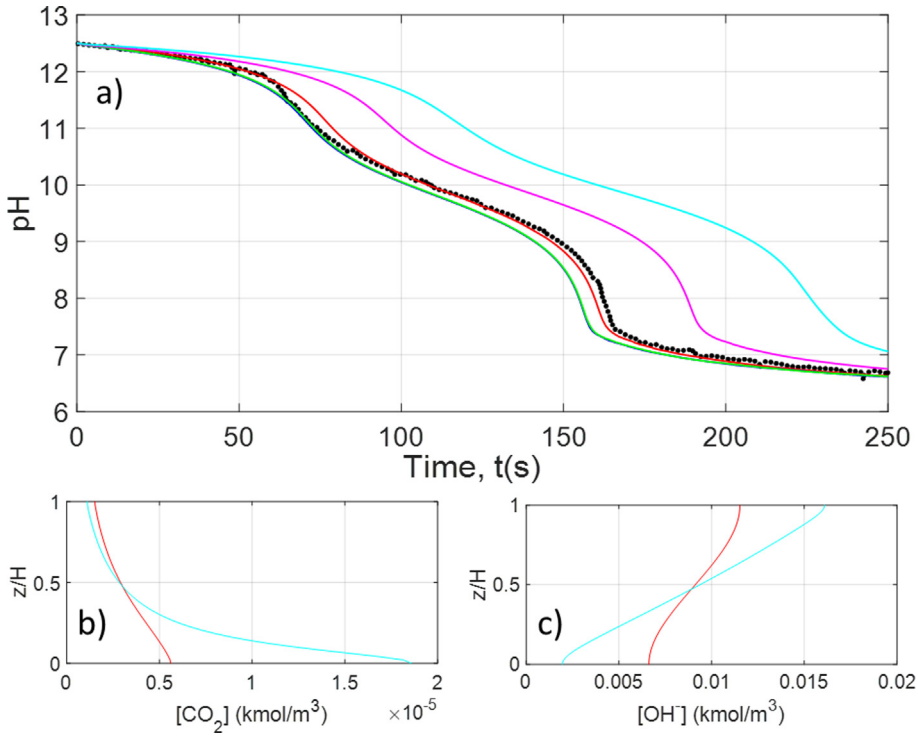

Fig. 10. (a) Time-dependent pH profile for different axial dispersion coefficient. Black dots from (Darmana et al., 2007) experimental results, Continuous lines from 1D model with Red lines D_L = 5x10^{-3} m^2.s^{-1} (default value estimated from (Deckwer et al., 1974)), Cyan lines D_L = 5x10^{-5} m^2.s^{-1}, Magneta line D_L = 5x10^{-4} m^2.s^{-1}, Green line D_L = 5x10^{-2} m^2.s^{-1}, Blue line D_L = 5x10^{-1} m^2.s^{-1}. (b) Spatial profile of [CO_2] at t = 50 s. (c) Spatial profile of [OH^-] at t = 50 s. Red lines D_L = 5x10^{-3} m^2.s^{-1}. Cyan lines D_L = 5x10^{-5} m^2.s^{-1}.

Fig. 10a shows that D_L has an immediate impact in reproducing experimental pH curve with 5x10^{-5} m^2.s^{-1} < D_L < 5x10^{-1} m^2.s^{-1}. The value of 5x10^{-5} is about one order of magnitude lower than the estimated turbulent diffusivity (10^{-4} m^2.s^{-1} as calculated in Section 2.2.1) and 5x10^{-1} is about two orders of magnitude higher than the spatial dispersion to illustrate the extreme case. Low axial dispersion coefficient will create spatial heterogeneities in terms of dissolved concentration, as evidenced in Fig. 10b & Fig. 10c. The lower the D_L, the greater the concentration difference between the top and the bottom of the column. As CO_2 is sparged at the bottom of the column, fast chemical reaction has already initiated at the lower half of the column, leaving less CO_2 at the top of the column to reacts with OH^- ions. Thus, with a low value of D_L, a moderate decline of pH is obtained, as evidenced in Fig. 10a. With a higher axial dispersion coefficient, dissolved CO_2 is homogenized in the column, it reaches the top with higher concentration at an earlier time, leading to an earlier decrease in pH in the similar manner. Nonetheless, the results become insensitive to D_L, for D_L higher than a magnitude of 10^{-3} m^2.s^{-1}. The two pH curves of D_L = 5x10^{-2} m^2.s^{-1} (green line) and D_L = 5x10^{-1} m^2.s^{-1} (blue line) superpose with each other, showing that at perfectly mixed liquid behavior, the pH description converge to the same shape. This is in line with the conclusion of Krauβ and Rzehak (2017) work whereby they captured the pH evolution with a perfectly mixed 0D model. Here, it is found that the value estimated from Deckwer et al. (1974) yields a good pH prediction, without additional fitting on other parameters.

The gaseous side axial dispersion coefficient D_G does not yield much influence to the results (results no shown). As mentioned in Section 3.2, the bubbles diameter varies between 5.5 mm and 3.7 mm during the chemisorption process, with almost identical u_{rel} at this range of bubble size. Thus, the spatial dispersion is expected to be less intense, which is typically the case in homogeneous regime at low gas holdup. Besides, considering the CO_2 diffusivity in air is three order of magnitude higher than that in water, the axial Peclet number is expected to be higher in the gaseous phase $\left(\frac{u_G d_b}{D_{CO_2,G}} > \frac{u_L d_b}{D_{CO_2,L}}\right)$, signifying less spatial dispersion.

5.2. Influence of enhancement factor

The enhancement factor E is defined as the ratio between mass transfer fluxes through the phase interface with and without reaction, based on the same concentration driving force (Westerterp et al., 1998). The effect of E has been highlighted in the work of Hlawitschka et al. (2016) and Liu et al. (2021). Without implementing E in the model, the mass transfer is underestimated, leading to a wrong pH temporal evolution that lags behind the experimental pH curve. In this work, the two E models presented in Section 2.2.3 are studied.

Krauβ and Rzehak (2017) applied a 0D model to solely investigate the chemical kinetics and enhancement factor. The authors stated that approximate or simplified expressions for the enhancement factor derived from simple conceptual models of mass transfer (film, penetration, and renewal models) that appear frequently in reaction engineering textbooks should be considered with care. They also showed that the E applied in the original work of Darmana is not suitable at small values of instantaneous enhancement factor E_i which even become less than one (violated the condition for equation (25)), leading to an underestimated value of E (see Fig. 8a of (Krauβ and Rzehak, 2017)). We agreed to this finding as an underestimated mass transfer flux was obtained when the enhancement factor model used by Darmana was applied to our 1D model (results not shown). This could partly explain why Darmana yielded a slower decrease in pH in the initial stage, as shown in Fig. 11 (black lines compared to black dots).

Many researchers (Hlawitschka et al., 2016; Huang et al., 2021; Liu et al., 2021) used a simple enhancement factor proposed by

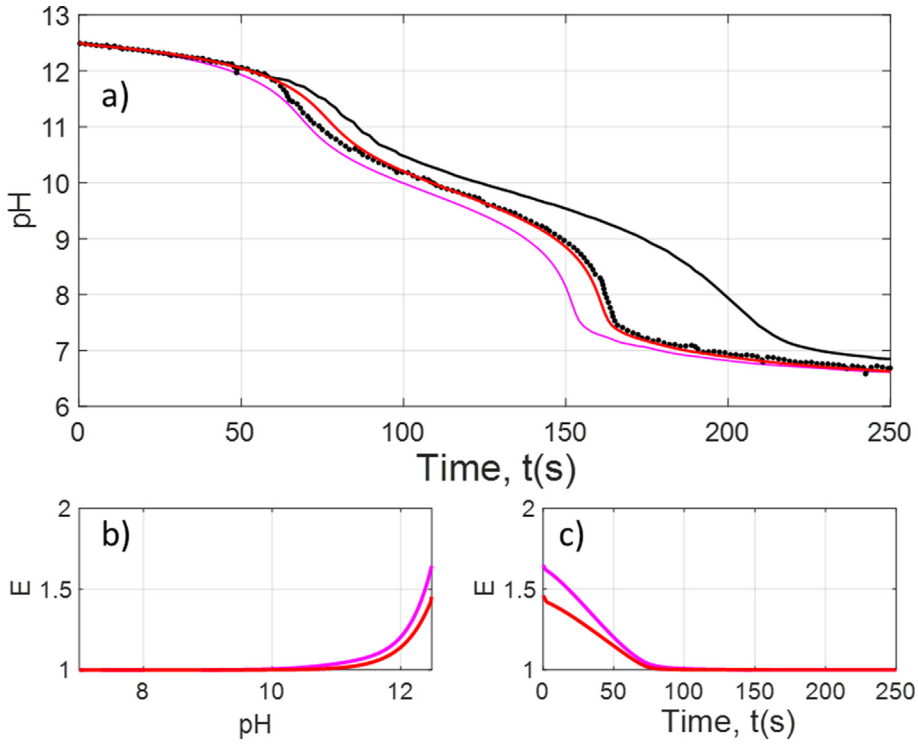

Fig. 11. (a) Time-dependent pH profile. Red lines with E from (Krauβ and Rzehak, 2017), and Magenta lines with E from (Fleischer et al., 1996) (b) E vs pH and (c) Time-dependent E value.

Fleischer et al. (1996) which is derived from experimental data to reproduce Darmana's case. Krauβ and Rzehak (2017) did not included this enhancement factor model in their comparison study. To the authors knowledge, the fit formula for the enhancement factor model proposed by Krauβ and Rzehak (2017), has only been used in Krauβ and Rzehak (2018) in the attempt to reproduce Darmana's case. Here, we compare the effectiveness between these two enhancement models of Fleischer et al. (1996) and Krauβ and Rzehak (2017).

Fig. 11a depicts the pH curve obtained from two different enhancement models. The enhancement factor model proposed by Fleischer et al. (1996) is derived theoretically via two-film model which supposed the bubble interface is flat. The flat interface assumption is unrealistic unless the radius of the interface curvature is infinitely large. This leads to an overoptimistic value of E, which is reflected in Fig. 11b and Fig. 11c, as the initial drop of pH (magenta line) is the strongest for Fleischer et al. (1996).

The enhancement factor proposed by (Krauβ and Rzehak, 2017) yields a slightly better description of the pH evolution at the beginning which extend to the overall pH curve. Nevertheless, the difference remains significantly small for these two models. This parameter should not be the determining factor to capture the overall pH curve, as it equals to 1 after 75 s.

It is also preferable to apply an analytical model such as that of Krauβ and Rzehak (2017) rather than empirical correlation to perform any predictive simulation. To conclude this subsection, it is clear that E is impactful to the pH prediction as early as the process starts. Therefore, it changes t_1, which causes a translation of the remaining pH curve. This has been initially proven by the asymptotic model as the parameter E appears only in the governing equation in Phase 1 (see equation (42)).

5.3. Influence of Sherwood number

Study of different mass transfer coefficient has been done in the recent work of (Huang et al., 2021; Liu et al., 2021) and it is also implemented here for the sensitivity analysis. Another mass transfer model tested is that proposed by Higbie (1935), which is often applicable for clean spherical bubbles over 2 mm (Cockx et al., 1999; Fayolle et al., 2007; Larsson et al., 2022; Solsvik, 2018). These mass transfer models are summarized in Table 9.

Fig. 12 demonstrates the importance of Sherwood closure model on the CO_2 mass transfer flux. These Sherwood closure models are developed for different bubble geometrical characteristic under different hydrodynamics and physicochemical conditions (see Table 9). The k_L derived by Brauer (1979) is found to be the most suitable model. It is also used by Darmana et al. (2007) in their simulation. It is derived for non-spherical bubbles in the wobbling regime – this is typically the case for the bubbles having a size of 5.5 mm as it considers the stochastic deformation of the interface induced by turbulent motion in the surrounding fluid (Clift et al., 1978; Tomiyama et al., 1998). Thus, it offers a higher mass transfer coefficient than $k_{L,2}$, leading to a much higher CO_2 interfacial mass transfer flux, hence, a larger drop in terms of pH. To our knowledge, the classical mass transfer model of Higbie $k_{L,3}$ has not been applied in earlier CFD work of this context. Fig. 12 shows that the mass transfer model proposed by Higbie (1935) overestimates the mass transfer flux, leading to a faster drop in pH than the experimental pH curve.

Table 9
Mass transfer models derived from different Sherwood correlations.

Sherwood correlation	Notation	Description	Reference
$Sh = 2 + 0.015Re^{0.89}.Sc^{0.7}$	$k_{L,1}$	Non-spherical bubbles with stochastic deformations of the interface	(Brauer, 1979)
$Sh = 2 + 0.6415Re^{0.5}.Sc^{0.5}$	$k_{L,2}$	Spherical bubbles	(Bird et al., 2002)
$Sh = 1.13Re^{0.5}.Sc^{0.5}$	$k_{L,3}$	Clean spherical bubbles	(Higbie, 1935)

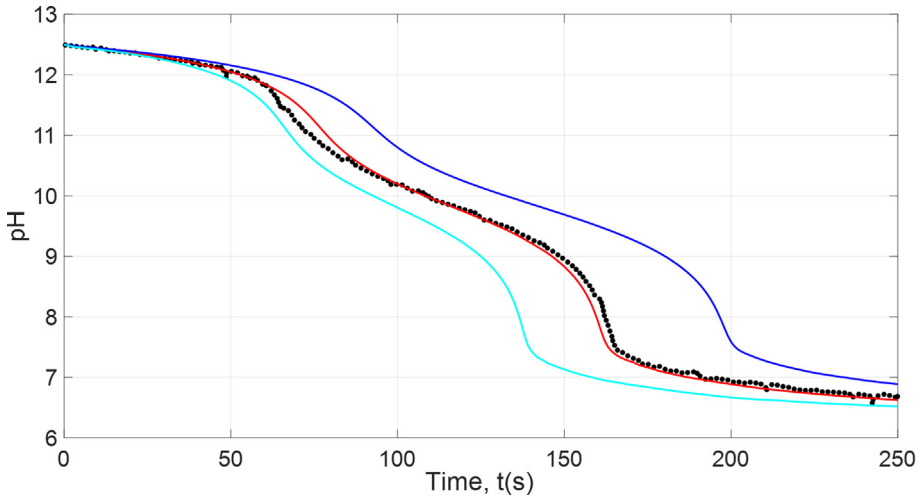

Fig. 12. Time-dependent pH profile using different k_L closure models. Black dots from (Darmana et al., 2007) experimental results, Colored lines from 1D model. Cyan lines from $k_{L,3}$, Red lines from $k_{L,1}$, and Blue lines from..$k_{L,2}$

Considering the Sherwood equation of Bird et al. (2002) and Higbie (1935), both has the classical exponent value of 0.5 for the Reynolds and Schmidt number, which is derived from the penetration model of mass transfer. The difference between the two equations is the factor before *Re* and *Sc*, with 0.6415 $\left(=\sqrt{\frac{4}{3\pi}}\right)$ and 1.13 $\left(=\sqrt{\frac{4}{\pi}}\right)$, respectively. The Sherwood number calculated from Bird et al. (2002) is developed for a spherical gas bubble surrounded by a liquid in creeping flow regime ($Re \ll 1$). For Sherwood number of Higbie (1935), the bubble is rising in liquids free of surface-acting agent and it undergoes a constant toroidal circulation (Rybczynski-Hadamard circulation). It is found that Sherwood model of Bird et al. (2002) underestimates the mass transfer rate, probably due to the *Re* is not in the applicable range.

Moreover, it is found that Re of the bubble is in the range of 1000–1600 for all studies. In this range of Re, these Sherwood correlations yield the mass transfer coefficient which ranks from the highest to the lowest as follows: $k_{L,3} > k_{L,1} > k_{L,2}$. This ranking is reflected in the pH curve whereby the highest Sherwood leads to an earlier decrease in pH. In terms of the ranking between $k_{L,1}$, $k_{L,2}$ and $k_{L,3}$. The choice of k_L remains a major factor in the pH prediction as it influences the rate of change of pH, right from the start to the end of the reactive process. The most suitable k_L is that applicable for non-spherical wobbling bubbles of Brauer (1979) in the configuration of the bubble plume of Darmana with large ellipsoîdal bubbles.

6. Conclusion

In this work, a two-way coupled spatio-temporal 1D model is applied to study CO_2 reactive absorption process in a bubble column, previously presented in the Darmana et al. (2007). It is found that 1D model performs just as well as previous studies performed with CFD model. The objective of this paper is not to combine all the improvements reported in the literature and to perform an updated CFD simulation of Darmana's case. In the contrary, it aims to integrate different strategies proposed from published works and compare with their results using the 1D model, like a novel insight of Darmana et al. (2007) case. Moreover, 1D model leads to an asymptotic 0D model that helps to capture the essential feature of reactive bubbly flow and to identify the underlying physical–chemical parameters which control these flows. Contrary to CFD simulation, 1D model yields fast results which is useful for probing a wide range of physical parameters and conducting series of sensitivity analysis. After identifying such specific parameters, advanced CFD model can be used to study the impact of these parameters on the local field structure and the phase interaction in more details without hypothesis on the flow. In CO_2-NaOH chemisorption case, the particular parameters to focus on in CFD are mass transfer coefficient k_L and inlet bubble diameter d_{b0}. The closure model applied to these two parameters must be given the utmost importance to successfully capture the interfacial mass transfer flux, and eventually the temporal pH curve. Several conclusions can be drawn from this work:

Gas phase hydrodynamics has to be closely modelled to give realistic mass transfer flux. In this work, it is well captured with a drift-flux loop model with a C_0 coefficient of 1.27 and an averaged liquid recirculation velocity of 4.2 cm.s^{-1}.

- Bubble size shrinkage due to CO_2 chemisorption is observed experimentally and it has to be well-characterized in order to yield a satisfactory pH prediction.
- A correct inlet bubble diameter d_{b0} is essential as it decides the bubble diameter evolution. It is shown that a good description of bubble size changes is important to determine the local mass transfer flux, as the value fluctuate in a factor of two between the top and the bottom of the column. The value of d_{b0} = 5.5 mm appears to be an accurate estimation, according to Darmana et al. (2007).
- The water pathway has to be considered to correctly describe the late stage of the neutralization process as proposed by Krauβ and Rzehak (2017).

An asymptotic model is proposed to describe the CO_2 reactive absorption process and to unravel the controlling parameters, such as *E*, k_L, and *a*.

- The axial dispersion coefficient of 5x10^{-3} m^2.s^{-1} calculated from the correlation of Deckwer et al. (1974) which is derived from circular bubble column is also reliable for pseudo-2D bubble column, as shown in the findings of Alexander and Shah (1976).
- The enhancement factor has a huge impact on the pH evolution only when pH > 10. The enhancement factor proposed by Krauβ and Rzehak (2017) has a better edge over that of Fleischer et al. (1996).
- The Sherwood correlation of Brauer (1979) seems to be the appropriate model. It corresponds well for non-spherical bubbles as the bubble with a size of 5.5 mm is typically situated in the wobbling regime. In this wobbling regime, the continuous

bubble oscillation motion contributes to a higher mass transfer coefficient as found in this work too.

Finally, it is shown that only by applying a suitable combination of closure models and chemical kinetics (d_{b0}, C_0, $u_{L,recirc}$, u_{dfloop}, D_L, E, k_L, reaction pathways), the experimental data can be reproduced perfectly by the two-way coupled spatio-temporal 1D model. In this work, it is found that the combination of enhancement factor from Krauβ and Rzehak (2017), 3 reactions pathway as proposed by Krauβ and Rzehak (2017), Sherwood correlation from Brauer (1979), d_{b0} of 5.5 mm and D_L correlation estimated from Deckwer et al. (1974) gives the closest results to that of Darmana et al. (2007) experimental data.

CRediT authorship contribution statement

Vincent Ngu: Methodology, Conceptualization, Writing – original draft, Software, Data curation, Validation. **Jérôme Morchain:** Supervision, Methodology, Conceptualization, Writing – review & editing. **Arnaud Cockx:** Supervision, Methodology, Conceptualization, Writing – review & editing.

Data availability

Data will be made available on request.

Declaration of Competing Interest

The authors declare that they have no known competing financial interests or personal relationships that could have appeared to influence the work reported in this paper.

Acknowledgement

The authors wish to thank Prof. Alain Liné for providing insightful comments to the manuscript.

Appendix A. Solubility

The solubility of CO_2 in water $C^*_{CO_2}$ is described by a Henry constant which can take several forms (Sander, 2015). For this work, the dimensionless ratio (H e) of the concentration in the liquid phase to the equilibrium concentration at the gas phase is used. The correlation for the temperature dependence dimensionless Henry constant for CO_2 in pure water ($He^w_{CO_2}$) proposed by Versteeg and Van Swaaij (1988) was used. This correlation was also applied in Huang et al. (2021) and Krauβ and Rzehak (2018).

$$He^w_{CO_2} = 3.54.10^{-7} RT \exp\left(\frac{2044}{T}\right) \tag{A.1}$$

Due to salting out effect in electrolyte solutions, the solubility of most gases decreases with salt concentration. Therefore, the solubility of CO_2 in alkaline solution can be estimated by that of Weisenberger and Schumpe (1996), expressed as.

$$He_{CO_2} = He^w_{CO_2} 10^{-\sum (h_i + h_G) C_i} \tag{A.2}$$

Where C_i is species concentration in kmol.m^{-3}, $h_G = h_{G,0} + h_T.(T - 298.15)$ and the corresponding constants h_i summarized in Table A.1.

Krauβ and Rzehak (2017) pointed out that the use of equation (A.2) leads to a maximum decrease of 1.5 % in CO_2 solubility compared with its solubility in pure water for the case of Darmana et al. (2007). Nevertheless, equation (A.2) is implemented in our model in order to have a full model without additional hypothesis. In the end, the solubility $C^*_{CO_2}$ is calculated using equation (A.3).

$$C^*_{CO_2} = He_{CO_2} C_{G,CO_2} \tag{A.3}$$

Appendix B. Diffusivity

Similar to solubility, the temperature dependence of CO_2 molecular diffusivity in water ($D^w_{CO_2}$) is calculated from the correlation of Versteeg and Van Swaaij (1988) as.

$$D^w_{CO_2} = 2.35.10^{-6} \exp\left(-\frac{2199}{T}\right) \tag{B.1}$$

The molecular diffusivity of CO_2 in electrolytes can be calculated from Ratcliff and Holdcroft (1963) correlation as.

$$D_{CO_2} = D^w_{CO_2}\left(1 + 0.624 \sum b_i \cdot C_i\right) \tag{B.2}$$

The b_i constants are given in Table B.1.

The temperature dependent molecular diffusion coefficient of other chemical species (D_i) is determined by the power-law fits proposed by Zeebe (2011) and it is expressed as.

$$D_i = D^0_i . \left(\frac{T}{T^{ref}_i} - 1\right)^{\gamma^i} \tag{B.3}$$

With the values of D^0_i, T^{ref}_i, and γ^i are given in Table B.2.

Again, Krauβ and Rzehak (2017) concluded that the decrease of CO_2 diffusivity due to ionic effect in Darmana et al. (2007) case is less than 0.5 %, considering negligible.

Table B1
Parameters for equation (B.2).

Species	b_i (m^3.kmol^{-1})
Na^+	−0.0857
OH^-	−0.1088
HCO_3^-	−0.1150
CO_3^{2-}	−0.2450

Table B2
Parameters for equation (B.3).

Ion	D^0_i. 10^9 (m^2.s^{-1})	T^{ref}_i (K)	γ^i
Na^+	5.391	209.7	1.619
OH^-	26.65	216.5	1.658
HCO_3^-	7.016	204.0	2.394
CO_3^{2-}	5.447	210.3	2.193

Table A1
Parameters for equation (A.2).

Liquid phase	h_i (m^3.kmol^{-1})	Gas phase	$h_{G,0}$ (m^3.kmol^{-1})	h_T (m^3.kmol^{-1}.K^{-1})
Na^+	0.1143	CO_2	−0.0172	$-0.338.10^{-3}$
OH^-	0.0839			
HCO_3^-	0.0967			
CO_3^{2-}	0.1423			

Appendix C. Reaction rate constants

The reaction rate constants mostly follow the work presented by Krauβ and Rzehak (2017). It is recalled here to a certain extend necessary for the model.

First reaction

The rate constant for the first forward reaction (equation (12)) is calculated by the correlation proposed by Pohorecki and Moniuk (1988), which is a function of ionic strength as follow.

$$k_{1,1} = k_{1,1}^{\infty}.10^{0.221I-0.016I^2} \tag{C.1.1}$$

Where $k_{1,1}^{\infty}$ is the temperature dependence first forward rate constant at infinite dilution of ions, given by.

$$k_{1,1}^{\infty} = 10^{11.895-\frac{2382}{T}} \tag{C.1.2}$$

I Represents the ionic strength and it can be calculated as

$$I = \frac{1}{2}\left([Na^+].Z_{Na^+}^2 + [OH^-].Z_{OH^-}^2 + \left[HCO_3^-\right].Z_{HCO_3^-}^2 + \left[CO_3^{2-}\right].Z_{CO_3^{2-}}^2\right) \tag{C.1.3}$$

Where Z represents the valency of the dissolved ions, with $Z_{Na^+} = 1$, $Z_{OH^-} = -1$, $Z_{HCO_3^-} = -1$ and $Z_{CO_3^{2-}} = -2$.

The first reaction (equation (12)) is coupled with the auto-dissociation of water. Thus, the backward reaction rate of the first reaction can be obtained through the ratio relation of the equilibrium constants. The backward reaction can therefore be expressed as.

$$k_{1,2} = \frac{K_W}{K_{eq}^3}k_{1,1} \tag{C.1.4}$$

where K_W is the equilibrium constant of the ionization of water and K_{eq}^3 is the equilibrium constant of the third reaction (equation (14)). Here, the temperature dependence K_W proposed by Tsonopoulos et al. (1976) is used. The equilibrium constant K_{eq}^3 is calculated from a relation proposed by Edwards et al. (1978).

$$K_W = [H^+][OH^-] = 10^{-\frac{5840}{T}-61.2062-22.48\log_{10}(T)} \tag{C.1.5}$$

$$K_{eq}^3 = \frac{\left[HCO_3^-\right][H^+]}{[CO_2]} = \exp\left(-\frac{12090}{T} + 235.5 - 36.78ln(T)\right) \tag{C.1.6}$$

Second reaction

The second reaction involves a proton transfer, implying that the rate of reactions is very rapid (Eigen, 1954). The forward reaction of the second reaction equation (13) $k_{2,1}$ is in the order of 10^{10}-10^{11} $m^3.kmol^{-1}.s^{-1}$. Nevertheless, as shown by Darmana et al. (2007) and Krauβ and Rzehak (2018), a much smaller value can be used, as long as $k_{2,1} \gg k_{1,1}$. Krauβ and Rzehak (2017) showed that with $k_{2,1}$ of 10^4 $m^3kmol^{-1}s^{-1}$ there is negligible influence on the results. A value of $k_{2,1} = 10^4$ $m^3.kmol^{-1}.s^{-1}$ is thus used in our study to allow numerical simulations to be performed at a larger time step.

The backward reaction $k_{2,2}$ is calculated with the equilibrium constant of the second reaction K_{eq}^2, as proposed by Hikita et al. (1976).

$$K_{eq}^2 = \frac{k_{2,1}}{k_{2,2}} = K_{eq}^{2,\infty}.10^{\left(\frac{1.01\sqrt{[Na^+]}}{1+1.27\sqrt{[Na^+]}}+0.125[Na^+]\right)} \tag{C.2.1}$$

where $K_{eq}^{2,\infty}$ is the temperature dependent rate at infinite dilution of sodium ions.

$$K_{eq}^{2,\infty} = 10^{\frac{1568.94}{T}+0.4134-0.00673.T} \tag{C.2.2}$$

The backward reaction is therefore calculated as.

$$k_{2,2} = \frac{k_{2,1}}{K_{eq}^2} \tag{C.2.3}$$

Third reaction

Since only uncharged molecules are involved in the third forward reaction (equation (14)), the forward reaction rate constant $k_{3,1}$ depends solely on the temperature and not ionic strength. It is determined by the equation proposed by Johnson (1982) as.

$$k_{3,1} = \exp\left(-\frac{6.19.10^4}{T} + 1247 - 183ln(T)\right) \tag{C.3.1}$$

The third backward reaction rate constant $k_{3,2}$ can be calculated with the equilibrium constant K_{eq}^3 introduced previously in equation (C.1.6).

$$k_{3,2} = \frac{k_{3,1}}{K_{eq}^3} \tag{C.3.2}$$

Appendix D. Supplementary data

Supplementary data to this article can be found online at https://doi.org/10.1016/j.ces.2022.117963.

References

Alexander, B.F., Shah, Y.T., 1976. Axial dispersion coefficients in bubble columns. Chemical Engineering J. 11, 153–156. https://doi.org/10.1016/0300-9467(76)80021-4.

Bird, R.B., Stewart, W., Lightfoot, E.N., 2002. Transport Phenomena, Second. ed. John Wiley and Sons Ltd, Inc.

Brauer, H., 1979. Particle/Fluid Transport Processes. Prog Chem. Eng. 19, 61–99.

Buffo, A., Vanni, M., Marchisio, D.L., 2017. Simulation of a reacting gas–liquid bubbly flow with CFD and PBM: Validation with experiments. Appl. Math. Model. 44, 43–60. https://doi.org/10.1016/j.apm.2016.11.010.

Camarasa, E., Carvalho, E., Meleiro, L.A.C., Maciel Filho, R., Domingues, A., Wild, G., Poncin, S., Midoux, N., Bouillard, J., 2001. Development of a complete model for an air-lift reactor. Chemical Engineering Science, 16th International Conference on Chemical Reactor Engineering 56, 493–502. 10.1016/S0009-2509(00)00253-0.

Camarasa, E., Vial, C., Poncin, S., Wild, G., Midoux, N., Bouillard, J., 1999. Influence of coalescence behaviour of the liquid and of gas sparging on hydrodynamics and bubble characteristics in a bubble column. Chem. Eng. Process. Process Intensif. 38, 329–344. https://doi.org/10.1016/S0255-2701(99)00024-0.

Chen, J., Brooks, C.S., 2021. Experiments and CFD simulation of mass transfer and hydrodynamics in a cylindrical bubble column. Chem. Eng. Sci. 234,. https://doi.org/10.1016/j.ces.2020.116435 116435.

Chou, P.Y., 1945. ON VELOCITY CORRELATIONS AND THE SOLUTIONS OF THE EQUATIONS OF TURBULENT FLUCTUATION. Q. Appl. Math. 3, 38–54.

Clift, R., Gurace, J.R., Weber, M.E., 1978. Bubbles, drops, and particles, 3. print. ed. Acad. Press, New York, NY.

Cockx, A., Do-Quang, Z., Liné, A., Roustan, M., 1999. Use of computational fluid dynamics for simulating hydrodynamics and mass transfer in industrial ozonation towers. Chem. Eng. Sci. 54, 5085–5090. https://doi.org/10.1016/S0009-2509(99)00239-0.

Colombet, D., Cockx, A., Guiraud, P., Legendre, D., 2013. Experiments and modelling of a draft tube airlift reactor operated at high gas throughputs. Chem. Eng. Sci. 104, 32–43. https://doi.org/10.1016/j.ces.2013.08.044.

Danckwerts, P.V., Lannus, A., 1970. Gas-Liquid Reactions. J. Electrochem. Soc. 117, 369C. https://doi.org/10.1149/1.2407312.

Darmana, D., Henket, R.L.B., Deen, N.G., Kuipers, J.A.M., 2007. Detailed modelling of hydrodynamics, mass transfer and chemical reactions in a bubble column using a discrete bubble model: Chemisorption of CO2 into NaOH solution, numerical and experimental study. Chem. Eng. Sci. 62, 2556–2575. https://doi.org/10.1016/j.ces.2007.01.065.

Deckwer, W.-D., Burckhart, R., Zoll, G., 1974. Mixing and mass transfer in tall bubble columns. Chem. Eng. Sci. 29, 2177–2188. https://doi.org/10.1016/0009-2509(74)80025-4.

Deckwer, W.-D., Adler, I., Zaidi, A., 1978. A comprehensive study on co2-interphase mass transfer in vertical cocurrent and countercurrent gas-liquid flow. The Canadian Journal of Chemical Engineering 56, 43–55. https://doi.org/10.1002/cjce.5450560107.

Deckwer, W.-D., Schumpe, A., 1993. Improved tools for bubble column reactor design and scale-up. Chem. Eng. Sci. 48, 889–911. https://doi.org/10.1016/0009-2509(93)80328-N.

DeCoursey, W.J., 1974. Absorption with chemical reaction: development of a new relation for the Danckwerts model. Chem. Eng. Sci. 29, 1867–1872. https://doi.org/10.1016/0009-2509(74)85003-7.

Edwards, T.J., Maurer, G., Newman, J., Prausnitz, J.M., 1978. Vapor-liquid equilibria in multicomponent aqueous solutions of volatile weak electrolytes. AIChE J. 24, 966–976. https://doi.org/10.1002/aic.690240605.

Eigen, M., 1954. Methods for investigation of ionic reactions in aqueous solutions with half-times as short as 10–9 sec. Application to neutralization and hydrolysis reactions. Discuss. Faraday Soc. 17, 194–205. https://doi.org/10.1039/DF9541700194.

Ertekin, E., Kavanagh, J.M., Fletcher, D.F., McClure, D.D., 2021. Validation studies to assist in the development of scale and system independent CFD models for industrial bubble columns. Chem. Eng. Res. Des. 171, 1–12. https://doi.org/10.1016/j.cherd.2021.04.023.

Fayolle, Y., Cockx, A., Gillot, S., Roustan, M., Héduit, A., 2007. Oxygen transfer prediction in aeration tanks using CFD. Chemical Engineering Science, 8th International Conference on Gas-Liquid and Gas-Liquid-Solid Reactor Engineering 62, 7163–7171. 10.1016/j.ces.2007.08.082.

Fleischer, C., Becker, S., Eigenberger, G., 1996. Detailed modeling of the chemisorption of CO2 into NaOH in a bubble column. Chemical Engineering Science, Chemical Reaction Engineering: From Fundamentals to Commercial Plants and Products 51, 1715–1724. https://doi.org/10.1016/0009-2509(96)00030-9.

Gaddis, E.S., Vogelpohl, A., 1986. Bubble formation in quiescent liquids under constant flow conditions. Chem. Eng. Sci. 41, 97–105. https://doi.org/10.1016/0009-2509(86)85202-2.

Gruber, M.C., Radl, S., Khinast, J.G., 2015. Rigorous modeling of CO2 absorption and chemisorption: The influence of bubble coalescence and breakage. Chem. Eng. Sci. 137, 188–204. https://doi.org/10.1016/j.ces.2015.06.008.

Higbie, R., 1935. The Rate of Absorption of a Pure Gas into a Still Liquid during Short Periods of Exposure. Trans. AIChE 31, 365–389.

Hikita, H., Asai, S., Takatsuka, T., 1976. Absorption of carbon dioxide into aqueous sodium hydroxide and sodium carbonate-bicarbonate solutions. The Chemical Engineering Journal 11, 131–141. https://doi.org/10.1016/S0300-9467(76)80035-4.

Hissanaga, A.M., Padoin, N., Paladino, E.E., 2020. Mass transfer modeling and simulation of a transient homogeneous bubbly flow in a bubble column. Chem. Eng. Sci. 218,. https://doi.org/10.1016/j.ces.2020.115531 115531.

Hlawitschka, M.W., Kováts, P., Zähringer, K., Bart, H.-J., 2017. Simulation and experimental validation of reactive bubble column reactors. Chemical Engineering Science, 13th International Conference on Gas-Liquid and Gas-Liquid-Solid Reactor Engineering 170, 306–319. 10.1016/j.ces.2016.12.053.

Hlawitschka, M.W., Drefenstedt, S, Bart, H.J., 2016. Local Analysis of CO2 Chemisorption in a Rectangular Bubble Column Using a Multiphase Euler-Euler CFD Code. Journal of Chemical Engineering & Process Technology 7. https://doi.org/10.4172/2157-7048.1000300.

Hori, Y., Hayashi, K., Hosokawa, S., Tomiyama, A., 2017. Mass transfer from single carbon-dioxide bubbles in electrolyte aqueous solutions in vertical pipes. Int. J. Heat Mass Transf. 115, 663–671. https://doi.org/10.1016/j.ijheatmasstransfer.2017.07.087.

Huang, Z., Yan, H., Liu, L., Gong, H., Zhou, P., 2021. Numerical modeling of reactive bubbly flows based on Euler-Lagrange approach. Chem. Eng. Sci. 239,. https://doi.org/10.1016/j.ces.2021.116640 116640.

Johnson, K.S., 1982. Carbon dioxide hydration and dehydration kinetics in seawater1. Limnol. Oceanogr. 27, 849–855. https://doi.org/10.4319/lo.1982.27.5.0849.

Kantarci, N., Borak, F., Ulgen, K.O., 2005. Bubble column reactors. Process Biochem. 40, 2263–2283. https://doi.org/10.1016/j.procbio.2004.10.004.

Kern, D.M., 1960. The hydration of carbon dioxide. J. Chem. Educ. 37, 14. https://doi.org/10.1021/ed037p14.

Krauß, M., Rzehak, R., 2018. Reactive absorption of CO2 in NaOH: An Euler-Euler simulation study. Chem. Eng. Sci. 181, 199–214. https://doi.org/10.1016/j.ces.2018.01.009.

Krauβ, M., Rzehak, R., 2017. Reactive absorption of CO2 in NaOH: Detailed study of enhancement factor models. Chem. Eng. Sci. 166, 193–209. https://doi.org/10.1016/j.ces.2017.03.029.

Larsson, T., Duran Quintero, C., Gillot, S., Cockx, A., Fayolle, Y., 2022. Development and validation of a comprehensive 1-D model to simulate gas hold-up and gas–liquid transfer in deep air–water bubble columns. Chem. Eng. Sci. 248,. https://doi.org/10.1016/j.ces.2021.117210 117210.

Launder, B.E., Spalding, D.B., 1974. The numerical computation of turbulent flows. Comput. Methods Appl. Mech. Eng. 3, 269–289. https://doi.org/10.1016/0045-7825(74)90029-2.

Liu, J., Zhou, P., Liu, L., Chen, S., Song, Y., Yan, H., 2021. CFD modeling of reactive absorption of CO2 in aqueous NaOH in a rectangular bubble column: Comparison of mass transfer and enhancement factor model. Chem. Eng. Sci. 230,. https://doi.org/10.1016/j.ces.2020.116218 116218.

McCann, D.J., Prince, R.G.H., 1971. Regimes of bubbling at a submerged orifice. Chem. Eng. Sci. 26, 1505–1512. https://doi.org/10.1016/0009-2509(71)86042-6.

McClure, D.D., Norris, H., Kavanagh, J.M., Fletcher, D.F., Barton, G.W., 2014. Validation of a Computationally Efficient Computational Fluid Dynamics (CFD) Model for Industrial Bubble Column Bioreactors. Ind. Eng. Chem. Res. 53, 14526–14543. https://doi.org/10.1021/ie501105m.

McClure, D.D., Wang, C., Kavanagh, J.M., Fletcher, D.F., Barton, G.W., 2016. Experimental investigation into the impact of sparger design on bubble columns at high superficial velocities. Chem. Eng. Res. Des. 106, 205–213. https://doi.org/10.1016/j.cherd.2015.12.027.

Ngu, V., Morchain, J., Cockx, A., 2022. Spatio-temporal 1D gas-liquid model for biological methanation in lab scale and industrial bubble column. Chem. Eng. Sci. 117478. https://doi.org/10.1016/j.ces.2022.117478.

Pohorecki, R., Moniuk, W., 1988. Kinetics of reaction between carbon dioxide and hydroxyl ions in aqueous electrolyte solutions. Chem. Eng. Sci. 43, 1677–1684. https://doi.org/10.1016/0009-2509(88)85159-5.

Ratcliff, G.A., Holdcroft, J.G., 1963. Diffusivities of gases in aqueous electrolyte solutions. Trans. Inst. Chem. Eng. 41, 315–319.

Rehman, U., Audenaert, W., Amerlinck, Y., Maere, T., Arnaldos, M., Nopens, I., 2017. How well-mixed is well mixed? Hydrodynamic-biokinetic model integration in an aerated tank of a full-scale water resource recovery facility. Water Sci. Technol. 76, 1950–1965. https://doi.org/10.2166/wst.2017.330.

Rzehak, R., Ziegenhein, T., Kriebitzsch, S., Krepper, E., Lucas, D., 2017. Unified modeling of bubbly flows in pipes, bubble columns, and airlift columns. Chemical Engineering Science, 12th International Conference on Gas-Liquid and Gas-Liquid-Solid Reactor Engineering 157, 147–158. 10.1016/j.ces.2016.04.056.

Rzehak, R., Krepper, E., 2016. Euler-Euler simulation of mass-transfer in bubbly flows. Chem. Eng. Sci. 155, 459–468. https://doi.org/10.1016/j.ces.2016.08.036.

Saito, T., Toriu, M., 2015. Effects of a bubble and the surrounding liquid motions on the instantaneous mass transfer across the gas–liquid interface. Chem. Eng. J. 265, 164–175. https://doi.org/10.1016/j.cej.2014.12.039.

Sander, R., 2015. Compilation of Henry's law constants (version 4.0) for water as solvent. Atmos. Chem. Phys. 15, 4399–4981. https://doi.org/10.5194/acp-15-4399-2015.

Schäfer, R., Merten, C., Eigenberger, G., 2002. Bubble size distributions in a bubble column reactor under industrial conditions. Exp. Therm Fluid Sci. 26, 595–604. https://doi.org/10.1016/S0894-1777(02)00189-9.

Shah, Y.T., Kelkar, B.G., Godbole, S.P., Deckwer, W.-D., 1982. Design parameters estimations for bubble column reactors. AIChE J. 28, 353–379. https://doi.org/10.1002/aic.690280302.

Siebler, F., Lapin, A., Takors, R., 2020. Synergistically applying 1-D modeling and CFD for designing industrial scale bubble column syngas bioreactors. Engineering in Life Sciences 20, 239–251. https://doi.org/10.1002/elsc.201900132.

Solsvik, J., 2018. Lagrangian modeling of mass transfer from a single bubble rising in stagnant liquid. Chem. Eng. Sci. 190, 370–383. https://doi.org/10.1016/j.ces.2018.06.002.

Taborda, M.A., Sommerfeld, M., 2021. Reactive LES-Euler/Lagrange modelling of bubble columns considering effects of bubble dynamics. Chem. Eng. J. 407,. https://doi.org/10.1016/j.cej.2020.127222 127222.

Takemura, F., Yabe, A., 1999. Rising speed and dissolution rate of a carbon dioxide bubble in slightly contaminated water. J. Fluid Mech. 378, 319–334. https://doi.org/10.1017/S0022112098003358.

Talvy, S., Cockx, A., Liné, A., 2007. Modeling hydrodynamics of gas–liquid airlift reactor. AIChE J. 53, 335–353. https://doi.org/10.1002/aic.11078.

Talvy, S., Cockx, A., Line, A., 2005. Global modelling of a gas–liquid–solid airlift reactor. Chemical Engineering Science, 7th International Conference on Gas-Liquid and Gas-Liquid-Solid Reactor Engineering 60, 5991–6003. 10.1016/j.ces.2005.04.067.

Tanaka, S., Kastens, S., Fujioka, S., Schlüter, M., Terasaka, K., 2020. Mass transfer from freely rising microbubbles in aqueous solutions of surfactant or salt. Chem. Eng. J. 387,. https://doi.org/10.1016/j.cej.2019.03.122 121246.

Tirunehe, G., Norddahl, B., 2016. The influence of polymeric membrane gas spargers on hydrodynamics and mass transfer in bubble column bioreactors. Bioprocess Biosyst. Eng. 39, 613–626. https://doi.org/10.1007/s00449-016-1543-7.

Tomiyama, A., Matsuoka, T., Fukuda, T., Sakaguchi, T., 1995. A Simple Numerical Method for Solving an Incompressible Two-Fluid Model in a General Curvilinear Coordinate System, in: Serizawa, A., Fukano, T., Bataille, J. (Eds.), Multiphase Flow 1995. Elsevier, Amsterdam, pp. 241–252. 10.1016/B978-0-444-81811-9.50026-3.

Tomiyama, A., Kataoka, I., Zun, I., Sakaguchi, T., 1998. Drag Coefficients of Single Bubbles under Normal and Micro Gravity Conditions. JSME International Journal Series B 41, 472–479. https://doi.org/10.1299/jsmeb.41.472.

Tomiyama, A., Tamai, H., Zun, I., Hosokawa, S., 2002. Transverse migration of single bubbles in simple shear flows. Chem. Eng. Sci. 57, 1849–1858. https://doi.org/10.1016/S0009-2509(02)00085-4.

Tsonopoulos, C., Coulson, D.M., Inman, L.B., 1976. Ionization constants of water pollutants. J. Chem. Eng. Data 21, 190–193. https://doi.org/10.1021/je60069a008.

Versteeg, G.F., Van Swaaij, W.P.M., 1988. Solubility and diffusivity of acid gases (carbon dioxide, nitrous oxide) in aqueous alkanolamine solutions. J. Chem. Eng. Data 33, 29–34. https://doi.org/10.1021/je00051a011.

Wachi, S., Nojima, Y., 1990. Gas-phase dispersion in bubble columns. Chem. Eng. Sci. 45, 901–905. https://doi.org/10.1016/0009-2509(90)85012-3.

Weisenberger, S., Schumpe, A., 1996. Estimation of gas solubilities in salt solutions at temperatures from 273 K to 363 K. AIChE J. 42, 298–300. https://doi.org/10.1002/aic.690420130.
Westerterp, A., Swaaij, K.R., Beenackers, W.P.M., 1998. Chemical Reactor Design and Operation. New York.
Zeebe, R.E., 2011. On the molecular diffusion coefficients of dissolved CO2, HCO3-, and CO32- and their dependence on isotopic mass. Geochim. Cosmochim. Acta 75, 2483–2498. https://doi.org/10.1016/j.gca.2011.02.010.
Zuber, N., Findlay, J.A., 1965. Average Volumetric Concentration in Two-Phase Flow Systems. J. Heat Transfer 87, 453–468. https://doi.org/10.1115/1.3689137.

5.5 Unpublished results

Some results are presented in this section as they are not included in the published paper. One of the results that are not featured in the article is the comparison of different mass transfer coefficient models, as has been done in the work of Liu et al. (2021) and Huang et al. (2021). Table 5.2 reports the list of Sherwood correlations used in this study.

Table 5.2: Mass transfer coefficient models derived from different Sherwood correlations

Sherwood correlation	Notation	Description	Reference
$Sh = 2 + 0.015Re^{0.89}.Sc^{0.7}$	$k_{L,1}$	Non-spherical bubbles with stochastic deformations of the interface	(Brauer, 1979)
$Sh = 2 + 0.6415Re^{0.5}.Sc^{0.5}$	$k_{L,2}$	Spherical bubbles	(Bird et al., 2002)
$Sh = 2 + 1.25Re^{0.5}.Sc^{0.33}$	$k_{L,3}$	Bubble swarm	(Jain et al., 2015)
$Sh = 1.13Re^{0.5}.Sc^{0.5}$	$k_{L,4}$	Clean spherical bubbles	(Higbie, 1935)

In terms of the ranking between $k_{L,1}$, $k_{L,2}$ and $k_{L,3}$, the 1D model finds that the pH has the fastest decline in the order of $k_{L,1} > k_{L,2} > k_{L,3}$, as shown in Figure 5.2(a). 1D model agrees with the finding of Huang et al. (2021) who reported the same ranking but not that of Liu et al. (2021). Interested readers can compare Figure 11 of Huang et al. (2021) to Figure 5 of Liu et al. (2021). Liu et al. (2021) reported a ranking of $k_{L,2} > k_{L,3} > k_{L,1}$. Huang et al. (2021) does not yield the same ranking as Liu et al. (2021) either. Huang et al. (2021) explained that the difference in ranking could due to different numerical approaches and different chemical reaction pathways considered as the third pathway is not considered in the work of Liu et al. (2021). This ranking is reflected in the pH curve whereby the highest Sherwood leads to an earlier decrease in pH, as shown in Figure 5.2(b). The higher the mass transfer coefficient, the higher the CO_2 mass transfer flux, the higher the consumption of hydroxyl ions, and the faster the drop in pH.

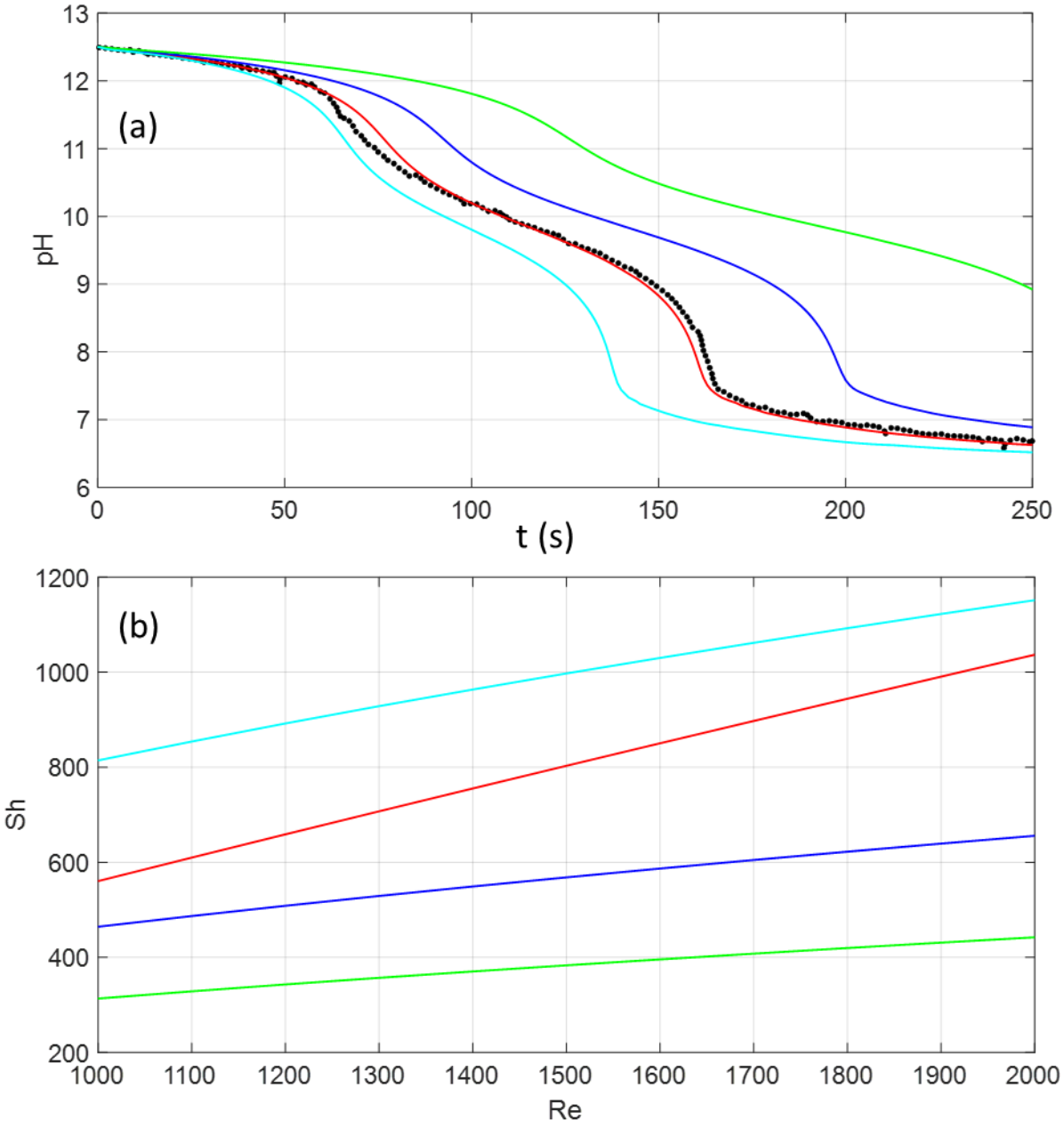

Figure 5.2: (a) Time-dependent pH profile using different k_L closure models. (b) Sherwood number vs Reynolds number for different mass transfer closure models from Table 5.2. Black dots from Darmana experimental results, Colored lines from 1D model. Cyan lines from $k_{L,4}$, Red lines from $k_{L,1}$, Blue lines from $k_{L,2}$, and Green lines from $k_{L,3}$

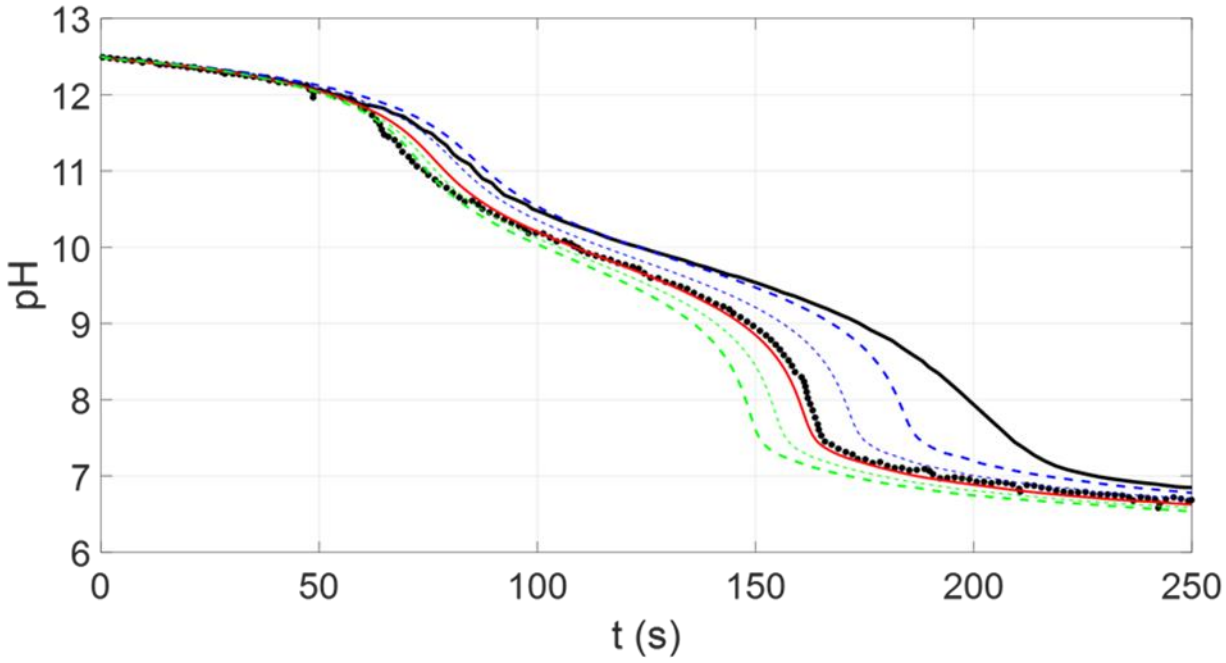

Figure 5.3: Sensitivity analysis on $k_L a$. Continuous red line: base case, dashed blue line ($k_L a - 10\%$), thick dashed blue line ($k_L a - 20\%$), dashed green line ($k_L a - 10\%$), thick dashed green line ($k_L a - 20\%$), Continuous black line: Darmana CFD model, dotted black line: Darmana experimental data

It is reported in the literature that bubble size distribution can be polydisperse even in the homogeneous bubbly flow regime. Besagni (2021) divided the homogeneous regime into mono-dispersed and poly-dispersed homogeneous flow regimes. A priori, the polydispersity has a direct impact on the $k_L a$. The $k_L a$ can be dissociated into two terms: k_L and a. The modelling of polydispersity on interfacial area a could be questionable in the homogeneous regime where bubble breakup and coalescence is mostly negligible. In particular, the superficial gas velocity applied in Darmana et al. (2007) is relatively low at 0.007 m.s^{-1}. The inlet bubble diameter measured at 5.5 mm in the experiment is already the Sauter mean diameter which considers the averaged polydisperse distribution, calculated in the mean volumetric interfacial area ($a = \frac{6\varepsilon_G}{d_{32}}$). As a consequence, the impact of bubble polydispersity is more questionable on the estimation of the mass transfer coefficient k_L than on the interfacial area a. For that, we have conducted a sensitivity analysis on k_L, the results have been reported in Figure 12 of our published paper.

When we compared some mass transfer models that appeared in Table 5.2, the variation of the Sherwood number depends in general on the square root of the Reynolds (and then the bubble size) except for the Brauer (1979) correlation where the power for Re is 0.9. This implies that the mass

transfer coefficient is nearly independent of the bubble size distribution with each bubble class having the same k_L. The d_b on the right-hand side is simplified with the d_b on the left-hand side of the correlation. Meanwhile, when the dependence of Sherwood is in the square root of the Reynolds, the relative standard deviation of the bubble size distribution will attenuate the mass transfer coefficient relative to this standard deviation (for example d_b increases 20% will reduce k_L to 10%). Figure 5.3 presents the sensitivity analysis of $\pm 10\%$ and $\pm 20\%$ on the $k_L a$ from the base case.

The sensitivity on bubble size distribution could be done via the sensitivity to $k_L a$ presented in Figure 5.3 or directly by changing the mean Sauter bubble size $\pm 1\ \mathrm{mm}$ as presented in Figure 4 of our published paper, as both achieve the same results. We observe that changing $k_L a \pm 20\%$ has the same impact as changing the bubble size in the same relative variation. It confirms the counterbalanced effect when a linear mass transfer model is used (whereby the power of Re is close to 1), as proposed by Brauer (1979).

Chapter 6 CFD modelling of biological methanation

As discussed in Section 1.3, bubble columns are multiphase contactors in which multiphysics coupled phenomena take place simultaneously at different spatial and temporal scales. Depending on the problem one needs to tackle, numerical simulation of bubble columns can be conducted using different modelling tools. Among these, CFD is a well-established tool, especially with the advent of powerful computational resources and the development of various simulation software. CFD models can be used to investigate the interactions between phases with excellent spatial resolution.

In this chapter, a Euler-Euler CFD model based on the two-fluid model is developed for the biological methanation process. The CFD simulations were performed using commercial CFD code ANSYS Fluent version 2021 R1. The model resolves the bubbly flow, the multispecies mass transfer and eventually couples with the bioreaction kinetics. To validate the multispecies mass transfer CFD model workflow, a step-by-step validation from the two-phase hydrodynamics to the multispecies mass transfer and bioreaction has been conducted. The validation studies can be found in the Appendix. Part of the CFD simulation work was conducted during a two-month mobility programme at the University of Sydney under the supervision of Associate Professor John M. Kavanagh and Adjunct Professor David F. Fletcher.

Our third paper entitled "*H_2 mass transfer – key factor for efficient biological methanation: Comparison between pilot-scale experimental data, 1D and CFD models*" has been submitted to Chemical Engineering Science on 15/06/2022. It is currently under review. The paper reports a comparison study between the experimental biological methanation results with the numerical predictions using 1D and CFD models. The same biological methanation model developed in Ngu et al. (2022a) is implemented in both modelling tools, as a function in the in-house code and as a user subroutine in the CFD software.

An analytical solution based on gas phase mass balance only was also developed with the aim to underline the most influential parameters governing the methane production. This simplified vision is also used to explain the asymptotic behaviour in 1D and CFD simulations. Lastly, sensitivity analysis is also presented to highlight the importance of H_2 mass transfer in biological methanation.

6.1 Pilot-scale biological methanation bubble column

H_2 mass transfer – a key factor for efficient biological methanation: Comparison between pilot-scale experimental data, 1D and CFD models

Vincent Ngu[1], David F. Fletcher[2], John M. Kavanagh[2], Yan Rafrafi[1], Claire Dumas[1], Jérôme Morchain[1], Arnaud Cockx[1,*]

[1] *Toulouse Biotechnology Institute, Université de Toulouse, CNRS, INRAE, INSA, Toulouse, France*

[2] *School of Chemical and Biomolecular Engineering, The University of Sydney, NSW 2006, Australia*

*Corresponding author: cockx@insa-toulouse.fr (A. Cockx)

Keywords: Bubble column, Multiscale modeling, Gas-liquid mass transfer, Power-to-Gas, CFD, Sparger

Highlights:

- Satisfactory numerical prediction of bioreactor performances using 1D and CFD models.
- Uniform porous plate leads to higher interfacial mass transfer.
- Analytical solutions unravel the impact of operating conditions on biological methanation efficiency.
- Sensitivity analysis reveals that CH_4 purity and productivity increases with H_2 mass transfer but is not impacted by the absolute pressure.

Submitted to Chemical Engineering Science on 15/06/2022

Revised on 28/11/2022

Abstract

Biological methanation is an emerging Power-to-Gas technology that provides a flexible, efficient, and long-term storage system to address the renewable energy intermittency issue. However, scaling-up a biological methanation plant requires overcoming the bottleneck of H_2 gas-liquid mass transfer. The current work demonstrates analytically, experimentally and numerically the importance of H_2 mass transfer on CH_4 purity and productivity. The influence of sparger design was investigated in a pilot-scale bubble column bioreactor. An increase of 265% in $k_L a$ and subsequently 81% in CH_4 purity is obtained when a uniform porous plate is used over a 4-points porous sparger. Numerical simulation of the bioreactor was performed using a multiscale modeling approach coupling 1D and CFD models. The numerical simulations were validated satisfactorily by the experimental data. Parametric studies were also performed using the 1D model to reveal the impact of operating conditions on the bioprocess. An analytical solution for the productivity of biomethanation reactors at steady-state is proposed based on mass balances and provides new insights into biological methanation. It is found that any modification of operating parameters that improve H_2 mass transfer, such as higher gas recirculation rate and smaller bubble size, leads to a better bioreactor performance.

6.1.1 Introduction

In the past decades, global warming and climate change have become the centerpiece of discussion among policymakers. The Paris Climate Agreement sets the framework for participating countries to limit the temperature rise well below 2°C. The European Commission has also set the goal of achieving a 32% renewable energy share in the energy mix by 2030 (European Commission, 2016b, 2016a). Therefore, renewable energies play an important role in mitigating the use of fossil fuels that have caused greenhouse gas emissions to reach a record high worldwide year-over-year. However, due to the intermittent behavior of renewable energy sources, such as wind and solar, an energy buffer is required. In this context, Power-to-Gas technologies play an important role in achieving deep decarbonisation and ensuring a green transition of the global energy system from carbon-emitting fossil fuels to renewable energy sources. Biological methanation has emerged as an interesting option for Power-to-Gas application. The product – methane (CH_4) is a promising energy vector as it can be directly injected into the existing natural gas network for transport and storage.

Compared with catalytic methanation, biological methanation operates under milder conditions and methanogens have higher resistance to feed gas impurities, which lower the CH_4 production costs (Jensen et al., 2021). Besides interconnecting with the renewable energy electricity grid, biological methanation can be integrated with wastewater treatment plants (WWTP) and anaerobic digestors, such as the biological methanation plant on BIOFOS site in Avedøre, Denmark (Lardon et al., 2018). Additionally, the H_2 produced from the electrolysis of water, oxygen (O_2) can be fed to nearby WWTP. The biogas from anaerobic digestion containing mainly CH_4 and carbon dioxide (CO_2) can be upgraded by biological methanation. The heat produced from biological methanation can be used to heat the anaerobic digestor. Such synergistic effects between industries have shown that a positive energy balance is achievable at large-scale (Lardon et al., 2018).

Despite numerous advantages of biological methanation, the overall process is strongly limited by hydrogen (H_2) mass transfer, as agreed by several researchers (Lecker et al., 2017; Rafrafi et al., 2020; Rusmanis et al., 2019). Only a few large-scale biological methanation plants with a range of volume between 3.5-100 m^3 are referenced in the literature, signifying that the technology is only at the early stage of its commercial application (Rafrafi et al., 2020). Extensive investigations on reactor design, system configurations and operating conditions are still mainly at the laboratory or pilot-scale. Several reactor designs, such as stirred tank reactors (Figueras et al., 2021; Martin et al., 2013; Peillex et al., 1990), bubble column reactors (Bassani et al., 2017; Kougias et al., 2017; Laguillaumie et al., 2022; Voelklein et al., 2019), membrane reactors (Díaz et al., 2015; Luo and Angelidaki, 2013), fixed-bed

reactors (Lee et al., 2012) and trickled bed reactors (Markthaler et al., 2020; Sieborg et al., 2020; Strübing et al., 2018; Ullrich et al., 2018), have been studied to demonstrate the feasibility of biological methanation. Different strategies for the operating configurations and conditions have been investigated to improve H_2 mass transfer efficiency (Bassani et al., 2017; Kougias et al., 2017; Ullrich and Lemmer, 2019). Two main configurations, namely in-situ and ex-situ biological methanation strategies are also reported (Angelidaki et al., 2018; Jensen et al., 2021; Lecker et al., 2017; Rafrafi et al., 2020). For the in-situ system, H_2 is directly injected into an anaerobic plant to increase biogas production through CO_2 consumption. Meanwhile, for the ex-situ system, H_2 and biogas or any CO_2 source are injected into another independent bioreactor for biogas upgrading through biological methanation. As most of the studies focus on experimental work, the development of numerical models is also necessary to elucidate the bioprocess and predict bioreactor performances. Therefore, extensive research and development is required to better understand the fundamental phenomena and the coupling in a biological methanation reactor in order to guide the scale-up of the technology. The multiphysics phenomena to couple in the numerical model include:

- Two-phase gas-liquid bubbly flow
- Multi-species mass transfer (H_2, CO_2, CH_4)
- Biological kinetics

In terms of biokinetics, the classical Monod-type law is not appropriate to describe biological methanation reaction, as discussed in Ngu et al. (2022a). When bioreaction is limited by mass transfer, the dissolved substrate concentration reaches zero, consequently, the Monod-type description forces the reaction to stop, but the mass transfer flux is still maintained. As the limiting factor of biological methanation is H_2 mass transfer, the detailed bioreaction description becomes less important (Markthaler et al., 2020). Therefore, a more practical and realistic model capable of switching between the biological and physical limited regime is necessary, especially when multiphysics phenomena are competing. In addition, computational fluid dynamics (CFD) models for biological methanation are still scarce in the literature and they mostly focus on the hydrodynamic behavior of bioreactors (Leonzio, 2016; Markthaler et al., 2020). Leonzio (2018, 2016) presents a CFD model to study the mixing and the mass transfer efficiency of in-situ biological methanation in a stirred tank reactor but no discussion on the bioreaction is provided. Meanwhile, liquid gas holdup of a lab-scale trickled bed bioreactor is predicted satisfactorily by the CFD model of Markthaler et al. (2020) but the biomethane production is underpredicted. In fact, a CFD model can unravel local flow structures precisely, hence, it can offer a good description of hydrodynamic coupling with mass transfer and bioreaction. Here, we attempt to

develop a CFD model that considers the mutual interactions of multiphase bubbly flow, multispecies mass transfer and biological reaction with the validation from biological methanation experimental data presented in Rafrafi et al. (2019).

The sparger design is very important as it largely determines the initial bubble size, and thus the bubble rise velocity (Kulkarni and Joshi, 2011). Different types of sparger design have been studied in the literature to determine the hydrodynamics and mass transfer properties, such as tree sparger, ring sparger, spider sparger, porous plate, perforated plate, and needle sparger. These spargers can be classified into two major categories: plate type spargers and pipe type spargesr (Kulkarni and Joshi, 2011). At a given superficial gas velocity, these spargers will produce different flow regimes, depending on the uniformity of gas injection, the pore size, and the number of holes (Besagni et al., 2018a; Sharaf et al., 2016; Veera and Joshi, 1999). Consequently, the flow pattern will impact the mass transfer and (bio)reaction rate (Li et al., 2021). In aerobic bioprocesses, the sparger plays an important role in supplying gas substrate to the biomass for growth and metabolism. For example, oxygen transfer is pivotal for wastewater treatment and aeration remains the major operating cost of such processes (Amaral et al., 2019; Fayolle et al., 2007). In biological methanation whereby the major substrates (H_2 and CO_2) are fed through the gaseous phase, the overall process can be limited by H_2 mass transfer. This is due to the poor solubility of H_2 (of the order 1 mg/L at atmospheric pressure compared with that of O_2 at 40 mg/L). To elucidate the importance of H_2 mass transfer, the hydrodynamics of two sparger designs and their impact on biological methanation are studied.

In this work, ex-situ biological methanation is studied experimentally and numerically in a pilot-scale bubble column bioreactor. In the same bubble column, the importance of the gas sparger system on the global hydrodynamics and the bioreactor performances was also demonstrated. Besides, a one-dimensional (1D) spatio-temporal multi-species mass transfer model considering bubble size changes due to pressure and mass transfer coupled with a newly proposed bioreaction closure model was applied to study the experimental system. The model was validated using experimental data and it can be used to identify certain key parameters for the optimization of the industrial-scale bubble column design for biological methanation through a series of sensitivity analyses. CFD simulations were also carried out to investigate the local hydrodynamics and the bioreactor performances equipped with two types of gas sparger. Lastly, an analytical solution based on gaseous mass balances at steady-state is proposed. It underlines the importance of mass transfer to the bioprocess. The objectives of this multiphysics modeling are threefold: to highlight the importance of sparger design on bioreactor performance, to perform numerical predictions of bioreactor performance using 1D and CFD models, and to identify underlying parameters impacting H_2 mass transfer. This work aims at offering some

guidelines for bubble column bioreactor design, and thus to accelerate the biological methanation technology transfer to the industry.

6.1.2 Experimental and Numerical Methods

6.1.2.1 Experimental setup

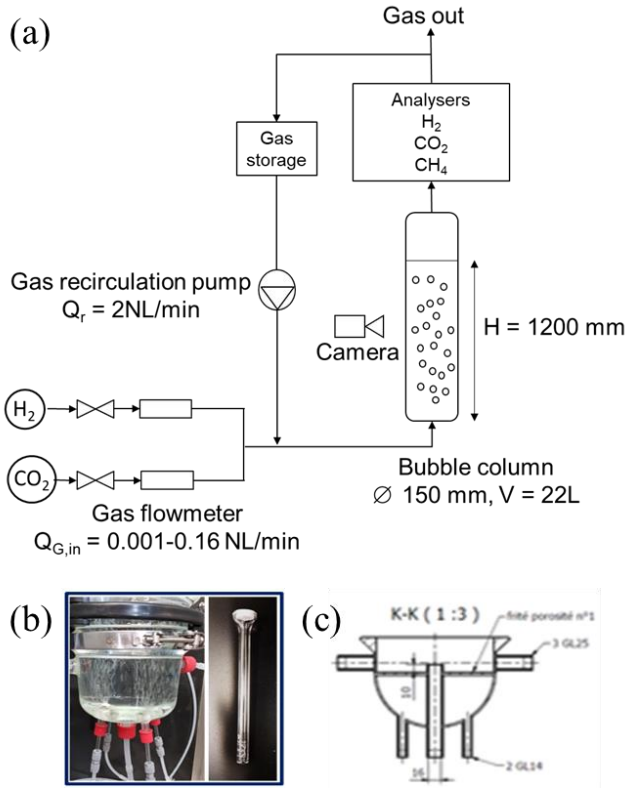

Figure 6.1: (a) Simplified experimental setup. (b) 4-points sparger (c) Porous plate.

The experiment setup as shown in Figure 6.1(a) is composed of a 22 L bubble column with an initial liquid height and internal diameter of 1200 mm and 150 mm, respectively. The experiment was conducted at atmospheric pressure and in thermophilic conditions (temperature at 328.15 K). The temperature was regulated with a thermostat (LAUDA®) by circulating water in the jacket of the bubble column. H_2:CO_2 with a ratio of 4:1 was fed to the column with any unreacted gas being recirculated at a rate (Q_r) of 2 NL/min. Two types of gas sparger, presented in Figure 6.1(b) and (c), were tested experimentally. The first, named the 4-points porous sparger, is composed by 4 small porous sintered diffusers with a diameter of 10 mm each. The second, a uniform porous plate, consists of a single porous sintered diffuser occupying the bottom cross-section of the column. Both spargers have the same properties with a pore size between 100-160 µm. The total area of the spargers is 0.000314 and 0.0177 m² for the 4-points sparger and porous plate respectively. The inlet gas flowrate ($Q_{G,in}$) was varied between 0.001 to 0.16 NL/min. The influence of uniform and non-uniform aeration is discussed

in Section 6.1.3.3.

The bubble diameter is required for the 1D and CFD models. However, it is not determined under bioreaction conditions, as it cannot be measured by optical means due to the turbid and muddy liquid medium. The bubble diameter was measured in air-tap water system and was used as an estimate of the inlet bubble diameter for the numerical models. A camera was installed at the column mid-height to measure the bubble size. The details on the bubble size measurement can be found in Ngu et al. (2022a). Figure 6.2(a) and (b) show that the bubbles formed using the 4-points sparger are larger than those from the porous plate. This shifts the bubble size distribution to larger sizes, resulting in a larger Sauter mean diameter, as shown in Figure 6.2(c) and (d). The bubble diameter used for the simulations is discussed in Section 6.1.2.3.

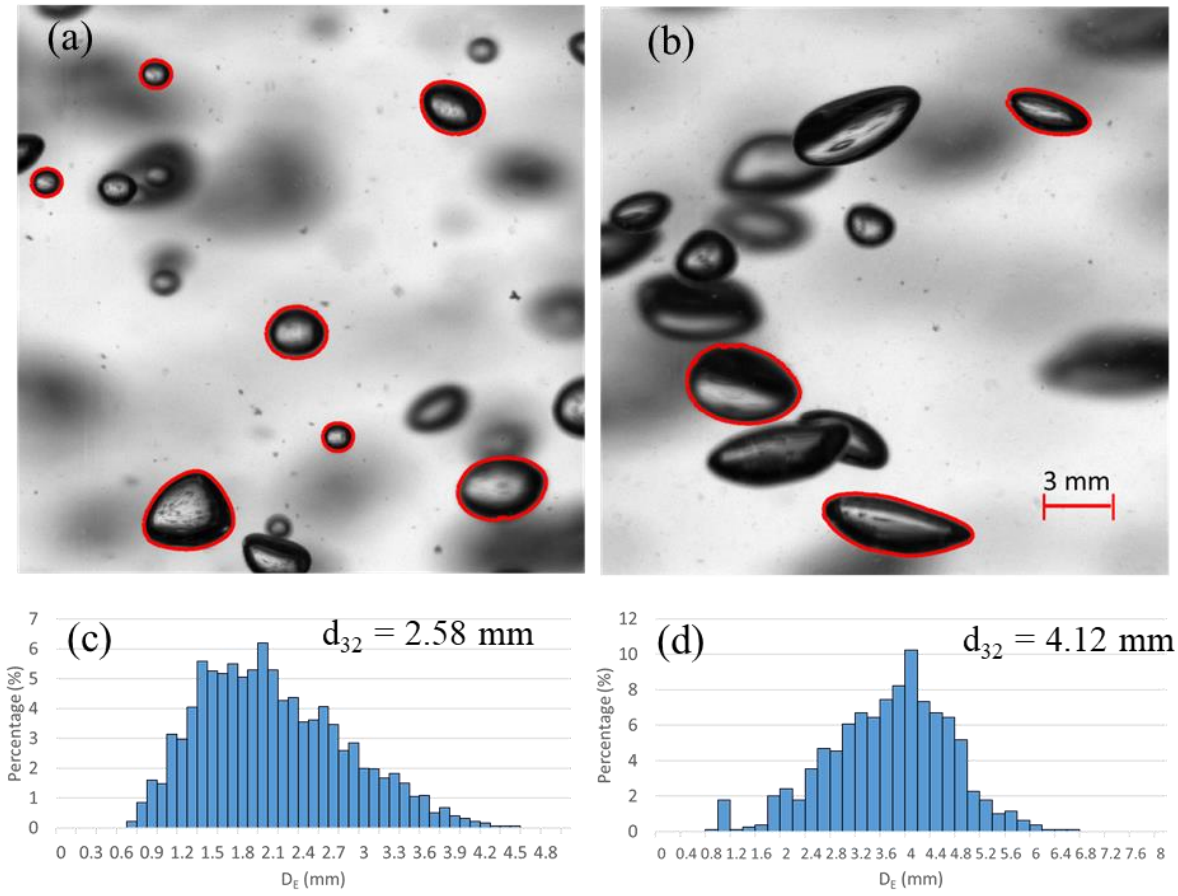

Figure 6.2: (a and b) Detected bubbles by the image processing algorithm at $Q_{G,in} = 1.6$ NL/min. (c and d) Histogram of bubble size distribution for a bin size of 0.2 mm equivalent diameter and the calculated Sauter mean diameter. (a) and (c) porous plate, (b) and (d) 4-points sparger.

To characterise the bioreactor performances, two parameters were chosen, namely outlet methane gas purity ($y_{CH_4,out}$) and methane production rate (MPR). MPR is defined in equation (2.9) as the outlet

methane volumetric flowrate per unit volume of reactor. These two parameters represent the quality and the quantity of methane contained in the off-gas.

$$MPR = \frac{y_{CH_4,out} \cdot Q_{G,out}}{V} \tag{6.1}$$

where $Q_{G,out}$ is outlet gas flowrate and V is the reactor volume.

6.1.2.2 1D model for multispecies bioreactive bubbly flow

A previously developed 1D model was applied in this work and is presented briefly here. The numerical discretization and the applied scheme were kept the same as in Ngu et al. (2022a). The 1D model consists of the following species transport equations (equations (6.2) and (6.3)), referring to the conservation of mass in an elementary volume of height dz. The resolution of this model provides the spatial and temporal profiles of gas holdup and species concentrations in both phases.

$$\frac{\partial \phi_{G,i}}{\partial t} + \frac{\partial u_G \phi_{G,i}}{\partial z} = D_G \frac{\partial}{\partial z}\left(\varepsilon_G \frac{\partial C_{G,i}}{\partial z}\right) - k_{L,i} a (C_i^* - C_{L,i}) \tag{6.2}$$

$$\frac{\partial \phi_{L,i}}{\partial t} + \frac{\partial u_L \phi_{L,i}}{\partial z} = D_L \frac{\partial}{\partial z}\left(\varepsilon_L \frac{\partial C_{L,i}}{\partial z}\right) + k_{L,i} a (C_i^* - C_{L,i}) \; + \varepsilon_L R_i \tag{6.3}$$

$$\varepsilon_G + \varepsilon_L = 1 \tag{6.4}$$

The key parameters of this model are u_G and u_L, the gas and liquid velocities, respectively. ε_G and ε_L are the gas and liquid holdup, summing to one, as stated in equation (6.4). $C_{G,i}$ and $C_{L,i}$ are the concentration of species i: mass per unit volume of the gas and liquid phase, respectively. Hence, $\phi_{G,i}$ is the concentration of species i in the gas phase: mass per unit volume of the column, i.e., $\phi_{G,i} = \varepsilon_G C_{G,i}$. Similarly, we have $\phi_{L,i} = \varepsilon_L C_{L,i}$. The liquid axial dispersion coefficient, D_L, was calculated from the correlation proposed by Deckwer et al. (1974), as presented in equation (6.5) while the gaseous axial dispersion coefficient, D_G, was estimated from the correlation of Wachi and Nojima, (1990), as written in equation (6.6). Both correlations are function of the superficial gas velocity, j_G, and bubble column diameter, D_r.

$$D_L = 2.7 \cdot 10^{-4} \cdot (D_r \cdot 100)^{1.4} \cdot (j_G \cdot 100)^{0.3} \tag{6.5}$$

$$D_G = 20 \cdot D_r^{1.5} \cdot j_G \tag{6.6}$$

The local volumetric interfacial area for mass transfer, a, was calculated from the local bubble diameter,

d_b, and gas holdup, ε_G, as expressed in equation (6.7). The liquid side mass transfer coefficient of each species $k_{L,i}$ was computed via equation (6.8) from Higbie (1935) and it involves the species dependent liquid-side diffusion coefficient, D_i, and the spatially dependent variables (ε_G, d_b, u_{rel}), with $u_{rel} = u_G - u_L$ the homogeneous slip velocity, as presented in equation (6.9).

$$a = 6\frac{\varepsilon_G}{d_b} \tag{6.7}$$

$$k_{L,i} = 2\sqrt{\frac{D_i . u_{rel}}{\pi . d_b}} \tag{6.8}$$

The corresponding diffusion coefficients at 328.15K are 1×10^{-8}, 4.5×10^{-9}, and 3.3×10^{-9} m².s^{-1} for hydrogen, carbon dioxide and methane, respectively (Thibodeaux and Mackay, 2010).

The calculation of the gas and liquid phase velocities is crucial in the 1D model as they impact the gas holdup. In uniform gas injection system, the hydrodynamics description in the 1D model is more straightforward. The bubble column operated in batch mode ($u_L = 0$), therefore, the bubbles ascend in a uniform manner and the bubbly flow can be modeled using the bubble terminal velocity, u_{rel}, as shown in equation (6.9). The drag coefficient C_D for contaminated system proposed by Tomiyama et al. (1998) was applied, as expressed in equation (6.10).

$$u_{rel} = \sqrt{\frac{4}{3}.\frac{g.(\rho_L - \rho_G).d_b}{\rho_L . C_D}} \tag{6.9}$$

$$C_D = \max\left\{\frac{24}{Re}(1 + 0.15 \cdot Re^{0.687}), \frac{8}{3}\frac{Eo}{(4 + Eo)}\right\}$$
$$Re = \frac{u_{rel}.d_b}{\nu_L} \qquad Eo = \frac{(\rho_L - \rho_G).g.d_b}{\sigma} \tag{6.10}$$

g is the acceleration due to gravity (9.81 m².s^{-1}), ρ_L and ρ_G are the liquid and gas density, respectively, Re is the Reynolds number and Eo is the Eötvös number. The viscosity and density of water were corrected to 328.15 K, whilst the surface tension of water at 293.15 K was applied which yields ρ_L = 985 kg.m^{-3}, μ_L = 5.10^{-4} Pa.s, and σ = 0.072 N.m^{-1}.

In the non-uniform gas injection system, a non-uniform hydrodynamics profile was observed due to complex gas and liquid circulation flow. Therefore, the bubble velocity was modeled using the drift-flux

approach, expressed as

$$u_G = C_0 . < j > + u_{rel} \quad (6.11)$$

The distribution coefficient C_0 describes the non-uniform flow profile and it is calculated from its definition $C_0 = \frac{<\varepsilon_G \cdot j>}{<\varepsilon_G> \cdot <j>}$ (Zuber and Findlay, 1965). $< j >$ is the averaged mixture volumetric flux which is the sum of the superficial gas and liquid velocities $<j_G + j_L>$. The liquid circulation velocity, u_c, was considered as j_L. Information on C_0 and u_c were obtained from the resolved 3D CFD simulation, as in Cockx et al. (1997) and Talvy et al. (2007). Further discussions on the hydrodynamics are reported in Section 6.1.3.2 and Table 6.3.

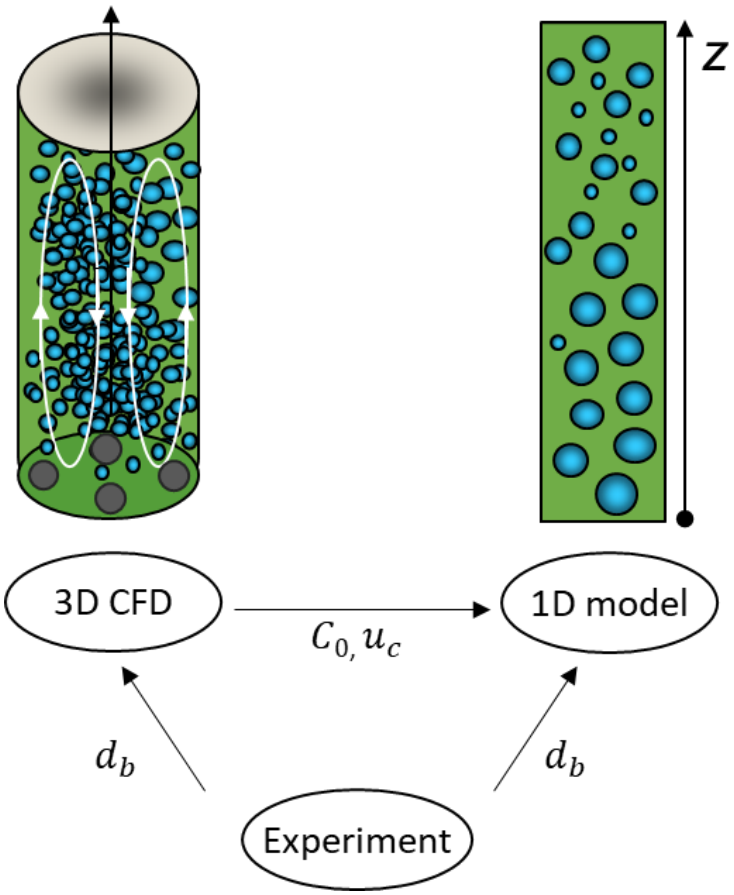

Figure 6.3: Workflow to predict bioreactor performances using 1D model coupled with CFD model.

In short, the detailed spatially resolved CFD model provides the fluid flow pattern in terms of simplified hydrodynamics parameters (C_0, u_c) to the 1D model, as depicted in Figure 6.3. This multiscale modeling approach is similar to the workflow proposed by Bauer and Eigenberger (1999) and Cockx et al. (1997) for bubble columns and loop reactors. This approach is useful when non-homogeneities in the flow are generated by the non-uniform gas sparger.

The calculation of the reaction rates, R_i, follows the previous work of Ngu et al. (2022a) and is briefly presented here. It is based on the magnitude of the hydrogen uptake rate, φ_{H_2} and the set of intracellular reactions describing the conversion of H_2 and CO_2 into CH_4 proposed by Schill et al. (1996):

$$H_2 + \nu_{CO_2,1} CO_2 + \nu_{NH_3,1} NH_3 \underset{r_1}{\rightarrow} \nu_{X,1}\, X + \nu_{CH_4,1} CH_4 + \nu_{H_2O,1} H_2O \tag{6.12}$$

$$H_2 + \nu_{CO_2,2} CO_2 \underset{r_2}{\rightarrow} \nu_{CH_4,2} CH_4 + \nu_{H_2O,2} H_2O \tag{6.13}$$

$$X \underset{r_3}{\rightarrow} \emptyset \tag{6.14}$$

The metabolic flux-based model is based on the computation of the reaction rate vector $\boldsymbol{r} = \{r_1, r_2, r_3\}$ in $g_{H_2}.L^{-1}.h^{-1}$. r_1, r_2, and r_3 signify growth, maintenance and death mechanisms, respectively, experienced by the biomass at different stage of its lifecycle, depending on the local availability of the substrates. The hydrogen uptake is used for growth and maintenance activity, such that $r_1 + r_2 = \varphi_{H_2}.X$. The priority is given to the specific maintenance rate, m, consequently two scenarios can be identified (i) $\varphi_{H_2} > m$ and (ii) $\varphi_{H_2} < m$. For the first case, the maintenance requirement is reached and therefore growth is ensured, and death is negligible, thus, $r = \{\varphi_{H_2} - m, m, 0\} \cdot X$. Otherwise, in the second case, growth halts as the hydrogen supply is insufficient for maintenance. The maintenance rate is now defined by φ_{H_2} and the cell death rate is proportional to the energy lacking for maintenance, thus, $r = \{0, \varphi_{H_2}, m - \varphi_{H_2}\} \cdot X$.

The calculation of the hydrogen specific uptake rate φ_{H_2} is presented in equation (6.15). It uses a standard approach in multiphase reactor modeling, which is to define the actual consumption rate as the smallest (limiting) rate between the biological uptake rate and the external physical transport rate (Ngu et al., 2022a; Pigou and Morchain, 2015).

$$\varphi_{H_2} = min\{\varphi_{bio}, \varphi_{phy}\} \tag{6.15}$$

The biological uptake capacity is calculated from the Monod model, involving the maximum specific hydrogen uptake capacity $q_{H_2}^{max}$, the saturation constant K_{H_2}, and the liquid phase hydrogen concentration C_{L,H_2}:

$$\varphi_{bio} = q_{H_2}^{max}.\frac{C_{L,H_2}}{K_{H_2} + C_{L,H_2}} \tag{6.16}$$

The physical transport rate involves two phenomena in parallel: the gas-liquid mass transfer rate and

the micromixing rate at the cell scale. The specific substrate flux supplied to the cell is thus calculated as the larger of the two rates:

$$\varphi_{phy} = \max\left(\frac{k_L a.\left(C^*_{L,H_2} - C_{L,H_2}\right)}{\varepsilon_L.X}, \frac{C_{L,H_2}}{X.\tau_m}\right) \tag{6.17}$$

This formulation provides a physically consistent and numerically stable way to handle the situation when the biological methanation is limited by H_2 mass transfer whereby the dissolved H_2 concentration approaches zero.

The reaction terms for each species R_i in equation (6.3) is summarized in equations (6.18)-(6.21):

$$R_{H_2} = (r_1 + r_2) = \varphi_{H_2} X \tag{6.18}$$

$$R_{CO_2} = \left(Y_{CO_2/H_2} r_1 + Y^m_{CO_2/H_2} r_2\right) \tag{6.19}$$

$$R_{CH_4} = \left(Y_{CH_4/H_2} r_1 + Y^m_{CH_4/H_2} r_2\right) \tag{6.20}$$

$$R_X = Y_{X/H_2}(r_1 - r_3) \tag{6.21}$$

with $Y_{i/j}$ being the yield coefficient in grams of i per gram of j consumed. The values for the biological methanation kinetic rates and yield coefficient are reported in Ngu et al. (2022a) and the same values are applied in this work.

6.1.2.3 CFD Eulerian model setup for multispecies bubbly flow

3D CFD simulations were performed using the commercial CFD code ANSYS Fluent® version 2021R1. The simulations were based on the Euler-Euler two fluid model, that solves the Reynolds-Averaged Navier-Stokes (RANS) equations. Turbulence was modeled using the standard k-ϵ model. Both phases were mixtures to investigate the concentration of each species. The closure relations required to complete the model are summarized in Table 6.1. In this work, the virtual mass and wall lubrication forces were neglected. It has been shown that the virtual mass force has no significant influence in bubble column reactors as the bubbles quickly reach its terminal velocity (Deen et al., 2001; McClure et al., 2014b; Tabib et al., 2008). The wall lubrication force is important for the near wall layer only if significant number of bubbles lie inside the boundary layer, as in the case for nucleate boiling, and thus it is also neglected here.

Table 6.1: Summary of interfacial force correlations used in the CFD model.

Force	Correlation
Drag	(Tomiyama et al., 1998)
Lift	(Tomiyama et al., 2002b)
Turbulent dispersion	(Simonin and Viollet, 1990)

The liquid phase was water with the density and surface tension described in Section 6.1.2.2. For the CFD model, the gas recycling was simulated by a pseudo-steady state, with a total gas flow (Q_{tot}) defined as the sum of inlet gas flowrate ($Q_{G,in}$) and gas recirculation flow rate (Q_r). The composition of the gas at the inlet was determined using the 1D model. For example, Q_{tot} for the reference case corresponds to 2.14 NL/min. The gas phase was considered as an ideal gas with a constant bubble diameter. No bubble coalescence or breakage were considered as the gas holdup was below 1% as previously measured in air-tap water system in Ngu et al. (2022a). Experimentally measured bubble size in air-tap water system serves as an estimate of the inlet bubble diameter for both the 1D and CFD models. For the reference case ($Q_{tot} = 2.14$ NL/min) the inlet bubble diameter for porous plate and 4-points sparger were set and assumed constant as 2 mm and 5 mm, respectively. Using the bubble diameter correlation of Abro et al. (2021) developed for porous sparger yields 1.7 mm for a gas flow of 2.14 NL/min, which corresponds well with the estimated 2 mm used for the porous plate. To elucidate the impact of bubble diameter, a sensitivity analysis on the bubble diameter was also performed and is presented in Section 6.1.5.

For the boundary conditions, all walls were set as no-slip condition for the liquid and free-slip for the gas. Gas entering through the inlet was modeled using a velocity-inlet boundary condition. The total gas flowrate Q_{tot} was set at the inlet, with the velocity magnitude set as the bubble terminal velocity of the imposed bubble diameter calculated using the Tomiyama et al. (1998) drag model. A turbulence intensity of 5% and a turbulent viscosity ratio of 10 were imposed at the inlet. The column outlet was modeled as an opening at zero gauge pressure, with a complete back-flow of gas, followed the suggestion of Nadal-Rey et al. (2022). The inlet composition of the gas phase followed that of 1D model. The inlet species mole fraction ratio of H_2:CO_2:CH_4 were 17.4%:2.5%:80.1% and 49.8%:5.6%:44.6% for the porous plate and 4-points sparger, respectively.

The solution strategy is detailed as follow. The hydrodynamics were first solved with the interphase forces presented in Table 6.1. Once the hydrodynamics converged, the species transport equations were then solved, determining the transport of gaseous species throughout the column. Lastly, all equations were solved simultaneously to capture the coupling between hydrodynamics, mass transfer

and bioreaction. Species transport equations were also solved to couple mass transfer and bioreaction with the bubbly flow. Given the short simulation time, the growth of biomass is negligible, thus the biomass concentration was not solved but was fixed set at 0.1 kg.m^{-3}. User-defined functions (UDFs) were developed to describe $k_{L,i}$ and R_i as expressed in equations (6.8) and (6.18).

The Phase Coupled SIMPLE scheme was used for pressure-velocity coupling. The first-order implicit temporal discretization scheme was used. For the spatial discretization schemes, QUICK was used for density and volume fraction, the first-order upwind scheme was used for the turbulence variables, and the second-order upwind scheme was used for the momentum and species transport equations. The scaled residual targets were set to 10^{-5} and a time step of 0.001 s with a maximum of 10 iterations per step were employed. Hydrodynamic simulations were run for a time of 20 s. An extra 10 s were run for the species transport equations. After all species in the gaseous phase are transported, the mass transfer together with bioreaction simulation were run for 20 s. The global mass balances for the gas phase were also assessed.

For the porous plate, direct comparison with the experimental data was carried out without performing CFD simulations in advance. For the 4-points sparger, CFD simulation was performed beforehand to obtain the fluid flow pattern and this information (C_0 and u_c) was then fed into the 1D model. The hydrodynamics was studied first and subsequently the bioreactor performance was compared with that of the 1D model. The goal was to compare the bioreactor performances ($y_{CH_4,out}$ and MPR) obtained from the two models with the experimental data from Rafrafi et al. (2019).

6.1.3 Results and Discussions

The hydrodynamic behavior of the two spargers is first evaluated using both the 1D and CFD models and the results of both models are then compared in terms of global gas holdup. To rectify the drawback of the 1D model in the hydrodynamic description of 4-points sparger, information from the CFD model is extracted and fed into the 1D model, as discussed in Section 6.1.2.2

6.1.3.1 Mesh convergence

For the porous plate, a swept mesh is used throughout the geometry. For the 4-points sparger, high gradients are expected near the inlet due to non-uniform gas injection. From the gas inlet up to a height of 3-column diameter, the poly-hexcore mesh is more refined, with a polyhedral transition layer between the two jet formation zones. After the 3-column diameter height, a coarser mesh is employed in the column center with polyhedral elements near the wall.

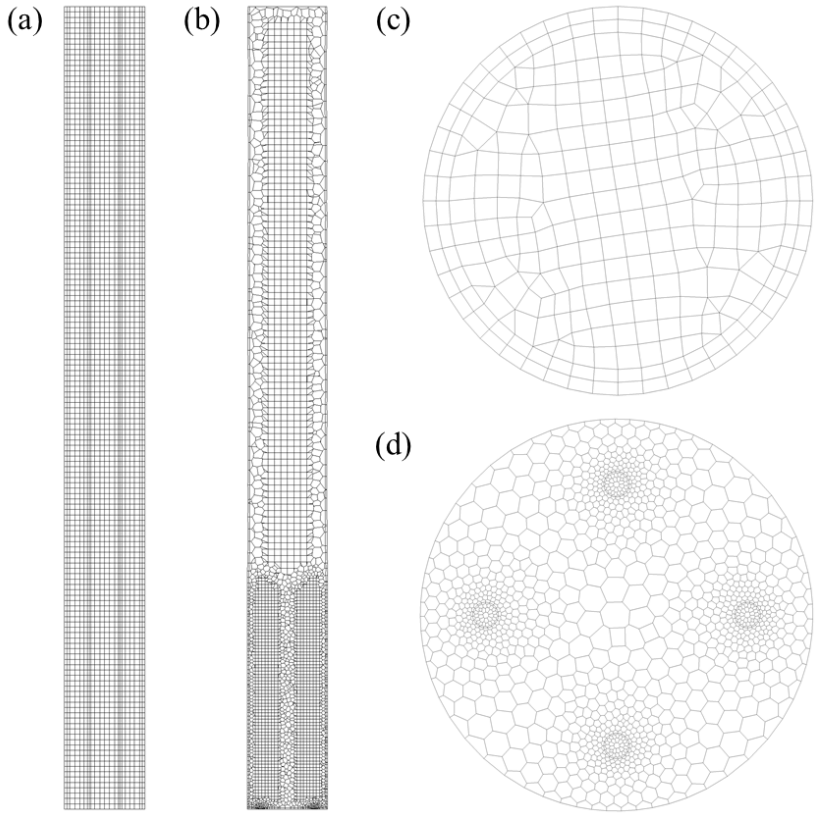

Figure 6.4: Axial and radial section of the coarse mesh. (a and c) porous plate (b and d) 4-points sparger.

Table 6.2 shows that the difference in gas holdup between the coarse and fine mesh for both spargers is relatively small. In both cases, a very low gas holdup (< 1%) was obtained as the superficial gas velocity is low. The two-phase bubbly flow generated by the porous plate is expected to be uniform with no significant gradients. It is not surprising to obtain very close gas holdups for the two meshes. To optimise the computational time, the coarse mesh for both spargers, as presented in Figure 6.4, was used in this work.

Table 6.2: Impact of grid size on the gas holdup for both spargers with the same superficial gas velocity of 0.136 cm.s^{-1}.

	Porous plate ($d_b = 2$ mm, $u_G = 0.29$ m.s^{-1})		4-points sparger ($d_b = 5$ mm, $u_G = 0.24$ m.s^{-1})	
	Coarse mesh	Fine mesh	Coarse mesh	Fine mesh
Number of elements	44,700	494,000	46,500	561,000
Typical element size (mm)	8	4	8	4
Gas holdup (%)	0.547	0.546	0.580	0.575

6.1.3.2 Extracting hydrodynamics parameters from the CFD model

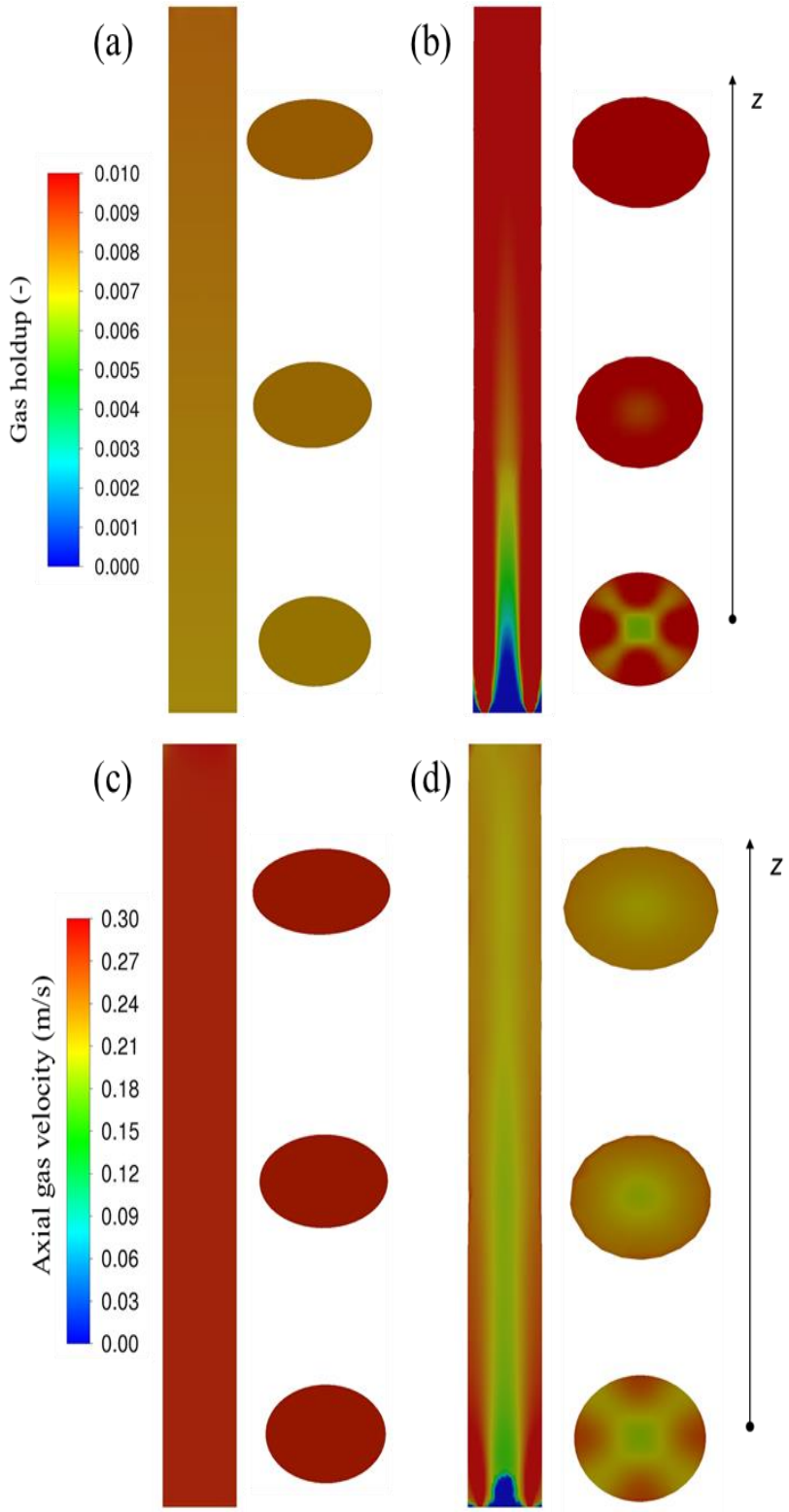

Figure 6.5: Contours of the gas hold-up (a and b) and axial gas velocity component (c and d) in a vertical plane passing through center and three cross sections (z/H = 0.25, 0.5, and 0.75) for the reference case. (a) and (c) porous plate, (b) and (d) 4-points sparger.

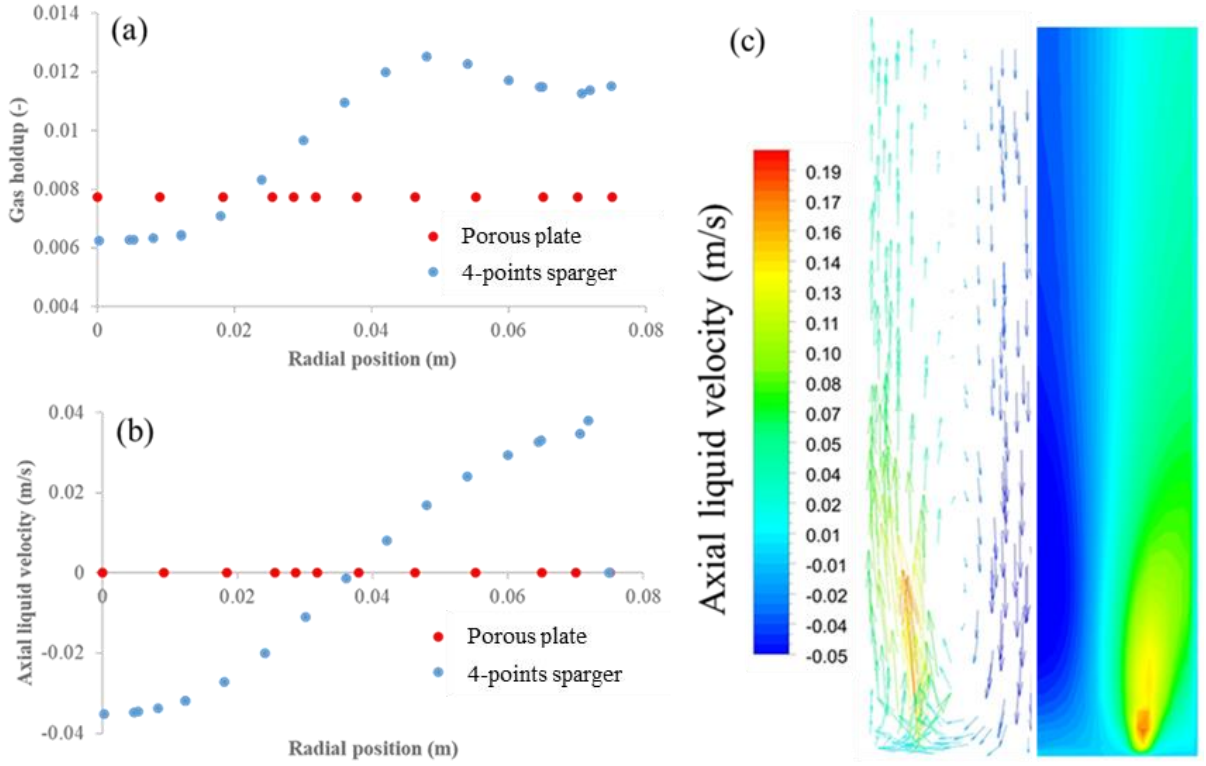

Figure 6.6: Radial profile of (a) gas holdup and (b) axial liquid velocity for the reference case at z/H = 0.25. (c) Axial liquid velocity component contour with the velocity vector profile from the bottom up to z/H = 0.25 for 4-points sparger. (The number of arrows does not correspond with the mesh density.)

Figure 6.5 depicts the gas holdup and gas velocity contour profiles obtained from CFD model for both spargers. Figure 6.5(a) and (c) show that the bubbly flow using the porous plate is rather uniform radially, which is a typical characteristic of homogeneous flow regime at this low superficial gas velocity. A slight increase of 8% in the gas holdup is observed from the inlet to the free surface, due to a decrease of pressure in the axial direction, in line with the ideal gas law. Figure 6.5(b) and (d) reveal the complex local flow structure created by the 4-points sparger. It is found that the 4-points sparger creates strong jets, which gives rise to high radial gradients at the bottom of the column which gradually homogenize at the top of the column.

Figure 6.6(a) shows that the radial profile of gas holdup for the porous plate is rather flat at the bottom of the column ($z/H = 0.25$). The liquid velocity is almost zero for the porous plate case, signifying a very weak liquid recirculation effect, as shown in Figure 6.6(b). At the same zone, the 4-points sparger case shows a non-uniform gas holdup profile. For the 4-points sparger case, higher gas holdup is located away from the center, as the local gas injection is located near the wall. This effect diminishes with

height, where a developed flow region occurs (see cross section contours in Figure 6.5(b) and (d)). The liquid is dragged upwards by the bubbles near the wall and recirculates downwards in the centre, as shown by the axial liquid velocity profile (Figure 6.6(b)). Figure 6.6(c) shows the large-scale recirculation structures due to non-uniformities in the aeration is captured by the CFD model near the inlet, which is also observed experimentally by Harteveld et al. (2003). The authors observed a static recirculation cell near the bottom of the column when the gas distributor was located at the wall, similar to the 4-points sparger whereby the bubbles are introduced near the wall.

Table 6.3 presents the overall hydrodynamics results. Under complex hydrodynamics conditions with large-scale coherent structures encountered in the 4-points sparger case, an axial hydrodynamics description is not sufficient. To tackle this issue, fluid flow information from the CFD model is provided to the 1D model in terms of simplified hydrodynamics (C_0 and u_c) as described in the workflow in Figure 6.3. The drift-flux coefficient C_0 is estimated from the local hydrodynamics profile using its definition (Zuber and Findlay, 1965). The liquid circulation velocity u_c is also computed from CFD spatially-averaged upward liquid velocity data. It describes the upward flow due to the recirculating liquid motion. As the gas holdup is low, u_c can be considered to be the superficial liquid velocity j_L in the mixture velocity of the drift-flux model <j>. This assumption is reasonable as the gas holdup is very low, the liquid circulation velocity is like j_L. On the contrary, as the velocity profile is flat, C_0 for the porous plate is one from the CFD calculation. The value of u_c is considered to be zero, therefore the bubble velocity is equal to the bubble terminal velocity, as discussed in Section 6.1.2.2.

Overall, the global gas holdup computed from the 1D model closely matches that of CFD model. It shows that for the same inlet gas flow rate, the 4-points sparger yields a slightly higher gas holdup compared with the porous plate. In contaminated system, the bubbles rise with a velocity of 0.24 $\pm$ 0.01 m.s^{-1} over a wide range of bubble sizes, leading to very close gas holdup between the two spargers. However, the interfacial area for mass transfer is higher for homogeneous sparger due to smaller bubble size. Table 6.3 reports that the interfacial area for the porous plate is almost double that for the 4-points sparger. It is found that the sparger design has a more profound effect to the interfacial area than the gas holdup at such low superficial gas velocity ($j_G \sim mm.s^{-1}$).

Table 6.3: Hydrodynamics results ($Q_{tot} = 2.14$ NL/min) for 1D and CFD model.

Sparger type	Numerical model	C_0	u_c	ε_G (%)	a (m^{-1})
Porous plate	CFD	-	-	0.80	24.0
	1D	1	0	0.82	24.6
4-points sparger	CFD	-	-	0.98	11.7
	1D	1.4	0.013	0.94	11.1

6.1.3.3 Comparison of 1D and CFD model predictions with experimental data

With the hydrodynamics resolved for both 1D and CFD models, the mass transfer and bioreaction are activated to compare with the biological methanation experimental data.

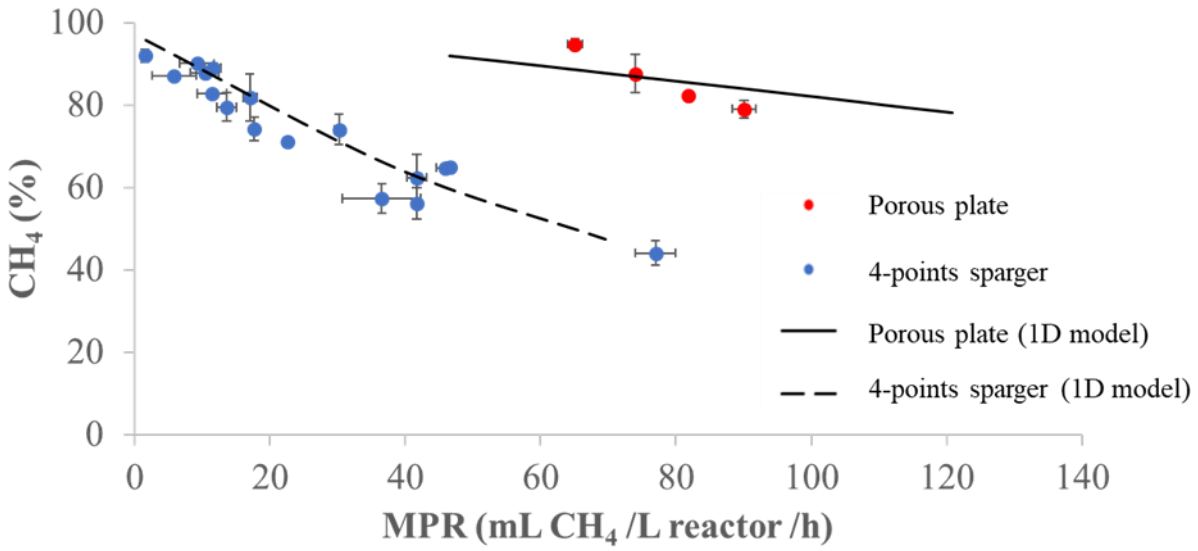

Figure 6.7: Numerical prediction of both sparger performances compared with experimental data. Symbols: Experimental data from Rafrafi et al. (2019), Solid line: 1D model with $d_b = 2$ mm, Dashed line: 1D model with d_b fitted according to the inlet gas flowrate.

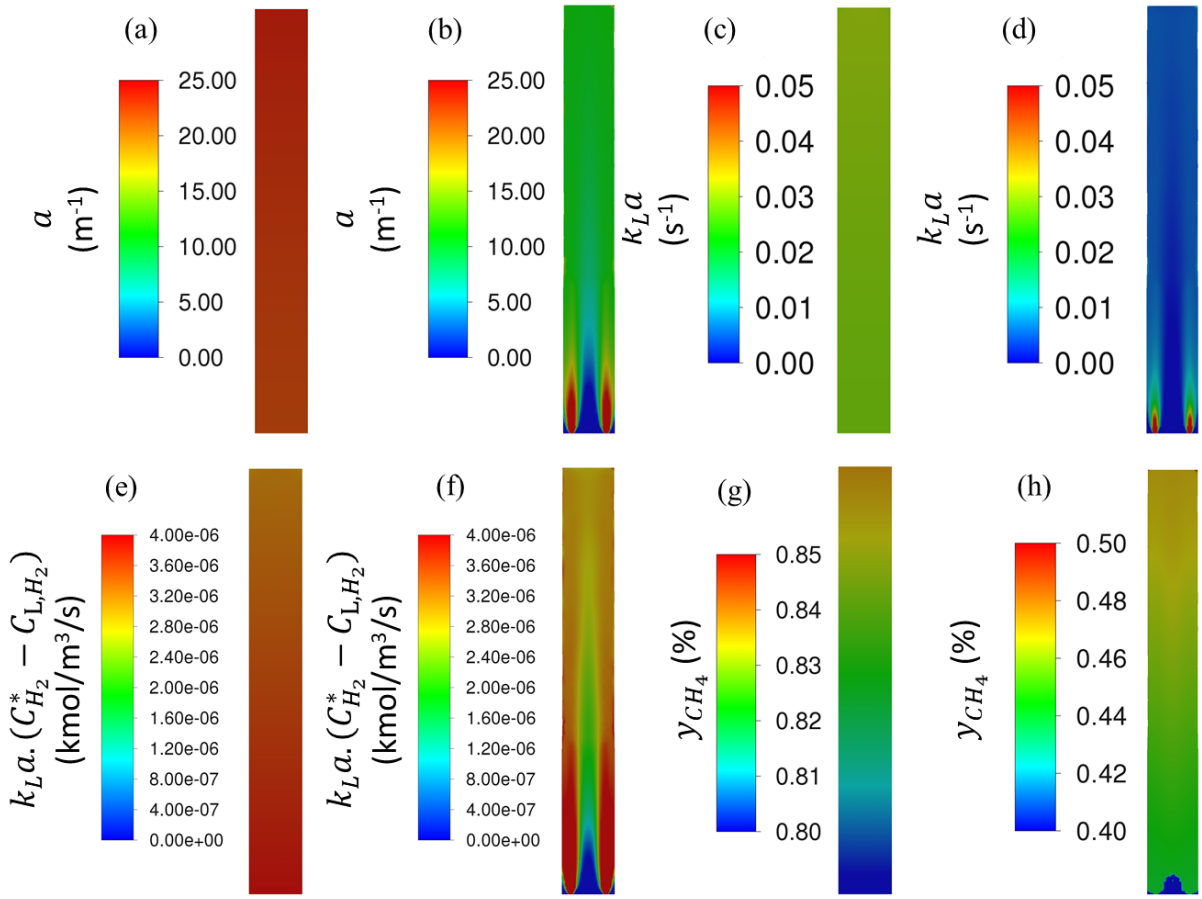

Figure 6.8: Contours of interfacial area (a and b), k_La (c and d), steady-state H_2 mass transfer flux (e and f) and methane fraction (g and h) in a vertical plane passing through the center. (a), (c), (e), and (g) porous plate, (b), (d), (f) and (h) 4-points sparger.

Figure 6.7 displays the experimental and 1D model results in terms of outlet methane purity versus methane production rate (MPR). A similar trend is observed in both spargers – lower inlet gas flowrate leads to higher CH_4 purity but with lower productivity. It also shows that the experimental results shift to the left, signifying that a yield loss is observed when the 4-points sparger is used. To achieve a certain CH_4 purity (y-axis isoline), the productivity is always lower when the 4-points sparger is used instead of the porous plate. The 1D model of the 4-points sparger case (dashed line) agrees relatively well with the experimental results, provided the inlet bubble diameter corresponds to the inlet gas flowrates. The inlet bubble diameter used varies between 3 to 5 mm in the range of experimentally imposed $Q_{G,in}$. Meanwhile, the 1D model for the porous plate results (continuous line) are obtained by setting a 2 mm inlet bubble diameter, regardless of the gas flowrate. The influence of inlet bubble diameter is discussed in Section 6.1.5.

Table 6.5 and Table 6.6 summarize the overall comparison between experimental results and numerical simulations. For the same inlet gas flowrate ($Q_{G,in} = 0.14$ NL/min), use of the porous plate produces

more methane (90 mL/L/h versus 77 mL/L/h experimentally) at a higher purity (80 % versus 44 % experimentally) compared with use of the 4-points sparger. For the same inlet gas flowrate, the bubble diameter for the 4-points sparger is always larger than that from the porous plate (see Figure 6.2). Despite having a higher gas holdup for the 4-points sparger, a larger bubble size leads to a lower interfacial area, as shown in Figure 6.8(a) and (b). These larger bubbles generated by the 4-points sparger could be primarily due to bubble coalescence at the inlet due to much higher local gas holdup as the injection area is 56 times lower, and marginally due to the presence of a liquid recirculation cell. Consequently, low interfacial area hinders the mass transfer efficiency, leading to a lower $k_L a$ (Figure 6.8 (c) and (d)). The spatial-averaged $k_L a$ for the porous plate case yields 113 h^{-1}, as opposed to 31 h^{-1} for the 4-points sparger case, showing an increase of 265 % in $k_L a$ by just switching the gas distributor from a non-uniform to uniform system. Figure 6.8(e) and (f) show that the H_2 mass transfer flux is uniform and globally higher in the porous plate case than in the 4-points sparger case. A slight decrease of H_2 mass transfer flux from the inlet to the outlet is observed due to decreasing C^*, and thus a lower driving force occurs at the top of the column. It is reported that a finer and uniform sparger is beneficial to mass transfer performance, in particular reactions which are mass transfer limited (Möller et al., 2017). Small openings and a large number of openings for the sparger have been found to promote higher interfacial area for mass transfer (Han and Al-Dahhan, 2007; Luo et al., 2011; Wongwailikhit et al., 2018).

At steady-state, the volume-averaged H_2 mass transfer flux for the porous plate case yields 7.83×10^{-5} mol/s compared with 6.42×10^{-5} mol/s for the 4-points sparger case. These low H_2 mass transfer fluxes are reflected in the CH_4 mole fraction profile (see Figure 6.8(g) and (h)) whereby the upgrade of biomethane is low (roughly 80% to 85% and 45% to 48% for the porous plate and 4-points sparger, respectively), signifying that a steady-state is reached. During this stage, the bubble diameter changes insignificantly, i.e. from 2 to 2.05 mm and from 5 to 5.1 mm for the porous plate and the 4-points sparger, respectively, as predicted by the 1D model. This justifies the assumption of constant bubble diameter used in the CFD simulations. At the steady-state, the bioreaction is limited by the H_2 physical supply (Ngu et al., 2022a), therefore, the description of $k_L a$ and C^* is important to capture the mass transfer flux that determines the bioreaction rate (Schill et al., 1996). An improvement in the sparger design that promotes smaller bubble size would lead to better mass transfer and a more efficient biomethane upgrading. The present 1D and CFD models obtained satisfactory results compared with the experimental data, signifying that the coupling of bubbly flow, interfacial mass transfer and bioreaction kinetics are correctly implemented.

6.1.4 Analytical solution of steady-state bioreactor performances

To elucidate the effect of different physical parameters involved in the bubble column on the biological efficiency, an analytical solution based on a global mass balance is derived here.

6.1.4.1 Calculation of methane purity ($y_{CH_4,out}$)

At steady-state, the flux-based metabolic formulation combined with the limiting flux approach imposes that the hydrogen supply is used entirely for maintenance activity, leading to $\boldsymbol{r}^{-} = \{0, \overline{\varphi}_{\mathrm{H_2}}, 0\}$, with $\overline{\varphi}_{\mathrm{H_2}} = \frac{k_L a.C^*_{L,H_2}}{\varepsilon_L.X}$ (Ngu et al., 2022a). Then, the outlet methane purity $y_{CH_4,out}$ can be derived from the mass balance of the gaseous phase. Due to the limitation of bioreaction by the H_2 mass transfer at steady-state, the local CO_2 transfer is stoichiometrically controlled by the bioreaction: with every 4 moles of H_2 transferred, 1 mole of CO_2 is transferred as well, and 1 mole of CH_4 is produced. The molar flux of each species is expressed as a function of the hydrogen conversion, η, as shown in Table 6.4.

$$4\mathrm{H_2} + \mathrm{CO_2} \rightarrow \mathrm{CH_4} + 2\mathrm{H_2O} \tag{6.22}$$

Table 6.4: Gas-side mass balance. Here $F_{i,in}$ is the molar flux of each species i in the fresh feed (before mixing with the recycling stream, see Figure 6.9a).

Species, i	H_2	CO_2	CH_4
Inlet molar flux, $F_{i,in}$ (mol/s)	$F_{H_2,in}$	$F_{CO_2,in}$	$F_{CH_4,in}$
Outlet molar flux $F_{i,out}$ (mol/s)	$F_{H_2,in} - \eta F_{H_2,in}$ $F_{H_2,in}(1-\eta)$	$F_{CO_2,in} - \frac{\eta F_{H_2,in}}{4}$ $F_{H_2,in}\left(\frac{y_{CO_2,in}}{y_{H_2,in}} - \frac{\eta}{4}\right)$	$F_{CH_4,in} + \frac{\eta F_{H_2,in}}{4}$ $F_{H_2,in}\left(\frac{y_{CH_4,in}}{y_{H_2,in}} + \frac{\eta}{4}\right)$

η the H_2 conversion is defined as

$$\eta = \frac{F_{H_2,in} - F_{H_2,out}}{F_{H_2,in}} = \frac{T_{H_2}}{F_{H_2,in}} \qquad \eta \in [0;1] \tag{6.23}$$

T_{H_2} is the overall hydrogen transfer flux in mol/s. The outlet methane purity $y_{CH_4,out}$ on a dry basis can therefore be written as:

$$y_{CH_4,out} = \frac{F_{CH_4,out}}{F_{H_2,out} + F_{CO_2,out} + F_{CH_4,out}} \tag{6.24}$$

Substituting the outlet molar flux of each species from Table 6.4 into equation (6.24) yields:

$$y_{CH_4,out} = \frac{\frac{y_{CH_4,in}}{y_{H_2,in}} + \frac{\eta}{4}}{(1-\eta) + \frac{y_{CO_2,in}}{y_{H_2,in}} + \frac{y_{CH_4,in}}{y_{H_2,in}}} \tag{6.25}$$

Equation (6.25) is the general form for $y_{CH_4,out}$ prediction. In case of an inlet injection of H_2:CO_2:CH_4 ratio of 4:1:0, equation (6.25) is simplified to:

$$y_{CH_4,out} = \frac{\eta}{5-4\eta} \tag{6.26}$$

6.1.4.2 Calculation of the methane productivity (MPR)

The productivity of methane is calculated using equation (6.1). The outlet gas flowrate $Q_{G,out}$ must be calculated based on the mass balance from the inlet gas molar flowrate and the mass transfer fluxes. First, the outlet gas flowrate can be defined using the ideal gas law as

$$Q_{G,out} = \frac{F_{out} \cdot R \cdot T}{P_{out}} \tag{6.27}$$

with F_{out} being the outlet molar flowrate in mol/s, R the ideal gas constant (8.3145 J/mol/K), T the temperature in K and P_{out} the outlet pressure in Pa. The outlet molar flowrate F_{out} can be calculated from the global mass balance as inlet molar flux F_{in} $\pm$ the mass transfer flux T_i. At steady-state, the CO_2 and CH_4 mass transfer are conditioned by the stoichiometry of the bioreaction, as stated in equation (6.22). Consequently, the CO_2 and CH_4 mass transfer cancel out each other, the outlet molar flowrate is written with equation (6.23) as

$$F_{out} = F_{in} - T_{H_2} = F_{in} - \eta F_{H_2,in} \tag{6.28}$$

The inlet molar flux can be defined in terms of H_2 molar flux $F_{H_2,in}$ as

$$F_{in} = F_{H_2,in}\left(1 + \frac{y_{CO_2,in}}{y_{H_2,in}} + \frac{y_{CH_4,in}}{y_{H_2,in}}\right) \tag{6.29}$$

Substituting equations (6.28) and (6.29) into (6.27), the outlet gas flowrate can be expressed as

$$Q_{G,out} = \frac{F_{H_2,in}\left(1 + \frac{y_{CO_2,in}}{y_{H_2,in}} + \frac{y_{CH_4,in}}{y_{H_2,in}} - \eta\right) \cdot R \cdot T}{P_{out}} \tag{6.30}$$

For an inlet H_2:CO_2:CH_4 ratio of 4:1:0, and assuming a weak pressure effect for a small-scale column

($P_{out} = P_{in}$), the methane production rate MPR can be obtained by substituting equations (6.26) and (6.30) into (6.1), which yields equation (6.31).

$$MPR = \frac{1}{V} \cdot \frac{\eta}{5 - 4\eta} \cdot \left(\frac{5}{4} - \eta\right) \cdot Q_{H_2,in} = \frac{1}{V} \cdot \frac{\eta}{4} \cdot Q_{H_2,in} \tag{6.31}$$

with $Q_{H_2,in} = \frac{F_{H_2,in} \cdot R \cdot T}{P_{out}}$. Considering the extreme case for equations (6.26) and (6.31), whereby the ideal situation of total consumption of H_2 supply in the bioreactor ($\eta = 1$), is accompanied by total consumption of CO_2 stoichiometrically, $y_{CH_4,out}$ of 100% will be obtained at a production rate of 25% $Q_{H_2,in}$.

Figure 6.9(b) shows that outlet methane purity $\frac{\eta}{5-4\eta}$ (blue points) increases non-linearly with η but $\frac{5}{4} - \eta$ (red points) decreases linearly with η. However, the product of the two terms, which is proportional to the methane production rate (black points) increases linearly with $\frac{\eta}{4}$. This shows that the bioreactor performances are strongly linked to the H_2 conversion rate η. The higher the H_2 mass transfer efficiency, the higher the H_2 conversion, the higher the CH_4 purity and productivity.

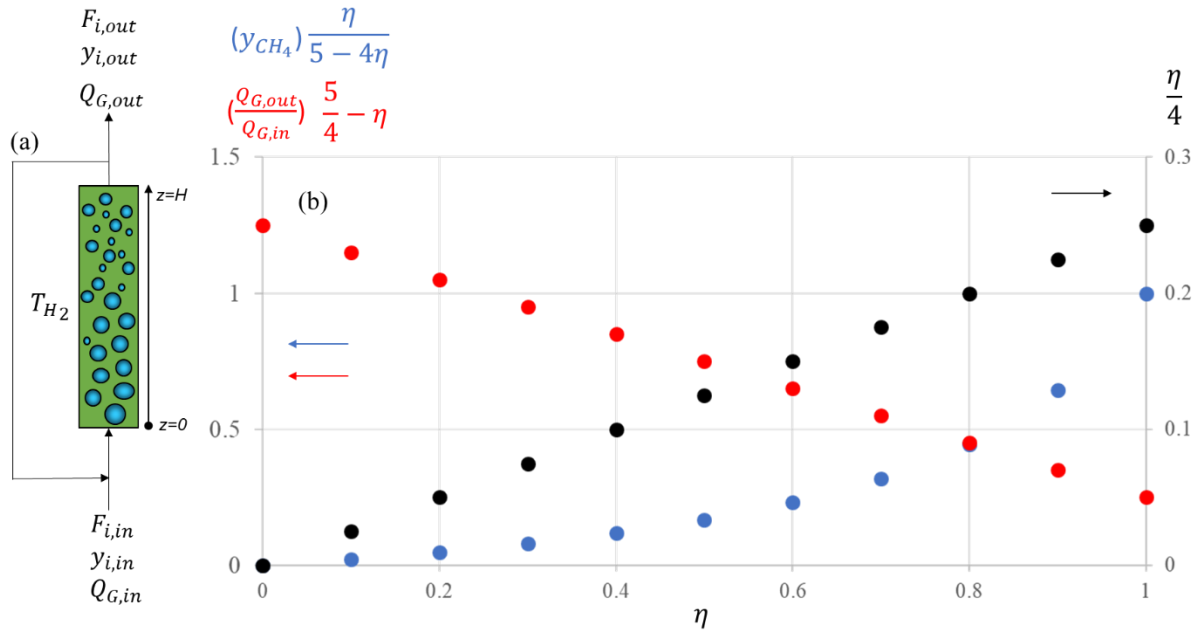

Figure 6.9: (a) Schematic representation of recycling reactor (b) Effect of η on methane purity and productivity.

From equations (6.26) and (6.31), it is clear that $y_{CH_4,out}$ and MPR are a function of η, which depends on the H_2 mass transfer efficiency. The overall H_2 mass transfer flux T_{H_2} throughout the column is expressed as the volume integral of the overall mass transfer rate, or in the case of 1D model, the axial

integration:

$$T_{H_2} = S.\int_0^z k_L a.\left(C^*_{H_2} - C_{L,H_2}\right).dz \tag{6.32}$$

with S being the cross-sectional area in m², $k_L a$ in s^{-1} and $C^*_{H_2}$ in mol/m³. Equation (6.32)(6.32) can be further simplified for a small-scale column (H < 1 m) where there are no non-linearities of the hydrodynamic variables in the axial direction. At steady-state, the dissolved hydrogen is depleted, thus, C_{L,H_2} = 0. $C^*_{H_2}$ can be calculated as $H^{cc}C_{G,H_2}$, with $H^{cc} = He_{H_2}RT$ = 0.018 being the dimensionless Henry solubility for T = 328.15K. The overall transfer flux can be estimated as

$$T_{H_2} = S.\int_0^z k_L a.H^{cc}.C_{G,H_2}dz \tag{6.33}$$

The hydrogen depletion in the gas along the column at steady-state can be described via

$$\frac{du_G\varepsilon_G C_{G,H_2}}{dz} = -k_L.a.C^*_{H_2} = -k_L\frac{6\varepsilon_G}{d_b}H^{cc}C_{G,H_2} \tag{6.34}$$

Assuming that the gas velocity, gas holdup, and bubble diameter are kept constant, the integration of equation (6.34) gives the variation of H_2 mass per unit volume of reactor ($\varepsilon_G C_{G,H_2}$) along z:

$$\varepsilon_G C_{G,H_2} = \varepsilon_{G0}C_{G0,H_2}e^{-\frac{6H^{cc}}{d_b}.\frac{k_L}{u_G}.z} \tag{6.35}$$

with $\varepsilon_{G0}C_{G0,H_2}$ being the inlet mass of H_2 per unit volume of reactor.

Substituting equations (6.7) and (6.35) into equation (6.33) yields

$$\mathrm{T_{H_2}} = S.\int_0^z k_L.\frac{6H^{cc}}{d_b}.\varepsilon_{G0}C_{G0,H_2}e^{-\frac{6H^{cc}}{d_b}.\frac{k_L}{u_G}.z}dz \tag{6.36}$$

The integration of equation (6.36) between 0 and H leads to

$$T_{H_2} = S.u_G.\varepsilon_{G0}.C_{G0,H_2}\left(1 - \exp\left(-\frac{6\cdot H^{cc}}{d_b}\cdot\frac{k_L}{u_G}\cdot H\right)\right) \tag{6.37}$$

The term $u_G.\varepsilon_{G0}.C_{G0,H_2}$ can be translated as the inlet H_2 molar flux and $\exp\left(-\frac{6\cdot H^{cc}}{d_b}\cdot\frac{k_L}{u_G}\cdot H\right)$ as the overall depletion factor throughout the column (Larsson et al., 2022). Equation (6.37) can be used as

an estimate of the global mass transfer flux. This gives access to the calculation of hydrogen conversion through (6.23) and finally the methane purity through (6.26).

Notice that the gas holdup ε_G in the volumetric interfacial area a of equation (6.7) and in C_{G,H_2} of equation (6.35) cancel each other out when equations (6.7) and (6.35) are substituted into equation (6.33). This simplification of ε_G indicates clearly that no positive pressure effect on the mass transfer will be observed in bubble column. At a fixed gas mass flowrate, increasing pressure will lead to higher $C^*_{H_2}$, but the gas compression will result in lower ε_G, and thus lower interfacial area. The positive impact of pressure on $C^*_{H_2}$ is counterbalanced by the drop in interfacial area, as shown in Maalej et al. (2003). Therefore, any attempt to increase mass transfer flux by increasing pressure is fruitless. Nevertheless, high pressure is necessary in industrial-scale bubble columns as it compresses the gas to enable the treatment of higher gas loading and at the same time maintains the bubbly flow in the homogeneous regime, which is beneficial for interfacial mass transfer.

The analytical model aims to shed light on the controlling parameters involved in the biological methanation process. It highlights that the bioreactor performance of biological methanation is heavily dependent on the H_2 mass transfer efficiency (η). For example, the proposed analytical solutions for a given H_2:CO_2 ratio of 4:1 in the gas inlet – equations (6.26) and (6.31) highlights that both CH_4 purity and productivity are related to η, and hence T_{H_2}, which is in line with the conclusion of Schill et al. (1996). The results are not surprising since the process operates in the H_2 mass transfer limitation regime at the stationary state. It shows that the change in k_La and C^* in the axial direction is crucial in modeling biological methanation, as the major substrates are fed to the reactor as a gaseous mixture and this physical supply can be limited by mass transfer due to poor solubility. This explains the importance of interfacial area on the biological methanation efficiency as it is related to k_La (see Figure 6.8) and subsequently to d_b, u_G, and k_L. These hydrodynamic variables were calculated from the steady-state spatial-averaged 1D model results. To assess correctly the overall mass transfer term T_{H_2}, a precise calculation of the spatial integration of $k_La(C^* - C_L)$ is required. In this work, the integration of equation (6.32) has been assessed using the 1D model. Hence, the so-called analytical model should be interpreted as an analytical demonstration that the bioreactor performances are determined by the volume integral of the mass transfer term. If non-linearity exists, the latter has to be evaluated using accurate models, such as 1D and CFD models (Deckwer et al., 1978; Ngu et al., 2022). Otherwise, for short column (H < 1 m), the mass transfer can be evaluated using equation (6.37), by using the conditions set at the inlet for d_b, k_L, and u_G. Here, the value of η is evaluated using two approaches: 1D model or inlet conditions, denoted by η_{1D} or η_0, respectively, as shown in Tables 5 and 6.

Table 6.5 and Table 6.6 report the bioreactor performance predicted by numerical models compared with the experimental data for the homogeneous and heterogeneous spargers, respectively. An increase of 81% in CH_4 purity and of 17% in productivity is obtained experimentally when the homogeneous sparger is used over the heterogenous sparger. For the 1D model, the results are reported with the variation of 0.5 mm on the referenced bubble diameter (2 mm for homogeneous and 5 mm for heterogeneous). For both spargers, all models slightly overpredict the methane fraction. Similarly, the CFD model overpredicts the methane production rate, whilst the 1D model underpredicts it. Overall, both the 1D and CFD models predict relatively well the bioreactor performances as the numerical results are close to the experimental data. A better prediction is achieved for the heterogeneous sparger case when the 1D model is coupled with the CFD model. This provides an efficient way to study bioreactors. Spatially resolved CFD simulations are a more efficient way to provide flow information to simpler model, such as the 1D model (Cockx et al., 1997; Siebler et al., 2020) and the compartment model (Delafosse et al., 2010; Nadal-Rey et al., 2021a; Pigou and Morchain, 2015).

Table 6.5: Comparison of numerical model predictions with experimental data for porous plate with $Q_{G,in} = 0.14$ NL/min.

Method	H_2 (%)	CH_4 (%)	Methane Production Rate (mL/L/h)
Experiment data	10 ± 2	80 ± 2	90 ± 2
CFD model ($d_b = 2$ mm)	14	84	103
1D model ($d_b = 2 \pm 0.5$ mm)	13 ± 5	85 ± 6	83 ± 2
Analytical ($\eta_{1D} = 0.963$ / $\eta_0 = 0.983$)	-	84/92	80/82

Table 6.6: Comparison of numerical model predictions with experimental data for 4-points sparger with $Q_{G,in} = 0.14$ NL/min.

Method	H_2 (%)	CH_4 (%)	Methane Production Rate (mL/L/h)
Experiment data	46 ± 3	44 ± 3	77 ± 3
CFD model ($d_b = 5$ mm)	47	48	78
1D model ($d_b = 5 \pm 0.5$ mm)	48 ± 4	48 ± 5	70 ± 3
Analytical ($\eta_{1D} = 0.808$ / $\eta_0 = 0.82$)	-	46/47	68/69

Upon validation with the experimental data, the analytical predictions were tested with another set of data from the work of Voelklein et al. (2019). The authors conducted similar experiments with the same configuration in a smaller bubble column (total volume of 9.5 L). The dataset of continuous ex-situ with H_2 and CO_2 as injected gases are used for comparison. The η value is given in Voelklein et al. (2019). As the H_2:CO_2 ratio is 4:1, equations (6.26) and (6.31) can be directly used to evaluate the CH_4 purity and productivity.

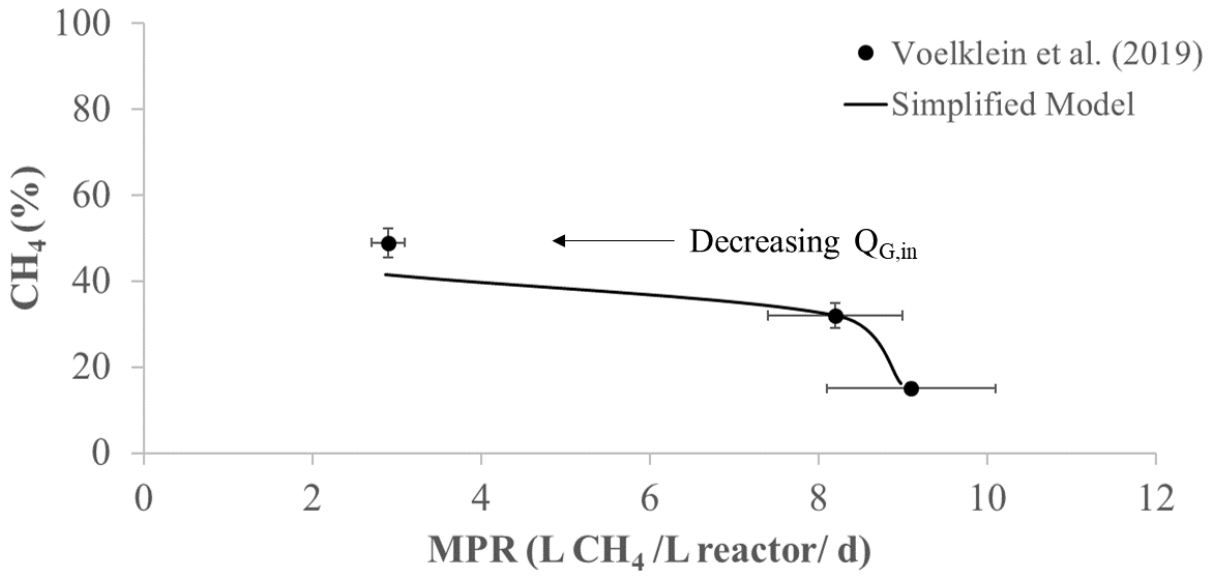

Figure 6.10: Evaluation of biological methanation efficiency calculated using the analytical solution.

Figure 6.10 presents the prediction of bioreactor performances using the analytical solution. The analytical solution agrees well with the experimental data of Voelklein et al. (2019). It also shows that the global mass balance is respected experimentally. Similar observations are drawn – higher H_2 loading leads to higher productivity but less H_2 is converted into CH_4, leading to lower purity. When the bioreaction is limited by H_2 mass transfer, which is the case in steady-state, the biokinetics become

negligible in predicting the biological production of methane, since the controlling parameters are $k_L a$ and C^*, as shown by the analytical solution.

6.1.5 Sensitivity analyses on inlet gas flowrate $Q_{G,in}$, inlet bubble diameter d_b, and gas recirculation flowrate Q_r

With the 1D model validated using the experimental data, sensitivity analyses can be conducted on several operating parameters. The 1D model yields faster computation and satisfactory predictions, thus, it is useful for sensitivity analyses rather than using the computationally-intensive CFD model. The sensitivity analysis was performed for the porous plate case. This sensitivity analysis provides insights into the process phenomena important for optimization of bioreactor design. Here, the influence of inlet gas flowrate, inlet bubble diameter and gas recirculation flowrate are studied.

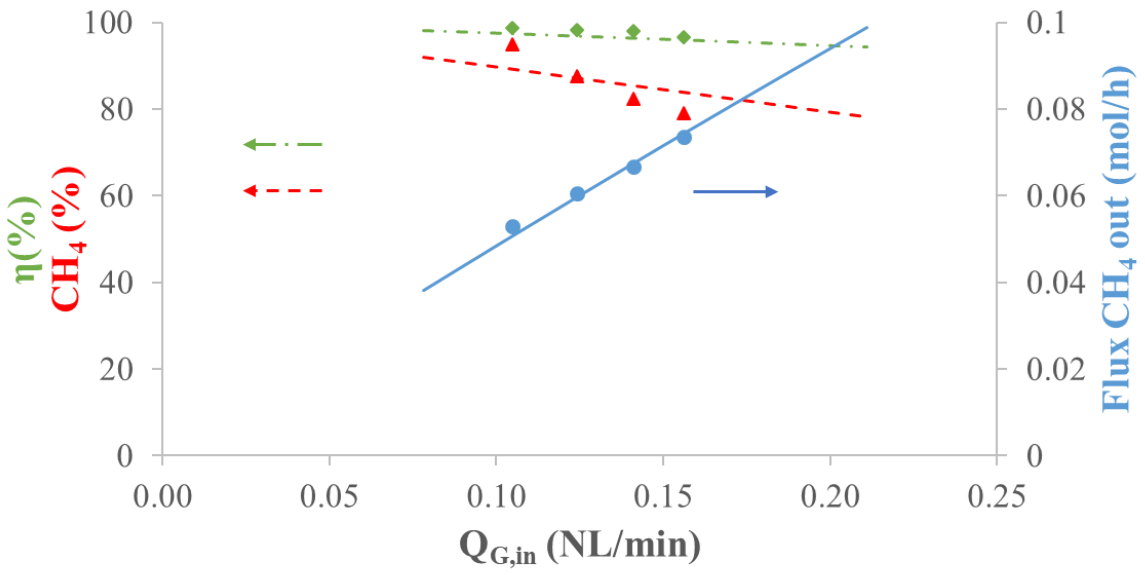

Figure 6.11: Outlet methane purity (▲), H_2 conversion (♦) and methane production (●) as a function of $Q_{G,in}$. Symbols: Experimental data, Lines: 1D model with $d_b = 2$ mm.

Figure 6.11 shows that an increase in $Q_{G,in}$ leads to higher productivity. However, higher methane production does not imply higher methane purity. As shown in Figure 6.11, the lower methane purity is due to a lower H_2 conversion defined in equation (6.23). For the same H_2 molar flux in the fresh stream $F_{H_2,in}$, the higher the $Q_{G,in}$, the lower the mass transfer efficiency, less H_2 is converted to CH_4, thus the CH_4 purity is lower. This effect is also reported by Ghofrani-Isfahani et al. (2021) and Voelklein et al. (2019) where the authors observed an increase in CH_4 productivity is counterbalanced by a decrease in CH_4 purity when the inlet gas flowrate is increased. For the same inlet gas flowrate ($Q_{G,in} = 0.14$ NL/min), the H_2 conversion when using the 4-points sparger and porous plate is 89% and 96%,

respectively. Therefore, higher CH_4 purity and productivity are achieved using the porous plate.

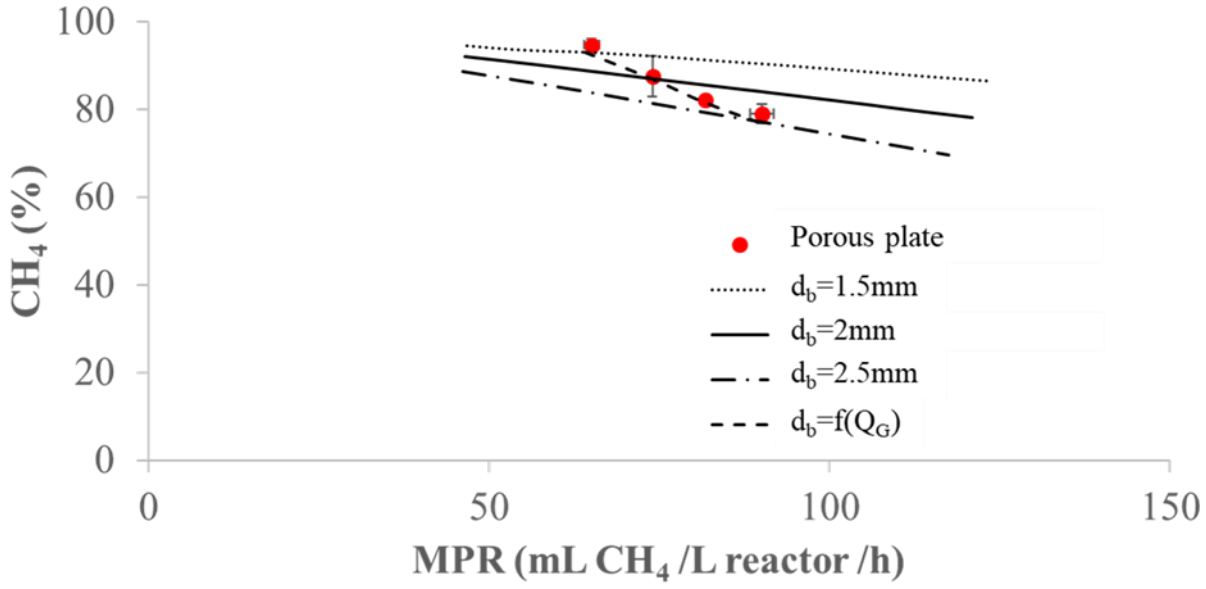

Figure 6.12: Effect of inlet bubble diameter on the reactor performances using 1D model.

Figure 6.12 shows that decreasing inlet bubble diameter leads to an increase in methane purity. Smaller bubbles offer a higher interfacial area for mass transfer, therefore a higher mass transfer efficiency (Merker et al., 2017). As the bubble diameter was not measured under bioreaction conditions, experimental measurement in air-tap water system and a literature correlation were applied to estimate the bubble diameter in real conditions. For the porous plate, the initial bubble diameter of 2 mm is of the same order of magnitude as for previous measurements in tap water using an optical method. Under bioreaction conditions, the bubble diameter size could be reduced due to limited coalescence (Li et al., 2019; McClure et al., 2013). The bioreactor performance is sensitive to bubble diameter, as the bioreaction is limited by the mass transfer phenomenon. Analogous to a heterogeneous reaction catalyst problem, the bioreaction could be limited by the species transport and mass diffusion phenomena. These phenomena arise when the locally available specific substrate flux is insufficient to fulfill the biological demand, typically when the gas flow rate is low or when the biomass concentration is high at the steady-state, as shown in Ngu et al. (2022a). Under such regimes, satisfactory descriptions of convective transport and interfacial mass transfer become crucial. The sensitivity analysis of bubble diameter for $\pm$0.5 mm for the reference case for both spargers was also performed and the results are reported in Table 6.5 and Table 6.6. Figure 6.12 reveals that at higher $Q_{G,in}$, a better fit is obtained by a larger bubble diameter, and vice versa, similar with the observation for the 4-points sparger, as shown in Figure 6.7. The gassing rate dependent inlet bubble size correlation for the porous plate is $\mathrm{d_b} = 0.034\mathrm{Q_{G,in}^{1.4}}$, while for the 4-points sparger is $\mathrm{d_b} = 0.007\mathrm{Q_{G,in}^{0.2}}$, with d_b in

m and $Q_{G,in}$ in NL.min^{-1}. This finding is consistent with the fact that the higher the $Q_{G,in}$, the larger the bubble diameter (Quintero, 2015). Also, from this study, it is observed that sparger design is pivotal for biological methanation as it determines the bubble size and subsequently defines the bioreactor performance.

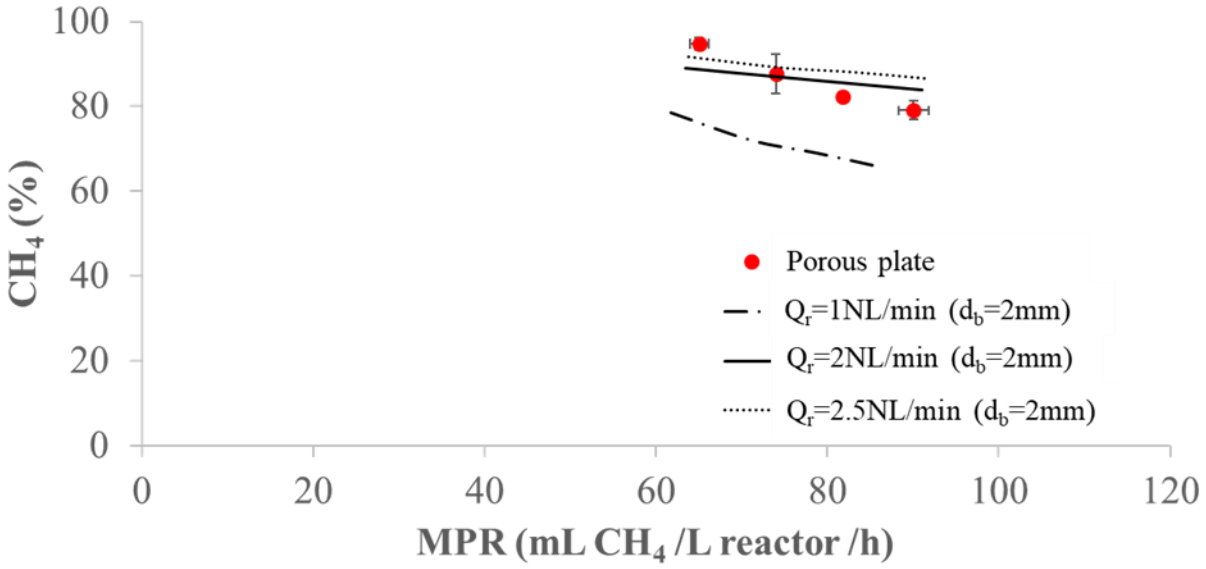

Figure 6.13: Effect of gas recirculation flowrate on the reactor performances using 1D model.

Moreover, Bassani et al. (2016) and Kougias et al. (2017) have shown that increasing the gas recycling rate improves the methane purity. Figure 6.13 shows that the methane purity increases when Q_r increases from 1 NL/min to 2.5 NL/min. For the same inlet H_2 molar flux, increasing the recycling flowrate leads to increasing ε_G, as more gas is present per unit volume of the bubble column. Besides, the gas residence time is also prolonged with gas recycling. In combination with higher gas residence time and gas holdup, this leads to higher $k_L a$, as more specific area is available for mass transfer, resulting in higher mass transfer efficiency, higher H_2 conversion, and thus higher methane purity. Although recycling will dilute the inlet reactive gas, lowering the saturation concentration C^*, the gain in $k_L a$ is much higher, resulting in higher overall mass transfer flux.

6.1.6 Conclusions

Successful bioconversion of H_2 and CO_2 to CH_4 was conducted in a pilot-scale bioreactive bubble column. Comprehensive 1D and CFD models that couple the hydrodynamics, mass transfer and bioreaction were validated and used to predict the CH_4 purity and productivity. The results of the 1D and CFD models are consistent with the experimental data. This work aimed to demonstrate the importance of reactor design and operating conditions on H_2 mass transfer efficiency which consequently defines the biological methanation performances. It is shown that the biological methanation process is favored

when a uniform porous plate is used. In terms of hydrodynamics, a marginal higher gas holdup was achieved with the 4-points porous sparger but a smaller bubble size was obtained with the porous plate. Due to uniform gas injection of the porous plate, no bubbles coalescence is expected at such low gas holdup, leading to smaller bubbles of 2 mm, as compared with the 4-points porous sparger with bubbles around 5 mm. Since the bioreaction is limited by H_2 mass transfer (due to very poor H_2 solubility), any improvement in H_2 mass transfer flux is critical to biological methanation. Therefore, having a higher interfacial area via the porous plate leads to better bioreactor performance. An increase of 265% in $k_L a$ and subsequently 81% in CH_4 purity is obtained when a porous plate is used instead of a 4-points sparger. However, it is less industrially applicable to use a homogeneous sintered sparger. The key is to use multiple gas spargers with large sparging area to generate bubbles as small as possible at birth and to distribute the gas the most uniformly possible to achieve better mass transfer performance.

The hydrodynamics of 4-points sparger can be described by the 1D model provided the fluid flow structure is obtained from the detailed CFD model. The 1D modelling approach leads to a simplified model which can be solved analytically and underlines the essential feature ($k_L a$) that impacts the biological methanation process. Sensitivity analyses reveal that any improvement on the mass transfer efficiency leads to better biological methanation efficiency. On the contrary, any attempt to increase mass transfer flux by increasing pressure is fruitless as the positive impact of pressure on hydrogen solubility is counterbalanced by the negative impact on gas holdup. Nevertheless, a high pressure allows the bubble column to operate in the homogeneous bubbly regime even at higher gas loading, which is particularly critical when the biological substrate comes from the gas phase as in the biological methanation process. It is shown that any optimization of hydrodynamics, gas recirculation, bubble size and interfacial area (thus $k_L a$) is beneficial to biological methanation.

This work shows that both the 1D and CFD models can be used to assess the impact of different parameters on the reactor performance, and thus serve as scale-up and optimization tools for biological methanation. The 1D model offers fast numerical prediction of CH_4 purity and productivity with a sufficient degree of accuracy at the pilot-scale which can be extended to industrial-scale. Previously developed metabolic flux-based model of Ngu et al. (2022a) is applied here in the 1D and CFD models to couple the two-phase bubbly flow, multispecies mass transfer and biological kinetics. At the pilot-scale, the gas holdup is low and the coupling between hydrodynamics and bioreaction is relatively weak, so the CFD model does not give a significant advantage over the 1D model, as shown by the almost identical results of the two models. Nevertheless, at industrial-scale, pressure effects with increasing height and longer gas residence time will have a stronger coupling with biokinetics.

Complex hydrodynamics prevail in large-scale bubble columns which will subsequently impact the mass transfer and coupling with the bioreaction, as well as heterogeneities or micro-mixing limitations. From this perspective, performing numerical prediction using the CFD model becomes attractive.

6.1.7 Acknowledgments

This work benefited from a State grant managed by the Agence Nationale de la Recherche (ANR) under the Investissements d'Avenir programme with the reference ANR-18-EURE-0021. The CFD work was performed using HPC resources of CALMIP supercomputing center under the 2022 grant (P22025). The authors would like to acknowledge Claude Le Men for his technical support for the optical setup for bubble image acquisition. The experimental work was conducted thanks to funding received from the Occitanie French Region, and the French ecological transition agency (ADEME) in the framework of HYCABIOME and HYDROMET projects.

6.2 Large-scale biological methanation bubble column (Electrochaea)

Successful scale-up of biological methanation reactors requires a deep understanding of the mass transfer efficiency, especially that of hydrogen to prevent poor methanation performance and high operational costs. Modelling large-scale bubble column bioreactors requires a detailed mechanistic description of the bubbly flow and the closures on the gas-liquid interfacial mass transfer as well as the biological kinetics. In this work, it is attempted to use a complete fully-resolved Eulerian CFD model to study local phenomena of an existing large-scale biological methanation plant operated by Electrochaea GmbH, Denmark. This has been done in our previous work using the spatio-temporal 1D model, as shown in Ngu et al. (2022a). Nevertheless, CFD models offer more precise spatially resolved local interactions between phases which is valuable to study large-scale multiphase flow, mass transfer, and bioreaction coupled problems. Despite the higher computational costs, the CFD model is a reliable conceptual reactor design tool for industrial-scale bubble column bioreactors, as demonstrated in the recent work of Puiman et al. (2022), Siebler et al. (2019), and Nadal-Rey et al. (2022), for example.

In the literature, CFD simulations of biological methanation with the validation of the bioreaction remain scarce. To our best knowledge, the only work with the full validation of CFD model for biological methanation focuses on a laboratory scale trickle bed reactor (Markthaler et al., 2022, 2020). Moreover, very few large-scale biological methanation plants are reported in the literature, which renders the CFD validation more hazardous in the absence of local measurements (Rafrafi et al., 2020). However, some open literature data ("Electrochaea - Carbon and Energy storage," 2017; Jensen et al., 2021; Lardon et al., 2018; Rusmanis et al., 2019; Sveinbjörnsson and Münster, 2017), including information published in the official website of Electrochaea (https://www.electrochaea.com/) are adequate for the global validation. It is mentioned that the biological methanation plant of Electrochaea in Avedore, Denmark is the world's first largest full-scale demonstration plant (Rusmanis et al., 2019). The bubble column is designed to treat up to 50 Nm^3/h of CO_2 issued from a nearby anaerobic digestor with a typical biogas mixture of 60% CH_4 and 40% CO_2. With the CO_2 sourced from the biogas, the bioreactor is expected to produce 125 Nm^3/h of CH_4 with the supply of 200 Nm^3/h of H_2 generated from the electrolysis of water using surplus renewable electricity. The electrolyser is supposed to operate at a full electrical power load capacity of 1 MW. The bubble column operates under thermophilic condition with a temperature of 65°C and with a pressure of 8 bar.

In this section, the objective is to perform pioneer CFD simulations of the large-scale biological methanation reactor of Electrochaea and to compare the bioreactor performance with the results

from the literature, similar to the work of Ngu et al. (2022a). If relevant, comparisons of the CFD results with those of the 1D model are also conducted.

6.2.1 Reactor geometry, mesh and model setup

Full details on the bioreactor design are absent in the literature. Therefore, the dimensions of the large-scale bubble column were estimated from openly available data and picture ("Electrochaea - Carbon and Energy storage," 2017; Lardon et al., 2018; Rusmanis et al., 2019). The 3D geometry has been built using cylinders and the gas sparger is supposed to occupy the total reactor base. The initial liquid height is assumed to be 10 m. Considering the increase in water level due to gassing, the total height of the column is set to 11 m. The internal diameter of the reactor is set to 0.72 m according to Rusmanis et al. (2019). The total volume of the reactor is 4.5 m^3 with an ungassed liquid volume of 4.1 m^3. The computational fluid dynamics mesh was generated using ANSYS Meshing. A swept mesh technique was used throughout the column with a similar meshing strategy as Siebler et al. (2019). In the end, a mesh with 141 000 hexahedral cells, 0.7 minimum orthogonal quality, 0.86 averaged skewness and 5.5 cm cell size was constructed, as shown in Figure 6.14.

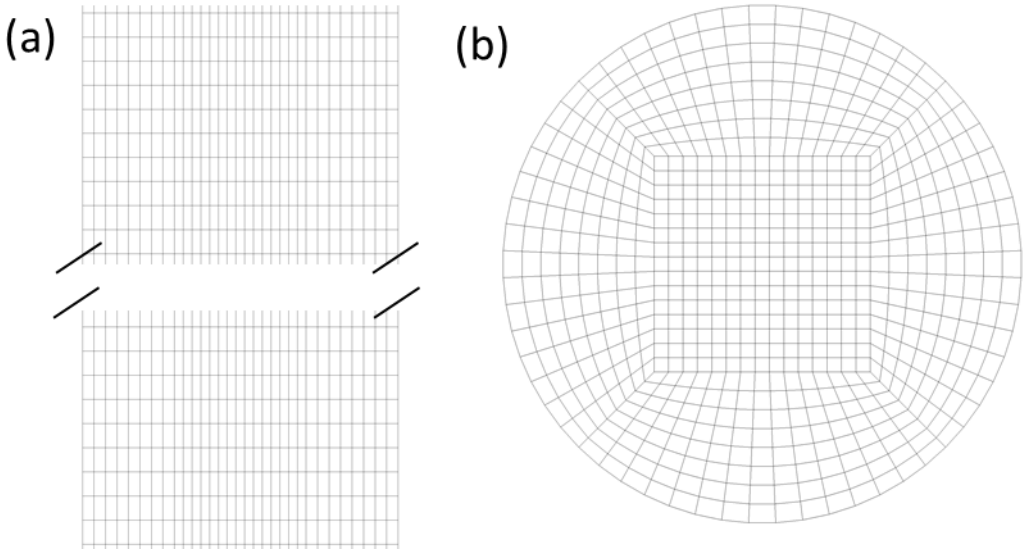

Figure 6.14: (a) Axial and (b) radial section of the mesh

The transient multiphase simulation was conducted in the Eulerian framework using ANSYS Fluent 2021R1. The CFD model setup of the large-scale bubble column followed mostly the work of Siebler et al. (2019). The Reynolds-Averaged Navier Stokes (RANS) equations are solved with dispersed RNG k-ϵ turbulence model. The interfacial forces solved followed the large-scale bioreactors simulations work of Puiman et al. (2022) and Siebler et al. (2019) who considered the drag, lift, wall lubrication, turbulent

dispersion, and turbulence interaction forces. The closure correlations used for these forces are summarised in Table 6.7. The inlet bubble diameter is supposed to be 2 mm as in the work of Ngu et al. (2022a). It is found that small bubble size ($\leq$ 2 mm) is necessary to ensure high H_2 mass transfer flux and to achieve high CH_4 purity.

Table 6.7: Summary of interfacial force correlations used in the CFD model for Electrochaea case.

Force	Correlation
Drag	(Tomiyama et al., 1998)
Lift	(Tomiyama et al., 2002b)
Wall	(Antal et al., 1991)
Turbulent dispersion	(Burns et al., 2004)
Turbulent interaction	(Sato and Sekoguchi, 1975)

A velocity-inlet boundary condition was used on the sparger inlet for the gas. A superficial gas velocity of 0.031 m.s^{-1} was set at the inlet with the velocity magnitude set as the bubble terminal velocity of the imposed bubble diameter calculated using the Tomiyama et al. (1998) drag model (0.286 m.s^{-1}). A turbulence intensity of 5% and a turbulent viscosity ratio of 10 were imposed at the inlet. A pressure-outlet with gas backflow was imposed at the top of the column, with the headspace pressure specified to 8 bar. All walls were set as no-slip condition for the liquid and free-slip for the gas. The inlet gas species mole fraction ratio of H_2:CO_2:CH_4 was 61.5%:15.3%:23.2%. The bubble column is closed to the liquid. The ideal gas law was applied to the gas phase.

The resolution strategy is detailed as follows. First, the unsteady gas-liquid flow field was solved to obtain a pseudo-stationary flow field without species transport. Then, species transport equations were solved together with the flow equations but without mass transfer and bioreaction, signifying the transport of gas mixture from the inlet to the outlet. Next, the mass transfer and bioreaction were activated, and all equations were solved simultaneously. Finally, the transient averaging was conducted for an additional 100 s with data sampling every second. Since the interest of study was not located in the transient state, the solution initialisation for the fluid flow equations was computed from the inlet (u_L = 0 m.s^{-1}, $u_{G,ax}$ = 0.286 m.s^{-1}, a = 330 m^{-1}, ε_G = 0.11). Therefore, a much shorter simulation time was required to achieve a pseudo-stationary flow field. The fluid flow equations were solved only for 100 s to reach a stable overall gas holdup. The species transport equations were solved for 50 s. For the initialisation of the species concentration field, the dissolved H_2 and CO_2 concentrations were patched at equilibrium with the gas phase while the dissolved CH_4 concentration was patched at zero. A total of 500 s simulation time was imposed for the full resolution of flow equations, mass transfer

and bioreaction. All simulations were performed with a timestep of 0.01 s and a maximum iterations per time step of 10. The resolution strategy was able to achieve solution convergence with residuals < $O(10^{-4})$ in the end. The Phase Coupled SIMPLE scheme was used for pressure-velocity coupling. The first-order implicit temporal discretisation scheme was used. For the spatial discretisation schemes, the first-order upwind scheme was used for the density, volume fraction and turbulence variables, and the second-order upwind scheme was used for the momentum and species transport equations.

6.2.2 Fluid dynamic model, mass transfer and bioreaction

The RANS equations were solved transiently by ANSYS Fluent in the Eulerian framework. Analogous to the 1D model established in Ngu et al. (2022a), the bubble size variation was considered due to (i) the hydrostatic pressure and (ii) the huge loss of mass in the gas phase (4 moles of H_2 and 1 mole of CO_2 reduced to 1 mole of CH_4), throughout the 10-m high bubble column. To model these effects, the transport equation of interfacial area was activated in ANSYS Fluent. In this representation, the local interfacial area is a new unknown of the problem. It is a scalar quantity, named interfacial area concentration (IAC) for which an additional equation (6.38) is added. In this model, the bubble size variation due to volume contraction or dilatation, mass transfer, bubble coalescence and breakup are translated into interfacial area changes. Similar to the spatio-temporal 1D model, coalescence and breakup phenomena are assumed to be balanced so that the bubble size variation is mostly dominated by pressure and mass transfer effects, corresponding to the first two terms of the RHS of equation (6.38), respectively.

$$\frac{\partial(\rho_G a)}{\partial t} + \nabla \cdot (\rho_G \overrightarrow{u_G} a) = \frac{1}{3}\frac{D\rho_G}{Dt} a + \frac{2}{3}\frac{\dot{m}_G}{\alpha_G} a + \rho_G (S_{RC} + S_{WE} + S_{TI}) \quad (6.38)$$

With

a: volumetric interfacial area

$\dot{m}_G$: interfacial mass transfer rate

S_{RC}: Coalescence due to random collision

S_{WE}: Coalescence due to wake entrainment

S_{TI}: Breakage due to turbulent eddies

Two user-defined functions (UDF) for mass transfer and the bioreaction uptake rate were developed. The species mass transfer rate $\dot{m}_{G,i}$ is given by equation (6.39),which is a function of species-dependent mass transfer coefficient $k_{L,i}$, interfacial area a and the driving force $(C_i^* - C_{L,i})$. The mass transfer coefficient is modelled as the Higbie (1935) correlation given as

$$\dot{m}_{G,i} = -\dot{m}_{L,\iota} = -k_{L,i} a (C_i^* - C_{L,i}) \tag{6.39}$$

$$k_{L,i} = 2\sqrt{\frac{u_{rel}\, D_i}{\pi\, d_b}} \tag{6.40}$$

$$a = \frac{6\alpha_G}{d_b} \tag{6.41}$$

With d_b is the Sauter mean diameter calculated from the resolved interfacial area transport equation. The diffusion coefficients D_i for the species H_2, CO_2, and CH_4 at 65°C are 1.2×10^{-8}, 5.4×10^{-9}, and 3.95×10^{-8} $m^2.s^{-1}$, respectively. The dimensionless Henry's constant was used to calculate the solubility C_i^* with the corresponding dimensionless Henry's constant for the species H_2, CO_2, and CH_4 being 56.27, 2.79, and 54, respectively (Sander, 2015).

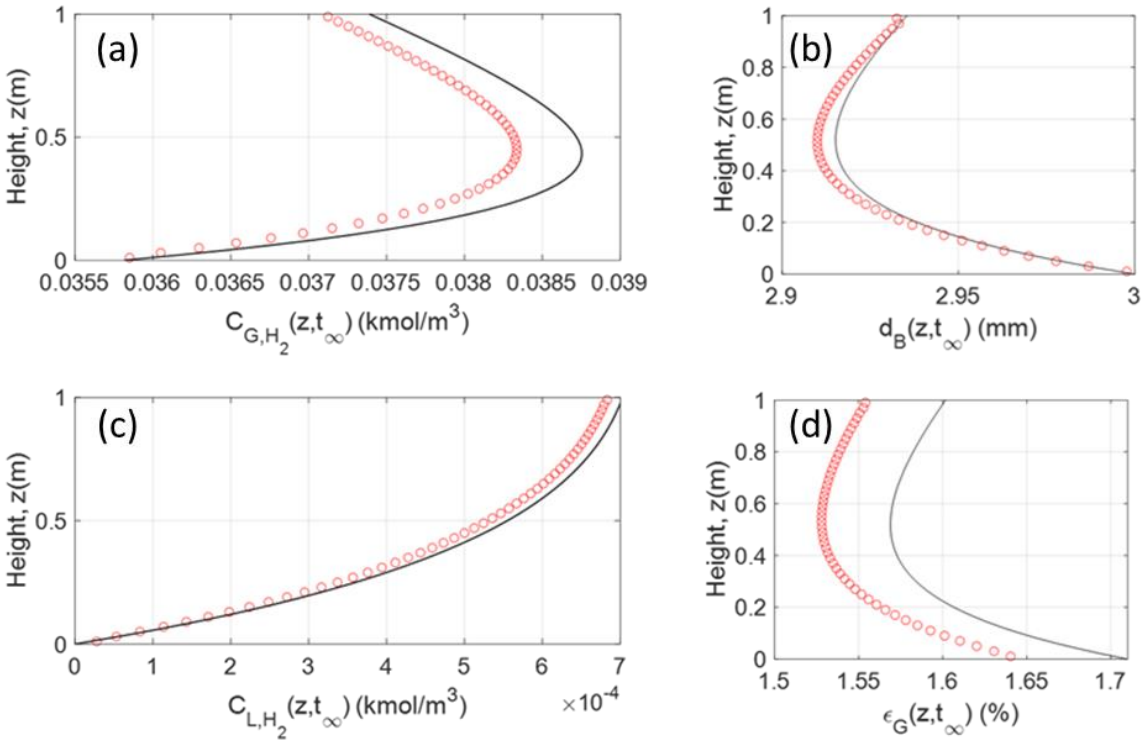

Figure 6.15: Comparison of CFD and 1D predictions for co-current mass transfer in a 1-m high bubble column. (a) Hydrogen gas concentration (b) bubble diameter, (c) hydrogen liquid concentration (d) gas holdup

It is shown in the Appendix that the CFD approach was validated in a 1-m high bubble column and the results were in line with the 1D model results. The test case was a gas-liquid co-current bubble column in a 2D geometry. Figure 6.15 shows an example of the axial profiles obtained for one of the validation cases. Here, the validation case consists of the hydrogen and carbon dioxide mass transfer in co-current bubbly flow (refers to case 1.2.4 in the Appendix). Figure 6.15(a) and (c) reports the hydrogen concentration evolutions in the gas and liquid phase, respectively. A roughly 10% increase in hydrogen gas concentration was observed due to the huge loss of carbon dioxide in the gas phase in the first half of the column. The hydrogen liquid concentration increases due to mass transfer, but the equilibrium concentration (vertical asymptotic value) was not reached due to lower liquid residence time. Figure 6.15(b) and (d) show that the bubble diameter and gas holdup decreased at the bottom half of the column due to high mass transfer flux but it increased slightly in the upper half of the column due to volume expansion brought on by decreasing hydrostatic pressure. Additional details on the comprehensive validation case were explained in Appendix.

For biological methanation, it is generally agreed that the H_2 gas-liquid mass transfer rate is the limiting factor of the overall biological methanation process (Jensen et al., 2021; Lecker et al., 2017; Rafrafi et al., 2020). It was proposed that the steady-state is characterised by a balance between the specific hydrogen uptake rate (mass transfer rate divided by the biomass concentration) and the utilisation rate for maintenance (Ngu et al., 2022a). From that moment, constant carbon dioxide consumption and methane production rates will be achieved, both being proportional to the H_2 mass transfer rate. The hydrogen mass transfer rate being the limiting factor for the metabolism, the specific hydrogen uptake rate at steady state is equal to the maximum hydrogen mass transfer rate per cell mass $\varphi_{H_2,max} = \frac{k_L a(C^*_{H_2} - 0)}{\varepsilon_L X}$ and the specific carbon dioxide and methane uptake rate are expressed stoichiometrically as $\varphi_{CO_2} = \frac{\varphi_{H_2,max}}{4} \cdot \frac{M_{CO_2}}{M_{H_2}}$ and $\varphi_{CH_4} = \frac{\varphi_{H_2,max}}{4} \cdot \frac{M_{CH_4}}{M_{H_2}}$, respectively. Since the objective here is to predict the bioreactor performance at the steady-state and to compare with the literature value, it is chosen to set a constant biomass concentration, X = 35 g.L^{-1}, the same steady-state concentration obtained with the 1D model for the Electrochaea case (Ngu et al., 2022a). As the methanogens growth rate is usually very low, it is not possible and therefore it is not attempted to simulate the transient growth using the CFD model.

6.2.3 Results on flow field pattern

In this section, the flow pattern and the species transport in the gas established after 150 s will be discussed. This situation corresponds to bubbly flow without mass transfer and bioreaction. Figure

6.16 shows the contours of the axial gas velocity, axial liquid velocity, gas holdup and species molar fraction in a vertical plane passing through the centre. It shows that the bubbles rise rather uniformly due to a homogeneous injection of gas covering the total cross-section surface of the column, with a bubble terminal velocity around 0.3 $m.s^{-1}$ according to the Tomiyama et al. (1998) drag model. The liquid axial velocity is nearly zero, signifying no liquid recirculation. The gas holdup increases slightly due to the decreasing hydrostatic pressure, in line with the ideal gas law. The overall gas holdup was 0.117 which was in good agreement with the values obtained from the 1D model at 0.116 (Ngu et al., 2022a). Following the work of Puiman et al. (2022) who also compared the averaged gas holdup with the global correlation of Zuber and Findlay (1965) and Heijnen and Van't Riet (1984), it is found that the correlations yield 0.109 and 0.124, respectively, which is close to the CFD predicted value. The gas species is also homogeneously distributed in the column. The fluid flow is uniform with very weak liquid recirculation, yielding a homogeneous bubbly regime.

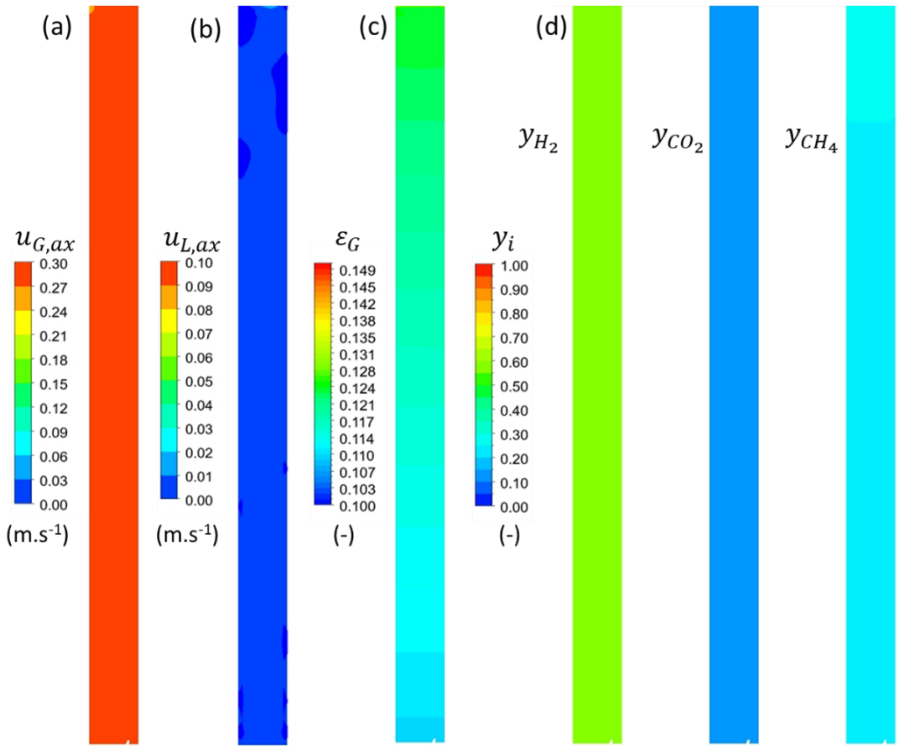

Figure 6.16: Contours of (a) axial gas velocity component (b) axial liquid velocity component (c) gas holdup (d) gas species molar fraction

Upon the establishment of the flow and species transport in the gas phase, the mass transfer and bioreaction kinetics were activated to study the impact of bioreaction on the hydrodynamics.

6.2.4 Results on biological methanation and comparison with the 1D model

In this section, the results of the large-scale biological methanation are discussed. First, the predictions of the hydrodynamic variables such as bubble diameter, gas holdup, gas velocity and interfacial area are presented, as shown in Figure 6.17. In each subfigure, an instantaneous coutour map is presented on the left and a time-averaged over 100 seconds contour map is shown on the right.

In the presence of bioreaction and mass transfer, the hydrodynamics behaviour differs from the previous case. The bubble diameter varies spatially and temporally due to density gradient effects. The time-averaged value reveals that the mean bubble size decreases from the bottom to the top of the column, as shown in Figure 6.17(a). The spatially dispersed axial gas velocity in Figure 6.17(b) reflects the influence of different bubble size on gas-liquid hydrodynamics as different bubble size rises at a different velocity. Due to huge consumption of H_2 and CO_2, the gas holdup varies significantly from the inlet to the outlet, ranging from roughly more than 10% to 5%, as presented in Figure 6.17(c). This nearly two-fold reduction in gas holdup creates an axial gradient of gas holdup, leading to “heavier” liquid at the top of the column compared to the bottom. The unsteadiness of the two-phase flow originates from that instability. Consequently, large-scale mixing is favoured, resulting in axial and radial dispersions. Figure 6.17(c) and (d) show gradient profiles of gas holdup and interfacial area with maximum values located at the bottom and the lowest values towards the top of the column. Combining higher interfacial area and hydrostatic pressure at the bottom, high mass transfer rate is expected at this region. The time-averaged radial profiles of gas holdup and interfacial area were mostly homogeneous after the mid-height till the top.

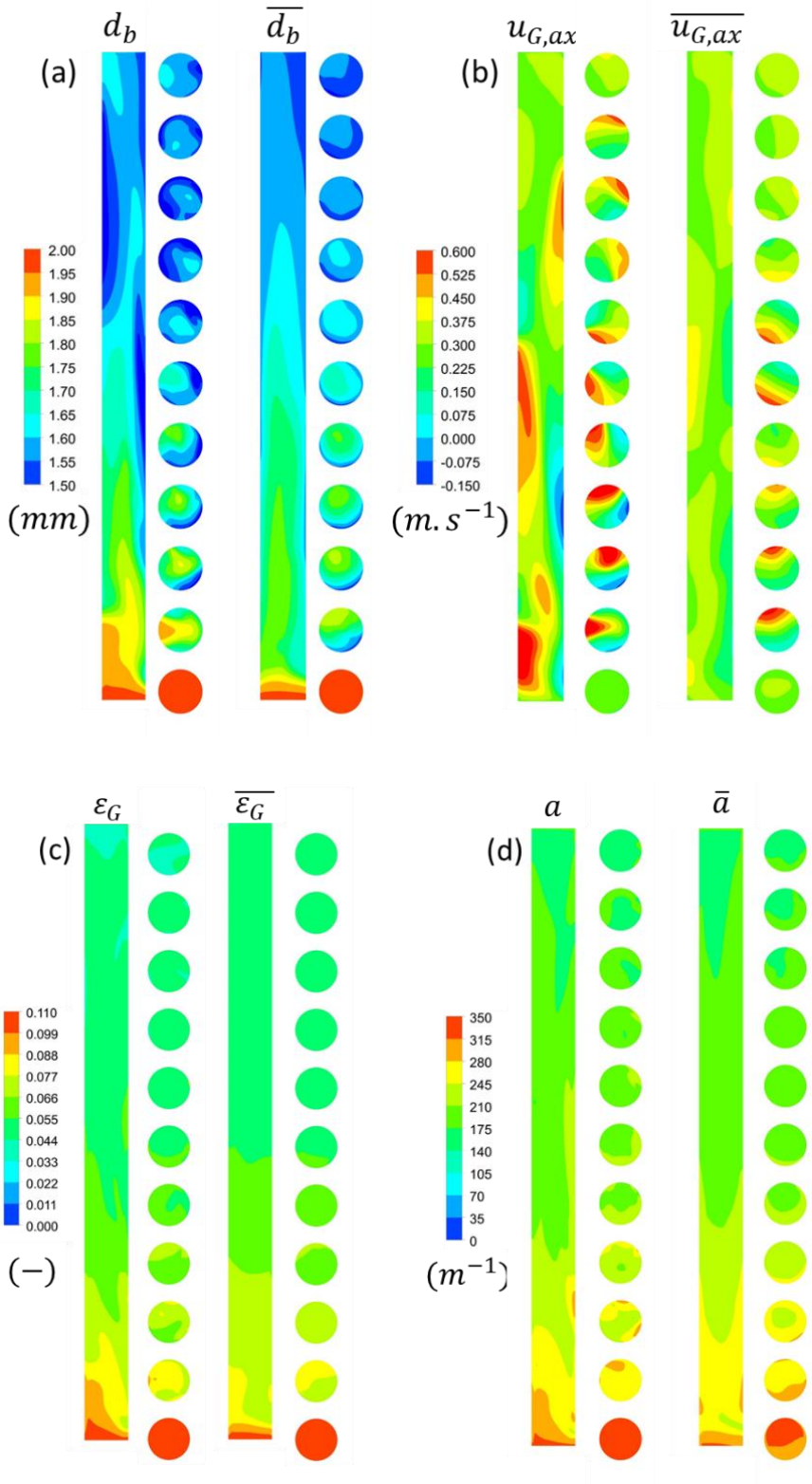

Figure 6.17: Contour plots of instantaneous and time-averaged profiles on a vertical plane and selected cross sections (every meter) for (a) bubble diameter (b) axial gas velocity component (c) gas holdup and (d) interfacial area. The instantaneous surface plots were obtained after 500 s of simulation time. The time-averaged contours were averaged over the last 100 s.

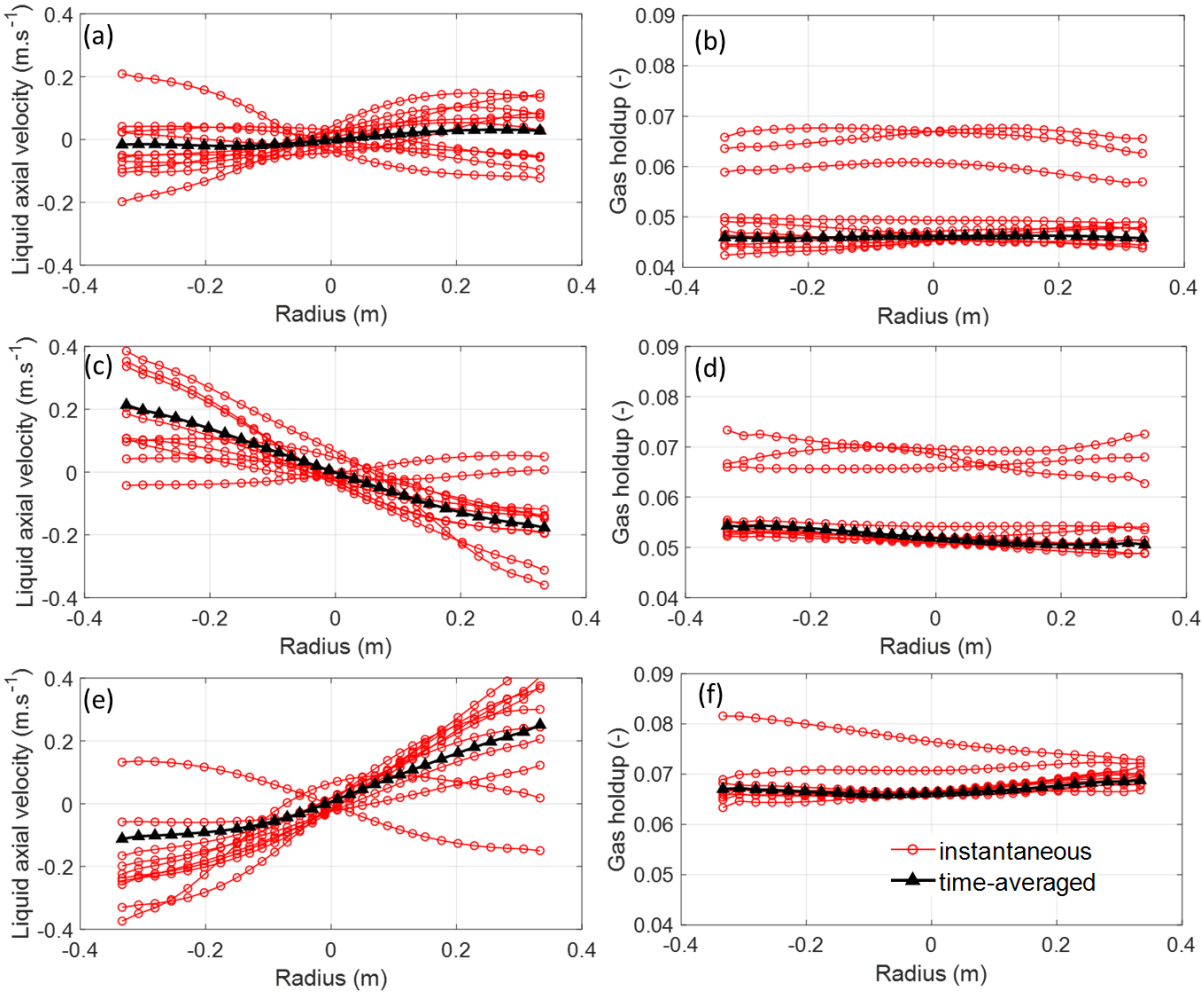

Figure 6.18: Radial profiles of (a, c, and e) liquid axial velocity and (b, d, and f) gas holdup for z/H of 0.25 (bottom row), 0.5 (middle row) and 0.75 (top row). Red circle lines are instantaneous profiles, Black triangle lines are time-averaged profiles. The instantaneous profiles are reported for every 10 s but no distinction is made for the sake of simplicity and to avoid confusions.

Figure 6.18 reports both the instantaneous (red lines) and 100 s time-averaged (black lines) radial profiles of liquid axial velocity and gas holdup for z/H of 0.25 (Bottom row, (e) and (f)), 0.5 (Middle row, (c) and (d)), and 0.75 (Top row, (a) and (b)). For the liquid axial velocity, it fluctuates roughly between $\pm$ 0.40 m.s^{-1} at $z/H = 0.25$ and 0.5 while between $\pm$ 0.20 m.s^{-1} at $z/H = 0.75$. At each height, all instantaneous radial profiles of liquid velocity are asymmetrical, reflecting the unsteady bubbly flow in the bubble column. At z/H of 0.25, the liquid ascends mostly at the right side and descends at the left but at certain time instant, inversion may also occur, as shown in Figure 6.18(e). For increasing z/H, it is found that the liquid velocity decreases. This shows that the two-phase flow becomes more stable with weaker liquid recirculation in the column. At the top of the column, the

liquid axial velocity becomes negligible. Moreover, for increasing z/H, the time averaged radial profiles (black triangle lines) become more uniform with less radial gradients. Meanwhile, the gas holdup varies approximately between 0.06 – 0.07 at z/H of 0.25, between 0.05 – 0.06 at z/H of 0.5, and between 0.04 – 0.05 at z/H of 0.75. For the gas holdup, the radial profiles are rather uniform. At z/H = 0.25 and 0.5, three of the ten radial profiles show a slightly higher values than other profiles, displaying the time-dependent behaviour of the column. This is also reflected in the gas holdup temporal profile in Figure 6.19(c).

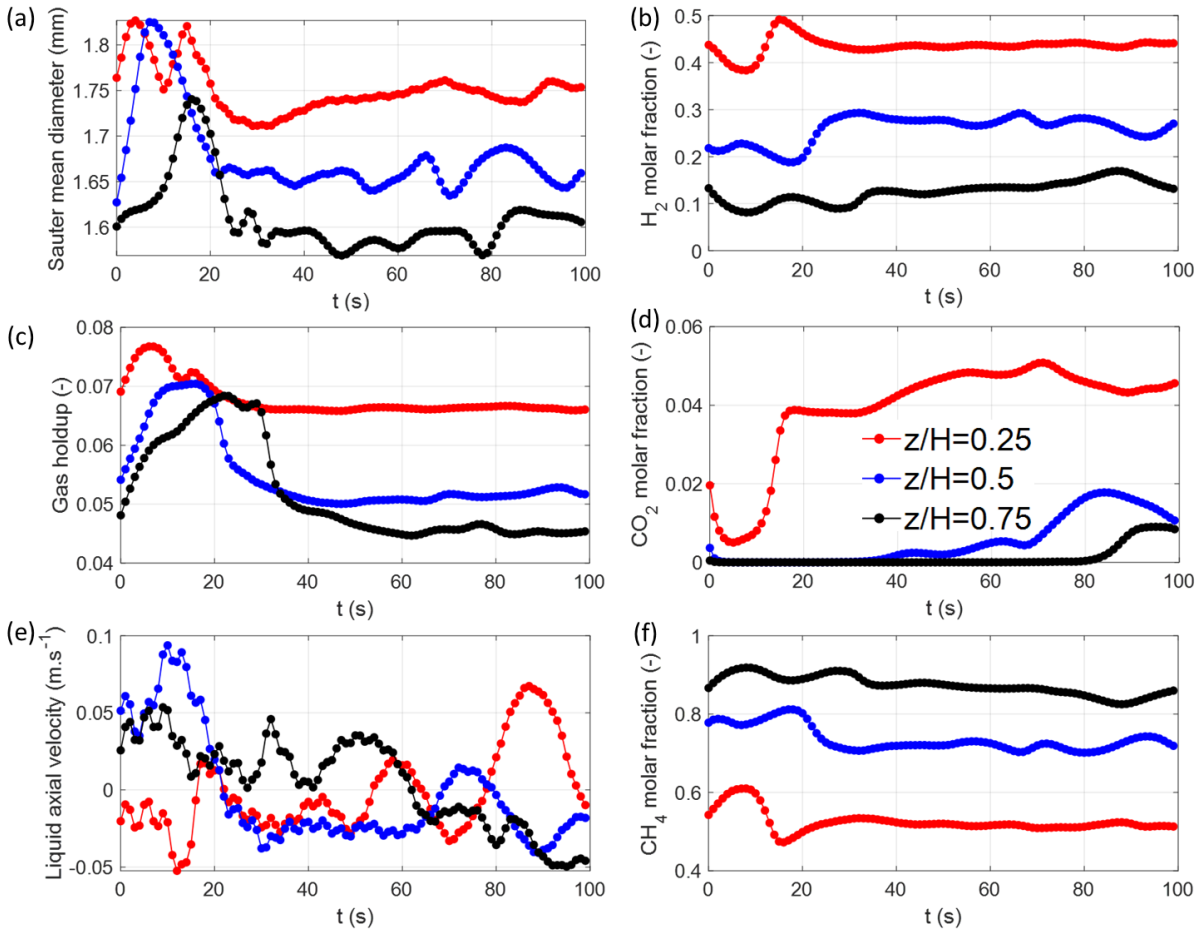

Figure 6.19: Temporal profiles of (a) Sauter mean diameter, (b) hydrogen gas molar fraction, (c) gas holdup, (d) carbon dioxide gas molar fraction, (e) liquid axial velocity, and (f) methane gas molar fraction for a centred point at z/H = 0.25 (red points), 0.5 (blue points) and 0.75 (black points).

Figure 6.19 shows the temporal profiles for different variables at three different z locations. The temporal profiles were recorded for 100 s at centred location (x = 0, y = 0) for three different heights. The Sauter mean diameter and the gas holdup show a slight increase in value at less than 20 s but immediately decrease right after. The gas holdup remains rather stable after 40 s, signifying the

pseudo-steady state is reached. At these measuring points, the liquid axial velocity fluctuates between $\pm$ 0.05 m.s^{-1}. The gas species molar fraction of the substrates (hydrogen and carbon dioxide) decreases with z, whilst the methane gas molar fraction increases, reflecting the successful conversion of substrates into the gas product. As for carbon dioxide, the substrate is mostly depleted after the mid-height.

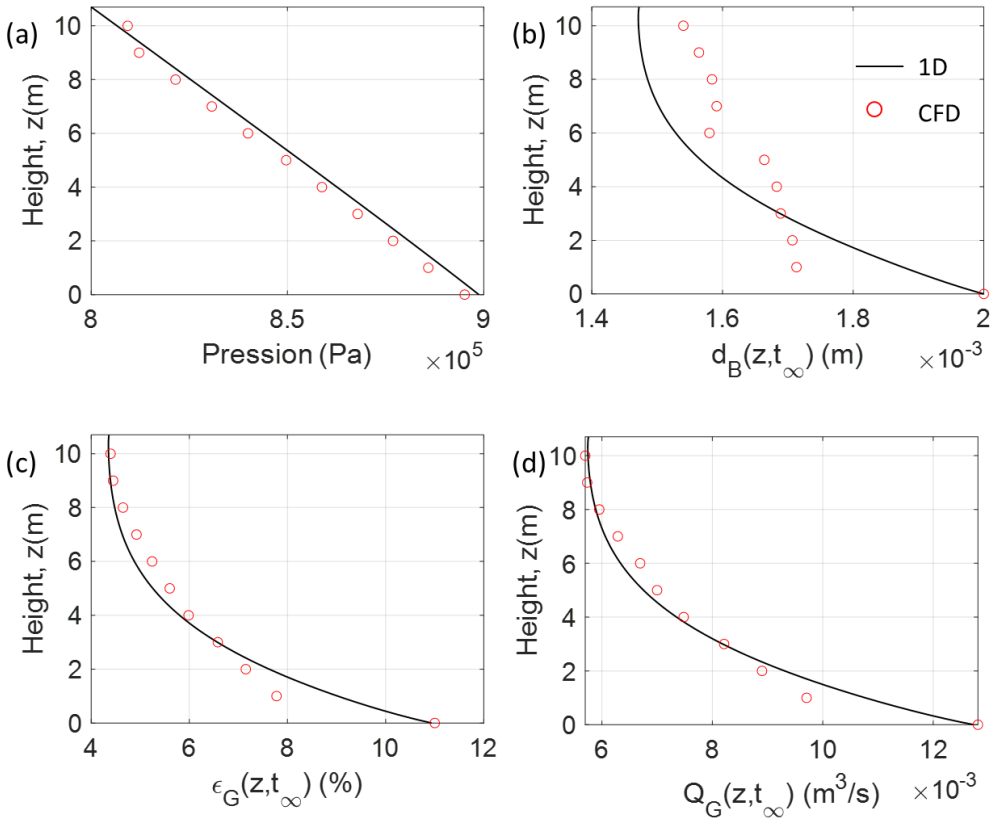

Figure 6.20: Comparison between CFD and 1D axial profiles. (a) Hydrostatic pressure (b) bubble diameter (c) gas holdup (d) Gas flowrate. CFD points were calculated from spatial-averaging of the time-averaged profiles.

Previously, we have developed a two-way coupled spatio-temporal 1D model and the 1D model has been used to predict the biological methanation performance of Electrochaea plant (Ngu et al., 2022a). Here, some CFD results were compared with these previously published results, as shown in Figure 6.20. Globally, the CFD model followed the same trend as the 1D model. Hydrostatic pressure decreases linearly from the bottom to the top, as shown in Figure 6.20(a). Along with the decreasing hydrostatic pressure and the bioreaction, gas holdup (Figure 6.20(c)) and volumetric gas flowrate (Figure 6.20(d)) decrease sharply from the bottom to the top of the column. As a result of decreasing gas holdup, the volumetric gas flowrate was also reduced by nearly two-fold. According to the

stoichiometry of the reaction, the flowrate should be reduced five-fold but since the hydrostatic pressure varies by a factor of two in a 10-m high column, the theoretical flowrate reduction is thus 2.5, which is consistent with the two-fold reduction. At the top of the column, the gas holdup remains almost stable around 5%, resulting in a more homogeneous bubbly flow. Figure 6.20(b) shows that two zones for the bubble diameter can be distinct with an average of 1.7 mm at the bottom half of the column and an average of 1.55 mm at the top. This reflects that at the bottom where the gas holdup is around 8%, liquid instabilities and swarm effects induce bubble mixing between large and small bubbles, leading to a stable bubble diameter.

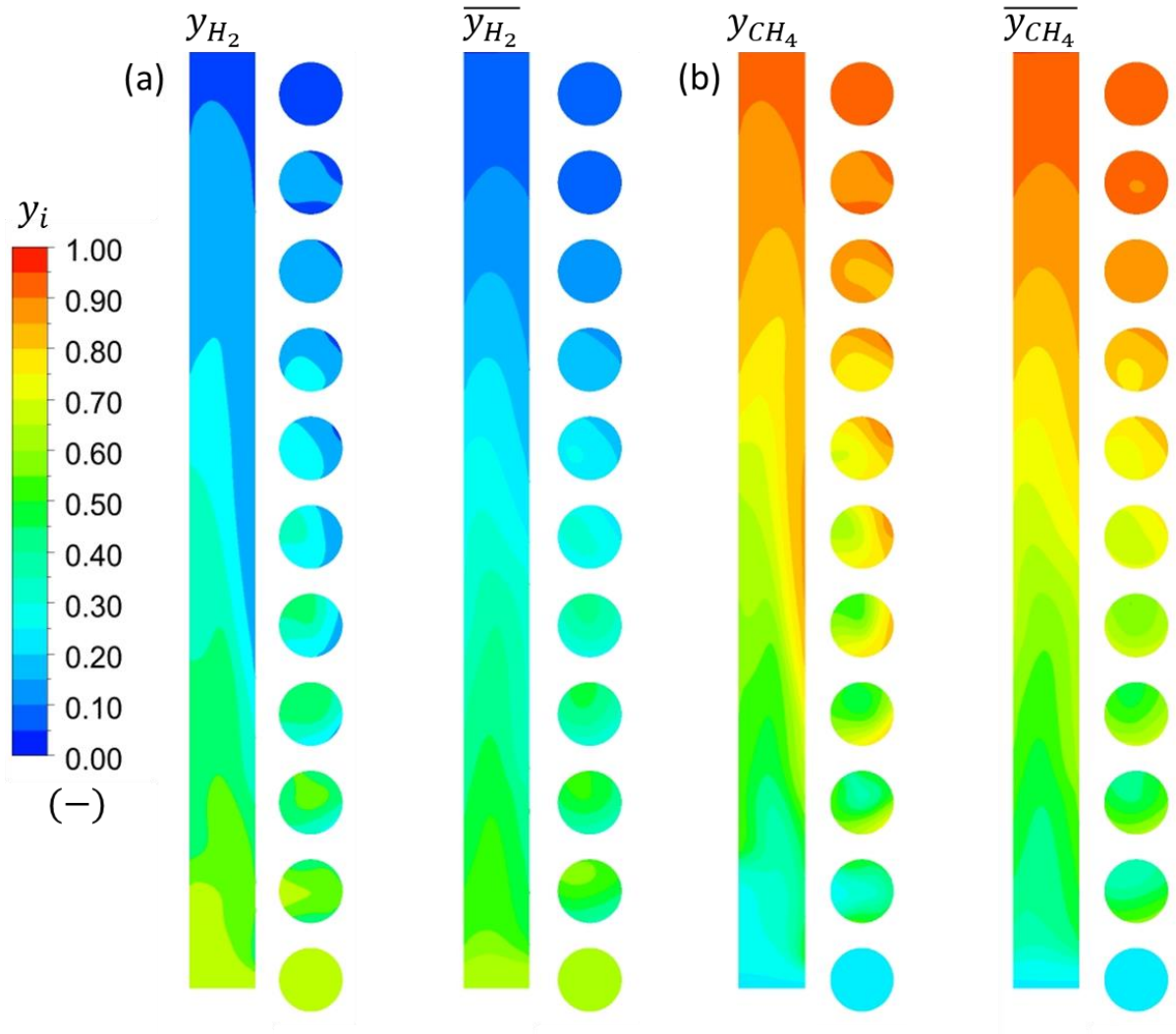

Figure 6.21: Contour plots of instantaneous and time-averaged profiles for (a) hydrogen gaseous molar fraction (b) methane gaseous molar fraction.

Figure 6.21 reports the molar fraction surface plots for hydrogen and methane. Figure 6.21(a) shows that hydrogen molar fraction decreases from approximately 60% at the inlet to less than 10% at the

outlet. Successful biogas upgrading was achieved as the methane molar fraction increases from 25% at the inlet to 95% at the outlet, as displayed in Figure 6.21(b). This proves that the chosen bioreactor design as a "slim and high bubble column" is suitable to produce high-quality methane by promoting H_2 gas-liquid mass transfer. High bubble columns are advantageous for mass transfer due to increased gas retention time and gas solubility (hydrostatic pressure) and this has been discussed previously in the literature (Deckwer et al., 1978; Ngu et al., 2022a; Siebler et al., 2019). Moreover, the CFD results showed that the radial gradients are negligible in comparison to the axial gradients $\left(\frac{\partial \phi}{\partial r} \ll \frac{\partial \phi}{\partial z}\right)$ for any variable ϕ.

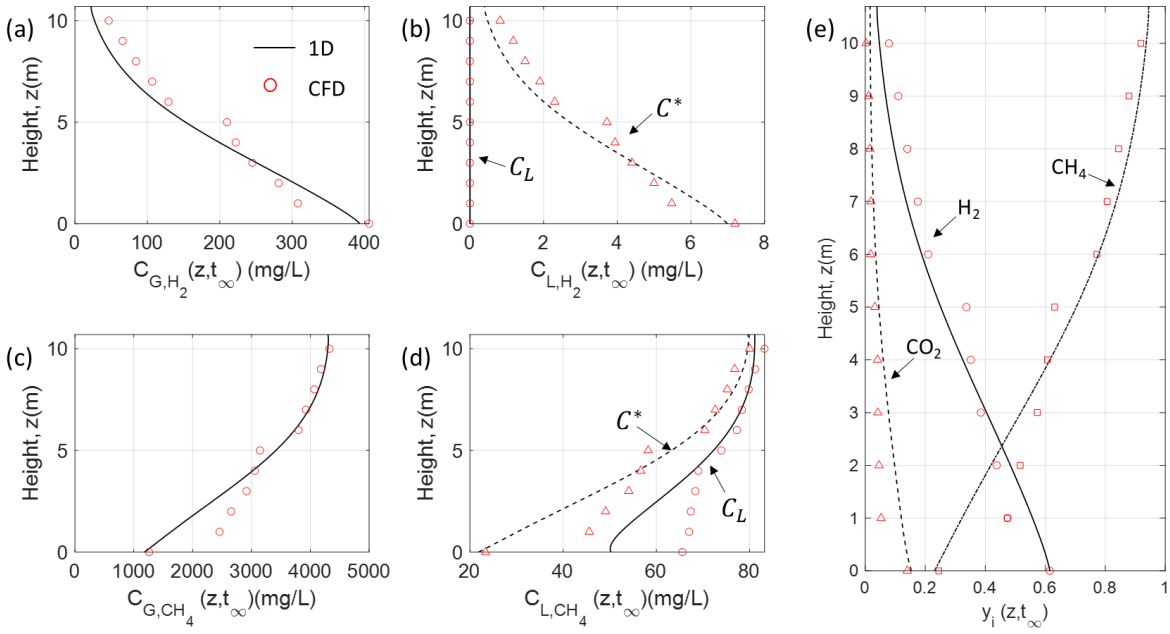

Figure 6.22: Comparison between CFD and 1D axial profiles. (a) Hydrogen gas concentration (b) Hydrogen liquid concentration (c) Methane gas concentration (d) Methane liquid concentration (e) Gas molar fraction. CFD points were calculated from spatial-averaging of the time-averaged profiles.

Figure 6.22 presents the gas and liquid concentration axial profiles for hydrogen (in Figure 6.22(a)-(b)) and methane (in Figure 6.22(c)-(d)) obtained with 3D and 1D approaches. It shows that the hydrogen gas concentration decreases throughout the reactor as all transferred hydrogen is converted into methane. In the liquid, hydrogen concentration reaches zero, signifying the total consumption of the dissolved hydrogen by the bioreaction. The hydrogen gas concentration and its solubility obtained from the CFD model agree with the 1D model predictions. For the methane concentrations, the differences between the CFD model and the 1D model were the largest at the bottom part of the column. This could be due to the unsteadiness of the two-phase flow in the large-scale bubble column with the presence of bioreaction. Due to the nature of the bioreaction, a huge loss of gas was awaited,

which contributes to high gas holdup axial gradients. The spatial evolutions lead to large-scale unsteady liquid recirculation and bubble plumes due to density gradients, as shown in Figure 6.23. Figure 6.23(a) and (b) illustrate the unsteady, oscillating behaviour of the bubble column. Near the inlet, the liquid recirculated down near the right-side wall and pushes the sparged gas to the left side, resulting in a higher local liquid velocity on the left side, hence forming a circulation loop. Figure 6.23(c) and (d) show the radial profiles of liquid axial velocity and gas holdup. Liquid axial velocity up to 0.2 $m.s^{-1}$ can be observed locally with asymmetric liquid recirculation profiles despite the sparger and the mesh being homogeneous at the bottom. The gas holdup radial profiles were fairly uniform with a slightly higher radial gradient observed at z/H = 0.5.

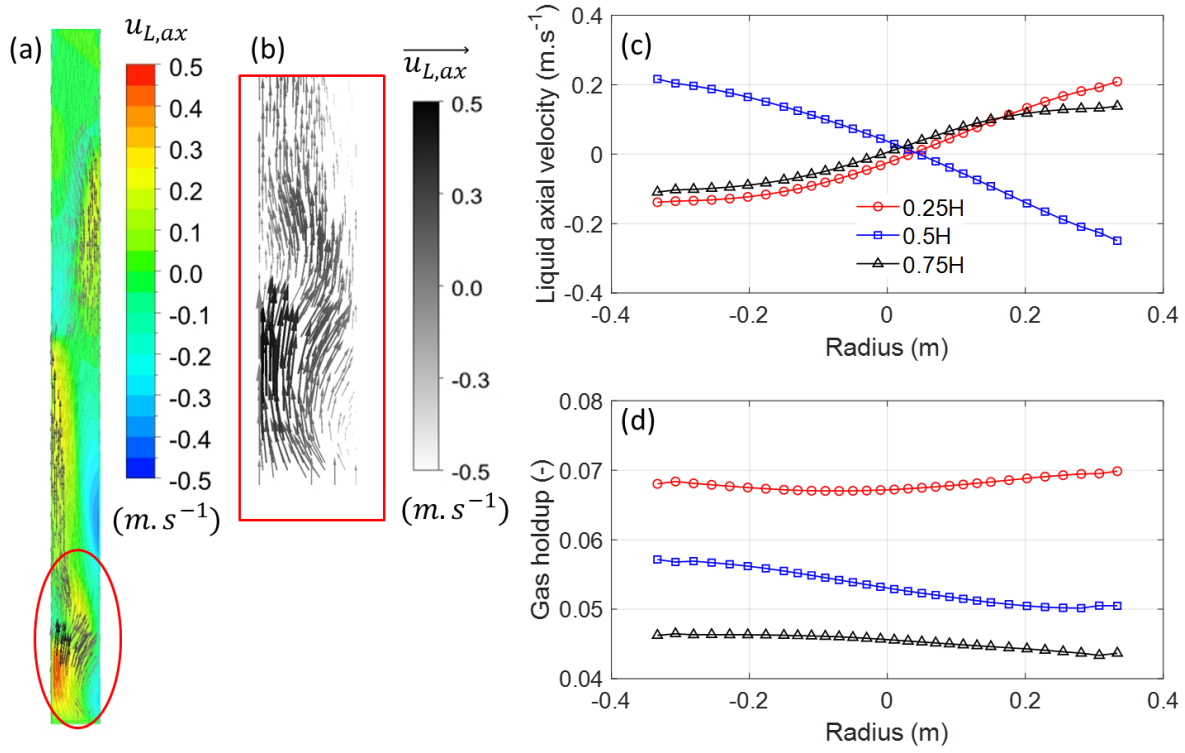

Figure 6.23: (a) Contour of liquid axial velocity superposed with the arrows indicating the velocity vectors. (b) Zoom of the liquid velocity vector near the inlet circled with red contours in (a). Radial profiles of (c) liquid axial velocity and (d) gas holdup for z/H = 0.25, 0.5, and 0.75.

Overall, after the mid-height, the CFD predictions coincide well with the 1D model results. This is expected as the radial gradients after this height were relatively weak, as shown in the radial contour plots in Figure 6.17 and Figure 6.21. It can also be noticed in Figure 6.20(c) that the axial evolution of the gas holdup was weaker at the top of the column which induced a relative stability of the two-phase flow. The slope of the gas holdup at the bottom of the column is steeper, reflecting a higher axial

gradient $\left(\frac{\partial \varepsilon_G}{\partial z}|_{6-10m} \approx 0.2\%/m < \frac{\partial \varepsilon_G}{\partial z}|_{0-5m} \approx 1\%/m\right)$. This justifies the choice of the 1D model to simulate the industrial reactor of Electrochaea as it is sufficient to yield satisfactory results. At the outlet, the CFD model predicts a CH_4 purity of 95% and a productivity of 126.5 Nm^3/h which agrees well with the 1D model prediction of 95% and 123 Nm^3/h (Ngu et al., 2022a) and the reported value 90-95 % and 125 Nm^3/h of CH_4 ("Electrochaea - Carbon and Energy storage," 2017; Sveinbjörnsson and Münster, 2017). The similarity in the results essentially confirms that the implementation of the various models and the selection of closure law are correct and physically consistent. The unsteadiness of the flow simulated in the 3D CFD study are modelled as a dispersion term in the 1D model. Usual correlation for the estimation of that dispersion coefficient are found to be satisfying in the configuration simulated here. It could be adjusted as the bubble column is found to be particularly sensitive to density gradient effects. As far as biology is concerned, the steady-state coincide with a balance between uptake and maintenance which translates into $\varphi_{H_2,max} =< \frac{k_L a C^*_{H_2}}{\varepsilon_L X} > = m$.

6.2.5 Conclusion

Fully-resolved CFD simulations for biological methanation in a large-scale bubble column were performed and it was compared with open literature data. To our best knowledge, this was the first CFD attempt on ex-situ large-scale biological methanation reactor.

The bioreactor performance predicted by the CFD model was also validated by comparison with that of the 1D model and the results were satisfactory. It was found that when the radial profiles were rather uniform in the second half of the column, the CFD model yielded a very close value to the 1D model. However, due to the nature of the reaction (5 moles of gas substrates are reduced to 1 mole of gas product), huge gas holdup depletions are expected axially. These density gradients lead to unsteadiness in the bubbly flow which is more pronounced at the bottom half of the column.

CFD modelling becomes pivotal and advantageous if one is interested in quantifying the local phenomena which are difficult to model using coarse 1D approach. In this case, the CFD model is the ideal tool to characterise the instabilities and the effects of spatiotemporal heterogeneities on the bioreaction. Through this study, it is found that the CFD model becomes useful in bioreactor modelling when the major substrates are gas-fed and the stoichiometry of the reaction leads to gas phase depletion and high density gradients in the two-phase flow. In the future, a finer mesh and further work on bubble induced turbulence might be necessary to better describe the bubble plume dynamics and recirculation flow structure (Laupsien, 2017).

Despite higher computational costs, detailed CFD simulations offer valuable insights of the fluid flow thanks to a higher spatial resolution that could not be achieved using the 1D model, especially the oscillating behaviour of the bubble plume near the gas sparger revealed by the CFD simulations. Nevertheless, the 1D model provides faster resolution and is a useful tool for probing a wide range of parameters before conducting computational-power constrained CFD calculations. Conceptual bioreactor design should rely upon the synergetic application of the high-resolution CFD model and the practical 1D model.

Chapter 7 Conclusion & Perspective

7.1 General conclusion

The modelling and the simulation of bioreactors form a challenging task encompassing a variety of physical and biochemical aspects, from the description and computation of fluid dynamics to (bio)reaction dynamics. In this PhD thesis, a fully-coupled gas-liquid spatio-temporal 1D model was proposed to simulate bubble column bioreactors. The 1D model has been validated using experimental and literature data. After comprehensive validations, numerical simulations using the 1D model have been performed on several chemical and biochemical processes, as shown in Table 7.1 and Table 7.2, highlighting the robustness of the model. Table 7.1 summarises the biological methanation reactors studied in this thesis, ranging from pilot-scale to industrial units. Other applications that have been investigated using the 1D model are also reported in Table 7.2.

Table 7.1: Different biological methanation reactor simulated using the 1D model.

Scale	Pilot-scale SYMBIOSE	Scale-up Demonstration unit	Scale-up Industrial unit	Industrial unit Electrochaea
Reactor design	H = 1.24 m D_r = 0.15 m V = 22 L	H = 2 - 7 m D_r = 0.3 - 0.5 m V = 100 - 500 L	H = 3 - 8 m D_r = 0.8 - 1.2 m V = 1.5 - 9.0 m^3	H = 10 m D_r = 0.72 m V = 4.4 m^3
Fresh gas feed H_2:CO_2:CH_4	80%:20%:0	61.5%:15.3%:23.2%		
Gas inlet flowrate	0.06 - 9.6 NL/h	13 Nm^3/h	221 Nm^3/h	325 Nm^3/h
Gas recirculation	With	With and without	With and without	Without
Operating conditions	T = 55°C $P = P_{atm}$	T = 55°C P = 4 bar	T = 55°C P = 13 bar	T = 65°C P = 8 bar
Hydrodynamics d_b, ε_G range	d_b = {1.5; 5} mm ε_G = {1.5; 2} %	d_b = 2 mm ε_G = {1; 6} %	d_b = 3 & 4 mm ε_G = {1; 5} %	d_b = {1.5; 2} mm ε_G = {5; 11} %
Max CH_4 purity (corresponding productivity)	93% (0.002 Nm^3/m^3/h)	84% (10 Nm^3/m^3/h)	78% (13 Nm^3/m^3/h)	95% (28 Nm^3/m^3/h)
Max CH_4 productivity (corresponding (purity)	0.12 Nm^3/m^3/h (80%)	26 Nm^3/m^3/h (73%)	43 Nm^3/m^3/h (38%)	-

Table 7.2: Other applications simulated using the 1D model

Applications	CO_2 physical absorption (Deckwer et al., 1978)	CO_2 chemical absorption (Darmana et al., 2007)	Yeast fermentation (Sarkizi Shams Hajian et al., 2020)
Reactor design	H = 4.4 m D_r = 0.14 m V = 680 L	H = 1 m D_H = 0.09 m V = 6 L	H = 6.6 m D_r = 2.1 m V = 22 m^3
Operating conditions	T = 14°C $P = P_{atm}$	T = 25°C $P = P_{atm}$	T = 55°C $P = P_{atm}$
Hydrodynamics d_b, ε_G range	d_b = 2.86 mm ε_G = {5; 20} %	d_b = {3; 5.5} mm ε_G = {1.5; 2} %	d_b = 9 mm $\varepsilon_G \sim$ 18 %

The successive paragraphs below recall and summarise the important findings of each chapter.

A thorough state-of-the-art of biological methanation, bioreactor modelling, and bubble columns was summarised in Chapter 1. It is found that the current biological methanation researches focus strongly on the proof-of-concept experimental studies and the optimisation of reactor design. Few numerical models on biological methanation can be found in the literature. Challenges in bioreactor modelling have been identified and discussed, namely the hydrodynamics coupling with the biological phase. Bubble columns are widely used as an industrial-scale bioreactor and a mini general review on this topic has been conducted to understand the fundamental physics and multiscale phenomena. Recent examples of CFD and 1D modelling of bubble columns were given and the contributions of each work were stated. Gaps in the 1D bioreactor modelling have been identified, **namely (i) constant gas holdup or imposed by empirical correlations (ii) one-way coupling of hydrodynamics and reactive mass transfer and (iii) mono-species mass transfer simulation.** One of the objectives of this thesis was to develop a 1D model framework and structure that attempt to solve the aforementioned gaps simultaneously, as illustrated in Figure 7.1.

In Chapter 2, we have presented the experimental setup used for hydrodynamics and biological methanation experiment. The instrumentation techniques and the image processing algorithm for the bubble size distribution and the transient gas holdup measurements were also explained. The two-way coupled spatio-temporal 1D model developed in this thesis was presented. Closure relations for multiphase flow, interfacial gas-liquid mass transfer, and bioreaction kinetics used in this work were also presented and discussed. **A novel bioreaction closure model for biological methanation relying upon physical substrate supply and biological demand** was proposed and detailed.

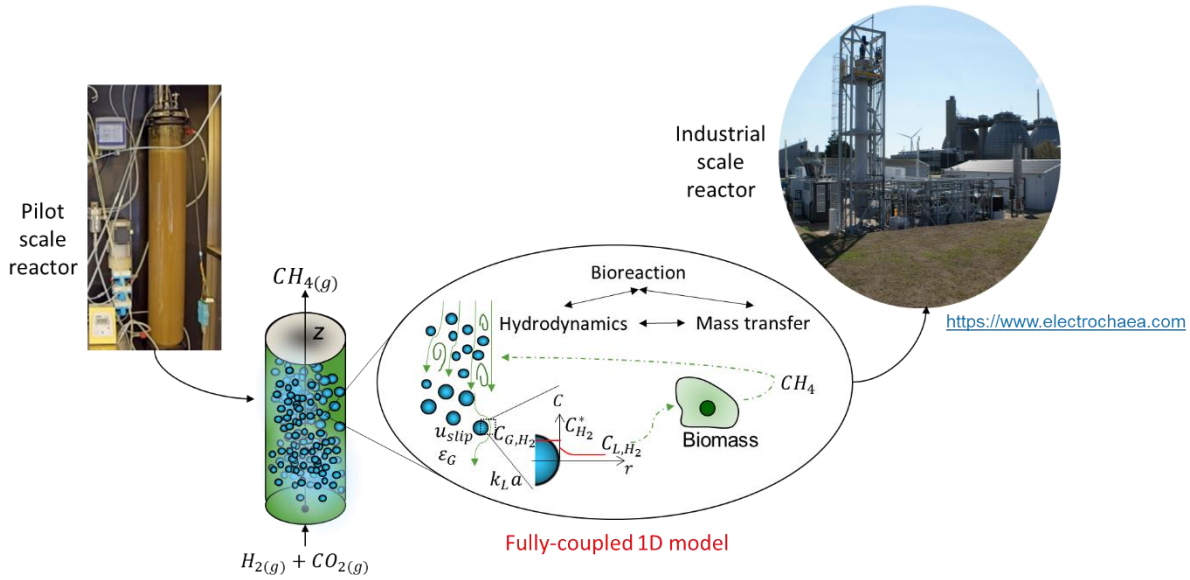

Figure 7.1: Multiscale fully-coupled spatio-temporal 1D model for bioreactors modelling. Pilot-scale reactor corresponds to 22 L bubble column used by the SYMBIOSE team. Industrial-scale reactor is the 4.5 m^3 column of Electrochaea.

Extensive work on the 1D model validation has been reported in Chapter 3 which was based on the hydrodynamics and mass transfer studies conducted in different bubble column configurations from the literature. It was shown that by applying the same experimental bubble diameter and suitable closures for the bubble drag and mass transfer coefficient, the 1D model was able to reproduce the literature data. A full-scale mass transfer validation was carried out based on Deckwer et al. (1978) data who investigated CO_2 absorption in a 4.4 m tall column. The non-linear gas holdup and CO_2 molar fraction axial profiles as observed in the experiments were well predicted by the spatio-temporal 1D model. **The gas holdup profile was influenced by the absorption taking place at the bottom where the mass transfer flux is higher (higher hydrostatic pressure) and desorption occuring at the top.** For example, the **gas holdup decreases by nearly 50% at the first half of the column and increases by roughly 33% at the outlet** for a superficial gas velocity of 3.42 cm.s^{-1} (experiment 17). It was also revealed that the $k_L a$ and subsequently the mass transfer rate are axial-dependent and making such constant $k_L a$ assumption could negatively impact the prediction of industrial-scale bubble column performance, such as the biological methanation reactor of Electrochaea.

Further industrial applications of the 1D model have been demonstrated in Chapter 4. In this chapter, the model was used for upscaling and designing biological methanation reactor. This work was conducted in conjunction with the industrial partner ENOSIS Energies. The goal was to provide scaleup guidelines for their bioreactors at two scales: the demonstration and industrial units. **The investigation**

showed that biological methanation performs better in high bubble columns as the CH_4 purity increases significantly with height. This increases the gas retention time and benefits from the hydrostatic pressure for achieving high mass transfer rate. The industrial biological methanation reactor of Electrochaea was also designed as a tall column. Through a comprehensive literature review, it was found that no **positive pressure effect on the mass transfer in high pressure bubble columns, provided the same molar flowrate of gas is injected.** This is because the **positive pressure effect on the solubility is always compensated by the negative impact on the gas holdup.** However, when a trickled bed reactor is used, the interfacial area is not impacted by the pressure, leading to a positive pressure effect on the mass transfer. In the second section, the 1D model was applied to another reactor geometry – industrial-scale stirred tank fermenter. The reference case was a well-documented 22 m^3 Stavanger fermenter. It was found that the 1D model was able to describe the bubbly flow in the tall stirred tank reactor as the predicted overall gas holdup and substrate gradients were very close to the literature data (experimental results and CFD numerical predictions), as the closure on the bubble drag coefficient was taken the same as the CFD model. For the yeast fermentation, the same metabolic model was implemented in the 1D model. In general, the axial gradients of oxygen and glucose were well predicted. The glucose concentration was also compared with the experimental measurements of Larsson et al. (1996) and the CFD Euler-Lagrange predictions of Haringa et al. (2017). **Interestingly, both CFD and 1D models underpredicted the glucose concentration near the feed, reflecting the need to refine the biological model.** Through this study, it was also revealed that dissolved CO_2 concentration predicted by the CFD model was overly high than that obtained from usual yeast fermentation operation. This could be due to the pressure taken for the solubility calculation was the hydrostatic pressure or absolute pressure instead of CO_2 partial pressure, leading to a lower stripping rate, and hence a higher dissolved CO_2 concentration. As the substrate gradients were well predicted, it demonstrated that the **1D model could be used as a practical tool for designing bioreactors and performance diagnostics since the computational costs are lower.** Moreover, sensitivity analysis of the uncertain biokinetics can be performed using the 1D model to narrow down the uncertainties before shifting the investigation to a more detailed CFD-based model.

Chapter 5 is devoted to the study of reactive bubble columns using the spatio-temporal 1D model. The work of Darmana et al. (2007) was chosen as the reference case for the reactive bubbly flow analysis. This reference case highlights detailed experimental and numerical investigations of CO_2 chemisorption in aqueous NaOH solution. It was found that the gas-liquid hydrodynamics (gas holdup, bubble diameter profile, reactive mass transfer flux) in a pseudo-2D reactive bubble column of Darmana et al. (2007) can be reproduced using the 1D model provided the closure models applied are

appropriate, i.e. inlet bubble diameter of 5.5 mm, drift flux hydrodynamics model (C_0 and u_{recirc} derived from Darmana et al. (2007) spatial-averaged CFD results), axial dispersions, mass transfer coefficient of Brauer (1979), and the latest enhancement factor and three reaction pathways proposed by Krauβ and Rzehak (2017). Asymptotic models and a new analytical solution have been reported to describe the transient bubble shrinkage and CO_2 chemisorption process. **The pH temporal evolution can be dissected into three periods and each period can be characterised by a simplified relation. The asymptotic models reveal that the first period is influenced by enhanced mass transfer, whilst the two last periods are mostly controlled by volumetric mass transfer. The bubble shrinkage can be described by an analytical solution relating the mass transfer characteristic time and convection characteristic time. Since the CO_2 chemisorption is controlled by the interfacial mass transfer, the most important parameters are k_L and d_b.** The enhancement factor model only plays a role when the pH and the reactive mass transfer rate are high (at the start of the process).

In Chapter 6, Eulerian CFD models for biological methanation were developed and the simulations were performed on the pilot and industrial scales. The CFD model was first applied to a pilot-scale bubble column and the CFD predictions were compared with the experimental data and 1D model results. In this section, **CFD models provide closures in terms of simplified hydrodynamics to the 1D model to describe the non-homogeneous flow generated by the heterogenous sparger.** In addition, analytical solutions for predicting biological methanation efficiency, particularly methane purity and productivity were proposed based on gas phase mass balance. **The analytical solution reveals that the key to high CH_4 purity and productivity is to obtain a high hydrogen conversion rate by means of an elevated mass transfer rate at high inlet gas flowrate.** The simplified analytical solution also yielded good quality predictions of the reactor performance when it was applied to a literature case in a similar reactor configuration. Then, the complete fully-resolved CFD model was extended to the large-scale biological methanation reactor of Electrochaea. Again, a similar result with the 1D model and literature data was obtained, signifying the large-scale CFD simulation was correctly implemented. **Due to the nature of the bioreaction, a huge depletion of gas was obtained from the inlet to the outlet.** This causes density gradients and contributes to the instabilities of the two-phase flow. In this regard, the CFD model has a better edge over the 1D model in capturing spatiotemporal gradients and transient phenomena. Through this example**, it is demonstrated that the practical use of CFD models of bioreactor modelling depends on the following factors: (i) the stoichiometry of the reaction when both substrate and product are in the gas phase (ii) the origin of the limitation and (iii) the reactor scale.** Indeed, depending on the substrate feeding method, the bioreaction could have different limitation mechanisms (liquid mixing or mass transfer), leading to the formation of liquid or gas spatial

gradients in large-scale bioreactors. For bioreaction that leads to gas depletion or expansion, density gradients will be formed. The ability to capture precisely these gradients at high spatial resolution is the driving reason to use CFD for large-scale bioreactor modelling. Once the hydrodynamics are resolved, the coupling with the bioreaction dynamics by either the Lagrangian tracking or the population balance approach can be performed by more computationally affordable hydrodynamic model such as compartment models, as has been typically done in the literature (Haringa et al., 2022; Pigou and Morchain, 2015). The study in Chapter 6 showed that **both CFD and 1D models are valuable and complementary tools for bioreactor design.** In this regard, the 1D model provides fast and satisfactory predictions whilst the CFD model provides fine resolution of bubbly flow and interactions between phases.

The major achievement of this work was to propose a **dynamic gas-liquid spatio-temporal 1D model** that encompasses (i) axial-dependent hydrodynamics variables such as gas holdup and bubble diameter, (ii) two-way coupling of hydrodynamics and (bio)reactive mass transfer, and (iii) multispecies mass transfer. From the 1D simulations, macroscopic models at the reactor scale were developed for asymptotic cases, leading to analytical solutions and correlations that provide insights into the controlling parameters of the chemical and biochemical processes. At the same time, mesoscopic models with a finer resolution than the 1D model, i.e. the CFD model was developed for biological methanation. The CFD model unravels the details of the local hydrodynamics and spatiotemporal heterogeneities in a 3D representation which cannot be obtained by the 1D model.

In short, through this PhD thesis, efficient numerical modelling tools (0D, 1D, and CFD models) have been developed for primarily bubble column applications to gain an understanding of the multiscale physical and biological phenomena to minimise the risk of upscaling the bioprocess. The multiscale modelling strategy has drawn new fundamental insights into multiphase reactor modelling, particularly the use of appropriate models according to the subject of research and the scale of interest, the implementation of suitable closures in the modelling of multiphysics coupling phenomena, and the identification of controlling parameters of such processes. For the three modelling approaches, there is still room left for improvements and additional research and development. The next section details the future outlooks for this work.

7.2 Outlooks

With the 1D model validated in different applications and configurations, several perspectives can be envisaged. The following are some brief discussions on the possible future perspectives.

Generally, the accuracy of the proposed biological methanation model can be improved and enhance their predictive capabilities. In this PhD, the biological methanation studied was limited to the ex-situ configuration which is considered to be more efficient and stable than the in-situ configuration. We recall that in-situ biological methanation refers to the direct injection of hydrogen into an anaerobic digestor whereas ex-situ biological methanation involves a second reactor whereby hydrogen and biogas are being fed into for bio-methanation to take place. If the interest of study is the transient behaviour and the stability of the bioreactor, additional equations need to be considered. Indeed, the pH dynamics were not solved as pH increase is less problematic in an ex-situ system than in an in-situ system. However, the pH is sensitive to ammoniacal and sulfuric compounds and if the pH dynamics are not well mastered, it would lead to reactor failure. The associated models can be implemented to analyse this behaviour and limit the risk of reactor failure.

Another perspective which involves minor modifications is to adapt the 1D and CFD model framework and closures to expand its use to other applications. Other gas-fed bioprocesses such as syngas fermentation for ethanol or acetate production can be studied using the 1D model. Similarly, the multispecies mass transfer CFD model developed in this work can be extended to bioprocesses involving oxygen uptake and carbon dioxide production, leading to simultaneous gas absorption and desorption. For bioprocesses involving multiple strains it its particularly advantageous to use the 1D model to study the process on the long term so as to access the dynamics of each populations.

In large-scale biological methanation reactors, the CFD model unravels the unsteady flow patterns due to density gradients formed during the bioreaction. It would be interesting to quantify the effect of such spatiotemporal heterogeneities on the bioreaction at a different stage of the process, by performing the simulation at different biomass concentrations. The analysis of these instabilities in terms of oscillation frequency and magnitude can be performed and its impact on mixing and bioreaction can be quantified. A more adapted turbulence model such as large eddy simulation (LES) model could be used to capture the transient flow structure. For that, a finer mesh may also be required to capture the relevant flow structures. However, such high resolution of hydrodynamic aspects require then an equivalent level of description can be developed and validated for the biological phenomena including uptake dynamics and metabolic response to repeated fluctuations. To validate thoroughly the CFD model, local measurements on both fluid dynamics and reaction dynamics are required. Future developments will focus on acquiring new experimental data on biological methanation at the demonstration unit of SOLIDIA.

References

Abro, M., Yu, L., Yu, G., Chen, X., Qazi, A.B., 2021. Experimental investigation of hydrodynamic parameters and bubble characteristics in CO2 absorption column using pure ionic liquid and binary mixtures: Effect of porous sparger and operating conditions. Chemical Engineering Science 229, 116041. https://doi.org/10.1016/j.ces.2020.116041

ADEME, 2018. Un mix de gaz 100% renouvelable en 2050?

Akita, K., Yoshida, F., 1973. Gas holdup and volumetric mass transfer coefficient in bubble columns: effects of liquid properties. Ind. Eng. Chem. Res. 12, 76–80.

Alitalo, A., Niskanen, M., Aura, E., 2015. Biocatalytic methanation of hydrogen and carbon dioxide in a fixed bed bioreactor. Bioresource Technology 196, 600–605. https://doi.org/10.1016/j.biortech.2015.08.021

Amaral, A., Gillot, S., Garrido-Baserba, M., Filali, A., Karpinska, A.M., Plósz, B.G., De Groot, C., Bellandi, G., Nopens, I., Takács, I., Lizarralde, I., Jimenez, J.A., Fiat, J., Rieger, L., Arnell, M., Andersen, M., Jeppsson, U., Rehman, U., Fayolle, Y., Amerlinck, Y., Rosso, D., 2019. Modelling gas–liquid mass transfer in wastewater treatment: when current knowledge needs to encounter engineering practice and vice versa. Water Science and Technology 80, 607–619. https://doi.org/10.2166/wst.2019.253

Angelidaki, I., Treu, L., Tsapekos, P., Luo, G., Campanaro, S., Wenzel, H., Kougias, P.G., 2018. Biogas upgrading and utilization: Current status and perspectives. Biotechnology Advances 36, 452–466. https://doi.org/10.1016/j.biotechadv.2018.01.011

Angenent, L.T., Usack, J.G., Xu, J., Hafenbradl, D., Posmanik, R., Tester, J.W., 2018. Integrating electrochemical, biological, physical, and thermochemical process units to expand the applicability of anaerobic digestion. Bioresource Technology 247, 1085–1094. https://doi.org/10.1016/j.biortech.2017.09.104

Antal, S.P., Lahey, R.T., Flaherty, J.E., 1991. Analysis of phase distribution in fully developed laminar bubbly two-phase flow. International Journal of Multiphase Flow 17, 635–652. https://doi.org/10.1016/0301-9322(91)90029-3

Aryal, N., Kvist, T., Ammam, F., Pant, D., Ottosen, L.D.M., 2018. An overview of microbial biogas enrichment. Bioresource Technology 264, 359–369. https://doi.org/10.1016/j.biortech.2018.06.013

Azizi, S., Yadav, A., Lau, Y.M., Hampel, U., Roy, S., Schubert, M., 2019. Hydrodynamic correlations for bubble columns from complementary UXCT and RPT measurements in identical geometries and conditions. Chemical Engineering Science 208, 115099. https://doi.org/10.1016/j.ces.2019.07.017

Bach, C., Yang, J., Larsson, H., Stocks, S.M., Gernaey, K.V., Albaek, M.O., Krühne, U., 2017. Evaluation of mixing and mass transfer in a stirred pilot scale bioreactor utilizing CFD. Chemical Engineering Science 171, 19–26. https://doi.org/10.1016/j.ces.2017.05.001

Bardin-Monnier, N., Guiraud, P., Gourdon, C., 2003. Lagrangian simulations contribution to the knowledge of discs and doughnuts pulsed solvent extraction columns hydrodynamics.

Chemical Engineering and Processing: Process Intensification 42, 503–516. https://doi.org/10.1016/S0255-2701(02)00072-7

Bashiri, H., Bertrand, F., Chaouki, J., 2016. Development of a multiscale model for the design and scale-up of gas/liquid stirred tank reactors. Chemical Engineering Journal 297, 277–294. https://doi.org/10.1016/j.cej.2016.03.102

Bassani, I., Kougias, P.G., Angelidaki, I., 2016. In-situ biogas upgrading in thermophilic granular UASB reactor: key factors affecting the hydrogen mass transfer rate. Bioresource Technology 221, 485–491. https://doi.org/10.1016/j.biortech.2016.09.083

Bassani, I., Kougias, P.G., Treu, L., Angelidaki, I., 2015. Biogas Upgrading via Hydrogenotrophic Methanogenesis in Two-Stage Continuous Stirred Tank Reactors at Mesophilic and Thermophilic Conditions. Environ. Sci. Technol. 49, 12585–12593. https://doi.org/10.1021/acs.est.5b03451

Bassani, I., Kougias, P.G., Treu, L., Porté, H., Campanaro, S., Angelidaki, I., 2017. Optimization of hydrogen dispersion in thermophilic up-flow reactors for ex situ biogas upgrading. Bioresource Technology 234, 310–319. https://doi.org/10.1016/j.biortech.2017.03.055

Bauer, M., Eigenberger, G., 2001. Multiscale modeling of hydrodynamics, mass transfer and reaction in bubble column reactors. Chemical Engineering Science 56, 1067.

Bauer, M., Eigenberger, G., 1999. A concept for multi-scale modeling of bubble columns and loop reactors. Chemical Engineering Science 54, 5109.

Becker, S., Sokolichin, A., Eigenberger, G., 1994. Gas--liquid flow in bubble columns and loop reactors: Part II. Comparison of detailed experiments and flow simulations. Chemical Engineering Science 49, 5747.

Besagni, G., 2021. Bubble column fluid dynamics: A novel perspective for flow regimes and comprehensive experimental investigations. International Journal of Multiphase Flow 135, 103510. https://doi.org/10.1016/j.ijmultiphaseflow.2020.103510

Besagni, G., Gallazzini, L., Inzoli, F., 2018a. Effect of gas sparger design on bubble column hydrodynamics using pure and binary liquid phases. Chemical Engineering Science 176, 116–126. https://doi.org/10.1016/j.ces.2017.10.036

Besagni, G., Guédon, G.R., Inzoli, F., 2018b. Computational fluid-dynamic modeling of the mono-dispersed homogeneous flow regime in bubble columns. Nuclear Engineering and Design 331, 222–237. https://doi.org/10.1016/j.nucengdes.2018.03.003

Besagni, G., Guédon, G.R., Inzoli, F., 2015. Annular Gap Bubble Column: Experimental Investigation and Computational Fluid Dynamics Modeling. Journal of Fluids Engineering 138. https://doi.org/10.1115/1.4031002

Besagni, G., Inzoli, F., 2017. The effect of liquid phase properties on bubble column fluid dynamics: Gas holdup, flow regime transition, bubble size distributions and shapes, interfacial areas and foaming phenomena. Chemical Engineering Science, 13th International Conference on Gas-Liquid and Gas-Liquid-Solid Reactor Engineering 170, 270–296. https://doi.org/10.1016/j.ces.2017.03.043

Besagni, G., Inzoli, F., 2016. Bubble size distributions and shapes in annular gap bubble column. Experimental Thermal and Fluid Science 74, 27–48. https://doi.org/10.1016/j.expthermflusci.2015.11.020

Besagni, G., Inzoli, F., De Guido, G., Pellegrini, L.A., 2016. Experimental investigation on the influence of ethanol on bubble column hydrodynamics. Chemical Engineering Research and Design 112, 1–15. https://doi.org/10.1016/j.cherd.2016.06.009

Besagni, G., Inzoli, F., Ziegenhein, T., 2018c. Two-Phase Bubble Columns: A Comprehensive Review. ChemEngineering 2, 13. https://doi.org/10.3390/chemengineering2020013

Besagni, G., Inzoli, F., Ziegenhein, T., Lucas, D., 2019. The pseudo-homogeneous flow regime in large-scale bubble columns: experimental benchmark and computational fluid dynamics modeling. Petroleum, SI: Experimental & Numerical Study of Multiphase Flow Phenomena and Models in Oil & Gas Industry 5, 141–160. https://doi.org/10.1016/j.petlm.2017.12.004

Besagni, G., Inzoli, F., Ziegenhein, T., Lucas, D., 2017. Computational Fluid-Dynamic modeling of the pseudo-homogeneous flow regime in large-scale bubble columns. Chemical Engineering Science 160, 144–160. https://doi.org/10.1016/j.ces.2016.11.031

Bhavaraju, S.M., Mashelkar, R.A., Blanch, H.W., 1978. Bubble motion and mass transfer in non-Newtonian fluids: Part I. Single bubble in power law and Bingham fluids. AIChE Journal 24, 1063–1070. https://doi.org/10.1002/aic.690240618

Bird, R.B., Stewart, W., Lightfoot, E.N., 2002. Transport Phenomena, Second. ed. John Wiley and Sons Ltd, Inc.

Bothe, D., Koebe, M., Wielage, K., Warnecke, H.-J., 2009. VOF-Simulations of Mass Transfer From Single Bubbles and Bubble Chains Rising in Aqueous Solutions. Presented at the ASME/JSME 2003 4th Joint Fluids Summer Engineering Conference, American Society of Mechanical Engineers Digital Collection, pp. 423–429. https://doi.org/10.1115/FEDSM2003-45155

Bouaifi, M., Hebrard, G., Bastoul, D., Roustan, M., 2001. A comparative study of gas hold-up, bubble size, interfacial area and mass transfer coefficients in stirred gas–liquid reactors and bubble columns. Chemical Engineering and Processing: Process Intensification 40, 97–111. https://doi.org/10.1016/S0255-2701(00)00129-X

Boyer, C., Duquenne, A.-M., Wild, G., 2002. Measuring techniques in gas–liquid and gas–liquid–solid reactors. Chemical Engineering Science, Jean-Claude Charpentier Festschrift Issue 57, 3185–3215. https://doi.org/10.1016/S0009-2509(02)00193-8

Brauer, H., 1979. Particle/Fluid Transport Processes. Prog. Chem. Eng. 19, 61–99.

Bredwell, M.D., Worden, R.M., 1998. Mass-transfer properties of microbubbles. 1. Experimental studies. Biotechnol. Prog. 14, 31–38. https://doi.org/10.1021/bp970133x

Breit, F., Mühlbauer, A., von Harbou, E., Hlawitschka, M.W., Bart, H.-J., 2021. A one-dimensional combined multifluid-population balance model for the simulation of batch bubble columns. Chemical Engineering Research and Design 170, 270–289. https://doi.org/10.1016/j.cherd.2021.03.036

Buffo, A., Vanni, M., Marchisio, D.L., 2017. Simulation of a reacting gas–liquid bubbly flow with CFD and PBM: Validation with experiments. Applied Mathematical Modelling 44, 43–60. https://doi.org/10.1016/j.apm.2016.11.010

Burkhardt, M., Busch, G., 2013. Methanation of hydrogen and carbon dioxide. Applied Energy 111, 74–79. https://doi.org/10.1016/j.apenergy.2013.04.080

Burkhardt, M., Jordan, I., Heinrich, S., Behrens, J., Ziesche, A., Busch, G., 2019. Long term and demand-oriented biocatalytic synthesis of highly concentrated methane in a trickle bed reactor. Applied Energy 240, 818–826. https://doi.org/10.1016/j.apenergy.2019.02.076

Burkhardt, M., Koschack, T., Busch, G., 2015. Biocatalytic methanation of hydrogen and carbon dioxide in an anaerobic three-phase system. Bioresource Technology 178, 330–333. https://doi.org/10.1016/j.biortech.2014.08.023

Burns, A.D., Frank, T., Hamill, I., Shi, J.M., 2004. The Favre averaged drag model for turbulence dispersion in Eulerian multi-phase flows. Presented at the Proceddings of the 5th International Conference on Multiphase Flow, Yokohoma, Japan.

Camarasa, E., Carvalho, E., Meleiro, L.A.C., Maciel Filho, R., Domingues, A., Wild, G., Poncin, S., Midoux, N., Bouillard, J., 2001. Development of a complete model for an air-lift reactor. Chemical Engineering Science, 16th International Conference on Chemical Reactor Engineering 56, 493–502. https://doi.org/10.1016/S0009-2509(00)00253-0

Campani, G., Ribeiro, M., Horta, A., Giordano, R., Badino, A., Zangirolami, T., 2015. Oxygen transfer in a pressurized airlift bioreactor | SpringerLink [WWW Document]. URL https://link.springer.com/article/10.1007/s00449-015-1397-4 (accessed 3.16.21).

Carton, J.G., Olabi, A.G., 2010. Wind/hydrogen hybrid systems: Opportunity for Ireland's wind resource to provide consistent sustainable energy supply. Energy, The 3rd International Conference on Sustainable Energy and Environmental Protection, SEEP 2009 35, 4536–4544. https://doi.org/10.1016/j.energy.2010.09.010

Charpentier, J.-C., 1981. Mass-Transfer Rates in Gas-Liquid Absorbers and Reactors, in: Drew, T.B., Cokelet, G.R., Hoopes, J.W., Vermeulen, T. (Eds.), Advances in Chemical Engineering. Academic Press, pp. 1–133. https://doi.org/10.1016/S0065-2377(08)60025-3

Chaumat, H., Billet, A.-M., Delmas, H., 2006. Axial and Radial Investigation of Hydrodynamics in a Bubble Column; Influence of Fluids Flow Rates and Sparger Type. International Journal of Chemical Reactor Engineering 4. https://doi.org/10.2202/1542-6580.1342

Chen, J., Brooks, C.S., 2021. Experiments and CFD simulation of mass transfer and hydrodynamics in a cylindrical bubble column. Chemical Engineering Science 234, 116435. https://doi.org/10.1016/j.ces.2020.116435

Chen, J., Gomez, J.A., Höffner, K., Barton, P.I., Henson, M.A., 2015. Metabolic modeling of synthesis gas fermentation in bubble column reactors. Biotechnology for Biofuels 8, 89. https://doi.org/10.1186/s13068-015-0272-5

Chen, J., Gomez, J.A., Höffner, K., Phalak, P., Barton, P.I., Henson, M.A., 2016. Spatiotemporal modeling of microbial metabolism. BMC Systems Biology 10, 21. https://doi.org/10.1186/s12918-016-0259-2

Chen, P., Sanyal, J., Dudukovic, M.P., 2004. CFD modeling of bubble columns flows: implementation of population balance. Chemical Engineering Science, ISCRE18 59, 5201–5207. https://doi.org/10.1016/j.ces.2004.07.037

Chen, S.L., Gutmanis, F., 1976. Carbon dioxide inhibition of yeast growth in biomass production. Biotechnology and Bioengineering 18, 1455–1462. https://doi.org/10.1002/bit.260181012

Clark, K.N., 1990. The effect of high pressure and temperature on phase distributions in a bubble column. Chemical Engineering Science 45, 2301–2307. https://doi.org/10.1016/0009-2509(90)80109-R

Clift, R., Grace, J.R., Weber, M.E., 1978. Bubbles, drops, and particles, 3. print. ed. Acad. Press, New York, NY.

Cockx, A., Do-Quang, Z., Audic, J.M., Liné, A., Roustan, M., 2001. Global and local mass transfer coefficients in waste water treatment process by computational fluid dynamics. Chemical Engineering and Processing: Process Intensification 40, 187–194. https://doi.org/10.1016/S0255-2701(00)00138-0

Cockx, A., Do-Quang, Z., Liné, A., Roustan, M., 1999. Use of computational fluid dynamics for simulating hydrodynamics and mass transfer in industrial ozonation towers. Chemical Engineering Science 54, 5085–5090. https://doi.org/10.1016/S0009-2509(99)00239-0

Cockx, A., Liné, A., Roustan, M., Do-Quang, Z., Lazarova, V., 1997. Numerical simulation and physical modeling of the hydrodynamics in an air-lift internal loop reactor. Chemical Engineering Science 52, 3787–3793. https://doi.org/10.1016/S0009-2509(97)00224-8

Colombet, D., 2012. Modélisation de réacteurs Gaz-Liquide de type colonne à bulles en conditions industrielles (These de doctorat). Toulouse, INSA.

Colombet, D., Cockx, A., Guiraud, P., Legendre, D., 2013. Experiments and modelling of a draft tube airlift reactor operated at high gas throughputs. Chemical Engineering Science 104, 32–43. https://doi.org/10.1016/j.ces.2013.08.044

Colombet, D., Legendre, D., Cockx, A., Guiraud, P., Risso, F., Daniel, C., Galinat, S., 2011. Experimental study of mass transfer in a dense bubble swarm. Chemical Engineering Science, 10th International Conference on Gas–Liquid and Gas–Liquid–Solid Reactor Engineering 66, 3432–3440. https://doi.org/10.1016/j.ces.2011.01.020

Colombet, D., Legendre, D., Risso, F., Cockx, A., Guiraud, P., 2015. Dynamics and mass transfer of rising bubbles in a homogenous swarm at large gas volume fraction. Journal of Fluid Mechanics 763, 254–285. https://doi.org/10.1017/jfm.2014.672

Copigneaux, P., 1993. Distillation. Absorption - Colonnes garnies. Techniques de l'ingénieur, Procédés chimie - bio - agro | Opérations unitaires. Génie de la réaction chimique 28.

Cuenot, B., Magnaudet, J., Spennato, B., 1997. The effects of slightly soluble surfactants on the flow around a spherical bubble. Journal of Fluid Mechanics 339, 25–53. https://doi.org/10.1017/S0022112097005053

Danckwerts, P.V., Lannus, A., 1970. Gas-Liquid Reactions. J. Electrochem. Soc. 117, 369C. https://doi.org/10.1149/1.2407312

Dani, A., Cockx, A., Guiraud, P., 2006. Direct Numerical Simulation of Mass Transfer from Spherical Bubbles: the Effect of Interface Contamination at Low Reynolds Numbers. International Journal of Chemical Reactor Engineering 4. https://doi.org/10.2202/1542-6580.1304

Dani, A., Cockx, A., Legendre, D., Guiraud, P., 2022. Effect of spheroid bubble interface contamination on gas-liquid mass transfer at intermediate Reynolds numbers: From DNS to Sherwood numbers. Chemical Engineering Science 248, 116979. https://doi.org/10.1016/j.ces.2021.116979

Darmana, D., Henket, R.L.B., Deen, N.G., Kuipers, J.A.M., 2007. Detailed modelling of hydrodynamics, mass transfer and chemical reactions in a bubble column using a discrete bubble model: Chemisorption of CO2 into NaOH solution, numerical and experimental study. Chemical Engineering Science 62, 2556–2575. https://doi.org/10.1016/j.ces.2007.01.065

Datar, R.P., Shenkman, R.M., Cateni, B.G., Huhnke, R.L., Lewis, R.S., 2004. Fermentation of biomass-generated producer gas to ethanol. Biotechnol. Bioeng. 86, 587–594. https://doi.org/10.1002/bit.20071

De Bere, L., 2000. Anaerobic digestion of solid waste: state-of-the-art. Water Science and Technology 41, 283–290. https://doi.org/10.2166/wst.2000.0082

de Medeiros, E.M., Noorman, H., Maciel Filho, R., Posada, J.A., 2020. Production of ethanol fuel via syngas fermentation: Optimization of economic performance and energy efficiency. Chemical Engineering Science: X 5, 100056. https://doi.org/10.1016/j.cesx.2020.100056

de Medeiros, E.M., Posada, J.A., Noorman, H., Filho, R.M., 2019. Dynamic modeling of syngas fermentation in a continuous stirred-tank reactor: Multi-response parameter estimation and process optimization. Biotechnology and Bioengineering 116, 2473–2487. https://doi.org/10.1002/bit.27108

de Swart, J.W.A., Krishna, R., 2002. Simulation of the transient and steady state behaviour of a bubble column slurry reactor for Fischer–Tropsch synthesis. Chemical Engineering and Processing: Process Intensification 41, 35–47. https://doi.org/10.1016/S0255-2701(00)00159-8

Deckwer, Schumpe, 1993. Improved tools for bubble column reactor design and scale-up. Chemical Engineering Science 48, 889–911. https://doi.org/10.1016/0009-2509(93)80328-N

Deckwer, W.-D., 1977. Blasensäulen-Reaktoren – ihre modellmäßige Erfassung und Berechnung. Chemie Ingenieur Technik 49, 213–223. https://doi.org/10.1002/cite.330490305

Deckwer, W.-D., Adler, I., Zaidi, A., 1978. A comprehensive study on co2-interphase mass transfer in vertical cocurrent and countercurrent gas-liquid flow. The Canadian Journal of Chemical Engineering 56, 43–55. https://doi.org/10.1002/cjce.5450560107

Deckwer, W.-D., Burckhart, R., Zoll, G., 1974. Mixing and mass transfer in tall bubble columns. Chemical Engineering Science 29, 2177–2188. https://doi.org/10.1016/0009-2509(74)80025-4

Deckwer, W.-D., Louisi, Y., Zaidi, A., Ralek, M., 1980. Hydrodynamic Properties of the Fischer-Tropsch Slurry Process. Ind. Eng. Chem. Proc. Des. Dev. 19, 699–708. https://doi.org/10.1021/i260076a032

Deen, N., 2001. An Experimental and Computational Study of Fluid Dynamics in Gas-Liquid Chemical Reactors.

Deen, N.G., Solberg, T., Hjertager, B.H., 2001. Large eddy simulation of the Gas–Liquid flow in a square cross-sectioned bubble column. Chemical Engineering Science, Proceedings of the 5th International Conference on Gas-Liquid and Gas-Liquid-Solid Reactor Engineering 56, 6341–6349. https://doi.org/10.1016/S0009-2509(01)00249-4

Deen, N.G., van Sint Annaland, M., Kuipers, J.A.M., 2004. Multi-scale modeling of dispersed gas–liquid two-phase flow. Chemical Engineering Science, Complex Systems and Multi-scale Methodology 59, 1853–1861. https://doi.org/10.1016/j.ces.2004.01.038

Delafosse, A., 2008. Analyse et étude numérique des effets de mélange dans un bioréacteur (These de doctorat). Toulouse, INSA.

Delafosse, A., Collignon, M.-L., Calvo, S., Delvigne, F., Crine, M., Thonart, P., Toye, D., 2014. CFD-based compartment model for description of mixing in bioreactors. Chemical Engineering Science 106, 76–85. https://doi.org/10.1016/j.ces.2013.11.033

Delafosse, A., Delvigne, F., Collignon, M., Crine, M., Thonart, P., Toye, D., 2010. Development of a compartment model based on CFD simulations for description of mixing in bioreactors.

Delvigne, F., Destain, J., Thonart, P., 2006. A methodology for the design of scale-down bioreactors by the use of mixing and circulation stochastic models. Biochemical Engineering Journal 28, 256–268. https://doi.org/10.1016/j.bej.2005.11.009

Delvigne, F., Goffin, P., 2014. Microbial heterogeneity affects bioprocess robustness: Dynamic single-cell analysis contributes to understanding of microbial populations. Biotechnology Journal 9, 61–72. https://doi.org/10.1002/biot.201300119

Deshpande, S.S., Kar, K., Pressler, J., Tebeka, I., Martins, B., Rosenfeld, D., Biggs, J., 2019. Mass transfer estimation for bubble column scale up. Chemical Engineering Science 205, 350–357. https://doi.org/10.1016/j.ces.2019.05.011

Díaz, I., Pérez, C., Alfaro, N., Fdz-Polanco, F., 2015. A feasibility study on the bioconversion of CO2 and H2 to biomethane by gas sparging through polymeric membranes. Bioresource Technology 185, 246–253. https://doi.org/10.1016/j.biortech.2015.02.114

Dijkhuizen, W., Roghair, I., Van Sint Annaland, M., Kuipers, J.A.M., 2010. DNS of gas bubbles behaviour using an improved 3D front tracking model—Drag force on isolated bubbles and comparison with experiments. Chemical Engineering Science 65, 1415–1426. https://doi.org/10.1016/j.ces.2009.10.021

Dupnock, T.L., Deshusses, M.A., 2019. Detailed investigations of dissolved hydrogen and hydrogen mass transfer in a biotrickling filter for upgrading biogas. Bioresource Technology 290, 121780. https://doi.org/10.1016/j.biortech.2019.121780

Dupuy, J., Fargeon, H., Martin-StPaul, N., Pimont, F., Ruffault, J., Guijarro, M., Hernando, C., Madrigal, J., Fernandes, P., 2020. Climate change impact on future wildfire danger and activity in southern Europe: a review. Annals of Forest Science 77, 1–24. https://doi.org/10.1007/s13595-020-00933-5

Electrochaea - Carbon and Energy storage, 2017.

Electrochaea GmbH, n.d. URL http://www.electrochaea.com/ (accessed 3.8.21).

Elqotbi, M., Vlaev, S.D., Montastruc, L., Nikov, I., 2013. CFD modelling of two-phase stirred bioreaction systems by segregated solution of the Euler–Euler model. Computers & Chemical Engineering 48, 113–120. https://doi.org/10.1016/j.compchemeng.2012.08.005

Enfors, S.-O., Jahic, M., Rozkov, A., Xu, B., Hecker, M., Jürgen, B., Krüger, E., Schweder, T., Hamer, G., O'Beirne, D., Noisommit-Rizzi, N., Reuss, M., Boone, L., Hewitt, C., McFarlane, C., Nienow, A., Kovacs, T., Trägårdh, C., Fuchs, L., Revstedt, J., Friberg, P.C., Hjertager, B., Blomsten, G., Skogman, H., Hjort, S., Hoeks, F., Lin, H.-Y., Neubauer, P., van der Lans, R., Luyben, K., Vrabel, P., Manelius, Å., 2001. Physiological responses to mixing in large scale bioreactors. Journal of Biotechnology, Twenty years of the European Federation of Biotechnology 85, 175–185. https://doi.org/10.1016/S0168-1656(00)00365-5

Ertekin, E., Kavanagh, J.M., Fletcher, D.F., McClure, D.D., 2021. Validation studies to assist in the development of scale and system independent CFD models for industrial bubble columns. Chemical Engineering Research and Design 171, 1–12. https://doi.org/10.1016/j.cherd.2021.04.023

European Commission, 2016a. Paris Agreement [WWW Document]. Climate Action - European Commission. URL https://ec.europa.eu/clima/policies/international/negotiations/paris_en (accessed 9.29.21).

European Commission, 2016b. 2030 climate & energy framework [WWW Document]. Climate Action - European Commission. URL https://ec.europa.eu/clima/policies/strategies/2030_en (accessed 9.29.21).

Fadavi, A., Chisti, Y., 2005. Gas–liquid mass transfer in a novel forced circulation loop reactor. Chemical Engineering Journal 112, 73–80. https://doi.org/10.1016/j.cej.2005.06.009

Falcone, M., Bothe, D., Marschall, H., 2018. 3D direct numerical simulations of reactive mass transfer from deformable single bubbles: An analysis of mass transfer coefficients and reaction selectivities. Chemical Engineering Science 177, 523–536. https://doi.org/10.1016/j.ces.2017.11.024

Fan, L.-S., Yang, G.Q., Lee, D.J., Tsuchiya, K., Luo, X., 1999. Some aspects of high-pressure phenomena of bubbles in liquids and liquid–solid suspensions. Chemical Engineering Science 54, 4681–4709. https://doi.org/10.1016/S0009-2509(99)00348-6

Farzan, P., Mistry, B., Ierapetritou, M.G., 2017. Review of the important challenges and opportunities related to modeling of mammalian cell bioreactors. AIChE Journal 63, 398–408. https://doi.org/10.1002/aic.15442

Fayolle, Y., Cockx, A., Gillot, S., Roustan, M., Héduit, A., 2007. Oxygen transfer prediction in aeration tanks using CFD. Chemical Engineering Science, 8th International Conference on Gas-Liquid and Gas-Liquid-Solid Reactor Engineering 62, 7163–7171. https://doi.org/10.1016/j.ces.2007.08.082

Felis, F., Strassl, F., Laurini, L., Dietrich, N., Billet, A.-M., Roig, V., Herres-Pawlis, S., Loubière, K., 2019. Using a bio-inspired copper complex to investigate reactive mass transfer around an oxygen

bubble rising freely in a thin-gap cell. Chemical Engineering Science 207, 1256–1269. https://doi.org/10.1016/j.ces.2019.07.045

Figueras, J., Benbelkacem, H., Dumas, C., Buffiere, P., 2021. "Biomethanation of syngas by enriched mixed anaerobic consortium in pressurized agitated column." Bioresource Technology 338, 125548. https://doi.org/10.1016/j.biortech.2021.125548

Fleischer, C., Becker, S., Eigenberger, G., 1996. Detailed modeling of the chemisorption of CO2 into NaOH in a bubble column. Chemical Engineering Science, Chemical Reaction Engineering: From Fundamentals to Commercial Plants and Products 51, 1715–1724. https://doi.org/10.1016/0009-2509(96)00030-9

Fletcher, D.F., McClure, D.D., Kavanagh, J.M., Barton, G.W., 2017. CFD simulation of industrial bubble columns: Numerical challenges and model validation successes. Applied Mathematical Modelling 44, 25–42. https://doi.org/10.1016/j.apm.2016.08.033

Fredrickson, A.G., Tsuchiya, H.M., 1963. Continuous propagation of microorganisms. AIChE Journal 9, 459–468. https://doi.org/10.1002/aic.690090410

Frössling, N., 1938. Über die verdunstung falender tropfen. Beitr Geophys 52, 170–216.

Gaddis, E.S., Vogelpohl, A., 1986. Bubble formation in quiescent liquids under constant flow conditions. Chemical Engineering Science 41, 97–105. https://doi.org/10.1016/0009-2509(86)85202-2

Garcia-Ochoa, F., Gomez, E., 2009. Bioreactor scale-up and oxygen transfer rate in microbial processes: An overview. Biotechnology Advances 27, 153–176. https://doi.org/10.1016/j.biotechadv.2008.10.006

Geary, N.W., Rice, R.G., 1991. Bubble size prediction for rigid and flexible spargers. AIChE Journal 37, 161–168. https://doi.org/10.1002/aic.690370202

Gemello, L., 2018. Modélisation de l'hydrodynamique des colonnes à bulles selon une approche couplant modèle à deux fluides et bilan de population (These de doctorat). Lyon.

Gemello, L., Cappello, V., Augier, F., Marchisio, D., Plais, C., 2018. CFD-based scale-up of hydrodynamics and mixing in bubble columns. Chemical Engineering Research and Design 136, 846–858. https://doi.org/10.1016/j.cherd.2018.06.026

Gemello, L., Plais, C., Augier, F., Marchisio, D.L., 2019. Population balance modelling of bubble columns under the heterogeneous flow regime. Chemical Engineering Journal 372, 590–604. https://doi.org/10.1016/j.cej.2019.04.109

Gernaey, K.V., Jeppsson, U. (Eds.), 2014. Benchmarking of Control Strategies for Wastewater Treatment Plants. IWA Publishing.

Gernaey, K.V., Lantz, A.E., Tufvesson, P., Woodley, J.M., Sin, G., 2010. Application of mechanistic models to fermentation and biocatalysis for next-generation processes. Trends in Biotechnology 28, 346–354. https://doi.org/10.1016/j.tibtech.2010.03.006

Ghofrani-Isfahani, P., Tsapekos, P., Peprah, M., Kougias, P., Zhu, X., Kovalovszki, A., Zervas, A., Zha, X., Jacobsen, C.S., Angelidaki, I., 2021. Ex-situ biogas upgrading in thermophilic up-flow reactors:

The effect of different gas diffusers and gas retention times. Bioresource Technology 340, 125694. https://doi.org/10.1016/j.biortech.2021.125694

Giovannettone, J.P., Gulliver, J.S., 2008. Gas transfer and liquid dispersion inside a deep airlift reactor. AIChE Journal 54, 850–861. https://doi.org/10.1002/aic.11449

Giovannettone, J.P., Tsai, E., Gulliver, J.S., 2009. Gas void ratio and bubble diameter inside a deep airlift reactor. Chemical Engineering Journal 149, 301–310. https://doi.org/10.1016/j.cej.2008.11.024

Götz, M., Lefebvre, J., Mörs, F., McDaniel Koch, A., Graf, F., Bajohr, S., Reimert, R., Kolb, T., 2016. Renewable Power-to-Gas: A technological and economic review. Renewable Energy 85, 1371–1390. https://doi.org/10.1016/j.renene.2015.07.066

Götz, M., Mörs, F., Baer, K., 2015. Comparison of Biological and Catalytic Methanation for Power-to-Gas Applications [WWW Document]. ResearchGate. URL https://www.researchgate.net/publication/278024062_Comparison_of_Biological_and_Catalytic_Methanation_for_Power-to-Gas_Applications (accessed 9.1.20).

Grimalt-Alemany, A., Skiadas, I.V., Gavala, H.N., 2018. Syngas biomethanation: state-of-the-art review and perspectives. Biofuels, Bioproducts and Biorefining 12, 139–158. https://doi.org/10.1002/bbb.1826

Gruber, M.C., Radl, S., Khinast, J.G., 2015. Rigorous modeling of CO2 absorption and chemisorption: The influence of bubble coalescence and breakage. Chemical Engineering Science 137, 188–204. https://doi.org/10.1016/j.ces.2015.06.008

Guiot, S.R., Cimpoia, R., Carayon, G., 2011. Potential of wastewater-treating anaerobic granules for biomethanation of synthesis gas. Environ. Sci. Technol. 45, 2006–2012. https://doi.org/10.1021/es102728m

Gunyol, O., Mudde, R.F., 2009. Computational Study of Hydrodynamics of a Standard Stirred Tank Reactor and a Large-Scale Multi-Impeller Fermenter. JMC 7. https://doi.org/10.1615/IntJMultCompEng.v7.i6.60

Hadamard, J.S., 1911. Mouvement permanent lent d'une sphere liquide et visqueuse dans un liquid visqueux. Comptes Rendus de l'Academie des Sciences 152, 1735–1738.

Han, L., Al-Dahhan, M.H., 2007. Gas–liquid mass transfer in a high pressure bubble column reactor with different sparger designs. Chemical Engineering Science, Fluidized Bed Applications 62, 131–139. https://doi.org/10.1016/j.ces.2006.08.010

Haringa, C., Deshmukh, A.T., Mudde, R.F., Noorman, H.J., 2017. Euler-Lagrange analysis towards representative down-scaling of a 22m3 aerobic S. cerevisiae fermentation. Chemical Engineering Science, 13th International Conference on Gas-Liquid and Gas-Liquid-Solid Reactor Engineering 170, 653–669. https://doi.org/10.1016/j.ces.2017.01.014

Haringa, C., Tang, W., Deshmukh, A.T., Xia, J., Reuss, M., Heijnen, J.J., Mudde, R.F., Noorman, H.J., 2016. Euler-Lagrange computational fluid dynamics for (bio)reactor scale down: An analysis of organism lifelines. Engineering in Life Sciences 16, 652–663. https://doi.org/10.1002/elsc.201600061

Haringa, C., Tang, W., Noorman, H.J., 2022. Stochastic parcel tracking in an Euler–Lagrange compartment model for fast simulation of fermentation processes. Biotechnology and Bioengineering 119, 1849–1860. https://doi.org/10.1002/bit.28094

Haringa, C., Tang, W., Wang, G., Deshmukh, A.T., van Winden, W.A., Chu, J., van Gulik, W.M., Heijnen, J.J., Mudde, R.F., Noorman, H.J., 2018. Computational fluid dynamics simulation of an industrial P. chrysogenum fermentation with a coupled 9-pool metabolic model: Towards rational scale-down and design optimization. Chemical Engineering Science 175, 12–24. https://doi.org/10.1016/j.ces.2017.09.020

Harmathy, T.Z., 1960. Velocity of large drops and bubbles in media of infinite or restricted extent. AIChE Journal 6, 281–288. https://doi.org/10.1002/aic.690060222

Harteveld, W.K., Mudde, R.F., Van Den Akker, H.E.A., 2003. Dynamics of a Bubble Column: Influence of Gas Distribution on Coherent Structures. The Canadian Journal of Chemical Engineering 81, 389–394. https://doi.org/10.1002/cjce.5450810308

Heavner, B.D., Smallbone, K., Barker, B., Mendes, P., Walker, L.P., 2012. Yeast 5 – an expanded reconstruction of the Saccharomyces cerevisiae metabolic network. BMC Systems Biology 6, 55. https://doi.org/10.1186/1752-0509-6-55

Heavner, B.D., Smallbone, K., Price, N.D., Walker, L.P., 2013. Version 6 of the consensus yeast metabolic network refines biochemical coverage and improves model performance. Database 2013, bat059. https://doi.org/10.1093/database/bat059

Hebrard, G., 1995. Etude de l'influence du distributeur de gaz sur l'hydrodynamique et le transfert de matière gaz-liquide des colonnes à bulles. INSA Toulouse, France.

Heijnen, J.J., Van't Riet, K., 1984. Mass transfer, mixing and heat transfer phenomena in low viscosity bubble column reactors. The Chemical Engineering Journal 28, B21–B42. https://doi.org/10.1016/0300-9467(84)85025-X

Heller, T., 2015. First commercial PtG-plant with biological methanation goes live. MicrobEnergy GmbH, presentation.

Higbie, R., 1935. The Rate of Absorption of a Pure Gas into a Still Liquid during Short Periods of Exposure. Trans. AIChE 31, 365–389.

Hikita, H., Asai, S., Takatsuka, T., 1976. Absorption of carbon dioxide into aqueous sodium hydroxide and sodium carbonate-bicarbonate solutions. The Chemical Engineering Journal 11, 131–141. https://doi.org/10.1016/S0300-9467(76)80035-4

Hikita, H., Asai, S., Tanigawa, K., Segawa, K., Kitao, M., 1981. The volumetric liquid-phase mass transfer coefficient in bubble columns. The Chemical Engineering Journal, An International Journal of Research and Development 22, 61–69. https://doi.org/10.1016/0300-9467(81)85006-X

Hissanaga, A.M., Padoin, N., Paladino, E.E., 2020. Mass transfer modeling and simulation of a transient homogeneous bubbly flow in a bubble column. Chemical Engineering Science 218, 115531. https://doi.org/10.1016/j.ces.2020.115531

Hlawitschka, M., Drefenstedt, S., Bart, H., 2016. Local Analysis of CO2 Chemisorption in a Rectangular Bubble Column Using a Multiphase Euler-Euler CFD Code. Journal of Chemical Engineering & Process Technology 7. https://doi.org/10.4172/2157-7048.1000300

Hlawitschka, M.W., Kováts, P., Zähringer, K., Bart, H.-J., 2017. Simulation and experimental validation of reactive bubble column reactors. Chemical Engineering Science, 13th International Conference on Gas-Liquid and Gas-Liquid-Solid Reactor Engineering 170, 306–319. https://doi.org/10.1016/j.ces.2016.12.053

Hori, Y., Hayashi, K., Hosokawa, S., Tomiyama, A., 2017. Mass transfer from single carbon-dioxide bubbles in electrolyte aqueous solutions in vertical pipes. International Journal of Heat and Mass Transfer 115, 663–671. https://doi.org/10.1016/j.ijheatmasstransfer.2017.07.087

Hosokawa, S., Tomiyama, A., Misaki, S., Hamada, T., 2009. Lateral Migration of Single Bubbles Due to the Presence of Wall. Presented at the ASME 2002 Joint U.S.-European Fluids Engineering Division Conference, American Society of Mechanical Engineers Digital Collection, pp. 855–860. https://doi.org/10.1115/FEDSM2002-31148

Hosokawa, S., Tomiyama, A., Misaki, S., Hamada, T., 2002. Lateral migration of single bubbles due to the presence of wall, in: Proceedings of ASME Fluids Engineering Division Summer Meeting.

Huang, Q., Yang, C., Yu, G., Mao, Z.-S., 2010. CFD simulation of hydrodynamics and mass transfer in an internal airlift loop reactor using a steady two-fluid model. Chemical Engineering Science 65, 5527–5536. https://doi.org/10.1016/j.ces.2010.07.021

Huang, Z., Legendre, D., Guiraud, P., 2011. A new experimental method for determining particle capture efficiency in flotation. Chemical Engineering Science 66, 982–997. https://doi.org/10.1016/j.ces.2010.12.006

Huang, Z., McClure, D.D., Barton, G.W., Fletcher, D.F., Kavanagh, J.M., 2018. Assessment of the impact of bubble size modelling in CFD simulations of alternative bubble column configurations operating in the heterogeneous regime. Chemical Engineering Science 186, 88–101. https://doi.org/10.1016/j.ces.2018.04.025

Huang, Z., Yan, H., Liu, L., Gong, H., Zhou, P., 2021. Numerical modeling of reactive bubbly flows based on Euler-Lagrange approach. Chemical Engineering Science 239, 116640. https://doi.org/10.1016/j.ces.2021.116640

Idogawa, K., Ikeda, K., Fukuda, T., Morooka, S., 1985. Behavior of bubbles in a bubble column under high pressure for air-water system. https://doi.org/10.1252/KAKORONBUNSHU.11.253

IEA Bioenergy, T. 37, 2018. Biological Methanation Demonstration Plant in Allendorf, Germany: An Upgrading Facility for Biogas | Bioenergy. URL https://www.ieabioenergy.com/blog/publications/biological-methanation-demonstration-plant-in-allendorf-germany-an-upgrading-facility-for-biogas/ (accessed 7.15.22).

IEA Data overview [WWW Document], 2019. . IEA. URL https://www.iea.org/data-and-statistics (accessed 7.9.22).

Inkeri, E., Tynjälä, T., 2020. Modeling of CO2 Capture with Water Bubble Column Reactor. Energies 13, 5793. https://doi.org/10.3390/en13215793

Inkeri, E., Tynjälä, T., Laari, A., Hyppänen, T., 2018. Dynamic one-dimensional model for biological methanation in a stirred tank reactor. Applied Energy 209, 95–107. https://doi.org/10.1016/j.apenergy.2017.10.073

Inoue, Kafarov, 1973. Method of determining the coefficient of longitudinal mixing for the continuous phase under conditions of a non flow-through system in high rate extractors. Theoreticheskie Osnovy Khimicheskoi Tekhnologii 550–556.

Ishii, M., Zuber, N., 1979. Drag coefficient and relative velocity in bubbly, droplet or particulate flows. AIChE J. 25, 843–855. https://doi.org/10.1002/aic.690250513

Jain, D., Kuipers, J.A.M., Deen, N.G., 2015. Numerical modeling of carbon dioxide chemisorption in sodium hydroxide solution in a micro-structured bubble column. Chemical Engineering Science 137, 685–696. https://doi.org/10.1016/j.ces.2015.07.025

Jakobsen, H.A., Grevskott, S., Svendsen, H.F., 1997. Modeling of Vertical Bubble-Driven Flows. Ind. Eng. Chem. Res. 36, 4052–4074. https://doi.org/10.1021/ie970276o

Jamialahmadi, M., Müller-Steinhagen, H., Sarrafi, A., Smith, J.M., 2000. Studies of Gas Holdup in Bubble Column Reactors. Chemical Engineering & Technology 23, 919–921. https://doi.org/10.1002/1521-4125(200010)23:10<919::AID-CEAT919>3.0.CO;2-R

Jensen, M.B., Kofoed, M.V.W., Fischer, K., Voigt, N.V., Agneessens, L.M., Batstone, D.J., Ottosen, L.D.M., 2018. Venturi-type injection system as a potential H2 mass transfer technology for full-scale in situ biomethanation. Applied Energy 222, 840–846. https://doi.org/10.1016/j.apenergy.2018.04.034

Jensen, M.B., Ottosen, L.D.M., Kofoed, M.V.W., 2021. H2 gas-liquid mass transfer: A key element in biological Power-to-Gas methanation. Renewable and Sustainable Energy Reviews 147, 111209. https://doi.org/10.1016/j.rser.2021.111209

Jones, R.P., Greenfield, P.F., 1982. Effect of carbon dioxide on yeast growth and fermentation. Enzyme and Microbial Technology 4, 210–223. https://doi.org/10.1016/0141-0229(82)90034-5

Joshi, J.B., Sharma, M.M., 1979. Circulation cell model for bubble columns. Transactions of the Institution of Chemical Engineers 57, 244–251.

Ju, D.-H., Shin, J.-H., Lee, H.-K., Kong, S.-H., Kim, J.-I., Sang, B.-I., 2008. Effects of pH conditions on the biological conversion of carbon dioxide to methane in a hollow-fiber membrane biofilm reactor (Hf–MBfR). Desalination, The Fourth Conference of Aseanian Membrane Society: Part 2The Fourth Conference of Aseanian Membrane Society 234, 409–415. https://doi.org/10.1016/j.desal.2007.09.111

Kantarci, N., Borak, F., Ulgen, K.O., 2005. Bubble column reactors. Process Biochemistry 40, 2263–2283. https://doi.org/10.1016/j.procbio.2004.10.004

Kastens, S., Timmermann, J., Strassl, F., Rampmaier, R.F., Hoffmann, A., Herres-Pawlis, S., Schlüter, M., 2017. Test System for the Investigation of Reactive Taylor Bubbles. Chemical Engineering & Technology 40, 1494–1501. https://doi.org/10.1002/ceat.201700047

Kazakis, N.A., Mouza, A.A., Paras, S.V., 2008. Experimental study of bubble formation at metal porous spargers: Effect of liquid properties and sparger characteristics on the initial bubble size

distribution. Chemical Engineering Journal 137, 265–281. https://doi.org/10.1016/j.cej.2007.04.040

Kemoun, A., Cheng Ong, B., Gupta, P., Al-Dahhan, M.H., Dudukovic, M.P., 2001. Gas holdup in bubble columns at elevated pressure via computed tomography. International Journal of Multiphase Flow 27, 929–946. https://doi.org/10.1016/S0301-9322(00)00037-9

Kentheswaran, K., Dietrich, N., Tanguy, S., Lalanne, B., 2022. Direct numerical simulation of gas-liquid mass transfer around a spherical contaminated bubble in the stagnant-cap regime. International Journal of Heat and Mass Transfer 198, 123325. https://doi.org/10.1016/j.ijheatmasstransfer.2022.123325

Kern, D.M., 1960. The hydration of carbon dioxide. J. Chem. Educ. 37, 14. https://doi.org/10.1021/ed037p14

Kexel, F., v.Kameke, A., Hoffmann, M., Schlüter, M., 2021. The influence of fluid dynamics on the selectivity of fast gas–liquid reactions in methanol. Chemical Engineering and Processing - Process Intensification 108650. https://doi.org/10.1016/j.cep.2021.108650

Kexel, Felix, von Kameke, A., Oßberger, M., Hoffmann, M., Klüfers, P., Schlüter, M., 2021a. Bildgebende UV/VIS-Spektroskopie zur Untersuchung des Einflusses der Fluiddynamik auf die Entstehung von Haupt- und Nebenprodukt in schnellen konkurrierenden konsekutiven Gas-Flüssig-Reaktionen. Chemie Ingenieur Technik 93, 297–305. https://doi.org/10.1002/cite.202000159

Kexel, Felix, von Kameke, A., Tenhaus, J., Hoffmann, M., Schlüter, M., 2021b. Taylor Bubble Study of the Influence of Fluid Dynamics on Yield and Selectivity in Fast Gas-Liquid Reactions. Chemie Ingenieur Technik 93, 830–837. https://doi.org/10.1002/cite.202000241

Kimmel, D.E., Klasson, K.T., Clausen, E.C., Gaddy, J.L., 1991. Performance of trickle-bed bioreactors for converting synthesis gas to methane. Appl Biochem Biotechnol 28, 457. https://doi.org/10.1007/BF02922625

Kipping, R., Kryk, H., Hampel, U., 2021. Experimental analysis of gas phase dynamics in a lab scale bubble column operated with deionized water and NaOH solution under uniform bubbly flow conditions. Chemical Engineering Science 229, 116056. https://doi.org/10.1016/j.ces.2020.116056

Kipping, R., Kryk, H., Schleicher, E., Gustke, M., Hampel, U., 2017. Application of a Wire-Mesh Sensor for the Study of Chemical Species Conversion in a Bubble Column. Chemical Engineering & Technology 40, 1425–1433. https://doi.org/10.1002/ceat.201700005

Kougias, P.G., Treu, L., Benavente, D.P., Boe, K., Campanaro, S., Angelidaki, I., 2017. Ex-situ biogas upgrading and enhancement in different reactor systems. Bioresource Technology 225, 429–437. https://doi.org/10.1016/j.biortech.2016.11.124

Kováts, P., Thévenin, D., Zähringer, K., 2017. Investigation of Mass Transfer and Hydrodynamics in a Model Bubble Column. Chemical Engineering & Technology 40, 1434–1444. https://doi.org/10.1002/ceat.201600679

Krauß, M., Rzehak, R., 2018. Reactive absorption of CO2 in NaOH: An Euler-Euler simulation study. Chemical Engineering Science 181, 199–214. https://doi.org/10.1016/j.ces.2018.01.009

Krauβ, M., Rzehak, R., 2017. Reactive absorption of CO2 in NaOH: Detailed study of enhancement factor models. Chemical Engineering Science 166, 193–209. https://doi.org/10.1016/j.ces.2017.03.029

Krepper, D.E., Rzehak, D.R., Lucas, D.D., Ziegenhein, T., 2014. Closure relations for CFD simulation of bubble columns.

Krepper, E., Reddy Vanga, B.N., Zaruba, A., Prasser, H.-M., Lopez de Bertodano, M.A., 2007. Experimental and numerical studies of void fraction distribution in rectangular bubble columns. Nuclear Engineering and Design 237, 399–408. https://doi.org/10.1016/j.nucengdes.2006.07.009

Krepper, E., Rzehak, R., Lucas, D., 2018. Validation of a closure model framework for turbulent bubbly two-phase flow in different flow situations. Nuclear Engineering and Design 340, 388–404. https://doi.org/10.1016/j.nucengdes.2018.09.042

Krishna, R., 2000. A Scale-Up Strategy for a Commercial Scale Bubble Column Slurry Reactor for Fischer-Tropsch Synthesis. Oil & Gas Science and Technology - Rev. IFP 55, 359–393. https://doi.org/10.2516/ogst:2000026

Krishna, R., Urseanu, M.I., van Baten, J.M., Ellenberger, J., 1999. Influence of scale on the hydrodynamics of bubble columns operating in the churn-turbulent regime: experiments vs. Eulerian simulations. Chemical Engineering Science 54, 4903–4911. https://doi.org/10.1016/S0009-2509(99)00211-0

Krishna, R., van Baten, J.M., 2003. Mass transfer in bubble columns. Catalysis Today, Catalysis in Multiphase Reactors 79–80, 67–75. https://doi.org/10.1016/S0920-5861(03)00046-4

Kulkarni, A.V., Joshi, J.B., 2011. Design and selection of sparger for bubble column reactor. Part I: Performance of different spargers. Chemical Engineering Research and Design 89, 1972–1985. https://doi.org/10.1016/j.cherd.2011.01.004

Kumar, A., Degaleesan, T.E., Laddha, G.S., Hoelscher, H.E., 1976. Bubble swarm characteristics in bubble columns. The Canadian Journal of Chemical Engineering 54, 503–508. https://doi.org/10.1002/cjce.5450540525

Kuschel, M., Siebler, F., Takors, R., 2017. Lagrangian Trajectories to Predict the Formation of Population Heterogeneity in Large-Scale Bioreactors. Bioengineering 4, 27. https://doi.org/10.3390/bioengineering4020027

Laguillaumie, L., Rafrafi, Y., Moya-Leclair, E., Delagnes, D., Dubos, S., Spérandio, M., Paul, E., Dumas, C., 2022. Stability of ex situ biological methanation of H2/CO2 with a mixed microbial culture in a pilot scale bubble column reactor. Bioresource Technology 354, 127180. https://doi.org/10.1016/j.biortech.2022.127180

Lamont, J.C., Scott, D.S., 1970. An eddy cell model of mass transfer into the surface of a turbulent liquid. AIChE Journal 16, 513–519. https://doi.org/10.1002/aic.690160403

Lapin, A., Müller, D., Reuss, M., 2004. Dynamic Behavior of Microbial Populations in Stirred Bioreactors Simulated with Euler−Lagrange Methods: Traveling along the Lifelines of Single Cells. Ind. Eng. Chem. Res. 43, 4647–4656. https://doi.org/10.1021/ie030786k

Lapin, A., Schmid, J., Reuss, M., 2006. Modeling the dynamics of E. coli populations in the three-dimensional turbulent field of a stirred-tank bioreactor—A structured–segregated approach. Chemical Engineering Science 61, 4783–4797. https://doi.org/10.1016/j.ces.2006.03.003

Lardon, L., Thorberg, D., Krosgaard, L., 2018. Biogaz valorization and efficient energy management [WWW Document]. URL http://powerstep.eu/system/files/generated/files/resource/d3-2-technical-and-economic-analysis-of-biological-methanationdeliverable.pdf

Larsson, G., Törnkvist, M., Wernersson, E.S., Trägårdh, C., Noorman, H., Enfors, S.-O., 1996. Substrate gradients in bioreactors: origin and consequences. Bioprocess Engineering 14, 281–289. https://doi.org/10.1007/BF00369471

Larsson, T., Duran Quintero, C., Gillot, S., Cockx, A., Fayolle, Y., 2022. Development and validation of a comprehensive 1-D model to simulate gas hold-up and gas–liquid transfer in deep air–water bubble columns. Chemical Engineering Science 248, 117210. https://doi.org/10.1016/j.ces.2021.117210

Launder, B., Spalding, D., 1972. Mathematical Models for Turbulence. Waltham: Academic Press.

Laupsien, D., 2017. Hydrodynamics, Mass Transfer and Mixing induced by Bubble Plumes in Viscous Fluids (These de doctorat). Toulouse, INSA.

Laupsien, D., Cockx, A., Line, A., 2017. Bubble Plume Oscillations in Viscous Fluids. Chemical Engineering & Technology 40, 1484–1493. https://doi.org/10.1002/ceat.201600690

Laupsien, D., Le Men, C., Cockx, A., Liné, A., 2019. Image processing for bubble morphology characteristics in diluted bubble swarms. Physics of Fluids 31, 053306. https://doi.org/10.1063/1.5088945

Laupsien, D., Men, C.L., Cockx, A., Liné, A., 2022. Effects of liquid viscosity and bubble size distribution on bubble plume hydrodynamics. Chemical Engineering Research and Design 180, 451–469. https://doi.org/10.1016/j.cherd.2021.09.025

Le Moullec, Y., Gentric, C., Potier, O., Leclerc, J.P., 2010. Comparison of systemic, compartmental and CFD modelling approaches: Application to the simulation of a biological reactor of wastewater treatment. Chemical Engineering Science, 20th International Symposium in Chemical Reaction Engineering—Green Chemical Reaction Engineering for a Sustainable Future 65, 343–350. https://doi.org/10.1016/j.ces.2009.06.035

Lecker, B., Illi, L., Lemmer, A., Oechsner, H., 2017. Biological hydrogen methanation – A review. Bioresource Technology 245, 1220–1228. https://doi.org/10.1016/j.biortech.2017.08.176

Lee, J.C., Kim, J.H., Chang, W.S., Pak, D., 2012. Biological conversion of CO2 to CH4 using hydrogenotrophic methanogen in a fixed bed reactor. J. Chem. Technol. Biotechnol. 87, 844–847. https://doi.org/10.1002/jctb.3787

Legendre, D., Magnaudet, J., 1998. The lift force on a spherical bubble in a viscous linear shear flow. Journal of Fluid Mechanics 368, 81–126. https://doi.org/10.1017/S0022112098001621

Leibson, I., Holcomb, E.G., Cacoso, A.G., Jacmic, J.J., 1956. Rate of flow and mechanics of bubble formation from single submerged orifices. I. Rate of flow studies. AIChE Journal 2, 296–300. https://doi.org/10.1002/aic.690020305

León-Becerril, E., Cockx, A., Liné, A., 2002. Effect of bubble deformation on stability and mixing in bubble columns. Chemical Engineering Science, Jean-Claude Charpentier Festschrift Issue 57, 3283–3297. https://doi.org/10.1016/S0009-2509(02)00199-9

Leonzio, G., 2018. Study of mixing systems and geometric configurations for anaerobic digesters using CFD analysis. Renewable Energy 123, 578–589. https://doi.org/10.1016/j.renene.2018.02.071

Leonzio, G., 2016. Biological Sabatier reaction with CFD analysis. AIP Conference Proceedings 1790, 150028. https://doi.org/10.1063/1.4968767

Letzel, H.M., Schouten, J.C., Krishna, R., van den Bleek, C.M., 1999. Gas holdup and mass transfer in bubble column reactors operated at elevated pressure. Chemical Engineering Science 54, 2237–2246. https://doi.org/10.1016/S0009-2509(98)00418-7

Levich, VG., 1962. Physicochemical hydrodynamics. Prentice-Hall, Englewood Cliffs, NJ.

Li, L., Zhao, Y., Lian, W., Han, C., Zhang, Q., Huang, W., 2021. Review on the Effect of Gas Distributor on Flow Behavior and Reaction Performance of the Bubble/Slurry Reactors. Ind. Eng. Chem. Res. 60, 10835–10853. https://doi.org/10.1021/acs.iecr.1c00609

Li, Xiangan, Griffin, D., Li, Xueliang, Henson, M.A., 2019. Incorporating hydrodynamics into spatiotemporal metabolic models of bubble column gas fermentation. Biotechnology and Bioengineering 116, 28–40. https://doi.org/10.1002/bit.26848

Liao, Y., Lucas, D., 2010. A literature review on mechanisms and models for the coalescence process of fluid particles. Chemical Engineering Science 65, 2851–2864. https://doi.org/10.1016/j.ces.2010.02.020

Liao, Y., Lucas, D., 2009. A literature review of theoretical models for drop and bubble breakup in turbulent dispersions. Chemical Engineering Science 64, 3389–3406. https://doi.org/10.1016/j.ces.2009.04.026

Liao, Y., Ma, T., Liu, L., Ziegenhein, T., Krepper, E., Lucas, D., 2018. Eulerian modelling of turbulent bubbly flow based on a baseline closure concept. Nuclear Engineering and Design 337, 450–459. https://doi.org/10.1016/j.nucengdes.2018.07.021

Lin, T.-J., Tsuchiya, K., Fan, L.-S., 1998. Bubble flow characteristics in bubble columns at elevated pressure and temperature. AIChE Journal 44, 545–560. https://doi.org/10.1002/aic.690440306

Linek, V., Kordač, M., Fujasová, M., Moucha, T., 2004. Gas–liquid mass transfer coefficient in stirred tanks interpreted through models of idealized eddy structure of turbulence in the bubble vicinity. Chemical Engineering and Processing: Process Intensification 43, 1511–1517. https://doi.org/10.1016/j.cep.2004.02.009

Linkès, M., 2012. Simulation numérique et modélisation de l'assimilation de substrat par des microorganismes dans un écoulement turbulent (These de doctorat). Toulouse, INPT.

Liu, J., Zhou, P., Liu, L., Chen, S., Song, Y., Yan, H., 2021. CFD modeling of reactive absorption of CO2 in aqueous NaOH in a rectangular bubble column: Comparison of mass transfer and enhancement factor model. Chemical Engineering Science 230, 116218. https://doi.org/10.1016/j.ces.2020.116218

Liu, K., Phillips, J.R., Sun, X., Mohammad, S., Huhnke, R.L., Atiyeh, H.K., 2019. Investigation and Modeling of Gas-Liquid Mass Transfer in a Sparged and Non-Sparged Continuous Stirred Tank Reactor with Potential Application in Syngas Fermentation. Fermentation 5, 75. https://doi.org/10.3390/fermentation5030075

Lochiel, A.C., Calderbank, P.H., 1964. Mass transfer in the continuous phase around axisymmetric bodies of revolution. Chemical Engineering Science 19, 471–484. https://doi.org/10.1016/0009-2509(64)85074-0

Lucas, D., Beyer, M., Kussin, J., Schütz, P., 2010a. Benchmark database on the evolution of two-phase flows in a vertical pipe. Nuclear Engineering and Design, Experiments and CFD Code Applications to Nuclear Reactor Safety (XCFD4NRS) 240, 2338–2346. https://doi.org/10.1016/j.nucengdes.2009.11.010

Lucas, D., Beyer, M., Szalinski, L., Schütz, P., 2010b. A new database on the evolution of air–water flows along a large vertical pipe. International Journal of Thermal Sciences 49, 664–674. https://doi.org/10.1016/j.ijthermalsci.2009.11.008

Lucas, D., Krepper, E., Liao, Y., Rzehak, R., Ziegenhein, T., 2020. General guideline for closure model development for gas-liquid flows in the multi-fluid framework. Nuclear Engineering and Design 357, 110396. https://doi.org/10.1016/j.nucengdes.2019.110396

Luo, G., Angelidaki, I., 2013. Hollow fiber membrane based H2 diffusion for efficient in situ biogas upgrading in an anaerobic reactor. Appl Microbiol Biotechnol 97, 3739–3744. https://doi.org/10.1007/s00253-013-4811-3

Luo, G., Angelidaki, I., 2012. Integrated biogas upgrading and hydrogen utilization in an anaerobic reactor containing enriched hydrogenotrophic methanogenic culture. Biotechnology and Bioengineering 109, 2729–2736. https://doi.org/10.1002/bit.24557

Luo, L., Liu, F., Xu, Y., Yuan, J., 2011. Hydrodynamics and mass transfer characteristics in an internal loop airlift reactor with different spargers. Chemical Engineering Journal 175, 494–504. https://doi.org/10.1016/j.cej.2011.09.078

Maalej, S., Benadda, B., Otterbein, M., 2003. Interfacial area and volumetric mass transfer coefficient in a bubble reactor at elevated pressures. Chemical Engineering Science 58, 2365–2376. https://doi.org/10.1016/S0009-2509(03)00085-X

Mandenius, C.-F., 2016. Challenges for Bioreactor Design and Operation, in: Mandenius, C.-F. (Ed.), Bioreactors. Wiley-VCH Verlag GmbH & Co. KGaA, Weinheim, Germany, pp. 1–34. https://doi.org/10.1002/9783527683369.ch1

Markthaler, S., Plankenbühler, T., Miederer, J., Kolb, S., Herkendell, K., Karl, J., 2022. Combined Two-Model CFD Simulation of Trickle Bed Reactors with Head-Sump Extension: Case Study on Hydrodynamics and Biological Methanation. Ind. Eng. Chem. Res. 61, 4134–4152. https://doi.org/10.1021/acs.iecr.1c04262

Markthaler, S., Plankenbühler, T., Weidlich, T., Neubert, M., Karl, J., 2020. Numerical simulation of trickle bed reactors for biological methanation. Chemical Engineering Science 226, 115847. https://doi.org/10.1016/j.ces.2020.115847

Martin, M.R., Fornero, J.J., Stark, R., Mets, L., Angenent, L.T., 2013. A Single-Culture Bioprocess of Methanothermobacter thermautotrophicus to Upgrade Digester Biogas by CO2-to-CH4 Conversion with H2 [WWW Document]. Archaea. https://doi.org/10.1155/2013/157529

Mata-Alvarez, J., Macé, S., Llabrés, P., 2000. Anaerobic digestion of organic solid wastes. An overview of research achievements and perspectives. Bioresource Technology 74, 3–16. https://doi.org/10.1016/S0960-8524(00)00023-7

Mayr, B., Horvat, P., Nagy, E., Moser, A., 1993. Mixing-models applied to industrial batch bioreactors. Bioprocess Engineering 9, 1–12. https://doi.org/10.1007/BF00389534

McClure, D.D., Aboudha, N., Kavanagh, J.M., Fletcher, D.F., Barton, G.W., 2015a. Mixing in bubble column reactors: Experimental study and CFD modeling. Chemical Engineering Journal 264, 291–301. https://doi.org/10.1016/j.cej.2014.11.090

McClure, D.D., Deligny, J., Kavanagh, J.M., Fletcher, D.F., Barton, G.W., 2014a. Impact of Surfactant Chemistry on Bubble Column Systems. Chemical Engineering & Technology 37, 652–658. https://doi.org/10.1002/ceat.201300711

McClure, D.D., Kavanagh, J.M., Fletcher, D.F., Barton, G.W., 2017. Experimental investigation into the drag volume fraction correction term for gas-liquid bubbly flows. Chemical Engineering Science, 13th International Conference on Gas-Liquid and Gas-Liquid-Solid Reactor Engineering 170, 91–97. https://doi.org/10.1016/j.ces.2016.12.066

McClure, D.D., Kavanagh, J.M., Fletcher, D.F., Barton, G.W., 2016a. Characterizing bubble column bioreactor performance using computational fluid dynamics. Chemical Engineering Science 144, 58–74. https://doi.org/10.1016/j.ces.2016.01.016

McClure, D.D., Kavanagh, J.M., Fletcher, D.F., Barton, G.W., 2015b. Oxygen transfer in bubble columns at industrially relevant superficial velocities: Experimental work and CFD modelling. Chemical Engineering Journal 280, 138–146. https://doi.org/10.1016/j.cej.2015.06.003

McClure, D.D., Kavanagh, J.M., Fletcher, D.F., Barton, G.W., 2014b. Development of a CFD Model of Bubble Column Bioreactors: Part Two – Comparison of Experimental Data and CFD Predictions. Chemical Engineering & Technology 37, 131–140. https://doi.org/10.1002/ceat.201300546

McClure, D.D., Kavanagh, J.M., Fletcher, D.F., Barton, G.W., 2013. Development of a CFD Model of Bubble Column Bioreactors: Part One – A Detailed Experimental Study. Chemical Engineering & Technology 36, 2065–2070. https://doi.org/10.1002/ceat.201300544

McClure, D.D., Lee, A.C., Kavanagh, J.M., Fletcher, D.F., Barton, G.W., 2015c. Impact of Surfactant Addition on Oxygen Mass Transfer in a Bubble Column. Chemical Engineering & Technology 38, 44–52. https://doi.org/10.1002/ceat.201400403

McClure, D.D., Norris, H., Kavanagh, J.M., Fletcher, D.F., Barton, G.W., 2015d. Towards a CFD model of bubble columns containing significant surfactant levels. Chemical Engineering Science 127, 189–201. https://doi.org/10.1016/j.ces.2015.01.025

McClure, D.D., Norris, H., Kavanagh, J.M., Fletcher, D.F., Barton, G.W., 2014c. Validation of a Computationally Efficient Computational Fluid Dynamics (CFD) Model for Industrial Bubble Column Bioreactors. Ind. Eng. Chem. Res. 53, 14526–14543. https://doi.org/10.1021/ie501105m

McClure, D.D., Wang, C., Kavanagh, J.M., Fletcher, D.F., Barton, G.W., 2016b. Experimental investigation into the impact of sparger design on bubble columns at high superficial velocities. Chemical Engineering Research and Design 106, 205–213. https://doi.org/10.1016/j.cherd.2015.12.027

Meegoda, J.N., Li, B., Patel, K., Wang, L.B., 2018. A Review of the Processes, Parameters, and Optimization of Anaerobic Digestion. Int J Environ Res Public Health 15, 2224. https://doi.org/10.3390/ijerph15102224

Mei, R., Klausner, J.F., Lawrence, C.J., 1994. A note on the history force on a spherical bubble at finite Reynolds number. Physics of Fluids 6, 418–420. https://doi.org/10.1063/1.868039

Mendelson, H.D., 1967. The prediction of bubble terminal velocities from wave theory. AIChE Journal 13, 250–253. https://doi.org/10.1002/aic.690130213

Merker, D., Böhm, L., Oßberger, M., Klüfers, P., Kraume, M., 2017. Mass Transfer in Reactive Bubbly Flows – A Single-Bubble Study. Chemical Engineering & Technology 40, 1391–1399. https://doi.org/10.1002/ceat.201600715

Miller, D.N., 1974. Scale-up of agitated vessels gas-liquid mass transfer. AIChE Journal 20, 445–453. https://doi.org/10.1002/aic.690200303

Möller, F., Seiler, T., Lau, Y.M., Weber, Mf., Weber, Mk., Hampel, U., Schubert, M., 2017. Performance comparison between different sparger plate orifice patterns: Hydrodynamic investigation using ultrafast X-ray tomography. Chemical Engineering Journal 316, 857–871. https://doi.org/10.1016/j.cej.2017.01.114

Monod, J., 1950. Technique, Theory and Applications of Continuous Culture. Ann. Inst. Pasteur 79, 390–410.

Moore, D.W., 1963. The boundary layer on a spherical gas bubble. Journal of Fluid Mechanics 16, 161–176. https://doi.org/10.1017/S0022112063000665

Moo-Young, M., Blanch, H.W., 1981. Design of biochemical reactors mass transfer criteria for simple and complex systems, in: Reactors and Reactions, Advances in Biochemical Engineering. Springer, Berlin, Heidelberg, pp. 1–69. https://doi.org/10.1007/3-540-10464-X_16

Morchain, J., 2017. Bioreactor Modeling. Elsevier Ltd.

Morchain, J., Fonade, C., 2009. A structured model for the simulation of bioreactors under transient conditions. AIChE Journal 55, 2973–2984. https://doi.org/10.1002/aic.11906

Morchain, J., Gabelle, J.-C., Cockx, A., 2014. A coupled population balance model and CFD approach for the simulation of mixing issues in lab-scale and industrial bioreactors. AIChE Journal 60, 27–40. https://doi.org/10.1002/aic.14238

Morchain, J., Gabelle, J.-C., Cockx, A., 2013. Coupling of biokinetic and population balance models to account for biological heterogeneity in bioreactors. AIChE Journal 59, 369–379. https://doi.org/10.1002/aic.13820

Morchain, J., Pigou, M., Lebaz, N., 2017. A population balance model for bioreactors combining interdivision time distributions and micromixing concepts. Biochemical Engineering Journal 126, 135–145. https://doi.org/10.1016/j.bej.2016.09.005

Morchain, J., Quedeville, V., Fox, R.O., Villedieu, P., 2021. The closure issue related to liquid–cell mass transfer and substrate uptake dynamics in biological systems. Biotechnology and Bioengineering 118, 2435–2447. https://doi.org/10.1002/bit.27752

Mudde, R.F., Simonin, O., 1999. Two- and three-dimensional simulations of a bubble plume using a two-fluid model. Chemical Engineering Science 54, 5061–5069. https://doi.org/10.1016/S0009-2509(99)00234-1

Munasinghe, P.C., Khanal, S.K., 2012. Syngas fermentation to biofuel: Evaluation of carbon monoxide mass transfer and analytical modeling using a composite hollow fiber (CHF) membrane bioreactor. Bioresource Technology, Membrane Bioreactors (MBRs): State-of-Art and Future 122, 130–136. https://doi.org/10.1016/j.biortech.2012.03.053

Munasinghe, P.C., Khanal, S.K., 2010. Biomass-derived syngas fermentation into biofuels: Opportunities and challenges. Bioresource Technology 101, 5013–5022. https://doi.org/10.1016/j.biortech.2009.12.098

Nadal-Rey, G., McClure, D.D., Kavanagh, J.M., Cassells, B., Cornelissen, S., Fletcher, D.F., Gernaey, K.V., 2022. Computational fluid dynamics modelling of hydrodynamics, mixing and oxygen transfer in industrial bioreactors with Newtonian broths. Biochemical Engineering Journal 177, 108265. https://doi.org/10.1016/j.bej.2021.108265

Nadal-Rey, G., McClure, D.D., Kavanagh, J.M., Cassells, B., Cornelissen, S., Fletcher, D.F., Gernaey, K.V., 2021a. Development of dynamic compartment models for industrial aerobic fed-batch fermentation processes. Chemical Engineering Journal 420, 130402. https://doi.org/10.1016/j.cej.2021.130402

Nadal-Rey, G., McClure, D.D., Kavanagh, J.M., Cornelissen, S., Fletcher, D.F., Gernaey, K.V., 2021b. Understanding gradients in industrial bioreactors. Biotechnology Advances 46, 107660. https://doi.org/10.1016/j.biotechadv.2020.107660

Nauha, E., 2019. Modeling of bioreactors. Aalto University.

Ngu, V., Morchain, J., Cockx, A., 2022a. Spatio-temporal 1D gas–liquid model for biological methanation in lab scale and industrial bubble column. Chemical Engineering Science 251, 117478. https://doi.org/10.1016/j.ces.2022.117478

Ngu, V., Morchain, J., Cockx, A., 2022b. In-depth analysis of reactive bubbly flow using two-way coupled spatio-temporal 1D model. Chemical Engineering Science 261, 117963. https://doi.org/10.1016/j.ces.2022.117963

Nienow, A.W., 1998. Hydrodynamics of Stirred Bioreactors. Applied Mechanics Reviews 51, 3–32. https://doi.org/10.1115/1.3098990

Orth, J.D., Tom M Conrad, Na, J., Lerman, J.A., Nam, H., Feist, A.M., Palsson, B.Ø., 2011. A comprehensive genome-scale reconstruction of Escherichia coli metabolism—2011. Molecular Systems Biology 7, 535. https://doi.org/10.1038/msb.2011.65

Paul, E.L., Atiemo-Obeng, V., Kresta, S.M., 2004. Handbook of Industrial Mixing: Science and Practice. Wiley-Interscience.

Pauss, A., Andre, G., Perrier, M., Guiot, S.R., 1990. Liquid-to-Gas Mass Transfer in Anaerobic Processes: Inevitable Transfer Limitations of Methane and Hydrogen in the Biomethanation Process. Appl Environ Microbiol 56, 1636–1644.

Peillex, J.-P., Fardeau, M.-L., Belaich, J.-P., 1990. Growth of Methanobacterium thermoautotrophicum on H2/CO2: High CH4 productivities in continuous culture. Biomass 21, 315–321. https://doi.org/10.1016/0144-4565(90)90080-4

Peillex, J.-P., Fardeau, M.-L., Boussand, R., Navarro, J.-M., Belaich, J.-P., 1988. Growth of Methanococcus thermolithotrophicus in batch and continuous culture on H2 and CO2: influence of agitation. Appl Microbiol Biotechnol 29, 560–564. https://doi.org/10.1007/BF00260985

Pesci, C., Weiner, A., Marschall, H., Bothe, D., 2018. Computational analysis of single rising bubbles influenced by soluble surfactant. Journal of Fluid Mechanics 856, 709–763. https://doi.org/10.1017/jfm.2018.723

Pfleger, D., Becker, S., 2001. Modelling and simulation of the dynamic flow behaviour in a bubble column. Chemical Engineering Science, 16th International Conference on Chemical Reactor Engineering 56, 1737–1747. https://doi.org/10.1016/S0009-2509(00)00403-6

Pigou, M., 2018. Modélisation du comportement cinétique, des phénomènes de mélange et de transfert locaux, et des effets d'hétérogénéité de population dans les fermenteurs industriels (These de doctorat). Toulouse, INSA.

Pigou, M., Morchain, J., 2015. Investigating the interactions between physical and biological heterogeneities in bioreactors using compartment, population balance and metabolic models. Chemical Engineering Science 126, 267–282. https://doi.org/10.1016/j.ces.2014.11.035

Pigou, M., Morchain, J., Fede, P., Penet, M.-I., Laronze, G., 2017. An assessment of methods of moments for the simulation of population dynamics in large-scale bioreactors. Chemical Engineering Science 171, 218–232. https://doi.org/10.1016/j.ces.2017.05.026

Porté, H., Kougias, P.G., Alfaro, N., Treu, L., Campanaro, S., Angelidaki, I., 2019. Process performance and microbial community structure in thermophilic trickling biofilter reactors for biogas upgrading. Science of The Total Environment 655, 529–538. https://doi.org/10.1016/j.scitotenv.2018.11.289

Pourbaix, M., 1974. Atlas of Electrochemical Equilibria in Aqueous Solutions, 2nd ed. National Association of Corrosion.

Prasher, B.D., Wills, G.B., 1973. Mass Transfer in an Agitated Vessel. Ind. Eng. Chem. Proc. Des. Dev. 12, 351–354. https://doi.org/10.1021/i260047a023

Pratofiorito, G., Hackbarth, M., Mandel, C., Madlanga, S., West, S., Horn, H., Hille-Reichel, A., 2021. A membrane biofilm reactor for hydrogenotrophic methanation. Bioresource Technology 321, 124444. https://doi.org/10.1016/j.biortech.2020.124444

Puiman, L., Abrahamson, B., Lans, R.G.J.M. van der, Haringa, C., Noorman, H.J., Picioreanu, C., 2022. Alleviating mass transfer limitations in industrial external-loop syngas-to-ethanol fermentation. Chemical Engineering Science 259, 117770. https://doi.org/10.1016/j.ces.2022.117770

Putra, R.A., Lucas, D., 2016. CFD Development for Multiphase Flows in HZDR. Publikasi Ilmiah. http://publikasiilmiah.ums.ac.id/handle/11617/7474

Quintero, C.D., 2015. Comportement rhéologique des boues activées : Mesures, modélisation et impact sur le transfert d'oxygène dans les bioréacteurs aérés (phdthesis). INSA de Toulouse.

Rachbauer, L., Voitl, G., Bochmann, G., Fuchs, W., 2016. Biological biogas upgrading capacity of a hydrogenotrophic community in a trickle-bed reactor. Applied Energy 180, 483–490. https://doi.org/10.1016/j.apenergy.2016.07.109

Rados, N., Muthanna H. Al-Dahhan, * and, Duduković, M.P., 2005. Dynamic Modeling of Slurry Bubble Column Reactors. ACS Publications. https://doi.org/10.1021/ie040227t

Rafrafi, Y., Contreras, V., Lefebvre, X., Mengelle, E., Delagnes, D., Dubos, S., Spérandio, M., Palmade, S., Guerré, V., Dumas, C., 2019. Développement et optimisation d'un procédé de méthanation biologique. Presented at the SFGP 2019, Nantes, France.

Rafrafi, Y., Laguillaumie, L., Dumas, C., 2020. Biological Methanation of H2 and CO2 with Mixed Cultures: Current Advances, Hurdles and Challenges. Waste Biomass Valor. https://doi.org/10.1007/s12649-020-01283-z

Rahimi, M.J., Sitaraman, H., Humbird, D., Stickel, J.J., 2018. Computational fluid dynamics study of full-scale aerobic bioreactors: Evaluation of gas–liquid mass transfer, oxygen uptake, and dynamic oxygen distribution. Chemical Engineering Research and Design 139, 283–295. https://doi.org/10.1016/j.cherd.2018.08.033

Rajeshwari, K.V., Balakrishnan, M., Kansal, A., Lata, K., Kishore, V.V.N., 2000. State-of-the-art of anaerobic digestion technology for industrial wastewater treatment. Renewable and Sustainable Energy Reviews 4, 135–156. https://doi.org/10.1016/S1364-0321(99)00014-3

Reactive Bubbly Flows, 2021. . Springer, Switzerland.

Reuter, M., 2013. Power to gas: microbial methanation, a flexible and highly efficient method. MicrobEnergy GmbH, presentation 8.

Royce, P.N.C., Thornhill, N.F., 1991. Estimation of dissolved carbon dioxide concentrations in aerobic fermentations. AIChE Journal 37, 1680–1686. https://doi.org/10.1002/aic.690371111

Rusmanis, D., O'Shea, R., Wall, D.M., Murphy, J.D., 2019. Biological hydrogen methanation systems – an overview of design and efficiency. Bioengineered 10, 604–634. https://doi.org/10.1080/21655979.2019.1684607

Rzehak, R., 2016. Modeling of mass-transfer in bubbly flows encompassing different mechanisms. Chemical Engineering Science 151, 139–143. https://doi.org/10.1016/j.ces.2016.05.024

Rzehak, R., Krauß, M., Kováts, P., Zähringer, K., 2017a. Fluid dynamics in a bubble column: New experiments and simulations. International Journal of Multiphase Flow 89, 299–312. https://doi.org/10.1016/j.ijmultiphaseflow.2016.09.024

Rzehak, R., Krepper, E., 2016. Euler-Euler simulation of mass-transfer in bubbly flows. Chemical Engineering Science 155, 459–468. https://doi.org/10.1016/j.ces.2016.08.036

Rzehak, R., Krepper, E., 2015. Bubbly flows with fixed polydispersity: Validation of a baseline closure model. Nuclear Engineering and Design 287, 108–118. https://doi.org/10.1016/j.nucengdes.2015.03.005

Rzehak, R., Krepper, E., 2013a. CFD modeling of bubble-induced turbulence. International Journal of Multiphase Flow 55, 138–155. https://doi.org/10.1016/j.ijmultiphaseflow.2013.04.007

Rzehak, R., Krepper, E., 2013b. Closure models for turbulent bubbly flows: A CFD study. Nuclear Engineering and Design 265, 701–711. https://doi.org/10.1016/j.nucengdes.2013.09.003

Rzehak, R., Krepper, E., Liao, Y., Ziegenhein, T., Kriebitzsch, S., Lucas, D., 2015. Baseline Model for the Simulation of Bubbly Flows. Chemical Engineering & Technology 38, 1972–1978. https://doi.org/10.1002/ceat.201500118

Rzehak, R., Ziegenhein, T., Kriebitzsch, S., Krepper, E., Lucas, D., 2017b. Unified modeling of bubbly flows in pipes, bubble columns, and airlift columns. Chemical Engineering Science, 12th International Conference on Gas-Liquid and Gas-Liquid-Solid Reactor Engineering 157, 147–158. https://doi.org/10.1016/j.ces.2016.04.056

Sa'adiyah, D.S., Matsuo, Y., Schlüter, M., Kurimoto, R., Hayashi, K., Tomiyama, A., 2021. Effects of chemical absorption on mass transfer from single carbon dioxide bubbles in aqueous sodium hydroxide solution in a vertical pipe. Chemical Engineering Science 245, 116852. https://doi.org/10.1016/j.ces.2021.116852

Sadhal, S.S., Johnson, R.E., 1983. Stokes flow past bubbles and drops partially coated with thin films. Part 1. Stagnant cap of surfactant film – exact solution. Journal of Fluid Mechanics 126, 237–250. https://doi.org/10.1017/S0022112083000130

Sáez, A.E., Márquez, M.A., Roberts, G.W., Carbonell, R.G., 1998. Hydrodynamic model for gas-lift reactors. AIChE Journal 44, 1413–1423. https://doi.org/10.1002/aic.690440619

Sander, R., 2015. Compilation of Henry's law constants (version 4.0) for water as solvent. Atmospheric Chemistry and Physics 15, 4399–4981. https://doi.org/10.5194/acp-15-4399-2015

Sarkizi Shams Hajian, C., Haringa, C., Noorman, H., Takors, R., 2020. Predicting By-Product Gradients of Baker's Yeast Production at Industrial Scale: A Practical Simulation Approach. Processes 8, 1554. https://doi.org/10.3390/pr8121554

Sasaki, S., Uchida, K., Hayashi, K., Tomiyama, A., 2017. Effects of column diameter and liquid height on gas holdup in air-water bubble columns. Experimental Thermal and Fluid Science 82, 359–366. https://doi.org/10.1016/j.expthermflusci.2016.11.032

Sato, Y., Sekoguchi, K., 1975. Liquid velocity distribution in two-phase bubble flow. International Journal of Multiphase Flow 2, 79–95. https://doi.org/10.1016/0301-9322(75)90030-0

Savvas, S., Donnelly, J., Patterson, T., Chong, Z.S., Esteves, S.R., 2017. Biological methanation of CO 2 in a novel biofilm plug-flow reactor: A high rate and low parasitic energy process. Applied Energy 202, 238–247. https://doi.org/10.1016/j.apenergy.2017.05.134

Schaaf, T., Grünig, J., Schuster, M.R., Rothenfluh, T., Orth, A., 2014. Methanation of CO2 - storage of renewable energy in a gas distribution system. Energ Sustain Soc 4, 2. https://doi.org/10.1186/s13705-014-0029-1

Schill, N., van Gulik, W.M., Voisard, D., von Stockar, U., 1996. Continuous cultures limited by a gaseous substrate: Development of a simple, unstructured mathematical model and experimental verification with Methanobacterium thermoautotrophicum. Biotechnology and Bioengineering 51, 645–658. https://doi.org/10.1002/(SICI)1097-0290(19960920)51:6<645::AID-BIT4>3.0.CO;2-H

Schiller, L., Nauman, A., 1933. VDI Zeits, 77, 318.

Schweitzer, J.M., Viguié, J.C., 2009. Reactor Modeling of a Slurry Bubble Column for Fischer-Tropsch Synthesis. Oil & Gas Science and Technology - Rev. IFP 64, 63–77. https://doi.org/10.2516/ogst/2009003

Seifert, A.H., Rittmann, S., Herwig, C., 2014. Analysis of process related factors to increase volumetric productivity and quality of biomethane with Methanothermobacter marburgensis. Applied Energy 132, 155–162. https://doi.org/10.1016/j.apenergy.2014.07.002

Shah, Y.T., Kelkar, B.G., Godbole, S.P., Deckwer, W.-D., 1982. Design parameters estimations for bubble column reactors. AIChE Journal 28, 353–379. https://doi.org/10.1002/aic.690280302

Sharaf, S., Zednikova, M., Ruzicka, M.C., Azzopardi, B.J., 2016. Global and local hydrodynamics of bubble columns – Effect of gas distributor. Chemical Engineering Journal 288, 489–504. https://doi.org/10.1016/j.cej.2015.11.106

Sharman, H., 2005. Why wind power works for Denmark. Proceedings of the Institution of Civil Engineers - Civil Engineering 158, 66–72. https://doi.org/10.1680/cien.2005.158.2.66

Shu, S., Vidal, D., Bertrand, F., Chaouki, J., 2019. Multiscale multiphase phenomena in bubble column reactors: A review. Renewable Energy 141, 613–631. https://doi.org/10.1016/j.renene.2019.04.020

Siebler, F., Lapin, A., Hermann, M., Takors, R., 2019. The impact of CO gradients on C. ljungdahlii in a 125 m3 bubble column: Mass transfer, circulation time and lifeline analysis. Chemical Engineering Science 207, 410–423. https://doi.org/10.1016/j.ces.2019.06.018

Siebler, F., Lapin, A., Takors, R., 2020. Synergistically applying 1-D modeling and CFD for designing industrial scale bubble column syngas bioreactors. Engineering in Life Sciences 20, 239–251. https://doi.org/10.1002/elsc.201900132

Sieborg, M.U., Jønson, B.D., Ashraf, M.T., Yde, L., Triolo, J.M., 2020. Biomethanation in a thermophilic biotrickling filter using cattle manure as nutrient media. Bioresource Technology Reports 9, 100391. https://doi.org/10.1016/j.biteb.2020.100391

Simonin, O., Viollet, P.L., 1990. Prediction of an oxygen droplet pulverization in a compressible subsonic coflowing hydrogen flow. ASME. FED (American Society of Mechanical Engineers. Fluids Engineering Division) 91, 73–82.

Simonnet, M., Gentric, C., Olmos, E., Midoux, N., 2007. Experimental determination of the drag coefficient in a swarm of bubbles. Chemical Engineering Science 62, 858–866. https://doi.org/10.1016/j.ces.2006.10.012

Sin, G., Gernaey, K.V., Lantz, A.E., 2009. Good modeling practice for PAT applications: Propagation of input uncertainty and sensitivity analysis. Biotechnology Progress 25, 1043–1053. https://doi.org/10.1002/btpr.166

Sokolichin, A., Eigenberger, G., 1994. Gas--liquid flow in bubble columns and loop reactors: Part I. Detailed modelling and numerical simulation. Chemical Engineering Science 49, 5735.

Sokolichin, A., Eigenberger, G., Lapin, A., Lübert, A., 1997. Dynamic numerical simulation of gas-liquid two-phase flows Euler/Euler versus Euler/Lagrange. Chemical Engineering Science 52, 611–626. https://doi.org/10.1016/S0009-2509(96)00425-3

Solsvik, J., 2018. Lagrangian modeling of mass transfer from a single bubble rising in stagnant liquid. Chemical Engineering Science 190, 370–383. https://doi.org/10.1016/j.ces.2018.06.002

Sonnleitner, B., Käppeli, O., 1986. Growth of Saccharomyces cerevisiae is controlled by its limited respiratory capacity: Formulation and verification of a hypothesis. Biotechnol Bioeng 28, 927–937. https://doi.org/10.1002/bit.260280620

Sposob, M., Wahid, R., Fischer, K., 2021. Ex-situ biological CO2 methanation using trickle bed reactor: review and recent advances. Rev Environ Sci Biotechnol 20, 1087–1102. https://doi.org/10.1007/s11157-021-09589-7

Stokes, G.G., 2005. Mathematical and physical papers, by George Gabriel Stokes. Reprinted from the original journals and transactions, with additional notes by the author.

Strübing, D., Huber, B., Lebuhn, M., Drewes, J.E., Koch, K., 2017. High performance biological methanation in a thermophilic anaerobic trickle bed reactor. Bioresource Technology 245, 1176–1183. https://doi.org/10.1016/j.biortech.2017.08.088

Strübing, D., Moeller, A.B., Mößnang, B., Lebuhn, M., Drewes, J.E., Koch, K., 2018. Anaerobic thermophilic trickle bed reactor as a promising technology for flexible and demand-oriented H2/CO2 biomethanation. Applied Energy 232, 543–554. https://doi.org/10.1016/j.apenergy.2018.09.225

Sveinbjörnsson, D., Münster, E., 2017. Gas conditioning and grid operation: Upgrading of Biogas to Biomethane with the Addition of Hydrogen from Electrolysis.

Sweere, A.P.J., Giesselbach, J., Barendse, R., de Krieger, R., Honderd, G., Luyben, K.C.A.M., 1988. Modelling the dynamic behaviour ofSaccharomyces cerevisiae and its application in control experiments. Appl Microbiol Biotechnol 28, 116–127. https://doi.org/10.1007/BF00694298

Tabib, M.V., Roy, S.A., Joshi, J.B., 2008. CFD simulation of bubble column—An analysis of interphase forces and turbulence models. Chemical Engineering Journal 139, 589–614. https://doi.org/10.1016/j.cej.2007.09.015

Taborda, M.A., Kipping, R., Hampel, U., Sommerfeld, M., 2021a. Advanced analysis of bubble columns: Comparison of Euler/Lagrange simulations and experiments under CO2 chemisorption conditions. Chemical Engineering Research and Design 170, 389–405. https://doi.org/10.1016/j.cherd.2021.04.020

Taborda, M.A., Sommerfeld, M., 2021. Reactive LES-Euler/Lagrange modelling of bubble columns considering effects of bubble dynamics. Chemical Engineering Journal 407, 127222. https://doi.org/10.1016/j.cej.2020.127222

Taborda, M.A., Sommerfeld, M., Muniz, M., 2021b. LES-Euler/Lagrange modelling of bubble columns considering mass transfer, chemical reactions and effects of bubble dynamics. Chemical Engineering Science 229, 116121. https://doi.org/10.1016/j.ces.2020.116121

Tajsoleiman, T., Spann, R., Bach, C., Gernaey, K.V., Huusom, J.K., Krühne, U., 2019. A CFD based automatic method for compartment model development. Computers & Chemical Engineering 123, 236–245. https://doi.org/10.1016/j.compchemeng.2018.12.015

Takemura, F., Yabe, A., 1999. Rising speed and dissolution rate of a carbon dioxide bubble in slightly contaminated water. Journal of Fluid Mechanics 378, 319–334. https://doi.org/10.1017/S0022112098003358

Talvy, S., Cockx, A., Liné, A., 2007a. Modeling hydrodynamics of gas–liquid airlift reactor. AIChE Journal 53, 335–353. https://doi.org/10.1002/aic.11078

Talvy, S., Cockx, A., Liné, A., 2007b. Modeling of oxygen mass transfer in a gas–liquid airlift reactor. AIChE Journal 53, 316–326. https://doi.org/10.1002/aic.11075

Talvy, S., Cockx, A., Line, A., 2005. Global modelling of a gas–liquid–solid airlift reactor. Chemical Engineering Science, 7th International Conference on Gas-Liquid and Gas-Liquid-Solid Reactor Engineering 60, 5991–6003. https://doi.org/10.1016/j.ces.2005.04.067

Taylor, T.D., Acrivos, A., 1964. On the deformation and drag of a falling viscous drop at low Reynolds number. Journal of Fluid Mechanics 18, 466–476. https://doi.org/10.1017/S0022112064000349

Thema, M., Weidlich, T., Hörl, M., Bellack, A., Mörs, F., Hackl, F., Kohlmayer, M., Gleich, J., Stabenau, C., Trabold, T., Neubert, M., Ortloff, F., Brotsack, R., Schmack, D., Huber, H., Hafenbradl, D., Karl, J., Sterner, M., 2019. Biological CO2-Methanation: An Approach to Standardization. Energies 12, 1670. https://doi.org/10.3390/en12091670

Thibodeaux, L.J., Mackay, D. (Eds.), 2010. Handbook of Chemical Mass Transport in the Environment. CRC Press, Boca Raton. https://doi.org/10.1201/b10262

Toerien, D.F., Hattingh, W.H.J., 1969. Anaerobic digestion I. The microbiology of anaerobic digestion. Water Research 3, 385–416. https://doi.org/10.1016/0043-1354(69)90002-5

Tomiyama, A., Kataoka, I., Zun, I., Sakaguchi, T., 1998. Drag Coefficients of Single Bubbles under Normal and Micro Gravity Conditions. JSME International Journal Series B 41, 472–479. https://doi.org/10.1299/jsmeb.41.472

Tomiyama, A., Matsuoka, T., Fukuda, T., Sakaguchi, T., 1995. A Simple Numerical Method for Solving an Incompressible Two-Fluid Model in a General Curvilinear Coordinate System, in: Serizawa,

A., Fukano, T., Bataille, J. (Eds.), Multiphase Flow 1995. Elsevier, Amsterdam, pp. 241–252. https://doi.org/10.1016/B978-0-444-81811-9.50026-3

Tomiyama, Celata, G.P., Hosokawa, S., Yoshida, S., 2002a. Terminal velocity of single bubbles in surface tension force dominant regime. International Journal of Multiphase Flow 28, 1497–1519. https://doi.org/10.1016/S0301-9322(02)00032-0

Tomiyama, Tamai, H., Zun, I., Hosokawa, S., 2002b. Transverse migration of single bubbles in simple shear flows. Chemical Engineering Science 57, 1849–1858. https://doi.org/10.1016/S0009-2509(02)00085-4

Troshko, A.A., Zdravistch, F., 2009. CFD modeling of slurry bubble column reactors for Fisher–Tropsch synthesis. Chemical Engineering Science 64, 892–903. https://doi.org/10.1016/j.ces.2008.10.022

Ullrich, T., Lemmer, A., 2019. Performance enhancement of biological methanation with trickle bed reactors by liquid flow modulation. GCB Bioenergy 11, 63–71. https://doi.org/10.1111/gcbb.12547

Ullrich, T., Lindner, J., Bär, K., Mörs, F., Graf, F., Lemmer, A., 2018. Influence of operating pressure on the biological hydrogen methanation in trickle-bed reactors. Bioresource Technology 247, 7–13. https://doi.org/10.1016/j.biortech.2017.09.069

Veera, U.P., Joshi, J.B., 1999. Measurement of Gas Hold-Up Profiles by Gamma Ray Tomography: Effect of Sparger Design and Height of Dispersion in Bubble Columns. Chemical Engineering Research and Design 77, 303–317. https://doi.org/10.1205/026387699526232

Versteeg, H.K., Malalasekera, W., 2007. An Introduction to Computational Fluid Dynamics: the Finite Volume Method. Prentice Hall.

Viessmann, 2021. Schmack Biogas Service GmbH and microbEnergy GmbH Become Part of Hitachi Zosen Inova [WWW Document]. URL https://www.viessmann.family/en/newsroom/company/schmack-biogas-and-microbenergy-become-part-of-hitachi-zosen-inova (accessed 7.15.22).

Voelklein, M.A., Rusmanis, D., Murphy, J.D., 2019. Biological methanation: Strategies for in-situ and ex-situ upgrading in anaerobic digestion. Applied Energy 235, 1061–1071. https://doi.org/10.1016/j.apenergy.2018.11.006

Vrábel, P., Van der Lans, R.G.J.M., Cui, Y.Q., Luyben, K.Ch.A.M., 1999. Compartment Model Approach: Mixing in Large Scale Aerated Reactors with Multiple Impellers. Chemical Engineering Research and Design 77, 291–302. https://doi.org/10.1205/026387699526223

Vrábel, P., van der Lans, R.G.J.M., Luyben, K.Ch.A.M., Boon, L., Nienow, A.W., 2000. Mixing in large-scale vessels stirred with multiple radial or radial and axial up-pumping impellers: modelling and measurements. Chemical Engineering Science 55, 5881–5896. https://doi.org/10.1016/S0009-2509(00)00175-5

Vrábel, P., van der Lans, R.G.J.M., van der Schot, F.N., Luyben, K.Ch.A.M., Xu, B., Enfors, S.-O., 2001. CMA: integration of fluid dynamics and microbial kinetics in modelling of large-scale fermentations. Chemical Engineering Journal 84, 463–474. https://doi.org/10.1016/S1385-8947(00)00271-0

Wachi, S., Nojima, Y., 1990. Gas-phase dispersion in bubble columns. Chemical Engineering Science 45, 901–905. https://doi.org/10.1016/0009-2509(90)85012-3

Wallis, G.B., 1969. One-Dimensional Two-Phase Flow. Courier Dover Publications.

Wallis, G.B., 1961. Some hydrodynamic aspects of two-phase flow and boiling. Int. Heat Transfer Conference, Boulder, Colorado, USA 2, 319–325.

Wang, G., Tang, W., Xia, J., Chu, J., Noorman, H., van Gulik, W.M., 2015. Integration of microbial kinetics and fluid dynamics toward model-driven scale-up of industrial bioprocesses. Engineering in Life Sciences 15, 20–29. https://doi.org/10.1002/elsc.201400172

Westerling, A.L., Bryant, B.P., 2008. Climate change and wildfire in California. Climatic Change 87, 231–249. https://doi.org/10.1007/s10584-007-9363-z

Westerterp, A., Swaaij, K.R., Beenackers, W.P.M., 1984. Chemical Reactor Design and Operation. Wiley, New York.

Westerterp, K.R., Swwaij, W.P.M.V., Beenackers, A.A.C.M., 1987. Chemical Reactor Design and Operation. Wiley, New York.

Wilkinson, P.M., 1991. Physical aspects and scale-up of high pressure bubble columns.

Wilkinson, P.M., Haringa, H., Van Dierendonck, L.L., 1994. Mass transfer and bubble size in a bubble column under pressure. Chemical Engineering Science 49, 1417–1427. https://doi.org/10.1016/0009-2509(93)E0022-5

Wilkinson, P.M., Spek, A.P., Dierendonck, L.L. van, 1992. Design parameters estimation for scale-up of high-pressure bubble columns. AIChE Journal 38, 544–554. https://doi.org/10.1002/aic.690380408

Wilkinson, P.M., v. Dierendonck, L.L., 1990. Pressure and gas density effects on bubble break-up and gas hold-up in bubble columns. Chemical Engineering Science 45, 2309–2315. https://doi.org/10.1016/0009-2509(90)80110-Z

Wongwailikhit, K., Warunyuwong, P., Chawaloesphonsiya, N., Dietrich, N., Hébrard, G., Painmanakul, P., 2018. Gas Sparger Orifice Sizes and Solid Particle Characteristics in a Bubble Column – Relative Effect on Hydrodynamics and Mass Transfer. Chemical Engineering & Technology 41, 461–468. https://doi.org/10.1002/ceat.201700293

Wright, M.R., Bach, C., Gernaey, K.V., Krühne, U., 2018. Investigation of the effect of uncertain growth kinetics on a CFD based model for the growth of S. cerevisiae in an industrial bioreactor. Chemical Engineering Research and Design 140, 12–22. https://doi.org/10.1016/j.cherd.2018.09.040

Wu, W.-T., Wu, J.-Y., Jong, J.-Z., 1992. Mass Transfer in an Airlift Reactor with a Net Draft Tube. Biotechnology Progress 8, 465–468. https://doi.org/10.1021/bp00017a015

Xu, B., Jahic, M., Enfors, S.-O., 1999. Modeling of Overflow Metabolism in Batch and Fed-Batch Cultures of Escherichiacoli. Biotechnology Progress 15, 81–90. https://doi.org/10.1021/bp9801087

Xu, J., Grumbine, R.E., Shrestha, A., Eriksson, M., Yang, X., Wang, Y., Wilkes, A., 2009. The Melting Himalayas: Cascading Effects of Climate Change on Water, Biodiversity, and Livelihoods. Conservation Biology 23, 520–530. https://doi.org/10.1111/j.1523-1739.2009.01237.x

Yagi, H., Yoshida, F., 1977. Desorption of carbon dioxide from fermentation broth. Biotechnology and Bioengineering 19, 801–819. https://doi.org/10.1002/bit.260190603

Zahradník, J., Mann, R., Fialová, M., Vlaev, D., Vlaev, S.D., Lossev, V., Seichter, P., 2001. A networks-of-zones analysis of mixing and mass transfer in three industrial bioreactors. Chemical Engineering Science, 16th International Conference on Chemical Reactor Engineering 56, 485–492. https://doi.org/10.1016/S0009-2509(00)00252-9

Zhen, T., Cheng, Y., Li, X., Wang, L., 2019. Bubble shape and rising velocity in viscous liquids at high temperature and pressure. Experimental Thermal and Fluid Science 102, 528–538. https://doi.org/10.1016/j.expthermflusci.2018.12.018

Ziegenhein, T., Rzehak, R., Lucas, D., 2015. Transient simulation for large scale flow in bubble columns. Chemical Engineering Science 122, 1–13. https://doi.org/10.1016/j.ces.2014.09.022

Ziegenhein, T., Rzehak, R., Ma, T., Lucas, D., 2017. Towards a unified approach for modelling uniform and non-uniform bubbly flows. The Canadian Journal of Chemical Engineering 95, 170–179. https://doi.org/10.1002/cjce.22647

Zuber, N., Findlay, J.A., 1965. Average Volumetric Concentration in Two-Phase Flow Systems. Journal of Heat Transfer 87, 453–468. https://doi.org/10.1115/1.3689137

Zwart, K., Nap, J.P., 2017. Power to methane.: state-of-the-art and future prospects of biological power-to-methane (BioP2M) approaches.

Appendix

A simple 2D case with a small geometry is considered for the validation of the CFD workflow before extending to 3D simulations. The simple geometry used is shown in Figure A.1. Since the 1D model is validated extensively, the CFD simulations are also compared with the 1D model.

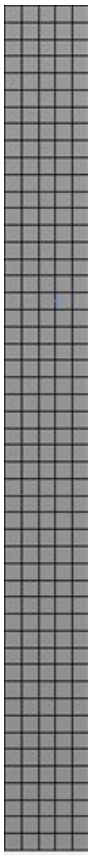

Figure A.1: Rectangular bubble column with a constant mesh size of 2 cm

For the test case, a rectangular 2D bubble column with a width of 0.1 m and a height of 1 m is considered. A constant face mesh of 2 cm was mapped to the geometry.

1.1 Hydrodynamics validation

The bubble column is supposed to operate in the co-current regime with superficial gas and liquid velocities of 0.005 $m.s^{-1}$ and 0.1 $m.s^{-1}$, respectively. We set up the following multiphase models, parameters and boundary conditions for the validation case. The initial conditions are also stated below. We first investigate the transient hydrodynamics of such column with a fixed time step of 0.1s.

- Models - Multiphase
    - Diameter: constant 3mm
    - Phase Interaction: Drag (Schiller Naumann)
- Viscous
    - Laminar
- Materials
    - Phase 1: Water-liquid
    - Phase 2: Air
- Boundary conditions
    - Velocity-inlet: Phase 1
        - Velocity Magnitude: 0.01 m/s
    - Velocity-inlet: Phase 2
        - Velocity Magnitude: 0.25 m/s
        - Volume Fraction: 0.02
    - Pressure-outlet
        - Gauge Pressure: 101325 Pa
    - Symmetry on both sides of the wall
- Operating conditions
    - Operating pressure: 0 Pa
    - Gravity: y – 9.81 m/s^2
    - Temperature: 300 K
- Initialization
    - Phase-1 X velocity: 0
    - Phase-1 Y velocity: 0.01
    - Phase-2 X velocity: 0
    - Phase-2 Y velocity: 0.25
    - Phase-2 Volume Fraction: 0

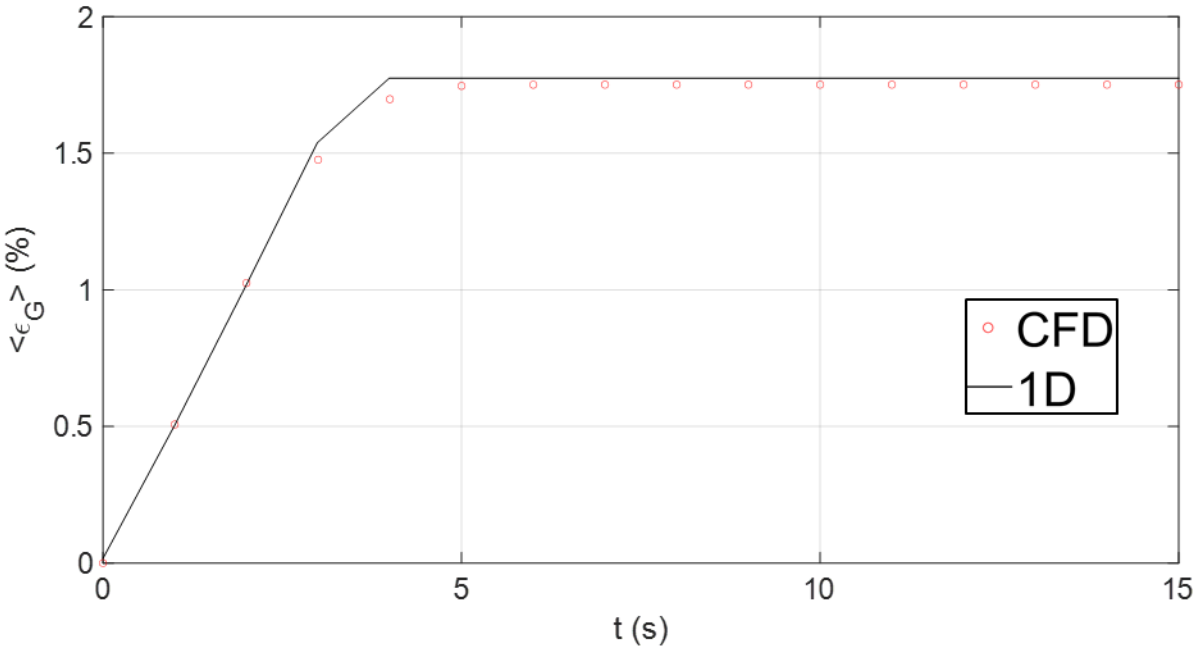

Figure A.2: Transient global gas holdup computed from the 1D and CFD models

Figure A.2 shows the simulation of transient gas loading in the column, starting from the absence of gas, follow by a linear increase, until reaching a stable global gas holdup. At the steady-state, the CFD model yields a global gas holdup of 1.75% compared with 1.78% obtained from the 1D model. After the hydrodynamic validation, the species transport and mass transfer mechanisms are investigated.

1.2 Mass transfer validation

The mass transfer modelling is conducted by solving the species transport equations to evaluate the species concentration. To model species transport in ANSYS Fluent, the energy and species transport equations in the model section have to be activated. The energy equation is not solved (it can be easily deactivated in the method section). Fluent solves for the local mass fraction ($Y_{i,k}$) of each species i in phase k through the solution of the following convection-diffusion equation (ANSYS Fluent, 2021a):

$$\frac{\partial(\rho_k \alpha_k Y_{i,k})}{\partial t} + \nabla \cdot (\rho_k \alpha_k \overrightarrow{u_k} Y_{i,k}) = -\nabla \cdot \alpha_k \overrightarrow{J_{i,k}} + \alpha_k R_{i,k} + S_{i,k} + \dot{m}_{i,k} \quad \text{(A.1)}$$

with $R_{i,k}$ is the homogeneous reaction rate, $S_{i,k}$ is the source of heterogeneous reaction and $\dot{m}_{i,k}$ is the mass transfer source term. The simulations are run in two steps: 1) simulation of species transport until steady-state without considering mass transfer; 2) once the species transport is converged, the mass transfer term is activated. This approach provides better stability and facilitates convergence

than direct simulation of mass transfer. The mass transfer term ($\dot{m}_{i,k}$) can be defined as a constant value or as a species mass transfer term. If species mass transfer is chosen, specifics have to be given for the calculation of mass transfer coefficient (k_L) and the equilibrium concentration (C^*). The mass transfer coefficient can be defined as a constant or using correlations predefined in Fluent or user-defined functions. The C^* can be defined via three methods: Raoult's Law, Henry's Law, and Equilibrium Ratio (ANSYS Fluent, 2021b). In the case of species mass transfer, it is recommended to use the equilibrium ratio method as the formulation is simple and direct to obtain the dissolved equilibrium concentration by knowing the concentration in the gas phase. It is also defined as the dimensionless Henry coefficient of C^*/C_G.

1.2.1 Constant k_L and bubble diameter

The interfacial mass transfer involves the bubble diameter for the calculation of interfacial area. The bubble diameter is first considered as a constant to facilitate the model validation. The k_L coefficient is also kept constant and it is calculated with the Higbie (1935) correlation, considering a bubble diameter of 3 mm, a diffusivity of species at 300 K, and a bubble velocity of 0.29 m.s^{-1} (bubble terminal velocity for a bubble of 3 mm calculated using Schiller Naumann drag coefficient). This yields a k_L for H_2 = 7 x 10^{-4} m.s^{-1} and H_2 = 5 x 10^{-4} m.s^{-1}. For the test case, a 4:1 molar ratio of H_2:CO_2 is applied as the boundary condition to the gas phase at the inlet. Zero mass fraction is applied to both H_2 and CO_2 in the liquid phase.

The same parameters, boundary and inlet conditions are set up in the 1D model. The objective is to compare the results obtained through these two approaches. Since the 1D model has been validated using experimental and literature data, the CFD model should yield similar results to be considered as validated. For each local variable, the mean absolute percentage error (MAPE) is calculated to quantify the difference between 1D and CFD models. It signifies the average relative difference between the two models.

The MAPE is computed as:

$$MAPE = \frac{1}{N}\sum_{i=1}^{N}\left(\frac{y_i^{CFD} - y_i^{1D}}{y_i^{CFD}}\right)$$

With N the discretization point and y any arbitrary comparative parameters between 1D and CFD models.

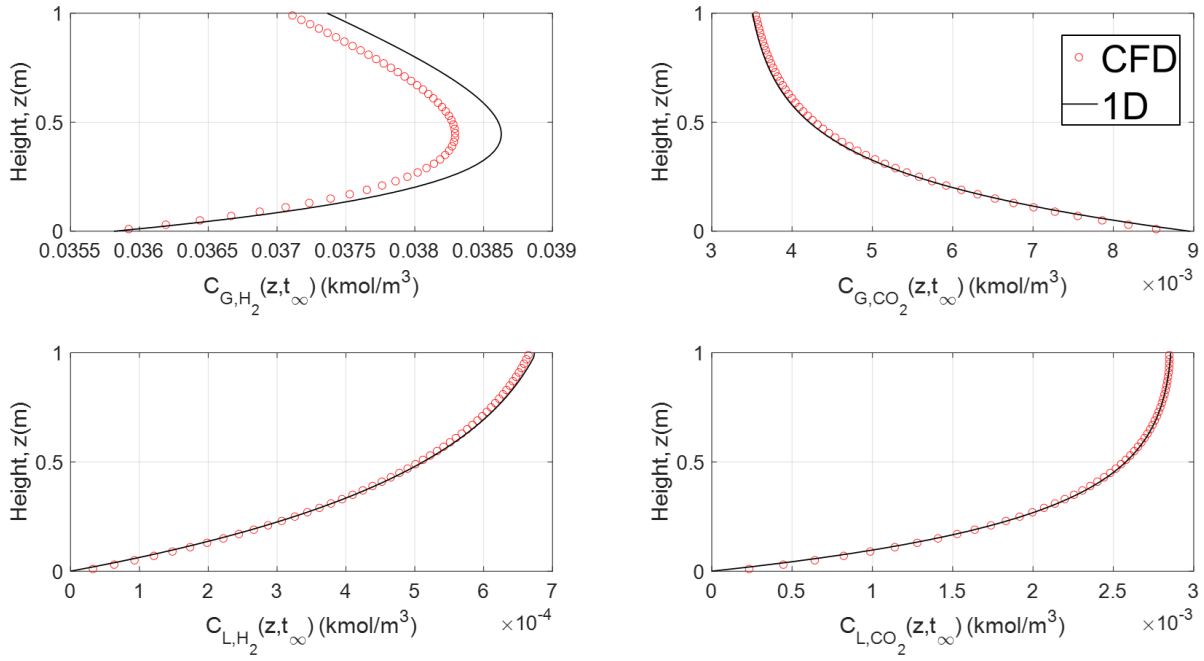

Figure A.3: Species concentrations in the gas and liquid phase

Figure A.3 shows the species concentration profiles obtained by the 1D and CFD models. The CFD model yields very good agreement with that of the 1D model. A weak multispecies mass transfer effect is showcased in this small-scale bubble column. An approximately 8.5% increase in H_2 concentration in the gas phase is shown. This is due to a higher CO_2 dissolution as the concentration drops nearly 60% from the inlet to the outlet. The CO_2 mass transfer enriches the H_2 concentration in the gas phase. Both H_2 and CO_2 liquid concentration increase with height. CO_2 almost reaches its asymptote value – with the equilibrium concentration at roughly 2.85×10^{-3} kmol.m^{-3} ($3.5/1.2 \times 10^{-3}$).

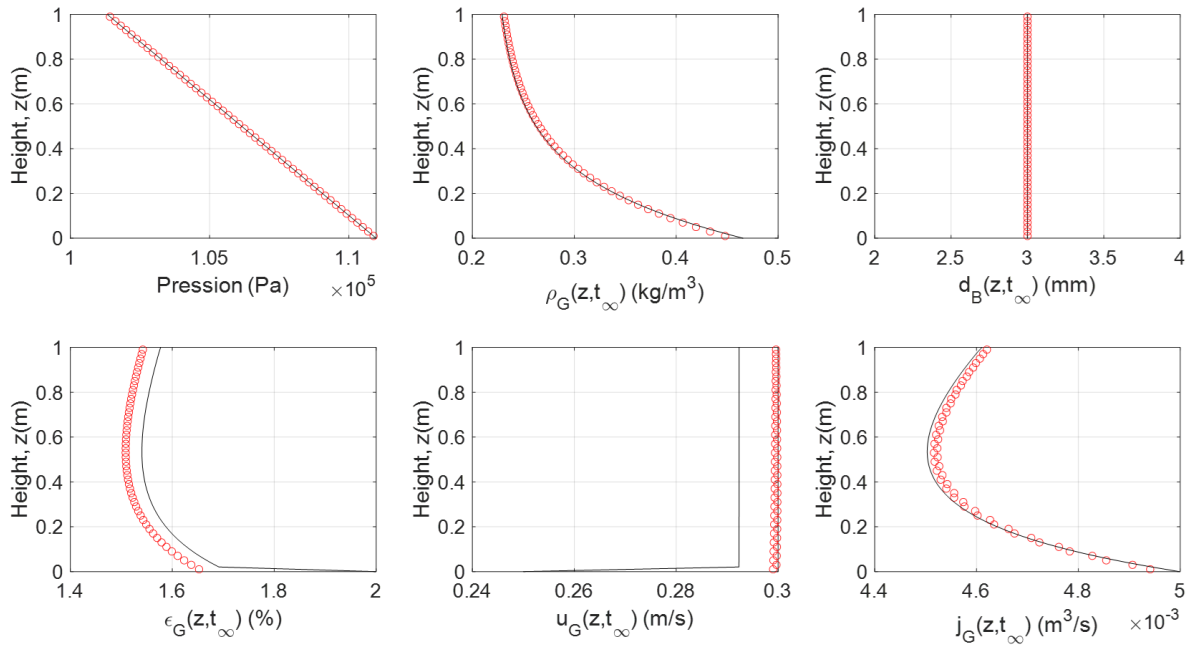

Figure A.4: Hydrodynamic variables at the steady-state

Figure A.4 shows that all hydrodynamic variables are well captured by the CFD model. Due to volume expansion, gas density decreases non-linearly with the height. The gas holdup profile is non-linear, showing the effect of mass transfer and gas expansion. This effect is also shown in the superficial gas velocity profile whereby an initial decrease due to the mass transfer, follow by a slight increase due to volume expansion, according to the ideal gas law. Table A.1 presents the MAPE calculated for each variable. Overall, the error is less than 5% showing that the CFD model is well validated.

Table A.1: MAPE between 1D and CFD model

C_{G,H_2}	C_{G,CO_2}	C_{L,H_2}	C_{L,CO_2}	P	ρ_G	d_B	ε_G	u_G	j_G
0.7%	1.78%	2.13%	1.34%	0.05%	1.29%	-	2.7%	2.67%	0.33%

1.2.3 Non-constant k_L and constant bubble diameter

Now, the CFD model is improved by implementing an expression for calculating the mass transfer coefficient. This can be done by defining a user-defined function (UDF). In this test case, the Higbie (1935) model is used to compute k_L. The UDF considers the local bubble slip velocity in calculating the k_L.

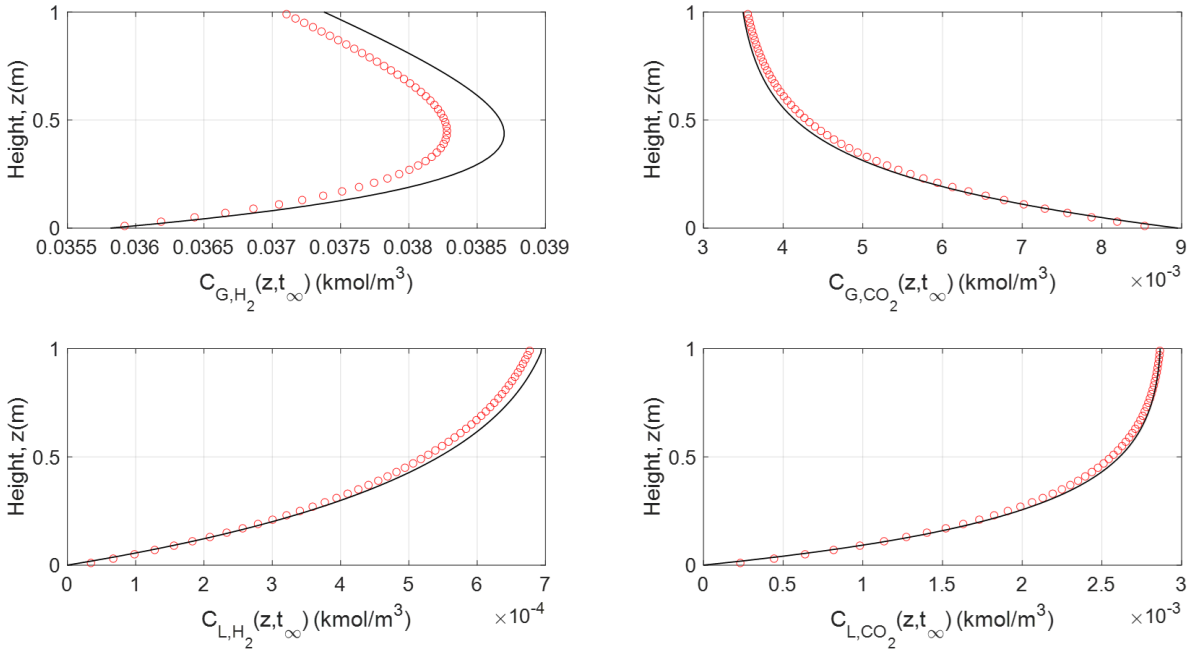

Figure A.5: Species concentrations in the gas and liquid phase with non-constant k_L

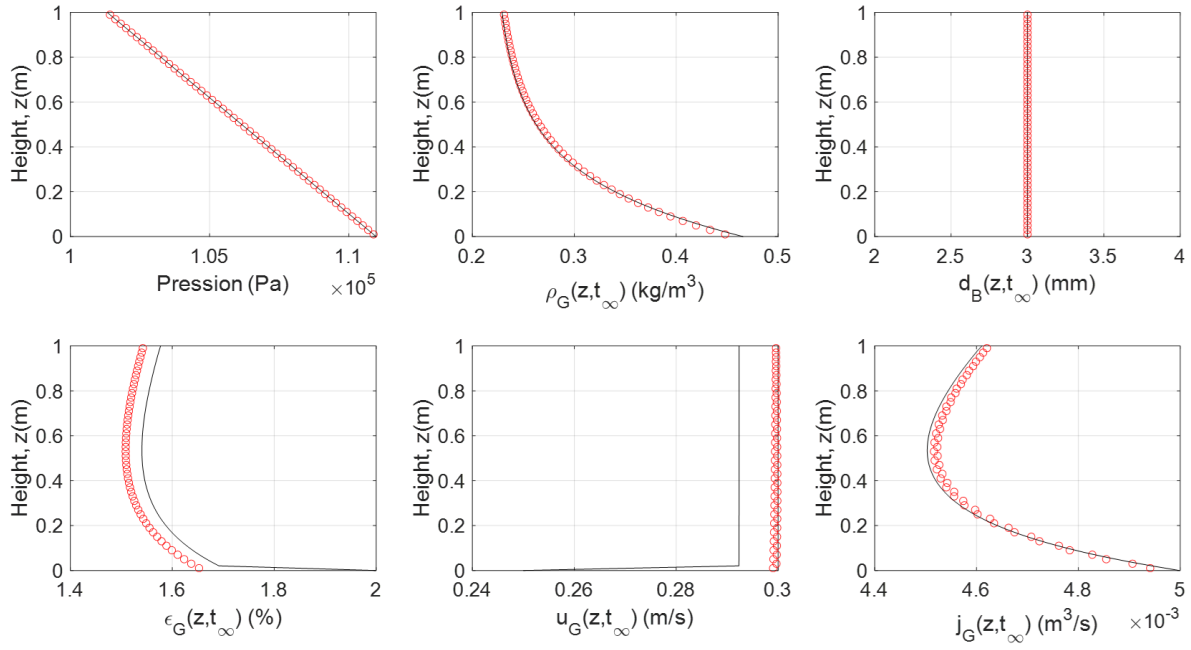

Figure A.6: Hydrodynamic variables at the steady-state with non-constant k_L

As awaited, Figure A.5 and Figure A.6 show that the profiles are practically the same as those obtained in Section 1.2.1. Table A.2 shows that the overall MAPE is still less than 5%, which signifies a very good agreement.

Table A.2: MAPE between 1D and CFD model with non-constant k_L

C_{G,H_2}	C_{G,CO_2}	C_{L,H_2}	C_{L,CO_2}	P	ρ_G	d_B	ε_G	u_G	j_G
0.86%	2.49%	3.83%	2.02%	0.05%	1.79%	-	2.47%	2.69%	0.5%

1.2.4 Constant k_L and non-constant bubble diameter

The bubble diameter remains as the most important parameter in bubble column bioreactor modelling. It decides the bubble terminal velocity, gas holdup, gas residence time, interfacial area, mass transfer and therefore the bioconversion. McClure et al. (2014) assumed a single bubble size in the development of CFD model for industrial bubble column. The assumption is also supported by the narrow bubble size distribution measured experimentally. In the case of homogeneous bubbly flow regime, the bubble size distribution is often narrow and the bubbles are uniformly distributed over the cross-sectional area. For physical absorption studies in bubbly flow, the bubble diameter is very often supposed as constant (Huang et al., 2010; Rzehak and Krepper, 2016). For the case of reactive mass transfer, a two-way coupling problem may occur. The mass transfer will cause the bubbles to lose a significant amount of mass during absorption, this will modify the bubble size and velocity, thus the gas holdup. To tackle this issue, some researchers include the bubble coalescence and breakup process and solve for bubble polydispersity in the CFD model (Buffo et al., 2017; Gemello et al., 2019; Wang and Wang, 2007; Wiemann and Mewes, 2005). In the case of homogeneous regime, it is generally supposed that bubble coalescence and breakage effect is weak. For this reason, the bubble coalescence and breakage phenomena are not included in our CFD model but the two effects is considered to be balanced so that the bubble diameter varies essentially due to hydrostatic pressure effect and mass transfer.

Fluent offers an option to describes the changes in bubble diameter by solving interfacial area concentration (IAC) equation, which is written as (ANSYS Fluent, 2021c):

$$\frac{\partial(\rho_G a)}{\partial t} + \nabla \cdot (\rho_G \overrightarrow{u_G} a) = \frac{1}{3}\frac{D\rho_G}{Dt} \cdot a + \frac{2}{3}\frac{\dot{m}_G}{\alpha_G} \cdot a + \rho_G (S_{RC} + S_{WE} + S_{TI}) \quad \text{(A.2)}$$

With a the interfacial area ($m^2.m^{-3}$), $\dot{m}_G$ is the mass transfer rate per unit mixture volume ($kg.m^{-3}.s^{-1}$). S_{RC} and S_{WE} are the coalescence sink terms due to random collision and wake entrainment, while S_{TI} is the breakage source term due to turbulent impact. The first two terms on the right-hand side

represents the change of interfacial area due to bubble compression/expansion and the mass transfer term. The coalescence and breakage phenomena are omitted.

This option can be activated in the model-multiphase section, and mean Sauter diameter is used to calculate the interfacial area. The inlet a has to be given at the boundary conditions. In this case, we use $a = \frac{6\varepsilon_G}{d_b} = \frac{6 \cdot 0.02}{0.003} = 40$.

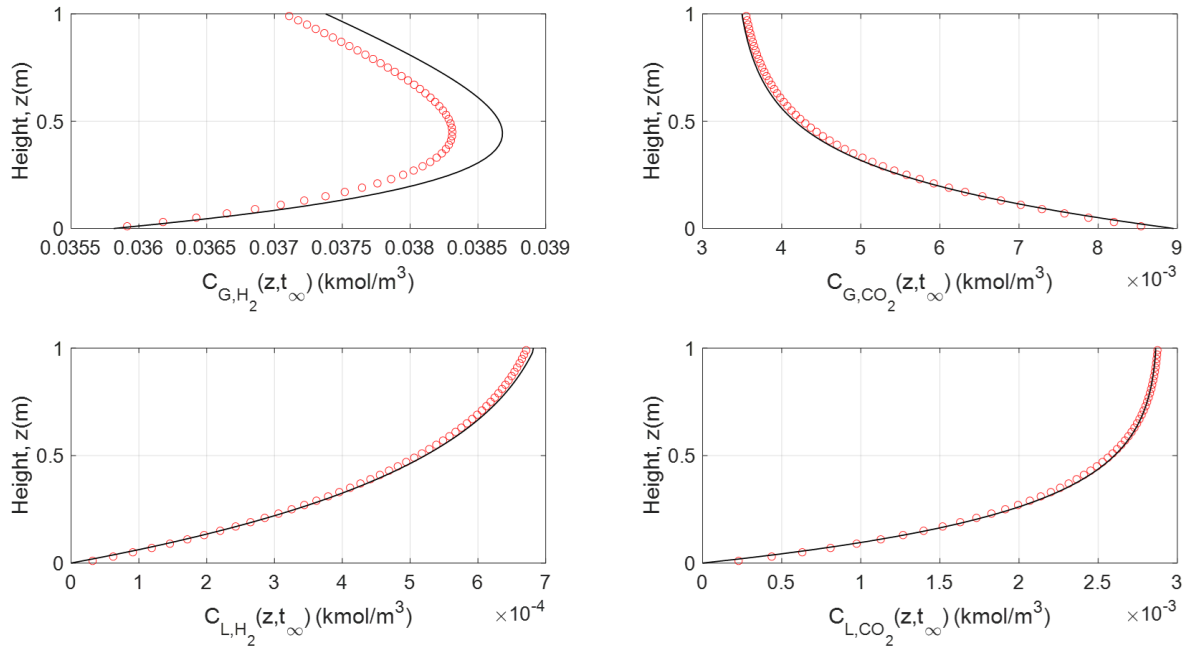

Figure A.7: Species concentrations in the gas and liquid phase with non-constant d_b

The species concentration profiles remain unchanged even with the implementation of IAC model, as shown in Figure A.7. In this small-scale column the mass transfer is not relatively high to observe the impact of two-way coupling, i.e. strong bubble diameter variation which leads to lower bubble velocity, higher gas residence time, higher mass transfer rate and thus, lower concentration profiles.

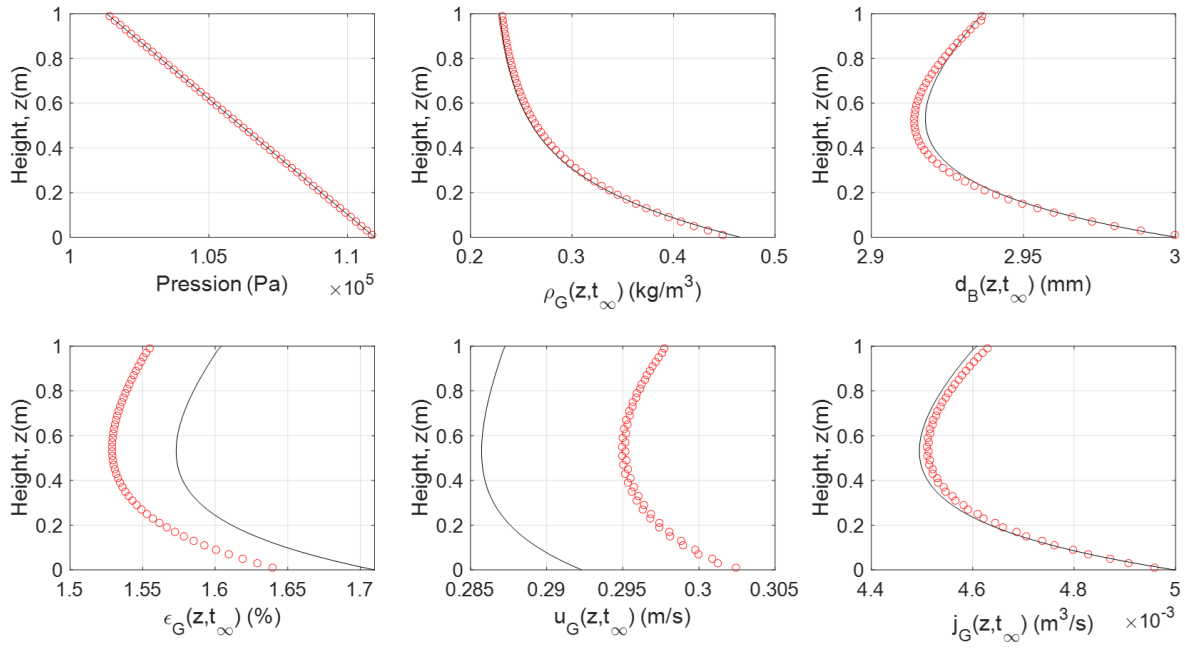

Figure A.8: Hydrodynamic variables at the steady-state with non-constant d_b

Figure A.8 shows that the bubble diameter changes non-linearly due to absorption and volume expansion. However, the changes are very modest at such small-scale bubble column. Nevertheless, the effect of bubble shrinkage due to mass transfer and bubble expansion due to lower hydrostatic pressure at the top column can be observed. Table A.3 shows that the overall MAPE is less than 5% signifying the approach is well implemented in the CFD model.

Table A.3: MAPE between 1D and CFD model with non-constant d_b

C_{G,H_2}	C_{G,CO_2}	C_{L,H_2}	C_{L,CO_2}	P	ρ_G	d_B	ε_G	u_G	j_G
0.78%	2.06%	2.38%	1.42%	0.05%	1.49%	0.09%	3.12%	3.25%	0.36%

1.2.5 Non-constant k_L and non-constant bubble diameter

Lastly, the species transport equations are coupled with the IAC transport equation and Higbie model is applied to the mass transfer term.

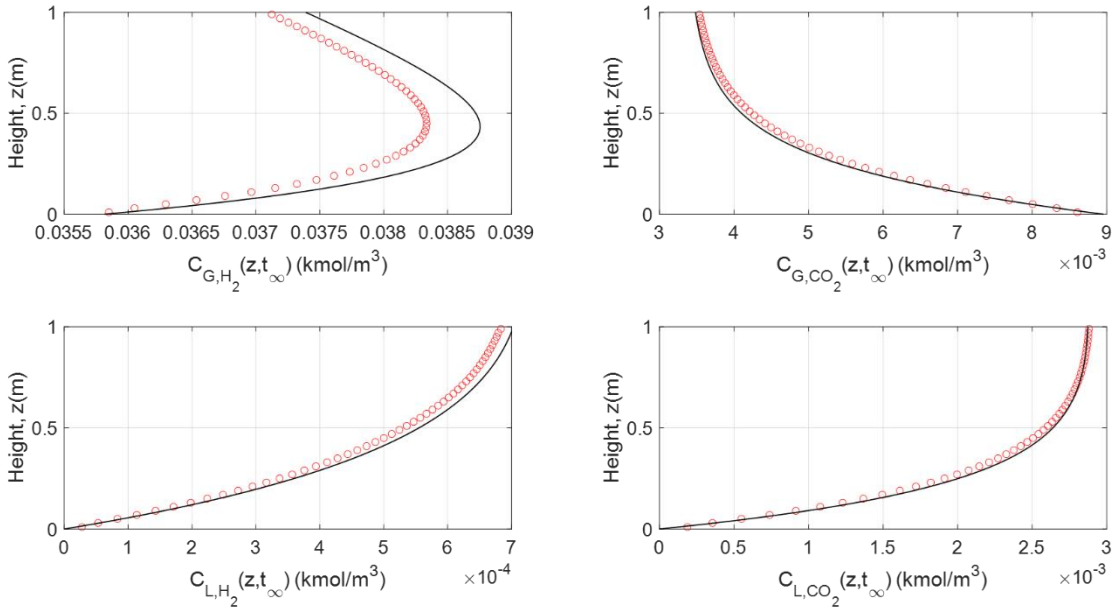

Figure A.9: Species concentrations in the gas and liquid phase with non-constant k_L and d_b

The concentration profiles again remain globally unchanged. The highest difference happens to be H_2 liquid concentration.

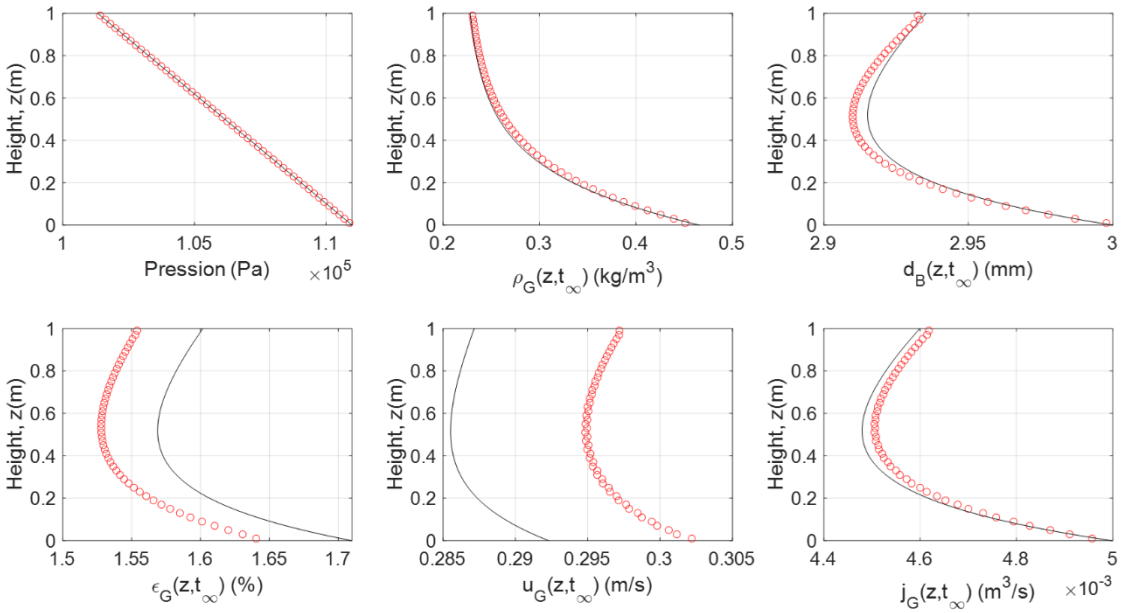

Figure A.10: Hydrodynamic variables at the steady-state with non-constant k_L and d_b

The species transport and mass transfer phenomena with variable bubble size are well captured by the CFD model, and the results resembles that of 1D model with MAPE less than 5%.

Table A.4: MAPE between 1D and CFD model with non-constant k_L and d_b

C_{G,H_2}	C_{G,CO_2}	C_{L,H_2}	C_{L,CO_2}	P	ρ_G	d_B	ε_G	u_G	j_G
0.91%	2.27%	4.19%	1.73%	0.05%	1.64%	0.14%	2.93%	3.23%	0.49%

1.3 Reaction validation

Upon validation of the species transport and mass transfer term, the reaction (source/sink) term is now added to the liquid phase species transport equation. The objective is to implement previously developed biological reaction term (Ngu et al., 2022) into the CFD model. Again, a step-by-step validation is followed. To ensure a better stability in the simulations, the species transport equation and the mass transfer term is first solved for H_2, CO_2 and CH_4. From the converged case, the bioreaction is then activated. The bioreaction is written as an UDF function. The inlet conditions for the gas phase and liquid phase are:

- Phase 1 (Liquid)
  - $Y_{H_2,L}$ = 0
  - $Y_{CO_2,L}$ = 0
  - $Y_{CH_4,L}$ = 0
- Phase 2 (Gas)
  - $Y_{H_2,G}$ = 0.8 (in molar fraction)
  - $Y_{CO_2,G}$ = 0.2 (in molar fraction)
  - $Y_{CH_4,G}$ = 0

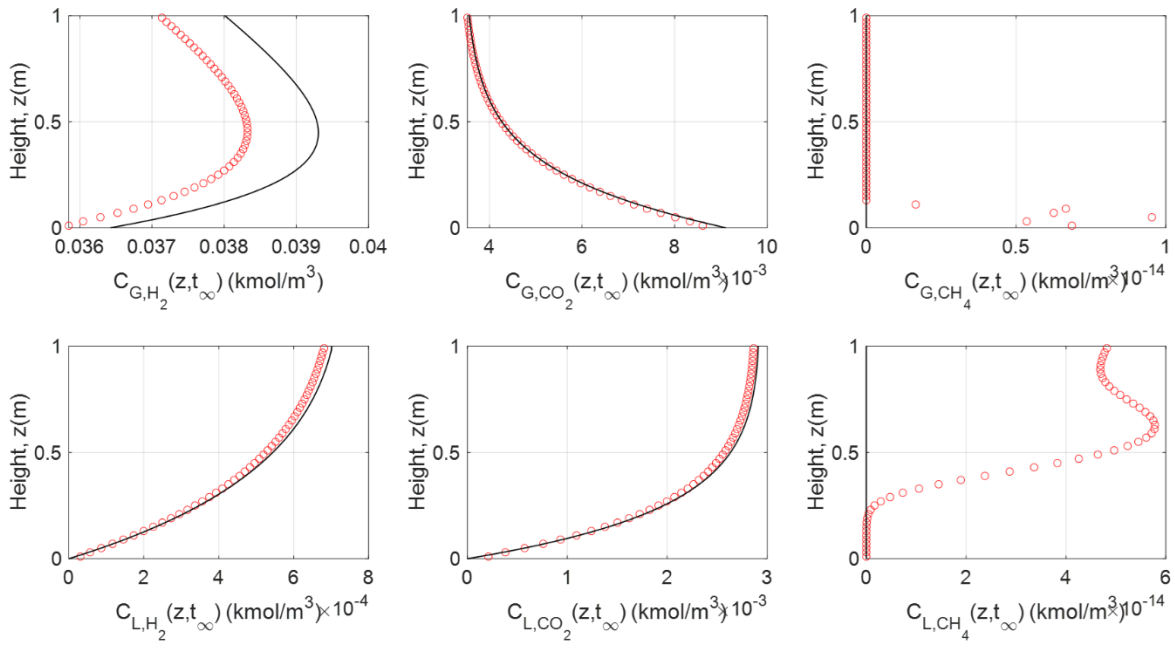

Figure A.11: Species concentrations in the gas and liquid phase with non-constant k_L and d_b

Figure A.11 presents the species concentration profiles. The H_2 and CO_2 profiles remain the same as those in the previous Section. The profile for CH_4 shows some numerical noises but it can be considered as 0. All subsequent test on the reaction term starts from this converged case.

1.3.1 First-order reaction term on H_2 only

The first test case is a first-order type reaction rate defined only on H_2 ($R_{H_2} = -k \cdot C_{H_2}$ with $k = 0.1/0.5$ s^{-1}). This test aims to check if the concentration variable of H_2 (C_{H_2}) for the definition of bioreaction is correctly called by the UDF.

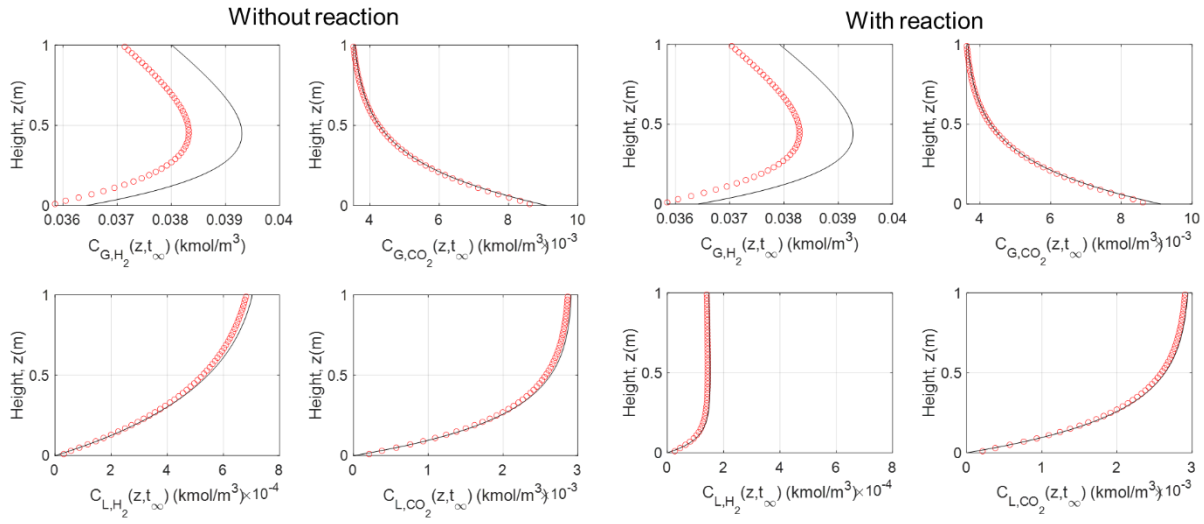

Figure A.12: Species concentrations in the gas and liquid phase with and without reaction

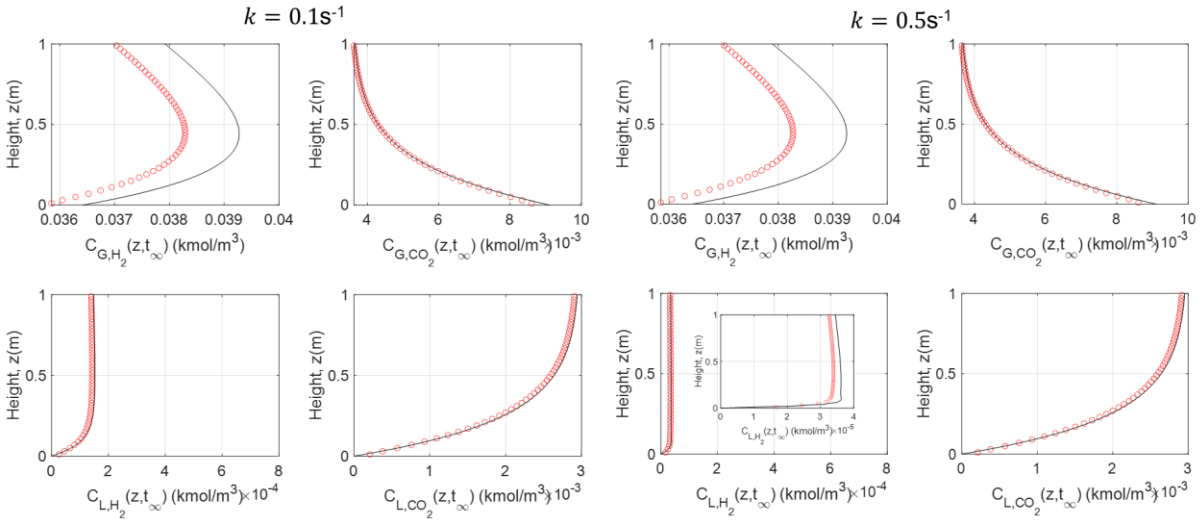

Figure A.13: Species concentrations in the gas and liquid phase with $k = 0.1\ s^{-1}$ and $k = 0.5\ s^{-1}$

Figure A.12 shows that only H_2 liquid concentration drops due to the only active consumption term presents in the equation. The CO_2 profiles remain unchanged as it is an inert species. If the reaction rate constant increases, a higher drop in H_2 liquid concentration is observed, as shown in Figure A.13.

1.3.2 First-order reaction term on H_2 and CO_2 ($k = 0.5\ s^{-1}$)

The next test case extends the reaction term to the CO_2.

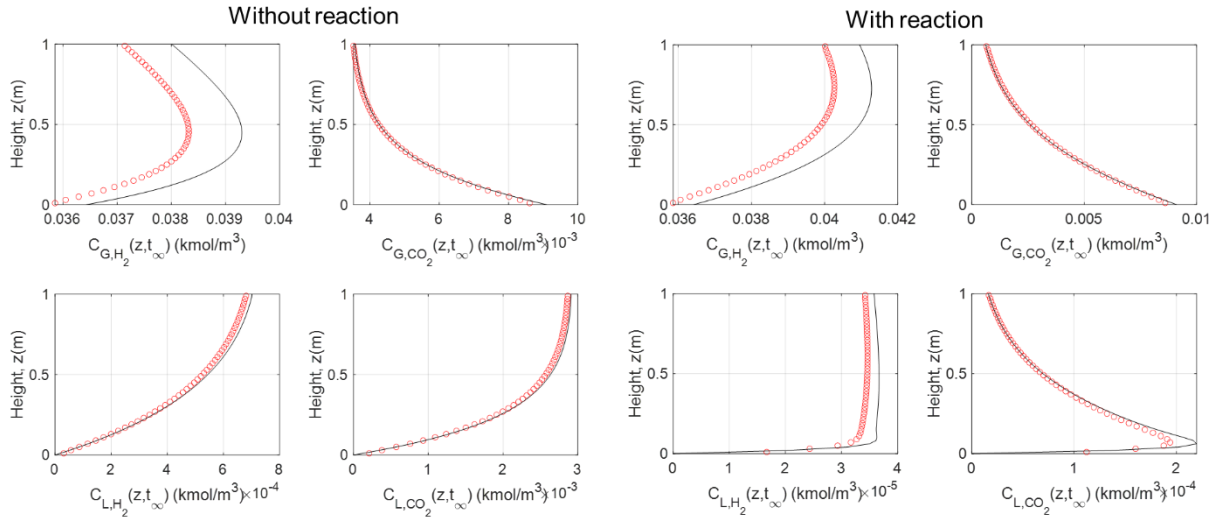

Figure A.14: Species concentrations in the gas and liquid phase with the presence of R_{H_2} and R_{CO_2}

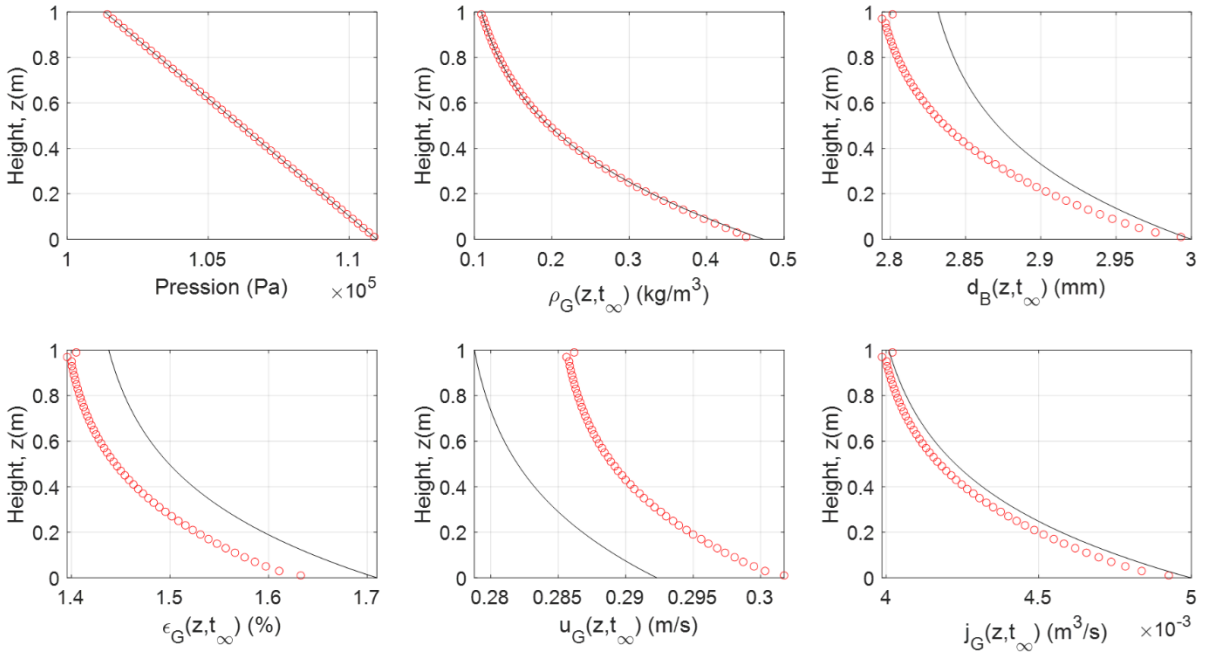

Figure A.15: Hydrodynamic variables at the steady-state with the presence of R_{H_2} and R_{CO_2}

Initially, the concentration of dissolved CO_2 increases due to mass transfer, but decreases subsequently from its peak due to the reaction. The H_2 liquid concentration profile remains unchanged, but the H_2 gas concentration profile increases comparing to the case without CO_2 reaction term. The CO_2 reaction enhance the CO_2 mass transfer which causes the CO_2 gas concentration decreases significantly. In return, it enriches the H_2 concentration in the gas phase. The multispecies mass transfer effect can be observed in this example as the CO_2 reactive mass transfer causes an increase in H_2 gas concentration. Figure A.15 shows the hydrodynamic variables profile when CO_2 reaction is activated. Due to CO_2 reactive mass transfer, the bubble diameter decreases along the axial location. The gas holdup decreases as well due to gas loss experienced during reactive mass transfer.

1.3.3 Second-order Arrhenius type reaction term

The Arrhenius type reaction rate has been used in the context of biological methanation in the work of Markthaler et al. (2020). Fluent offers in-built Arrhenius reaction definition box for users to defined easily the Arrhenius reaction rate. Regarding the overall reaction of $4H_2 + CO_2 \rightarrow CH_4 + H_2O$, the following reaction term for each of the species is considered:

- $R_{H_2} = -4 \cdot k \cdot C_{H_2} \cdot C_{CO_2}$
- $R_{CO_2} = -R_{CH_4} = -k \cdot C_{H_2} \cdot C_{CO_2}$

With $k = k_0 . e^{-\frac{E}{RT}}$. In this test case, arbitrary values of $k_0 = 10^4\ m^3 . kmol^{-1} . s^{-1}$, $E = 10^3\ J . mol^{-1}$, and $T = 300\ K$ is used. The objective for this test case is to validate the implementation of the reaction term in the species transport equation.

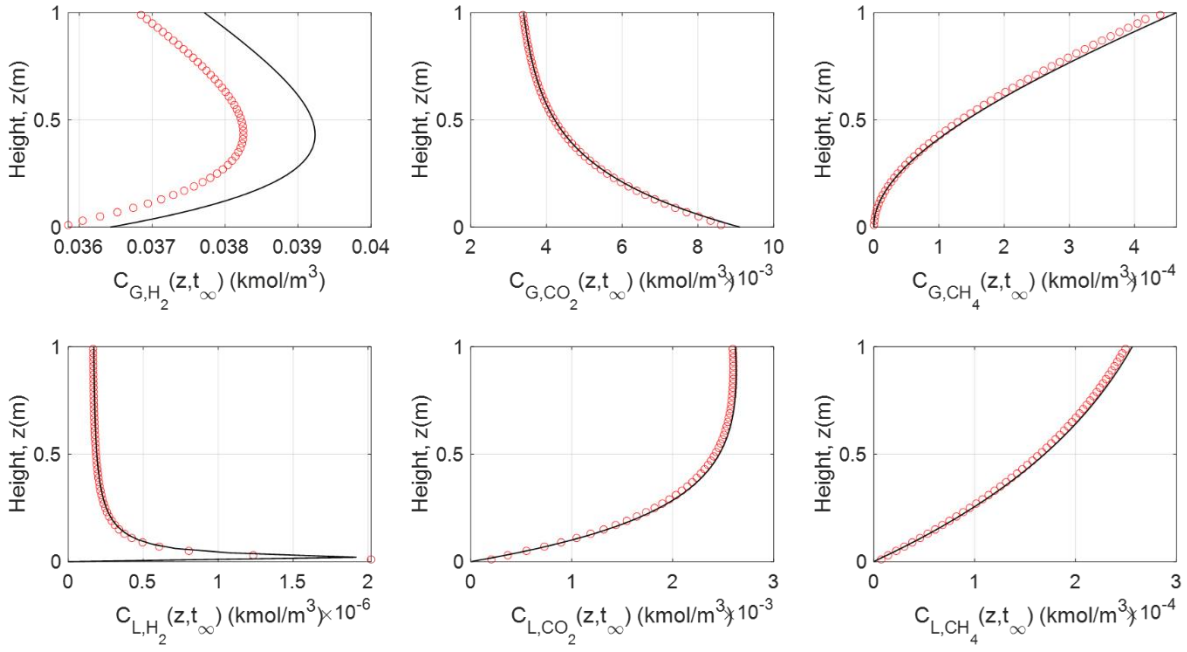

Figure A.16: Species concentrations in the gas and liquid phase with the presence of Arrhenius reaction

Figure A.16 shows that CH_4 is produced as its production term is defined in this test case. The H_2 concentration remains close to zero, signifying that H_2 remains as the limiting species.

1.3.4 Biological methanation with fixed biomass

Now, the validation is extended to the bioreaction as defined in Ngu et al. (2022). The biomass concentration is first set to constant to avoid complexity. To mimic the situation at steady-state whereby the biological methanation is limited by mass transfer, a very high biomass concentration of 35 kg.m^{-3} is applied.

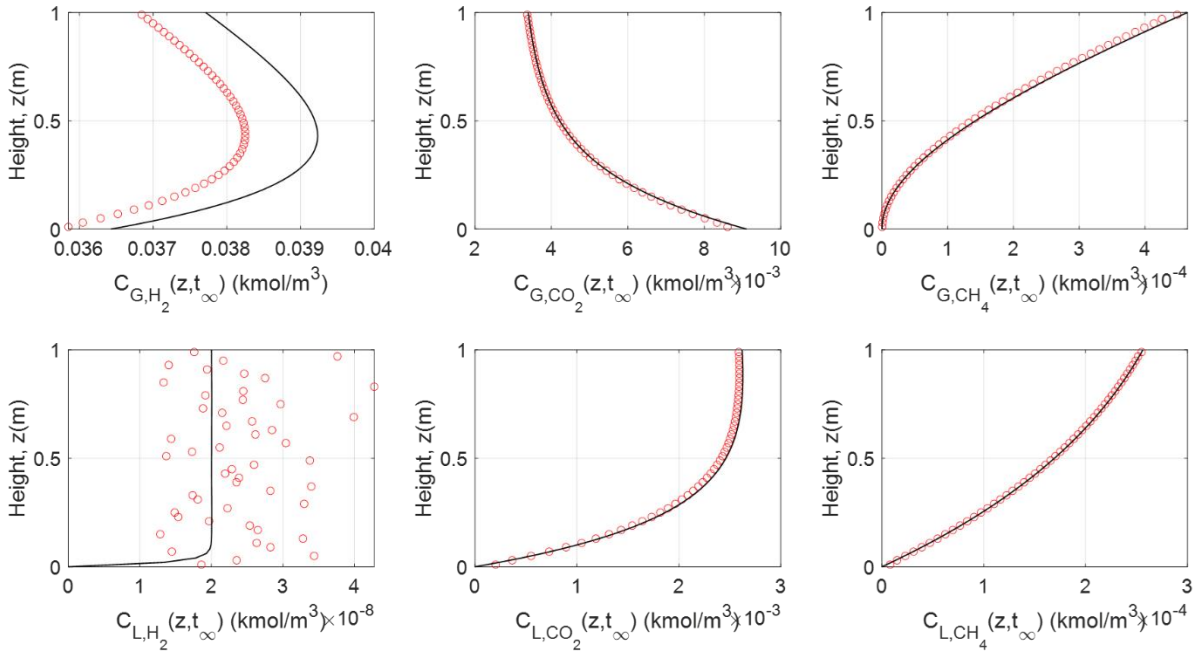

Figure A.17: Species concentrations in the gas and liquid phase during biological methanation with fixed biomass

During steady-state, the H_2 liquid concentration oscillates around values at the order of 10^{-8} kmol.m^{-3}. At this weak concentration, the bioreaction can be considered as limited by H_2 mass transfer. All the concentrations agree with that predicted by the 1D model.

1.3.5 Biological methanation with resolved biomass

For the last test case, the biomass is no longer treated as a constant, but instead a new transport equation of the biomass is now considered.

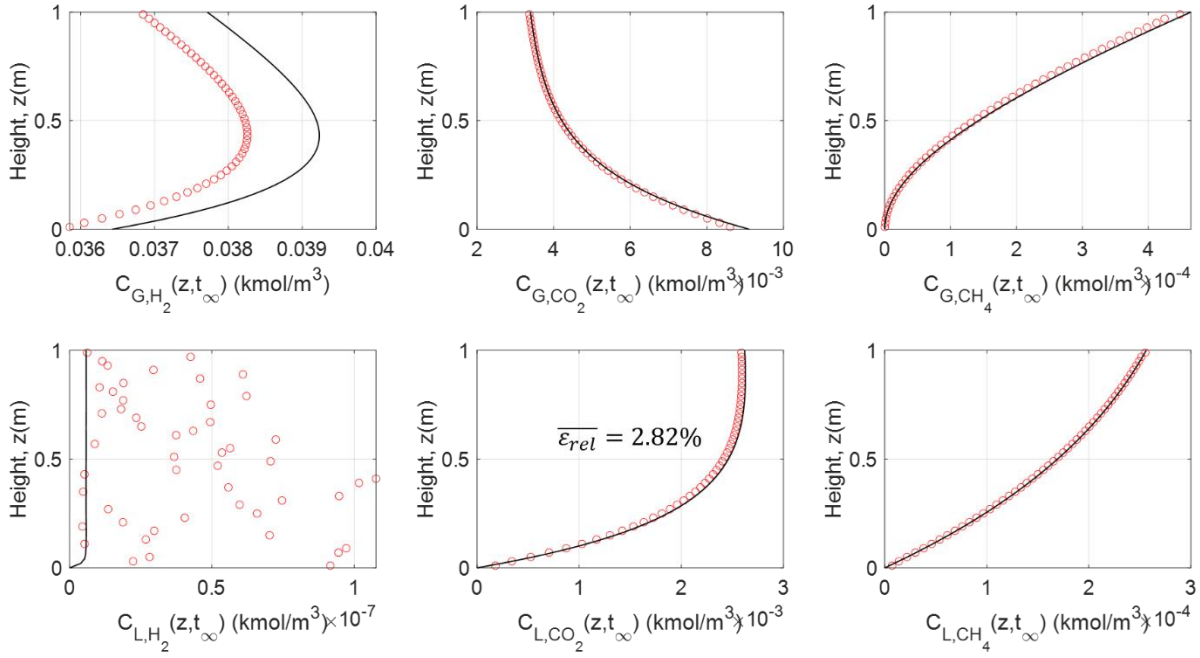

Figure A.18: Species concentrations in the gas and liquid phase during biological methanation

The H_2 concentration still oscillates around very small value but it can be considered as zero concentration.

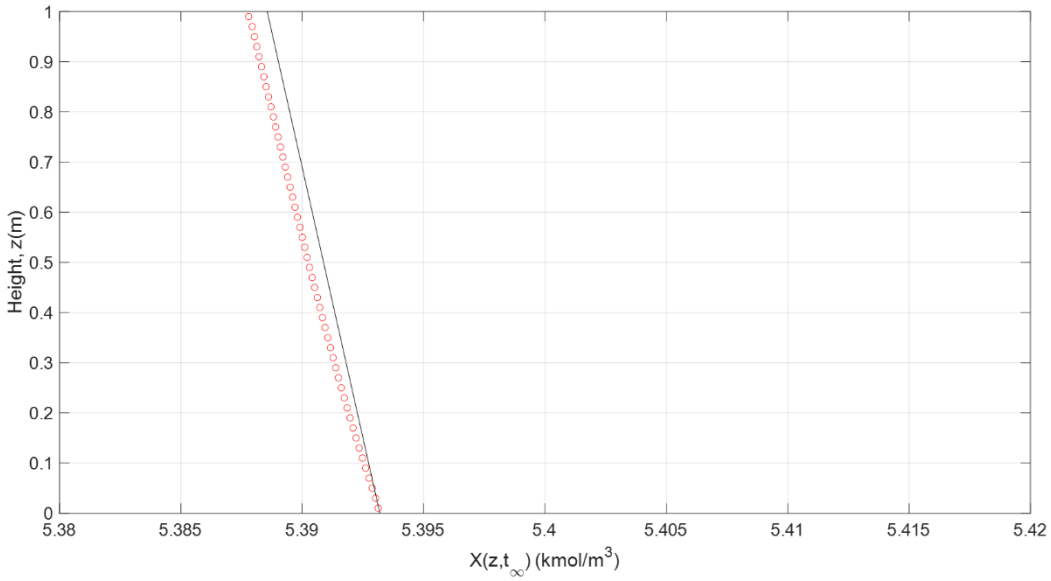

Figure A.19: Biomass concentration profile

In this test case, it seems like the biomass has reached steady-state as the concentration decreases slightly throughout the column. The changes can be considered as negligible.

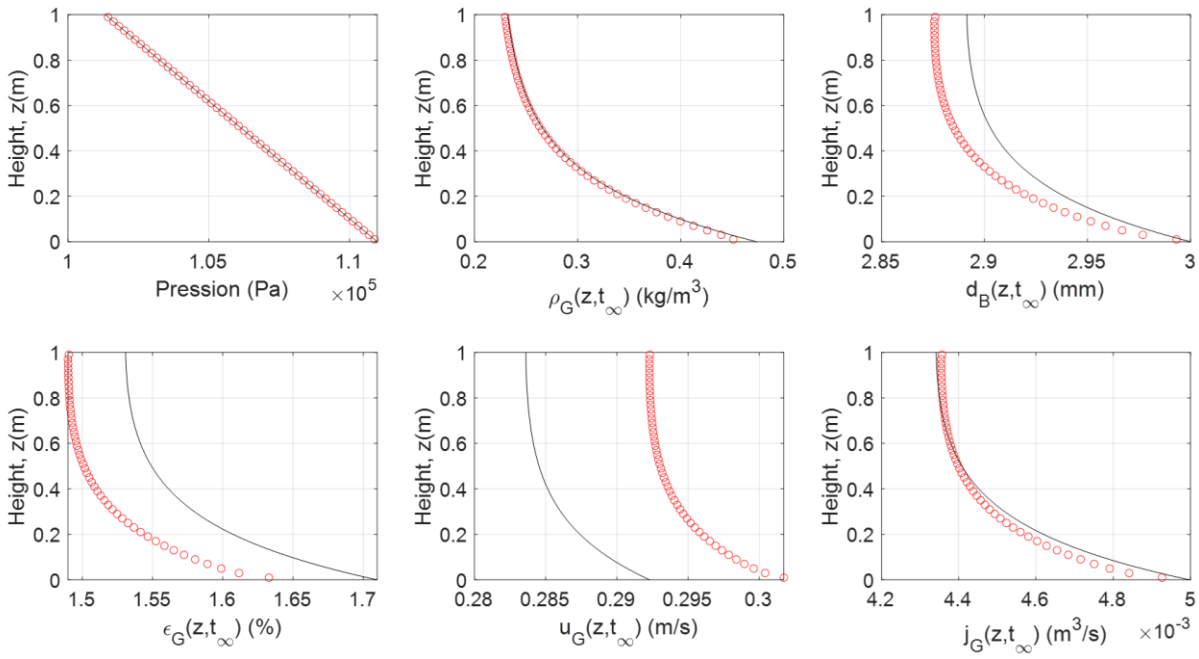

Figure A.20: Hydrodynamic variables

References for this chapter

ANSYS Fluent, 2021a. Fluent Theory Guide, Chapter 18.8. Modeling Species Transport in Multiphase Flows.

ANSYS Fluent, 2021b. Fluent Theory Guide, Chapter 18.7.7. Interphase Species Mass Transfer.

ANSYS Fluent, 2021c. Fluent Theory Guide, Chapter 18.4.11. Interfacial Area Concentration.

Buffo, A., Vanni, M., Marchisio, D.L., 2017. Simulation of a reacting gas–liquid bubbly flow with CFD and PBM: Validation with experiments. Applied Mathematical Modelling 44, 43–60. https://doi.org/10.1016/j.apm.2016.11.010

Gemello, L., Plais, C., Augier, F., Marchisio, D.L., 2019. Population balance modelling of bubble columns under the heterogeneous flow regime. Chemical Engineering Journal 372, 590–604. https://doi.org/10.1016/j.cej.2019.04.109

Higbie, R., 1935. The Rate of Absorption of a Pure Gas into a Still Liquid during Short Periods of Exposure. Trans. AIChE 31, 365–389.

Huang, Q., Yang, C., Yu, G., Mao, Z.-S., 2010. CFD simulation of hydrodynamics and mass transfer in an internal airlift loop reactor using a steady two-fluid model. Chemical Engineering Science 65, 5527–5536. https://doi.org/10.1016/j.ces.2010.07.021

Markthaler, S., Plankenbühler, T., Weidlich, T., Neubert, M., Karl, J., 2020. Numerical simulation of trickle bed reactors for biological methanation. Chemical Engineering Science 226, 115847. https://doi.org/10.1016/j.ces.2020.115847

McClure, D.D., Norris, H., Kavanagh, J.M., Fletcher, D.F., Barton, G.W., 2014. Validation of a Computationally Efficient Computational Fluid Dynamics (CFD) Model for Industrial Bubble Column Bioreactors. Ind. Eng. Chem. Res. 53, 14526–14543. https://doi.org/10.1021/ie501105m

Ngu, V., Morchain, J., Cockx, A., 2022. Spatio-temporal 1D gas–liquid model for biological methanation in lab scale and industrial bubble column. Chemical Engineering Science 251, 117478. https://doi.org/10.1016/j.ces.2022.117478

Rzehak, R., Krepper, E., 2016. Euler-Euler simulation of mass-transfer in bubbly flows. Chemical Engineering Science 155, 459–468. https://doi.org/10.1016/j.ces.2016.08.036

Wang, T., Wang, J., 2007. Numerical simulations of gas–liquid mass transfer in bubble columns with a CFD–PBM coupled model. Chemical Engineering Science, 8th International Conference on Gas-Liquid and Gas-Liquid-Solid Reactor Engineering 62, 7107–7118. https://doi.org/10.1016/j.ces.2007.08.033

Wiemann, D., Mewes, D., 2005. Calculation of flow fields in two and three-phase bubble columns considering mass transfer. Chemical Engineering Science, 7th International Conference on Gas-Liquid and Gas-Liquid-Solid Reactor Engineering 60, 6085–6093. https://doi.org/10.1016/j.ces.2005.04.054